Thermo-mechanical evolution of the subcontinental lithospheric mantle in an extensional environment Insights from the Beni Bousera peridotite massif (Rif belt, Morocco)

Erwin Frets

Thermo-mechanical evolution of the subcontinental lithospheric mantle in an extensional environment

Insights from the Beni Bousera peridotite massif
(Rif belt, Morocco)

Erwin C. FRETS

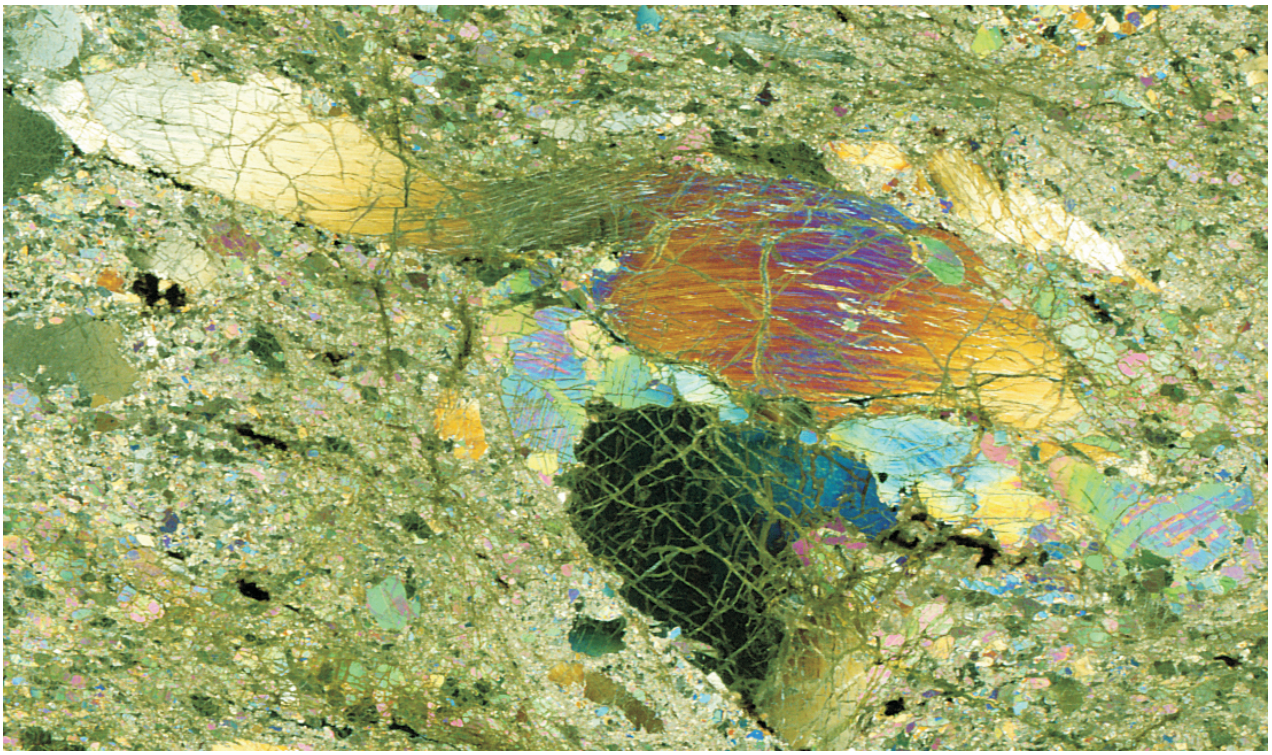

Tesis Doctoral 2012

Universidad de Granada

Instituto Andaluz de Ciencias de la Tierra
Consejo Superior de Investigaciones Científicas – Universidad de Granada
Université de Montpellier 2

THERMO-MECHANICAL EVOLUTION OF THE SUBCONTINENTAL LITHOSPHERIC MANTLE IN AN EXTENSIONAL ENVIRONMENT:

Insights from the Beni Bousera peridotite massif (Rif belt, Morocco)

PhD. Thesis · Tesis Doctoral

Memoria de Tesis Doctoral presentada por el Licenciado en Geología
D. Erwin C. Frets para optar al Grado de Doctor por la Universidad de Granada y de la Université de Montpellier 2.

Granada, septiembre de 2012

Esta Tesis Doctoral ha sido dirigida por el Dr. Carlos Jesús Garrido Marín, Investigador Científico del CSIC, del Instituto Andaluz de Ciencias de la Tierra (CSIC-UGR), y la Dra. Andréa Tommasi, Investigadora Científica del CNRS – Université de Montpellier 2 (Francia)

INSTITUTO ANDALUZ DE CIENCIAS DE LA TIERRA
CONSEJO SUPERIOR DE INVESTIGACIONES CIENTÍFICAS – UNIVERSIDAD DE GREANADA

UNIVERSITE DE MONTPELLIER 2
SCIENCES ET TECHNIQUES DU LANGUEDOC

THESE

Pour obtenir le grade de

DOCTEUR DE L'UNIVERSITE DE GRENADE ET DE L'UNIVERSITE DE MONTPELLIER 2

Discipline: Structure et évolution de la Terre et des autres planètes

Ecole Doctorale : SIBAGHE

Présentée et soutenue publiquement

Par

Erwin C. FRETS

Le 26 Octobre 2012

Thermo-mechanical evolution of the subcontinental lithospheric mantle in an extensional environment. Insights from the Beni Bousera peridotite massif (Rif belt, Morocco)

JURY

György FALUS	Chargé de Recherche (GGIH)	Rapporteur
Laurent JOLIVET	Professeur (Univ. Orléans)	Rapporteur
Fernando GERVILLA	Professeur (Univ. de Granada)	Président
Guillermo BOOTH-REA	Professeur (Univ. de Granada)	Secrétaire
Jean-Louis BODINIER	Directeur de Recherche (UM2)	Examinateur
Vicente LÓPEZ SÁNCHEZ VIZCAÍNO	Professeur (Univ.de Jaén)	Examinateur
Andréa TOMMASI	Directrice de Recherche	Directrice de thèse

El doctorando Erwin C. Frets y los directores de la tesis Carlos J. Garrido y Andréa Tommasi garantizamos, al firmar esta tesis doctoral, que el trabajo ha sido realizado por el doctorando bajo la dirección de los directores de la tesis y hasta donde nuestro conocimiento alcanza, en la realización del trabajo, se han respetado los derechos de otros autores a ser citados, cuando se han utilizado sus resultados o publicaciones.

Granada, de septiembre de 2012

Director/es de la Tesis

Fdo.: Carlos J. Garrido

Fdo.: Andréa Tommasi

Doctorando

Fdo.: Erwin C. Frets

Foreword

From crystal to plate: This thesis in the framework of "Crystal2Plate"

This thesis is part of a larger European Commission "FP 7 - funded Marie Curie Action" research project, named "*Crystal2Plate*[1] – From Crystal Scale Processes to Mantle Convection with Self-Consistent Plates". This Initial Training Network (ITN) is highly collaborative and involves the participation of 7 European institutions that are specialized in different geoscientific specialities:

- ✓ IACT (CSIC – Universidad de Granada) - Granada, Spain. (Petrology)
- ✓ Géosciences Montpellier (CNRS - Université de Montpellier 2) - Montpellier, France (Petrophysics)
- ✓ Earth Sciences Department of ETH - Zürich, Switzerland (Geodynamic Numerical Modeling)
- ✓ Earth Sciences Department of the University of Bristol - Bristol, UK (Seismology)
- ✓ FAST laboratory (CNRS – Université Paris VI) - Orsay, France (Analogue Experimental Modelling, Fluid Mechanics),
- ✓ Universiteit Utrecht - Utrecht, the Netherlands (Seismology)
- ✓ University of "Roma TRE" – Rome, Italy (Analogue Experiments, Geodynamics)

and four industrial partners *Rockfield*, *Schlumberger*, *Total* and *Oxford Instruments*..

The main goal of *Crystal2Plate* is to better constrain global plate tectonics processes by (i) implementing the microscopic-scale physical properties of minerals into global-scale numerical convection simulations and (ii) constrain plate-scale processes such as subduction, delamination, plumes etc. in laboratory experiments. Altogether, *Crystal2Plate*, as already quite straightforward the name itself, aims to combine observations covering a wide range of scales, from the (sub-) crystal (10^{-7} - 10^{-6} m) to the plate (10^{+5} - 10^{+6} m). This thesis forms the linking bridge between these two extremes: in addition to the crystal-scale, it integrates microstructure- (10^{-5} – 10^{-3} m), outcrop- (10^{-2} – 10^{+1} m) and massif-scale (10^{+2} - 10^{+4} m) observations.

From the laboratory to Nature (the Beni Bousera peridotite massif)

Over geological time scales, the mantle may be regarded as a viscous fluid. The mantle is mainly composed of olivine (50 – 100 %) and, hence, the physical laws of mantle rocks that are implemented in numerical models are derived from semi-empirical flow-laws obtained from high pressure and high temperature experiments of deformation of olivine. However, laboratory experiments, although nowadays technologically able to reproduce virtually any Earth-like pressure and temperature condition and even beyond, obviously may not reproduce (and most probably never will) geologically representative time-scales. Hence, although experiments may tell us about the general trends of the physics behind the processes involved, geoscientists have no other option than to over-extrapolate these trends way beyond the page containing them (if not even way beyond the table carrying this page…). Geophysicists and mathematicians that use the laboratory-derived flow laws in global convection simulations thus implement (hopefully consciously) huge uncertainties to predict plate-tectonic behavior. Geologists may add some additional constraints to these delicate extrapolations by sampling the relatively rare pieces of exhumed mantle that can be found at the surface of the Earth. These samples consist either of hand-sized xenoliths brought to the surface by volcanic eruptions, or constitute large bodies of up to several hundred kilometers that were tectonically emplaced within

[1] For a complete description of the project, the reader is referred to the following website: http://www.gm.univ-montp2.fr/CRYSTAL2PLATE/home.html

mountain belts. They represent the only witnesses of mantle deformed under "natural" conditions, i.e. at geological strain rates. The counterpart is that (i) these rocks only sample the shallowest part of the mantle, i.e. the lithospheric mantle (roughly the first 200 km) and are thus poorly representative of the deformation conditions down to the core-mantle transition (ii) these rocks exhibit only the finite state of a wide panel of physical processes (deformation, melting, metasomatism etc.) that they might have experienced during their ascent from mantle depths to the surface. However, *orogenic-type* peridotite massifs, due to their kilometer-scale continuity, form unique natural laboratories in the world to investigate "large"-scale (plurikilometric) mantle processes. This work focuses on the Beni Bousera peridotite massif of northern Morocco. This massif is located in the Rif mountains that outline the Gibraltar arc in northern Morocco. It is 15 km long, 5 km wide, and covers an area of approximately 75 km^2. It has gained some "fame" in the late 1980s when Pearson and co-workers (1989) published the discovery of graphite pseudomorphs after diamond in Beni Bousera garnet pyroxenite (Pearson et al., 1989), which brought evidence for the deep origin (>150km) of these rocks. Understanding how mantle rocks can be exhumed from such depths has profound implications on both our understanding of the rheology of the lithosphere (in particular the lithospheric mantle) and plate- (or "lithosphere-") tectonics as a whole.

Abstract

The mantle deformation processes that control the thinning and break-up of continental lithosphere remain poorly understood. Our knowledge is restricted to either lithospheric scale thermo-mechanical models —that use experimentally derived flow laws—, geophysical imaging and/or rare xenoliths from active continental rifts, such as the East African Rift System. The originality of this work relies on the study of the two largest outcrops of diamond facies subcontinental lithospheric mantle in the world: the Beni Bousera and Ronda peridotite massifs in N Morocco and S Spain, respectively. The structures and petrologic and metamorphic zoning preserved in these massifs —implying a polybaric and polythermal evolution— provides a unique opportunity to investigate the thermo-mechanical evolution of thick subcontinental lithospheric mantle in extensional settings.

In this thesis we studied the deformation mechanisms in both peridotites and pyroxenites to constrain the modes of exhumation of subcontinental lithospheric mantle from garnet-, to spinel-, and finally, to plagioclase lherzolite facies conditions. We combined field mapping of tectono-metamorphic domains and structural mapping of ductile structures, microstructural analysis, crystal preferred orientations (CPO) measurements and conventional thermobarometric calculations and thermodynamic modeling (Perple_X) to unravel the pressure and temperature conditions of deformation. We showed that exhumation from garnet- to spinel lherzolite facies conditions was accommodated by fast shearing —in thermal disequilibrium—along a lithospheric scale transtensional shear zone. In this context, the petrological zoning and the large temperature gradient (ca. 100ºC/km) preserved in the Beni Bousera massif represent the mechanical juxtaposition of progressively deeper and hotter lithospheric levels at depths of ca. 60 km in the latest Oligocene (ca. 25 Ma). Final exhumation from spinel- to plagioclase facies lherzolite and emplacement into the crust is best recorded in the Ronda massif where it occurred by inversion and lithospheric scale folding of the highly attenuated continental lithosphere in a back-arc region, probably in relation with southward slab rollback and subsequent collision with the palaeo-Maghrebien passive margin in the early Miocene (21-23 Ma).

Key Words: Mantle, deformation, microstructures, olivine, pyroxenes, CPO, thermobarometry, Beni Bousera

Resumen

Los procesos de deformación que controlan el adelgazamiento de la litosfera continental no son aún bien comprendidos. Nuestro conocimiento de estos procesos proviene fundamentalmente de la modelización termo-mecánica de la extensión litosférica utilizando leyes reológicas derivadas experimentalmente, de las imágenes geofísicas y del estudio de enclaves profundos de peridotitas que aparecen en el volcanismo en zonas de rifting activo tal y como el Rift del África oriental. La originalidad del presente trabajo reside en la investigación de este proceso mediante el estudio petrológico y estructural de dos de los macizos de peridotitas subcontinentales más extensos que registran condiciones primarias en facies de diamante: los macizos de Beni Bousera (norte de Marruecos) y de Ronda (sur de España). Las estructuras y la zonación petrológica y metamórfica —que implica una evolución polibárica y politérmica— que se preservan en estos macizos ofrecen una oportunidad única para abordar el estudio de la evolución térmica y mecánica del manto subcontinental en un contexto extensional.

En este trabajo hemos investigado los mecanismos de deformación de las peridotitas y piroxenitas con el objeto de averiguar cómo se exhuma el manto subcontinental desde condiciones de facies de lherzolitas con granate, pasando por facies de lherzolitas con espinela y, finalmente, emplazándose en facies de lherzolitas con plagioclasa. Con este objetivo hemos combinado una cartografía detallada de las diferentes facies tectono-metamórficas y estructuras de deformación dúctil con el análisis de microestructuras—medidas mediante la orientación preferente de la red cristalina (OPR)— y geotermobarometría —convencional y mediante la modelización termodinámica de diagramas de facies. Nuestro estudio muestra que la exhumación precoz, desde facies de lherzolitas con granate hasta facies con espinela, tuvo lugar en una falla transtensional de escala litosférica. En este contexto, la zonación tectono-metamórfica y el alto gradiente térmico (ca. 100ºC/km) que se registra en Beni Bousera resultó de la yuxtaposición mecánica de diferente dominios litosféricos —originalmente equilibrados a diferentes profundidades a lo largo de una misma geoterma— a una profundidad de unos 60 km en el Oligoceno superior (ca. 25 Ma). La exhumación final, desde facies de lherzolitas con espinela hasta facies con plagioclasa, y el emplazamiento intracortical de las peridotitas —procesos que sólo se registran en el macizo de Ronda— se produjeron por el plegamiento dúctil y obducción de la sección litosférica fuertemente adelgazada durante la inversión de la cuenca de rifting de trasera de arco. Este evento estuvo ocasionado por colisión de la zona de subducción que se retiraba hacia el sur con el paleomargen magrebí en el Mioceno (21-23 Ma).

Palabras Clave: Manto, deformación, micro-estructuras, olivino, piroxenos, OCP, termobarometría, Beni Bousera

Résumé

Les processus de déformation contrôlant l'amincissement de la lithosphère continentale sont encore mal contraints. Nos connaissances sont principalement basées sur la modélisation thermomécanique d'extension à l'échelle de la lithosphère—utilisant des lois rhéologiques derivées expérimentalement, l'imagerie géophysique et l'analyse de xénolithes provenant de rift continentaux actifs à ce jour, tels que le Rift Est-Africain. L'originalité de ce travail reside dans l'étude des deux plus grands massifs de péridotites sous-continentales ayant enregistrées des conditions primaires du facies à diamant: les massifs de Beni Bousera au nord du Maroc et de Ronda au sud de l'Espagne, respectivement. Les structures et la zonation petrologique et métamorphique —impliquant une évolution polybarique et polythermique— préservéees dans ces massifs offrent une opportunité unique pour étudier l'évolution thermo-mécanique du manteau sous-continental dans un contexte extensif.

Dans ce travail, nous avons étudié les mécanismes de déformation des péridotites et des pyroxénites afin de contraindre les modes d'exhumation du manteau lithosphérique sous-continental, depuis des conditions du facies des lherzolites à grenat, jusqu'au facies à spinelle et enfin à plagioclase. Nous avons combiné la cartographie des faciès tectono-métamorphiques et des structures ductiles de déformation, l'analyse des microstructures, la mesure d'orientations préférentielles de réseau (OPR), et la géothermobarométrie conventionelle couplée à la modélisation thermodynamique (PerpleX) afin de contraindre les conditions de pression et température de la déformation. Nous avons montré que l'exhumation précoce du facies à grenat au facies à spinelle était accomodée par une faille transtensive affectant le manteau lithosphérique. Dans ce contexte, la zonation tectono-métamorphique et le gradient thermique important (ca. 100°C/km) préservés à Beni Bousera résultent de la juxtaposition mécanique de domaines lithosphériques initialement équilibrés à différentes pressions et températures, fossilisée à une profondeur de ca. 60 km durant l'Oligocène supérieur (ca. 25 Ma). L'exhumation finale du facies de lherzolite à spinelle au facies à plagioclase et l'emplacement final dans la croûte, mieux enregistrés dans Ronda, se sont produits par inversion et plissement de la section lithosphérique fortement amincie dans un contexte arrière-arc, probablement lors du retrait vers le sud de la lithosphère subduite et la collision de l'arc avec les paléo-marges maghrébines au Miocène inférieur (21-23 Ma).

Mots clés: Manteau, déformation, microstructures, olivines, pyroxènes, OPR, thermobarométrie, Beni Bousera

Acknowledgements – Agradacemientos – Remerciements

Esta aventura de tres años de aprendizaje, de trabajo y de investigación (en este orden) ha sido para mí una gran aventura humana, que, en primer lugar, ha sido posible gracias a la confianza que **Carlos J. Garrido** (director principal de mi Tesis Doctoral) y **Andréa Tommasi** (codirectora de la Tesis y coordinadora del proyecto *Crystal2Plate*) pusieron en mi candidatura durante la primavera del año 2009.

Carlos, me acuerdo de nuestro primer encuentro en Bruselas: tuve que salir el "gran juego"… Para convencerte durante este entrevista, utilize dos armas de destrucción masiva: medio litro de "*Hoegaerden Grand Cru"* y una "*Westmalle Double*" un día (rarísimo) de sol en la terraza de un bar en un callejón del centro de Bruselas. Las cervezas probablemente te facilitarón hablar con una pasión sobre la increíble geodinámica de Mediterráneo y, a tu manera, me convenciste. Te agradezco por haberme enseñado con gran entusiasmo lo que se hoy de petrología metamorfica y de rocas del manto. Me has abierto los ojos sobre un aspecto de la geología que ahora me apasiona. Tendré siempre buenos recuerdos de los días de campo en Beni Bousera y en Ronda. Las numerosas risas a pesar de las condiciones adversas del trabajo de campo en el Rif, la "cresta de la muerte" con Kaz, Karoly y Zolli, los chipirones acompañados de fino y el "Flying Pig" como postre. Gracias para haber confiando en mi, y echarme una mano cuando era necesario. Las discusiones que te han llevado a que pongas todo tu arte y pasión en los dibujos explicativos, que al final, creo, podrián venderse caros en exposiciones de arte contemporáneo. ¡Me lleve unos ejemplaros preciosos! ¡Gracias!

Andréa, comme Carlos, tu m'as ouvert à un nouveau monde en géologie: celui des "rondelles". Grâce à de nombreuses discussions et la passion qui t'anime, tu as réussi à me donner envie d'avancer dans cette recherche. Lors de mes nombreux stages à Montpellier, j'ai particulièrement apprécié que tu aies pris le temps (et il en fallait!) afin de m'orienter dans mon travail. Tu as toujours su me donner la direction sans m'indiquer le chemin pour autant. Sans cela, ce travail ne serait ce qu'il est aujourd'hui. Je reste admiratif devant ton efficacité, ton insatiable curiosité et ta motivation pour aller au bout des choses, même si cela a fait perler mon front, bien plus que la chaleur estivale du sud de la France. Merci!

Il m'est difficile de parler d'Andrea sans passer naturellement à **Alain**, que je remercie de tout coeur pour avoir eu sa porte ouverte à n'importe quel moment. J'en ai d'ailleurs usé et abusé, mais ce fût un plaisir de retrouver ta zen-attitude pour des discussions pas moins passionnantes, ou ne serait-ce que pour raconter des âneries pour détendre l'atmosphère derrière HKL. J'espère que ce travail animera encore un peu plus le feu des linéations parallèles à la chaîne entre Carlos et toi. Ayant eu les deux sons de cloche, j'en ai beaucoup ri mais surtout appris!

Agradezco a **Fernando Gervilla**, **Guillermo Booth-Rea**, **Gyorgy Falus**, **Jean-Louis Bodinier**, **Vicente López Sánchez-Vizcaíno**, **Antonio Jabaloy** y **Laurent Jolivet** por aceptar formar parte del tribunal de tesis y su interés por mi trabajo.

Le travail de terrain et d'échantillonnage sur lequel est basé ce travail a été rendu possible par la collaboration avec nos collègues marocains: Tout d'abord **Isma Amri** et **Kamal Targuisti**, grâce à leur soutien logistique ainsi que leur accueil chaleureux, ils ont participé au bon déroulement des missions. Je salue aussi mon ami **Hassana** qui m'a fait découvrir un nouveau type de pyroxénites —les "pyroxénites à Smitou"—, **Arbi** de la station essence "ZIZ" et ses excellents tajines de poisson et couscous, dévorés après les dures journées de terrain, et bien sûr **Abslam** et **l'âne** pour avoir allégé nos sacs remplis de cailloux. Shokran bezèf!

El trabajo técnico de calidad de **Chari** y **Miguel** a quienes les lleve decenas de muestras por semana durante mi primer año de Tesis ha contribuido decisivamente a la finalización de este trabajo.

Del IACT agradezco al "Granada Dream Team": **Claudio** —nos fou-rires et sorties à Grenade resteront dans les annales—, **Amel** — pour ta tranquilité et ton humanité—, los "Hungaros" **Zolli** y **Karoly**—"Köszönöm!"—, y la recién llegada **Mari**.

A mis dos amigos y compañeros de bici de montaña, **Sudaka** y **Flavio**: nuestras salidas al campo haciendo "bajadas de la muerte" han contribuido a pensar en algo más que en el trabajo. Pedalear con vosotros en los alrededores de Sierra Nevada fue "una maravilla".

A mis compañeras y compañeros del famosísimo "**despacho 29**" de la Facultad de Ciencias, que fueron mis primeros contactos con "E'paña" y que han hecho posible que el "guiri" se sienta inmediatamente un poco menos "guiri". Os llevo a todos en el corazón.

Debo mucho a **José Alberto** quién también ha contribuido a este trabajo y que me ha enseñado los encantos del PerpleX! Siempre tenías respuesta a mis preguntas, lo que era un poco irritante, y siempre me has acogido con los brazos abiertos ¡Me has ayudado un montón!

Saludo también a los montañeros **Silvia** y **Chema**, y a **Laura** y **David** que guardarón mis cosas en sus casas (¡sin venderlas!), y a todos con los quien fui a tapear y festejar: **Pili**, **Pedroncito** y **Antonio**.

J'ai passé un quart de ma thèse à Montpellier au sein de l'Equipe Manteau et Interfaces, que je remercie, dont notamment **Jean-Louis Bodinier** qui participé à certaines missions de terrain. De l'orchestre instrumental Montpelliérain, j'ai pu bénéficier du professionalisme de: **Fabrice** à l'EBSD, **Claude et Bernard** à la microsonde et **Olivier** au laser.

Je salue bien sûr mes deux compagnons "*C2P*", **Kate** — pour ta British touch — et **Roberto** — che palle!— qui ont tous les deux contribué à mon bien-être culinaire à Montpellier! Un clin d'œil à toute la bande de doctorants de Géosciences Montpellier, et aussi **Mickaël**, **Shantanu** et **Vinc'**, et évidemment **Cédric** —que ce soit autour du stade Philippidès ou d'une bonne Chouffe.

Of course a big "*Cry-stal to Plaaaaaaaaate*!" to the whole **Crystal2Plate** - breed with whom I spent many workshops and congreses and, of course, thanks to **Nathalie** our project coordinator.

Enfin, j'aimerais remercier chaleureusement toute la « petite » **famille Déome** et en particulier **Brigitte** et **Thierry** pour m'avoir toujours si gentiment accueilli lors de mes retours à Bruxelles et pour l'intérêt qu'ils ont porté à l'avancée de cette thèse au cours de ces trois années.

Je remercie de tout cœur **ma famille** qui croît toujours en moi et me soutient quelles que soient les circonstances : **Maman** merci pour ton écoute et tes supers « ondes positives » qui ont toujours traversé l'océan et qui arrivent toujours à bon port ; **Papa**, merci pour les innombrables conseils pratiques que tu m'as donnés avec passion, et qui ont toujours porté leur fruit. **Nouch**, je te remercie d'être là pour moi si j'en ai besoin, et bien sûr j'embrasse **ma petite mamy Lulu** qui m'a apporté réconfort et espoir.

Ma biche, sans toi rien de tout ca n'aurait été possible. En plus de ton amour, tu m'as donné avec la plus grande générosité tout ton respect pour mon choix qui nous a éloignés pendant ces trois années. Tu m'as fait confiance, quotidiennement tu as cru en notre couple et infailliblement tu m'as soutenu. Jour après jour tu m'as conseillé, m'a écouté, en t'oubliant toi-même et en prenant ton mal en patience. Connaissant ta nature impatiente, la signification de ces efforts prend pour moi une dimension que peu seraient amenés à percevoir, et qui révèle ce qui est à mes yeux la plus belle preuve d'amour : le respect. Tu as fait que cette thèse soit la chose la moins importante. Merci.

Erwin C. Frets

Septiembre de 2012

The research leading to these results has been funded by Crystal2Plate, an EU-FP7 Marie Curie Action under grant agreement PITN-GA-2008-215353. We also acknowledge funding from the Spanish "Ministerio de Ciencia e Innovación" Grant CGL2010-14848, Junta de Andalucía research grants RNM-131 and 2009RNM4495, and the International Lithosphere Program (CC4-MEDYNA).

Ter herinnering aan mijn oom, Dr. Dick C. Frets, geoloog.

"I have no dress except the one I wear every day. If you are going to be kind enough to give me one, please let it be practical and dark so that I can put it on afterwards to go to the laboratory."

Marie Curie.

(about a wedding dress)

Part I - Introduction, Aims and Methodology

1. Introduction

1.1. Lithosphere Tectonics

The large quantity of energy that the Earth has accumulated since its accretion, more than 4.5 Gyr ago (Kaula, 1994), by the still ongoing decay of long-lived radioactive isotopes (e.g. Wasserburg et al., 1964) and due to its potential (gravitational) energy is mainly converted into heat. Heat dissipation at the surface occurs through long-wave radiation into space (Davies, 1980; Pollack et al., 1993) and transformation into potential energy such as tidal dissipation (Platzman, 1984). The large temperatures prevailing in the Earth mantle (T~600-700°C at 35 km depth, T~2500-3500°C at 2900 km at the core-mante boundary) associated with relatively small strain rates (10^{-11} – 10^{-14} s^{-1}) enable the ductile deformation of minerals. This mechanical behavior together with the large temperature gradient between the lowermost mantle and the surface enable heat transport by convection. The strong temperature dependence of the viscosity in the mantle results, however, in development of an upper boundary layer, where heat is mainly transferred by conduction. This colder and hence stiffer layer defines the "lithosphere". The coupling between large-scale convection currents in the deeper mantle induces the fragmentation of the lithosphere into plates (Fig. 1-1). Subducted lithospheric plates form the cold downwellings of this complex convective system, whereas mantle plumes form the upwellings.

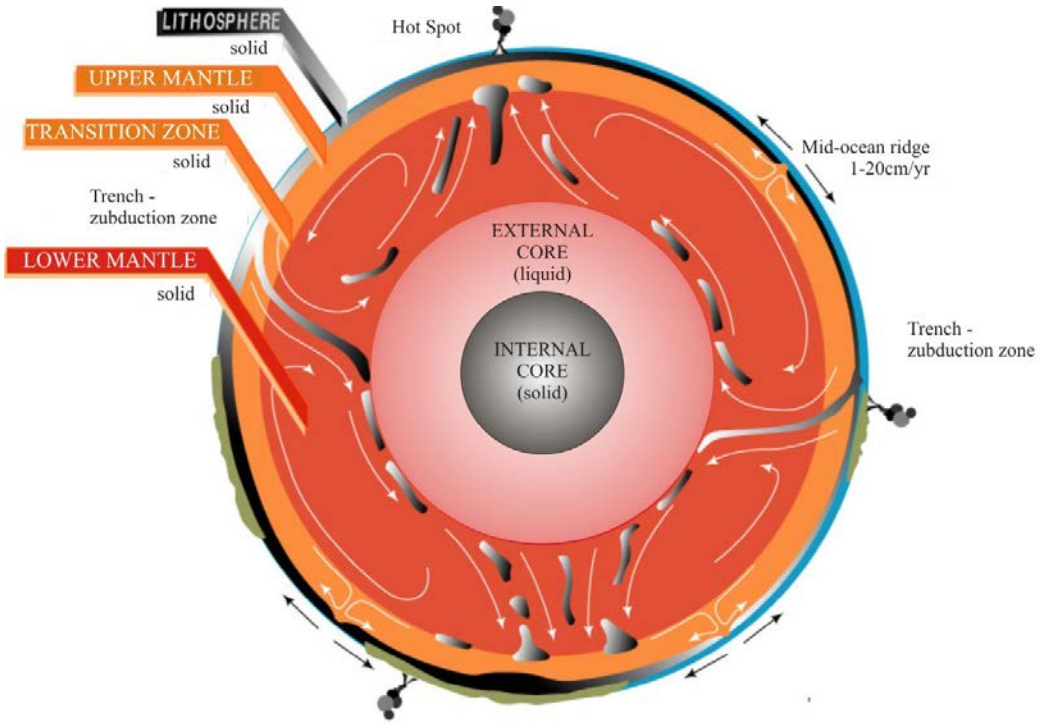

Figure 1-1. Cartoon illustrating the internal structure of the Earth and mantle convection generating lithosphere tectonics

The interaction between lithospheric plates expresses itself at the near-surface in the form of seismic and volcanic activity and has a major impact on human societies worldwide (Fig 1-2a,b). Most of the deformation of lithospheric plates occurs at their margins, supporting the idea of their mechanical rigidity. Active plate margins may be subdivided into 3 endmembers: divergent, convergent and strike-slip (transcurrent) boundaries (Isacks et al., 1968).

Convergent margins are characterized by thousand kilometers long volcanic provinces, like the Andean Cordillera, and by mountain belts, like the Alpine-Himalayan belt, (Fig. 1-2a, c). They are classically divided into "subduction" at ocean-continent (e.g. circum-Pacific subduction belt) and ocean-ocean boundaries (e.g. Antilles), or continental collision boundaries (e.g. Dewey & Bird, 1970; Ernst, 2005). Continental collision subsequent to oceanic subduction marks the end of a Wilson cycle (Wilson, 1966) due to the smaller buoyancy of continental crust that inhibits further subduction (McKenzie, 1969; Dewey & Bird, 1970; see historical review by Schellart & Rawlinson, 2010).

Except transform faults at mid-ocean ridges, strike-slip plate boundaries are rather rare and comprise the San Andreas Fault, the Anatolian Fault, the Alpine Fault in New-Zealand, the boundary between S-American and Caribbean plates among few others.

Divergent boundaries also form thousand kilometer long topographic features, such as mid-ocean ridges and continental rifts (Fig. 1-2a,c). Recent continental rifts comprise the Baikal Rift in Mongolia, the Rio Grande Rift in North America, the East-African rift, the North-east China rift or the Rhine graben in Europe. Fossil rifts include the East Brazilian and West-African rifts formed during the opening of the Atlantic more than 150 Myr ago (see Vauchez et al., 1997).

Continental break-up through rifting may, in favorable cases, lead to the opening of a new ocean and thus constitutes a major tectonic process, not only on Earth but also on other planets. Indeed, recently, image analyses of Mars revealed the presence of thousand kilometer-long linear topographic depressions interpreted as palaeo-rifts (Hauber et al., 2010).

On Earth, however, it remains unclear how thick, stable continental lithosphere may break up. Indeed, laboratory based flow laws extrapolated to natural conditions (Evans & Goetze, 1979) suggest that plate tectonic forces do not suffice to break-up an initially 100 km thick lithosphere (Brace & Köhlstedt, 1980). With the development of numerical techniques and enhanced computing capacities, geoscientists have gained increasing insight in the physical mechanisms controlling the distribution of the deformation in extensional settings (e.g. Huismans & Beaumont, 2003, 2007, 2008; Lavier & Manatschal, 2006; Buck, 2007 and references therein). These models together with many studies of deformation processes in exhumed crustal rocks allowed a better understanding of the physical mechanisms behind the deformation of the crust in the extensional regime (e.g. Handy, 2007; and references therein). However, the rarity of naturally deformed lithospheric mantle samples (xenoliths, peridotite massifs) at the surface has hindered the study of the deformation mechanisms allowing for extension and thinning of the subcontinental lithospheric mantle.

This work attempts to bring new constraints into the natural processes that allow subcontinental mantle to be thinned and exhumed in extensional settings. We gathered new structural and petrological data from the Beni Bousera massif in N Morocco, composed of a ~ 2 km-thick lithopheric section that outcrops over an area of approximately 75 km^2: We performed structural and petrological mapping, microstructural and crystal preferred orientations analyses, mineral and whole rock chemistry in order to perform thermobarometric calculations. These data allows unravelling the P-T-deformation history of both peridotites and pyroxenites. We couple these data with the analysis of the kinematics markers at the scale of the whole massif to build a dynamical model of the evolution of this mantle section.

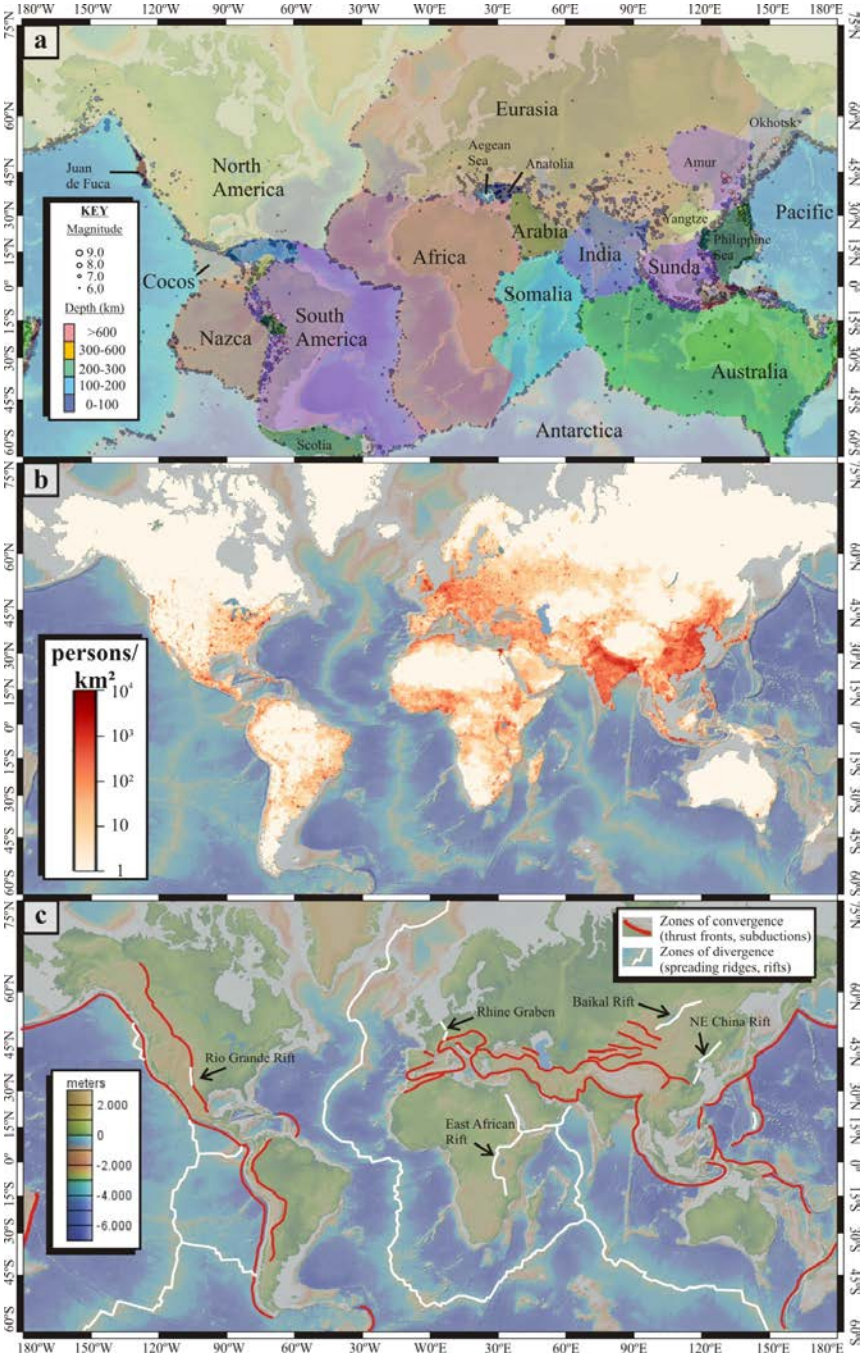

Figure 1-2. (a) Distribution of seismicity on Earth and plates (Bird, 2003). (b) Human population density on Earth. (c) Major divergent and convergent margins. Maps constructed with GeoMapApp.

1.2. Strength of the lithosphere

Before considering the evolution of a strained lithosphere, it is necessary to introduce some basic principles of rheology and the concept of lithospheric strength, on which rely most numerical models of lithospheric deformation.

1.2.1. Basic principles of rheology

The rheology describes the macroscopic behavior of continuum materials (liquids *and* solids) by constitutive (or rheological) equations that relate stress and strain (or deformation) and their time-derivatives (generally strain rate). Although the variety of materials is nearly infinite, 3 main behaviors exist: elastic, plastic and viscous.

A linear proportional relationship between stress (σ) and strain (ε) characterizes an **elastic** rheology, independent of strain rate ($\dot{\varepsilon}$), comparable to a Hooke's law for a spring:

$$\sigma = k \,.\, \varepsilon$$

where k is the elastic modulus, characteristic of the material, comparable to the Hooke's constant for a spring. In theory, this also implies complete recovery of strain when stress is released. For solids, elastic behavior applies mainly in the case of small finite strains. The elasticity of minerals is responsible for the propagation of waves through the Earth. For most minerals such as olivine, elasticity is an anisotropic property (Kumazawa and Anderson, 1969), described by a 4th rank elastic tensor.

Plastic materials generally show an elastic response up to a critical applied stress or "yield" stress (for $\sigma \leq \sigma_{el}$) above which strain is irreversible. For a perfectly plastic solid, the stress never exceeds the yield stress, as any increase in stress is instantaneously relaxed by strain. When stresses are released, in contrast to elastic rheology, no recovery of deformation occurs. Brittle failure for instance is a form of plastic deformation. Solids like crystals deformed at high homologous temperatures (i.e. for $T > 0.3\, T_m$) show an elastic response up to a certain stress (called the *critical resolved shear stress)* before behaving in a plastic manner (e.g. Poirier, 1985, 1995).

Any material that flows is said to be **viscous**, and its ability to flow is inversely correlated to its viscosity. Theoretically, an ideal solid has an infinite viscosity and does not flow, but in Nature, solids have very large (but not infinite) viscosities (conventionally $\mu_{solid} \geq 10^{14} Pa.s$, by comparison $\mu_{water} \approx 10^{-3} Pa.s$). Hence, when considered over large (geological) time scales, even solid rocks do flow.

A viscous rheology is characterized by the dependence between stress (σ) and strain rate ($\dot{\varepsilon}$) in the form of:

$$\sigma = k \,.\, \dot{\varepsilon}^{(1/n)}$$

where n is the stress exponent, characteristic of the deformation process used to accommodate strain.

For the particular case of $n = 1$, we obtain the constitutive equation for a *"Newtonian"* fluid:

$$\sigma = k \,.\, \dot{\varepsilon}$$

For most coarse-grained minerals and rocks, however, strain rate increases faster than stress, typical of a *"non-Newtonian", "non-linear" or "power-law"* viscous rheology. In this case $n > 1$, and is generally comprised in the interval $1 \leq n \leq 5$.

Depending on the time-scale considered, more complex stress-strain and stress-strain rate relations describe composite rheological behaviors, such as visco-elastic or visco-plastic. A solid, for instance, may show an elastic response over short time-scales but behave in a viscous manner at longer time scales. Visco-plasticity is also relevant in geosciences and characterizes geological materials such as quick clay (e.g. Pusch, 1970) or partially crystallized magma containing relatively high amounts of crystals (e.g. Féménias et al., 2004).

However, these macroscopic rheological behaviors, although dependent from them, do not carry full information on the *physical* processes of deformation, which occur essentially at the crystals scale. In the next sections we will recall the ductile (and hence plastic) deformation mechanisms relevant for mantle rocks deformed under lithospheric mantle conditions.

1.2.2. Ductile deformation processes under lithospheric mantle conditions

Experimental deformation and theoretical works have shown that the rheology of rocks, metals and ceramics deformed at high homologous temperatures may be described by a power-law creep in the general form of:

$$\dot{\varepsilon} = A\sigma^n d^{-p} f H_2O^r \exp(\alpha\phi) \exp\left(-\frac{E^* + PV^*}{RT}\right)$$

Where A is a constant, n is the stress exponent, d is grain size, p is the grain size exponent, fH_2O is the water fugacity, r is the water fugacity exponent, ϕ is melt fraction, α is a constant, E^* is the activation energy, V^* is the activation volume, R is the gas constant and T is absolute temperature (Hirth & Köhlstedt, 2003).

Depending on deformation conditions, high temperature ductile deformation of rocks may involve several processes, such as dislocation creep, dynamic recrystallization, diffusion creep and grain boundary sliding.

In the following, we briefly review these mechanisms that will be extensively discussed in the case of Beni Bousera peridotites and pyroxenites in chapters 4 and 5

1.2.2.1. - Dislocation glide

1.2.2.1.a) Mechanisms and terminology

One way a crystal may accommodate deformation under a given applied stre is by glide on specific planes in the lattice of the crystal (Fig. 1-3 for quartz for incremental strain).

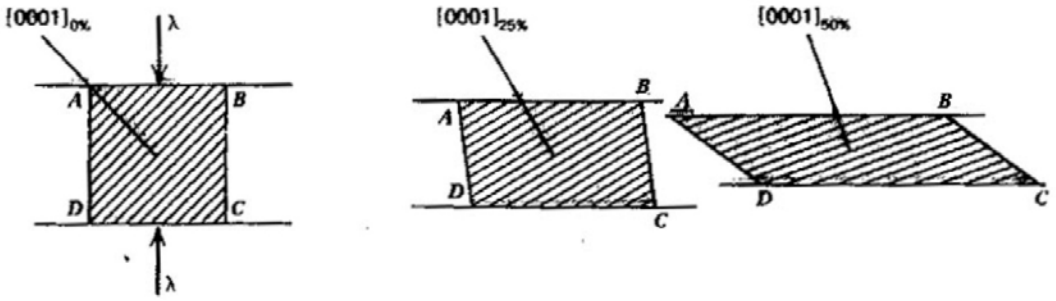

Figure 1-3. Cartoon illustrating the crystal preferred orientation of quartz. The [0001] axis progressively rotates towards 90º to the foliation with increasing strain. (A. Vauchez, pers. Comm.)

This movement occurs by translation of lattice imperfections or dislocations (Fig. 1-4). The slip direction in this plane is called the *Burgers vector* and depending on whether the slip direction is perpendicular or parallel to the dislocation line, we speak of an "*edge*" or a "*screw*" dislocation, respectively.

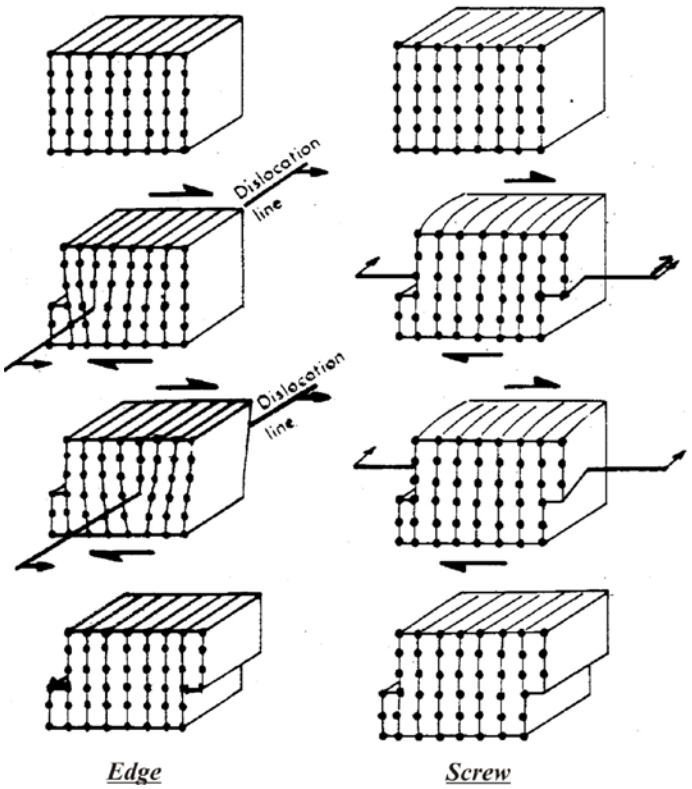

Figure 1-4. Cartoon illustrating the movement of dislocations in a lattice submitted to simple shear. Burgers vectors parallel and perpendicular to shear direction define edge and screw dislocations, respectively.

When the system gets locked due to accumulation of dislocations for instance, a jump to another slip plane may occur to resolve the shear stress. This type of recovery process is called *dislocation climb* in the case of edge dislocations, and *cross-slip* in the case of screw dislocations. Recovery by dislocation climb or cross-slip implies the migration of a lattice defect by diffusion (see next section). It is worth noticing that the term *dislocation creep* involves the association of dislocation glide, recovery and dynamic recrystallization (see next sections).

A slip *system* of a mineral is characterized by one or several slip planes and directions and the magnitude of the associated Burgers vector (Lister, 1974). The planes that can be activated depend on the crystal symmetry (cubic, hexagonal, trigonal, tetragonal, orthorhombic, monoclinic and triclinic), as exemplified in Fig. 1-5 for olivine (orthorhombic) and clinopyroxene (monoclinic).

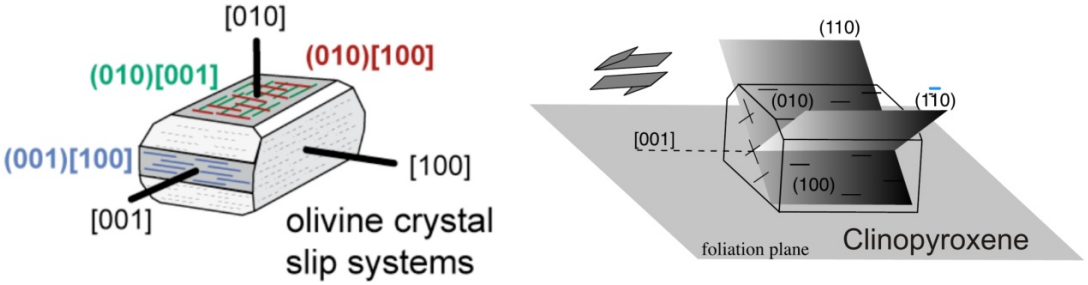

Figure 1-5. Olivine and clinopyroxene slip systems.

Each slip system in a given mineral has a different critical resolved shear stress ("*crss*"), which represents the resistance for a dislocation to glide in this direction and plane. Therefore, the slip system(s) that will accommodate the largest part of the deformation will be the one for which the *crss* is the smallest at given conditions (e.g. Fig. 1-5 for olivine; Bai et al., 1991). For instance, for olivine crystals at 1250°C and 300MPa confining pressure, strain rates may vary by 2 orders of magnitude depending on the orientation of the crystal with respect to the direction of compression (Durham et al., 1977; Bai et al., 1991). In these conditions, for olivine, slip on [100](010) and on [100](001) are thus easier than on [001](010).

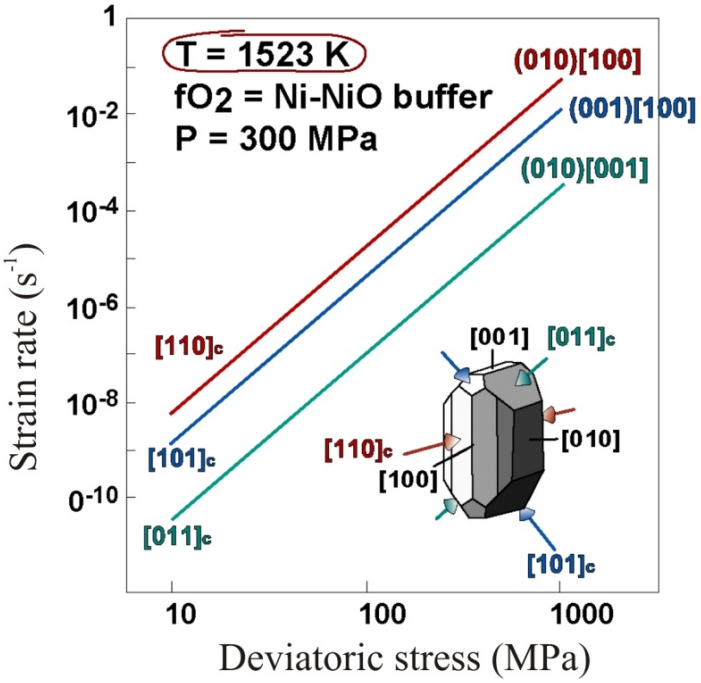

Figure 1-5. Strength of olivine slip systems at 1250ºC (Bai et al., 1991). {0kl}[100] are the easiest slips under these conditions.

However, the relative strength of the slip systems varies in function of extrinsic parameters such as stress and temperature (Fig. 1-6; Duram & Goetze, 1977 for olivine), but also water

contents (Chopra & Paterson, 1984; Mackwell et al., 1985), pressure (Couvy et al., 2004; Mainprice et al., 2005; Raterron et al., 2007, 2009, 2011, 2012) or the presence of melt at the scale of the aggregate (e.g. Beeman & Kohlstedt, 1993; Holtzman et al., 2003).

For olivine, for instance, at decreasing temperature and under laboratory strain rates, slip on [001]{hk0} may result easier (*crss* smaller) than slip on [100](0kl) (Durham & Goetze, 1977), the latter being the most commonly observed slip system in naturally deformed peridotites (e.g. Nicolas & Poirier, 1976).

Lithostatic pressure may also play a role, albeit pressures are usually only relevant for the deep mantle or extremely thick lithosphere underneath cratons. For instance, experiments suggest that for olivine the transition from [100](010) to [001](010) slip occurs at $p > 7\ GPa$ (Couvy et al., 2004; Mainprice et al., 2005; Raterron et al., 2007, 2009, 2011, 2012). The physical effect of pressure on the slip systems is its influence on the activation volume.

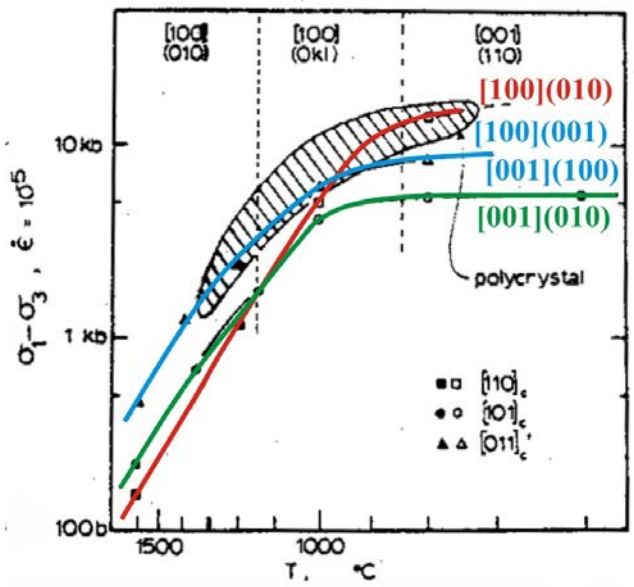

Figure 1-6. Strength of olivine slip systems in function of temperature and stress (Durham et al., 1977). Note the inversion towards [001]{hk0} slip below ca. 1000ºC.

Experiments have shown that the presence of melt tends to align olivine [100]-axes perpendicular to the shear direction (Holtzman et al., 2003), due to strain partitioning between melt rich and melt poor domains in simple shear. Field studies consistent with these experiments have been reported in the Oman ophiolite (Higgie & Tommasi, submitted).

1.2.2.1.b) CPO development

Depending on the activated slip systems, and hence deformation conditions (see above), crystallographic axes align preferentially with respect to the macroscopic shear plane (XY) and direction (X). Most observations on naturally deformed peridotites show alignment of olivine [100] subparallel to the shear direction with [010] - axes at high angle or in a girdle perpendicular to the macroscopic shear plane. Fig. 1-7 shows the main types of olivine CPO encountered in naturally deformed peridotites, i.e. (A) orthorhombic, (B) axial-(100) and (C) axial (010) patterns (Ben Ismaïl & Mainprice, 1998; Tommasi et al., 2000).

Transmission electron microscopy observations on experimentally deformed single-crystals and peridotites under lithospheric mantle conditions indicate dominant deformation essentially by dislocation creep accommodated on [100](0kl) slip systems (Phakey et al., 1972; Durham & Goetze, 1977; Durham et al., 1977; Doukhan et al., 1984; Bai et al., 1991; Bai & Köhlstedt, 1992; Jung et al., 2006; Demouchy et al., 2009), consistent with the observed CPO (A), (B) and (C) in Fig. 1-7. In (C), the dispersion of (100)-axes is either related to transpression (Tommasi et al., 1999) or simultaneous activation of [001]{hk0} slip systems.

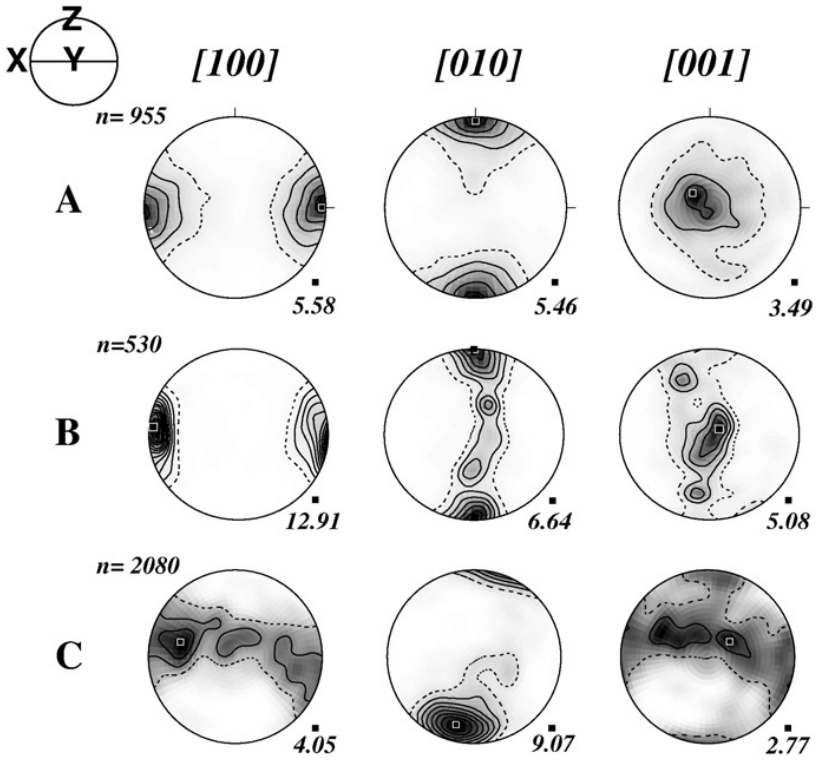

Figure 1-7. The three most frequent crystallographic preferred orientation (CPO) of olivine in peridotites. (A) orthorhombic symmetry CPO characterized by three point maxima for [100], [010] and [001], this CPO results from dominant activation of the (010)[100] slip system. (B) [100]-fiber or [100]-axial symmetry CPO, characterized by a point maximum concentration for the [100]-axes and a dispersion of the [010]- and [001]-axes in a girdle with a [100] symmetry axis; this CPO results fromthe activation ofmultiple (0kl)[100] slip systems. (C) [010]-fiber or [010]-axial symmetry CPO with a point concentration of the [010]-axes and the [100]- and [001]-axes dispersed in a girdle with a [010] symmetry axes; this CPO results either fromsimultaneous activation of the [100] and [001] slip directions or fromtranspressional deformation. n is the number of measurements, XYZ are the main finite strain axes. The filled square and the value attached indicate the maximum concentration for each axis (Vauchez et al., 2012).

The effect of the amount of strain on the evolution of the CPO has been experimentally tested by Bystricky et al. (2000), and is shown in Fig. 1-8. Interestingly, a weak, but well developed

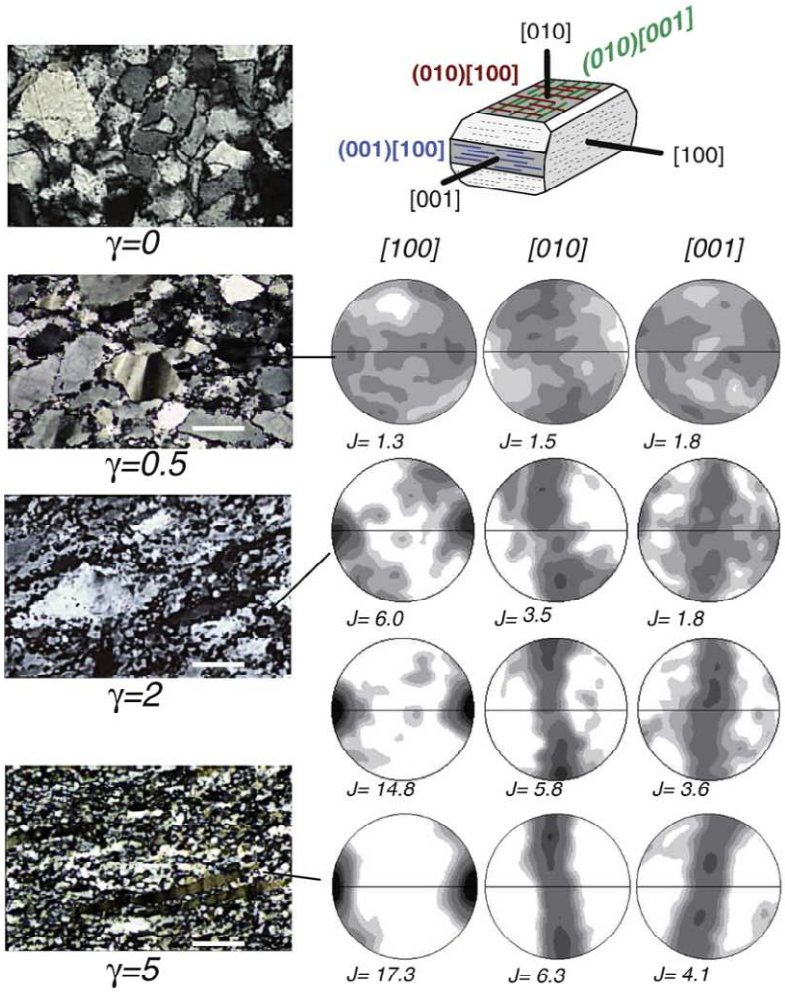

Figure 1-8. Progressive evolution of the microstructure and texture (CPO) with increasing strain during torsion experiments on olivine aggregates (Bystricky et al., 2000) deformed at 6.3×10^{-5} s^{-1}, 1200 °C, 300 MPa confining pressure and oxygen fugacity near the Fe/FeO buffer (10^{-7} Pa). Shear sense is dextral, γ is the shear strain and the initial grain size is ~20 μm. The microstructure shows progressive stretching of crystals then dynamic recrystallization. The CPO shows a fast strengthening up to γ =3–4 then tends to stabilize. The CPO shows a concentration of [100] close to the shear direction and a repartition of [010] and [001] in a girdle around the shear direction (from Vauchez et al., 2012).

CPO already develops after an equivalent strain of 0.5. The intensity of the CPO climbs up rapidly but then stabilizes strains due to dispersion related to dynamic recrystallization that counteracts CPO development by dislocation glide (Bystricky et al., 2000).

The CPO patterns observed in naturally deformed peridotites and in experiments are well reproduced by visco-plastic self-consistent numerical modelling of olivine aggregates using experimental data of high-temperature deformation of olivine (Wenk et al., 1991; Tommasi et al., 1999, 2000) (compare Figs. 1-7, 1-8 and 1-9). For instance, axial shortening results in axial-[010] fabrics, consistent with CPO obtained from experimentally deformed dunite at high temperature (1200°C) in axial compression (Nicolas et al., 1973; see Tommasi et al., 2000).

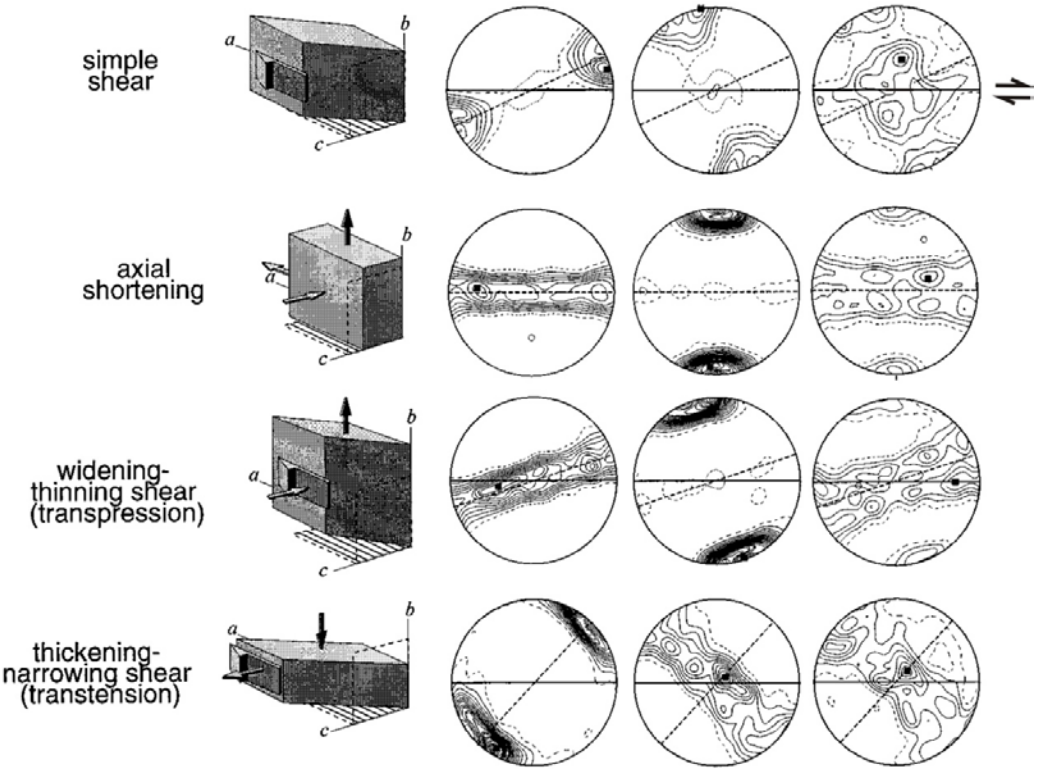

Figure 1-9. Fabric symmetries developed for dominant [100]{0kl} slip at equivalent strains of 1. Orthorhombic pattern in simple shear, axial-[010] in axial shortening ans transpression and axial-[100] in transtension.

1.2.2.2. - Dynamic recrystallization

1.2.2.2.a) Basics

Under upper mantle conditions, the precursor microstructural analyses and olivine crystal preferred orientation measurements (on U-stage microscope) of naturally deformed peridotites from massifs and xenoliths from kimberlites and basalts (Avé Lallemant, 1967; Nicolas et al., 1971, 1972, Nicolas & Boudier, 1975; Green & Radcliffe, 1972; Mercier, 1972; Boullier & Nicolas 1973, 1975; Mercier & Nicolas, 1975; Nicolas & Poirier, 1976; Boullier, 1975; Gueguen & Boullier, 1975) already suggested that solid state flow in the upper mantle was mainly accommodated by a combination of dislocation glide and dynamic recrystallization.

Dynamic recrystallization processes involve nucleation, subgrain rotation and grain boundary migration or bulging (White, 1977; Etheridge, 1975; Bell & Etheridge, 1973; Mercier et al., 1977, Etheridge & Wilkie, 1979). Dynamic recrystallization has major influence on the final microstructure of a deformed rock. Dynamic recrystallization involves two competing processes: (i) the accumulation of dislocations that tends to enhance grains' internal energy and (ii) recovery by diffusive processes that allow reorganization and reduction of the dislocation population in a crystal. Dynamic recrystallization may modify the CPO (e.g. Urai et al., 1986; Zhang & Karato, 1995; Tommasi et al., 2000). Recently, based on the analysis of a xenoliths suite from the Carpathians, Falus et al. (2011) proposed that

dynamic recrystallization resulted in the dispersion of the olivine CPO, as the CPO intensity is negatively correlated to the volume proportion of recrystallized grains.

1.2.2.2.b) Palaeopiezometry and palaeowattmetry

Twiss (1977) showed that the average recrystallized grain size d_s in dominant dislocation creep was inversely correlated to stress and could hence be used as a palaeopiezometric proxy in the form of:

$$d_s = A\sigma^{-m}$$

With A and m empirically determined constants. Van der Wal et al. (1993) scaled this relation for olivine. However, more recent work suggests that the dependence of recrystallized grain size is not only related to stress but also to strain rate (de Bresser et al., 1998). Austin & Evans (2007) also proposed that the rate of external mechanical work $\dot{W}$ (approximated to $\dot{W} = \sigma\dot{\varepsilon}$ at constant stress) is correlated with the rate of change of internal energy, and hence the recrystallized grain size. The latter is thus rather a palaeowattmeter than a palaeopiezometer. This may explain why shear zones that recorded a single deformation event (presumably under the same stress conditions) show grain size decrease towards the center of the shear zone. It would rather result from higher strain rates due to strain softening than different amounts of stress within the same shear zone (Austin & Evans, 2009, Austin, 2011).

1.2.2.3. - Diffusion and diffusion creep

Mass transfer via diffusion involves the migration (jump) of point defects, be it atoms of the crystal, impurities or vacancies in the lattice controlled by a gradient of concentration. The mobility of the atoms is thermally activated, so that the probability Γ of a successful "jump" of a point defect may be written as follows:

$$\Gamma = \nu . \exp\left(-\frac{\Delta G_m}{RT}\right)$$

With ν the oscillation frequency of atoms on their site, ΔG_m the variation in migration enthalpy, R the gas constant and T the absolute temperature.

Diffusion allows for recovery at high homologous temperatures. Recovery includes dislocation climb (or cross-slip), migration of dislocations to form subgrain boundaries, grain boundary migration, static recrystallization and abnormal grain growth.

Deformation solely accommodated by diffusion is called diffusion creep (see Fig. 1-10). The stress-induced diffusion creep rate is strongly dependent on grain size (generally as $1/d^3$), therefore it is also called "*grain size sensitive creep*" compared to dislocation creep that is "*grain size insensitive*". The smaller the grain size, the more effective diffusion creep. The diffusion creep rate is also directly dependent on the effective diffusivity D_{eff}, as follows:

$$\dot{\varepsilon} = A\frac{\sigma V}{kTd^2} \cdot D_{eff}$$

With k is the Boltzman constant, d is the grain size, T is absolute temperature, σ is stress, V is molar volume and D_{eff} given by:

$$D_{eff} = D_{gm}\left(1 + \frac{\pi\delta D_{gb}}{d.D_{gm}}\right)$$

With D_{gb} the grain boundary diffusion ("Coble creep"), D_{gm} the grain matrix diffusion ("Nabarro-Herring" creep) and δ the grain boundary width.

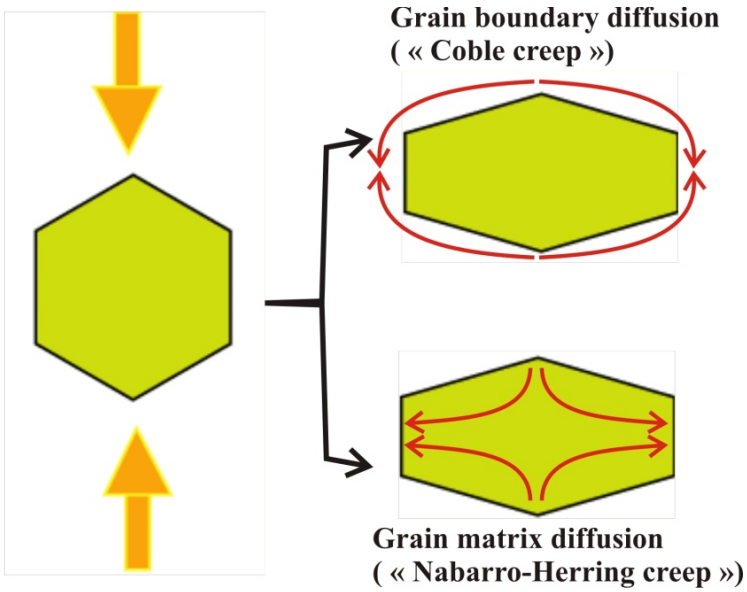

Figure 1-10. Modes of diffusion creep. (A. Vauchez, pers. Comm..)

Diffusion creep does modify the shape of crystals, but not the CPO (Fig.1-11). However, effective grain boundary migration may promote selective growth of crystals in easy glide orientations (see Chapter 5) and hence allow for stronger CPO.

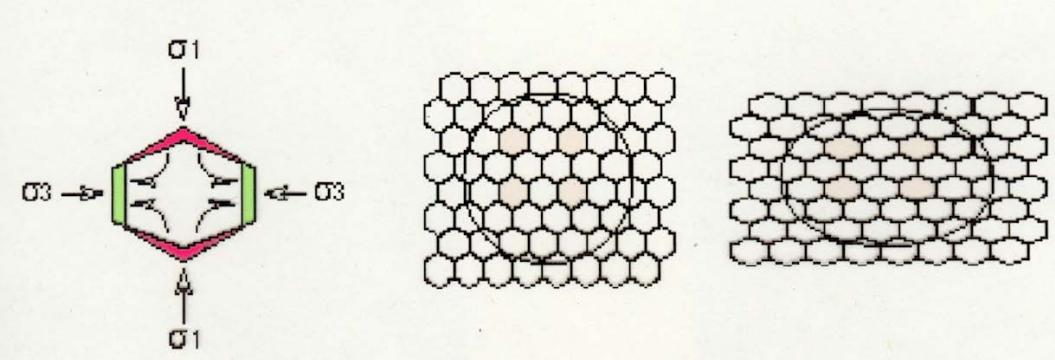

Figure 1-11. Cartoon illustrating the change in shape during diffusion creep accommodated deformation. Crystal orientations remain constant.

1.2.2.4. - Dry Grain Boundary Sliding (dry GBS)

Dry GBS-creep has been proposed as a potential ductile deformation mechanism based on the observation of strain rate dependence on grain size in the dislocation creep regime for fine grain sizes

near the transition from dislocation creep to diffusion creep (Hirth & Köhlstedt, 1995, 2003). The rounded grain shapes observed in these experiments supported this observation. This mechanism seems, however, quite rare in naturally deformed peridotites (Warren & Hirth, 2006; Précigout et al., 2007). Dry GBS-creep should disperse the CPO due to rotation of crystals with respect to each other.

1.2.3. Steady-state rheological profiles of the lithosphere

Classically, the strength of the lithosphere with depth is represented by a Brace-Goetze profile (Goetze & Evans, 1979; Brace & Kohlstedt, 1980; Kirby, 1983; Ranalli, 1986), also known as "Christmas Tree" (Fig. 1-12). Each stratification or "layer" of this profile is described as a compositionally uniform layer. The simplest profile assumes a linearly depth-dependent brittle upper layer (typically a Byerlee's law; Byerlee, 1978) with a strain-rate dependent viscous lower layer (e.g. an empirical flow law for dry dunite; Chopra & Paterson, 1981). The strength of the viscous layer may be described by a power-law

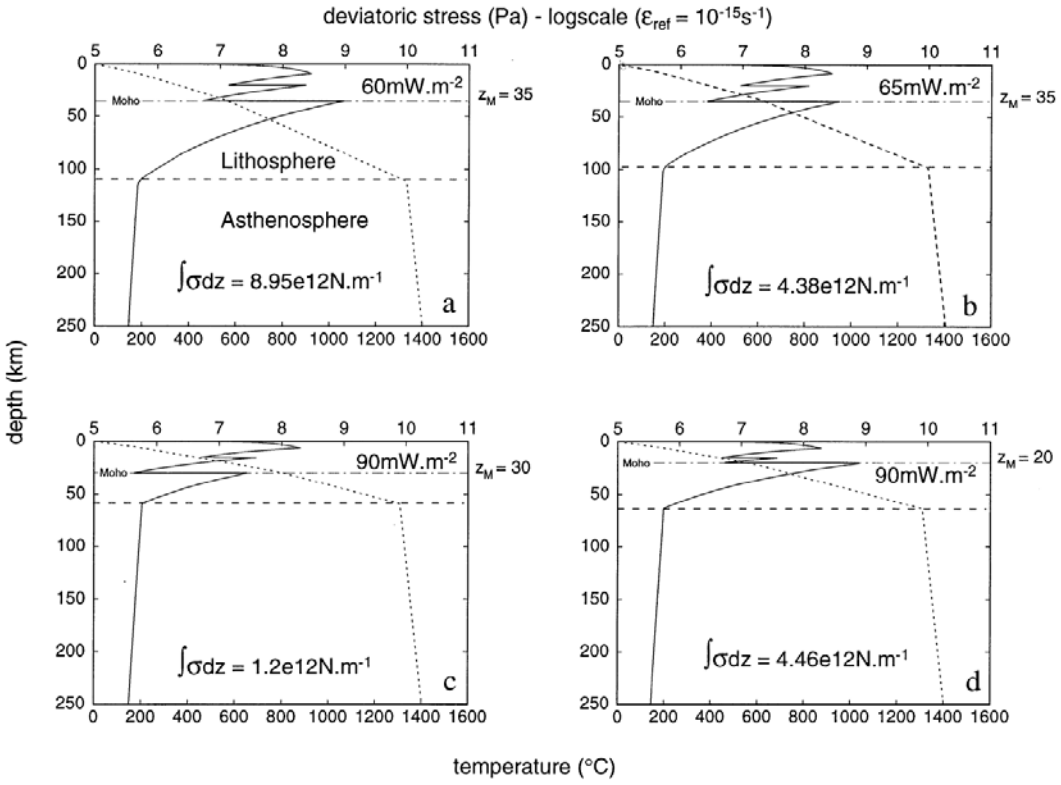

Figure 1-12. Rheological profiles calculated considering that the lithosphere is composed of a quartz-dominated 'upper=middle crust layer', overlaying a plagioclase-dominated 'lower-crust' layer and an olivine-dominated 'upper-mantle' layer. Constitutive equations used to describe the deformation are the Byerlee law (Byerlee, 1978) for the brittle crust and a power law (e.g., Weertman, 1978) for ductile deformation. Input rheological parameters are from Paterson and Luan (1990) for quartz, Wilks and Carter (1990) for granulite, and Chopra and Paterson (1981) for dunite. Strength profiles are for a 'normal lithosphere' with two slightly different geotherms (a,b) and an extended lithosphere with a high surface heat flow and two different crustal thickness (c,d). It should be noticed that an increase of 5 mW m^{-2} in surface heat flow can halve the integrated lithospheric strength, and a reduction of the crustal thickness from 30 to 20 km would increase almost four times the lithosphere strength, assuming the same surface heat flow (From Vauchez et al., 1998).

at constant strain rate, typically 10^{-15} - 10^{-14} s^{-1}. The intersection of the two curves than gives the depth of the brittle-ductile transition. Although more complex rheologies and additional stratifications may provide more realistic models, this approach remains oversimplified (Ranalli, 1986; Paterson, 1987).

However it enables (i) to have an idea of the integrated strength $\int_0^b \sigma dz$ (with b is the depth of the base of the lithosphere) of the whole lithospheric section (England, 1983) and (ii) to predict first-order effects of variations of some parameters such as the geothermal gradient, or the Moho depth (see Fig. 1-12; Vauchez et al., 1998), or the influence of a wet rheology in the mantle and in the crust etc. For instance, Vauchez et al. (1998) calculated that a slight increase of the surface heat flow from 60 $mW.m^{-2}$ may half the integrated lithospheric strength. Similarly, reducing the crustal thickness only from 30 to 20 km would strengthen the whole lithosphere by a factor 4.

1.3. Extension of continental lithosphere

One fundamental problem that arises from Brace-Goetze profiles is that plate tectonic related forces (mantle convection) are not large enough to break up an initially 100 km thick continental lithosphere (Köhlstedt et al., 1995). Consequently, Brace-Goetze strength profiles yield over-estimates of lithospheric strength (Kusznir & Park, 1984; Ranalli & Murphy, 1987; Buck, 2006; Regenauer-Lieb et al., 2008). Additional weakening mechanisms have been proposed to account for continental break-up from both modelling and geological observations such as the presence of magma (Kendall et al., 2005; Buck, 2006), the presence of structural (Vauchez et al., 1997) or rheological (Vauchez et al., 1998) heterogeneities, for instance mechanical anisotropy due to frozen olivine CPO (Tommasi & Vauchez, 2001; Tommasi et al. 2009).

Another limitation of strength-envelopes is the abrupt change of strength at rheological interfaces. These rheological jumps have been in some cases interpreted as horizontal decoupling surfaces, especially at the crust-mantle transition (e.g. Oldow et al. 1990). However, similarities between crustal and mantle deformation observed by geological mapping and shear-wave splitting, respectively, suggest coupling between these interfaces (Tikoff et al., 2002; 2004). Similarly, the brittle-ductile transition in the crust display regions of maximum strength, which is inconsistent with strain localization observed from geological mapping in exhumed extensional detachments (e.g. Jolivet et al., 1998; see Regenauer-Lieb et al., 2008).

The use of Brace-Goetze envelopes is therefore not fully adapted to explain lithospheric scale deformation considering geologically realistic forces.

1.3.1. Conceptual models of continental extension

1.3.1.1. - Pure shear and simple shear models

The first conceptual models of lithospheric scale continental extension are two end-member cases that result in different patterns in the lithospheric mantle (Vauchez et al., 2000). The first involves symmetric, homogeneous pure shear thinning (Fig. 1-13; McKenzie, 1978) that would result in almost flat-lying foliations with lineations perpendicular to the rift-axis. The second corresponds to an asymmetric lithospheric scale shear zone (Fig. 1-13; Wernicke, 1981, 1985). In this model, deformation in the lithospheric mantle is highly localized, which would result in a gently dipping foliation with lineation perpendicular to the rift-axis overprinting a pre-existing fabric. Interestingly, the area where the lithospheric mantle is thinned the most is offset from the rift valley.

An implicit and interesting aspect of the Wernicke-model, however, is the fact that the fault penetrates the lower crust and the lithospheric mantle till the lithosphere-asthenosphere boundary.

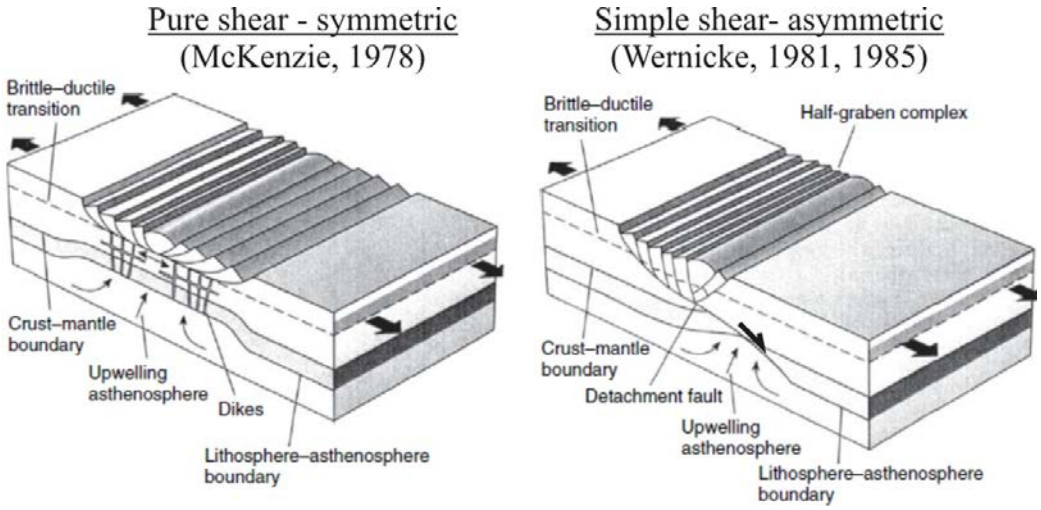

Figure 1-13. Conceptual models of lithospheric scale extension. Symmetric, pure shear model of McKenzie (1978), and asymmetric, simple shear model of Wernicke (1981, 1985).

There is now growing geophysical and geological evidence of faults penetrating down the lithosphere (see review in Vauchez et al., 2012). One of the most striking is probably the detection of Moho-offsets in seismic reflection data, for instance in the North Sea. These were interpreted as extensional shear zones affecting the lithospheric mantle developed during opening of the Atlantic (McBride et al., 1995; McGeary & Warner, 1985; Reston, 1990). The question of whether faults do penetrate down to the lithospheric mantle is a major issue, not only for the understanding of geodynamic processes, but also the rheology of the lithospheric mantle (Vauchez et al., 2012).

1.3.1.2. - Transtensional models: Reconciling geological observations with conceptual models

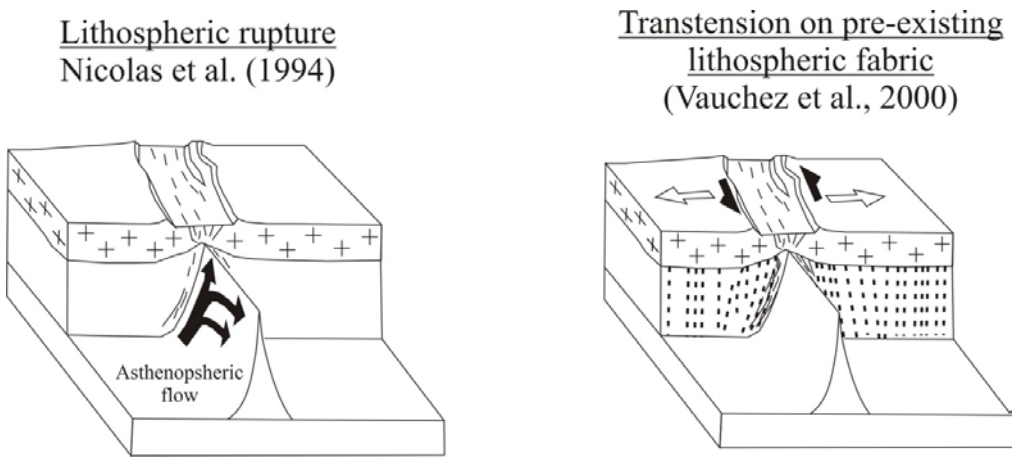

Figure 1-14. Transtensional models of Nicolas et al. (1994) and Vauchez et al. (2000).

To account for the presence of narrow low P-wave velocity anomalies just below the Kenya rift following to the rift trend, Nicolas et al. (1994) proposed a model in which rifting initiates by localized lithospheric rupture, most likely in transtension, leading to a narrow asthenospheric upwelling parallel to the rift axis, and followed by homogeneous extension (Fig. 1-14).

The striking parallelism between continental rift structures with ancient orogenic belts has been interpreted as evidence that rheological heterogeneity of the lithosphere is a good candidate to account for localization of the deformation at the scale of the lithosphere (Vauchez et al., 1997, 1998, 2000; Fig. 1-14). Indeed, numerical models of the deformation of a mechanically anisotropic lithosphere due to frozen olivine fabrics in the lithospheric mantle show that rift initiation and propagation along preexisting structures with a foliation oblique to the imposed extension are facilitated and that these zones deform in transtension (Tommasi & Vauchez, 2001; Knoll et al., 2009; Tommasi et al., 2009).

Teleseismic shear-wave splitting measurements beneath active continental rifts such as the Rio Grande rift (Sandvol et al., 1992) and the Kenya rift (Gao et al., 1997) show the fast split waves are mainly polarized parallel or slightly oblique to the rift trend, corroborating that transtension plays a major role in the rifting process (Vauchez et al., 2000). Based on geological observations from several geodynamic environments that suggest strong or at least partial mechanical coupling between crust and mantle, Tikoff et al. (2004) modeled the strain patterns that would be generated in the lithospheric mantle in different strain regimes. Fig. 1-15 shows their predicted strain pattern in two styles of oblique divergence (transtension). Simple shear dominated transtension better accounts for the abovementioned geophysical observations as it results in steeply-dipping foliations towards the center and more shallowly dipping ones farther away, and lineations at low angle to the rift axis. From these models, however, strain is distributed over a wide area and no localization of deformation occurs, in other words no fault penetrates the lithospheric mantle as in the Wernicke-model.

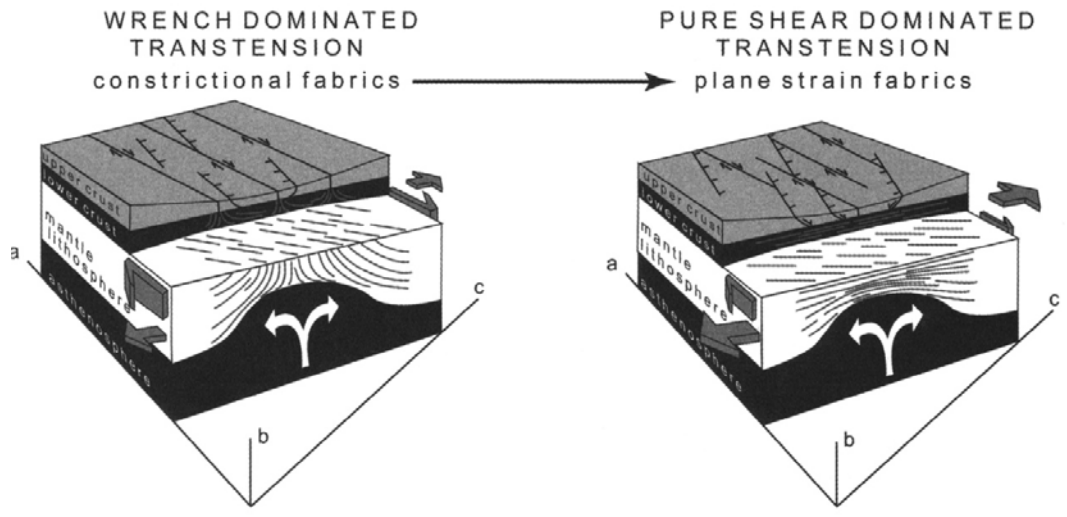

Figure 1-15. Oblique divergence results in wrench-dominated transtension (b) or pure shear-dominated transtension (c), both of which result in constrictional fabrics. Pure shear-dominated transtension causes horizontal foliations (from Tikoff et al., 2004).

1.3.2. Numerical models

1.3.2.1. - Extension at divergent margins

Though numerical models simulating extension of the crust are ubiquitous (Buck, 2007; and references therein), those taking into account the whole lithosphere are rare (e.g. Huismans & Beaumont, 2007; Regenauer-Lieb et al., 2008; Brune et al., 2012). Depending on initial conditions (rheological laws of lithospheric layers, addition of pre-existing weak zones or strain weakening laws, strain rate, time etc.), models are able to reproduce different widths and modes of extension (e.g. narrow, wide and core complex styles of rifting; Buck, 1991; Buck et al., 1999; Huismans & Beaumont, 2007) or the symmetric vs. asymmetric style of narrow rift basins (Lavier et al., 1999; Huismans & Beaumont, 2002, 2003; Huismans et al., 2005). Interestingly, regardless of the style (asymmetric or symmetric), normal-type (extensional) high strain zones develop. In Fig. 1-16, the model of Huismans & Beaumont (2007) highlights the presence of approximately 5-15 km wide zones where strain is localized. These "faults" crosscut the upper (frictional) lithospheric mantle and penetrate over ca. 20 km in the ductile lithospheric mantle (Fig. 1-16) down to ca. 60 km depth, consistent with asymmetric simple shear type model of Wernicke (1981, 1985).

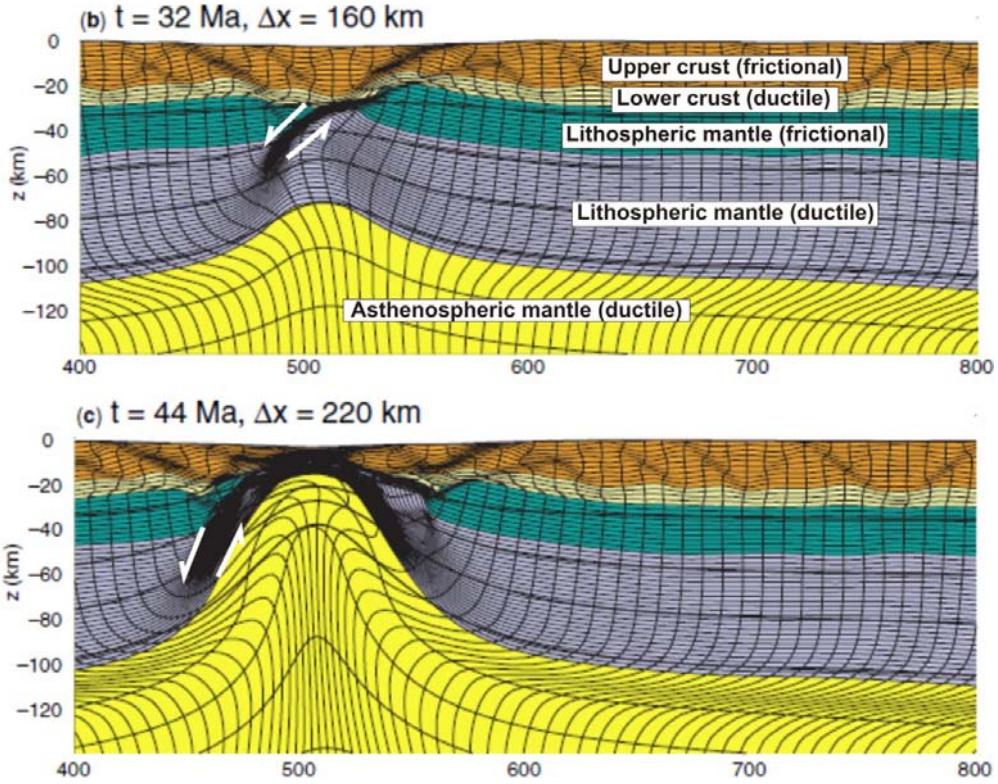

Figure 1-16. 2D-lithospheric scale numerical model, modified from Huismans & Beaumont (2007). Snapshots at 160 km and 220 km of extension, respectively, for an extension velocity of 0.5 cm/an. Weak lower-crust with statistical noise applied only to the crust. Note the development of high strain zones (normal shear sense) at the scale of the lithosphere.

Such models prescribe pre-existing heterogeneities ("weak seeds") or arbitrary weakening mechanisms in order to develop asymmetric geometries. This initial weakening may correspond to a pre-existing mechanical anisotropy as suggested by Tommasi & Vauchez (2001). However, more complex models that do not prescribe *ad hoc* weakening mechanisms to localize strain also display detachment structures both in the crust and the mantle (Regenauer-Lieb et al., 2008), supporting localization of strain in the lithospheric mantle.

Continental rifting is fundamentally a 3D-problem (van Wijk, 2005; Allken et al., 2011; Brune et al., 2012). Indeed, transtension occurred in many ancient rifted margins, as in the South Atlantic rifted margins (Nürnberg & Müller, 1991; Edwards et al., 1997; Macdonald et al., 2003; Torsvik et al., 2009; Moulin et al., 2010), the oblique separation of Africa and Madagascar (de Wit, 2003) and of Madagascar and India (Storey et al., 1995) in the Indian ocean, the opening of the oceanic basin between Antarctica and Australia (Whittaker et al., 2007), the Gulf of Aden between Somalia and the Arabian peninsula (Bellahsen et al., 2003), the Red Sea (Hempton, 1987) and the Dead Sea pull-apart (Weber et al., 2009) basins, and in presently active rifts. Analogue models of continental extension (e.g. Corti et al., 2003; and references therein) may reproduce some of the 3D-features of rifts, like surface structural patterns, but they are intrinsically limited by the independence of temperature (and pressure) of the analogue materials used, and hence their utility for deep lithospheric processes is much restricted. On the other hand, 3D-numerical models are highly demanding in terms of computation capacities and hence time consuming. Fig. 1-17 shows a recent 3D thermomechanical model of lithospheric scale oblique extension (transtension) of Brune et al. (2012). Like in 2D-models they predict necking of the base of the lithosphere with high strain (and strain rate) zones that penetrate the entire lithosphere (black arrow in Fig. 1-17). They resemble much to the conceptual model of wrench-dominated transtension of Tikoff et al. (2004), and also reproduce en-echelon type patterns in the upper crust usually observed in the analogue models.

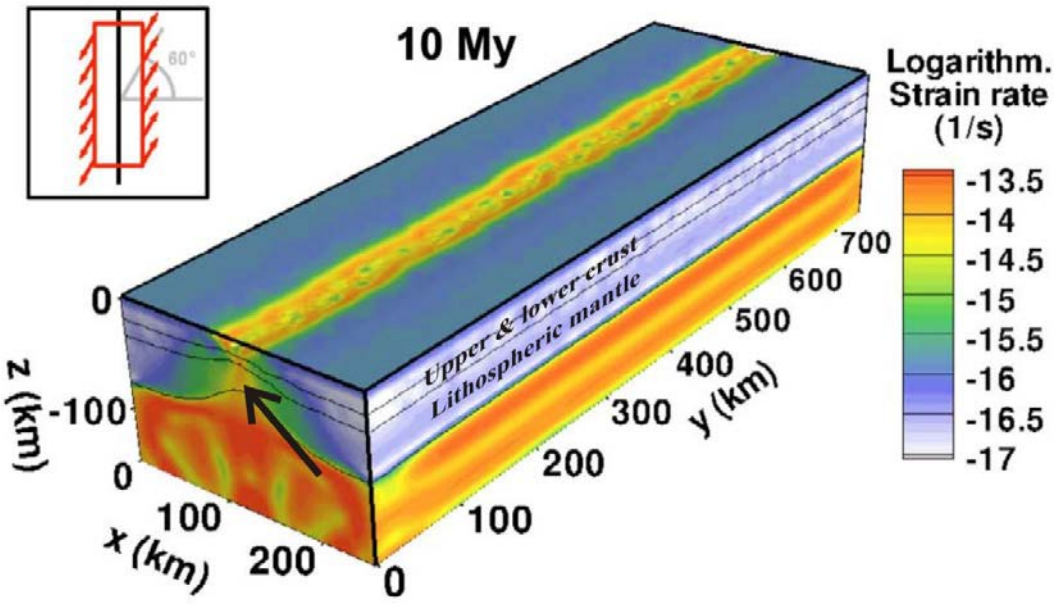

Figure 1-17. 3D-lithospheric scale numerical model (modified from Brune et al., 2012). High obliquity (60º) transtensional deformation results in lithospheric necking (black arrow) and relatively thin high strain rate zones crosscutting the entire lithospheric mantle parallel to the rift axis.

1.3.2.2. - Extension at convergent margins

Paradoxically, extension of continental lithosphere is not restricted to divergent plate boundaries. Indeed, syn- to late-orogenic crustal extension is a well-known phenomenon that has been largely documented both in currently deforming orogenic belts like the Himalayas (e.g. Burchfiel & Royden, 1985), the Alps (Sue et al., 1999), the Andes (Dhont et al., 2005), the Taiwan arc-continent collision (Crespi et al., 1996) as in ancient ones, such as the Alpine (Jolivet et al., 1998, 2003, 2010; Jolivet & Faccenna, 2000) and Variscan (Malavieille et al., 1990; Aerden & Malavieille, 1999) orogenies.

Syn-convergence extension of the overriding lithosphere may be the consequence of time-dependent processes in the life of the convergent system such as slab-breakoff (Davies & von Blanckenburg, 1995), mantle delamination (Bird, 1979), gravitational Rayleigh-Taylor instability of the viscous mantle lithosphere (Houseman et al., 1981) and slab-rollback (Royden, 1993; Doglioni et al., 2007; Vanderhaeghe & Duchêne, 2010). The huge intrinsic complexity of convergent zones has engendered a flourishing literature on this subject (e.g. Faccenda et al., 2008; Li et al., 2011, 2012; Li & Ribe, 2012). Here we will restrict ourselves to recall a synthetic model of Burov et al. (2001) where extension in the back-arc region during subduction of young (hot) oceanic crust is unequivocal (Fig. 1-18). Although thermo-mechanical studies of convergent zones do not generally focus on this particular region of the convergent system, numerical models in pure divergence are most probably a good first-order approximation to understanding lithospheric rifting processes in back-arc regions too.

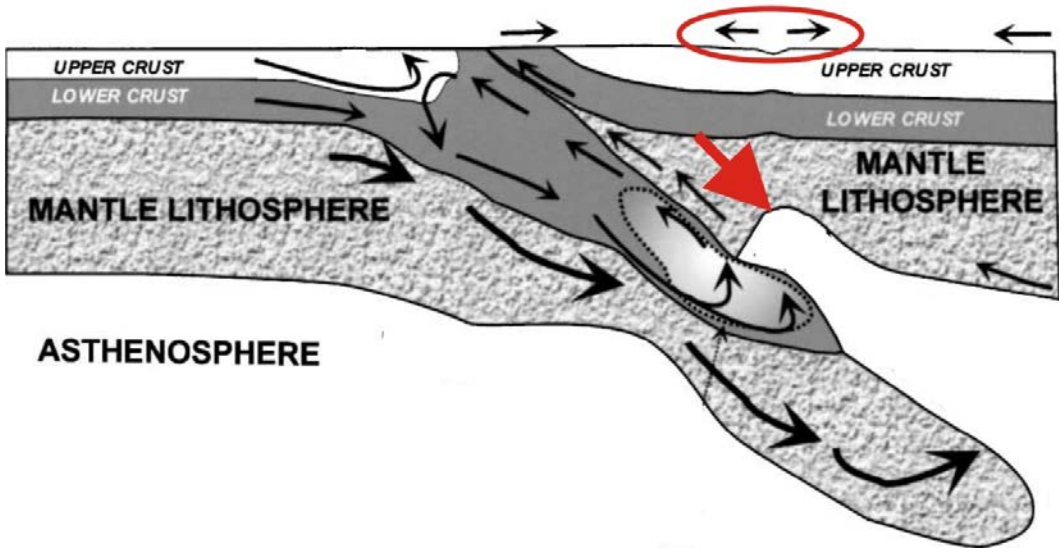

Figure 1-18. Lithospheric scale extension in the backarc of a convergent zone (modified from Burov et al., 2001).

1.4. Geological setting of the studied case

1.4.1. Tectonic evolution of the Betic-Rif belt

The Rif Mountains in northern Morocco together with the Betic Cordillera in southern Spain form an arcuate belt (Fig. 1-19a, b) that represents the westernmost segment of the peri-Mediterranean orogenic Alpine orogenic system in southern Europe (Fig. 1-19a). The Rif and the Betics surround the Alboran Sea basin, floored by thin continental crust (15-20 km; e.g. Torné et al., 2000). This region as a whole is bounded to the north and the south by the Iberian and African continental forelands, to the west, the system is connected through the Gibraltar Arc with the Atlantic Ocean, and to the east with south Balearic oceanic basin. The Betic-Rif belt is located between two large lithospheric plates (Africa

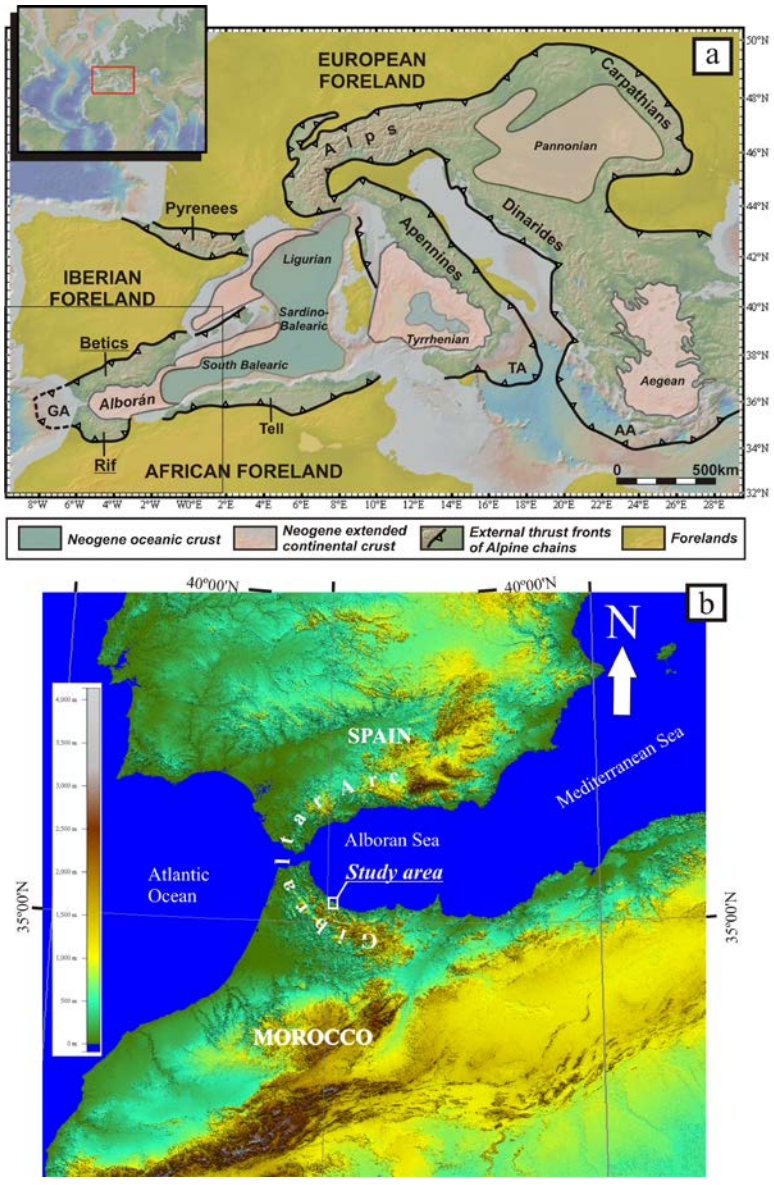

Figure 1-19. (a) Tectonic sketch of the Mediterranean Sea, showing Alpine external thrust fronts and Neogene extensional basins. AA= Aegean Arc, GA=Gibraltar Arc, TA=Tyrrhenian Arc. (after Comas et al., 1999, base map created with GeoMapApp). (b) The Gibraltar Arc surrounding the Alboran Sea between Spain and Morocco.

and Eurasia) that have had variable amounts of convergence since the late Cretaceous (Dewey et al, 1973, 1989; Dercourt et al., 1986; Rosenbaum et al., 2002).

The Betic-Rif belt is generally subdivided into three distinct palaeogeographic domains (Fig. 1-20; see Booth-Rea et al., 2007; and references therein): the External Zones, the Flysch units, and the Internal Zones (Fallot, 1948; Suter, 1980). The External Zones correspond to the Mesozoic thinned continental margins of the Iberian and African plates, respectively; the allochtonous Flysch units were deposited on highly-thinned continental or oceanic crust in the Liassic to Oligocene (Durand-Delga et al., 2000). The Internal Zones of the Rif and the Betics, named the Sebtides and Alpujarrides, respectively, represent the Alboran Crustal Domain (Balanyá & García-Dueñas, 1987) and contain relicts of pre-Miocene HP metamorphism (e.g. Booth-Rea et al., 2002 in the Betics, Bouybaouène et al., 1995 in the Rif) most probably of Paleogene age (ca. 50Ma in the Betics; Monié et al., 1991, 1994; Platt et al., 2005). This nappe stacking event occurred in a most easterly position, when the Alborán Domain was a segment of the continuous Alpine orogenic belt (e.g. Malinverno and Ryan, 1986; Dewey et al., 1989). From the latest Oligocene and early Miocene, the Alborán Crustal Domain was thrust westward onto the South-Iberian and Maghrebian continental margins, which formed the present-day arcuate shape of the belt. At the same time, crustal extension occurred in the inner part of the arc, which resulted in subsidence of much of the region below sea-level developing the Alborán Sea basin (Comas et al., 1999; and references therein).

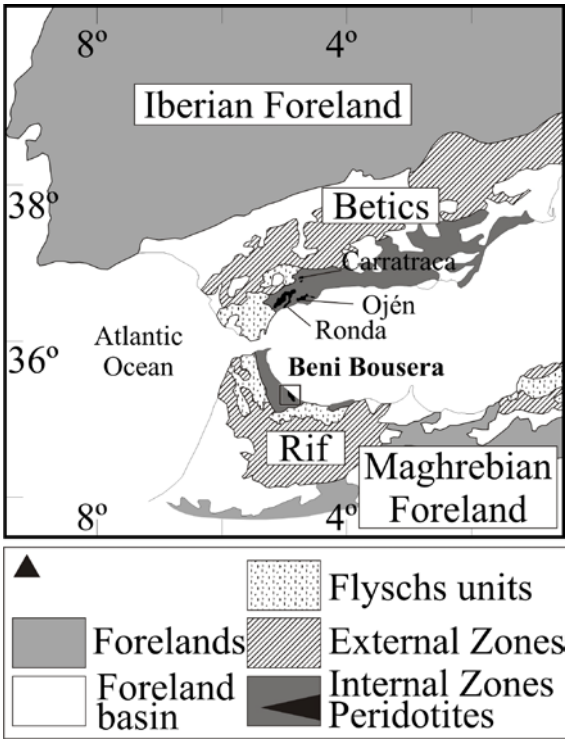

Figure 1-20. Simplified geological map of the Betic-Rif mountain belt showing the outcrops of peridotite bodies.

The belt underwent large scale extensional collapse in the Late Oligocene – Early Miocene (e.g. Platt & Vissers, 1989; Galindo-Zaldívar et al., 1989; Platt et al., 1998). The causes of the late-orogenic extension have been extensively debated and involve back-arc extension driven by the westward slab rollback of oceanic lithosphere (Royden, 1993; Lonergan and White, 1997; Jolivet al., 2006), slab break-off (Blanco and Spakman, 1993; Carminati et al., 1998), delamination of lithospheric mantle (Comas et al., 1992; Docherty & Banda, 1995; Seber et al., 1996) or convective removal of the overthickened lithospheric root (Platt and Vissers, 1989). The implications of our results regarding the geodynamic implications of the Betic-Rif belt and West-Mediterranean geodynamics are brielfly discussed in chapters 5 and 6, albeit this is not the primary purpose of this dissertation, which is focused on the mantle deformation processes that can be clearly constrained from the observations within the Beni Bousera massif.

1.4.2. The Rif Internal Zones

The Beni Bousera peridotite massif crops out in the Rif Internal Zones (Fig. 1-21). They are composed of two metamorphic ensembles, downsection the Ghomarides and the Sebtides. All are overlain by the quasi-unmetamorphosed "Dorsale Calcaire". The Ghomarides are composed of Palaeozoic to Tertiary sediments. They recorded LP-LT metamorphism of Late-Variscan age (Chalouan & Michard, 1990), but were partly overprinted by higher temperatures during their Alpine evolution (Negro et al., 2006).

The Sebtides (Fig. 1-21) are subdivided into the structurally upper Federico and lower Filali units (Kornprobst, 1974; Michard et al., 1997). The first is a 1-2 km-thick metasedimentary sequence that has recorded peak metamorphic conditions ranging from HP-LT blueschist facies (0.8 – 1.5 GPa, 380-450ºC) to HP-MT eclogite facies (2.0 GPa, 550ºC; Bouybaouène et al., 1995). Late cordierite and andalusite crystallization attests, however, for partial reequilibration at higher temperatures and lower pressures (Bouybaouène, 1993; Michard et al., 1997).

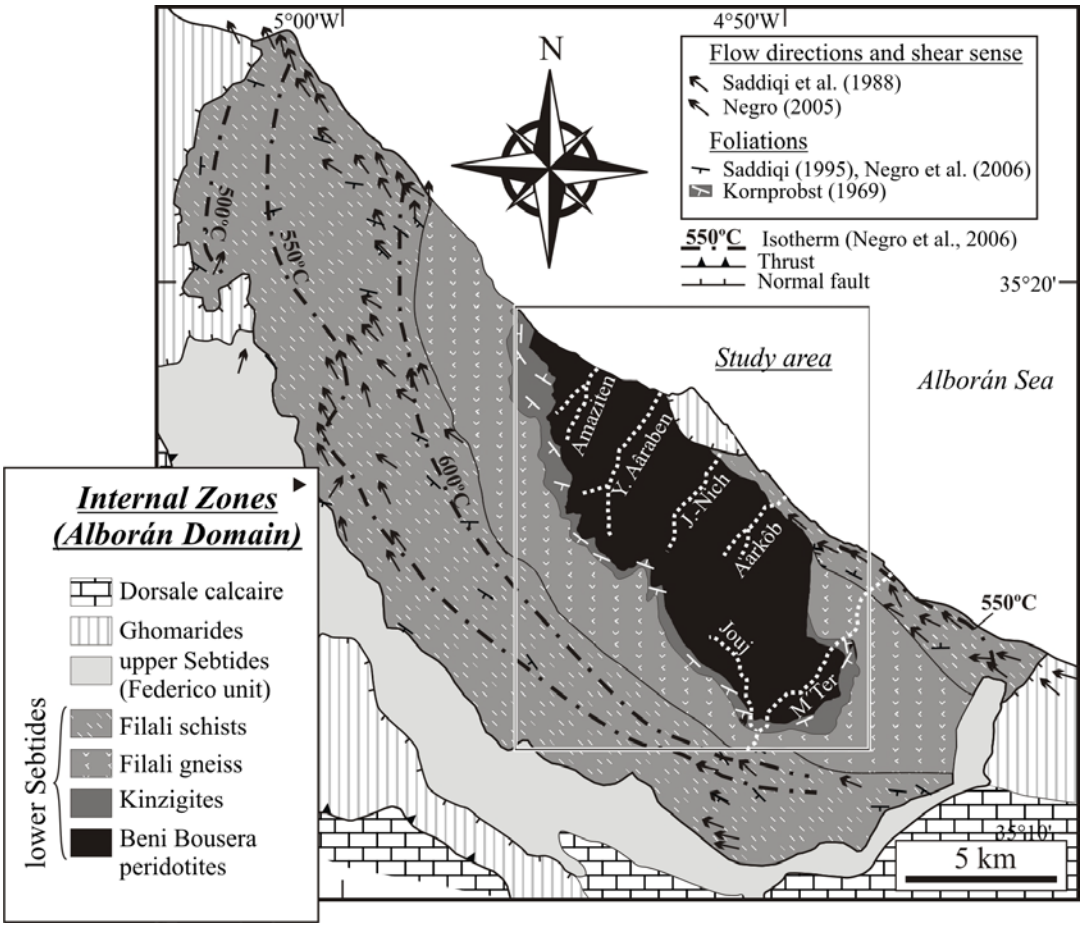

Figure 1-21. Geological and structural setting of the Beni Bousera peridotite in the Internal Zones of the Rif. Inset shows study area. Palaeo-isotherms are peak Raman Spectroscopy on Carbonaceous Material (RSCM) from Negro et al. (2006).

The metamorphic grade in the Filali unit increases downward, towards the contact with the peridotites (Negro et al., 2006; Fig. 1-21). The topmost phyllites were equilibrated at MP-MT amphibolites facies conditions (P = 0.7 - 0.8 GPa; Bouybaouène, 1993) and show a marked

temperature gradient from 500 to >640ºC in <5 km towards the underlying gneisses (Negro et al., 2006; isotherms in Fig. 1-21). The gneisses record peak MP-HT amphibolite / granulite facies conditions of 0.7 – 0.8 GPa, 750-800˚C (Kornprobst & Vielzeuf, 1984; Bouybaouène, 1993; El Maz & Guiraud, 2001) and grade into granulite facies, HP-HT kinzigites with peak metamorphic conditions of 1.6 – 2.0 GPa, 760-820ºC (Bouybaouène et al., 1998). Recent studies have documented ultra-high pressure metamorphism assemblages such as diamond and coesite-bearing gnesises and kinzigites (Ruiz-Cruz and Sanz de Galdeano, 2012). The age of this UHP event is unknown.

Foliations in upper and lower Sebtides units trend NW-SE in average (Fig. 1-21), subparallel to the Rif chain. They dip shallowly towards the SW (Saddiqi, 1995; Negro et al., 2006). Lineations trend NW-SE in average, but N-S to NE-SW directions are observed locally, with top to the NW and N-NE senses of shear, respectively (Saddiqi et al., 1988; Negro et al., 2006). In the kinzigites, the few available foliation data are consistent with the structures in the schists and tend to wrap around the peridotites (Kornprobst, 1974). Except for a few measurements indicating SE-dipping lineations (Afiri et al., 2011), there are, to our knowledge, no lineation data for the kinzigites in the literature.

1.4.3. The Beni Bousera peridotite

The Beni Bousera massif is mainly composed of lherzolite with minor harzburgite and dunite (Kornprobst, 1969; Reuber et al., 1982). Previous studies recognized different tectono-metamorphic domains, from SW to NE: (i)mylonitic garnet and spinel mylonites (Kornprobst, 1969; Reuber et al., 1982; Saddiqi et al., 1988; Tabit et al., 1997) that overlie (ii) porphyroclastic spinel peridotites containing garnet pyroxenite layers (Ariègite subfacies; Targuisti, 1994), which in turn overlie (iii) coarse grained porphyroclastic to granular spinel peridotites with differing amounts of spinel pyroxenite layers (Seiland subfacies; Targuisti, 1994).

Garnet- and/or spinel pyroxenite layers are common in the entire massif and may locally comprise up to 50% of an outcrop section. Detailed geochemical studies from both Beni Bousera and Ronda pyroxenites highlighted that these rocks represent either the product of crystallization of magmas at high pressure in the mantle or recycled oceanic crust (Davies et al., 1993; Kornprobst et al., 1990; Pearson et al., 1989, 1991, 1993; Pearson and Nowell, 2004; Gysi et al., 2011). Graphite pseudomorphs after diamond discovered in garnet pyroxenites indicate that Beni Bousera (and Ronda) equilibrated at some point at depths of >150 km (Pearson et al., 1989; Davies et al., 1993). More recent studies on Beni Bousera pyroxenites focused on melting and subsolidus reequilibration of these pyroxenites during exhumation of the massif (El Atrassi et al., 2011; Gysi et al., 2011).

Radiometric age constraints in Beni Bousera and also Ronda peridotite fairly constrain the exhumation history. Osmium systematics suggests that the peridotites were isolated from the convecting mantle at ca. 1.2-1.4 Ga (Reisberg and Lorand, 1995; Pearson and Nowell, 2004; Marchesi et al., 2010). U-Pb dating of zircons in garnet pyroxenites reveal Mesozoic ages (in the range 183 – 131 ±3 Ma) interpreted as early magmatic crystallization during Pangeae break-up (Sánchez-Rodriguez and Gebauer, 2000). Lu-Hf cooling ages in cpx-grt pairs, with blocking temperature of ca.

800 °C, in Beni Bousera garnet pyroxenite yield ages of 24 ± 3 Ma (Pearson and Nowell, 2004). Final emplacement into the crust occurred at ca. 21 Ma (Priem et al., 1979).

Studies addressing the relations between the peridotites deformation and the metamorphic evolution of the massif, similar to those performed in the Ronda massif (Obata, 1980; Remaïdi, 1993, Van der Wal & Vissers, 1996; Van der Wal & Bodinier, 1996; Lenoir et al., 2001; Vauchez & Garrido, 2001; Soustelle et al., 2009; Garrido et al., 2011) are still lacking and are one of the goals of the present study.

1.4.4. Emplacement models of Betic-Rif peridotite bodies

A rather unique feature of the Betic-Rif cordillera is the existence of the largest exposure of diamond and garnet facies subcontinental peridotites worldwide (Obata, 1980; Pearson et al., 1990; Davies et al., 1993; El Atrassi et al., 2011; Garrido et al., 2011). Models proposed for the uplift and final emplacement of these subcontinental peridotites may be broadly grouped into three types: in situ diapiric models, emplacement along transpresive, transcurrent or normal faults, and emplacement in subduction setting.

1.4.4.1.a) In situ diapiric models

Early models for the uplift of peridotite bodies in the Betic-Rif realm involved in situ diapirism (Loomis, 1972; Obata, 1980) or nested mantle core complexes (Doblas and Oyarzun, 1989). Seismic and geological studies showed, however, that the bodies formed sheet-like bodies interlayered within the high-grade metamorphic rocks of the Alboran Domain (e.g. Lundeen, 1978; Barranco et al., 1990; Torné et al., 1992).

A significant refinement of the "diapir" model was made by Obata (1980) that accounted for the unique petrological zoning preserved in the peridotites, ranging from HP-LT garnet-bearing

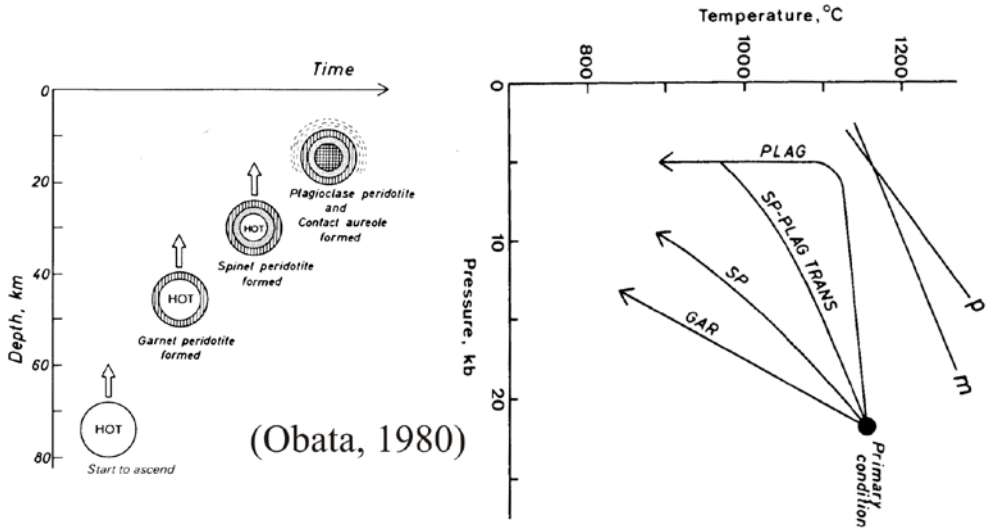

Figure 1-19. Polybaric and polythermal evolution of the Ronda peridotite during diapiric uplift from HP-HT "primary conditions". Progressive overprinting of lower pressure assemblages during differential cooling of the initial hot rising peridotite mass.

assemblages grading structurally downwards to LP-HT (plagioclase in the Ronda peridotite, spinel in Beni Bousera), suggesting the progressive rising and inward cooling of an initially hot mantle diapir (Fig. 1-19; Obata, 1980). However, the highly condensed metamorphic sequence ranging from high-pressure granulites at the peridotites contact upwards to unmetamorphosed rocks in just a few kilometers suggests a relationship between the extensional late-orogenic evolution of the Alboran Domain and at least part of their emplacement history (Argles et al., 1999). Tubía et al. (2004) suggested later that the hot plagioclase peridotites represented an asthenospheric mantle diapir, which rise was induced by slab break-off or delamination.

1.4.4.1.b) Emplacement along transcurrent and/or normal faults

Structural and kinematic analyses of the peridotites (e.g. Darot, 1973, 1974 in the Ronda massif; Tubía and Cuevas, 1986, 1987 in the nearby Ojén peridotite massif) highlighted consistency between crustal rocks and peridotites, which led Tubía (1994) to propose the in situ emplacement of peridotites through initial lithospheric scale transtension followed by transpressive emplacement into the crust. In their view, garnet-bearing peridotites developed upon high – temperature plagioclase peridotites that represented asthenospheric mantle uplift during the initial transtensional continental rift. Reuber et al. (1982) conducted detailed structural work in Beni Bousera peridotite and proposed a pre-Alpine extensional uplift followed by Alpine emplacement into the crust.

More recently purely extensional models have been proposed for Ronda (Platt et al., 2003) and Beni Bousera (Afiri et al., 2011). Platt et al. (2003) based their interpretation upon thermal modeling of available radiometric ages and P-T conditions from both crustal rocks and peridotites. They suggest that the Ronda peridotite exhumed from 66 km in about 5 Ma (starting at around 25 Ma), shortly after the removal of part of the lithospheric mantle beneath the Betic orogen. Thermal modeling also suggests an asthenospheric heat source to account for near-isothermal decompression of the crustal rocks. Afiri et al. (2011) interpreted peridotite foliation patterns in the peridotites and in the crustal units due to decompression and cooling in an extensional shear zone.

1.4.4.1.c) Subduction related models

Subduction related models are of two kinds: the first considers an evolution in the hanging-wall of a subduction zone (Fig. 1-20; Van der Wal & Vissers, 1993, 1996), whereas the second involves a back-arc setting (Fig. 1-21; Garrido et al., 2011; Marchesi et al., 2012).

Van der Wal and Vissers (1993, 1996) proposed that Ronda peridotites uplifted from the diamond stability field into the Ariègite subfacies spinel peridotite conditions (Fig. 1-21) in Mesozoic times. Ariègite subfacies spinel tectonites and garnet-spinel mylonites were supposed to reflect progressive ductile deformation in the subduction hanging-wall by near-isobaric cooling. Further uplift from garnet-spinel peridotite transition to spinel- and plagioclase lherzolitee stability was triggered by asthenospheric ascent in response to slab break-off (Blanco and Spakman, 1993). Final emplacement into the crust was accommodated by plagioclase peridotite extensional shear zones that accommodated tectonic denudation. This suprasubduction setting for the Ronda peridotite heavily relies on the

calculation of primary and recrystallization condtions. Primary conditions of Van der Wal and Vissers (1993, 1996) were estimated assuming an ad hoc choice of pressure, within the spinel lherzolite facies stability field.

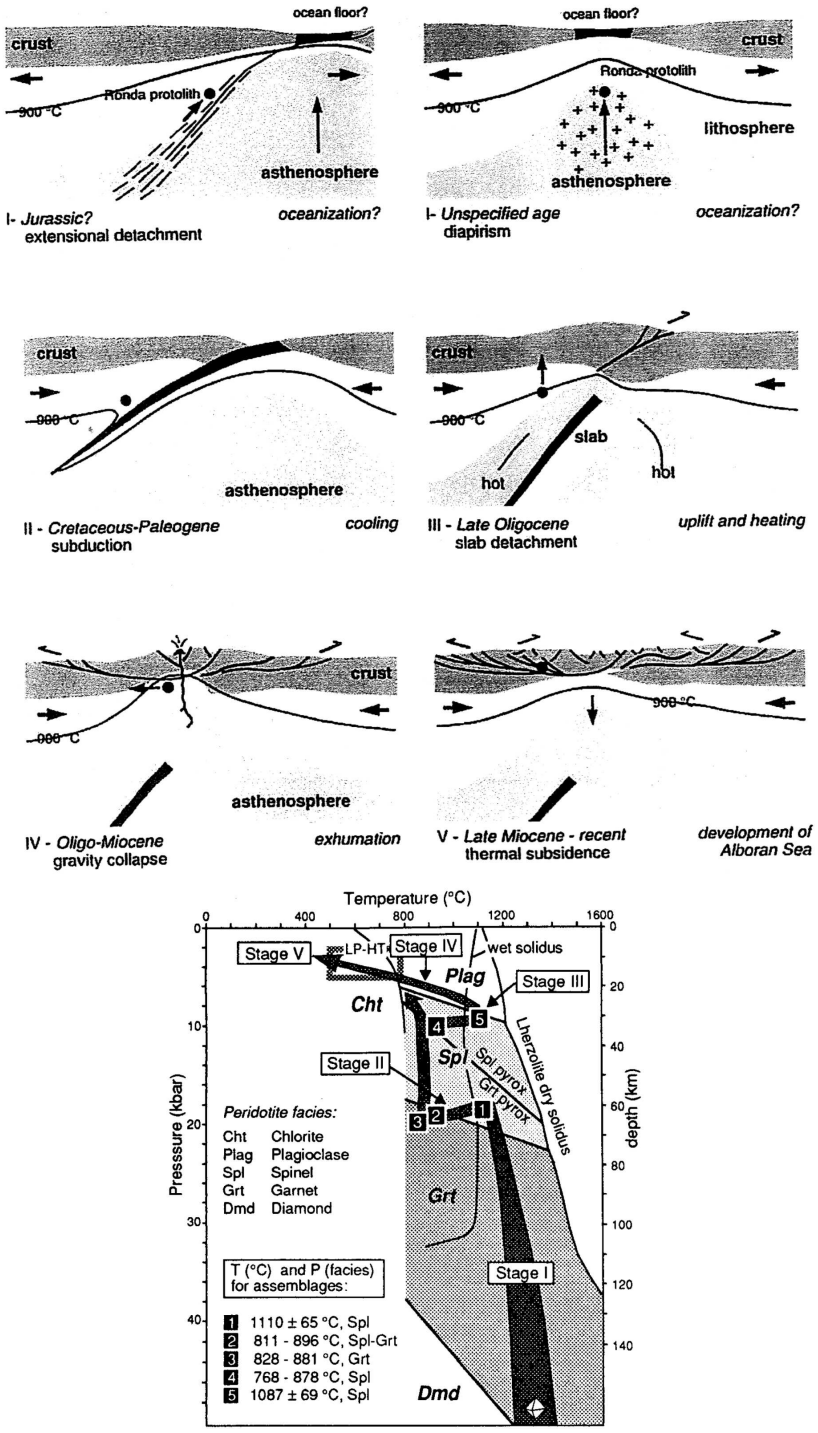

Figure 1-20. P-T-t path for the Ronda peridotite from Van der Wal & Vissers (1993). Early uplift from diamond facies to spinel-lherzolite stability field occurred by a first extensional event, possibly Jurassic in age. Near-isobaric cooling (slight compression) is interpreted as strain localization in the hangingwall of a subduction zone. Subsequent slab break-off resulted in asthenospheric upwelling leading to heating at LP conditions, forming plagioclase-lherzolite facies tectonites.

Garrido et al. (2011) found unequivocal prekinematic, HP-HT garnet-lherzolite assemblages (2.4-2.7 GPa, 1020-1100ºC) in garnet-spinel mylonites, demonstrating that Ronda peridotite equilibrated at 85 km before shearing (P-T diagram in Fig. 1-21). Garnet-spinel mylonites formed during cooling and decompression from this primary garnet peridotite, invalidating the near-isobaric cooling above a subduction proposed by Van der Wal and Vissers (1993). Garrido et al. (2011) proposed that garnet-spinel mylonite represents the vestiges of early back-arc lithospheric mantle extensionsal shear zone most likely initiated by Late Oligocene-Early Miocene slab roll back of African lithosphere (Fig. 1-21), coeval thinning of the overlying Alboran Domain crustal units. This model is supported by the geochemical signature of late Cr-rich pyroxenite dikes intrusive in Ronda garnet-spinel mylonites. Marchesi et al. (2012) showed that the trace elements and Sr-Nd-Pb radiogenic isotopic compositions of these intrusive dikes indicate a mantle source contaminated by a subduction component released by detrital sediments. This indicates that thinning and thermal erosion of the subcontinental lithosphere mostly likely occurred in a back-arc setting (Marchesi et al., 2012).

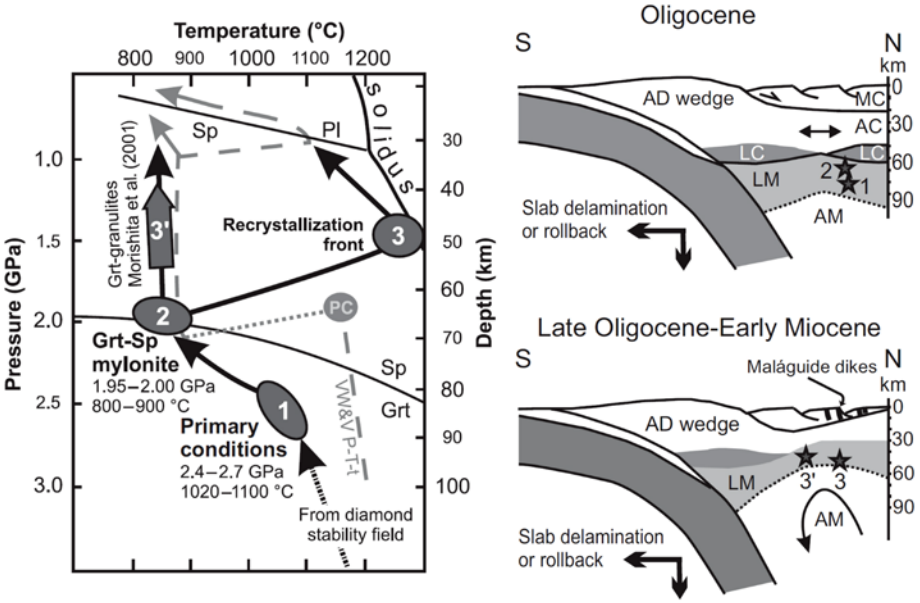

Figure 1-21. Left: PTt time path from Garrido et al. (2011) and Van der Wal & Vissers (1993). Right: Tectonic scenario proposed by Garrido et al. (2011) for the uplift of the westernmost Mediterranean subcontinental lithospheric mantle, represented by the Ronda peridotite, on a schematic southnorth cross section between early Oligocene (top) and late Oligocene to early Miocene (bottom). AC—Alpujárride Complex; AD wedge—Alborán crustal domain; AM—Asthenospheric mantle; LC—lower crust; LM—lithospheric mantle; MC—Maláguide complex.

2. Aims and Thesis structure

2.1. Synthesis of the state of the art

The processes that account for the thinning and/or break-up of continental lithosphere are a major issue in geodynamics, as this happens both at purely divergent as well as at convergent margins. Thinning and exhumation of middle and lower crust is now increasingly understood, as the vast exposures of these rocks at the surface of the Earth enable to study their deformation mechanisms under a wide range of P-T conditions. Additionally, efficient radiometric dating of crustal rocks also allows putting temporal constraints on exhumation and cooling rates that may constrain strain rates in natural conditions.

On the other hand, very little is known on the deformation processes that allow accommodating thinning (and exhumation) of the lithospheric mantle, which composes about 2/3 of a stable continental lithosphere. Conceptual models of lithospheric scale extension involve either symmetric, pure shear homogeneous stretching, or asymmetric, localized simple shear along a lithopsheric scale normal fault.

Depending on initial parameters, 2D- numerical models display either symmetric or asymmetric rift styles, but in both cases high strain zones that crosscut, at least partly, the lithospheric mantle develop. This is consistent with growing geophysical and geological evidences suggesting that faults may penetrate deep in the lithospheric mantle (Vauchez et al., 2012; and references therein). However, numerical models use oversimplified rheologies for the lithospheric and asthenospheric mantle, that are at odds to the wealth of deformation processes observed in peridotite microstructures deformed under natural conditions.

Kinematics of faults related to fossil rifted margins and active continental rifts suggest that transtensional deformation regimes are ubiquitous. Furthermore, analysis of shear wave splitting data in active continental rifts shows that the lithospheric mantle too deforms underneath continental rifts. However, the strain regime associated is neither pure nor simple shear, but transtension (Vauchez et al., 1997).

2.2. Working objectives

Orogenic peridotites preserving petrological zoning implying a polybaric and polythermal evolution, such as the Ronda and Beni Bousera peridotite in the Betic-Rif belt, provide a unique opportunity to investigate the thermo-mechanical evolution during extension of thick subcontinental lithospheric mantle. The aim of the presented work here is two-fold:

1) **To constrain the deformation mechanisms of mafic (pyroxenites) and ultramafic (peridotites) lithologies that were deformed under various P-T conditions in the lithospheric mantle (from garnet- to spinel- and finally plagioclase-lherzolite facies conditions**
2) **To couple these results with kilometer-scale mapping of foliations and lineations and petrological observations to unravel the spatial and temporal evolution of the kinematics during the thinning and exhumation of subcontinental lithospheric mantle.**

To attain these two principle objectives, we focused on the following goals:

I. To Map
   - Beni Bousera peridotite tectono-metamorphic domains by combining field observations at the outcrop/sample scale and microstructural analysis
   - Beni Bousera peridotite foliations and lineations at the scale of the massif, corroborated by analysis of olivine crystal preferred orientation measurements obtained on > 100 geographically oriented thin sections.
   - The lowermost spinel- and plagioclase-lherzolite facies structures in the Ronda peridotite

II. To describe in detail the microstructures of peridotites and pyroxenites

III. To provide new crystal preferred orientation data of olivine and pyroxenes from both peridotites and pyroxenites samples, as well as mineral chemistry and bulk rock analyses in order to assess the metamorphic conditions (pressure and temperature) prevailing during deformation.

IV. To discuss the implications of our observations in Beni Bousera peridotite for the thinning, the exhumation and the emplacement into the crust of subcontinental lithospheric mantle.

V. Finally, we built up a unique set of > 400 thin sections of peridotites and associated pyroxenites from the remote, difficultly accessible and poorly studied Beni Bousera peridotite massif.

2.3. Organization of the Thesis

The present work is subdivided into three parts:

PART I contains some introductory concepts relevant for the present study. In the **Introduction (Chapter 1)**, we summarized some basic knowledge concerning the static strength of the lithosphere and the dynamic behavior of a model continental lithosphere in extensional settings, with emphasis on the lithospheric mantle. We also briefly recalled the high-temperature deformation mechanisms of crystals, with particular emphasis on olivine, which is the most abundant mineral in the upper mantle. The statement of the studied question and the presentation of the selected work program **(Chapter 2)** is followed by the description of the **Methodology (Chapter 3)**, highlighting the multi-disciplinary and multi-scale approach used in the present work, involving field mapping, microstructures analysis (grain size analysis), measurement of crystal orientation data (SEM-EBSD), mineral chemistry (EPMA), thermodynamic calculations (conventional) and modeling (Perple_X) and whole rock (XRF) geochemistry. Because of their importance for the interpretation of the evolution of deformation conditions and relative novelty of the technique, most of this work involves, special attention has been paid regarding the presentation of crystal preferred orientation data acquisition and treatment.

PART II contains the **Results** from this study and is subdivided in two chapters.

- **Chapter 4** is a detailed study of the **deformation processes of a set of 12 pyroxenite samples** from various tectono-metamorphic domains of the Beni Bousera massif. Although pyroxenite is globally a minor constituent in the upper mantle, their mafic composition allows more accurate P-T estimates than ultramafic compositions. Moreover, little is known on the deformation processes of these rocks under lithospheric mantle conditions that locally, may constitute up to 50% of an outcrop section. We couple microstructural observations, crystal preferred orientations (CPO) measurements, conventional thermobarometric calculations coupled with thermodynamic modelling using Perple_X to unravel the P-T conditions of deformation. This chapter, published in *Journal of Structural Geology,* forms the basis to constrain the synkinematic P-T conditions in Beni Bousera peridotites.
- **Chapter 5** deals with the early thinning from garnet- to spinel lherzolite facies conditions of the subcontinental mantle. This chapter aims to shed light on the primary objective of the present work, i.e. **integrating the kinematics at the scale of the Beni Bousera massif with the deformation processes and conditions recorded in peridotites and pyroxenites**. We synthetize our results and interpretations from this chapter and chapter 3 in a comprehensive model and discuss the implications for the early exhumation of subcontinental lithospheric mantle. This chapter has been submitted to *Journal of Petrology* and is currently under review.
- **Chapter 6** contains a **co-authored article** in collaboration with other researchers from the University of Granada. It is related to the latest stages of exhumation of the subcontinental mantle, i.e. from spinel- to plagioclase lherzolite facies conditions and subsequent crustal emplacement in the crust. This study is based on detailed structural mapping in the Ronda massif (southern Spain).

PART III

- **Chapter 7** synthetizes the main **conclusions and future perspectives** from this study, both in English and Spanish.

PART IV

- **Chapter 8** contains the **references** cited in the present work

PART V

- **Chapter 9** contains synthetic tables of field structural data and sampling
- **Chapters 10, 11 and 12** list the microstructural and CPO characteristics, the mineral major element compositions and the calculated temperatures respectively of peridotite samples described in *chapter 5,*
- **Chapter 13** is *a compilation of s*ynthetic **EBSD data sheets** of each analyzed peridotite samples.

3. Methodology

3.1. From crystal to plate

To understand large scale geodynamic processes, be it by numerical simulations (e.g. Agrusta et al., submitted; Li et al., 2011, 2012; Rolf & Tackley, 2012; Rolf et al., accepted; Thielman & Kaus, submitted) or seismic anisotropy (e.g. Di Leo et al., 2012), huge scale jumps are made between crystal-scale rheological properties and plate- or even Earth-scale geodynamics. In this thesis, additionally to gathering new data at the crystal scale, we also contribute to the bridging of plate-scale processes by observations at intermediate scales, i.e. hand sample/outcrop-scale and kilometer-scale integration of these data over the whole Beni Bousera massif (Fig. 3-1).

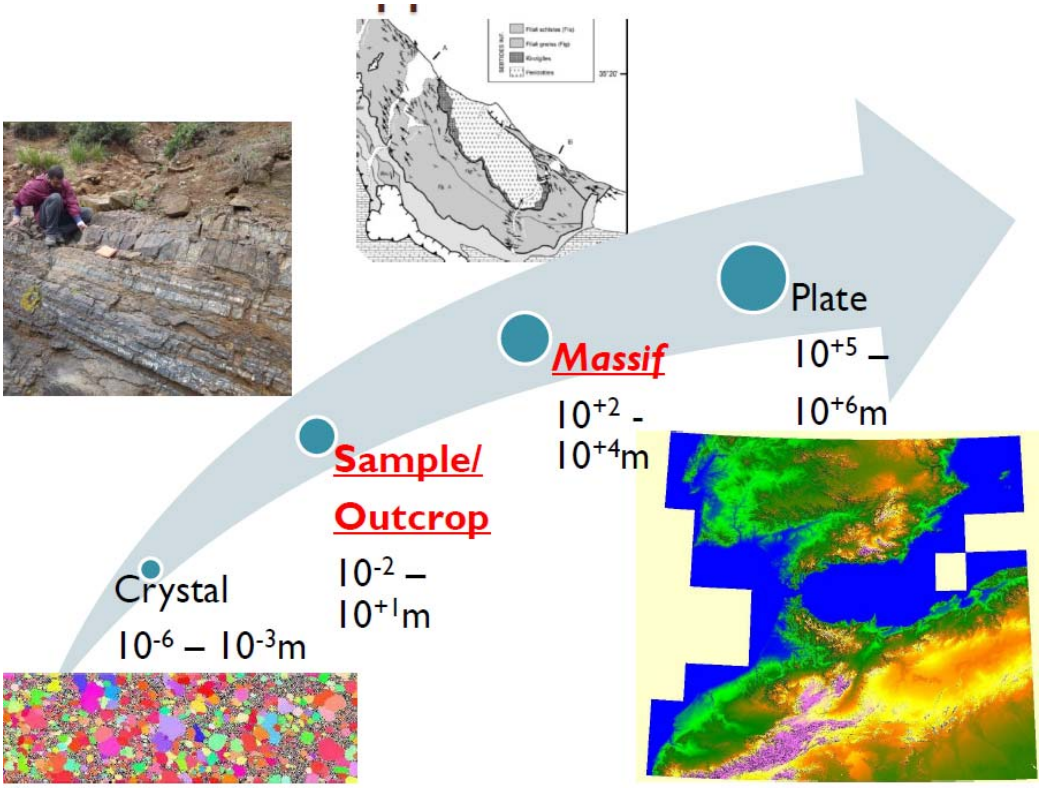

Figure 3-1. Cartoon illustrating the various scales of observations in this study and the importance of field observations as a linking bridge between the crystal- and plate scales.

3.2. Field work and sampling

Figure 3-2. Oriented sampling Beni Bousera "Oueds" and structural mapping

This thesis is based on the study of the Beni Bousera peridotite massif located in the Rif mountains of northern Morocco. Not less than 4 campaigns of 10-15 days each (15-30 Nov. 2009; 07-17 Apr., 20-29 Sept. & 22-28 Nov. 2010) were conducted in the study area. Field observations and sampling were carried out in a highly collaborative international framework involving researchers and students from several institutions: the CSIC-IACT (Granada, Spain), the University of Montpellier (France), the University of Tetuan and the University of Rabat (Morocco). On-site logisitics were extremely facilitated by our colleagues of the University of Tetuan (Dr. Kamal Targuisti, Dr. Isma Amri).

Field work can be synthesized in 3 main objectives:

i) mapping of peridotites and pyroxenites petrological and metamorphic facies,

ii) measuring meso- and macroscopic structures (foliations, layerings, lineations, fold axes, faults). These measurements were gathered using a Topochaix (see Fig. 3-2) or Freiberg compass. A synthetic table of ductile structures is given in the Appendices (Chapter 9).

iii) Systematic oriented sampling of peridotites and pyroxenites with a step of the order of ~10-100 m depending of outcrop availability. A total of 275 oriented samples of around 2-5 kg each to ensure a homogenous and representative bulk rock analysis were extracted (see Figs. 3-2 and 3-4). From these 275 oriented hand samples 411 oriented thin sections were later produced.

3.2.1. Topographic base map from Digital Elevation Model

Many maps available for the Rif (topographical, geological etc.) are based on the sequent conical "Lambert Nord-Maroc" projection, using the reference ellipsoid of Clarke (1880) and the reference geodetic datum of "Merchich". In this configuration, the longitudes are counted in *grades*, from the *Moroccan reference meridian*, as follows:

0 grades (Morocco) = -6 grades (Greenwich) = -5°24'00" (Greenwich)

This leads to significant difficulties to overlay GPS-acquired positions on top of the available maps. It is worth noting that because of the unawareness of this particularity, many (published) maps are distorted (they appear as stretched horizontally). To solve this problem, 2 options are possible:

i) In any GIS-type software, manually reconfigure the ellipsoid parameters[2], which is not straightforward for a lambda GIS-software user,

ii) Apply a systematic transformation to the GPS-position (see footnote). This results in the introduction of an additional systematic error in the x, y and z coordinates to the precision of the points, albeit this error is relatively small (a few meters).

Instead, we eventually created our own topographic maps by using free Digital Elevation Models (DEM) data (see below). DEM were processed by the International Centre for Tropical Agriculture (CIAT, http://srtm.csi.cgiar.org) from original SRTM dataset (Farr et al., 2007) distributed by the USGS/NASA (http://www2.jpl.nasa.gov/srtm/cbanddataproducts.html) to provide seamless continuous topography surfaces (Jarvis et al., 2008). Areas with regions of no data in the original SRTM data have been filled using interpolation methods described by Reuter et al. (2007). The data are distributed in several formats ARC GRID, ARC ASCII and Geotiff, in decimal degrees and datum WGS84.

Global Mapper 11 software was used to open ARC ASCII (".asc") files and plot the area in square UTM coordinates. Elevation data transformed in UTM coordinates were exported in Surfer grid (ASCII format). *Surfer 8* software enabled enhanced graphical processing of the topography.

3.2.2. Location and geomorphology of the study area

The study area is located southeast of the nearest BouAhmed village. The ~70 km^2 study area is elongated along a N140 - 150 axis roughly parallel to the shore, is ~15 km long and ~5 km in width. Part of its northern side is cut by the shores of the Alboran Sea and lies thus beneath present day sea level. The topography is very steep (Fig. 3-3) and strongly influences the accessibility of the area and thus the sampling procedure; the highest peak near the village of Azarhar reaches 1194 m only 5 km away in horizontal distance from the sea. From NW to SE the massif is cut by 5 roughly parallel N30 – N40 striking valleys or "oueds": O. Amaziten, O. Yahia Aârab, O. Jenane Nich, O. Aârkoub and O. M'Ter. To the South, O. Jouj (parallel to the elongation of the massif) links the highest peak with O. M'Ter.

[2] For more information on the transformation parameters between WGS84 and Merchich systems, please refer to the French National Geographic Institute (IGN) website: http://geodesie.ign.fr/contenu/fichiers/Systeme_Algerie_Tunisie_Maroc.pdf

Because the valleys crosscut the whole massif nearly perpendicularly and they are characterized by quasi-continuous and fresh outcrops, we mainly focused our field work in these areas. Figure 3-4 shows the locations of the 275 oriented hand samples collected.

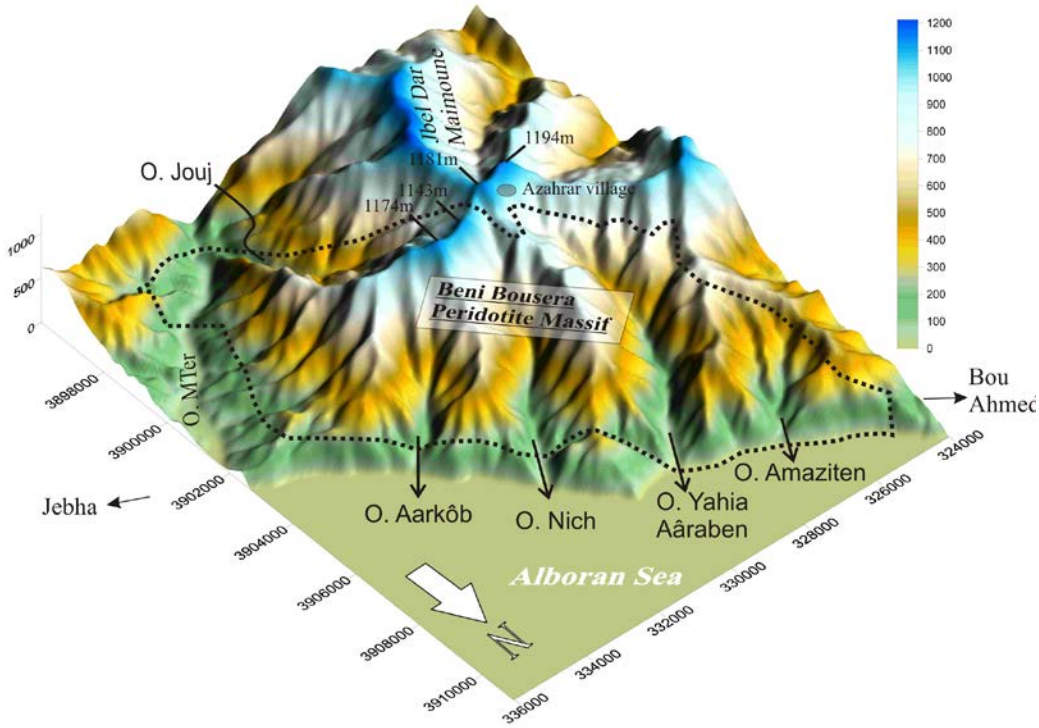

Figure 3-3. (a) The Beni Bousera peridotite massif crosscut by the main valleys or “oueds”.

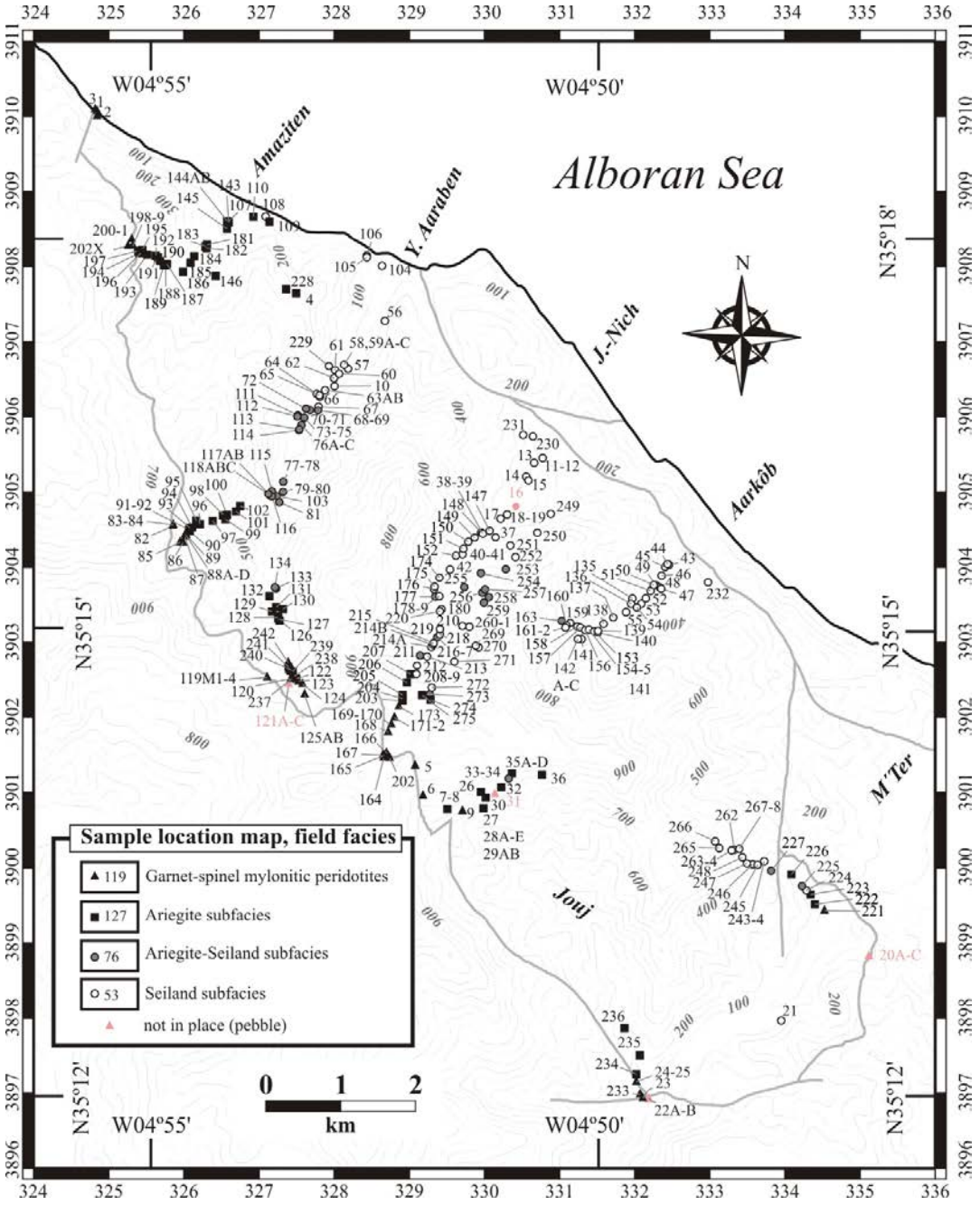

Figure 3-4. (a) Map showing the coverage of oriented sampling in Beni Bousera. All the main valleys have been sampled with a spacing less than 100-200m.

3.2.3. Calculating distances from the contact

3.2.3.1. - Assigning an altitude to each station

To calculate the altitude of each samples, we used their UTM coordinates as a Cartesian reference frame (Fig. 3-5). For the (x, y)-coordinates we simply used the UTM values (N, E) given by the GPS. Because of the variable precision of the altitude value of the GPS, we assigned the altitude corresponding to the DEM-values at the given (x, y)-position. In *Global Mapper 11* software, this can be done relatively easily by importing a text-file containing (x, y) coordinates of samples over the

DEM. Then select all the points, right-click and choose "assign altitude from DEM". This generates an output text-file containing the (x, y, z) coordinates of the points.

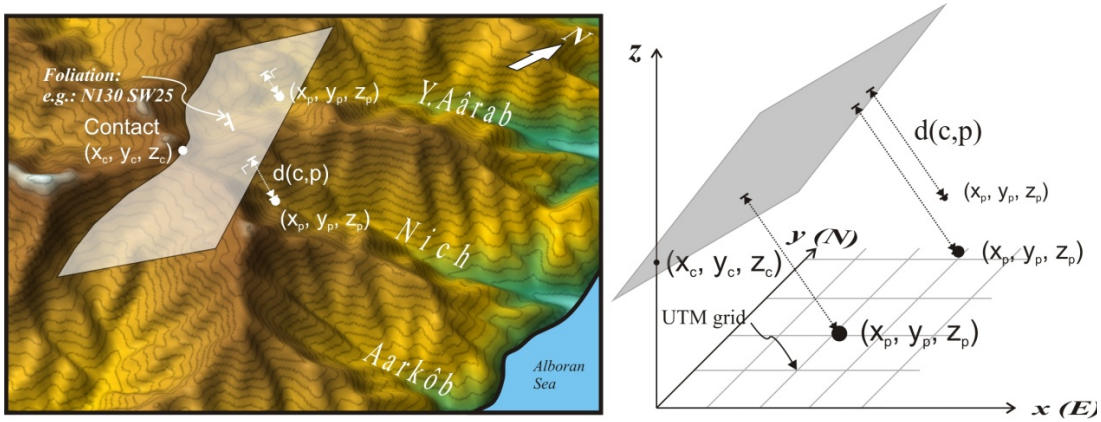

Figure 3-5. Cartoon illustrating the plane defining the contact between peridotites and the crustal units (left) and how UTM coordinates were used to solve the distance plane-sample distances analytically (right).

3.2.3.2. - Analytical solving of plane (foliation) – point distance

In an orthonormal reference frame, the general equation of a plane containing a given point A with coordinates (x_A, y_A, z_A) is given by:

$$a(x - x_A) + b(y - y_A) + c(z - z_A) = 0,$$

where $(\vec{a}, \vec{b}, \vec{c})$ are the coordinates of the normal-vector $\vec{n}$ of the plane.

In our particular case, the point A corresponds to the observed contact between peridotites and crustal units. It is defined by (x_C, y_C, z_C) where (x_C, y_C) are the UTM-coordinates and z_C the previously assigned altitude. Thus, the equation of the plane containing the contact in a Cartesian reference frame is:

$$P_{contact} \equiv \vec{a}(x - x_C) + \vec{b}(y - y_C) + \vec{c}(z - z_C) = 0$$

We now need to extract the values (a, b, c) of the normal-vector $\vec{n}$ from our structural measurements in spherical (geological) coordinates (θ, φ) and transform them into a Cartesian coordinates system (a, b, c). For this purpose we first extract the angular values of the normal-vector from the values of the plane in strike and dip notation (right-hand convention):

$$\begin{cases} \theta = strike - 90º \\ \varphi = 90º - dip \end{cases}$$

Then, the transformation from spherical to Cartesian coordinates is given by:

$$\begin{cases} a = \cos\varphi \ \sin\theta \\ b = \cos\varphi \ \cos\theta \\ c = -\sin\varphi \end{cases}$$

The resulting equation of the plane can be written as:

$$ax + by + cz + (-ax_C - by_C - cz_C) = 0, \text{ with}$$

$$(-ax_C - by_C - cz_C) = d,$$

so that the distance D from the contact of a point p with coordinates (x_p, y_p, z_p) can be calculated as:

$$D = \frac{\|ax_p + by_p + cz_p + d\|}{\sqrt{a^2 + b^2 + c^2}}$$

Because the contact appears at highly variable altitude atop of the different valleys, and because the values of strike and dip of the foliations differ due to faulting at the contact, we used an average foliation that was most representative of the general structural trend around this particular point.

Valley, location	x_c (m)	y_c **(m)**	y_c **(m)**	**Mean foliation /** (θ, φ)
Beach	324727	3910165	1	N100 S20 / (10, 70)
Amaziten	325308	3908403	407	N155 SW25 / (65, 65)
Yahia 1	325674	3904914	722	N160 SW15 / (70, 75)
Yahia 2	327108	3902567	743	N122 SW22 / (32, 68)
Nich & Aarkôb	328786	390523	1028	N093 S19 / (3, 71)
Azarhar	328999	3901421	1034	N166 SW12 / (76, 78)
Jouj	332105	3897043	119	N119 SW38 / (29, 52)
M'Ter	334524	3899525	49	N356 E62 / (266, 28)

3.3. Preparation of geographically-oriented thin sections

To be able to check field measurements of foliations and lineations, we systematically compared them with both shape and crystal preferred orientation of olivine and pyroxenes. Because these minerals only exhibit few slip systems with highly variable strengths, the dominant slip direction tends to align parallel to the shear direction and the slip plane-normal with the shear plane-normal (or foliation) in either simple or pure shear deformation (Zhang & Karato, 1995; Tommasi et al., 1999; Bystricky et al., 2000).

Most thin sections were cut in a geographic reference frame, i.e. in a vertical N-S plane, with their long axis pointing towards the North, pasted either on the left (West) or right (East) slab-face when looking to the North. In either case, the letters "W" or "E" have been added to the sample name to retrieve this information at any time. Reorientation of the hand sample before slab sectioning, reorientation of the slab before final cutting and cleaning and sectioning of samples for bulk geochemistry with a diamond saw were done by the author.

Part of the procedure to generate geographically oriented thin sections is shown in the cartoon of Fig. 3-6. Oriented samples from the field were first re-oriented in the laboratory. For this purpose,

very simple material was used, i.e. an empty carton box of Belgian chocolate as a support and some plasticine.

i) Knead a fist-size ball of plasticine in your hands during several minutes until it gets soft enough. Put it on the carton support.

ii) Take the oriented sample and squeeze it onto the plasticine so that it is able to "stand on its own". Check all the horizontals of the sample with a spirit level and "adapt" progressively the orientation of the sample. Repeat operation until all horizontals are horizontal. This may take a while as adapting one horizontal often results in the perturbation of the others.

iii) With an alcohol marker, draw several parallel traces of vertical planes that pass through the N-S direction. Use the spirit level vertically to guide your tracings onto the more vertical sides of the samples, with the marker always pointing in the N-S direction. This is the trickiest part as marking the sample may result in moving the samples and hence restart operations 1) and 2).

iv) Once done, saw the sample in 2 through one of the marked traces. One half is for the thin sections; the other may be used for other types of analyses, such as WR-geochemistry.

v) To help us cutting well parallel to the first plane and guide our movement smoothly on the sawing surface, we will first saw an additional perpendicular plane to the former. Put the sample face-down on the cut face and saw the perpendicular plane.

vi) Flip the sample onto the newly cut surface. Take a set square and stall one side with the NS-plane and the other with the edge of the sawing table. In this way, a slab with perfectly parallel sides will be cut.

Do not forget to carefully mark the N-position on each newly cut part of the samples. The sawing itself and the water of the saw tend to erase all the marked orientations.

vii) Dry the slab and the remaining part(s) of the sample associated with the slab. Mark on both faces of the slab which is the East- and which is the West-facing one.

viii) Re-put the slab and its associated part again together to "fit". Carefully hold them both together and squeeze them back into the plasticine. Reiterate 1) and 2).

ix) Mark carefully the horizontal on one of the faces of the slab with the spirit level, and then draw the rectangular thin section area(s) with the long side parallel to the horizontal. Mark the North with an arrow and name thin section area with "E" or "W" at the end, depending on which face of the slab has been used.

Thin sections for EBSD analysis were carefully polished at CSIC-IACT (Armilla, Spain). After two 90 min-long standard polishing with respectively 6 and 3 mm polycrystalline diamond suspension thin sections were polished for 1-2 h with 1 mm polycrystalline diamond suspension at 180 rpm. The last step of the procedure consisted of a chemical polish using colloidal silica for 45 min at 110e135 rpm.

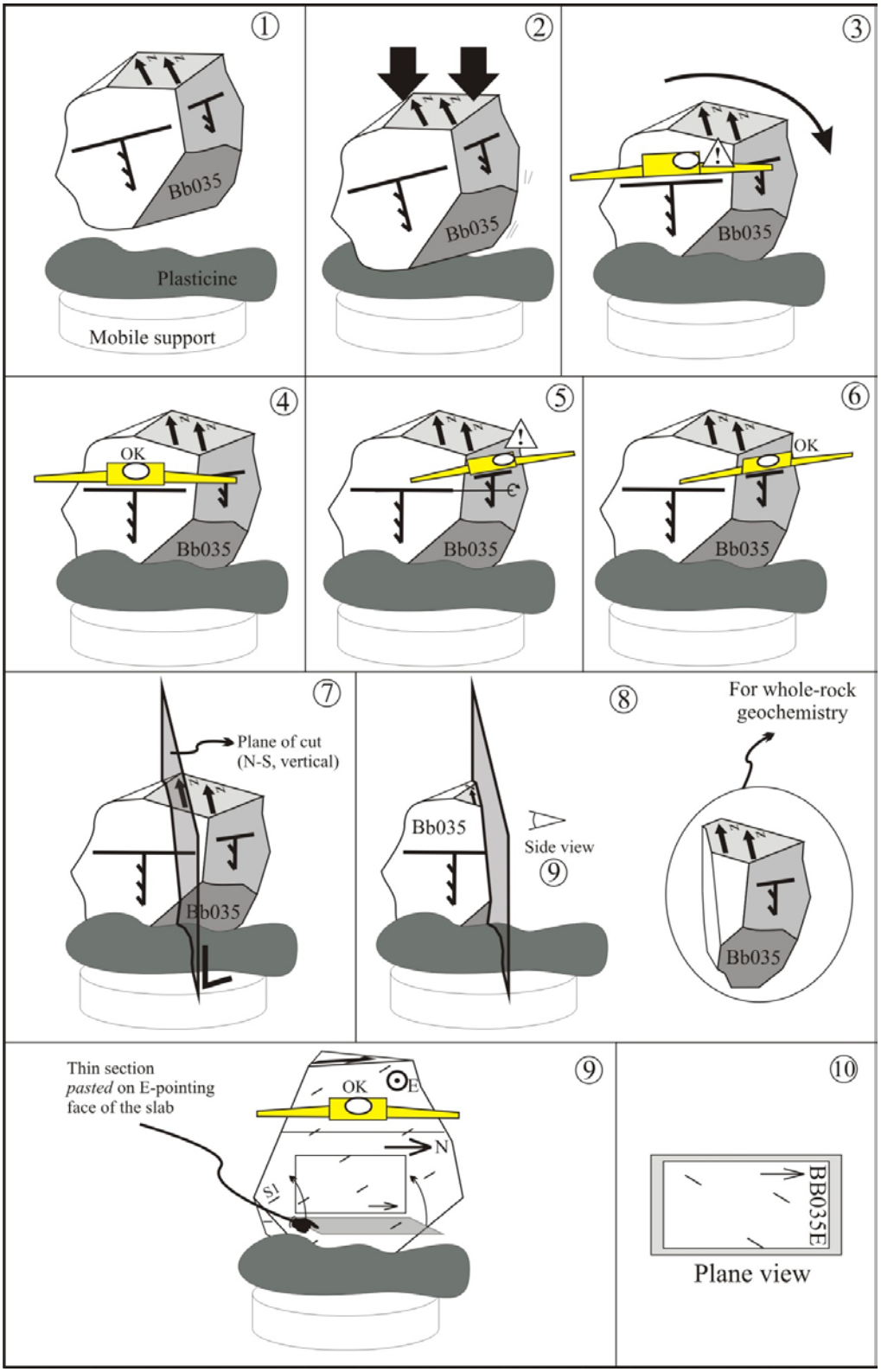

Figure 3-6. Cartoon illustrating the different steps during the procedure for cutting geographically oriented slabs and thin sections. See text for further explanation.

3.4. Electron Backscattered diffraction (EBSD) – SEM

3.4.1. Data acquisition

Crystal preferred orientations (CPO) of olivine (forsterite), orthopyroxene (enstatite), clinopyroxene (diopside), garnet (pyrope) and spinel (chromite) of peridotites and pyroxenites were measured by indexing backscattered patterns. These so-called "Kikuchi" patterns (see Fig. 3-7) are generated by interaction of high-energy electrons of an electron beam with the surface of a sample that is tilted at 70° with respect to the incident beam (Prior et al., 1999).

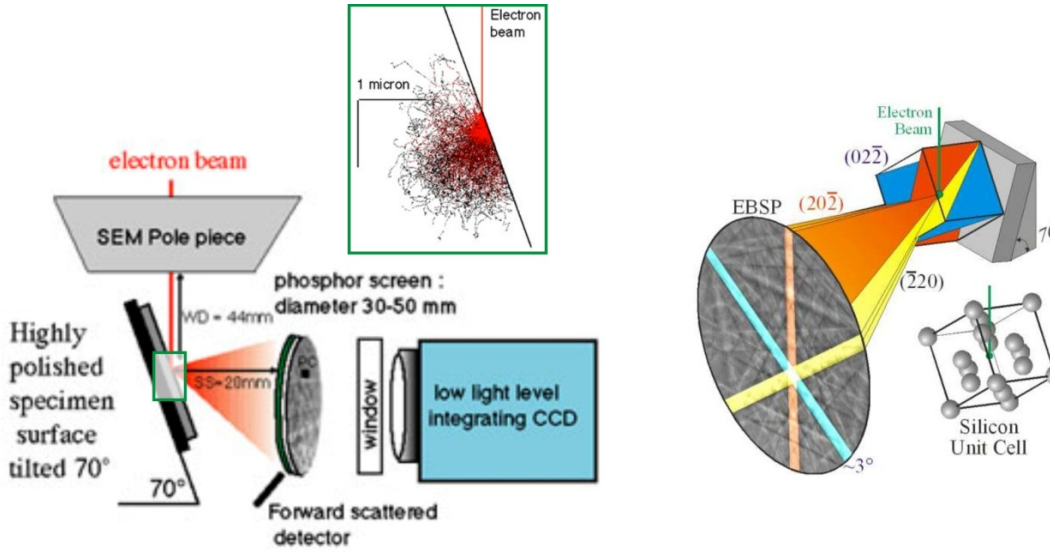

Figure 3-7. (a) Illustration of the Electron Backscattered Diffraction technique. The sample is tilted at 70° from the incident beam. Electron backscaterred Patterns (EBSP) and associated Kikuchi Bands.

EBSD patterns (EBSP) were acquired using the SEM-EBSD systems at Géosciences Montpellier (CNRS-Université de Montpellier 2, France). Indexing was performed by automatic EBSD mapping of whole thin sections on a JEOL JSM 5600, covered by a rectangular grid with regular step size varying from 5 – 100 µm depending on average grain size of the samples. For high-resolution mapping of selected areas, the CamScan X5000FE CrystalProbe (Fig. 3-8) was used in a low vacuum mode and a grid step size of 5 µm. We used an acceleration voltage of 17 kV and a working distance of 23 mm.

Figure 3-8. JEOL JSM 5600 (left) and CamScan X5000FE CrystalProbe facilities et Geosciences Montpellier (France).

The *CHANNEL 5* software package from HKL Technology coupled with the instruments enables automatic indexing of Kikuchi patterns and acquisition of lattice orientation using the Hough transform and five to seven detected band edges and their zone axes in the diffraction pattern (Fig. 3-9).

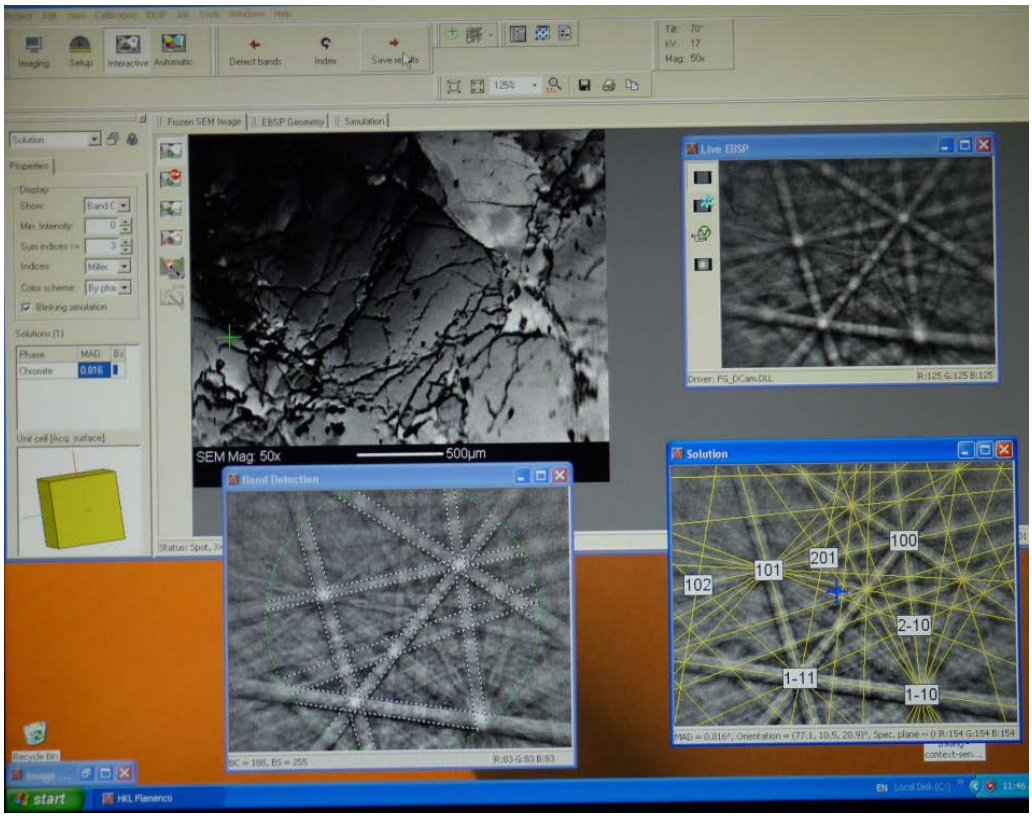

Figure 3-9. Screenshot of CHANNEL 5 software during acquisition of EBSD patterns. Top left frame is sample surface backscattered image. Bottom right shows indexing Kikuchi patterns using band centers for chromite.

Detailed parameters and acquisition settings are given in the following table:

Lattice parameters

Mineral	HKL phase name	Unit cell parameters		
		α; β; γ	a; b; c	Laue Group
Olivine	Forsterite	90; 90; 90	4.756; 10.207; 5.98	mmm
Orthopyroxene	Enstatite Opx AV77	90; 90; 90	18.2406; 8.8302; 5.1852	mmm
Clinopyroxene	Diopside $CaMgSi_2O6$	90; 105.63; 90	9.746; 8.99; 5.251	2/m
Spinel	Chromite	90; 90; 90	8.378; 8.378; 8.378	m3m
Garnet	Pyrope 11	90; 90; 90	11.459; 11.459; 11.459	m3m

Analytical parameters

Binning	4x4
Gain	low
Band detection criterion	edges
Nb. of frames averaged	3
Hough resolution	75
Numbe of bands	min=5, max=7
Number of reflectors	50

3.4.2. Post-acquisition treatment

In order to increase the indexing rate, we performed the following procedure:

i) Filling non-indexed pixels that have up to 8 identical neighbours with the same orientation.
ii) Iterating this operation for respectively 7, 6 and 5 identical neighbours.
iii) Identifying the grains that present less than 15° of internal misorientation.
iv) For olivine, searching and correcting for systematic indexing errors due to the olivine hexagonal pseudosymmetry, which results in similar diffraction patterns in the case the orientations differ by a rotation of 60° around [100].

In both pyroxenites and peridotites, systematic misindexing of orthopyroxene as clinopyroxene was common and particularly affected the study of the pyroxenites (chapter 4). Therefore, manual

post-acquisition treatment was necessary; the *Channel 5* software enables to assign a new phase (e.g. orthopyroxene instead of clinopyroxene) to a subset of manually selected misindexed pixels. Although the lattice parameters differ from one mineral to another, *Channel 5* enables to retrieve the orientation of the Euler angles (see below) by normalizing the unit cell parameters.

3.5. Crystal Preferred Orientations

3.5.1. Theoretical background

3.5.1.1. - Orientation distribution and Euler angles

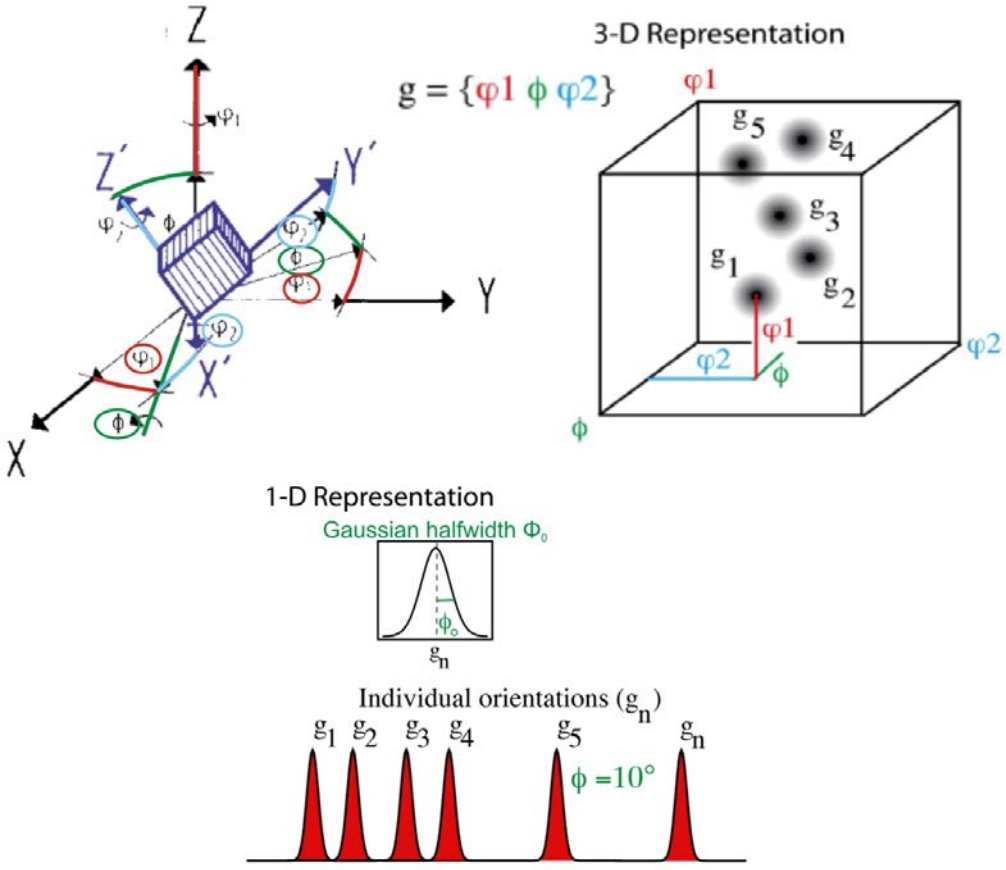

Figure 3-10. Graphical representation of Euler angles (top left), orientation distribution function *f(g)* (top right) and Gaussian halfwidth (modified from D. Mainprice, pers. Comm..)

The orientation of a pixel (or grain) with respect to the external reference frame (in our case the sample) is described by a rotation matrix g. For practical reasons, Bunge (1982) described this rotation matrix as a triplet of Euler angles $g(\varphi_1, \phi, \varphi_2)$ that define the rotations in Euler space (or orientation space) allowing for coincidence between crystallographic and external reference frames (Fig. 3-10). The distribution of g in Euler space is given by a function $f(g)$, called the Orientation Distribution Function (ODF).

The contribution of an orientation g in the whole volume of orientation space (V) is given by the volume fraction $\left(\frac{dV_g}{V}\right)$ in the interval $[g,\ (g+dg)]$, so that:

$$\frac{dV_g}{V} = f(g).dg$$
$$\Leftrightarrow \frac{1}{V}\int dV_g = \int f(g).dg$$
$$\Rightarrow \frac{\Delta V_g}{\mathrm{V}} = \int f(g).dg$$

The infinitesimal volume of integration dg is given by:

$$dg = {}^{1}/_{8}\,\pi^2 sin\Phi d\psi_1 d\Phi d\varphi_2$$

In practice, $f(g)$ is discretized into a series of spherical harmonics using the method of Bunge (1982):

$$f(g) = \sum_{l=0}^{L_{max}} \sum_{m=1}^{M(l)} \sum_{n=-1}^{l} C_i^{mn} T_l^{mn}(g)$$

where C_i^{mn} are the coefficients of the series development of $f(g)$, T_l^{mn} are the generalized spherical harmonic functions, $M(l)$ is the number of linearly independent spherical harmonics and L_{max} is the maximum degree used in the expansion, typically $L_{max} = 22$ (Mainprice & Silver, 1993).

Then we arbitrarily discretize the Euler space in bins of 1º. Within one of this "Euler-box", we assign a Gaussian probability function centered on the discrete data points. The Gaussian half-width of this function is defined by the angular distance for which the probability decreases by a factor $1/e$, arbitrarily chosen at 10º (see review in Skemer et al., 2005).

3.5.1.2. - Pole figure density

The density P that is measured in a direction y in specimen coordinates, and parallel to the normal of a low-index lattice plane with Miller indices $[hkl]$ (see Fig. 3-11), is formulated as follows (Ben Ismaël & Mainiprice, 1998):

$$P_{hkl}(y) = \frac{1}{2\pi}\int_{hkl||y} f(g)d\chi$$

With $d\chi$ given by:

$$d\chi = \frac{\pi}{4} sin\alpha\ d\alpha\ d\beta$$

and where $\chi(\alpha,\beta)$ is the angle in spherical coordinates of [hkl] in specimen reference frame and $d\chi$ is a unit element of solid angle in the unit lower hemisphere of the stereographic projection. The angle α is measured from the center and β is the azimuth. To obtain a representative CPO of a rock, at least 100 - 150 grains for each phase should be measured (Ben Ismaël & Mainprice, 1998).

3.5.1.3. - Fabric strength

In order to quantify the degree of crystal preferred orientation of a given mineral, we used the dimensionless *J*-index (Bunge, 1982). It is calculated as follows:

$$J = \int f(g)^2 dg$$

The J-index has a theoretical value of 1 for a completely random fabric and ∞ for a single crystal. Practically, it does not exceed a value of 250 due to the truncation of the expanded spherical harmonics (see above).

Skemer et al. (2005) claimed that the J-index is an ambiguous indicator of the fabric strength due to the arbitrary choices made related to the discretization of the Euler space and the cutting of the expanded ODF into spherical harmonics at degree 22. They proposed the *M*-index as an alternative texture-index. However, recent studies showed the correlation between these indexes for olivine (Soustelle et al., 2010; Kusbach et al., 2012) and clinopyroxene and garnet (Muramoto et al., 2011). We thus preferred to use the *J*-index, which is most commonly used, not only in geology but also in material sciences.

pfJ gives the degree of crystal preferred orientation for each of the crystallographic axes (see Fig. 3-11), and is given by:

$$pfJ = \int P_{hkl}(\alpha, \beta)^2 d\omega$$

with $d\omega$ given by:

$$d\omega = \frac{\pi}{2} sin\alpha \; d\alpha \; d\beta$$

3.5.1.4. - Fabric geometry

Besides the strength of a CPO, one may also investigate its geometry (or "symmetry"). Vollmer (1990) defined three indices characterizing the geometry of the CPO: Point (P), Girdle (G) and Random (R) (see bottom of Fig. 3-7a). These are calculated from the eigenvalues $\lambda_1, \lambda_2, \lambda_3$ ($\lambda_1 \geq \lambda_2 \geq \lambda_3$ and $\lambda_1 + \lambda_2 + \lambda_3 = 1$) of the normalized orientation matrix for each principal crystallographic axis (Woodcock & Naylor, 1983; Humbert et al., 1996):

$$\begin{cases} P = \lambda_1 - \lambda_3 \\ G = 2 * (\lambda_2 - \lambda_3) \\ R = 3 * \lambda_3 \end{cases}$$

With the property that $P + G + R = 1$

Fig. 3-11a illustrates well these parameters: [100]- and [001]-axes have large G-values as they show well-developed girdles and [010]-axes show very strong P-values that characterizes its strong clustering around the maximum density. All the axes, have, however, low R-values as they all show a high degree of preferred orientation.

Pole figures were plotted using average Euler angles values for each grain instead of plotting all the raw data. This avoids overrepresentation of large grains (e.g., porphyroclasts in a fine-grained matrix).

3.5.2. Reference frames and rotations

Sample coordinates only define the position of the sample in the microscope (U-stage optical microscope, SEM-EBSD). The foliation and the lineation have on their turn a certain orientation with respect to the sample. In geosciences, a rectangular thin section (~4.5cm long, ~2.5cm wide) is the most common type of support. Hence, its position in the microscope is solely defined by the orientation of its long (or short) axis. In this study, thin sections were always inserted with their long axis ("X-stage" or "Xs") parallel to the sample holder long axis and the North (arrow on thin section) pointing towards the East in map view (Xs=90°).

The geometrical relationship of CPO with macroscopic shear plane and direction is generally used to constrain the active slip systems in ductilely deformed rock-forming minerals. For this reason, in Earth Sciences samples are generally cut in a plane perpendicular to the foliation and parallel to the lineation that defines the **structural reference frame**. This makes it possible to plot pole figure densities in XZ coordinates without any additional rotation. This is particularly true for mantle xenoliths that have lost any orientation with respect to their "host rock" (i.e. the mantle) when brought to the surface during the volcanic eruption.

On the other hand, additional valuable structural information may be gathered from samples from orogenic peridotite massifs such as Beni Bousera when cut in the **geographical reference frame**. Indeed, when sampled over the whole massif, we may then map kilometer scale variations of the orientations of mineral crystallographic axes, and hence get a glimpse of the evolution of crystal-scale deformation that start to be representative of orogenic –scale flow processes. For this purpose, the pole figures must be rotated from the sample reference frame back to the geographic by 2 successive rotations: one around a vertical axis, and another around a horizontal one (Fig. XXb). Rotating and plotting CPO were performed with the *Fortran* based programs *ROTctf4_PC* and *PFCH5,* respectively (Mainprice, 1990, 2007; Mainprice & Humbert, 1994).

The rotations must be handled very carefully: the sense of rotation (clockwise [-] or anticlockwise [+]) is considered looking towards the center of the hemisphere and the dip of the rotation axis is always negative when working in a lower hemisphere, which is usually the case for geologists. For instance, when rotating around a horizontal axis, the latter must have a dip of – 0°.

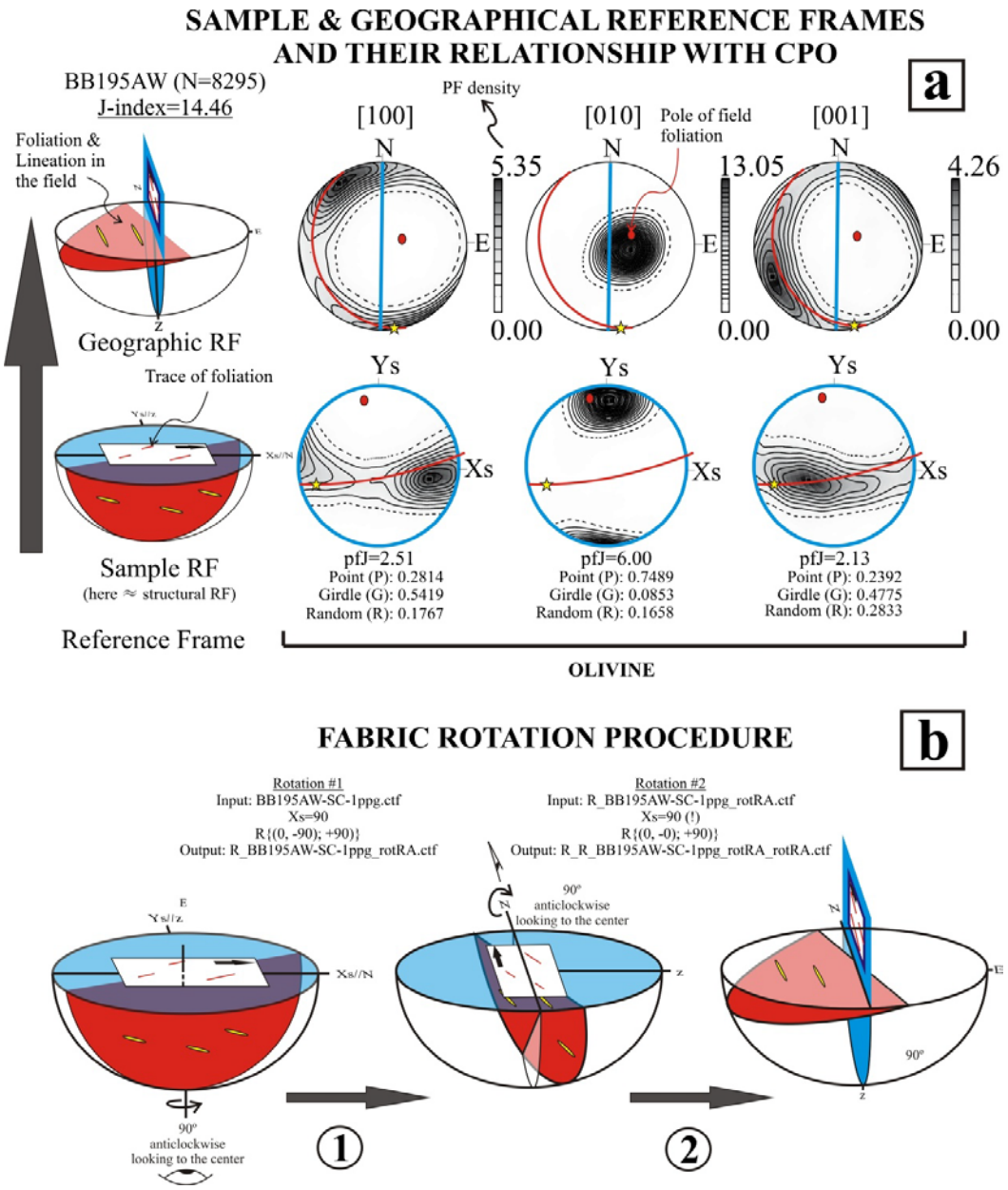

Figure 3-7. (a) Rotating fabrics from sample to geographic reference frames. Top: example from sample BB195AW, plotted before rotation (sample RF) and after rotation procedure (Geographic RF). (b) Rotation procedure for a West-pasted thin section.

3.5.3. Semi-automated method for plotting large numbers of files

Because of the large number of samples analyzed for olivine, orthopyroxene, clinopyroxene, spinel and garnet CPO in this study (>100 peridotites, >15 pyroxenites), we developed a semi-automated procedure first for rotating the measurements, then for plotting CPO and finally for calculating J-indexes, all using raw and "one point per grain" datasets.

The programs are based upon multiple answers questionnaires. Typing one of the options automatically brings the user to the next question. The default answer, denoted by a star, may be chosen just by typing "*0*". We created a text-file containing all the answers that the programs can automatically read (e.g. "*inputPF.txt*", Fig. 3-12). In the following example we show how such a file looks like for input into the program *PFch5.exe* (i.e. plotting pole figures). One "run" corresponds to the plotting of 1 mineral of 1 sample. This series of answers is then "copy-pasted" below one another and only the part corresponding to the nature of the mineral and its lattice parameters must be changed (Olivine=2, 1; orthopyroxene=3, 1; clinopyroxene = 4, 4; spinel=5, 5; garnet= 6, 5). The whole set of 4 or 5 runs (depending on the presence of garnet in the sample) is then copy-pasted for each sample, and the file name is changed in each set.

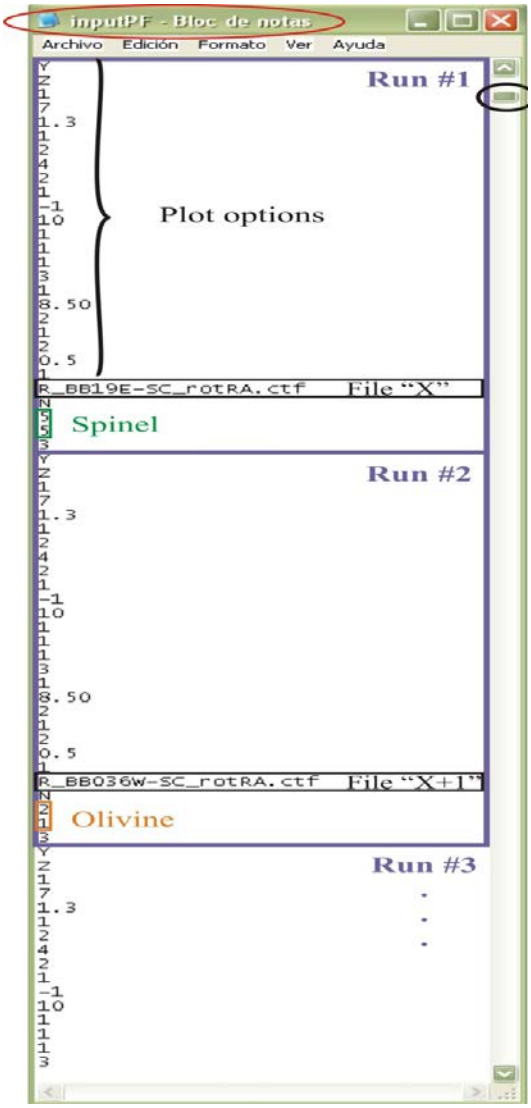

Figure 3-12. Typical batch file for semi-automated plotting of EBSD data. Each "Run" corresponds to a given mineral for a given sample.

The batch-file, the application and all the used data files must be located in the same folder. Open the "Command" window and type the following command: *PFch5.exe<inputPF.txt*

An absolutely similar procedure may be used for rotating large numbers of files. However, calculating J-indexes with *SuperJctfPC.exe* (Mainprice, 1990; ftp://www.gm.univ-montp2.fr/mainprice//CareWare_Unicef_Programs/) requires a slightly different procedure, because the program automatically shuts down after one run without asking the user whether he/she wants to continue or not. To get around this:

i. Create a text-file for each sample (e.g. "BB001W.txt", … , "BB272E.txt") containing the desired options in *SuperJctfPC.exe*

ii. Put all these files in a folder containing *SuperJctfPC.exe.*

iii. In a new text-file, type the command line to launch *SuperJctfPC.exe* for each sample

iv. Save this file a "batch"-file by adding the extension ".bat" and selecting "All files"-type, instead of "Text document":

v. In the Command window, run Super_J.bat

3.6. Texture analysis

3.6.1. Microstructural maps

The Channel 5 software offers an enormous amount of possible EBSD data processing, including plotting microstructural maps, misorientation angle histograms, pole figures, inverse pole figures in crystal coordinates, colored orientation maps in different reference frames (sample, crystal or a particular crystallographic axis of interest). All of them were used for the analysis of deformation processes in pyroxenites in chapter 4.

Much information on the deformation history of mantle rocks can be gathered through the study of their texture or microstructure (e.g. Mercier & Nicolas, 1975). The *Channel 5* software enables one to produce rapidly high quality microstructural maps by drawing phase-, grain- and sub-grain boundaries. Commonly, misorientation values of >15º and >3º respectively are chosen for grain- and sub-grain boundaries. The description of Beni Bousera peridotite microstructures is described in chapter 5.

3.6.2. Grain size analysis

The quantification of a microstructure is of great importance not only in the study of deformed rocks but also in the metallurgy because of the strong dependence between recrystallized grain size (d_s) and flow stress (σ), usually in the form of:

$$d_s = A\sigma^{-k}$$

Where A and k are constants, depending on the nature of the material. Twiss (1977) had addressed this problematic in the late 1970s for metals and ceramics. Later on, several works have provided insight into these relations for olivine (Karato et al., 1980; Van der Wal et al., 1993), quartz (Stipp & Tullis, 2003) and calcite (Schmid et al., 1980; Barnhoorn et al., 2004). However, determining a mean grain size in polymineralic aggregates is not straightforward because of both the usual complexity of grain size and shape distribution, and additionally the reduction of the 3D-distribution in 2D (e.g. Higgins, 1994; Morgan & Jerram, 2006). For trivial distributions such as piled spheres of equal diameter (see Exner, 1972), theoretical correction factors have been derived, but the problem becomes very complex for anisotropic textures depending on the orientation of the sections (Garrido et al., 2001). Berger et al. (2011) compared many methods for estimating grain size distribution and their characterisitic values. Although the used method depends on the scientific question, they suggested that apart from 3D computer tomography, the 2D area-weighted grain size distribution remains the best proxy and concluded that, regardless of the method, all should be better used in comparative studies.

Following this idea in chapter 5, we estimated mean olivine grain sizes as mean 2D equivalent circular diameters ($\bar{d}$) calculated as described in Berger et al. (2011) using the MTEX toolbox (Bachmann et al., 2010):

$$\bar{d} = \frac{w}{\sum_{i=1}^{n_{tot}} A_i} \cdot \sum_{j=1}^{j_{tot}} \left(j \cdot \sum_{i=1}^{i} A_{ji} \right)$$

With w: class width, A_i: area of the ith grain, n_{tot}: total number of measurements and j: the jth class. In chapter 5, $j_{tot} = 50$ for all samples.

Grain size and aspect ratios of olivine in 29 samples distributed along the Aaraben, Aarkôb and J. Nich valleys were obtained using the MTEX software (Hielscher & Schaeben, 2008; Bachmann et al., 2010) from digital EBSD grain boundary maps of peridotite thin sections. Non-indexed areas were automatically filled extrapolating grain neighbours or, in a few instances, manually.

3.7. Wavelength Dispersive Spectroscopy (WDS-) Electron Probe Microanalyses (EPMA)

Mineral contents of major and minor elements were obtained using the following Wavelength Dispersion Sprectroscopy (WDS-) Electron Probe Microanalyses (EPMA). In Chapter III we characterized the chemistry of pyroxenes, garnet, spinel and olivine in pyroxenites deformed under different P-T conditions. In chapter V, mineral compositions were used for geothermometry of peridotites. We used both CAMECA SX-100 from the "Centro de Instrumentacion Científica" (CIC, University of Granada, Spain) and the Service Microsonde Sud-Géosciences Montpellier (CNRS-Université Montpellier II, Montpellier, France).

3.7.1. Principle of the method

Incidence of high-energy electrons with an atom results in both elastic and inelastic interactions. Elastic interactions with the solid generate back-scattered electrons. It has been found experimentally that the fraction η of elastic versus inelastic interactions varies as a function of the atomic number Z. This provides a first order tool to image phases that carry different mean Z values. The brightest phases are thus the heaviest. Backscattered electrons are also used in SEM-EBSD systems. Inelastic interactions are multiple but here we will focus on the X-ray spectrum used in EPMA analysis (Fig. 3-

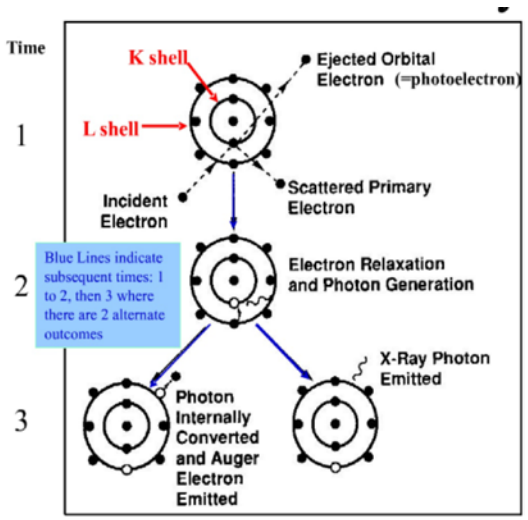

Figure 3-13. Principle of the EPMA.

13; Castaing, 1951). If an incident electron carries enough energy, it may ionize an inner-shell (K-level) electron of an atom. To retrieve a stable energy, an electron from a more external, higher-energy level will "fill the gap". The excess energy ΔE will be either emitted as an X-ray with a characteristic wavelength given by $\lambda = {}^{hc}/_{\Delta E}$ (0.01 – 10 nm) or direct emission of an outer shell or "Auger"-electron. The energy ΔE is correlated to the nature of the atom and increases with Z.

3.7.2. Quantitative analysis and sample preparation

The WDS-spectrometer (Fig. 3-14) consists of a monochromatic crystal, an argon flux detector and a counting device, all geometrically located on the Rowland circle. For a given wavelength λ the monochromatic crystal may lie in the right Bragg angle to diffract the X-ray towards the counter. Because this may happen for a very narrow range of wavelength and is dependent on the nature of the crystal, several crystals are used at the same time. When an X-ray photon hits an argon atom in the Argon flux detector, an electron will be emitted by photo-electric effect. The amplitude of the impulsion generated in the counter will be proportional to the energy of the emitted electron. The intensity of the X-ray will be counted as the number of impulsions per second in a given (narrow) energy range. WDS-EPMA has a precision of less than 1%. Analyses of samples from this study were performed with accelerating voltage and beam current of 20 kV–10 nA, respectively. Counting times were 20–30 s. Samples consisted of ~80 km thick thin sections, polished up to 1 µm and coated with a $25.0 \pm 2.0\ nm$ carbon layer under vacuum.

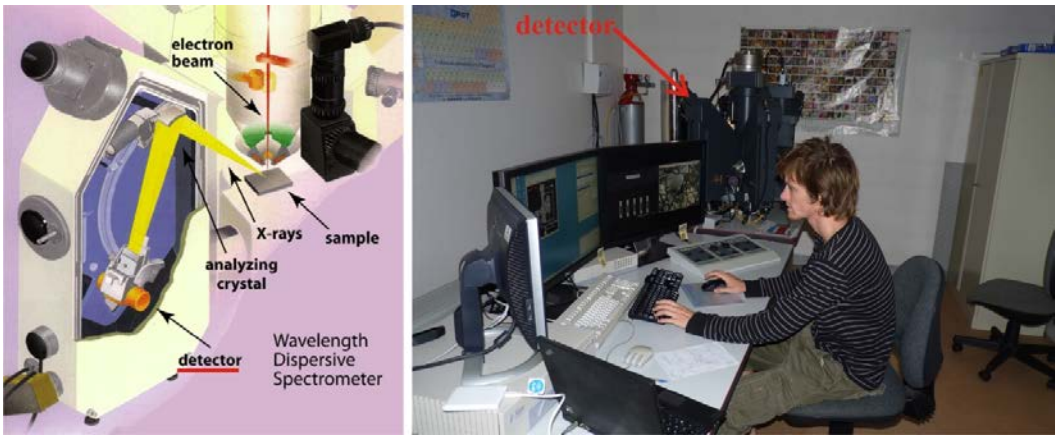

Figure 3-14. Left: Experimental setup of WDS-EPMA. Right: Cameca SX-100 facility at Géosciences Montpellier (France).

The standards used for element calibrations were wollastonite (Si, Ca), corundum (Al), chromium oxide (Cr), rutile (Ti), albite (Na), forsterite (Mg), manganese (Mn), hematite (Fe), orthoclase (K) and nickel (Ni).

Kα lines of Si and Al were measured by a spectrometer equipped with a TAP crystal, Kα of Ca and K, Mn and Fe, Cr and Ti, and Na and Mg with LPET-, LLiF-, PET- and a second TAP-equipped spectrometer, respectively.

3.8. Peridotite conventional thermobarometry

3.8.1. Sampling strategy

In chapter 5, samples analyzed for mineral chemistry and used for thermobarometric calculations were collected from all tectono-metamorphic domains in order to cover the whole massif (75 km2) in the most homogeneous way possible (Fig. 3-15). The samples the least affected by late serpentinization were selected keeping a maximum vertical distance with the contact of < 200 m between samples along a given profile (Fig. 3-15). In each sample, at least 3 crystals have been analyzed for each mineral and different textural occurrences, for both "core" and "rim" compositions.

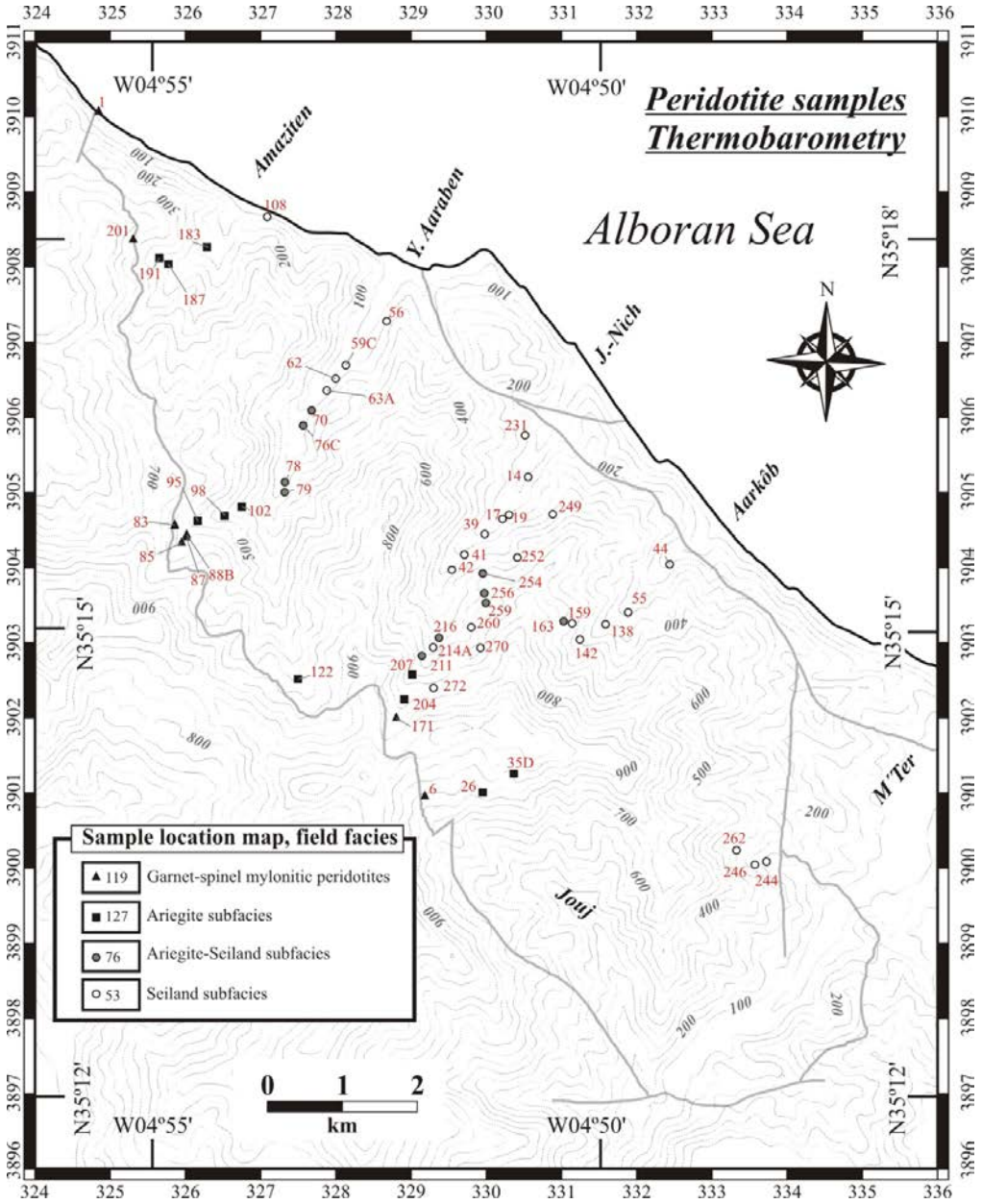

Figure 3-15. Map of the study area showing the selected samples analyzed for major elements mineral chemistry (EPMA) and used for thermobarometric calculations.

3.8.2. Used thermobarometric calculations

Synkinematic pressures for Grt-Sp Mylonites samples were calculated using the geobarometer calibration of the Grt-Sp lherzolite transition in the CMAS-Cr system (Webb & Wood, 1986), corrected for the effect of FeO in olivine (O'Neill, 1981) for those samples exhibiting spinel in textural equilibrium with fresh garnet or elongated spinel neoblasts adjacent to garnet and olivine neoblasts in the recrystallized matrix (Garrido et al., 2011). We generated an iterative solution by combining this geobarometric calculation with the recommended thermometer formulations (Nimis & Grutter, 2010) of Brey & Köhler (1990), Taylor (1998), Witt-Eickschen & Seck (1991) and Nimis & Grutter (2010). For other tectono-metamorphic domains, we used the same thermometer formulations as previously mentioned, but fixed the pressure at 1.8 GPa, which was obtained from thermodynamic modelling in Perple_X from chapter 4. The effect of pressure on the previously mentioned thermometers, remains, however, negligible. Parts of these results were used in chapter 5, but a synthetic table is given in the Appendix (chapter 12).

3.1. Whole Rock major and trace elements using X-ray Fluorescence

Whole rock major elements were analyzed using standard X-ray fluorescence procedure at the CIC (University of Granada, Spain). Hand size samples were cleaned from alteration and cut in blocks of ~100 cm^3 using a diamond saw. They were then crushed using steel jaws and then quartered with a riffle-splitter. The samples were first run for loss on ignition and then fused with borate flux to produce a glass bead. Transitional elements compositions were measured in pressed pellets. Whole rock major compositions were used in chapter 4 for computing isochemical P-T-phase diagrams for pyroxenites.

3.2. P-T-phase diagram modeling using Perple_X

In chapter 4, we used Perple_X software (Connolly, 1990, 2005) to compute phase diagrams for one particular bulk chemical composition in function of pressure and temperature, also known as a "pseudosection". In such an isochemical system, Perple_X calculates the amounts and the compositions of the phases that minimize the Gibbs free energy G at a given pressure and temperature (at a certain grid node in the diagram). Because G for a solid solution phase varies upon the composition of the solid solution, this non-linear function is approximated by a series of pseudocompounds that are used in the linear approximation of the minimization of the free Gibbs energy of the system, i.e. including all phases (Connolly, 2005; see review in Padrón-Navarta, 2010).

Pseudosections are a powerful tool to compare petrological observations such as stable mineral assemblages or reaction textures (e.g. symplectites in pyroxenites in chapter 4) and hence to unravel PT paths of rocks. In chapter 4, we linked these P-T-phase diagrams to conventional local equilibrium thermobarometric calculations.

Part II - Results

Journal of Structural Geology **39** (2012) 138-157, DOI:10.1016/j.jsg.2012.02.019

Received: 17 November 2011 / Received in revised form: 27 February 2012 / Available online: 15 March 2012

4. Deformation processes and rheology of pyroxenites under lithospheric mantle conditions

Erwin Frets [a,b,*], Andréa Tommasi [b], Carlos J. Garrido [a], José Alberto Padrón-Navarta [b,c], Isma Amri [d], Kamal Targuisti [d]

We combined microstructural observations and high-resolution crystallographic preferred orientation (CPO) mapping to unravel the active deformation mechanisms in garnet clinopyroxenites, garnet-spinel websterites, and spinel websterites from the Beni Bousera peridotite massif. All pyroxenites display microstructures recording plastic deformation by dislocation creep. Pyroxene CPO are consistent with dominant slip on [001]{110} in clinopyroxene and on [001](100) or [001](010) in orthopyroxene. Garnet clinopyroxenites have however high recrystallized fractions and finer grain sizes than spinel websterites. Recrystallization mechanisms also differ: subgrain rotation dominates in garnet clinopyroxenites, whereas in spinel websterites nucleation and growth also contribute. Elongated shapes and strong intracrystalline misorientations suggest plastic deformation of garnet, but CPO are weak. Clinopyroxene porphyroclasts in spinel websterites show deformation twins underlined by orthopyroxene exsolutions. Thermodynamic calculations indicate that garnet clinopyroxenites deformed at 2.0 GPa and 950-1000ºC and spinel pyroxenites at 1.8 GPa and 1100-1150 ºC. The lower temperatures may explain the faster work rates implied by the finer grained microstructures in garnet clinopyroxenites. Greater stresses may have also reduced the competence contrast between garnet and pyroxene in the garnet pyroxenites and, at the outcrop scale, lowered the competence contrast between pyroxenites and peridotites, favoring mechanical dispersion of pyroxenites in the cooler lithospheric mantle.

[a] *Instituto Andaluz de Ciencias de la Tierra (IACT), CSIC and UGR, Avenida de las Palmeras 4, 18100 Armilla, Granada, Spain*

[b] *Geosciences Montpellier, CNRS & Université de Montpellier 2, F-34095 Montpellier Cedex 5, France*

[c] *Research School of Earth Sciences, The Australian National University, Building 61, Mills Road, ACT0200 Canberra, Australia*

[d] *Département de Géologie, Faculté des Sciences, Université Abdelmalek Essaâdi, Tetouan, Morocco*

Journal of Structural Geology **39** (2012) 138-157, DOI:10.1016/j.jsg.2012.02.019

Received: 17 November 2011 / Received in revised form: 27 February 2012 / Available online: 15 March 2012

Keywords: mantle, pyroxenite, plastic deformation, rheology, microstructure, crystal preferred orientations, garnet, clinopyroxene, orthopyroxene, Beni Bousera

Highlights:

- Pyroxenites deform by dislocation creep under lithospheric mantle conditions
- EBSD maps reflect dynamic recrystallization in garnet and clinopyroxene
- High stresses result in smaller rheological contrasts

4.1. Introduction

Pyroxenite is an important constituent of the upper mantle. Lithological mapping in continental peridotite massifs, like Lherz in the Pyrenees, Lanzo in the Alps, Beni Bousera and Ronda in the Betics-Rif belt, shows that pyroxenite layers are ubiquitous in these massifs (Kornprobst, 1969, 1970; Dickey, 1970; Garrido and Bodinier, 1999; Bodinier et al., 2008; Gysi et al., 2011). Mantle pyroxenites have been inferred as source material of ocean island basalts in Hawaii (Sobolev et al., 2005) and to a lesser extent, of mid-ocean ridge basalts (Hirschmann and Stolper, 1996).

Three origins are classically proposed for mantle pyroxenites: recycling of oceanic crust into the convective mantle due to subduction (Polvé and Allègre, 1980; Allègre and Turcotte, 1986), partial crystallization of basaltic melts at depth, or melting and melt-rock reaction products (Loubet and Allègre, 1982; Bodinier et al., 1987; Suen and Frey, 1987; Pearson et al., 1993; Garrido and Bodinier, 1999; Bodinier et al., 2008). Regardless of their origin, pyroxenites usually occur as layers parallel to the peridotite foliation, suggesting that deformation during mantle flow probably controls their distribution and, hence, the scale of expression of compositional heterogeneity in the upper mantle. However, data on pyroxenes deformation mechanisms and rheology are still limited.

Deformation experiments and TEM observations on diopside (Avé Lallemant, 1978; Kollé and Blacic 1982, 1983; Raterron and Jaoul, 1991; Ingrin et al., 1992; Jaoul and Raterron, 1994; Zhang et al., 2006; Amiguet et al., 2009), orthopyroxene (Turner et al.; 1960; Raleigh, 1965; Green and Radcliffe, 1972; Lally et al., 1972; Kohlstedt and Vandersande, 1973; Ross and Nielsen, 1978; Skrotsky, 1994), and garnet (Ando et al., 1993; Doukhan et al., 1994; Voegelé et al., 1998, 1998a,b; Ji et al., 2003) showed that these minerals may deform by crystal-plastic processes, while identifying the dominant slip systems. For diopside, these studies also determined the pressure and temperature dependence of the critical resolved shear stresses of the various slip and twinning systems. In addition, flow laws were determined for diopside polycrystals under dry (Bystricky and Mackwell, 2001) and hydrous conditions (Chen et al. 2006). Yet, the extrapolation of these results to natural conditions remains delicate. Most studies for natural garnet-bearing pyroxene-rich lithologies focused on eclogites from subduction-related metamorphic terranes deformed under high to ultra-high pressure and low temperature conditions or high-pressure granulitic conditions (e.g., Buatier et al., 1991; Abalos 1997; Bascou et al., 2001; Bascou et al., 2002; Mainprice et al., 2004; Padrón-Navarta et al., 2008). Fewer data exist for mantle pyroxenites deformed under lithospheric or asthenospheric mantle conditions (e.g., Muramoto et al. 2011).

The Beni Bousera peridotite massif encompasses a large variety of mantle pyroxenites from garnet clinopyroxenite to spinel websterite deformed under a variety of pressure and temperature conditions (Kornprost, 1969. 1970; Pearson et al., 1989, 1991,1992; Targuisti, 1994). We use these rocks to present detailed analyses of outcrop-scale structures, microstructures, and crystallographic preferred orientations (CPO) for garnet pyroxenite, garnet-spinel websterite, and spinel websterite from the Beni Bousera ultramafic massif. We couple these microstructural data to petrological modeling to constrain the deformation mechanisms and rheological behavior of pyroxenite in the subcontinental lithospheric mantle for a range of pressure and temperature conditions.

4.2. Sampling strategy

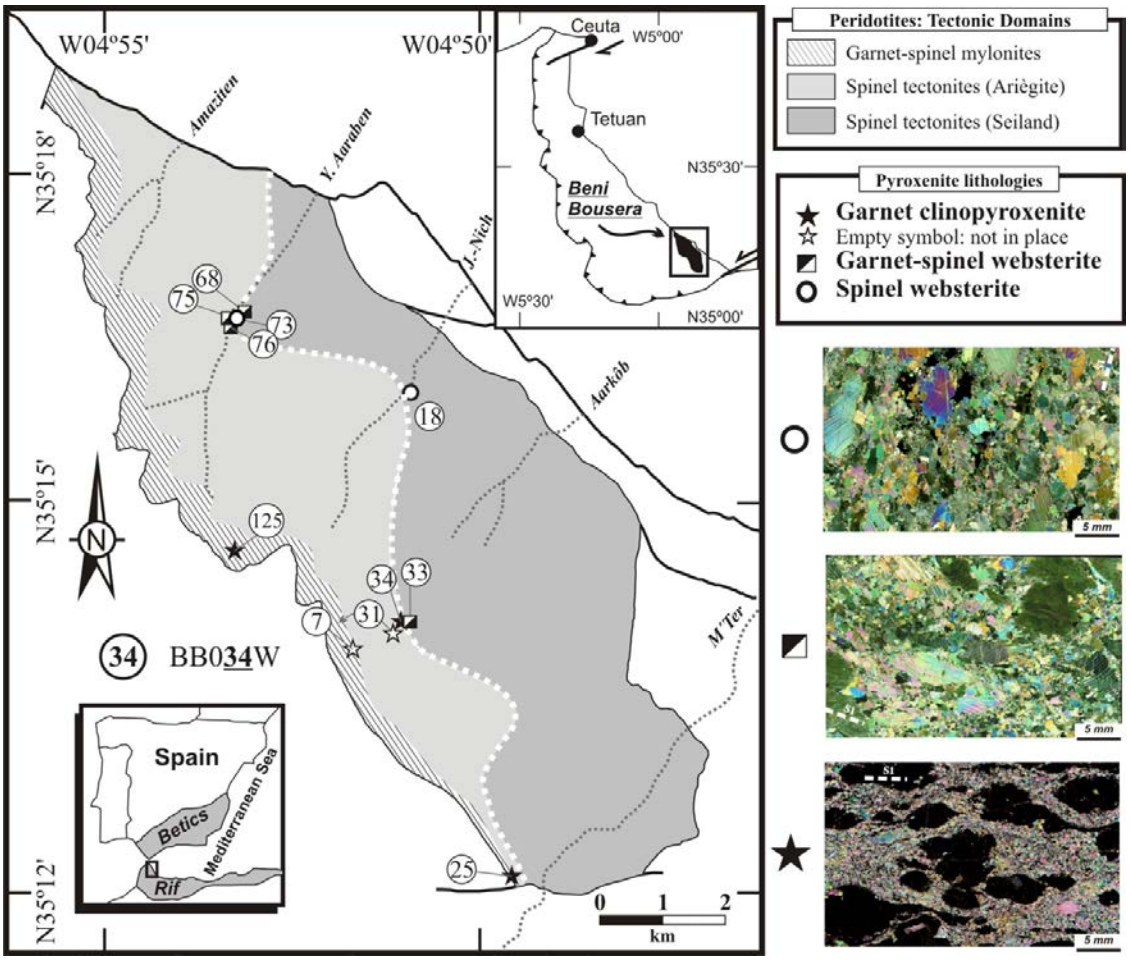

Figure 4-1. Geological map of the Beni Bousera peridotite massif showing the locations of the studied pyroxenites samples. Photomicrographs show the variation of pyroxenites microstructures.

We collected samples across a wide range of pyroxenite microstructures and rock types (Fig. 4-1). Pyroxenites were sampled at varying distances to the Ariegite-Seiland transition, from the garnet-spinel mylonite, through the Ariègite domain to the Ariègite-Seiland transition (Obata, 1980; Targuisti, 1994). Detailed microstructural analyses were conducted on: (i) five orthopyroxene-bearing garnet clinopyroxenites (<10 vol.% of orthopyroxene), (ii) four garnet-spinel websterites (BB033W, BB068E, BB075W, and BB076BBE), and (iii) two spinel websterites (BB073CW and BB018W). From group (i), four were collected from the garnet-spinel mylonite domain (BB007, BB025E, BB031 and BB125BW) and one from the Ariègite domain (BB034W) near the Ariègite-Seiland transition. Group (ii) pyroxenites were sampled at varying distance to the Ariègite-Seiland transition; including an orthopyroxene-rich websterite (opx/cpx > 3:1; BB033W). The spinel websterites from group (iii) were sampled from thick websterite layers (Fig.4-2f) that preserve garnet-spinel websterite in their central part. We did not analyze the centimeter-thick websterite layers with diffuse limits that crop out in the lower parts of the Seiland subdomain because they contain large amounts of olivine (up to 30%). Modal compositions, microstructures, and J-indexes of all samples are presented in Table 1.

Table 1
Sample location, mineralogy, and calculated mineral J-indexes.

Facies	Grt-Spl Lherzolite				Spinel Lherzolite						
Subfacies					Ariègite	Ariègite–Seiland					
Rock type	Grt clinopyroxenites					Grt-Spl websterites				Spl websterites	
Microstructure	Fine-grained porphyroclastic						Coarse porphyroclastic				
Sample	BB007	BB031	BB125BW	BB025E	BB034W	BB068E	BB033W	BB075W	BB076BBE	BB018W	BB073CW
Lat (°N)	35°14′10″	35°14′18″	35°14′57″	35°12′10″	35°14′26″	35°17′03″	35°14′26″	35°17′00″	35°16′55″	35°16′18″	35°17′00″
Long (°W)	4°52′29″	4°52′03″	4°53′41″	4°50′44″	4°51′56″	4°53′41″	4°51′56″	4°53′47″	4°53′46″	4°52′00″	4°53′48″
Mineralogy (modal vol.%)											
Grt	65	60	55	50	42–44	34–38	15	30	15–17	–	–
Cpx	35	40	45	40	55	60	35	55	65	50	40
Opx	<1	<1	<1	10	1–3	1–3	45	15	15	35	35
Spl	–	–	–	–	–	1–3	5	1–3	3–5	10–12	12
Ol	–	–	–	–	–	–	–	–	–	3–5	13
$D_{Se\text{-}Ar}$ (m)	847	780	1047	1082	5	102	0	29	0	−195	−29
J_{cpx} (raw)	2.59	3.37	1.77	3.93	4.59	9.51	4	7.1	11.73	7.08	5.43
J_{cpx} (1 ppg)	2.24	2.94	1.64	2.97	4.1	7.6	3.23	4.76	9.13	5.34	3.36
J_{opx} (raw)	–	–	–	–	–	–	3.83	4.13	5.64	8.72	5.33
J_{opx} (1 ppg)	–	–	–	–	–	–	2.69	3.76	6.04	4.58	4.8
$^{*}J_{grt}$ (1 ppg)	1.02	1.14	1.01	1.04	1.31	–	–	–	–	–	–

$D_{Se\text{-}Ar}$ = distance from the Seiland-Ariègite transition; 1 ppg = 1 point per grain calculation; $^{*}J_{grt}$ = J-indexes calculated using the MTEX code.

4.3. Field occurrences and macroscopic structures

Figure 4-2. Field occurences of Beni Bousera pyroxenites (px). (a) Garnet clinopyroxenite layers parallel to the peridotite foliation from the mylonitic domain. Note the boudinage of the finer pyroxenite layers (white arrow). (b) Flattened garnets marking the foliation (S1) in a garnet clinopyroxenite. (c) Extreme boudinage of a garnet clinopyroxenite in the Ariegite domain. Note the peridotite foliation warping around the boudin. (d) Elongate garnets marking the lineation in a garnet clinopyroxenite. (e) Abundant garnet-spinel websterites layers from the Arièigite-Seiland transition. Note the absence of boudins. (f) Thick “composite” pyroxenite from the Arièigite-Seiland transition.

Garnet pyroxenites crop out in the garnet-spinel mylonite zone and in the spinel tectonite domain of the Ariègite subfacies (Fig. 4-1). They occur as centimeter- to meter-scale layers with rather sharp contacts to the host peridotite and are commonly isoclinally folded or boudinaged (Fig.4-2a-c). Pyroxenite layering is parallel to the peridotite foliation (Fig. 4-2a). At the outcrop scale, the foliation in the clinopyroxenite, which is marked by the shape-preferred orientation of garnet, is parallel to that of the host peridotite. In most cases, garnet is pancake-shaped (Fig. 4-2b), but in some pyroxenites, garnets are elongate and define a stretching lineation on the foliation plane (Fig. 4-2d). In thicker pyroxenite layers, variation of the garnet modal content defines a compositional layering parallel to the foliation.

Garnet-spinel websterites characterize the transition between the Ariegite and Seiland subfacies domains (Fig. 4-1). Similarly to the garnet clinopyroxenites, these websterites crop out as layers parallel to the peridotite foliation, which are often boudinaged (Fig. 4-2e). Thick websterite layers in the central part of the massif those in Figure 4-2 may have a composite structure, containing spinel in its external part and keliphitized garnet in its central part. Finally, the structurally lowest part of the Seiland subfacies domain is characterized by centimeter-thick olivine-bearing websterite layers with diffuse limits.

4.4. Microstructures

4.4.1. Garnet pyroxenites

Both garnet clinopyroxenite and opx-bearing garnet clinopyroxenite have porphyroclastic microstructure characterized by coarse garnet porphyroclasts (up to 10 mm long) enclosed in a finer grained (250-300 μm) matrix of recrystallized clinopyroxene and garnet neoblasts (Fig. 4-3a). Garnet porphyroclasts occur either as isolated grains or as aggregates forming a compositional layering parallel to the foliation (Fig. 4-3b). They are usually pancake-shaped with aspect ratios that vary between 1.5:1 and 4:1. Their elongation marks the lineation and their flattening the foliation. The latter is also defined by the shape-preferred orientation of garnet and clinopyroxene in the matrix (Fig. 4-3c). All garnet porphyroclasts have irregularly-shaped grain boundaries with embayments filled by clinopyroxene (arrows in Fig. 4-3d) and may contain clinopyroxene inclusions (Fig. 4-3a,d). The largest garnet porphyroclasts also contain oriented rutile inclusions. Garnet in the matrix is also lens-shaped, but less elongate than the porphyroclasts, which are up to 500 μm long with average aspect ratios of 2:1 (Fig. 4-3c). Matrix clinopyroxenes have more irregular shapes and tend to be less elongate (300-400-μm long on average) than matrix garnets; plus mm-size porphyroclasts are rare. They usually display undulose with the local occurrence of subgrains (Fig. 4-3e). Clinopyroxene grain boundaries are serrated, with very short length-scale embayments, which grade into a very-fine grained matrix (5-10μm, Fig. 3e-f) that coats most grain boundaries. Most clinopyroxenes show fine, closely spaced orthopyroxene exsolutions limited to the central part of the crystals (Fig. 4-3e,f). Orthopyroxene occurs as isolated recrystallized grains in the clinopyroxene matrix with a size similar to recrystallized clinopyroxene crystals.

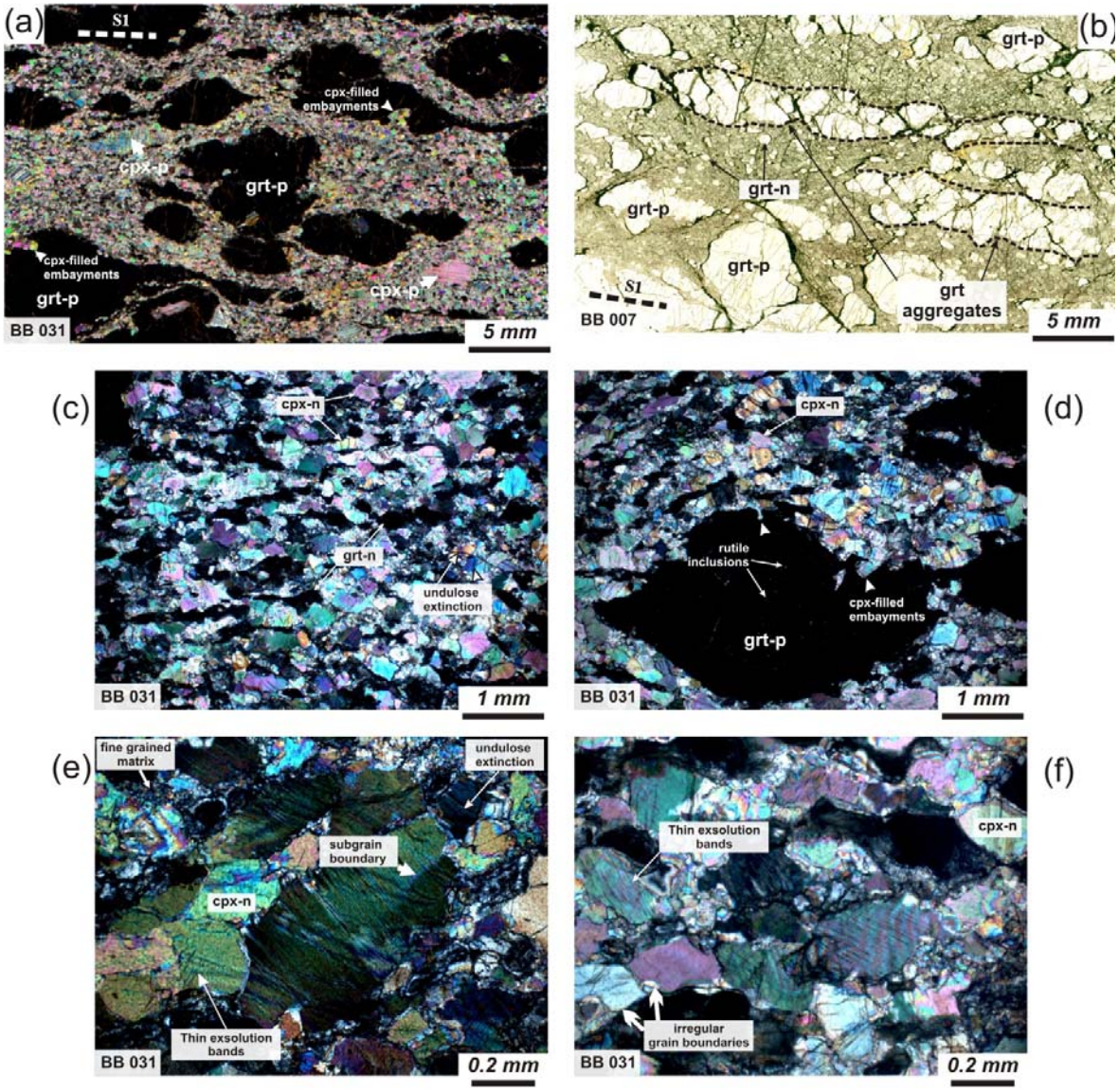

Figure 4-3. Photomicrographs of typical microstructures of garnet pyroxenites (cross-polarized light, except b, plane polarized light). (a) Fine-grained porphyroclastic microstructure of garnet clinopyroxenite. Flattening of garnet porphyroclasts (grt-p) marks the foliation (S1) and clinopyroxene is almost entirely recrystallized. Note the few remaining clinopyroxene porphyroclasts (cpx-p) and the embayments in garnet porphyroclasts filled with clinopyroxene (white arrows). (b) Foliation (S1) defined by variations in the garnet modal content and by the elongation of garnet porphyroclasts (grt-p, garnet porphyroclasts; grt-n, garnet neoblasts). (c) Detail of the recrystallized matrix of a garnet clinopyroxenite (garnet marked by white arrow). (d) Garnet porphyroclasts (grt-p) with rutile exsolutions presenting sinuous grain boundaries filled with clinopyroxene. (e) Undulose extinction and subgrains in clinopyroxene; grain boundaries are coated by a fine-grained matrix (cpx-n, clinopyroxene neoblasts). (f) Detail of recrystallized clinopyroxene crystals -p indicates porphyroclasts and -n, neoblasts.

4.4.2. Garnet-spinel websterites

Garnet-spinel websterites differ from the garnet pyroxenites because of their coarser clinopyroxene grain sizes (Fig. 4-4), their higher orthopyroxene modal contents, and the presence of spinel. Garnet in these rocks is completely transformed to kelyphite aggregates up to 5 mm wide. Kelyphite aggregates have irregular shapes, but tend to be more rounded than garnet porphyroclasts in garnet clinopyroxenites. However, the compositional layering parallel to the foliation is preserved in some samples (Fig. 4-4b). Spinel occurs as a minor phase within kelyphite or along pyroxene grain boundaries. Clinopyroxene occurs as large porphyroclasts up to 2 cm long enclosed in a rather coarse grained (~1 mm on average) matrix of ortho- and clinopyroxene (Fig. 4-4a-d). Clinopyroxene porphyroclasts are strongly deformed and often bent. They show thick orthopyroxene exsolutions up to 15μm wide parallel to (100), strong undulose extinction, and kinks (Fig. 4-4a-d). They also have very

irregular shapes, being partially replaced by the recrystallized matrix that occurs preferentially along exsolution planes (Fig. 4-4a,d). Clinopyroxene porphyroclasts may also enclose orthopyroxene crystals (Fig. 4-4c). Orthopyroxene porphyroclasts are rarer and smaller than clinopyroxene ones, but extremely deformed, reaching aspect ratios of 10:1 (Fig. 4-4c). Larger, but less deformed orthopyroxene crystals characterize however the orthopyroxene-rich websterite BB033W.

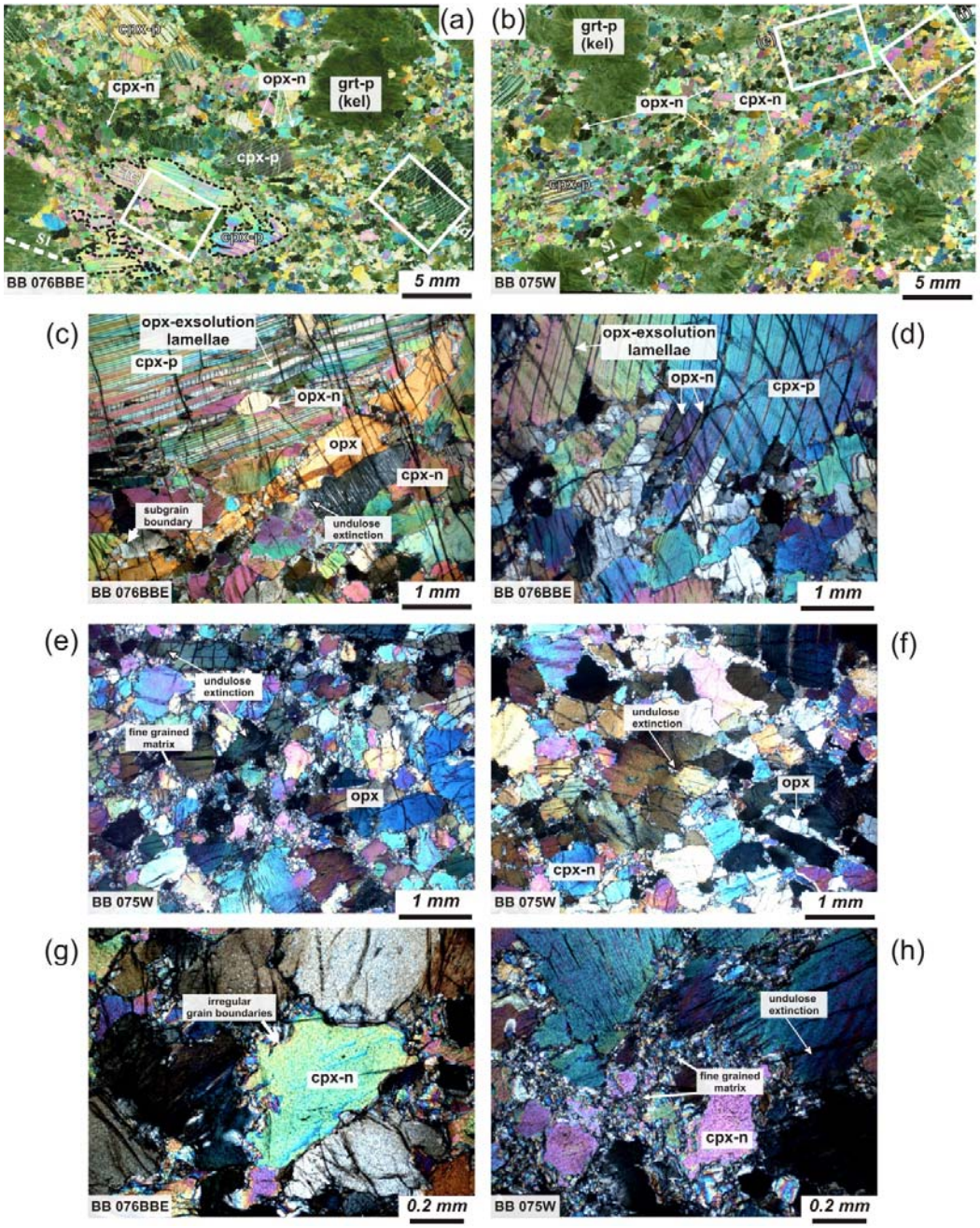

Figure 4-4. Photomicrographs of coarse porphyroclastic garnetespinel websterites (cross-polarized light). (a and b) Elongation of large clinopyroxene porphyroclasts marks the foliation (S1, dashed line). Garnet is completely transformed into greenish post-kinematic kelyphite aggregates, which are more rounded than garnet crystals in garnet clinopyroxenites. (c) Detail of a displaying a large elongated orthopyroxene crystal and a large clinopyroxene porphyroclast (cpx-p) with thick orthopyroxene lamellae parallel to (100). (d) Detail of a showing a bent and twinned clinopyroxene crystal with orthopyroxene exsolutions along the (100) twin lamellae. (e) Detail of the recrystallized matrix in b showing undulose extinction in clinopyroxene, elongated orthopyroxene crystals, and the intergranular fine-grained matrix. (f) Detail of b; note the elongation of orthopyroxene crystals slightly oblique to the foliation. (g) Detail showing the shape of recrystallized clinopyroxene grains. (h) Fine-grained matrix partially replacing clinopyroxene crystals along grain boundaries and exsolution planes. -p indicates porphyroclasts, -n, neoblasts, kel means kelyphitized garnet.

Recrystallized grains have irregular, interlocking shapes (Fig. 4-4c-f). They have no clear shape-preferred orientation, but tabular clinopyroxene crystals rimmed by orthopyroxene occur dispersed in the matrix (arrow in Fig 4-4f). These tabular crystals are interpreted to represent fragments of ancient porphyroclasts limited by planar orthopyroxene exsolutions. Recrystallized clinopyroxenes display undulose extinction and subgrains (Fig. 4-4e-f), but are not twinned. They have serrated grain boundaries (Fig. 4-4g) that are often rimmed by a very fine-grained matrix composed of ortho- and clinopyroxene. This matrix differs in abundance through the samples and when most abundant, it completely coats all grains (Fig. 4-4e-g) and partially replaces them (Fig. 4-4h).

4.4.3. Spinel websterites

Compared to the garnet-spinel websterites, kelyphite is absent and spinel is a major phase (5-10 vol.%) of spinel websterites. Spinel occurs either in intergrowth with ortho- and clinopyroxene (Fig. 4-5b,d) or forming interstitial aggregates along pyroxene grain boundaries aligned parallel to the foliation (Fig. 4-5a,c,e). Automorphic spinel is rare. Close to the contacts with the peridotite, olivine occurs as coarse (~1cm) crystals elongated parallel to the foliation. Farther within the pyroxenite, olivine occurs as rare small interstitial crystals (~1mm or less). Both show undulose extinction and subgrains (Fig. 4-5g).

Clinopyroxene occurs as large porphyroclasts up to 2 cm long elongate parallel to the foliation (Fig. 4-5a-b). These porphyroclasts are strongly deformed, often bent, and show polysynthetic mechanical twins typically parallel to (100), strong undulose extinction, and kinks. They have very irregular shapes, being partially replaced by recrystallized grains. This recrystallization occurred preferentially along twinning planes that are usually marked by orthopyroxene exsolution (Fig. 4-5c,e). Orthopyroxene porphyroclasts are less elongated and show strong undulose extinction and kinks. They display thinner and more closely-spaced clinopyroxene exsolution (Fig. 4-5a). Their boundaries are irregular with embayments filled by ortho-and clinopyroxene. Large, undeformed ortho- and clinopyroxene grains mostly occur in rounded aggregates with spinel (Fig. 4-5d). Pyroxene porphyroclasts are surrounded by medium sized (0.5 – 1 mm) anhedral pyroxene crystals with sutured grain boundaries. Some pyroxenes show intracrystalline structures such as undulose extinction. Porphyroclasts and matrix neoblasts are commonly coated by a very fine-grained matrix composed of ortho- and clinopyroxene grains (Fig. 4-5c-f, h). This matrix occurs differing abundance through the samples and in spinel-pyroxenite BB018W, it forms lens-shaped pockets, slightly flattened in the foliation plane that contain fibrous orthopyroxene, clinopyroxene, olivine, and plagioclase (Fig. 4-5f).

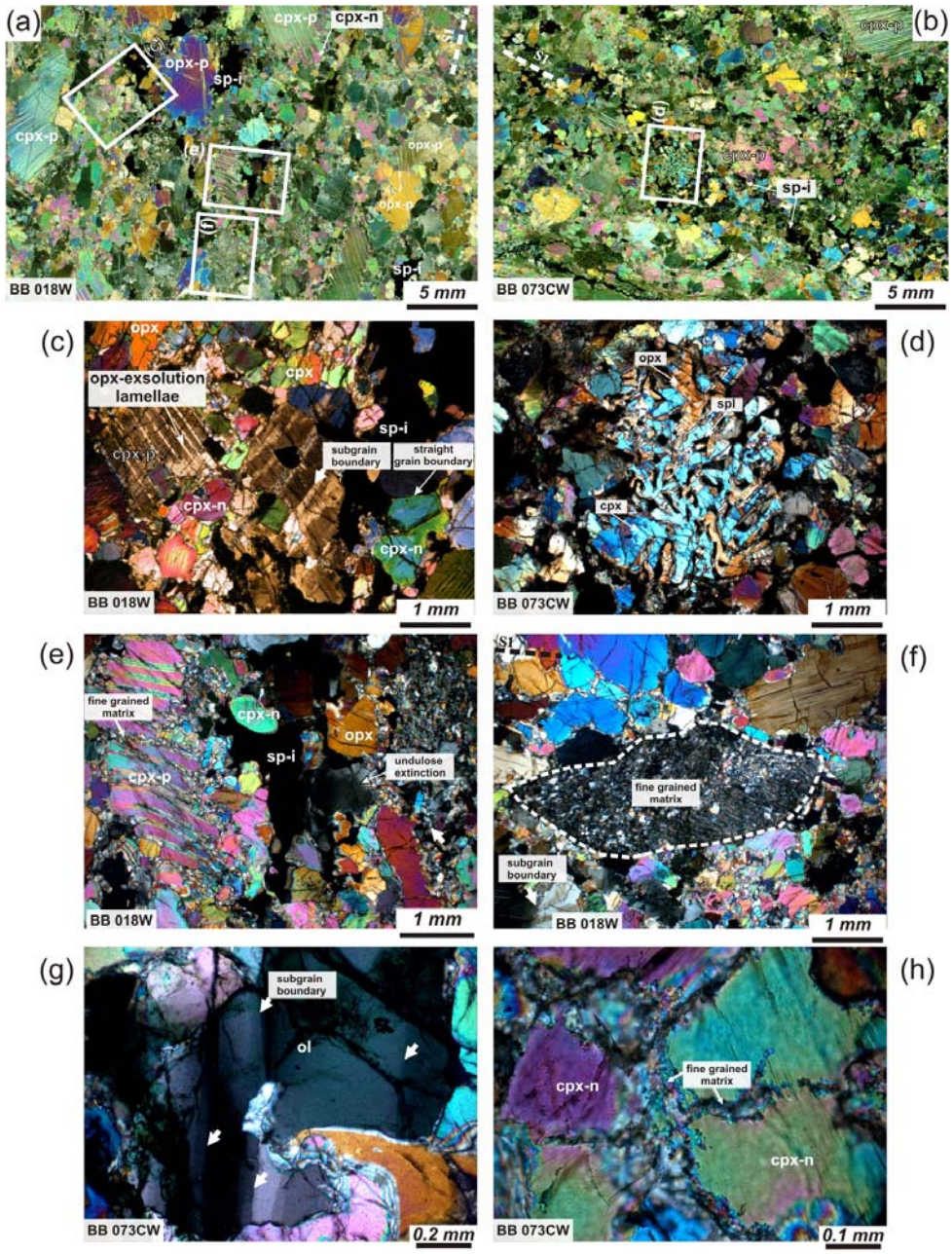

Figure 4-5. Photomicrographs of coarse porphyroclastic spinel websterites (cross-polarized light). (a and b) Foliation (S1) defined by the shape-preferred orientation of clinopyroxene (cpx-p) and orthopyroxene (opx-p) porphyroclasts. (c) Detail of a showing clinopyroxene crystals with coarse exsolutions and subgrains and spinel (spl) with interstitial habitus. Recrystallized clinopyroxene shows undulose extinction and straight grain boundaries (white arrows). (d) Detail of b showing an undeformed clinopyroxene-orthopyroxene-spinel symplectite. (e) Detail of a displaying a partially recrystallized orthopyroxene (opx) and an elongated clinopyroxene porphyroclast (cpx-p) replaced by fine-grained matrix along boundaries and exsolution planes (white arrows). (f) Detail of a showing a "pocket" of fine-grained plagioclase-bearing aggregates (fine grained matrix) elongated parallel to the foliation (S1). (g) Olivine crystal (ol) showing well developed subgrains and undulose extinction. (h) Fine-grained matrix along clinopyroxene neoblast (cpx-n) grain boundaries. -p indicates porphyroclasts, -n, neoblasts, and -i, interstitial crystals.

4.5. Crystal Preferred Orientations (CPO) data

4.5.1. Clinopyroxene, orthopyroxene and garnet CPO

All pyroxenite samples display a clear clinopyroxene CPO (Figs. 4-6 and 4-7) characterized by a concentration of [001] axes sub-parallel to the lineation and, in most cases, [010] axes at high angle to the foliation. In most samples, the clinopyroxene CPO has a clear asymmetry to the foliation that indicates simple shear deformation. However, detailed analyses highlight second-order variations in clinopyroxene CPO that do not correlate to provenance nor lithology. In all samples, [001] axes show some dispersion in the XY plane (foliation) or in the XZ plane. [001] forms a weak girdle in the foliation plane in garnet pyroxenites BB025E, BB034W, BB125W, in garnet-spinel websterites BB076BBE and BB068E, and in spinel websterites BB073CW and BB018W. It is dispersed in the XZ plane in garnet pyroxenites BB007 and BB0125BW and in garnet-spinel websterites BB033W and BB075W. Dispersion of [001] in the foliation plane is accompanied by a [010] maximum normal to the foliation and preferred orientation of [100] axes in the foliation plane with weak maxima normal to the lineation. In contrast, dispersion of [001] in the XZ plane is associated with dispersion of [010] in a plane normal to the lineation. Among the first group, spinel-websterite BB073CW and, to a lesser extent, garnet-spinel websterite BB068E exhibit clinopyroxene CPO characterized by bimodal [001] and [100] maxima in the foliation plane with the lineation as the bissectrix of the angle formed by the [001] maxima.

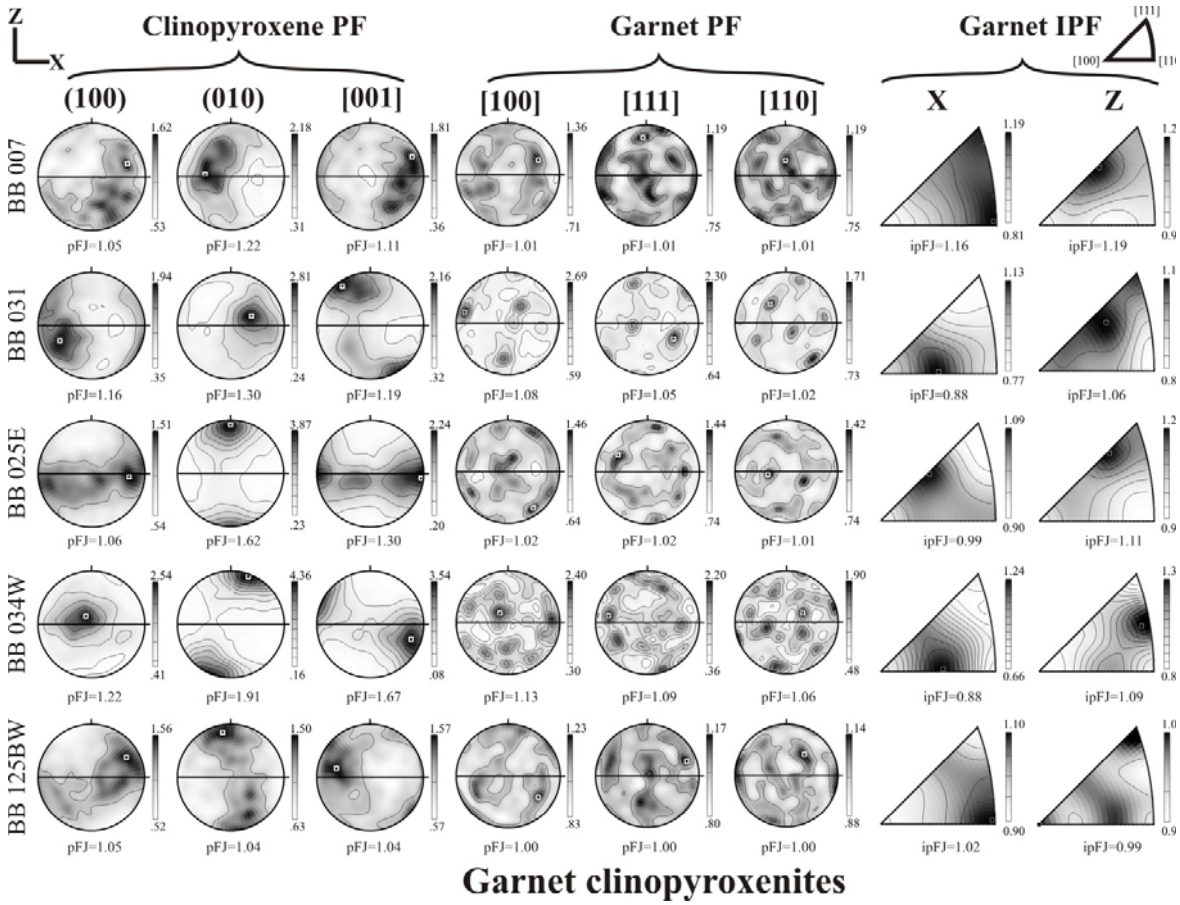

Figure 4-6. Clinopyroxene, orthopyroxene, and garnet CPO. PF ¼ Pole Figure, IPF ¼ Inverse Pole Figure. Pole figures are lower-hemisphere stereoplots; contours at 0.5 multiples of a uniform distribution (m.u.d.) for clinopyroxene and 0.25 m.u.d. for garnet. In garnet IPFs, contours at 0.05 m.u.d. (except for the normal to the foliation IPF of sample BB125BW where contours are at 0.02 m.u.d.).

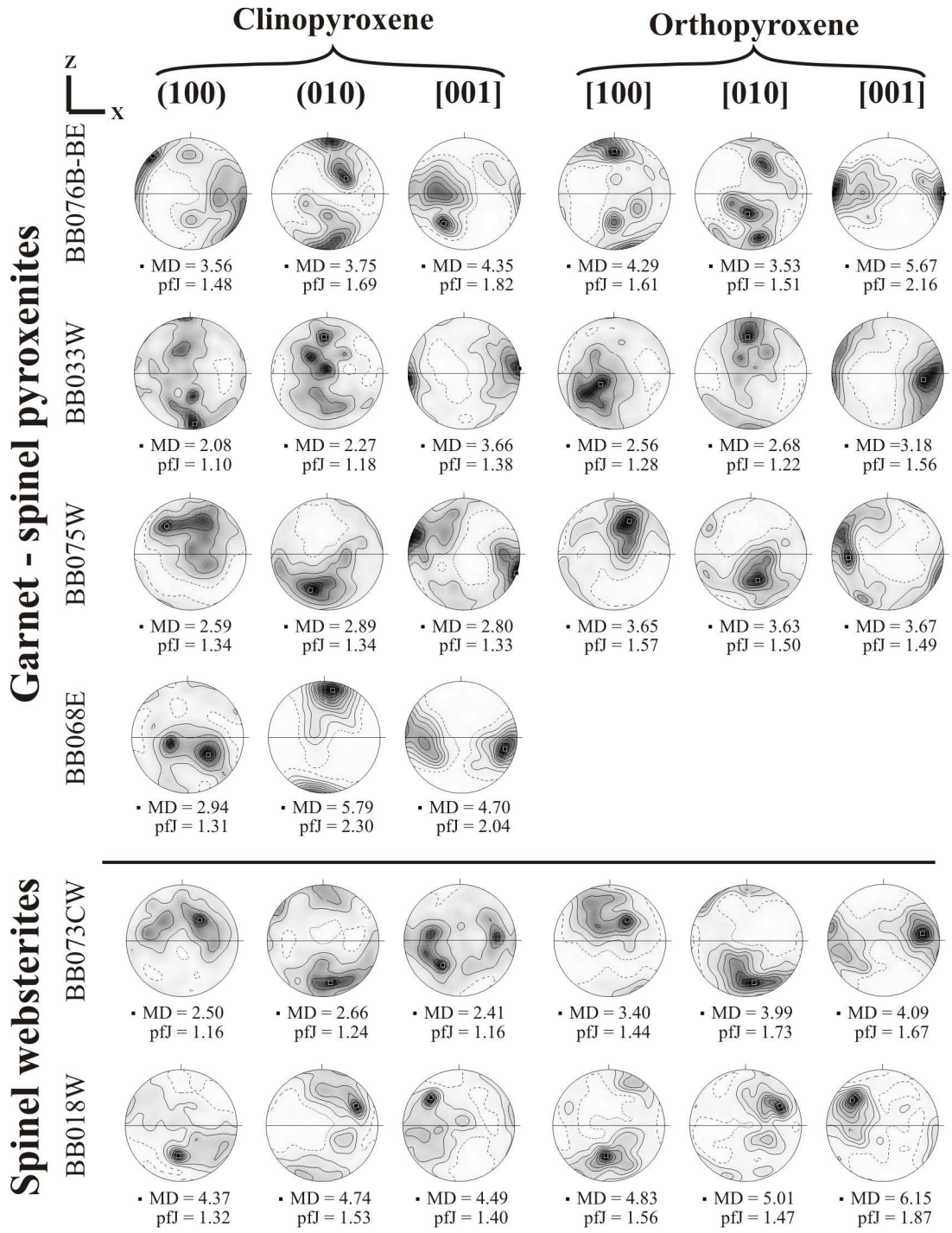

Figure 4-7. Clinopyroxene and orthopyroxene CPO in garnetespinel and spinel websterites. Pole figures are lower-hemisphere stereoplots; contours at 0.5 multiples of a uniform distribution (m.u.d.).

Although the patterns are similar, the intensity of the clinopyroxene CPO varies as a function of the lithology and provenance (Fig. 4-8). Garnet clinopyroxenites from the mylonitic domain generally display weak clinopyroxene CPO, characterized by J-indexes < 4, while garnet-spinel websterites from the Arièg ite-Seiland transition have strong clinopyroxene CPO with J-indexes as high as 12 (average of 8.1). Spinel websterites display intermediate J-indexes. In addition, the abundance of very coarse clinopyroxene porphyroclasts in the spinel websterites results in significantly higher J-indexes when the latter is calculated using one measurement point per pixel (raw EBSD data, full symbols in Fig. 4-8).

Orthopyroxene displays a clear CPO, which is well-correlated with the clinopyroxene CPO when orthopyroxene is present as a major phase (Fig. 4-7). Orthopyroxene [001] axes cluster at low angle to the lineation and either [100] or [010] form a slightly weaker maximum at high angle to the foliation. It is striking to note that the bimodal distribution of clinopyroxene [001] axes in sample BB073CW is accompanied by a bimodal distribution of orthopyroxene [001] axes. J-indexes for orthopyroxene (Table 1) vary between 2.7 and 6. Since most orthopyroxene-bearing samples were collected close to the Ariègite-Seiland transition, the relation between CPO strength and provenance could not be tested.

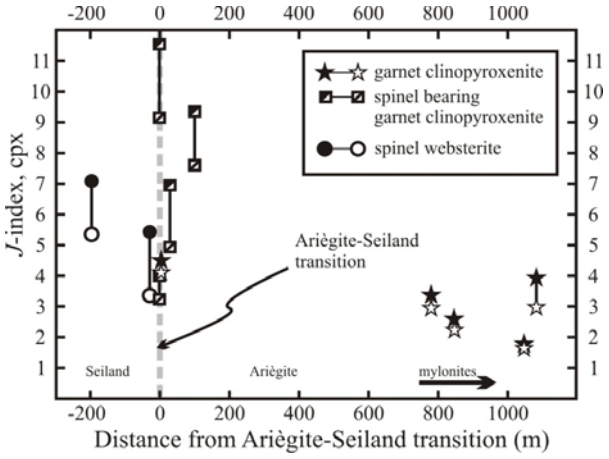

Figure 4-8. J-index as function of the distance to the AriègiteSeiland transition. Full symbols are calculated using one data point per pixel of the orientation map; empty symbols are calculated using one point per grain.

Garnet CPO could only be measured in the garnet clinopyroxenites. It is always very weak with J-indexes close to 1 (Table 1). The more pronounced CPO of sample BB034W might be due to the smaller number of grains measured, which were at least an order of magnitude less than in the other samples. Garnet CPO patterns vary from sample to sample (Fig. 4-6). Samples BB125BW and BB007 are characterized by weak ⟨110⟩ clusters subparallel to the lineation. Sample BB125BW shows weak ⟨111⟩ clusters normal to the foliation. The remaining samples have low Miller indices directions ⟨100⟩, ⟨110⟩, or ⟨111⟩ maxima neither parallel to the lineation, nor to the foliation.

4.5.2. Crystallographic Orientation Maps

Analysis of the crystallographic orientation maps shows that garnet porphyroclasts in garnet clinopyroxenites are strongly bent and display continuous crystallographic orientation gradients and even subgrains (Fig. 4-9a). Within a single porphyroclast, the rotation of the crystalline lattice may be as large as 30° over a distance of 5 mm (Fig. 4-9b,d). When the magnitude of the gradient is greater than 10°/mm, subgrains are present and more common at the edges of the garnet porphyroclasts (white arrows in Fig. 4-9a). Misorientation profiles parallel to the long axis of a garnet porphyroclast highlight rotations dominantly around ⟨111⟩, whereas profiles perpendicular to the crystal elongation show rotations around both ⟨111⟩ and ⟨110⟩ (Fig. 4-9c). The strongest orientation gradients are observed in the most elongate crystals, such as those in garnet clinopyroxenites BB031 and BB125BW that transition into recrystallized aggregates with average grain sizes of 500 μm (Fig. 4-9e). Misorientation between neighboring grains within these aggregates may be greater than 45° (Fig 4-9e). In more equidimensional garnets from garnet and spinel websterites BB007 and BB125BW, orientation gradients are limited to the crystal rims.

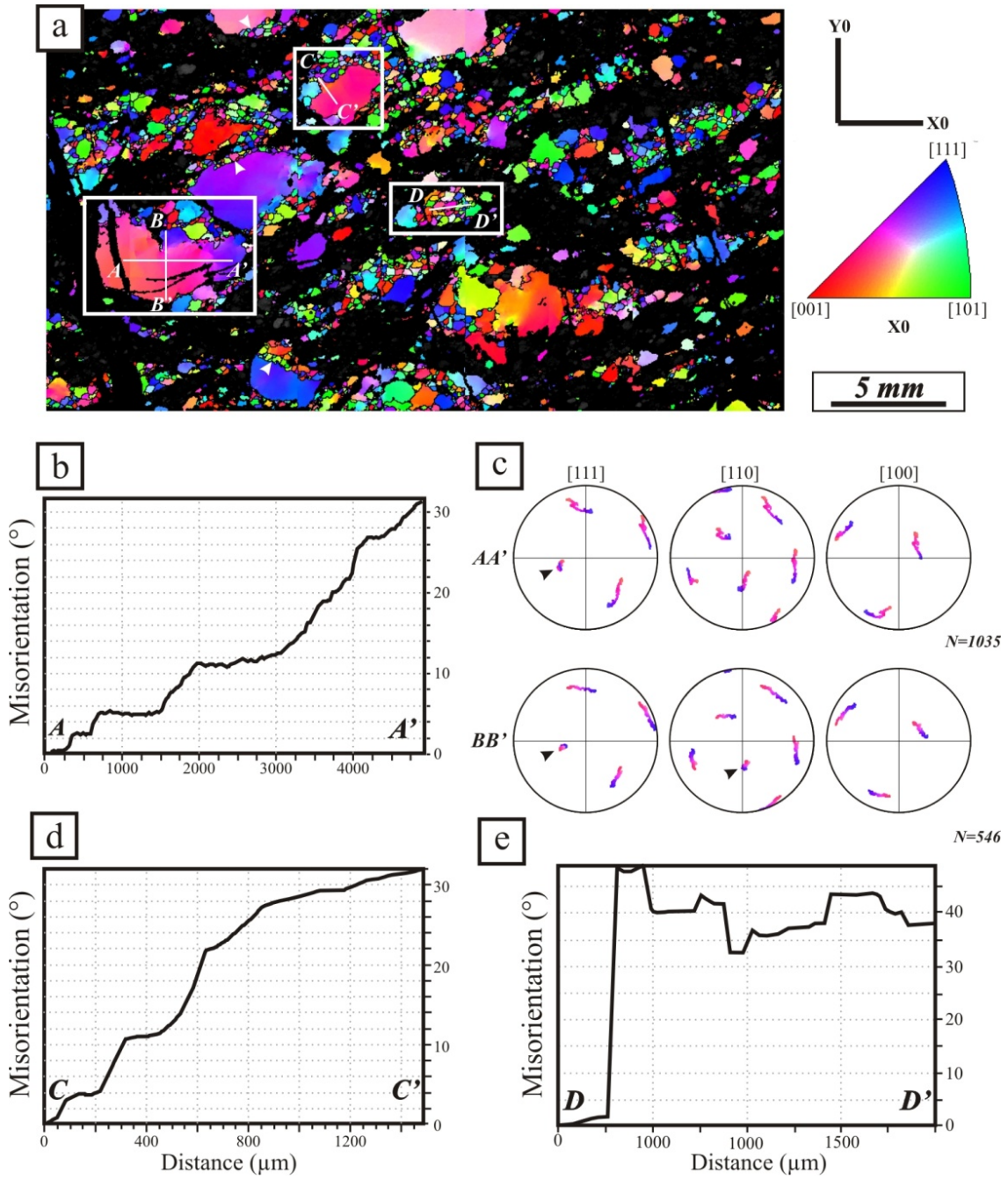

Figure 4-9. (a) Crystal orientation map of a garnet pyroxenite; garnet crystals are colored as a function of the X0 Inverse Pole Figure (insert on the left), pyroxene crystals are black. White arrow indicates recrystallized crystals at the rim of large porphyroclast. (b) Misorientation profile A-A' parallel to the long axis of a porphyroclast; note the continuous variation in orientation at the core and the development of subgrains toward the rim. (c) Stereoplots showing the internal misorientation in the same crystal; coloring as in (a); black arrows indicate rotation axes. (d) Misorientation profile C-C'. (e) Misorientation profile D-D' along a polycrystalline aggregate; weak misorientations on the left part of the profile are consistent with an origin by recrystallization.

Figure 4-10 illustrates the differences in microstructure between garnet clinopyroxenites and spinel websterites. First, clinopyroxene grain sizes in garnet pyroxenites are noticeably smaller than in spinel websterites and show a rather continuous grain-size distribution (20 μm - 1mm), which renders the discrimination between porphyroclasts and recrystallized grains difficult. In contrast, spinel websterites show a strongly bimodal grain-size distribution characterized by recrystallized grains 80-100 μm wide or even larger that surround and partially

replace large strained porphyroclasts that may attain several mm. Analysis of misorientations within these porphyroclasts reveals 180° rotations around [001] that represent deformation twins (Figs. 4-10a, c). These twins, which are also highlighted in the correlated (between neighbouring points in a map) misorientation distribution (Fig. 4-10f), are almost always outlined by coarse orthopyroxene exsolutions (Fig. 4-10a). The high proportion of low-angle grain boundaries in the correlated misorientation distribution of both garnet clinopyroxenite and spinel pyroxenite (Fig. 4-10f) highlights the abundance of subgrains in both rocks (in red in Fig. 4-10a,b). On the other hand, uncorrelated misorientation distributions differs more from the random one in the spinel pyroxenite than in the garnet clinopyroxenite (Fig. 4-10f), in agreement with the stronger clinopyroxene CPO of the former (Table 1).

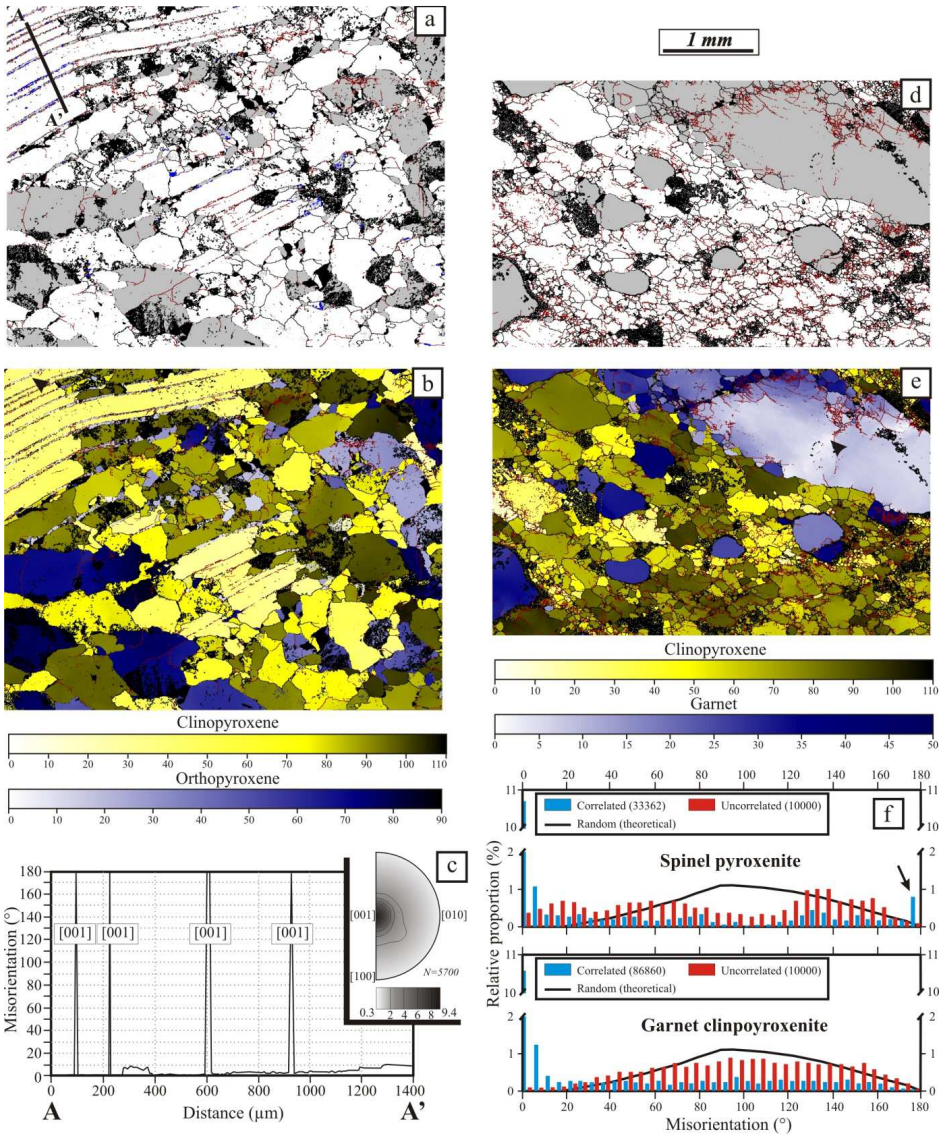

Figure 4-10. Detailed (5 µm step size) crystal orientation maps of a spinel websterite (a,d) and a garnet pyroxenite (d,e). (a,d) Phase distribution and grain boundary structure: clinopyroxene in white, orthopyroxene and garnet in gray, respectively. Red, black, and blue lines indicate grain boundaries with misorientations between 2º-15º, 15-179º, and >179º (twins), respectively. Thick black line AA' in a indicates the trace of the misorientation profile in c. (b,e) Crystallographic misorientation maps relative to an "ideal" orientation (black arrows indicate the grains used for defining this orientation); clinopyroxene are shown in yellow and garnet or orthopyroxene in blue. Grain boundaries as in (a,d). (c) Misorientation profile (AA') in a clinopyroxene porphyroclast: 180º misorientations with [001] rotation axes correspond to twinning. Inset shows that rotation axes in crystal coordinates for misorientations >179º in the entire map strongly cluster around [001]. (f) Clinopyroxene misorientation histogram for correlated and uncorrelated distributions in the spinel websterite (top) and in the garnet pyroxenite (bottom). Both show a predominance of low-angle misorientations, that is of subgrain boundaries. Twinning, recorded as 180º misorientations, is only observed in the spinel websterite.

The intracrystalline structures also differ between garnet pyroxenites and spinel websterites. Most clinopyroxene crystals in garnet pyroxenites are segmented in subgrains (in red in Fig. 4-10d-e) with sizes similar to the recrystallized grains in the matrix. In spinel websterites, subgrains are less common (cf. lower proportion of low-angle grain boundaries in Fig. 4-10f), occurring mainly parallel to the (100) exsolution planes of the large clinopyroxene porphyroclasts (Fig. 4-10a-b). This occurrence suggests that shearing along twinning lamellae produced an additional rotation of a few degrees that transformed the lamellae into subgrains. In the spinel websterites, clinopyroxene and orthopyroxene neoblasts located up to 2 mm away from the porphyroclast and its exsolutions, respectively, show similar crystallographic orientations (Fig. 4-10b). This geometry illustrates how dynamic recrystallization created significant grain-size reduction in these initially very coarse-grained rocks. Presence of neoblasts with strong misorientations relative to the porphyroclast within domains where the continuity of exsolutions indicates that they were initially part of the porphyroclast (upper left corner of Fig. 4-10a), implying that nucleation and growth are also involved in the recrystallization process.

Finally, EBSD analyses on undeformed clinopyroxene-orthopyroxene-spinel aggregates in spinel websterite BB073CW (Fig. 4-11a) highlight topotaxic crystallographic relations between the three phases. Orthopyroxene and clinopyroxene have almost identical CPO and their [010] axes are parallel to the spinel [110] axes. In addition, orthopyroxene [100] axes are parallel to spinel ⟨110⟩ axes. In garnet-spinel

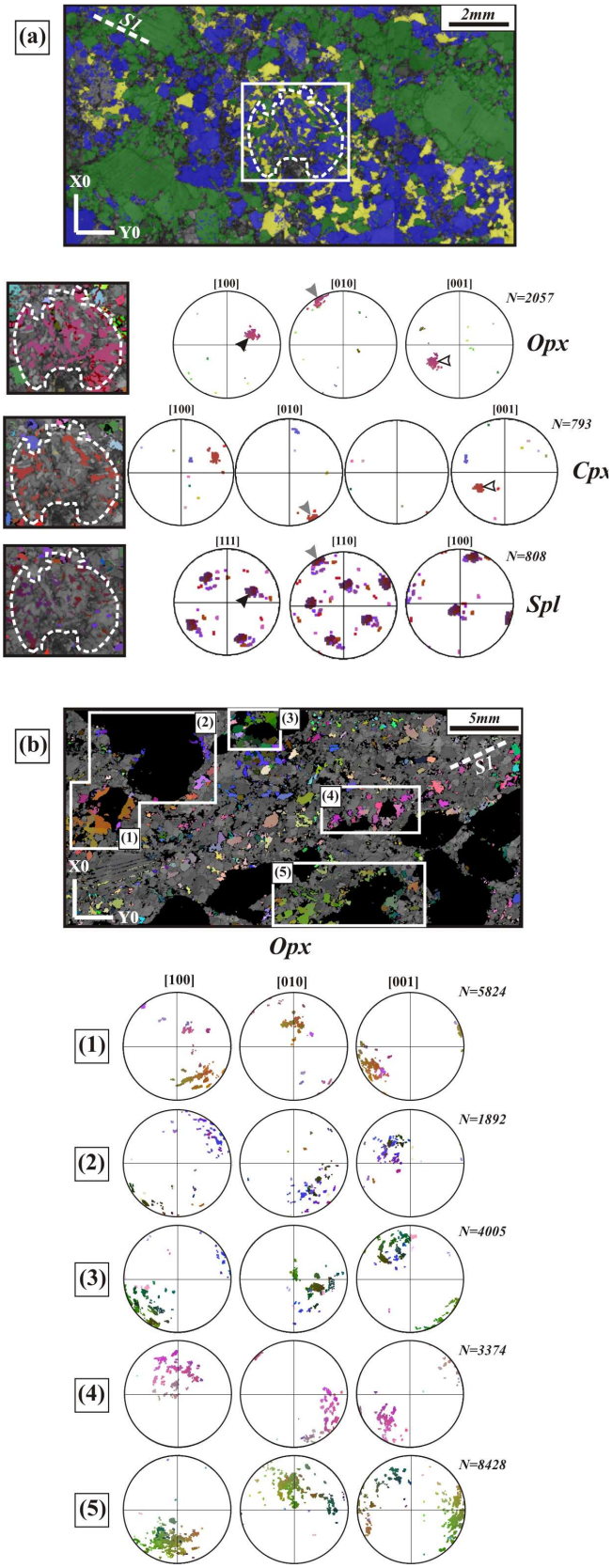

Figure 4-11. (a) Phase distribution map showing an undeformed clinopyroxene (green), orthopyroxene (blue), and spinel (yellow) symplectite sharing topotactic relations related to the breakdown of former garnet. Black, gray and white arrows indicate shared crystallographic orientations between the different minerals in stereoplots. (b) Orthopyroxene rims around kelyphite with quasi-single-crystal orientations suggesting topotaxic growth at the expense of garnet.

websterite BB075W, orthopyroxene coronas developed around kelyphitized garnets also show almost single-crystal CPO (Fig. 4-11b). Similar topotaxial relationships among spinel and pyroxenes were observed in kelyphite from retrograde garnet peridotites by Odashima et al. (2008) and Obata and Ozawa (2011). Padrón-Navarta et al. (2008) also identified topotaxial and homoepitaxial relations during the formation of garnet after pyroxenes from prograde mafic garnet granulites.

4.6. Mineral Chemistry

Table 2 lists representative analyses of pyroxenites constituent minerals. **Garnet** is always pyrope-rich: $Prp_{35–70}$, $Alm_{17–45}$,$Grs_{3-26,}$ with minor spessartine (Sps) and andradite (Adr) components ($Sps_{0–2}$ Adr_{0-4}). Garnet porphyroclasts show no significant zoning, except for 2 garnets found respectively in samples BB007 and BB031 that show a rimward decrease of the Prp content accompanied by an increase in the Grs content.

In all studied pyroxenites, **clinopyroxene** is rich in Al (0.37 ±0.07 atoms per formula unit [a.p.f.u.], calculated on the basis of 6 oxygens), and in Na (0.13 ±0.03). It also has large amounts of non-quadrilateral Tschermak (0.12 ±0.04) and acmite-jadeite (0.13 ±0.03) components. These non-quadrilateral components show a slight rimward increase in the few preserved porphyroclasts from garnet clinopyroxenites, but a rimward decrease in the large porphyroclasts of the spinel websterites. No significant zoning was observed in the neoblasts.

Orthopyroxene in the websterites is rich in Ca (0.02 ± 0.01 a.p.f.u. based on 6 oxygens) and in Al (0.26 ± 0.04). Porphyroclasts may be slightly zoned with a rimward decrease in Al coeval with a slight increase in Ca. Small orthopyroxene neoblasts in garnet clinopyroxenites (sample BB025E) yield much less Al (0.12 ± 0.04).

Spinels are Mg-rich (average Mg # = 0.73 ±0.04) in both garnet-spinel websterites and spinel-websterites and yield average Cr # of 0.03 ± 0.01, except for sample BB033W that yields a higher Cr # of 0.07.

Finally, **olivine** in the olivine-spinel websterite BB073CW is rather Mg-poor (Mg# = 0.85±0.01).

Table 2 . Representative analyses of minerals

	Garnet clinopyroxenite					Spinel bearing garnet pyroxenite							Spinel websterite							
Sample	BB034W				BB025E	BB076BBE		BB033W		BB076BBE			BB073CW							
Texture	por		nco			por				nco			por				nco			int
Core/Rim	c	r	c	c	c	c	r	c	r	c	c	c	c	r	c	r	c	c	c	
Mineral	Grt	Grt	Grt	Cpx	Opx	Cpx	Cpx	Opx	Opx	Cpx	Opx	Spl	Cpx	Cpx	Opx	Opx	Cpx	Opx	Ol	Spl
SiO_2 (wt.%)	41.26	41.36	41.13	52.28	53.09	50.68	50.99	54.53	54.98	51.13	53.90	0.02	51.00	51.40	53.12	54.04	51.53	53.82	40.05	0.01
TiO_2	0.14	0.17	0.11	0.41	0.16	0.48	0.43	0.18	0.11	0.46	0.04	0.08	0.68	0.72	0.13	0.13	0.70	0.16	0.00	0.05
Al_2O_3	22.90	22.86	22.88	7.01	3.46	9.05	8.86	5.77	5.37	8.86	5.34	60.69	9.19	7.74	6.76	5.54	8.22	5.61	0.00	63.09
Cr_2O_3	0.10	0.12	0.10	0.15	0.08	0.22	0.22	0.31	0.35	0.13	0.08	3.13	0.45	0.33	0.25	0.21	0.40	0.18	0.01	3.77
FeO*	15.36	15.43	15.86	6.46	17.07	4.01	4.84	6.54	6.63	4.28	10.29	18.42	3.44	3.84	9.15	9.50	3.73	9.19	15.19	13.19
MnO	0.35	0.36	0.37	0.16	0.25	0.13	0.15	0.15	0.19	0.13	0.21	0.26	0.09	0.12	0.17	0.22	0.07	0.15	0.17	0.17
NiO	0.00	0.00	0.01	0.06	0.17	0.00	0.04	0.10	0.10	0.03	0.08	0.37	0.05	0.01	0.05	0.09	0.04	0.10	0.34	0.51
MgO	16.08	15.90	15.77	12.95	25.93	13.00	15.10	32.10	32.58	13.65	30.06	16.94	12.84	13.85	29.98	30.26	13.70	30.02	45.03	19.28
CaO	4.65	4.71	4.70	18.54	0.58	20.21	17.22	0.58	0.37	19.30	0.47	0.00	19.72	19.98	0.42	0.48	19.48	0.80	0.02	0.00
Na_2O	0.02	0.03	0.01	2.11	0.03	1.82	1.68	0.02	0.01	1.71	0.01	0.00	2.14	1.69	0.02	0.02	1.87	0.04	0.00	0.01
K_2O	0.01	0.01	0.01	0.02	0.02	0.03	0.02	0.03	0.02	0.02	0.02	0.02	0.02	0.02	0.02	0.01	0.02	0.01	0.01	0.01
Total	100.95	101.05	101.05	100.17	100.83	99.64	99.56	100.33	100.69	99.69	100.50	99.92	99.61	99.69	100.09	100.50	99.77	100.10	100.82	100.09
O†	12	12	12	6	6	6	6	6	6	6	6	4	6	6	6	6	6	6	4	4
Si	2.986	2.995	2.981	1.906	1.913	1.847	1.8501	1.879	1.887	1.857	1.885	0.001	1.853	1.869	1.856	1.883	1.869	1.882	0.999	0.000
Ti	0.006	0.009	0.006	0.011	0.004	0.013	0.0117	0.005	0.003	0.013	0.001	0.002	0.018	0.020	0.004	0.003	0.019	0.004	0.000	0.001
Al_{tot}	1.953	1.951	1.954	0.301	0.147	0.389	0.3788	0.234	0.217	0.379	0.220	1.878	0.394	0.332	0.278	0.228	0.351	0.231	0.000	1.901
^{IV}Al				0.094	0.087	0.153	0.1499	0.121	0.113	0.143	0.115		0.147	0.131	0.144	0.117	0.131	0.118		
^{VI}Al				0.207	0.059	0.236	0.2289	0.114	0.104	0.237	0.105		0.247	0.201	0.134	0.111	0.220	0.113		
Cr	0.006	0.007	0.006	0.004	0.002	0.006	0.0063	0.009	0.009	0.004	0.002	0.065	0.013	0.009	0.007	0.006	0.012	0.005	0.000	0.076
Fe^*_{tot}	0.930	0.935	0.962	0.197	0.514	0.122	0.1467	0.189	0.190	0.130	0.301	0.404	0.104	0.117	0.267	0.277	0.113	0.269	0.317	0.282
Fe^{2+}‡	0.877	0.900	0.895	0.182		0.100	0.131			0.130			0.100	0.115			0.113			
Fe^{3+}‡	0.053	0.035	0.067	0.015		0.022	0.016			0.000			0.004	0.002			0.000			
Mn	0.022	0.022	0.023	0.005	0.008	0.004	0.0047	0.005	0.005	0.004	0.006	0.006	0.003	0.004	0.005	0.007	0.002	0.005	0.004	0.004
Mg	1.735	1.716	1.704	0.704	1.392	0.707	0.8168	1.649	1.667	0.739	1.567	0.663	0.696	0.751	1.562	1.572	0.741	1.565	1.674	0.735
Ca	0.360	0.365	0.365	0.724	0.022	0.789	0.6694	0.022	0.014	0.751	0.018	0.000	0.767	0.778	0.016	0.018	0.757	0.030	0.000	0.000
Na				0.149	0.002	0.129	0.1183	0.001	0.000	0.121	0.001	0.000	0.151	0.119	0.002	0.001	0.131	0.003	0.000	0.001
K				0.001	0.000	0.001	0.000	0.001	0.001	0.001	0.001	0.001	0.001	0.001	0.001	0.001	0.001	0.000	0.000	0.000
Ni				0.002	0.005	0.000	0.0012	0.003	0.003	0.001	0.002	0.008	0.001	0.000	0.001	0.002	0.001	0.003	0.007	0.010
Total	8.000	8.000	8.000	4.005	4.010	4.007	4.005	3.996	3.997	3.999	4.004	3.027	4.001	4.001	3.999	3.998	3.997	3.997	3.001	3.011
X_{Mg}**	0.664	0.656	0.656	0.782	0.730	0.876	0.862	0.897	0.898	0.850	0.839	0.621	0.874	0.867	0.854	0.850	0.868	0.853	0.841	0.723
Cr#**												0.033								0.039
X_{Prp}	0.579	0.571	0.570																	
X_{Alm}	0.300	0.299	0.299																	
X_{Grs}	0.088	0.098	0.084																	
X_{Sps}	0.007	0.007	0.008																	
X_{Adr}	0.028	0.019	0.035																	
CaTs				0.101		0.133	0.143			0.144			0.094	0.107			0.117			
Ac				0.036		0.016	0.015			0.017			0.002	0			0.003			
Jd				0.112		0.103	0.063			0.100			0.119	0.128			0.116			
AcJd				0.148		0.119	0.078			0.117			0.121	0.128			0.119			

*FeO and Fe calculated as total iron.† Number of oxygens for which cations are calculated. ‡ Fe^{2+} and Fe^{3+} based on garnet and clinopyroxene stoichiometry.

** $X_{Mg} = Mg / (Mg + Fe^{2+})$. Fe_{tot} was used for orthopyroxene, olivine and spinel. Cr# = Cr / (Cr + Al).

Ac = Fe^{3+}, CaTs = CrCaTs+AlCaTS, CrCaTs = Cr, AlCaTs = ^{VI}Al-Jd, Jd = Na-Ac (if Na-Ac < ^{VI}Al), Jd= ^{VI}Al (if Na-Ac ? ^{VI}Al).

4.7. Geothermobarometry

Phase equilibria were computed by free energy minimization in the system Cr_2O_3–Na_2O-CaO-FeO-MgO-Al_2O_3-SiO_2 (CrNCFMAS) using Perple_X (Connolly, 2009) and the internally consistent thermodynamic data of Holland and Powell (1998) with additional data for Cr-spinels and Cr-garnets from Klemme et al. (2009). Other solid solutions used were orthopyroxene and clinopyroxene (Holland and Powell, 1996; both modified for ideal Cr, see Perple_X documentation for more details), olivine (Holland and Powell, 1998), and plagioclase (Newton et al., 1980).

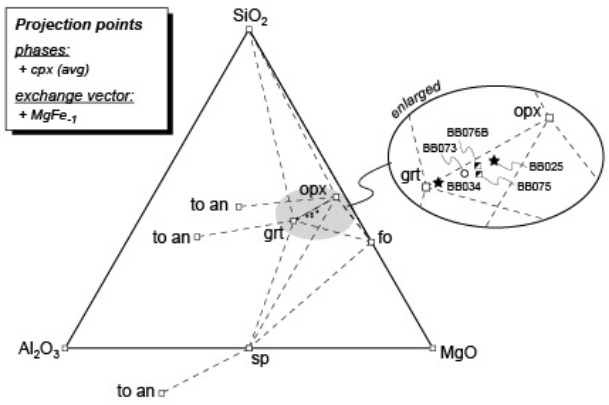

Figure 4-12. Bulk-rock composition of selected samples projected from the NCFMAS system. Projection through the exchange vector $MgFe_{-1}$ using an average clinopyroxene composition (cf. Table 2) computed with CSpace (Torres-Roldán et al., 2000).

Bulk-rock compositions of five representative garnet-clinopyroxenite, garnet and spinel websterite, and spinel websterite samples projected into the SiO_2-Al_2O_3-MgO compatibility diagram from the NCFMAS system are presented in Fig. 4-12. Irrespective of the mineral assemblage, all samples plot in the same region supporting the application of equilibrium thermodynamic calculation assuming the same bulk-rock composition so as to constrain their pressure and temperature evolution. Figure 13a displays the pseudosection computed for the bulk-rock composition of garnet clinopyroxenite BB034W, which has a homogeneous texture, in the NCFMAS system between 700 and 1300˚C and a pressure range of 1.0 – 3.0 GPa. A pseudosection for the same bulk-composition was also calculated in the CMAS system (not shown) to test the effect of the Cr_2O_3 component. The phase relation topology remains the same except for the reaction,

$$grt + ol = opx + spl + cpx \quad [1]$$

that is invariant in the CMAS simplified system, which is displaced to lower pressure (ca.0.4 GPa). This supports the importance of the Cr_2O_3 component in modeling the garnet to spinel transition as previously stressed by Klemme (2004) and Klemme et al. (2009).

The pseudosection in Fig. 4-13a shows that for the computed temperature range, the garnet clinopyroxenite field is constrained to pressures above 1.2 GPa. The olivine-bearing garnet spinel websterites that characterize the Ariègite-Seiland transition in Beni Bousera are limited to a narrow 5-phase field (orthopyroxene, olivine, garnet, clinopyroxene, and spinel), constraining pressures to 1.1-1.2 GPa at 700˚C and 1.8 GPa at 1200˚C. Finally the garnet-out curve and the pyroxenite solidus for similar bulk compositions from Lambart et al. (2009) constrain the spinel websterite to have equilibrated at pressures less than 1.8 GPa. As mentioned above, at the sample/outcrop scales, these rocks still exhibit kelyphitized garnet and could therefore have been equilibrated close to the Ariègite-Seiland transition. The presence of the fine-grained plagioclase-bearing assemblages in the matrix of some spinel websterites indicates late to post-kinematic partial re-equilibration in the plagioclase stability field (pressures ≤ 1.2 – 1.3 GPa).

Synkinematic PT conditions for garnet clinopyroxenites were estimated from the composition of the recrystallized exsolution-free pyroxenes in the matrix using several well-calibrated conventional barometers and thermometers. Pressure was estimated from the Al content in orthopyroxene of Nickel and Green (1985) and Taylor (1998) using the orthopyroxene compositions in sample BB025E. Temperatures were estimated using the Fe-Mg exchange in clinopyroxene-orthopyroxene pairs (Taylor, 1998), the Ca content in orthopyroxene (Brey and Köhler, 1990, modified by Nimis and Grutter, 2010), and the enstatite activity in clinopyroxene (Nimis and Taylor, 2000). These three methods give similar results. Synkinematic recrystallized assemblages in garnet clinopyroxenites yield pressures of 1.9-2.2 GPa and temperatures of 950-1000°C. The modeled phase assemblage in the pseudosection under these PT conditions (orthopyroxene, olivine, garnet and clinopyroxene, Fig. 4-13a) is in good agreement with observed modal composition of garnet-clinopyroxenites, where garnet and clinopyroxene represent more than 90 vol. % and orthopyroxene and olivine are minor phases.

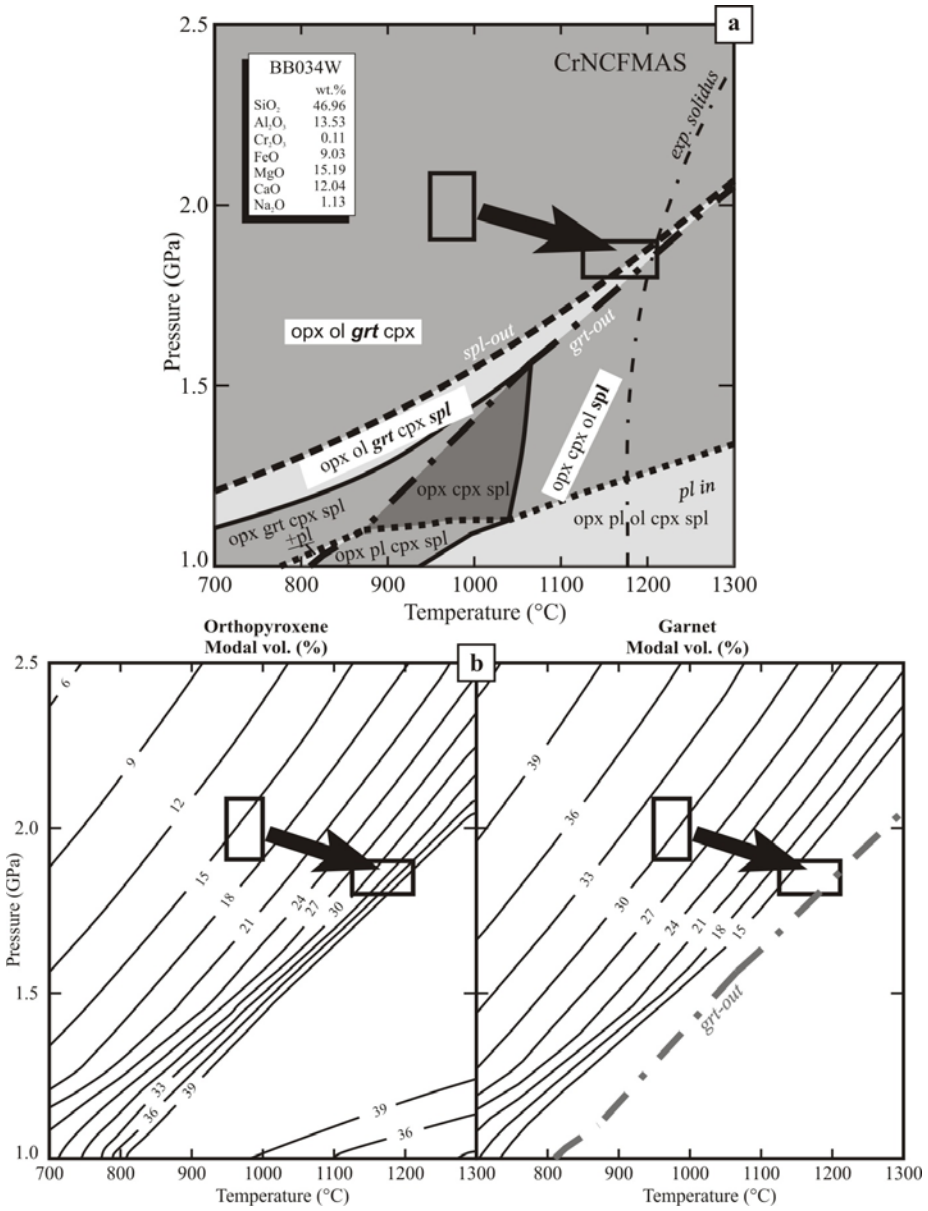

Figure 4-13 (a) P-T-phase diagram for the bulk-rock composition of garnet clinopyroxenite BB034W. Experimental solidus of Beni Bousera garnet clinopyroxenite from Lambart et al. (2009). (b) Variation of garnet and orthopyroxene modal volumes during the proposed PT path. Mineral abbreviations after Whitney and Evans (2010).

The transition between garnet clinopyroxenite and spinel pyroxenites could be reached either by a decrease in pressure resulting in the assemblage orthopyroxene-clinopyroxene-spinel or by an increase in temperature during decompression. The latter path should however result in small amounts of olivine (ca. 2 vol. %) in the spinel pyroxenite assemblage (Fig. 4-13a). The observation of olivine (Table 1) together with the microstructural data in the spinel pyroxenites, in particular the larger recrystallized grain sizes and the evidence for grain boundary migration supports higher temperatures (T>1040-1050°C) during the deformation of the spinel websterites. Pressure calculations using the Cr content in spinel (O'Neill, 1981) for these temperatures yield ~ 1.8 GPa. These results are slightly inconsistent with the calculated pseudosection, which implies a temperature of 1170-1180°C at 1.8 GPa. Using these higher temperatures increases the calculated pressure for the same geobarometer to 1.9 GPa. Conventional geothermometers that satisfied T > 1040-1050°C yielded 1113 ± 31°C for the Taylor (1998) thermometer, 1151 ± 16°C for the Brey and Köhler (1990) two-pyroxene thermometer, and 1157°C for the Wood and Banno (1973) one.

The PT evolution derived from both conventional geothermometry and microstructural observations is corroborated by the observed increase in modal volume of orthopyroxene (from 0 to 35%, and up to 45% for orthopyroxene-rich sample BB033W, Table 1) and decrease in garnet modal volume (from 45 to 17% and down to 0% for the garnet free samples BB073CW and BB018W) from the garnet clinopyroxenites to the spinel websterites. The crystallization of orthopyroxene at expenses of olivine can be modeled in the CMAS system. It results from two different reactions: the invariant reaction [1], which is limited by the small amount of olivine in the garnet clinopyroxenite protolith, and the exchange reaction involving a Tschermaks-type substitution (the subscript "ss" indicates solid solution):

$$grt_{ss} + cpx_{ss} = opx_{ss} + cpx_{ss}, \quad [2]$$

that occurs in divariant fields containing Grt and Cpx. Reaction [2] has a positive slope in the PT diagram and therefore the garnet breakdown may result either from a decrease in pressure and/or an increase in temperature (see isopleths of modal proportion in Fig. 4-13b). Crystallization of orthopyroxene at the expense of garnet is also consistent with microstructural observations that show orthopyroxene coronas with single-crystal like orientations around former garnets (Fig. 4-11b).

The PT conditions calculated for equilibration of the garnet-spinel websterites and spinel websterite are close to the solidus of Beni Bousera garnet clinopyroxenite (Lambart et al., 2009). This prediction is consistent with previous work on Ronda pyroxenites that concluded that olivine-bearing spinel websterite formed by melting of garnet clinopyroxenites upstream of the peridotites' melting front (Garrido and Bodinier, 1999; Soustelle et al., 2009).

4.8. Discussion

4.8.1. Deformation mechanisms

4.8.1.1. - Garnet

Clear evidence for plastic deformation of garnet in mantle rocks is rather rare (Carstens, 1969, 1971). However, the present observations in pyrope-rich garnets (Table 2) are similar to microstructures interpreted from dislocation creep in almandine-rich garnets in granulites (Dalziel and Bailey, 1968; Ross, 1973; Ji and Martignole, 1994; Kleinschodt and McGrew, 2000; Kleinschrodt and Duyster, 2002; Prior et al., 2000) and in

more ferro-magnesian garnets from eclogites from HP/UHP metamorphic terranes (Chen et al., 1996; Bascou et al. 2001; Mainprice et al. 2004). These observations include: the lens shape of garnet porphyroclasts and their alignment marking the lineation and foliation in garnet clinopyroxenites (Figs. 4-2b,c and 4-3) as well as the strong intracrystalline misorientations accommodated by rotations around low-order crystallographic axes, dominantly <111>, and presence of subgrains within elongated garnet porphyroclasts (Figs. 4-9 and 4-10). In the most deformed samples, garnet porphyroclasts are almost fully recrystallized and the pancake-like garnets observed in hand samples are actually polycrystalline aggregates (Fig. 4-9e).

TEM observations of experimentally (Voegelé et al., 1998, 1998a,b) and naturally deformed garnets (Ando et al., 1993; Doukhan et al., 1994; Voegelé et al., 1998; Ji et al., 2003) reveal both ½ ⟨100⟩ and ½ ⟨111⟩ dislocations. Viscoplastic self-consistent modelling of the evolution of garnet CPO in simple and pure shear shows that activation of these slip systems, with ⟨111⟩ slip easier than ⟨100⟩, results in alignment of ⟨110⟩ axes parallel to the lineation and of {100} and {111} planes parallel to the foliation (Mainprice et al., 2004). CPO is nevertheless always weak, due to the cubic structure of garnet, which results in a large number of equivalent slip systems. For instance, the ⟨111⟩{110} mode that accommodates most deformation in the models is composed of 12 slip planes/directions.

Garnet CPO in the Beni Bousera garnet clinopyroxenites are always weaker than the model predictions ($J \leq 1.3$, Table 1), but this difference is also the case for the naturally deformed eclogites analyzed in Mainprice et al. (2004). Among our samples, only BB007 and BB125BW show concentrations of ⟨110⟩ axes parallel to the lineation (Fig. 4-6) as predicted by the numerical models of garnet deformation. The remaining samples do not show concentration of any of the main crystallographic axes parallel the lineation or foliation. It is important to note, however, that the VPSC models in Mainprice et al. (2004) were calculated for pure garnet aggregates, whereas in the Beni Bousera pyroxenites most deformation has probably been accommodated by the pyroxenes, which are almost fully recrystallized. In those samples with weaker garnet shape-preferred orientations, rotation of garnet crystals in a less-viscous pyroxene matrix may also have contributed to the dispersion of the garnet CPO.

Strong keliphitization hinders the analysis of garnet deformation in the garnet-spinel websterites, but the more rounded shapes of the coarse garnet crystals in these samples suggest that they are less deformed. Finally, the embayments filled by pyroxenes along garnet grain boundaries in garnet clinopyroxenites (Fig. 4-3d) cannot have formed by plastic deformation. They rather suggest syn- to late-kinematic reactions that crystallize pyroxenes at the expense of garnet.

4.8.1.2. - Clinopyroxene

Microstructures and CPO of clinopyroxenes of the Beni Bousera pyroxenites record a variety of deformation processes: from mechanical twinning on [001](100) (Fig. 4-10a) to dislocation glide assisted by dynamic recrystallization by subgrain rotation (Fig. 4-10) and in a lesser extent, grain boundary migration (Fig. 4-3f). The abundance of subgrains with grain sizes similar to the recrystallized matrix (Fig. 4-10a), together with the large proportion of low angle grain boundaries with misorientations <15° (Fig. 4-10f) and their dominant rotations around [001] (Fig. 4-10c), indicates that subgrain rotation was the dominant recrystallization mechanism in garnet pyroxenites .Figure 4-3f shows that some bulging recrystallization did occur. However, the grain size of these bulges and of the pyroxene crystals formed by this process (5-10μm) is an order of magnitude smaller than

recrystallized crystals that compose most of the matrix. In the spinel websterites that were equilibrated at higher temperatures, nucleation and growth probably contributed more to recrystallization, as indicated by the presence of strongly misoriented crystals in domains where the continuity of the exsolutions indicates that they were part of a former porphyroclast (Fig. 4-10a). Stress concentration at the tips of the exsolution lamellae might have favored the nucleation.

Mechanical twinning of diopside on [001](100) was first recorded in the pioneering experiments of Avé Lallemant (1978), who deformed single crystals at temperatures below 850 ºC and strain rates of 10^{-3} s^{-1} in a Griggs apparatus. Twinning on [100](001) was observed at higher temperatures (1000°C) and lesser strain rates (10^{-6} s^{-1}). Similar results were reported by Kollé and Blacic (1982, 1983) for Cr-diopside and hedenbergite. However, to our knowledge, our observation are the first that clearly evidenced mechanical twinning along [001](100) in clinopyroxenes deformed at high temperature (1100-1150ºC) and natural strain rates.

TEM observations on experimentally deformed diopside crystals enabled the identification of dislocation glide systems active as a function of the temperature for laboratory strain rates: between 800 - 900°C, [001](100) is the easiest slip system, but [100](010), ½ ⟨110⟩{1-10} and [001]{110} are also activated (Ingrin et al., 1992). Above 1000°C, the most favorable slip system is ½ ⟨110⟩{1-10}, but [001]{110} and [001](100) are also active (Raterron and Jaoul, 1991; Jaoul and Raterron, 1994).

Experimentally deformed diopside aggregates (Boland and Tullis, 1986; Lavie, 1998; Mauler et al., 2000; Bystricky and Mackwell, 2001), naturally-deformed omphacite-bearing eclogites (Van Roermund and Boland, 1981; Van Roermund, 1983; Buatier et al., 1991; Godard and Van Roermund, 1985) and lower crustal gabbros (Barruol and Mainprice, 1993) usually have clear clinopyroxene CPO characterized by [001] and [010] axes aligned subparallel to the lineation and normal to the foliation, respectively. Al- and Na-rich clinopyroxenes (Table 2) from Beni Bousera pyroxenites show similar CPO patterns, except for garnet pyroxenite BB031 (Fig. 4-6). These patterns are consistently reproduced by viscoplastic self-consistent models in which much the deformation is accommodated by glide on [001]{110} (Bascou et al., 2002). Based on these results and on the petrological data, we conclude that clinopyroxene in the Beni Bousera pyroxenites deformed by dislocation creep with dominant activation of the [001]{110} system over a temperature range of 950-1150ºC. The transition to dominant glide on ½ ⟨110⟩{1-10} observed at 1000°C in experiments occurs therefore at higher temperatures in nature. This difference suggests that the transition might be strain-rate dependent, being favored under high strain rates.

CPO evolution models also showed that the strain regime controls the CPO symmetry (Bascou et al. 2002). Transpression, for instance, results in a dispersion of [001] in the foliation plane similar to that observed in many Beni Bousera pyroxenites. The anastomosed pattern of the foliation around the more competent garnet crystals may account, on the other hand, for the dispersion of [001] in the XZ plane observed in the remaining samples. This geometry may also explain the obliquity between the clinopyroxene CPO and the foliation observed in some samples. However, it cannot explain the bimodal distribution of [001] relative to the lineation displayed by spinel websterites BB076BBE, BB068E, and BB073CW. Finally, BB031 has a clinopyroxene CPO that is not consistent with glide on any known clinopyroxene slip system.

4.8.1.3. - Orthopyroxene

As in previous microstructural studies of naturally deformed orthopyroxenites (Etheridge, 1975), lattice bending and kinking are common in our samples. In addition, like clinopyroxene, orthopyroxene also shows evidence for

dynamic recrystallization. The strong misorientation of recrystallized grains (Fig. 4-10a) suggests that nucleation and growth contribute to this process. These processes are likely favored by the high temperatures recorded in the spinel websterites.

The most commonly observed slip system in experimentally deformed enstatite is [001](100) (Turner et al., 1960, Raleigh, 1965, Green and Radcliffe, 1972). Ross and Nielsen (1978) also observed slip on [001](010) in wet polycrystalline enstatite deformed at high temperature. [010] dislocations (Lally et al. 1972, Kohlstedt and Vandersande, 1973) and even longer Burger vectors ones (Skrotzky, 1994) were also reported in naturally deformed rocks, but they remain minor.

Measured CPO of Al- and Ca-rich orthopyroxene crystals (Table 2) from Beni Bousera pyroxenites are characterized by clustering of [001] subparallel to the lineation and [100] axes near the normal to the foliation. This is consistent with dominant slip on [001](100). Two garnet-spinel pyroxenites, BB076BBE and BB075W, show [010] axes clustered perpendicular to the foliation plane and are more consistent with dominant slip on [001](010). There is however no independent indication that these two pyroxenites were deformed under different hydration conditions. Similar orthopyroxene CPOs are also observed in peridotites deformed under lithospheric and asthenospheric conditions (e.g. Tommasi et al., 2006; Tommasi et al., 2008; Soustelle et al., 2009), suggesting that both planes may be activated in nature. Finally, the topotaxic relations between orthopyroxene and clinopyroxene observed in the symplectite might explain the strong correlation with clinopyroxene CPO.

4.8.2. Changes in deformation processes and rheological contrasts as a function of synkinematic P-T conditions

Based on the microstructures and CPO data analyzed above, we conclude that the deformation of Beni Bousera pyroxenites was essentially accommodated by dislocation creep of the volumetrically dominant clinopyroxene. Consistent orientations of the pyroxenite layering and of the foliation of the host peridotite at the massif scale (Reuber et al., 1982) suggest similar kinematics and hence a continuous deformation across the different metamorphic domains. Thermobarometric modeling indicates however that deformation of the garnet clinopyroxenites took place under lower temperatures and higher pressures than the deformation of the spinel websterites, respectively 950°C-2.0GPa and 1150°C-1.8GPa (Fig. 4-13).

The finer recrystallized grain sizes in the garnet clinopyroxenites relative to the spinel websterites suggests greater work rates in the former (Austin and Evans, 2007). Assuming a non-linear viscous rheology typical of crystal-plastic deformation by dislocation creep, we estimated the stresses during deformation of both garnet clinopyroxenites and spinel websterites using experimentally-derived dislocation creep flow laws for dry (Bystricky et al., 2001) and wet clinopyroxenite (Chen et al., 2006). As garnet clinopyroxenites are associated with mylonitic peridotites, we assume that they deformed under faster strain rates than the spinel websterites. We assume therefore that the strain rate was $10^{-12}s^{-1}$ for garnet clinopyroxenite versus $10^{-14}s^{-1}$ for spinel websterites. Calculations for clinopyroxene creep under dry conditions yielded ca. 185 MPa for the garnet clinopyroxenites and ca. 7MPa for the spinel websterites. Stresses calculated for wet conditions are substantially smaller, down to ca. 10 MPa and 7 x 10^{-2} MPa, respectively. In both cases, however, stresses for the garnet clinopyroxenites are greater by more than one order of magnitude than those predicted for the spinel websterites.

If strain rates are supposed similar in both domains, stresses in the garnet pyroxenites are still one order of magnitude larger.

The extremely small stresses obtained using wet clinoyroxene rheologies are consistent with the conclusion by Chen et al. (2006) that for hydrated conditions pyroxenites are weaker than peridotites. An inversion in the rheology contrast between pyroxenites and peridotites is however not corroborated by our field observations. The systematic boudinage of the pyroxenite layers (Fig. 4-2) indicates that pyroxenites are more competent than peridotites in all domains. Thus, although the deformation of garnet in the garnet clinopyroxenites indicates a small rheological contrast relative to the clinopyroxene, this reduction in competence contrast cannot be explained by hydration of the garnets, as proposed by Muramoto et al. (2011) to account for plastic deformation of garnet in pyroxenites in supra-subduction environments. The more rounded shapes of garnets in garnet-spinel websterites close to the Ariegite-Seiland transition and the coarser clinopyroxene grain size suggest a greater competence contrast between garnet and clinopyroxene during deformation of this domain, which occurred at higher temperature and lower pressure conditions. Based on these observations, we propose that the reduction in the competence contrast between garnet and clinopyroxene is due to the greater stresses implied in the deformation of the colder garnet pyroxenites.

Although the analysis of field structures does not corroborate an inversion of the competence contrast between the garnet clinopyroxenites and the host peridotite, it points to a reduced competence contrast between the two rocks. Garnet clinopyroxenites in garnet-spinel mylonites often outcrop as extremely stretched, partially disrupted layers (Fig. 4-2a,c). Even in thicker garnet pyroxenites, macroscopic boudins in the Beni Bousera massif are symmetric boudins that could be classified as "drawn" boudins in the sense of Goscombe et al. (2004) and require small competence contrasts (Fig. 4-2c). Deformation under high stress conditions is probably an effective mechanism for compositional homogeneization of the lithospheric mantle through mechanical mixing. Stretching of pyroxenite layers also increases the effective contact surface with the host peridotites and decreases grain sizes, enhancing the kinetics of pyroxenite-peridotite reactions during heating/exhumation.

4.9. Conclusions

Analysis of the microstructure, CPO, and thermobarometric data of pyroxenites from the Beni Bousera massif evidences that under lithospheric and near asthenospheric mantle conditions pyroxenites deform by dislocation creep. Strain was essentially accommodated by the pyroxenes, which deformed by dislocation creep involving glide on [001]{110} in clinopyroxene and on [001](100) and [001](010) in orthopyroxene, recovery, and dynamic recrystallization by subgrain rotation. Grain boundary migration also contributed to recrystallization during the deformation of the spinel websterites that deformed under higher synkinematic temperature conditions. In the latter, mechanical twinning also played an important role in the deformation and recrystallization of large clinopyroxene crystals.

Garnet in garnet clinopyroxenites also deformed plastically. Crystal orientations maps show strong intracrystalline misorientations accommodated by rotations around ⟨111⟩ and ⟨110⟩ and subgrains, suggesting deformation by dislocation creep. However, garnet CPO are weak and only two out of five analyzed samples show CPO consistent with those predicted by viscoplastic self-consistent modeling for dominant slip ⟨111⟩{110}.

Garnet pyroxenites and spinel websterites display contrasting microstructures characterized by distinct grain size distributions, as well as different volumes of the recrystallized grain fractions. Plastic deformation of

garnet and almost complete recrystallization of clinopyroxene to fine grain sizes in the garnet clinopyroxenites indicate deformation for large work rates (and large stresses and strain rates), consistent with the higher pressure and lower temperatures conditions inferred from petrological data in these samples (2.0 GPa and 950-1000°C). These strong stress conditions might account for the reduction in the competence contrast between garnet and clinopyroxene in these rocks.

Submitted to Journal of Petrology

5. Petrostructural evolution of the Beni Bousera peridotite massif (Rif belt, Morocco)

Erwin C. Frets[*1,2], Andréa Tommasi[2], Carlos J. Garrido[1], Alain Vauchez[2], David Mainprice[2], Kamal Targuisti[3], Isma Amri[3]

Detailed structural and petrological mapping associated with a thorough microstructural study in the Beni Bousera orogenic peridotite (Rif Belt, N Morocco) allows constraining the tectono-metamorphic evolution produced by exhumation of the subcontinental lithospheric mantle in a lithospheric-scale shear zone. The Beni Bousera massif is composed by four tectono-metamorphic domains showing consistent kinematics, marked by a pervasive shallowly-dipping foliation bearing a NW-SE stretching lineation, which progressively rotates towards a N20-N30 trend in the NE, lowermost part of the massif. From top to bottom: garnet-spinel mylonites, Ariègite subfacies fine-grained porphyroclastic spinel peridotites, Ariègite-Seiland subfacies porphyroclastic- and Seiland subfacies coarse-porphyroclastic to coarse-granular spinel peridotites. Microstructures and crystal preferred orientations (CPO) in the four domains are consistent with deformation by dominant dislocation creep, but the continuous increase in average olivine grain size and decrease in the recrystallized volume fraction indicate decreasing work rates from top to bottom. The microstructures are consistent with the variation in synkinematic pressure and temperature conditions, which range from 900°C-2.0 GPa in grt-sp mylonites and 1150°C-1.8 GPa in the Seiland domain. The diffuse compositional layering as well as the microstructures and CPO in the Seiland domain suggest deformation in presence of melt. Gravitational instabilities due to local melt accumulation may account for the small areas bearing a vertical lineation in this domain. To account for the consistent kinematics and for the large temperature gradient (ca. 100ºC/km) preserved in Beni Bousera, we propose that the massif records the functioning of a lithospheric mantle transtensional shear zone, arrested at a depth of 60 km. In this scenario, partial melting in the Ariègite-Seiland and Seiland domains results from decompression and does not require an exotic heat source.

Key words: Mantle, continental lithosphere, shear zone, deformation, microstructures, olivine, crystal preferred orientations, Beni Bousera

[1] *Instituto Andaluz de Ciencias de la Tierra (IACT), CSIC and UGR, Avenida de las Palmeras 4, 18100 Armilla, Granada, Spain.*

[2] *Geosciences Montpellier, CNRS & Université de Montpellier 2, F-34095 Montpellier Cedex 5, France.*

[3] *Département de Géologie, Faculté des Sciences Université Abdelmalek Essaâdi, Tetouan, Morocco.*

5.1. Introduction

Extension of continental lithosphere occurs in continental rifts, such as the East African, Baikal and Rio Grande rifts, and active convergent continental margins, such as in the Himalayas and the Alps (e.g. Burchfiel et al., 1992; Sue et al., 1999). While the mechanisms of crustal thinning are increasingly understood (Buck, 1997; and references therein), the processes governing the thinning of the lithospheric subcontinental mantle still remain barely constrained. Strength envelopes calculated using empirical flow laws for olivine deformation indicate that the strength of a 100 km thick continental plate largely overcomes the stresses that may be produced by mantle convection (or plate tectonics).

Another poorly understood issue is the deformation regime involved in the thinning of the subcontinental mantle. Conceptual models propose either pure (McKenzie, 1978) or simple shear (Wernicke, 1981, 1985). Lithospheric-scale thermomechanical models of continental extension (e.g. Lavier & Manatschal, 2006; Huismans & Beaumont, 2007) often show development of asymmetric normal shear zones into the lithospheric mantle, consistent with simple shear conceptual models. However, analysis of shear wave splitting data in continental rifts suggests that the lithospheric mantle in continental rifts deforms by neither pure nor simple shear, but in transtension (Vauchez et al., 1997).

Structural studies of subcontinental peridotite massifs provide a unique opportunity to constrain large-scale deformation processes of the lithospheric mantle. Among these, orogenic peridotites preserving petrological zoning implying a polybaric and polythermal evolution, such as the Ronda and Beni Bousera peridotite in the Betic-Rif belt, provide a unique opportunity to investigate the thinning and exhumation of thick, subcontinental mantle. Here we combined a petrostructural and microstructural study of peridotites in the Beni Bousera orogenic peridotite massif (Rif, NE Morocco) to study the spatial and temporal evolution of deformation processes in the subcontinental lithospheric mantle. These data allows constraining the mechanisms responsible for thinning and exhumation of subcontinental lithospheric mantle.

5.2. Tectono-metamorphic domains

We have mapped four main tectono-metamorphic domains in the Beni Bousera massif on the basis of the metamorphic facies and subfacies of peridotite defined by mineral assemblages of peridotites and host pyroxenite (e.g. O'Hara, 1967; Obata, 1980; Targuisti, 1994; Frets et al., 2012)—and microstructure of peridotite. From SW to NE, and towards structurally lower levels, these domains are (Fig. 5-1):

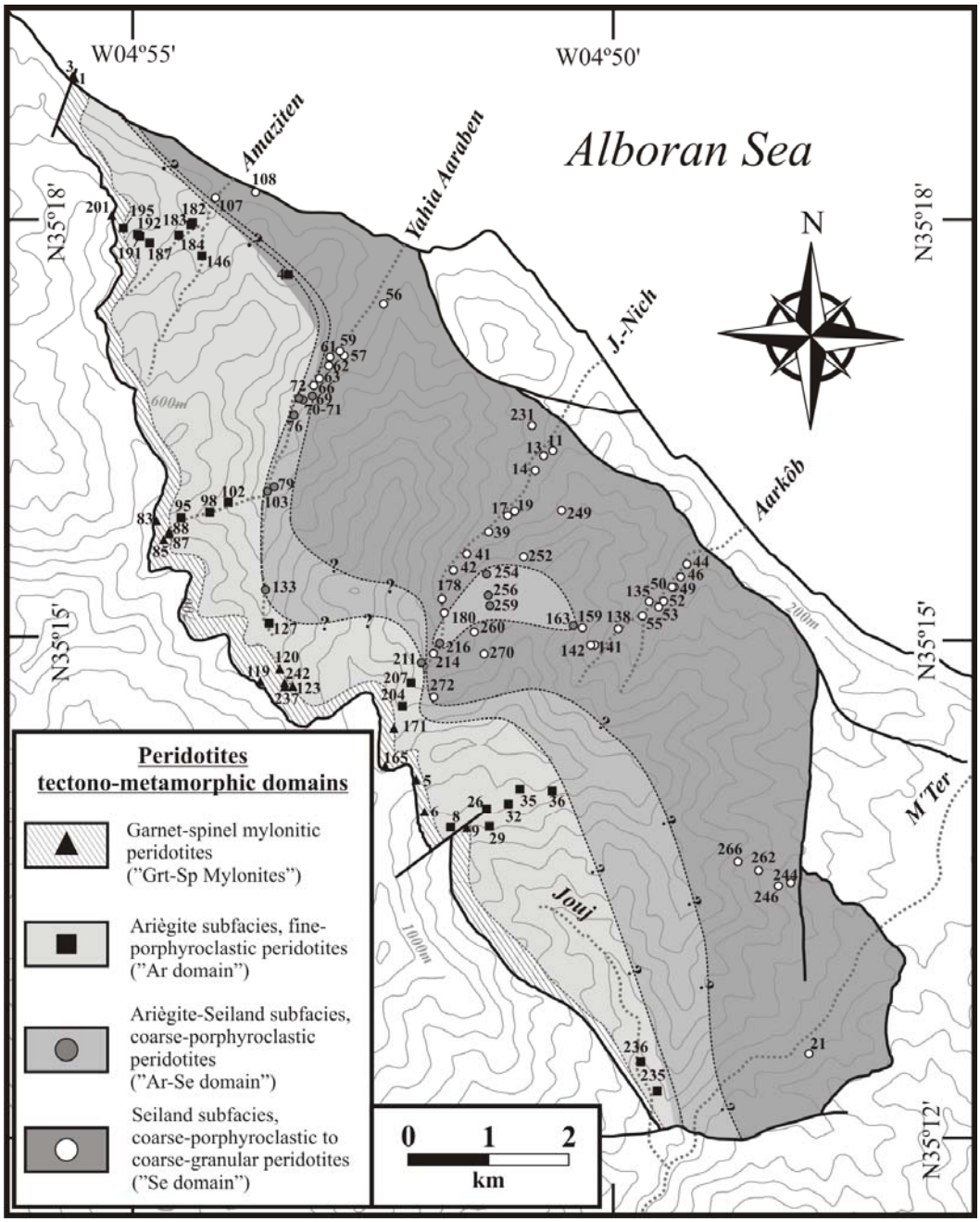

Figure 5-1. Map of the tectono-metamorphic domains of the Beni Bousera peridotite massif displaying the samples analyzed for EBSD in this study. Number refers to numeric part of sample name (e.g. BB072W="72")

(i) Garnet and spinel mylonites (hereafter referred to as "Grt-Sp Mylonites") constituting a 100-200 m wide domain below the contact with the overlying crustal garnet granulite. This domain is composed of garnet- and spinel-bearing mylonitic peridotite, displaying penetrative foliation (Fig. 5-2a-d) and lineation marked by elongated (aspect ratios reaching > 10:1) orthopyroxene porphyroclasts and spinel (Fig. 5-2a, d). Asymmetric orthopyroxene porphyroclasts and pressure shadows around garnets indicate a dominantly top to the SE shear sense. A compositional layering composed of discrete garnet pyroxenite bands <1 cm to tens of cm wide, or by more continuous variations in garnet and pyroxenes modal volume in the peridotites, parallels the foliation (Fig. 5-2a-d). The garnet

pyroxenite bands show rather sharp contacts with the host peridotite and are systematically stretched and boudinaged (Fig. 5-2c-d) (Frets et al., 2012). Thinner pyroxenite layers (≤ 5 mm) are spinel wehrlites and websterites showing more diffuse contacts with host peridotite.

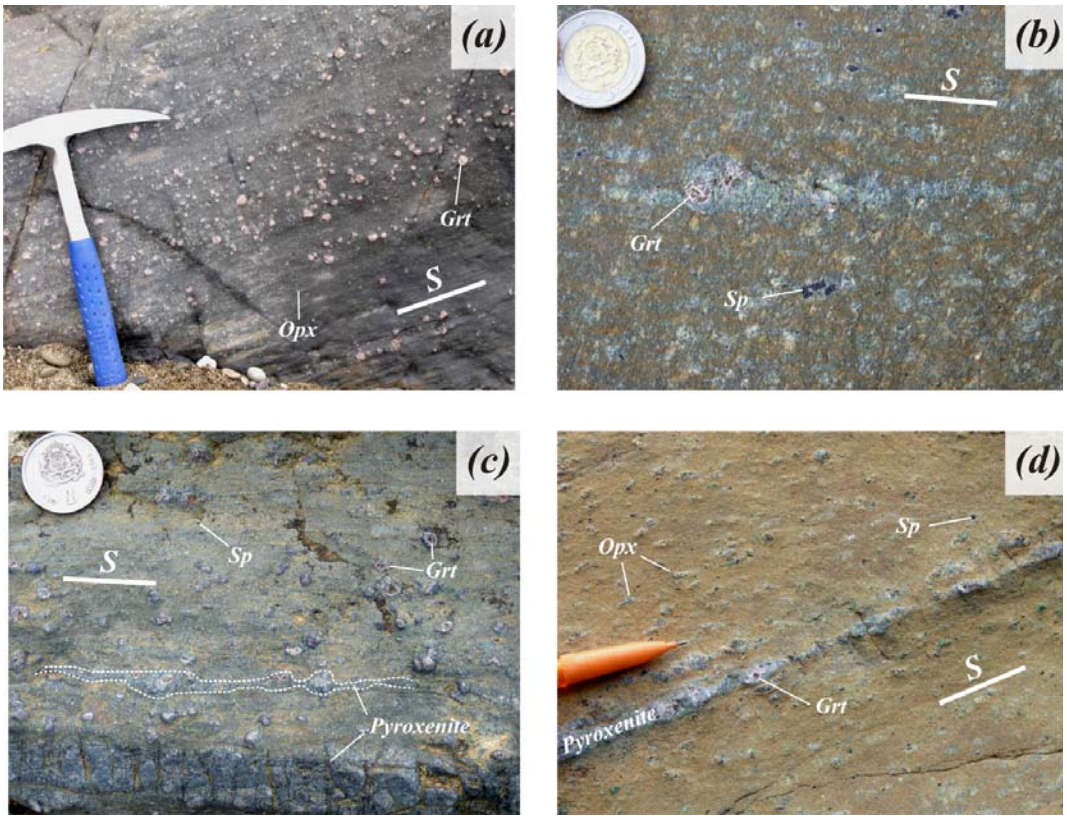

Figure 5-2. Typical macroscopic structures in the Grt-Sp Mylonites. (a-b) Foliation marked by elongation of orthopyroxene in Grt-Sp Mylonites. (c-d) Mm- to cm-scale boudinaged garnet pyroxenite layers parallel to the foliation.

(ii) The Ariègite domain (hereafter referred to as "Ar domain"): This domain grades downwards into fine-grained porphyroclastic spinel peridotites enclosing centimetric to decimetric garnet pyroxenites (Fig. 5-3a-d) and granulite (Kornprobst et al., 1990; Frets et al., 2012). Garnet pyroxenites in this domain have sharp contacts with host peridotite, too (Frets et al., 2012).

(iii) The Ariègite to Seiland transition (hereafter referred to as "Ar-Se domain") is characterized by coarse-grained, porphyroclastic spinel peridotites (Fig. 5-3e). We have mapped this transition on the basis of the coexistence of garnet—usually completely transformed to dark, greenish kelyphite—and rounded, green spinel (Frets et al., 2012; Fig. 4-4) in pyroxenite layers, taken as mineral indexes of the the Ariègite to Seiland subfacies transition (O'Hara, 1967; Obata, 1980; Targuisti, 1994). In contrast with the Ronda peridotite (Obata, 1980; Van der Wal & Vissers, 1996; Lenoir et al., 2001), the Ar-Se transition is rather gradual and has a variable thickness ranging from over 500 m in the Y. Aaraben valley to less than 300 m in the J. Nich section (Fig. 2). Pyroxenites occur as cm- to dm- wide layers (Fig. 5-3f).

(iv) The Seiland domain (hereafter referred to as "Se domain") constitutes the lowermost exposed levels of the massif (Fig. 5-1). It is characterized by coarse-grained porphyroclastic to granular

spinel peridotites containing dark to greenish, spinel websterite commonly showing diffuse olivine-rich boundaries with host peridotite (Fig.5-4). At the transition from the Ar-Se to the Se domain increases the abundance of spinel wehrlites parallel to the foliation, with dunite wall rocks within harzburgite (Fig. 5-4d). Although harzburgite and lherzolite predominate in this domain, in decametric domains locally predominates dunite and wehrlite (Fig. 5-4a,b,d,e). Down section, Se domain peridotites usually display a diffuse, centimetric to decametric compositional layering marked by variations in pyroxenes modal content (Fig. 5-4). This compositional layering is parallel or slightly oblique to the peridotite foliation defined by flattened olivine crystals; this foliation is only patent in grain boundary maps and is hardly observable on the field. In lherzolite, pyroxenes shows elongations defining different sets of directions in the same outcrop (Fig. 5-4c); they can be parallel to foliation or conjugate at certain angle of the peridotite foliation.

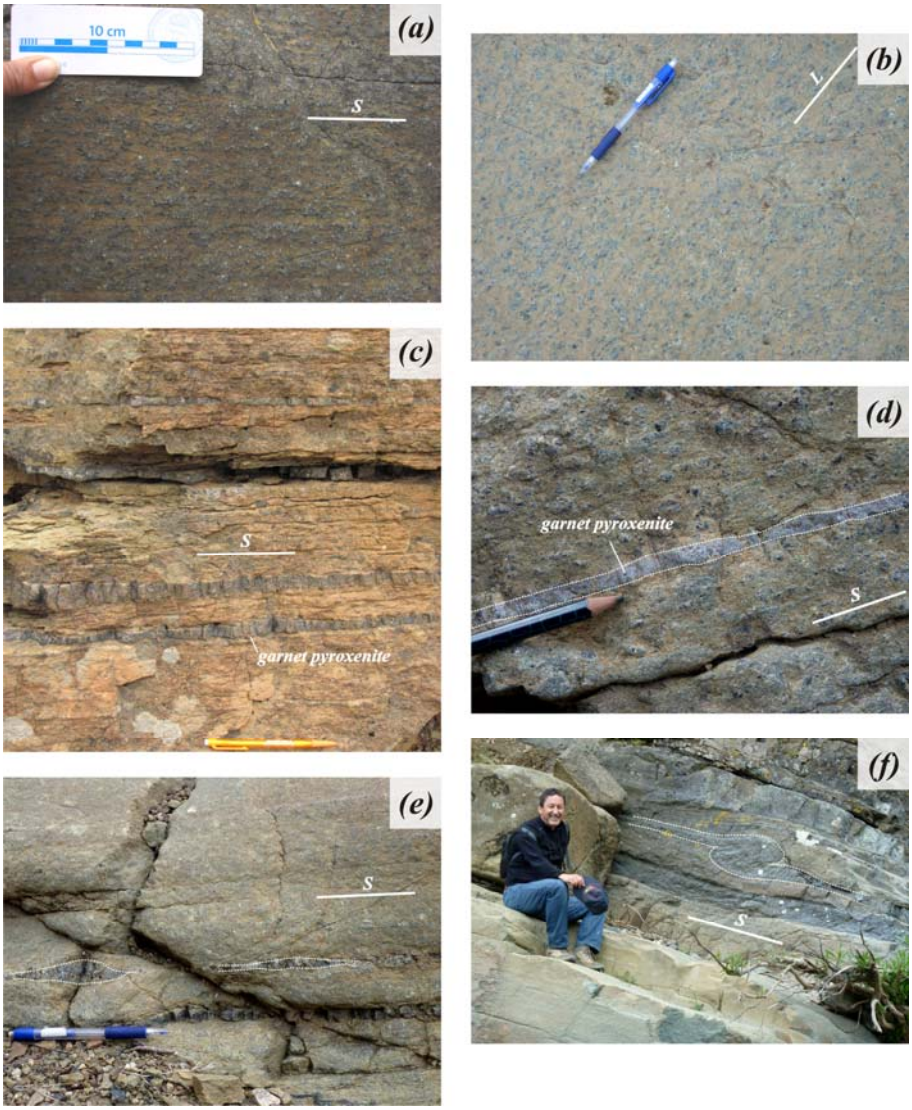

Figure 5-3. Typical macroscopic structures in the Ar (a-d) and Ar-Se (e-f) domains. (a-b) Foliation and lineation marked by the elongation of pyroxenes and spinel, respectively. (c-d) Cm-scale boudinaged garnet pyroxenites layering parallel to the foliation. (e) Boudinaged sp-bearing pyroxenites layers parallel to the foliation. (f) Pluridecimetrical pyroxenite layers exhibiting synfolial folds.

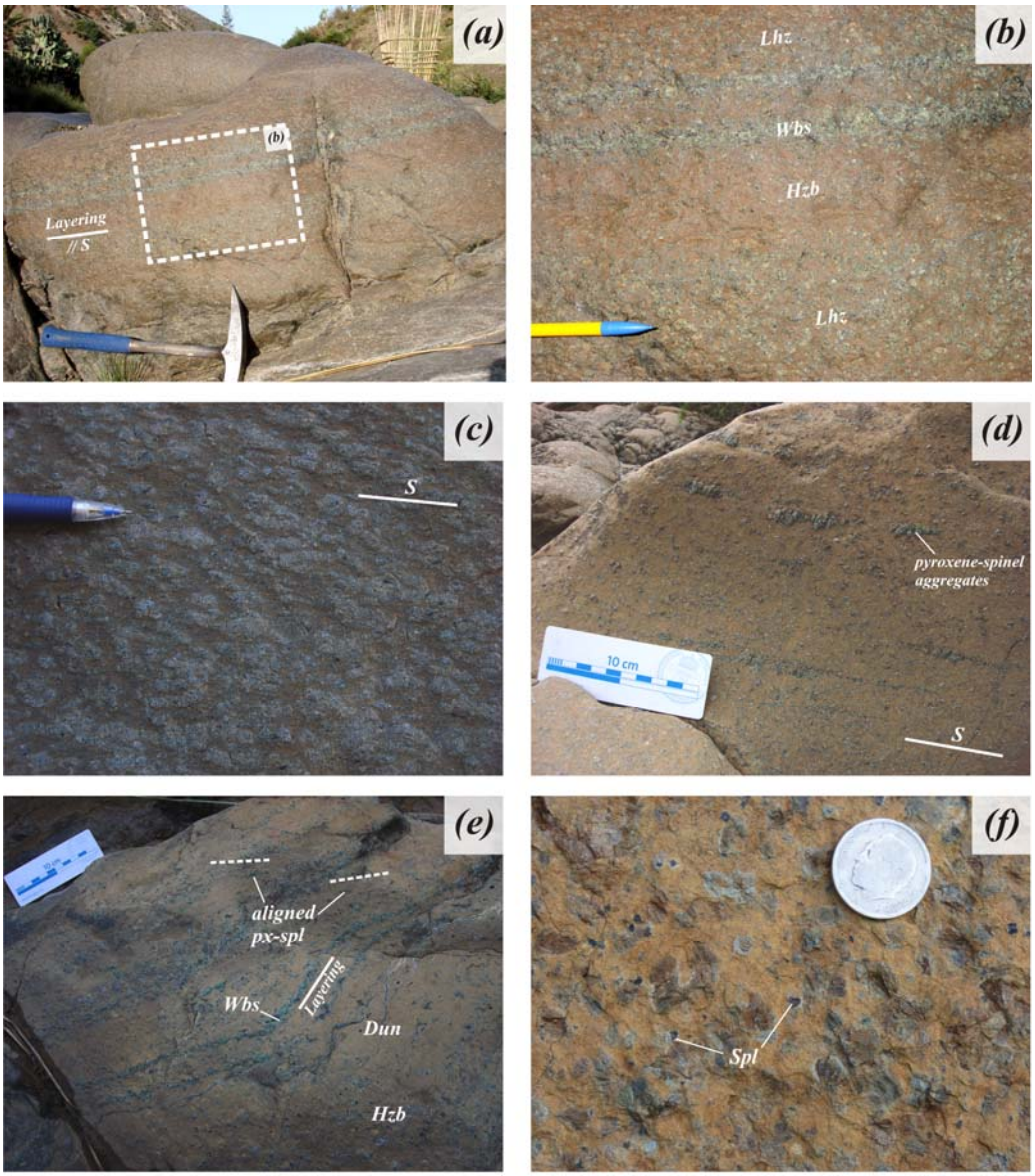

Figure 5-4. (a-b) Diffuse compositional layering from the Se domain. (c) Typical coarse-granular to coarse-porphyroclastic facies from the Seiland domain with a foliation marked by a weak shape preferred orientation of the pyroxenes and spinel. (d) Alignment of pyroxene-sp aggregates parallel to the foliation near the contact with the Ar-Se domain. (e) Dunites associated with harzburgites and diffuse websterites layers parallel to the foliation. Arrows indicate alignments of pyroxene-spinel aggregates at low angle to the layering, parallel to stippled lines. (f) Coarse-granular peridotites near the Ar-Se transition. Note the presence of coarse, rounded spinel grains. (Lhz: Lherzolite, Wbs: Websterite, Hzb: Harzburgite, Dun: Dunite)

5.3. Large scale structure of the massif

We conducted structural mapping and geographically oriented sampling (over 100 samples) of peridotite over a 75 km^2 area of the massif (Fig. 5-5), mostly along valleys—roughly perpendicular to the long axis of the massif—that exhibit continuous and fresh peridotite outcrops (Fig. 5-1). Field measurements of peridotite foliation were checked against—and wherein non apparent in the field,

retrieved from—the foliation obtained from the average shape preferred orientation of olivine grains derived from automatic grain boundary mapping of geographically oriented thin sections.

Because olivine and pyroxenes exhibit few slip systems with highly variable strengths, their dominant slip direction tends to align parallel to the shear direction and the slip plane-normal with the shear plane-normal (or foliation) in either simple or pure shear deformation (Zhang & Karato, 1995; Tommasi et al., 1999; Bystricky et al., 2000). Therefore, where spinel lineation was not apparent in the field—mostly in the Seiland-subfacies coarse-granular porphyroclastic peridotites—lineations were retrieved from crystal preferred orientation mapping as the dominant slip direction of olivine rotated back into the geographical reference frame (see Fig. 5-15).

Despite some local dispersion of peridotite foliation directions and dips, peridotites at the scale of the massif exhibit a dominantly flat-lying foliation with a NW-SE trending lineation, which rotates progressively towards a N20-N30 trend in the NE, lowermost part of the massif (Fig. 5-5a,b). Grt-Sp Mylonites and Ar domain peridotites are characterized by gently SW-dipping foliation striking N120-N140 (Fig. 6). Variability in foliation of the Grt-Sp Mylonites results from rotation along late brittle faults near the SW-contact. The Ar domain peridotites have rather constant gently dipping foliation striking N110-N145. The Ar-Se domain peridotites show foliations with orientations intermediate between those in the Ar- and Se domains (Fig. 5-5a). The Se domain has more variable foliations, both in strike and dip. This dispersion is probably due to late metric to decametric folds, as those observed at the base of the J. Nich section (Fig. 5-5a). The relatively lesser dispersion of lineations compared with that of foliation indicates that folds have mainly subhorizontal N-S to NNW-SSE axes. Another unique structural feature of the Se domain is the presence of subvertical E-W and N-S striking foliations and lineations in five small areas (≤ 200-300m in radius) in the northern and eastern parts of this domain (Fig. 5-5b). Dunite, wehrlite, and very coarse-grained spinel lherzolite are particularly abundant in these areas. These structures with vertical foliation and lineations are reminiscent of those mapped at a larger scale as diapirs in the mantle section of the Oman ophiolite (Nicolas & Boudier, 2000; Jousselin et al., 1998).

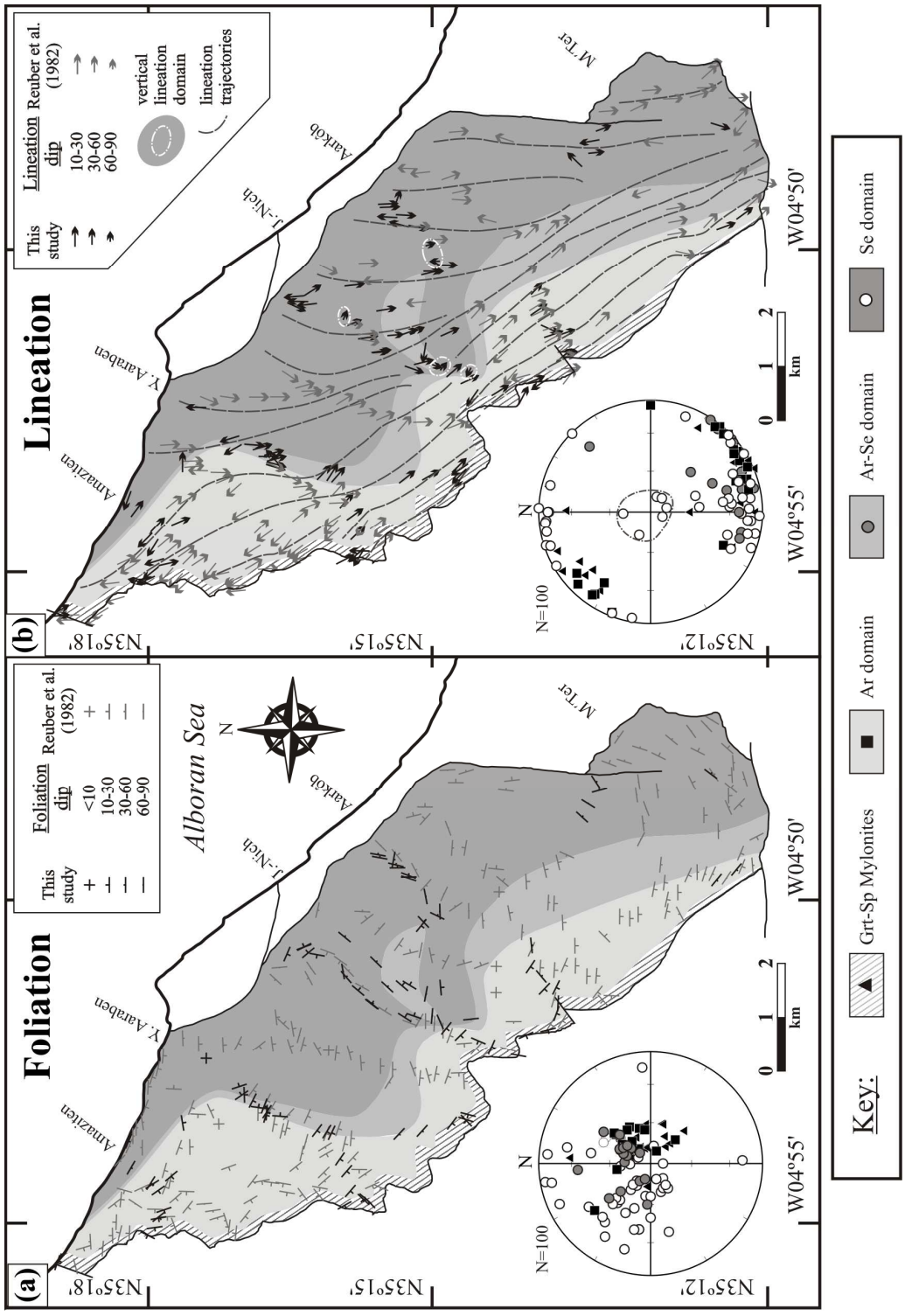

Figure 5-5. (a) Map of foliations based on original data collected in this study and on Reuber et al. (1982). The background shading represents the different tectono-metamorphic domains. Lower hemisphere stereoplot displays the poles of foliation measured in this study as a function of the tectono-metamorphic domain. (b) Map of lineations and lineation trajectories based on original data collected in this study and on Reuber et al. (1982). Dip for Reuber et al. (1982) data was inferred from the orientation of neighboring foliation data. Lower hemisphere stereoplot shows the lineations measured in this study as a function of the tectono-metamorphic domain. Note the progressive clockwise rotation of the lineation from NW-SE towards N-NNE orientations and the small domains containing subvertical lineations in the Seiland domain. All foliations and lineations from this study were checked by comparison between field measurements and CPO data on geographically-oriented thin sections.

5.4. Petrography and Microstructure

The massif is characterized by large scale variation in the grain size of olivine, which increases from Grt-Sp Mylonites towards the Se domain (Fig. 5-6). The Se domain is generally marked by coarsening of the olivine grain size (Fig. 5-6). The size and proportion of olivine porphyroclasts varies also across the massif from a bimodal distribution—constituted by few porphyroclasts embedded in a fine-grained olivine recrystallized matrix—in Grt-Sp Mylonites, Ar- and Ar-Se domain peridotites (Fig. 5-7a-c) to a more homogeneous distribution in the coarse-granular porphyroclastic peridotites in the Se domain (Fig. 5-7g-j). This transition in the olivine grain size distribution occurs across the Ar-Se domain, where peridotites show intermediate grain size distribution with evidence of abnormal grain growth (Fig. 5-7d-f).

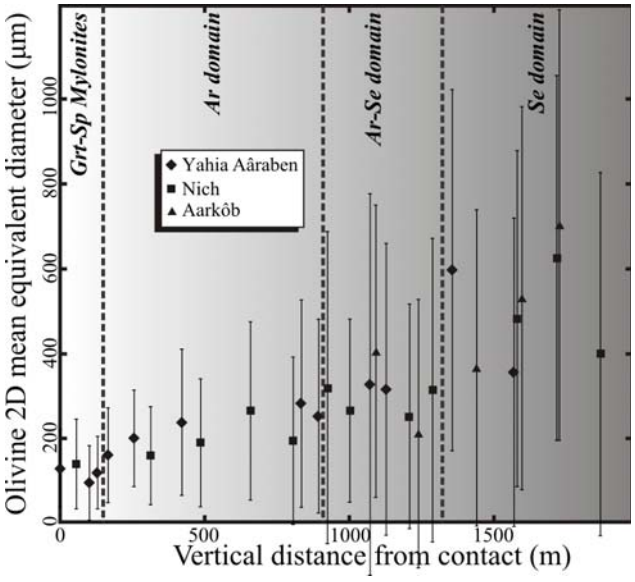

Figure 5-6. Olivine 2D area-weighted equivalent grain diameter (grain size) in function of the vertical distance to the contact. Bars represent the standard deviation. Note the coeval increase in average grain size and variability with increasing distance from the contact.

5.4.1. Grt-Sp Mylonites

Grt-sp peridotite mylonites are characterized by mm-sized garnet- and pyroxene porphyroclasts (Fig. 5-7a,b) embedded in a fine grained matrix of olivine and pyroxene neoblasts, which commonly show a shape preferred orientation parallel to the mylonitic foliation (Fig. 5-8b). Rounded garnet porphyroclasts—usually partly transformed to kelyphite and with lobate grain boundaries and embayements filled with pyroxene—mostly occur in mm-sized, clinopyroxene-rich lenses parallel to the foliation (Figs. 5-7a-b, 5-8a-b). Locally, garnet porphyroclasts also occur as isolated porphyroclasts (up to 10 mm wide; Fig. 5-7a-b) in clinopyroxene-rich domains or showing pressure shadows made up of coarse olivine (Figs. 5-7b and 5-8b). Isolated porphyroclasts occasionally contain rare reddish–brown spinel (Fig. 5-8g), pyroxene and olivine inclusions. Spinel coronae surrounding garnet also occur.

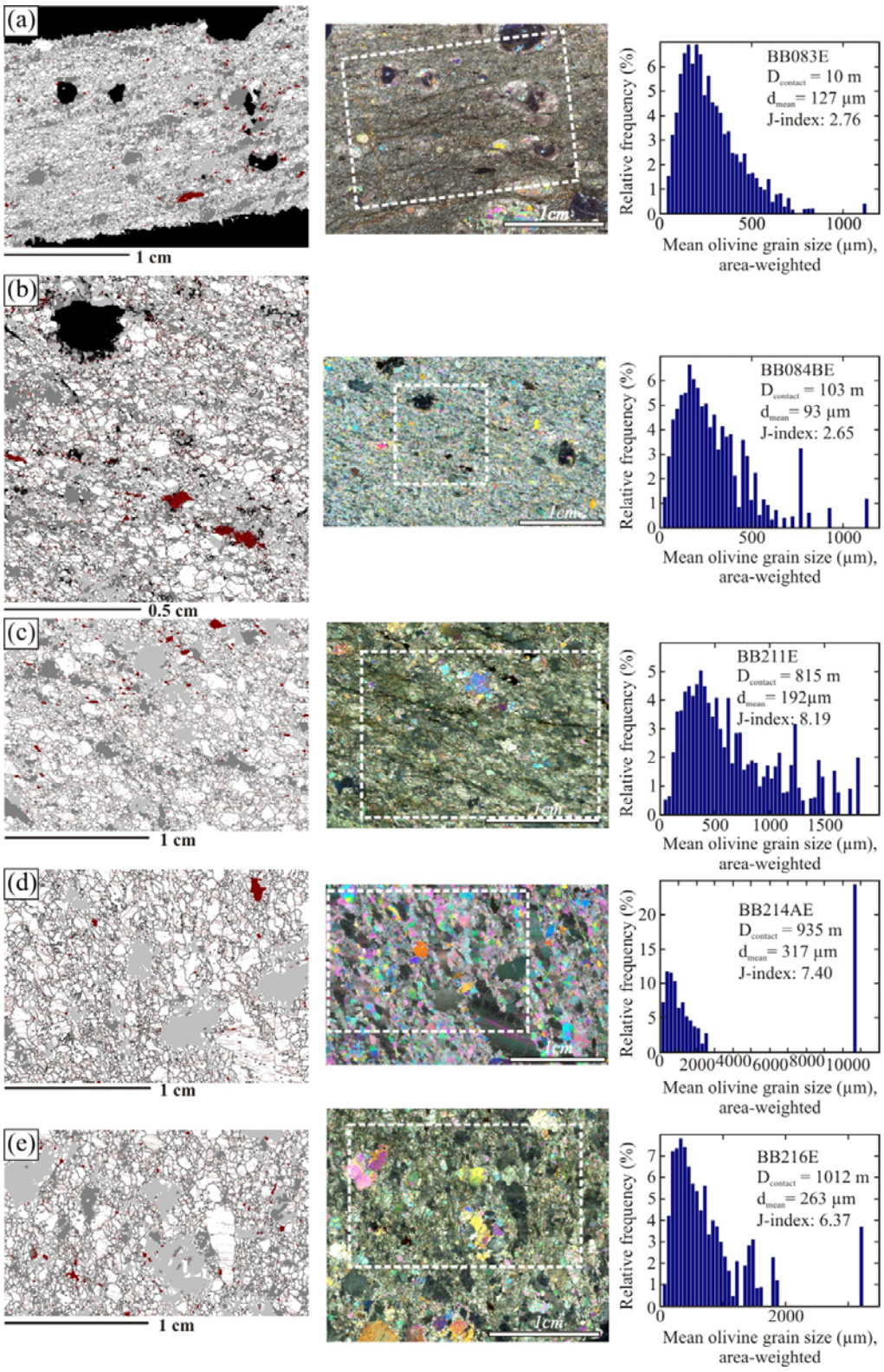

Figure 5-7. Microstructural evolution from the Grt-Sp Mylonites to the Se domain with increasing distance from the contact. Left = phase map with grain boundaries (black; misorientations >15º) and subgrain boundaries (dark red; misorientations > 3º) White = olivine, light grey = orthopyroxene, dark grey = clinopyroxene, black = unindexed (kelyphite), maroon = spinel. Center = investigated area of thin section corresponding to left frame. Right = area-weighted grain size distribution of olivine. (a-b) Mylonitic peridotites (c) fine-grained porphyroclastic peridotites (d-g) porphyroclastic peridotites with abnormal grain growth. Note vertical foliation marked by the elongation of olivine porphyroclasts in (d) and (e). (h-j) Coarse-porphyroclastic to coarse-granular peridotites. See text for further explanation.

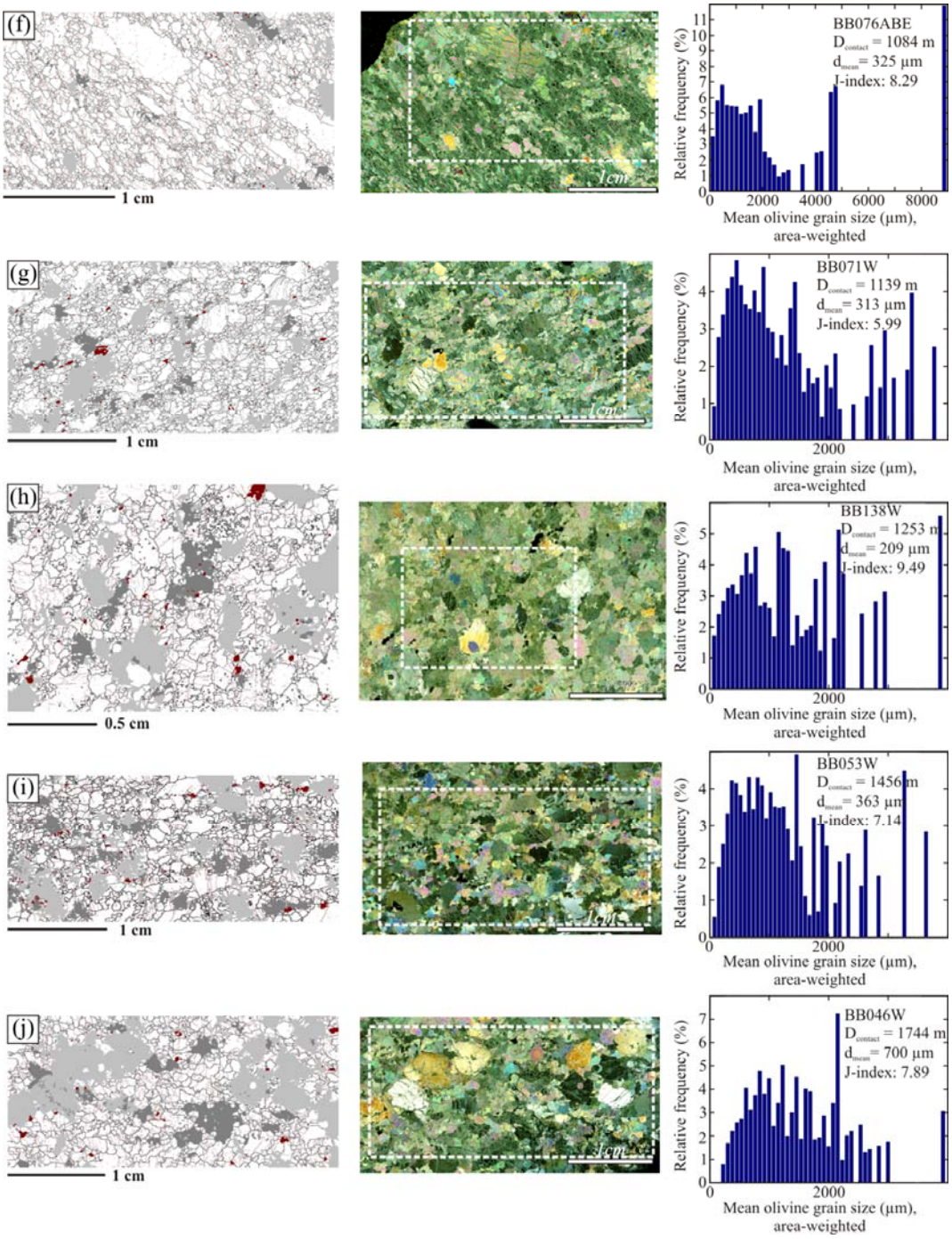

Figure 5-7. Continued

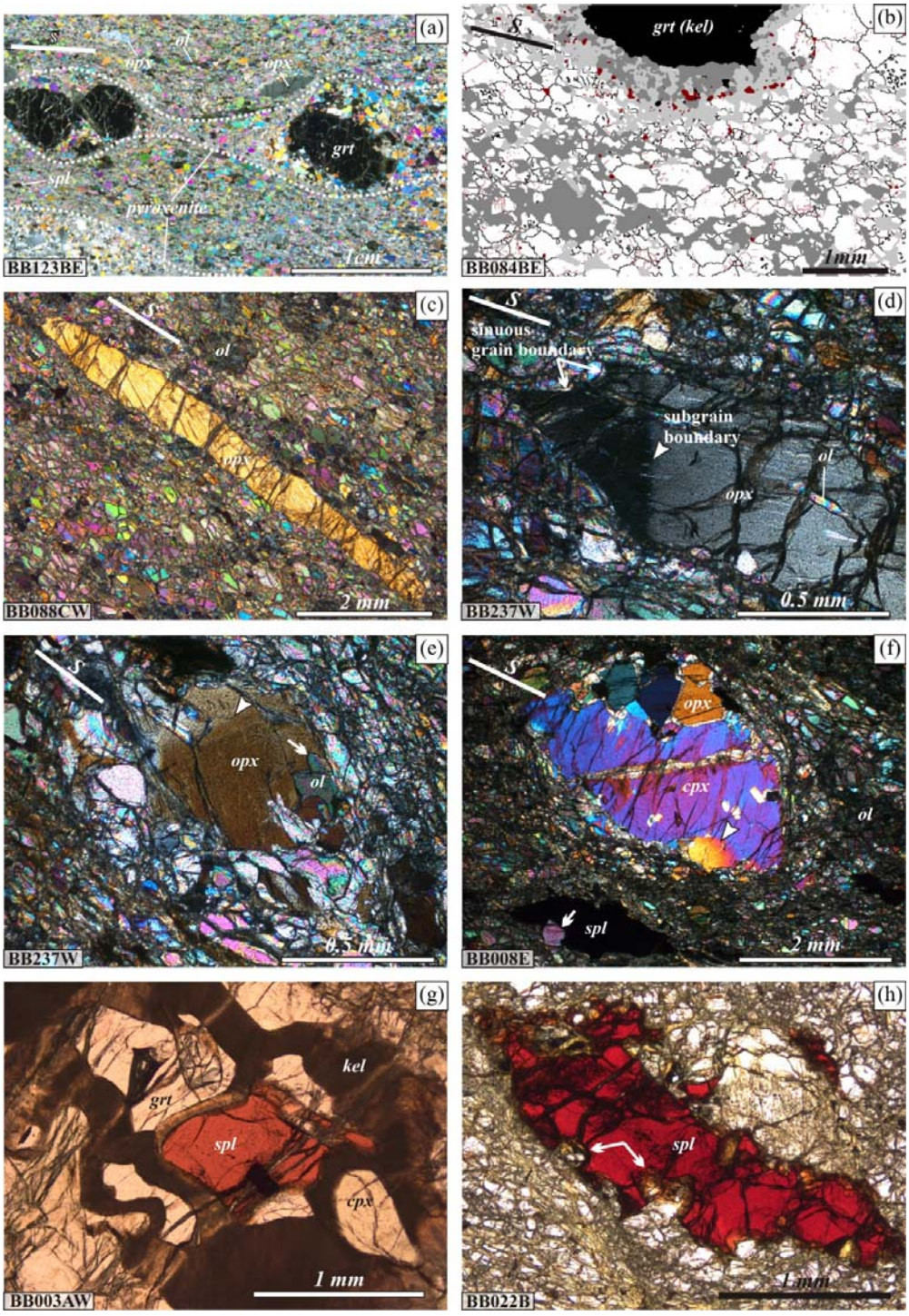

Figure 5-8. Detailed petrographic features of Grt-Sp Mylonites. (a) Cm-scale garnet pyroxenite lens boudinaged parallel to the foliation. Note the wrapping of the foliation around the pyroxenite lens and the elongation of orthopyroxene crystals in the peridotite. (b) Detail of Fig. 8b. Note the elongation of olivine crystals, the presence of subgrains, the irregular shape of pyroxenes and the compositional layering of pyroxene-rich and olivine-rich domains, and finally the pyroxene-spinel symplectites around garnet (kelyphite). Color code as in Fig. 8 (c) Stretched orthopyroxene with axial ratio of 10:1 parallel to the foliation with irregular grain boundaries. The foliation is also marked by the elongation of olivine crystals. (d-e) Irregular shape of orthopyroxene porphyroclast elongate parallel to the foliation showing grain boundaries and fractures filled by olivine. White arrows indicate subgrain boundaries. Also note the elongation of olivine crystals in (e). (f) Aggregate of ortho-and clinopyroxene and neighbouring spinel elongated parallel to the foliation. (g) Polarized light photomicrograph of reddish-brownish spinel surrounded by garnet, clinopyroxene and kelyphite. (h) elongated spinel parallel to the foliation with irregular grain boundaries.

Orthopyroxene porphyroclasts (1-10 mm) are highly elongated (aspect ratio 3:1, and up to 10:1; Figs. 5-8a,c and 5-9a) and commonly show undulose extinction and kink bands at high angle to clinopyroxene exsolutions (Fig. 5-8d). Orthopyroxene grain boundaries are irregular with common olivine-filled embayements (Fig. 5-8e). Clinopyroxene porphyroclasts are relatively smaller and less elongated (Figs. 5-7a and 5-9a), show undulose extinctions and irregular grain boundaries less indented than those of orthopyroxene porphyroclasts. Coarse two-pyroxene aggregates—a few mm wide—are rare (Fig. 5-8f). Pyroxenes neoblasts are intermixed with olivine neoblasts (Fig. 5-8b). Locally, they occur as clinopyroxene or orthopyroxene-rich neoblast domains parallel to the foliation (Fig. 5-7a-b). Pyroxene neoblasts in these domains have very irregular shapes, sinuous grain boundaries in contact with olivine and are elongated parallel to the foliation (Fig. 9b).

Olivine porphyroclasts (>1 mm) are rare; olivine mostly constitutes the recrystallized matrix (average grain sizes of 90-160 microns; Fig. 7) of Grt-Sp Mylonites. The homogeneity of the olivine grain size distribution and the area fraction of larger grain sizes systematically increase away from the contact with the overlying crustal granulites (cf. Fig. 5-7a-b). Olivine crystals have irregular shapes with sinuous grain boundaries (Figs. 5-7a-b and 5-8b), undulose extinction and, less commonly, rounded to subhedral shapes. High-resolution EBSD grain boundary maps reveal the presence of subgrains in olivine crystals irrespectively of their size; in larger grains, well-developed and closely-spaced subgrain boundaries occur at high angle to the grain elongation (Fig. 5-8b). Average aspect ratios for olivine range between 1.7 and 2 for all grain size populations (Fig. 5-9a).

Reddish–brown spinel occurs in the matrix as holly-leaf shaped crystals (0.2 – 2 mm) strongly elongated parallel to the foliation (Fig. 5-8h) or spatially associated to garnet.

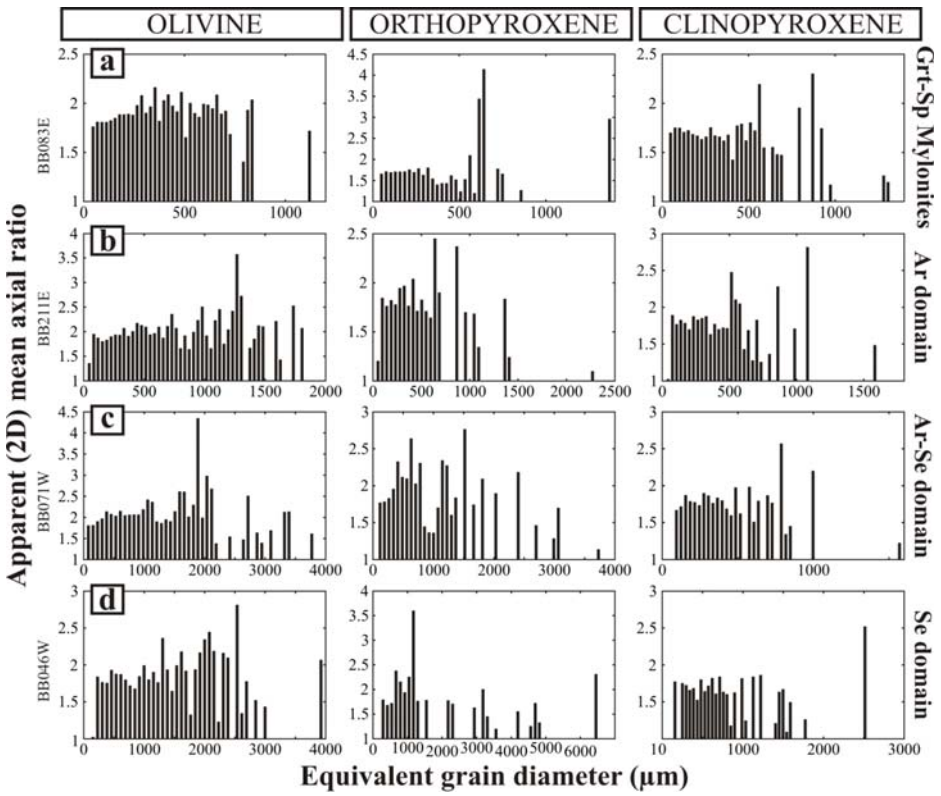

Figure 5-9. Mean axial ratios of olivine, orthopyroxene for the (a) Grt-Sp Mylonites, (b) Ar, (c) Ar-Se and (d) Se domains.

5.4.2. The Ar domain peridotites

The microstructure of peridotites evolves from Grt-Sp Mylonites to Ar domain tectonites by progressive coarsening of porphyroclasts and neoblasts (Figs. 5-6, 5-7c). Ar domain peridotites are unequivocal, spinel porphyroclastic peridotites entirely lacking garnet porphyroclasts either as isolated grains or associated to mm-size clinopyroxene-rich layers or domains (Figs. 5-3a-b, 5-7c, 5-10a-c). They are also characterized by the lack of mm-size layering of pyroxene neoblasts, which are less abundant than in the recrystallized matrix of Grt-Sp Mylonites. Fine-grained porphyroclastic peridotites of the Ar domain have a bimodal texture characterized by mm-sized olivine and pyroxene porphyroclasts embedded in a fine-grain recrystallized matrix of olivine and pyroxene neoblasts (Fig. 5-7c) with a shape preferred orientation (average aspect ratios 1.7:1 and 2:1, respectively; Fig. 10b) parallel to the foliation. Flattened, elongated olivine and pyroxenes define the foliation and elongated spinel and aligned pyroxene the lineation (Fig. 5-7c; Fig. 5-10a).

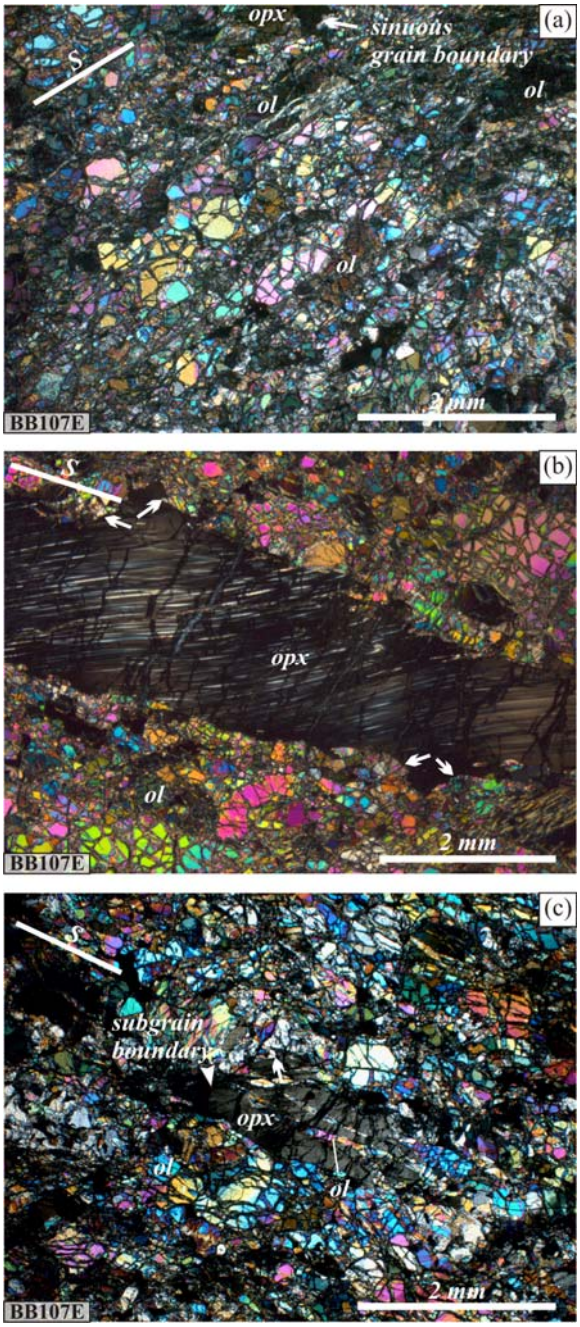

Figure 5-10. Microstructures of the Ar domain peridotites. (a) Elongate olivine crystals parallel to the foliation. (b-c) Large orthopyroxene porphyroclast with thin exsolution lamellae and irregular grain boundaries and fractures filled by olivine.

Olivine has a bimodal grain size distribution (Fig. 5-7c). The average grain size of olivine and the volume fraction of olivine porphyroclasts are greater than in Grt-Sp Mylonites. The olivine mean grain size increases from ~175 μm to >250 μm as function of the distance from the Grt-Sp Mylonites (Fig. 5-6). The main grain size population—i.e., the grain size class occupying the largest volume— is twice of that in Grt-Sp Mylonites (~400 μm vs. <200 μm; Fig. 5-7a-c). Olivine porphyroclasts and matrix crystals—with interlobated grain boundaries—have undulose extinctions and closely-spaced subgrains at high angle to their elongation (Fig. 5-7c).

Pyroxenes occur as single, elongated porphyroclasts—mostly orthopyroxene with kink bands, undulose extinction and exsolutions of the counterpart pyroxene—aligned parallel to foliation (Figs. 5-7c and 5-10b) or as elongated aggregates parallel to the foliation. Orthopyroxene porphyroclasts are coarser and less elongated than those in Grt-Sp Mylonites and show highly irregular shapes and embayements (Fig. 5-10b) and flame-like indentations filled with olivine (Fig. 5-10c). Matrix pyroxene neoblasts are finely intermixed with olivine neoblasts; they are elongated (aspect ratios of 1.5-2.5:1; Fig. 5-9b) with irregular shapes and lobate grain boundaries (Fig. 5-10c).

Spinel is coarser (0.5-2 mm) than that in Grt-Sp Mylonites and occurs as holly-leaf shaped elongated crystals parallel to the foliation (Fig. 5-10a).

5.4.3. The Ar-Se domain peridotites

Ar-Se domain peridotites show transitional porphyroclastic textures characterized by coarser olivine grain size (250-350 μm) and a reduction of the volume fraction of neoblasts relative to Ar domain peridotites (Figs. 5-6 and 5-7d-f). Elongated olivine porphyroclasts (aspect ratio of 2:1; Fig. 5-9c) and neoblasts display undulose extinctions, well-developed subgrain boundaries normal to the grain elongation (Fig. 5-7d-f); olivine-olivine grain boundaries are commonly lobated and, locally, straights developing triple junctions (Fig. 5-11a). A characteristic feature of Ar-Se domain peridotites is the presence of large (up to 1cm), irregularly shaped crystals of olivine—elongated along the foliation—within a rather heterogeneous coarse olivine matrix; this texture is symptomatic of abnormal grain growth (e.g. Hillert, 1965). This is patent in the olivine crystal size distribution as spikes in the larger size classes of Ar-Se domain peridotites that are absent in the olivine grain size distribution of Grt-Sp Mylonites and Ar domain peridotites (Fig.5-7d-f).

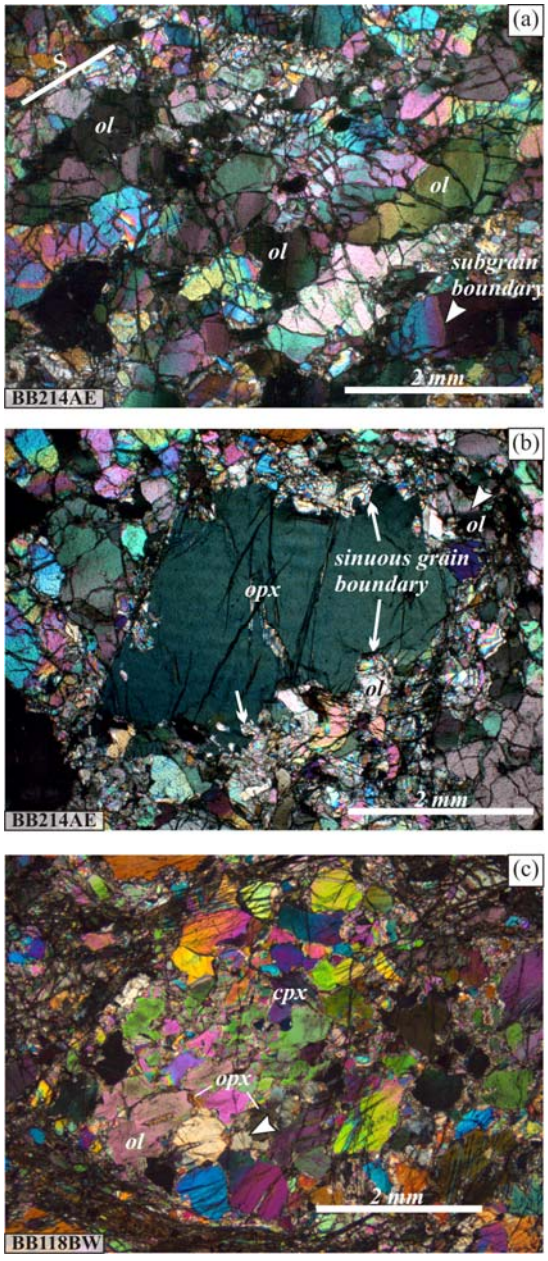

Figure 5-11. Microstructures of the Ar-Se domain peridotites. (a) Elongation of olivine crystals parallel to the foliation withundulose extinctions and subgrains. Orthopyroxene porphyroclast with irregular grain boundaries and fractures filled by olivine. Lens shaped px-ol-aggregates.

Orthopyroxene porphyroclasts are coarser (up to 4mm) than in the overlying domains. Clinopyroxene porphyroclasts—occurring as aggregates elongated parallel to the foliation (Fig. 5-7d, e)—show irregular shapes and have similar sizes than those in Ar domain, fine-grained porphyroclastic peridotites. Orthopyroxene porphyroclasts have also very irregular shapes; the embayements are usually filled by olivine (Fig. 5-7d-f and 5-11b). Both pyroxenes have undulose extinction. Kink bands in orthopyroxene are rarer. Fertile samples also show fine-grained ortho- and clinopyroxene intermixed with olivine in the matrix. These pyroxenes have irregular, but elongated shapes, and form a diffuse compositional banding parallel to the foliation (Fig. 5-7d-e). Aggregates of intermixed pyroxenes and olivine with interpenetrating boundaries are also locally observed (Fig. 5-11c). Spinel occurs as large holly-leaf shaped crystals or as small rounded grains included in olivine (Fig. 5-7d-f).

5.4.4. The Se domain peridotites

Se domains peridotites show coarse-grained porphyroclastic to granular textures (Fig. 5-6). The transition to the Se domain is characterized by a marked increase in the average olivien grain size (Fig. 5-6). The grain size distribution is rather homogenous without a clear dominant grain size; area fractions occupied by small and large grains tend to be similar (Fig. 5-7h-j).

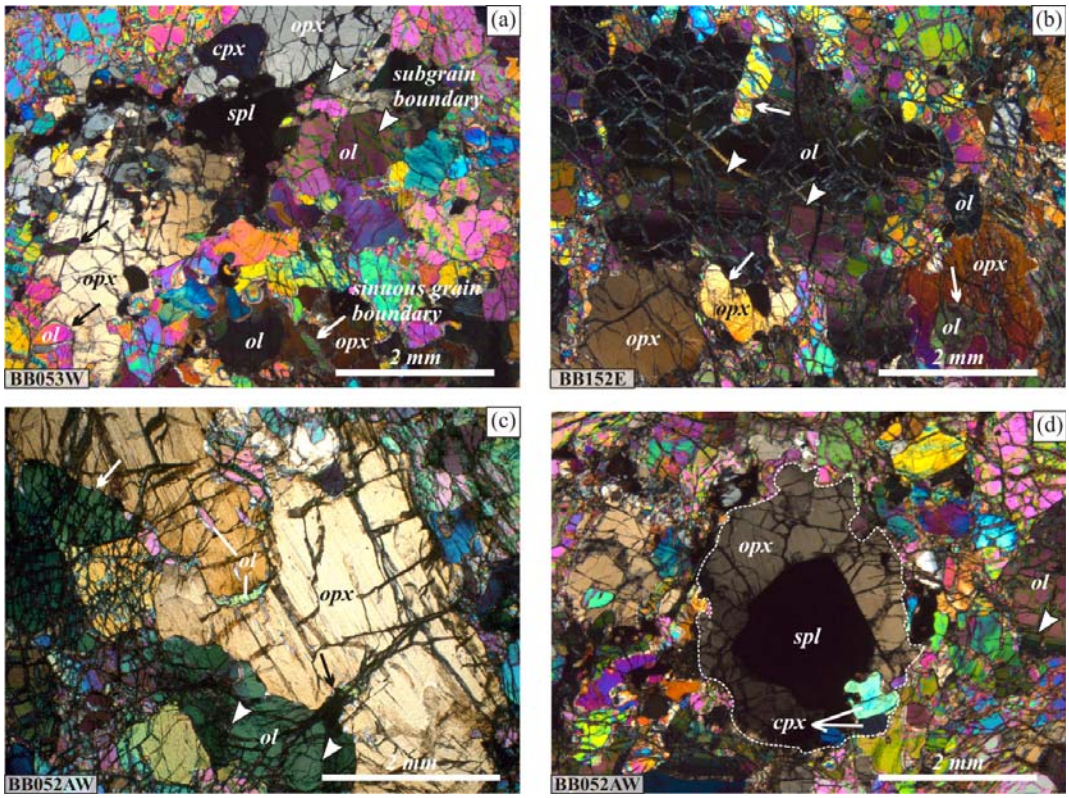

Figure 5-12. Microstructures of the Se domain peridotites. (a) Very irregular interpenetrating grain boundaries of all phases, all showing undulose extinctions and subgrains. (b) Large olivine olivine porphyroclast with closely spaced subgrain boundaries and corroded orthopyroxene porphyroclast. (c) Large orthopyroxene porphyroclast with wide grian boundary embayments and fractures filled by olivine. (d) Symplectitic aggregate of spinel surrounded by ortho-and clinopyroxene with irregular shapes. Note the undulose extinction of the surrounding orthopyroxene crystal.

The foliation and the lineation are mainly defined by the flattening of olivine and alignment of spinel. Olivine crystals of all sizes show sinuous grain boundaries, undulose extinctions, and ubiquitous subgrains (Fig. 5-12a-b. Orthopyroxene has rounded to very irregular shapes (Fig. 5-12a-d) and locally shows a weak shape preferred orientation (aspect ratios <2; Fig.5-9d). Embayements in the grain boundaries or fracture-like features are filled with olivine (Fig. 5-7h-j and 5-12a-d) in optical continuity with larger crystals displaying well-developed subgrains (Fig. 5-12c). Coarse orthopyroxene crystals usually have finely-spaced clinopyroxene exsolution lamellae, undulose extinctions, and kink-bands (Fig. 5-12c-d). Clinopyroxenes occur either as isolated crystals or in aggregates, with irregular shapes in both cases (Fig. 5-7h-j and 5-12b) and show exsolution lamellae and undulose extinction (Fig. 5-12b).

Spinel usually occurs as irregular, holly leaf shaped grains. Large (>2 mm wide) rounded spinel aggregates of subhedral spinel crystal occurs surrounded by two-pyroxene coronae.(Fig. 5-12d).

5.5. Geothermometry

Previous geothermobarometric studies of the Beni Bousera massif have focused on establishing the pressure and temperature equilibration conditions of Grt-Sp Mylonites (Tabit et al., 1997; Afiri et al., 2011) and pyroxenites (Kornprobst et al., 1990; Frets et al., 2012). Maximum prekinematic pressures of Grt-Sp Mylonites are ca. 2.3 GPa (Tabit et al., 1997; Afiri et al., 2011). These pressures are slightly larger than those recorded in P-T calculations of synkinematic assemblages in garnet pyroxenites in this domain (2.0 GPa; 950°C GPa; Frets et al., 2012). No accurate geobarometric formulation exists for spinel peridotite (e.g. Nimis & Grütter, 2010) that composes most of the Beni Bousera massif. Thermodynamic pseudosection modeling of pyroxenite provides a lower-bound pressure estimate for the equilibration of the Ar-Se domain of 1.8-1.9 GPa between 1050-1150°C (Frets et al., 2012).

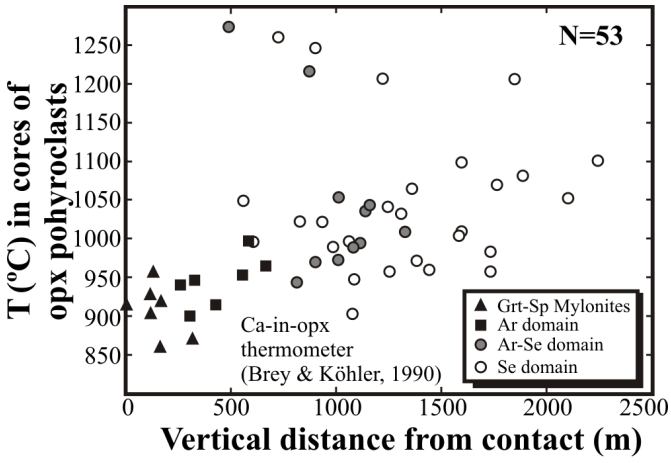

Figure 5-13. Calculated equilibration temperatures (Ca-in-opx; Brey & Köhler, 1990) using orthopyroxene core compositions in function of vertical distance to the contact with crustal units.

To investigate the P-T equilibration temperatures across all tectono-metamorphic domains, we have carried out a detailed thermometric study of 53 peridotites sampled across the whole massif in all tectono-metamorphic domains. Previous studies have shown that cores of orthopyroxene in spinel lherzolites commonly preserve Al-rich plateaus that reflect metastable equilibrium in the garnet lherzolite facies (Takazawa et al., 1996; Ozawa,

2004). Equilibration with garnet is, however, only detectable through careful analysis of REE in Al-rich orthopyroxene cores showing HREE–depleted patterns. Ca-in-opx temperatures in Beni Bousera peridotites were calculated using the formulation of Brey & Köhler (1990) at P=1.8 GPa, except in Grt-Sp Mylonites we chose P=2.0 GPa that was recorded in synkinematic garnet pyroxenites from this domain (Frets et al., 2012)—albeit the effect of pressure on Ca-in-opx thermometer is negligible. Temperatures vary continuously in the range 850-1150ºC with increasing distance from the contact, except for 5 samples located near the Ar-Se transition that yield even higher temperatures of >1200ºC (Fig. 5-13).

5.6. Crystallographic Preferred Orientations (CPO)

5.6.1. CPO patterns

Olivine CPO patterns vary systematically with increasing distance from the contact with crustal units (Fig. 5-14 and 5-15). Axial-[010] olivine CPO patterns (Fig. 5-14), characterized by a strong clustering of [010] axes perpendicular to the foliation and dispersion of [100] and [001] axes in the foliation plane, clearly predominate in Grt-Sp Mylonites and in Ar domain fine-grained porphyroclastic peridotites. With increasing distance from the contact, orthorhombic olivine CPO, characterized by point maxima of [100] and [010], and axial-[100] patterns, where a point maximum of [100] parallel to the lineation is accompanied by a girdle distribution of [010] and [001], become more common (Fig. 5-14). The latter represent half of the measured patterns in the Ar-Se and Se domains. Although much more dispersed than olivine, pyroxenes too, display well-developed CPO. Olivine, orthopyroxene, and clinopyroxene CPO illustrating the observed patterns in each domain are presented in Figure 5-14.

5.6.1.1. - Grt-Sp Mylonites and Ar domain peridotites

Grt-Sp Mylonites and Ar domain fine-grained porphyroclastic peridotites show consistent olivine, orthopyroxene and clinopyroxene CPO, indicating a significant contribution of dislocation creep to the deformation of all three main rock-forming minerals. Peridotites from these two domains exhibit mainly axial-[010] olivine CPO patterns (Fig. 5-14) characterized by a strong clustering of [010] axes perpendicular to the foliation and dispersion of [100] and [001] axes in the foliation plane (Fig. 5-15). [100] and [001] axes usually define, however, a weak maximum subparallel and at high angle to the lineation, respectively. In the Ar domain, axial-[100] to orthorhombic olivine CPO patterns are also observed, but they remain rare (Fig. 5-14). The latter is characterized by point maxima of [100] and [010] parallel to the lineation and normal to the foliation (Fig. 16), whereas the former displays a point concentration of [100] subparallel to the lineation and girdle distributions of [010] and [001] normal to it.

Orthopyroxene and clinopyroxene CPO in Grt-Sp Mylonites and Ar domain peridotites are well correlated (Fig. 5-15). Both show a strong clustering of the [001] axes subparallel to the lineation and, in a lesser extent, [010] axes aligned at high angle to the foliation. Unlike clinopyroxene [100]-axes that tend to align at high angle to the lineation (in particular in the mylonites), orthopyroxene

[100]-axes show no systematic orientation. They may either show a weak concentration normal to the foliation, be dispersed in a girdle normal to the lineation, or display a weak concentration in the foliation plane at high angle to the lineation.

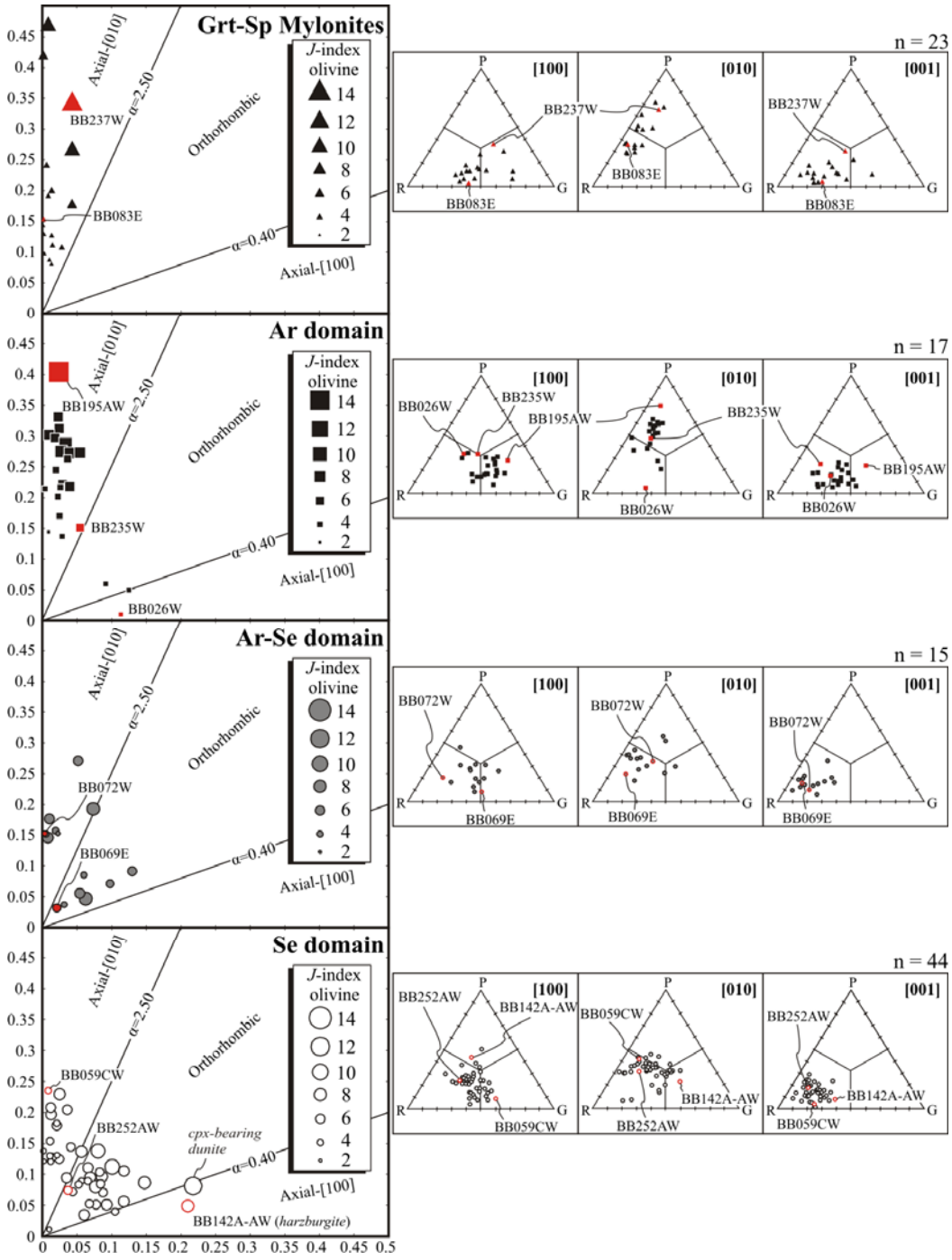

Figure 5-14. Frequency distribution of olivine CPO types in Beni Bousera peridotites and associated ternary P(point), G(Girdle) and R(Random) plots for olivine [100], [010] and [001] axes. Note the continuous evolution across the different domains. Red dots represent the samples plotted in Fig. 16.

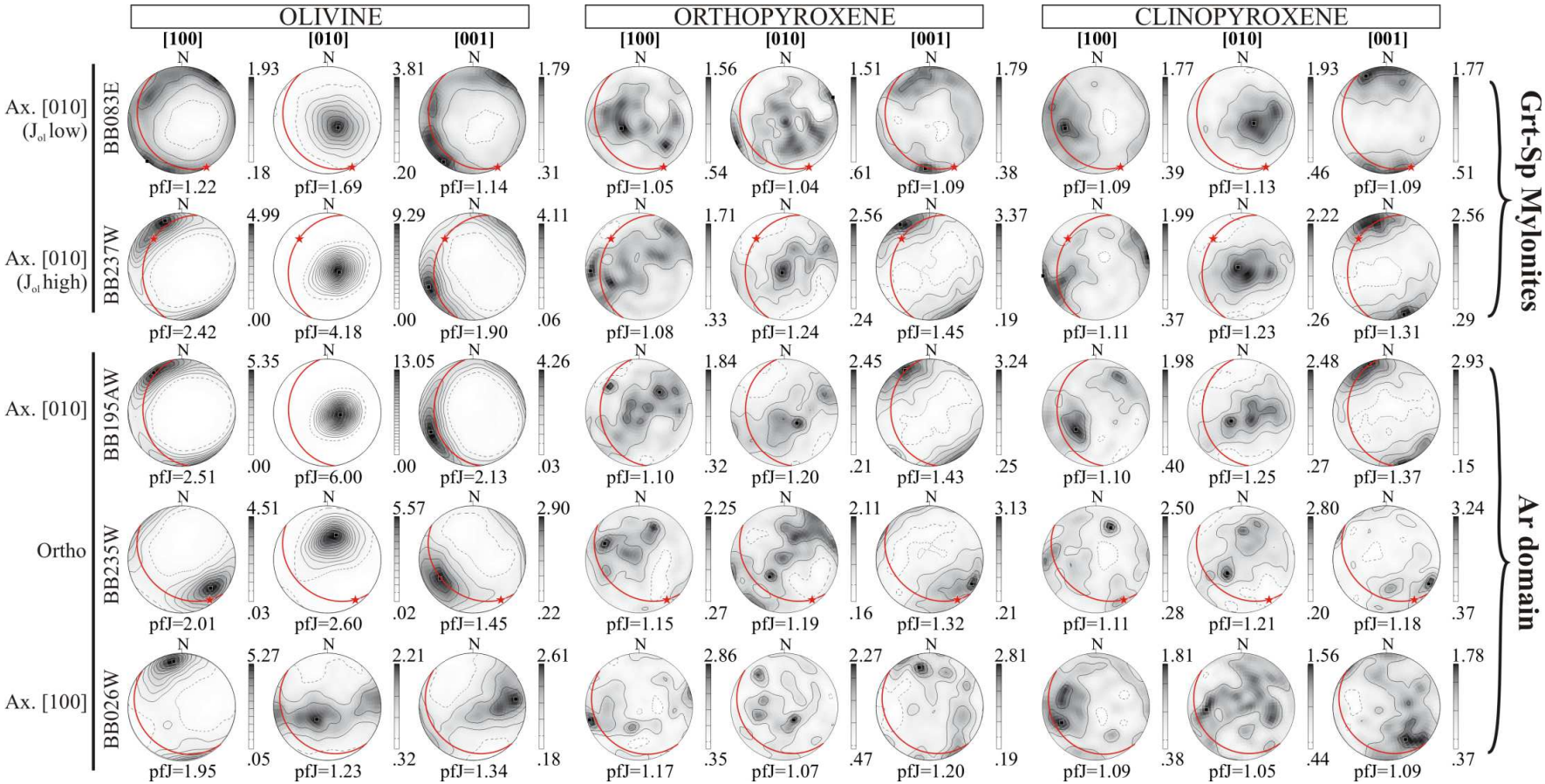

Figure 5-15. Olivine, ortho- and clinopyroxene CPO for Beni Bousera peridotites per tectono-metamorphic domain. Lower hemisphere stereoplots, contours at 0.5 multiples of a uniform distribution, inverse log grey scale colouring. Red and green great circles represent foliation and layering, respectively. Red star is the field measurement of the lineation.

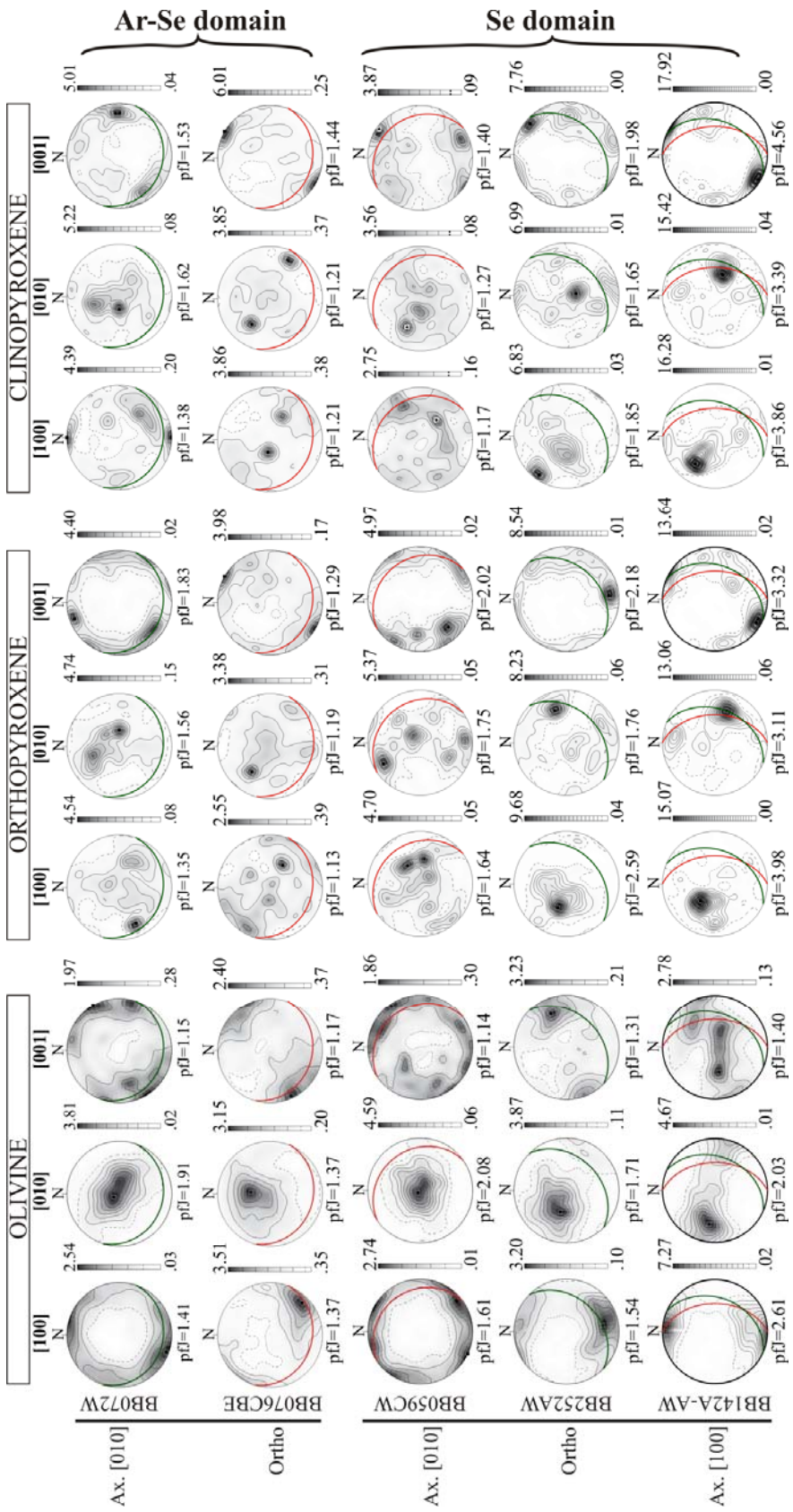

Figure 5-15. Continued

5.6.1.2. - Ar-Se and Se domain peridotites

Compared to Grt-Sp Mylonites and Ar domain peridotites, the Ar-Se- and Se domain peridotites are characterized by more variability of olivine CPO symmetry (Fig. 5-14) and intensity (see next section). Although axial-[010] patterns are still common, orthorhombic ones predominate, and axial-[100]-patterns remain rare (Fig. 5-14). All olivine CPO are characterized by clustering of [010] axes subperpendicular to the foliation and of [100] close to the lineation (Fig. 5-15). [001]-axes are usually more dispersed than the two others, but tend to align at high angle to the lineation in the foliation plane.

Ortho- and clinopyroxene CPO are correlated (Fig. 5-15). A striking characteristic of these two domains is, however, the total or partial decorrelation between the olivine and pyroxenes CPO. Most samples, like BB072W and BB059CW, display, in addition to the usual concentration of pyroxenes [001] axes subparallel to the olivine [100] maximum and the lineation, another [001] concentration at low angle to the foliation, but almost normal to the lineation. In some samples, like BB076CBE, only this [001] maximum is subparallel to the foliation plane, but at high angle to the lineation and this is observed for both ortho- and clinopyroxene. In contrast, peridotite BB142A-AW, which has an axial-[100] olivine CPO, has strong ortho- and clinopyroxene CPO well-correlated with the olivine CPO. Orthopyroxene [100] and clinopyroxene [010] axes tend to concentrate normal to the foliation, but those samples with a concentration of [001] at high angle to the lineation have weak [100] or [010] maxima subparallel to the lineation. For large pyroxene porphyroclasts (especially orthopyroxene), bad polishing and/or ubiquitous exsolution lamellae result in the incomplete indexing of these crystals and are recorded in the maps as isolated patches with a similar orientation. This leads to the overrepresentation of these orientations when plotted one point per grain and, hence the presence of local maxima in the stereoplots.

5.6.2. Strength of olivine CPO

The evolution of the intensity of the olivine CPO across the massif was quantified by calculating the dimensionless J-index (Bunge, 1982) for 100 peridotites sampled along 5 profiles normal to the massif trend (Appendix 2). Figure 5-16 presents the evolution of the olivine CPO strength as a function of the vertical distance to the contact (that is, the distance measured normal to the average foliation, which is mainly shallowly-dipping) along these profiles. All curves show similar first order variations. The J-indexes in Grt-Sp Mylonites are low, between 3 and 4, except in the Amaziten cross section, where stronger olivine CPO are observed (J-index of 6). In Ar domain peridotites, J-index of olivine first increases, reaching values between 7 and 14 at ~300 m from the contact, and then decreases more or less sharply, depending on the profile. The lower part of the Ar domain is usually characterized by rather weak olivine CPO. A second peak in J-index roughly coincides with the entrance in the Ar-Se domain. This peak is either sharp or smooth, depending on the profile. The double crossing of the Ar-Se and Se domain limits in the Nich profiles (see Fig. 5-1) is recorded by a smooth double peak in the J-index curves. Finally, Se domain peridotites are characterized by a strong variability in the olivine CPO strength, with J-index values ranging from 3 to 11.

In Grt-Sp Mylonites and Ar domain fine-porphyroclastic peridotites, the intensity of olivine CPO is positively correlated with the average olivine grain size (Fig. 5-17). However, the strongest and weakest olivine CPO in these domains are observed for harzburgites and clinopyroxene-rich lherzolites, respectively, illustrating that the olivine CPO strength is also anticorrelated with clinopyroxene modal content (Fig. 5-18). The first observation may easily explain the increase in J-index from Grt-Sp Mylonites to Ar domain peridotites. The decrease of the J-index in the lower part of the Ar domain is, however, difficult to reconcile with continuous increase of the average olivine grain size with increasing distance from the contact (Fig. 5-6). It might result from a variation in clinopyroxene modal content, but the correlation between the J-index and the clinopyroxene modal content in the Ar domain is weak (black squares in Fig. 5-18). The dominant process is rather related to the symmetry of the CPO itself (Fig. 5-14), the strongest axial-[010] pattern also exhibiting the highest J-indexes.

In the Ar-Se and Se domains, in contrast, the olivine CPO strength is highly variable and shows no correlation with average olivine grain size nor clinopyroxene modal content (Figs. 5-17 and 5-18). The second peak in the J-index profiles (Fig. 5-16) may be, however, linked to the abnormal grain growth that characterizes Ar-Se domain peridotites (Fig. 8d-f).

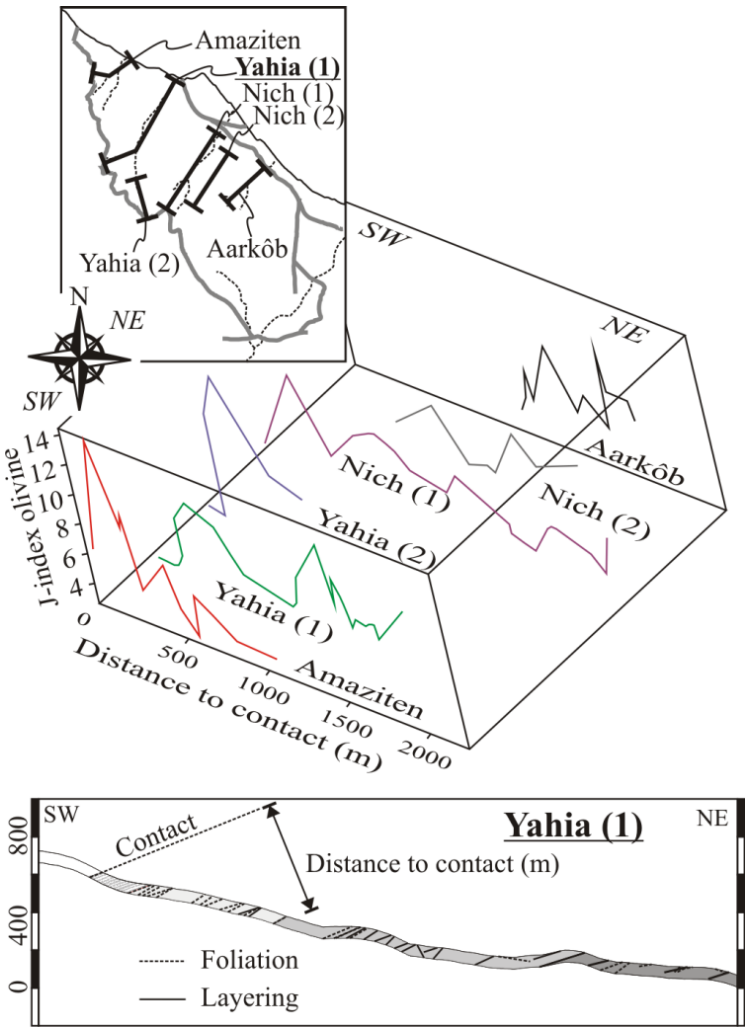

Figure 5-16. Evolution of the J-index across the different analyzed profiles in function of the vertical distance to the contact (distance increases from SW to NE). Map shows the location of the profiles.

5.7. Discussion

5.7.1. Deformation mechanisms and conditions

The Beni Bousera peridotite massif is characterized by a continuous metamorphic zoning and coherent foliations and lineations from the Grt-Sp Mylonites to the Se domain, lacking any crosscut relationship. The lowermost Se domain is, however, characterized by a gradual reorientation of the flow direction from NW-SE to NNE-SSW and the presence of local domains with contrasting kinematics (vertical lineations). The metamorphic zoning goes along with a microstructural gradient and variations in olivine and pyroxenes CPO. Below we discuss the deformation processes in each domain in the light of a polybaric and polythermal evolution recently inferred from the study of Beni Bousera pyroxenites (Frets et al., 2012). We relate the conditions of deformation with massif-scale kinematics and discuss a possible tectonic scenario integrating our observations and interpretations and finally the implications of the latter for the evolution of the Rif-Betic belt.

5.7.1.1. - Grt-Sp Mylonites: deformation under high stress and low temperature

The well-developed foliation and lineation, as well as the intense boudinage of pyroxenite layers (Fig. 5-2), imply that Grt-Sp Mylonites accommodated large finite strains. Locally, sigma-type asymmetries attest for dominant simple shear deformation. The peridotites (and pyroxenites, cf. Frets et al. 2012) from this domain are characterized by the finest grain sizes (mean olivine grain size is 90-160 μm, Figs. 5-6 and 5-7a,b) indicating high work rates (Austin and Evans, 2007). Large work rates may either result from high stress or strain rate, or a combination of both. High stresses are consistent with the low synkinematic temperature conditions recorded in peridotites and garnet pyroxenite layers from this domain (900 - 950ºC; Frets et al., 2012; this study). High stresses and large finite strains are also indicated by the intense deformation of the high strength garnet pyroxenite layers (Figs. 5-2c-d and 5-8a, Frets et al., 2012) and by the extreme elongation of orthopyroxene porphyroclasts in peridotite (Figs. 5-2a,d, 5-8c and 5-9). Strain rates cannot be estimated accurately, as the duration of deformation is unknown, but it is likely that they were high too.

Ubiquitous undulose extinction and subgrains in olivine, extreme stretching and kinks in orthopyroxene (Figs. 5-7 and 5-8), and neat CPO of olivine and pyroxenes (Fig. 5-15) indicate that, despite their fine grain sizes, deformation of peridotite in this domain was accommodated dominantly by dislocation creep. Coexistence of subgrains and recrystallized grains of similar sizes to the sinuosities of the olivine grain boundaries point to subgrain rotation and bulging as the active deformation mechanisms. Finally, the elongated shapes of olivine and pyroxenes in the recrystallized matrix (Fig. 5-9) and their sinuous grain boundaries (Fig. 5-8) preclude a large contribution of dry grain boundary sliding to the deformation in Grt-Sp Mylonites.

Grt-Sp Mylonites show well-developed olivine CPO with an axial-[010] symmetry and a weak concentration of [100] subparallel to the lineation (Figs. 5-14 and 5-15). However, the olivine CPO strength is highly variable; it is positively correlated to the mean olivine grain size and anti-correlated to the modal content of clinopyroxene (Figs. 5-17 and 5-18). Axial-[010] patterns of olivine

CPO patterns may result from various processes including axial compression/transpression (Nicolas et al., 1973; Tommasi et al., 1999), dynamic or static recrystallization (Falus et al., 2011; Tommasi et al., 2008), deformation in presence of melt (Holtzman et al., 2003) or simultaneous activation of [100](010) and [001](010) slip systems under high stress (Durham & Goetze, 1977) or high pressure (Couvy et al., 2004; Mainprice et al., 2005; Raterron et al., 2009).

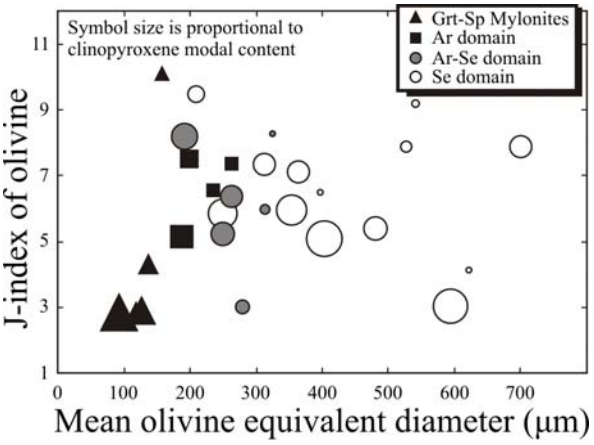

Figure 5-17. Olivine J-index in function of both mean olivine 2D equivalent diameter, and modal content of clinopyroxene (proportional to the size of the symbol) for those samples for which grain size analysis was performed. See text for explanation.

Axial compression/transpression and static recrystallization may be ruled out based on: (i) the well-developed and consistent stretching lineations, (ii) the analysis of the pyroxenes CPO, which are characterized by a point concentration of the main glide direction in pyroxenes—[001] subparallel to the lineation— and (iii) the well-developed intracrystalline deformation features. The synkinematic pressure — ~2.0 GPa recorded by the equilibrium mineral assemblages in pyroxenites from this domain (Frets et al. 2012) is also too low to produce a transition from [100] to [001]-glide in olivine.

Both high stress conditions and extensive dynamic recrystallization are corroborated by the microstructural observations and might explain both the positive correlation of the olivine CPO strength with the mean grain size and the axial-[010] patterns. In addition, the irregularly-shaped pyroxene-rich lenses parallel to the foliation (Fig. 8a-b), which are characterized by interpenetrating olivine-pyroxene grain boundaries (Fig. 5-8b), support syn- to late-kinematic crystallization of pyroxenes at the expense of olivine. These observations together with the low synkinematic temperatures (900-950ºC, Frets et al., 2012; this study) suggest synkinematic percolation of a Si-poor, Ca-rich magma (probably carbonatitic). Indeed, Grt-Sp Mylonites containing the highest amounts of clinopyroxene (>6 %) exhibit the most dispersed olivine CPO (Figs. 5-17 and 5-18).

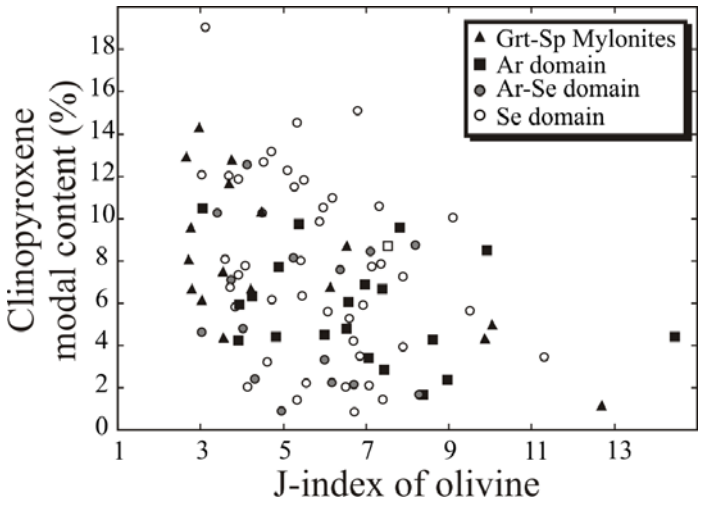

Figure 5-18. Olivine J-index as a function of the clinopyroxene modal content.

Pyroxenes CPO are consistent with dominant slip on [001]{110} (Bascou et al. 2002). Such CPO, although common for clinopyroxenes, is rather rare for orthopyroxenes. It has however already been reported in naturally deformed peridotites (Jackson, 1961; Avé Lallemant, 1967; Carter et al., 1972; Naze et al., 1987; Toy et al., 2010; Soustelle et al., 2010) and pyroxenites (Frets et al., 2012), and in wet polycrystalline enstatite experimentally deformed under high stresses and high temperatures (Ross & Nielsen, 1978). Topotaxic relationships between orthopyroxene and clinopyroxene in symplectites around garnet porphyroclasts (Fig. 5-8b) may also explain the similarity between the CPO of these two minerals, as suggested for Beni Bousera pyroxenites (Frets et al., 2012).

In summary, field and microstructural observations in Beni Bousera Grt-Sp Mylonites are consistent with previous data on pyroxenite layers in this domain (Frets et al. 2012); both imply strong deformation by dislocation creep under high stress, moderate temperature (~900-950°C) and pressure (~2.0 GPa) conditions with local synkinematic percolation of Si-poor, Ca-rich magmas.

The significance of Grt-Sp Mylonites in the Beni Bousera and the Ronda peridotites has been long controversial (Kornprobst, 1969; Obata, 1982; Reuber et al., 1982; Tabit et al., 1997; Van der Wal & Vissers, 1993, 1996, 1997; Zeck et al, 1997). The precursor of Grt-Sp Mylonites likely were coarse-grained garnet and spinel peridotites spatially coexisting in domains with variably FeO/MgO content (Tabit et al., 1997; Garrido et al., 2011), and locally interbedded with layered garnet pyroxenites (Pearson et al., 1993; El Atrassi, 2011). Grt-Sp Mylonites formed due to variable mechanical and compositional mixing of peridotite and pyroxenite by decompression and cooling leading to complex garnet and spinel textural relationships due to local mosaic equilibrium (Tabit et al, 1997; Garrido et al., 2011).

5.7.1.2. - The Ar domain peridotites: progressive delocalization of strain under increasing temperature conditions

The Ar domain is characterized by a continuous textural evolution from fine-grained porphyroclastic peridotites at the contact with Grt-Sp Mylonites towards coarse-grained porphyroclastic peridotites at the Ar-Se transition: the mean olivine average and recrystallized grain sizes increase (Fig. 5-6) and the volume fraction of recrystallized grains decrease (Fig. 5-7), which is consistent with decreasing work rates and finite strains and, hence with a more distributed deformation under lower stress conditions.

The transition from Grt-Sp Mylonites to Ar domain fine-porphyroclastic peridotites is coupled to a decrease of olivine CPO strength (Fig. 5-16). There is, however, no microstructural evidence for a change in deformation mechanism. Elongation of olivine and pyroxenes parallel to the lineation exhibiting undulose extinctions (Fig. 5-11a) and well-developed CPO (Fig. 5-15) of these minerals indicate dominant dislocation creep. Dynamic recrystallization, which could account for the olivine CPO dispersion, is less extensive in this domain, as indicated by the increase in the area fraction occupied by porphyroclasts (Fig. 5-7b-c). Evidence for synkinematic reactive melt percolation is also poor. Although pyroxene porphyroclasts display irregular shapes filled by olivine, this feature remains extremely limited in extent compared to the diffuse pyroxene bands in Grt-Sp Mylonites and Ar-Se domain peridotites. The decrease in olivine CPO strength in the Ar domain should therefore

imply lower finite strains. This interpretation is consistent with the less intense boudinage of the pyroxenite layers as one approaches the Ar-Se domain (Fig. 5-3 c-f).

Olivine CPO symmetry also changes progressively (Fig. 5-14). A few samples show olivine CPO with axial-[100] patterns, but most peridotites in this domain still have olivine CPO with an axial-[010] symmetry, even if the recrystallization is less complete. The coarser recrystallized grain sizes also imply lower work rates and, probably, lower stress conditions. As in grt-spl mylonites, both pyroxenes CPO are correlated with the olivine CPO and do not show a dispersion of [001] in the foliation plane that could be interpreted as an indicator of transpression (Fig. 5-15).

5.7.1.3. - The Ar-Se transition: synkninematic, melt-present abnormal coarsening under low stress

The transitional Ar-Se domain, defined by the apparition of spinel in pyroxenites is also marked by the presence of more abundant dunites with alignments of pyroxene-spinel aggregates parallel to the foliation.especially towards the structurally lower Se domain (Fig. 6d,e).

The microstructures are characterized by elongated cm-scale olivine crystals with lobated grain boundaries and frequent (100) subgrains (Figs. 5-7d-f and 5-11), which record abnormal grain growth during deformation. In addition, although the average olivine grain size does not vary continuously within this domain (Fig. 5-6), the grain size heterogeneity and the area fraction occupied by large crystals increase (Fig. 5-7d-f). All crystals, independently of their size, are elongated, marking the lineation, and show undulose extinction, well-developed subgrains, and sinuous grain boundaries (Fig. 5-11a). The above association of microstructures is characteristic of synkinematic grain boundary migration.

Abnormal grain growth is a well-known phenomenon in metallurgy that involves fast growth of some grains at the expense of the others (Hillert, 1965). It requires high-temperature conditions, consistent with the equilibrium temperatures recorded in garnet-spinel pyroxenites from this domain (T> 1100 ºC, P = 1.8GPa, Frets et al., 2012). High-temperature, near-solidus conditions during the deformation in this domain are also suggested by a series of microstructures characteristic of synkinematic reactive melt percolation: (i) the lobate shapes of large orthopyroxene crystals, which show embayments filled by olivine (Fig. 5-7d-f and 5-11b), (ii) the aggregates of intermixed pyroxenes and olivine with interpenetrating boundaries and undulose extinctions (Fig. 5-11c), and (iii) the lack of correlation between olivine and pyroxene CPO (Fig. 5-15).

The presence of small melt fractions in the system may have enhanced mass transport during deformation. Yet the transition from the Ar to the Ar-Se domain is characterized by a marked strengthening of the olivine CPO (Fig. 5-16). This increase in the J index is due to the abnormal growth, which tends to reinforce the volume of the texture components representing the coarse crystals. Analysis of Fig. 5-16, where the data is plotted as one point per grain shows indeed that olivine CPO in the Ar-Se are not so strong. A similar interpretation was proposed to explain the strong olivine CPO in coarse-grained peridotites from the Ronda recrystallization front (Vauchez & Garrido, 2001). Finally, this domain is characterized by a higher proportion of orthorhombic olivine

CPO (Fig. 5-14), consistent with an effective grain boundary migration, which counteracted the dispersion of the CPO with a preferential rotation around the [010] produced by subgrain rotation recrystallization (Falus et al., 2011).

5.7.1.4. - The Se domain: deformation of a partially molten (asthenospherized) lithospheric mantle

The peridotites in the Seiland domain are characterized by coarse grain sizes (Figs. 5-4c,f, 5-6 and 5-7g-j), interpenetrating grain boundaries indicative of extensive grain boundary migration in olivine (Fig. 5-12a,b) and melt-rock reactions leading to crystallization of olivine at the expenses of orthopyroxene (Figs. 5-7g-j and 5-12c) or to secondary crystallization of pyroxenes and spinel (Figs. 5-7g-j and 5-12a), and ubiquitous undulose extinctions and subgrains or kinks in olivine and pyroxenes, respectively. These microstructures, together with the ubiquitous diffuse dunitic lenses and websteritic layering (Fig. 5-4a,b,d,e), subparallel to the foliation, are indicative of high-temperature, low-stress deformation in presence of low melt fractions. Si saturation probably varied in time and space, leading to either pyroxene dissolution or crystallization (e.g. Berger & Weber, 1991; Kelemen et al., 1992; Le Roux et al., 2007).

This domain is also characterized by high variability in both olivine CPO strength and symmetry (Figs. 5-14, 5-15 and 5-16). There is no clear correlation between the olivine CPO strength and the average grains size or the clinopyroxene modal content, in contrast with the grt-spl mylonites and the Ar domain (Figs. 5-17 and 5-18). Harzburgites and dunites tend, however, to display more orthorhombic or even axial-[100] patterns (Fig. 5-14). This variability in olivine CPO symmetry and intensity is likely related to variations in the instantaneous melt fraction during deformation, which cannot be inferred from the present modal composition. High instantaneous melt fractions may favour diffusion, leading to a lower contribution of dislocation creep to the deformation (Hirth & Kohlstedt, 1995b) and thus to a decrease of the CPO intensity (Holtzman et al., 2003; Le Roux et al., 2008). Small melt/fluid fractions at triple junctions and along grain boundaries reduce, however, the contact area between, locally enhancing stresses and favouring dislocation creep and CPO development (Hirth and Köhlstedt, 1995a). A similar interpretation was proposed to account for the variability in olivine CPO intensity in the lherzolites from the Ronda peridotite massif (Soustelle et al., 2009).

Pyroxenes, in particular clinopyroxenes, show a bimodal CPO pattern, with one texture component, usually the strongest one, well correlated with the olivine CPO and another characterized by [001] axes in the foliation plane but at high angle to the lineation, similar to the one observed in the Ar-Se domain (Fig. 5-15). We interpret these CPO as recording synkinematic crystallization of pyroxenes due to reactive melt percolation, the change in orientation recording variations in finite strain accommodated since their crystallization. Following this interpretation, the difference in pyroxenes CPO between the Ar-Se- and the Se domain may record a spatial evolution in the relative timing between partial melting and deformation. A similar conclusion may be reached from the analysis of symplectites of opx-cpx-spl after garnet in both domains. The peridotites from the Se domain display coarse spinels surrounded by orthopyroxene with undulose extinctions and minor clinopyroxene (Fig. 5-4f and 5-12d), while pyroxenites sampled in the lower part of the Ar-Se domain

display undeformed opx-cpx-spl-symplectites (Frets et al., 2012) indicating that heat in the Ar-Se domain outlasted the deformation.

Together these data point to deformation in presence of variable melt fractions in the Se domain. The four small (<200m wide) domains with vertical foliations (Fig. 5-5) in the upper part of the Se domain might represent small gravitational instabilities (diapirs) formed in response to local melt accumulation. Larger than average melt fractions in these domains are consistent with the abundance of dunites and diffuse websterites in their vicinity.

Finally, the gradual reorientation of the lineation in the Se domain with respect to all overlying units (both mantle and crust) indicates progressive mechanical decoupling at the base of the lithospheric section. We propose that such partial decoupling was made possible due to a viscosity drop generated by the higher melt fractions in the partially molten "asthenospherizing" Se domain. Partial mechanical (de-)coupling or so-called "clutch-tectonics" (Tikoff et al., 2004) was proposed as a potential mechanism at the LAB, but to our knowledge this is the first time that this phenomenon is shown to be preserved in exhumed orogenic peridotite.

5.7.2. A tectonic model for the petro-structural zoning and exhumation of the Beni Bousera peridotite

5.7.2.1. - Previous models

Wealth of tectonic models have been proposed for the exhumation and intra-crustal emplacement of the Rif and Betic mantle peridotites. However, only a few of these models try to explain the petrostructural zoning of these orogenic peridotites, which implies deformation under polybaric and polythermal conditions (Obata, 1980; Van der Wal & Vissers, 1993, 1996; Tubía, 1994, Tubía et al., 2004, Précigout et al., 2007; Garrido et al., 2011; Hidas et al., in press). Obata (1980) proposed that the petrological zoning of the Ronda peridotite was formed during progressive inward cooling of an upwelling mantle diapir; however, his diapiric model fails to account for the predominant subhorizontal and consistent lineations in Beni Bousera peridotite and for the structural data indicating that the garnet-spinel mylonites formed at HP-LT in the earlier stages at the margins of the diapir. Van der Wal & Vissers (1993, 1996) claimed that Ronda garnet-spinel mylonites developed during Alpine oceanic subduction upon pre-existing Mesozoic Ariègite-subfacies spinel tectonites. The Seiland facies coarse-granular peridotites were interpreted as due to static recrystallization and melting at LP-HT conditions in response to slab break-off and asthenospheric upwelling. This was followed by intracrustal emplacement of plagioclase lherzolite facies peridotites along extensional faults. This model does not explain, however, the similar kinematics of the different tectono-metamorphic domains in the Beni Bousera peridotite. Furthermore, the existence of prekinematic garnet in Ronda garnet-spinel mylonites (Garrido et al., 2011) invalidates a near-isobaric cooling path for the formation garnet-spinel mylonites (Van der Wal & Vissers, 1993, 1996). The observed assemblages are more consistent with shear localization during decompression (Tabit et al., 1997; Précigout et al., 2007; Garrido et al., 2011; Afiri et al., 2011).

Emplacement along transcurrent faults, triggered or not by lithospheric delamination, as proposed for the Ojén and Carratraca peridotites in the Betics (Tubía et al., 2004), accounts for the internal kinematics of peridotite and their crustal envelope, but fails to provide an explanation for the internal petrological zoning of peridotite. Thinning and exhumation of subcontinental mantle lithosphere during slab rollback induced continental back-arc rifting (Précigout et al., 2007; Garrido et al., 2011), seems a feasible process for explaining the internal structure, petrology and geochemistry of the Ronda peridotite and provides a unifying setting for the emplacement of the Betic-Rif massifs in the late Oligocene (Hidas et al., in press). However, a common thread of this and previous tectonic and petrological models for the evolution of the Betic-Rif peridotites (Kornprobst, 1970; Kornprobst et al., 1990; Obata, 1980; Van der Wal & Vissers, 1993; Tabit et al., 1997; Précigout et al., 2007; Afiri et al., 2011; Garrido et al., 2011) is that all tectono-metamorphic domains are considered as originating at similar HP-HT prekinematic ("primary") conditions. This P-T-t evolution requires sequential overprinting of the earliest HP-LT structures upon decompression and heating (Van der Wal & Vissers, 1993, 1996; Van der Wal & Bodinier, 1996; Lenoir et al., 2001; Soustelle et al. 2009; Afiri et al., 2011). This tectonic evolution appears thermally not realistic, because it requires a heat sink atop of the peridotites for development of garnet-spinel mylonites by cooling and decompression, followed by heating and decompression by an extrinsic (unknown) heat source at the base of the massif to generate the HT-LP partially melted Se domain. In addition, the extreme thermal gradient implied by the preservation of HP-LT assemblages in garnet-spinel mylonites less than 1 km from the melting front (>100°C/km) is incompatible with conductive heating.

5.7.2.2. - Mantle exhumation along an asymmetrical extensional (transtensional) shear zone

These previous models neglect, however, three essential observations: (1) the P,T equilibrium conditions in the different domains are all syn- to late kinematic, (2) the consistency of the orientation of the foliations and lineations across the massif, and (3) the continuity in the variation of the microstructures and metamorphic assemblages over the entire massif. The structures mapped in the Beni Bousera massif record therefore the activity of a single tectonic object: a shear zone. As a shear zone accommodates, by definition, a relative displacement between two blocks, the different domains of Beni Bousera cannot have originated at the same 'primary conditions'.

If the subvertical lineations in the Se domain formed in diapiric-like structures, they record the paleovertical and indicate that the current orientation of the deformation structures and of the petrostructural zoning of the massif is roughly that in the pristine mantle shear zone. Grt-Sp Mylonites and Se domain constituted therefore the hanging and the footwall of the shear zone. Shearing resulted in tectonic juxtaposition at a final depth of 60 km (1.8 GPa) of domains that were initially equilibrated at different depths along the same geotherm (Fig. 5-19, t_0). The deeper and hotter levels, which are now represented by the Se domain, were submitted to the largest displacements. Fast shearing avoided significant thermal re-equilibration by conduction and as shearing put into contact domains with different temperatures, deformation migrated towards the hotter footwall (Fig. 5-19, t_1 and t_2). Together these two processes allowed the preservation of metastable HP assemblages,

accounting for the variation in temperature by > 200 °C and in pressure of at least 0.5 GPa presently recorded in a mantle section barely 2 km thick (Fig. 5-19, t_f).

In the shallower and colder lithospheric levels (P, T), lower temperatures resulted in strain localization forming Grt-Sp Mylonites. Sluggish reaction kinetics in this relative colder lithospheric level favored preservation of metastable HP assemblages, whereas mechanical mixing of garnet pyroxenites and peridotites produced chemical heterogeneities and garnet-spinel- and spinel-garnet assemblages in peridotites (Tabit et al., 1997). The higher temperatures conditions allowed for faster kinetics of decompression reactions in the Se domain peridotites erasing most petrological vestiges of earlier HP assemblages (only locally preserved as opx-cpx-spl symplectites, Fig. 5-12d). Microstructural evidence for melt-present deformation in the Se domain indicates that these hotter lithospheric levels crossed the lherzolite wet solidus upon decompression. Decompression may account for small degrees of melting of this domain, in particular if the peridotites were hydrated, without the need for an extrinsic heat source, which had been proposed for the Ronda peridotite (Van der Wal & Vissers, 1993, 1996; Garrido & Bodinier, 1999; Lenoir et al., 2001; Garrido et al., 2011). Paradoxally, this tectonic evolution implies that the apparently less strained Se peridotites accommodated higher displacements and upwelling then the porphyroclastic peridotites from the Ar domain and the Grt-Sp Mylonites.

High strain rates were necessary to avoid thermal re-equilibration and ensure the preservation of metastable high pressure assemblages and high stress deformation microstructures in Grt-Sp Mylonites and Ar domain. These data might be only accounted for if uplift rates were faster than the characteristic time for thermal equilibration by conduction. Evidence for thermal reequilibration in Beni Bousera, such as the static garnet-spinel transformation in pyroxenites in the Ar-Se domain, is limited to <1 km. Considering a peridotite thermal diffusivity of $6x10^{-7}$ m^2s^{-1} (at temperatures of 900°C, Tommasi et al., 2001), thermal equilibrium over such a distance should be reached in ca. 50 ka. Therefore, not only strain rates in the shear zone were high, but further exhumation and emplacement of peridotites in the crust, accommodated by another, deeper fault, must have occurred right after the deformation recorded in the Beni Bousera massif.

One may roughly estimate the order of magnitude of displacement on the shear zone based on the orientation of the foliation and lineation. In Beni Bousera, lineations are dominantly subparallel to the metamorphic zoning (Fig. 5-5). This implies a substantial strike-slip component of motion in the shear zone. Considering the end-member case, in which all decompression from 90 to 60 km depth is accommodated by the Beni Bousera shear zone, which has an average foliation dip of 30º of foliation and lineation pitch of 30º, the maximum displacement in the shear zone would attain ca. 120 km. Strain rates therefore need to be higher than 10^{-11} s^{-1} to avoid conductive re-equilibration at the km scale. Such high strain rates are consistent with extremely rapid exhumation and cooling rates of the overlying crustal granulites (ca. 3 km/Ma, 250º-450ºC/Ma, Haissen et al., 2004), but they are most likely overestimated, as latent heat sink effects during partial melting might have slowed thermal reequilibration.

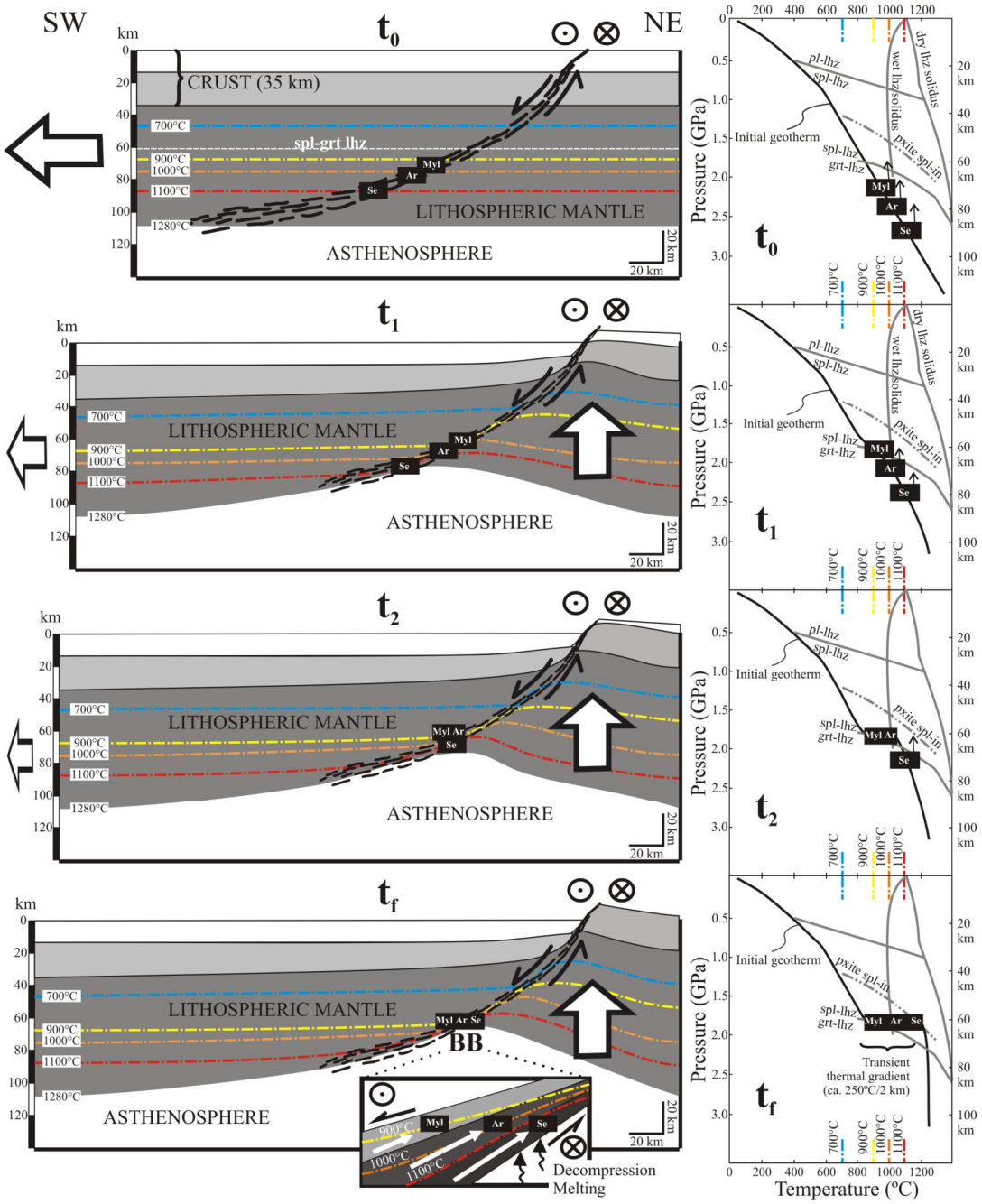

Figure 5-19. 2D-conceptual model showing different stages of the continuous P-T-deformation evolution of the Beni Bousera tectono-metamorphic domains in the context of a transtensional shear zone affecting the lithospheric mantle. (t_0) We consider a thermally equilibrated continental lithosphere with an aribitrary 35 km-thick crust. Grt-Sp Mylonites ("Myl"), Ar- ("Ar") and Se- domains ("Se") start from different, increasing P-T conditions along the same geotherm, respectively. The different domains sample different parts of the shear zone and have thus different lateral provenances in the lithospheric mantle. The geotherm was calculated considering a surface temperature of 27ºC, heat flows of 65 and 30 mW.m^{-2} at the surface and the base of the lithosphere, respectively. Thermal conductivity values for the crust and the mantle are 2.50 and 3.35 W.m^{-1}.ºC^{-1} respectively, and thickness of the radiogenic layer is 10 km. (t_1) All domains deform along the shear zone and record a near-isothermal decompression until Grt-Sp Mylonites reach 60 km. (t_2) Deformation migrates towards the lower stress, higher temperature domains (Ar domain, at this stage) towards the footwall of the shear zone, due to the compaction of the isotherms in the shear zone. (t_f) Further migration of the deformation towards the Se domain coeval with decompression melting. Dry and wet lherzolite solidi from Takahashi & Kushiro (1983) and Kushiro et al. (1968), respectively. Spinel-plagioglase lherzolite reaction from Green & Ringwood (1967b). Spinel-garnet reaction applying the geobarometer calibration in the CMAS-Cr system (Webb & Wood, 1986), corrected for the effect of FeO in olivine (O'Neill, 1981) using mineral compositions of garnet-spinel mylonite BB001W (not shown). Sp-in curve in Beni Bousera pyroxenite from Frets et al. (2012).

Although the proposed tectonic scenario accounts for the essentials of the petrostructural evolution of the Beni Bousera, it seems in conflict with the predominant axial-[010] olivine CPO of Beni Bousera peridotites, and in some Ronda peridotites (Vauchez & Garrido, 2001; Soustelle et al., 2009), that are thought to be symptomatic of transpressive deformation (Tommasi et al, 1999). However, an increasing number of studies show that they are also produced by melt-present deformation, irrespectively of the regional deformation regime (Holtzman et al. 2003; Le Roux et al. 2008; Higgie & Tommasi, submitted).

Fabric and metamorphic zoning such as in Beni Bousera peridotites are common in exhumed normal shear zones, both in the crust (e.g Handy et al., 2007) and in the shallow sublithospheric mantle (Kaczmarek & Tommasi, 2011). We propose a similar mechanism for the uplift of the deep, sub-continental mantle. As pointed out by Vauchez et al. (2012), lithospheric faults may penetrate deep (here ca. 90km) in the lithospheric mantle, albeit the width of these shear zones at depth remains hardly predictable. Observations in Beni Bousera only allow estimating minimum thicknesses from the actual thicknesses of the domains: the shear zone would be at least 100 m thick at ca. 60 km, 900 ^{o}C, and at least 1 km at ca. 90 km, 1150 ^{o}C.

Thinning accommodated by a lithospheric-scale extensional shear zone is also consistent with (1) the near-isothermal decompression and ductile thinning of the metamorphic sequence in the overlying crustal units with a sharp temperature increase towards the peridotites (Loomis, 1972; Negro et al., 2006; Janots et al., 2006) (2) the pressure gap between peridotites and kinzigites without the need to invoke a mechanism of lower crustal excision (Argles et al., 1999) and (3) the upper crustal detachments (e.g. Booth-Rea et al., 2002b).

5.7.2.3. - Geodynamic context

Exhumation of subcontinental mantle peridotites in the western Mediterranean has been attributed, among others, to pure extension (Platt et al., 2006), transpression (Tubía, 1994), or alternating contractional and extensional processes related to continental subduction followed by extension (Balanyá et al., 1997). An increasing number of multidisciplinary studies have shown that slab rollback has played a major role in the Cenozoic geodynamic evolution of the Betic-Rif chain (Jolivet et al., 2003; Faccenna et al, 2004; Booth-Rea et al., 2007, and references therein; Garrido et al, 2011; Marchesi et al., 2012; Hidas et al., in press). Slab rollback promoted drifting from the Provençal coast of Eurasian plate and extension of the proto-Alborán lithospheric domain, which was subsequently accreted onto the Iberian and the Moroccan passive margins. We relate the petrological zoning of the Beni Bousera to the earliest stages of exhumation of the proto-Alboran lithospheric mantle in the late Oligocene during asymmetrical extensional thinning of continental lithosphere, induced by slab-rollback in a backarc basin situated in eastward position. The observed structures in Beni Bousera, however, cannot account for the emplacement of the massif into the crust that must have been accomodated along other lithospheric structures. A potential scenario proposed on the basis of structural study of Ronda plagioclase-facies tectonites—unexposed in the Beni Bousera massif—is intracrustal emplacement during inversion of the back-arc rift due to southward collision of the

retreating slab with the Algerian margin in the late Oligocene (Hidas et al., in press). This theory provides a unifying scenario for the synchronous emplacement peridotites in the Rif, Betic and Tell belts (Hidas et al., in press).

5.8. Conclusions

Field mapping and analyses of microstructures and CPO in Beni Bousera peridotites evidence that the four tectono-metamorphic domains (downsection and from SW to NE: grt-spl mylonites, Ar-, Ar-Se- and Se domains, see legend of Fig. 5-1 for description) are characterized by consistent kinematics of predominant shallowly SW-dipping foliations with NW-SE striking lineations in average, lacking any crosscut relationship. A change in kinematics is only observed in lowest part of the Se domain, which is characterized a gradual rotation of the lineation towards a NNE-SSW strike and the presence of small zones ca. 100m wide bearing vertical lineations (Fig. 5-5).

Ubiquitous subgrains and undulose extinctions in olivine and pyroxenes and the well developed CPO are consistent with dominant deformation by dislocation creep in all domains. The increase in average olivine grain sizes and decrease in the volume fractions of recrystallized grains from the grt-spl mylonites to the Se domain indicate, however, deformation under decreasing work rates. This evolution in deformation microstructures is consistent with petrological data, which indicate an increase in synkinematic temperatures and decrease in synkinematic pressures from Grt-Sp Mylonites (900^{o}C, 2.0 GPa) to the Seiland domain (1150^{o}C, 1.8GPa).

Olivine displays dominantly axial-[010] CPO patterns, characterized by a strong concentration of [010] normal to the foliation and variable dispersion of [100] in the foliation plane, with a maximum parallel to the lineation. The processes producing thes CPO are different in Grt-Sp Mylonites and Ar domain than in Ar-Se- and Se domains. In the former, dispersion of [100] results from extensive dynamic recrystallization due deformation under high stress and strain rates. In the latter, it results from deformation in the presence of melt under low stress, near-solidus temperatures. These high temperature conditions are consistent with abnormal grain growth in the Ar-Se domain. Local melt accumulations, leading to development of small (ca. 100 m wide) diapirs may also account for the vertical lineations areas in the Se domain.

Based on these observations, we propose that the petrostructural zonation in the Beni Bousera massif records exhumation of the lithospheric mantle in a extensional (transtensional) shear zone. Fast advection of deep and hot peridotites (strain rates $\geq 10^{-10}$ s^{-1}) allowed development of an abnormal transient temperature gradient (100^{o}C/km); the temperature contrast resulted in migration of the deformation and accretion of progressively deeper domains to the shear zone hanging wall, allowing for the preservation of metastable HP assemblages. In this model, no external heat source is needed to account for partial melting at low pressure of the Se domain, which can only result from near-isothermal decompression allowing crossing the wet lherzolite solidus. The preservation of such temperature gradient implies large strain rates of the order of up to 10^{-10} – 10^{-11} s^{-1}.

In press in Journal of the Geological Society London

6. Backarc basin inversion and subcontinental mantle emplacement in the crust: Kilometer-scale folding and shearing at the base of the proto-Alborán lithospheric mantle (Betic Cordillera, South Spain)

Károly Hidas[1*], Guillermo Booth-Rea[1,2], Carlos J. Garrido[1], José Miguel Martínez-Martínez[1,2], José Alberto Padrón-Navarta[3,4], Zoltán Konc[1], Flavio Giaconia[1,2], Erwin C. Frets[1,3], Claudio Marchesi[1]

To constrain the latest evolutional stages and mechanisms of exhumation and emplacement of subcontinental peridotites in the Westernmost Mediterranean, we present here a detailed structural study of the transition from granular spinel peridotite to plagioclase tectonite in the western Ronda Peridotite (Betic Cordillera, southern Spain). We show that the plagioclase tectonite foliation represents an axial surface particularly well developed in the reverse limb of a downward facing moderately-plunging and -inclined synform at the base of the Ronda massif. The fold limbs are cut by several mylonitic and ultramylonitic shear zones with top-to-the-SW sense of shear. After restoring the middle to late Miocene vertical axis paleomagnetic rotation and the early Miocene tectonic tilting of the massif, these studied structures record southward directed kinematics. We propose a geodynamic model where folding and shearing of an attenuated mantle lithosphere occurred by backarc basin inversion during late Oligocene (23-25 Ma) southward collision of the Alborán Domain with the paleo-Maghrebian Passive Margin, leading to the intracrustal emplacement of peridotites in the earlymost Miocene (21-23 Ma).

[1] *Instituto Andaluz de Ciencias de la Tierra, CSIC & UGR, Avenida de las Palmeras 4, 18100 Armilla (Granada), Spain*

[2] *Department of Geodynamics, University of Granada, Fuentenueva s/n, 18002 Granada, Spain*

[3] *Géosciences Montpellier, Université Montpellier-2 & CNRS, CC 60, Place E. Bataillon, 34095 Montpellier, France*

[4] *Research School of Earth Sciences, The Australian National University, Building 61, Mills Road, ACT0200 Canberra, Australia*

6.1. Introduction

One of the most peculiar features of the arcuated Betic-Rif orogenic belt (western Mediterranean) is the occurrence of massive outcrops of subcontinental lithospheric mantle, i.e. the Ronda and Beni Bousera peridotite massifs (Fig. 6-1a). Several contrasting models have been proposed to explain the exhumation of these massifs and its relationship to the geodynamic evolution of the western Mediterranean, including the rollback of an eastward subducted oceanic lithosphere slab (Royden, 1993; Lonergan and White, 1997; Wortel and Spakman, 2000; Gutscher et al., 2002; Spakman and Wortel, 2004; Bokelmann and Maufroy, 2007; Bokelmann et al., 2011), convective removal (Platt and Vissers, 1989) or delamination (García-Dueñas et al., 1992; Seber et al., 1996; Calvert et al., 2000; Duggen et al., 2003; Tubía et al., 2004) of overthickened continental lithospheric mantle or transpressional emplacement during oblique plate convergence (Mazzoli and Martín Algarra, 2011). Most of these models agree that extension affected the orogenic wedge during the latest Oligocene to Early Miocene explaining the majority of geological and geophysical observations in the area (Calvert et al., 2000) but only a few of them try to account for the presence of Ronda Peridotite massif (the largest outcrop of subcontinental lithospheric mantle on Earth; ~450 km^2) which was exhumed from diamond facies (>140 km; Davies et al., 1993) and emplaced to middle crustal HP-LT to LP-HT metamorphic units (e.g. Tubía and Cuevas, 1986; Tubía, 1994; Zeck, 1997; Argles et al., 1999; Esteban et al., 2011).

The polybaric and polythermal history of the Ronda exhumation is preserved as a protracted record in different tectono-metamorphic domains (Fig. 6-1b:

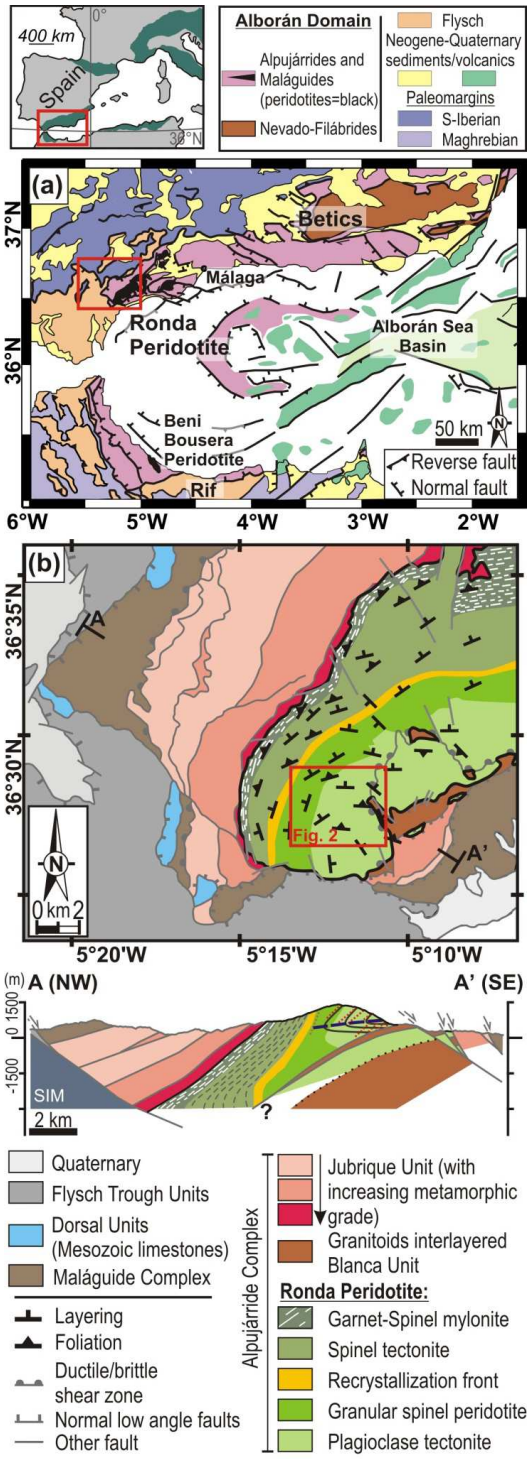

Figure 6-1. (a) Simplified geological map (modified after Comas et al., 1999; Booth-Rea et al., 2007) with the main tectonic domains forming the Betic-Rif orogenic belt (see inset for location). The figure also highlights the Ronda Peridotite in southern Spain and Beni Bousera Peridotite in northern Morocco. The red square is enlarged in (b). **(b)** Simplified geological map and cross section of the westernmost Alborán Domain in the Betic chain with the tectono-metamorphic domains and internal structures of the western Ronda Peridotite (mapped by Darot, 1973; Obata, 1980; Van der Wal and Vissers, 1996; Lenoir et al., 2001; Precigout et al., 2007; Soustelle et al., 2009). The Ronda Peridotite is outlined in black.

Figure 6-1. (a) – continued. The A-A' cross section is modified after García-Dueñas et al. (1992) and Sánchez-Gómez et al. (2002) showing the appearance of the reconstructed fold (solid black lines) with fold axial plane trace (dashed blue line) and axial planar S_2 tectonite. foliation (red dotted line). SIM: South Iberian Margin. Study area is enlarged in Fig. 2.

garnet, spinel and plagioclase peridotite e.g. Obata, 1980; Van der Wal and Vissers, 1996) of which plagioclase peridotite developed at the lowest pressure related to the latest evolutional stages of the massif. Nevertheless, previous structural studies have not satisfactorily integrated the LP-HT structures of this domain in the evolution of the Betic-Rif chain and in the emplacement of the Ronda massif because plagioclase peridotite has been interpreted as either formed by delamination-derived diapiric asthenospheric flow (Tubía, 1994; Tubía et al., 2004), or ductile extensional shear zones affecting partially molten lithosphere prior to its intracrustal emplacement (Van der Wal andVissers, 1996).

The main issues we discuss include the understanding of (i) the transition from a kilometer-scale partially melted domain (represented by the Ronda recrystallization front e.g., Van der Wal and Bodinier, 1996; Lenoir et al., 2001; Soustelle et al., 2009) to the formation of late, ductile structures in the plagioclase peridotite domain (Van der Wal and Vissers, 1996), and (ii) the relation of this transition to the exhumation and crustal emplacement of the massif. Here we present new structural data from this transition indicating massif-scale rotation of the compositional layering that evolved continuously from the spinel to the plagioclase facies and developed contemporaneously with the plagioclase tectonite foliation, recording *kilometer-scale* folding of the shallow subcontinental lithospheric mantle. After restoring the clockwise vertical axis rotation and the counter-clockwise horizontal axis tectonic tilting of the massif (García-Dueñas et al., 1992; Crespo-Blanc and Campos, 2001; Villasante-Marcos et al., 2003), our detailed structural mapping shows that the fold formed before crustal emplacement of the Ronda Peridotite during southward thrusting in the backarc setting of the Alborán Domain (western Mediterranean basin).

6.2. Structure of the Ronda Peridotite massif

The Ronda massif is a coherent lithospheric mantle section zoned into several kilometer-scale petrological, geochemical and structural domains (Obata, 1980; Van der Wal and Bodinier, 1996; Van der Wal and Vissers, 1996; Lenoir et al., 2001; Esteban et al., 2007; Précigout et al., 2007; Soustelle et al., 2009). Results of these extensive studies provide a basis to summarize the temporal and structural evolution of the domains from older to younger structures and from the top to the bottom of the massif (from NNW to SSE) as: (i) the *garnet-spinel (grt-sp) mylonite* and *spinel tectonite domains* representing the vestiges of Proterozoic lithospheric mantle with the grt-sp mylonites interpreted either as younger structures formed by high-pressure shearing of an older spinel tectonite domain (Van der Wal and Vissers, 1996), or as formed coevally with spinel tectonites by increasing strain localization and cooling at the top of the massif (Précigout et al., 2007; Garrido et al., 2011); (ii) *granular spinel peridotite domain* composed of coarse granular spinel peridotites formed by annealing of the spinel tectonites during thermal erosion and partial melting (>1250°C, 1.5 GPa) above the upwelling asthenosphere, at the base of the extremely attenuated lithospheric section (Van der Wal and Bodinier, 1996; Van der Wal and Vissers, 1996; Lenoir et al., 2001; Vauchez and Garrido 2001; Bodinier et al., 2008; Soustelle et al., 2009). The transition from the spinel tectonite to the granular spinel peridotite domain is a narrow (~200-400 m wide) and continuous (~20 km long) transitional zone referred to as the *recrystallization front* that is considered as a former isotherm overlying partially molten granular peridotites (Van der Wal and Bodinier, 1996; Lenoir et al., 2001); and (iii) the youngest, underlying *plagioclase tectonite domain*, overprinting the granular spinel peridotite domain, and recording the latest evolutional stages of the Ronda Peridotite under progressive cooling (800-900°C) and decompression (0.5-0.7 GPa, Obata, 1980).

6.3. Structure of the transition from granular spinel peridotite to plagioclase tectonite

Our study focuses on the westernmost Ronda Peridotite massif where granular spinel peridotite grades into plagioclase tectonite (Fig. 6-1b). We selected this area because the transition here is well exposed and unaffected by the late mantle imbrications overthrusting crustal rocks. These imbricated structures were previously interpreted as crustal lenses deformed synchronously with the ductile deformation of the plagioclase tectonite domain (e.g. Van der Wal and Vissers, 1996) but more recent studies have shown that intercalation of peridotites among layers of crustal Blanca Units is postkinematic to peridotite deformation and, in addition, is strongly modified by superimposed extensional faulting (Sánchez-Gómez et al., 2002).

The oldest structures in western Ronda Peridotite occur in the garnet-spinel mylonite and the underlying spinel tectonite domains (Van der Wal and Vissers, 1996; Précigout et al., 2007; Soustelle et al., 2009) as garnet pyroxenite compositional layering (S_0) and high-temperature (high-*T*) ductile peridotite foliation (S_1) with a NE-SW trending stretching lineation (L_1) defined by spinel aggregates and, in the garnet-spinel mylonite, by elongated orthopyroxene (Darot, 1973; Balanyá et al., 1997; Precigout et al., 2007; Soustelle et al., 2009). The S_1 foliation is subparallel to the S_0 compositional layering and dips generally 70-80° to the WNW (Van der Wal and Vissers, 1996; Soustelle et al., 2009; Fig. 6-1b). In the most intensely foliated spinel tectonites, the S_0 compositional layering exhibits boudins and meter-scale isoclinal folds with axial planes parallel to the S_1 foliation (Van der Wal and Vissers, 1996; Garrido and Bodinier, 1999). The S_1 spinel tectonite foliation disappears at the recrystallization front, which is interpreted as a peridotite solidus isotherm that annealed and melted the spinel tectonite domain giving way to underlying apparently undeformed granular spinel peridotite (Van der Wal and Bodinier, 1996; Van der Wal and Vissers, 1996; Lenoir et al., 2001). Due to melting and decompression the S_0 compositional layering is represented by spinel pyroxenite in the granular spinel peridotite domain (Seiland Facies of Obata, 1980) and by plagioclase-spinel pyroxenite in the plagioclase tectonite domain (Garrido and Bodinier, 1999; Bodinier et al., 2008). In the study area only these pyroxenites were considered as the markers of S_0 compositional layering. In addition to S_0, two newly developed structures characterize the lower part of the granular spinel peridotite and the plagioclase tectonite domains (study area, Fig. 6-2a): (i) a higher-temperature peridotite foliation S_2 (hereafter referred as high-*T* structure) and (ii) a lower-temperature and/or higher strain (hereafter referred as low-*T* structure) mylonitic to ultramylonitic foliation (S_m) developed in shear zones that cut the high-*T* structures.

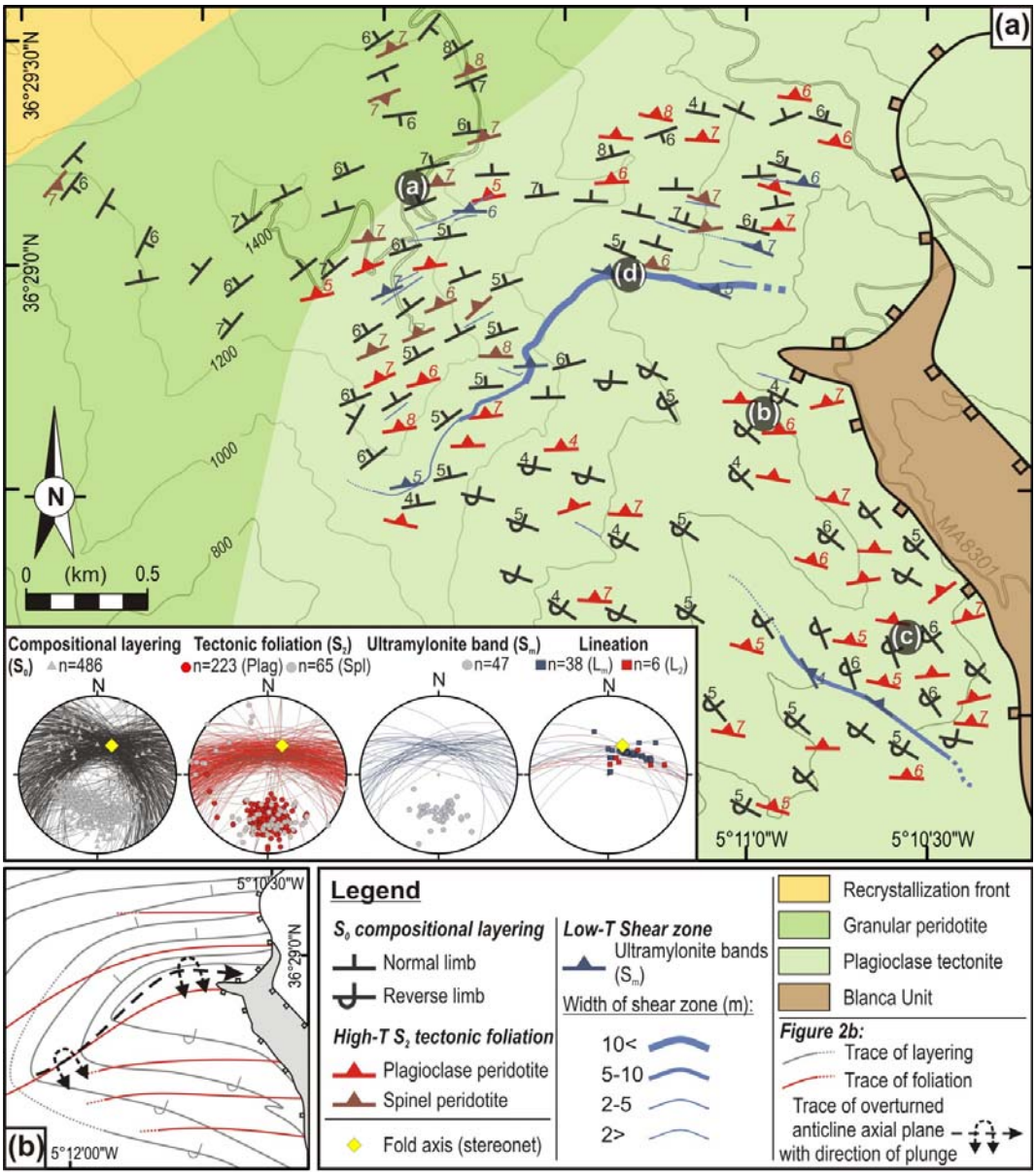

Figure 6-2. (a) Structural map of the study area. White letters in black shaded circles refer to the location of outcrops shown in Fig. 6-3. Numbers beside the symbols of layering, high-*T* and low-*T* foliation indicate the dip values where, for example, 4 should be read as a 40° dip. Inset in the bottom left corner shows lower hemisphere, equal angle (Wulff) stereographic projections of all field measurements as traces of planes and their poles for compositional layering (S_0, black), high-*T* tectonite foliation (S_2, red and dark red), and low-*T* shear zone foliation (S_m, blue). In the pole figure of the S_2 foliation (second pole figure from the left), dark red lines refer to plagioclase-free foliation, whereas red lines belong to plagioclase tectonites. Stretching lineations in high-*T* (L_2) and low-*T* (L_m) structures are plotted on their corresponding foliation planes (S_2 and S_m, respectively). Yellow diamond in pole figures corresponds to the fold axis. n: number of data; Plag: plagioclase tectonite foliation; Spl: plagioclase-free tectonite foliation. **(b)** Interpretative map of the large-scale folding of the S_0 compositional layering with the S_2 axial plane foliation in the study area. Note the changes from NW to SE cleavage vergence in normal and reverse limbs of the fold that corresponds to the 'north-vergent' and 'south-vergent' domains of Van der Wal and Vissers (1996), interpreted by them as shear zones with opposite kinematics. Note also a small inversion in cleavage vergence in the southeastern part of the study area, which is interpreted as a minor fold developed on the reverse limb of the fold.

At the highest topographic levels of our study area (Fig. 2a), located immediately below the recrystallization front (see Fig. 6-1b), the S_0 compositional layering is marked by spinel pyroxenite dipping 70-80° to the NW thus being subparallel to the garnet pyroxenite S_0 of the overlying spinel tectonite domain (Fig. 6-1b, Van der Wal and Vissers, 1996). Down the section, at the transition from granular spinel peridotite to plagioclase tectonite domain the S_0 compositional layering rotates gradually clockwise, at the base of the massif having a dip of 40-60º to the ENE (Fig. 6-2a). The first occurrence of the new high-*T* S_2 foliation is found close

to the recrystallization front in the northwestern part of the study area (Fig. 6-2a), where plagioclase-free spinel lherzolite show foliation dipping 60-80° to the N that crosscuts the spinel pyroxenite S_0 (Fig. 6-3a). Further to the SSE in the plagioclase tectonite domain the S_2 foliation becomes increasingly penetrative in porphyroclastic lherzolite that shows plagioclase rims around spinel (Fig. 6-3b,d) and it is slightly weaker in more refractory peridotite that lacks plagioclase. In both cases the S_2 foliation crosscuts S_0 compositional layering and former isoclinal folds (Fig. 6-3c), and shows a quite uniform dip of 50-70° to the NNE (Fig. 6-2a) with stretching lineation (L_2) trending NE-SW in the foliation plane (inset in Fig. 6-2a).

The younger low-*T* structure in the studied area is marked by the development of mylonitic-ultramylonitic microstructures in shear zones (Fig. 6-3d) with olivine grain sizes <200 μm (10-50 μm for ultramylonites, Fig. 6-3f). Although, Van der Wal and Vissers (1996) interpreted the whole plagioclase tectonite domain as a shear zone, they only reported high-*T* ductile S_2 structure in this domain and did not recognize the low-*T* ultramylonite bands. These shear zones first occur as thinner (<10 cm) and discontinuous bands at the base of the granular spinel peridotite domain and as much wider shear zones (up to 5-10 m width, Fig. 6-3d) in the plagioclase tectonite domain (Fig. 6-2a). In the eastern part of the study area, a thick ultramylonite shear zone (10 m wide, Fig. 6-3d) can be tracked westward for two kilometers where it progressively narrows down to

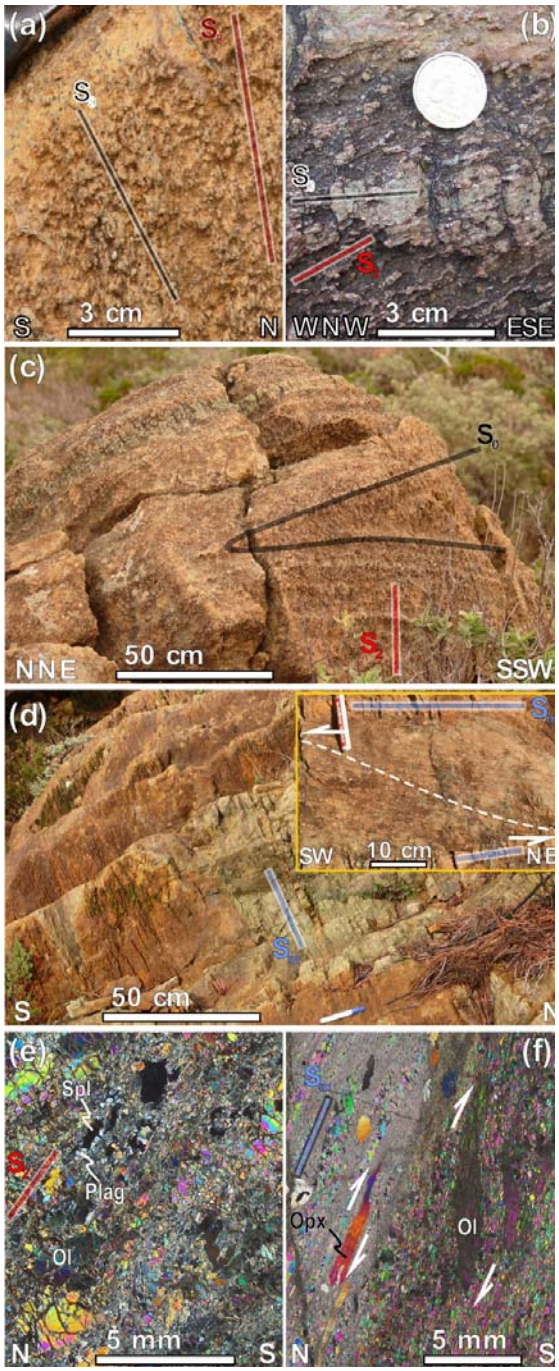

Figure 6-3. (a-d) Field view of the main structural features of the study area discussed in the text. Color coding is the same as for Fig. 6-2, where the (a-d) outcrop locations are also shown.

Figure 6-3. – continued. **(a)** Crosscutting relationship between high-*T* S_2 tectonite foliation and S_0 compositional layering observed in plagioclase-free spinel lherzolite indicating that large scale folding initiated in the spinel lherzolite facies. **(b)** Crosscutting relationship between high-*T* S_2 foliation and S_0 compositional layering observed in plagioclase tectonite. **(c)** Meter-scale unsheared isoclinal folding of the S_0 compositional layering crosscut by high-*T* S_2 plagioclase tectonite foliation indicating that isoclinal folds, similar to those observed in the overlying domains by Van der Wal and Vissers (1996) and Garrido and Bodinier (1999), formed earlier than the plagioclase tectonite foliation and are not related to the km-scale folded structure studied here. **(d)** 10 m wide shear zone developed in peridotite with low-*T* S_m shear zone foliation. Inset shows sigmoidal character of high-*T* S_2 foliation (white dashed line) between low-*T* ultramylonite bands (S_m). **(e-f)** Cross-polarized light photomicrographs of plagioclase tectonite (e) and mylonitic-ultramylonitic shear zone (f). White arrows in (f) and inset of (d) indicate top-to-the-SW sense of shear in the low-*T* structures.

less than a meter (Fig. 6-2a). The strike of the low-*T* S_m mylonitic foliation is subparallel to that of the high-*T* S_2 foliation but it dips more gently, 30-50º to the NNE (inset in Fig. 6-2a). Elongated orthopyroxene porphyroclasts and spinel denote a NE-SW trending lineation L_m, subparallel to the high-*T* L_2 lineation of plagioclase tectonite (inset in Fig. 6-2a). Microstructure of the low-*T* mylonites implies top-to-the-SW sense of shear (Fig. 3f) in accordance with the sigmoidal character of S_2 foliation in the shear zones (inset in Fig. 6-3d).

6.4. Origin and significance of plagioclase tectonites

Our detailed mapping of the granular peridotite and the plagioclase tectonite domains clearly shows large-scale gradual rotation of the S_0 compositional layering (Fig. 6-2a) that cannot be accounted solely by shearing as suggested by Van der Wal and Vissers (1996). Instead, the S_0 compositional layering forms two limbs of a km-scale fold with a high-*T* axial-plane foliation (S_2) (inset in Fig. 6-2a), which is well developed in the reverse limb (Fig. 6-2a,b). The fold axial surface dips 50° to the N (average orientation of the S_2 foliation) and the fold axis plunges approximately 45° to the NE (intersection between the layering in both limbs and between the S_2 foliation and the layering; inset in Fig. 6-2a). This single fold has only two major limbs, which involves that the fold asymmetry or fold vergence cannot be reconstructed. However cleavage vergence, defined here as the horizontal direction of the sense of acute angle towards which the S_2 foliation needs to be rotated so that it becomes parallel to S_0 layering (*cf.* Bell, 1981; and references therein), further clarifies internal fold geometry. As reported by Van der Wal and Vissers (1996) elsewhere in the plagioclase tectonite domain, we also observed in our study area a NW cleavage vergence to the north and a SE cleavage vergence to the southeast (Fig. 2a,b). Local vergence changes related to minor folds at a scale of 10-100 meters are also present, of which the largest one is shown in the southeastern part of the study area in Fig. 6-2b. Because the Ronda Peridotite is a coherent lithospheric mantle section (Obata, 1980; Van der Wal and Vissers, 1996) that is also continuous with its overlying crustal envelope (Tubía, 1994; Balanyá et al., 1997; Argles et al., 1999; Platt et al., 2003), the polarity in the northern side of the massif is upwards. It follows that the km-scale fold at the base of the mantle section is a non-cylindrical, moderately plunging, moderately inclined, downward facing synform (*i.e.*, anticline) (Fig. 6-2b). It should be noted that its fold axis is subparallel to the trace of the stretching L_2 lineation in the S_2 peridotite foliation plane (inset in Fig. 6-2a) but this geometry is similar to that observed in large scale folding of other orogenic peridotites like the central part of the Lanzo Peridotite Massif in the Alps (Nicolas and Boudier, 1975; Boudier, 1978). In fact, the parallelism between fold axis and mineral lineation is a common feature in rocks deformed by folding associated to shearing (*e.g.* Bell, 1978; and references therein), where the fold is formed initially by flattening but the increase of simple shear component progressively rotates fold axis within its own axial plane until it lays parallel to lineation (*cf.* sheath fold). In the study area, high-*T* (S_2-L_2) and low-*T* (S_m-L_m) structures show alike orientation (Fig. 6-2a inset), which indicates that they must record similar kinematics. Therefore, low-*T* shear zones are interpreted to be formed synkinematic to the folding by increasing strain localization upon cooling at the brittle-ductile transition of peridotite (Boullier and Gueguen, 1975).

Van der Wal and Vissers (1996) concluded that the high-*T* foliation S_2 in the plagioclase tectonite domain developed in two diachronous km-scale shear zones with opposite kinematics: an older 'south-vergent' shear zone, as wide as the entire plagioclase tectonite domain, with top-to-the-north sense of shear that was overprinted by a younger and narrower 'north-vergent' shear zone recording top-to-the-south sense of shear. At the borders of the oppositely directed shear zones, they observed minor folds (*ca.* 100 m length scale) with the

high-*T* S_2 foliation as axial plane (see Van der Wal and Vissers, 1996; pp. 36, their Fig. 11) that they suggested to form as shear folds due to strain gradients preserved in the margins of shear zones with opposite kinematics. In contrast, our structural data show that the local change in cleavage vergence corresponds to changes from the normal to the reverse limbs of the large-scale fold (Fig. 6-2a, b) instead of two opposite shearing senses in diachronous shear zones. Small scale folds described by Van der Wal and Vissers (1996) are explained here as minor folds developed on the normal limb of the km-scale anticline. The presence of undeformed granular spinel peridotite lenses within foliated plagioclase tectonite, and the occurrence of crustal lenses of the underlying Blanca unit within the younger, north-vergent shear zones were claimed by Van der Wal and Vissers (1996) as further support for increasing strain localization and their relation with the emplacement of the Ronda Peridotite. However, later studies have demonstrated that these crustal lenses represent brittle imbrications of the plagioclase tectonite overthrusting crustal rocks and that are unrelated to the ductile high-*T* deformation of peridotite (Sánchez-Gómez et al., 2002) (Fig. 6-1b, cross section). In our study area crustal lenses are not present in the SE-vergent domains, supporting that those crustal lenses are due to brittle tectonics (Sánchez-Gómez et al., 2002) unrelated to the processes that originated the ductile S_2 peridotite foliation. Alternative models for the origin of plagioclase tectonites is that they represent an upwelling asthenospheric mantle diapir at the base of a thinned continental lithosphere during mantle extrusion in a transform-fault context (Tubía 1994) or triggered by sublithospheric delamination (Tubía et al., 2004). However, mapping structures related to three-dimensional mantle diapirs below a fast paleo-spreading ridge in the Oman ophiolite shows that diapirs are composed of coarse-granular peridotite formed by high-temperature deformation producing steep peridotite lineations and warped vertical foliation trajectories (Ceuleneer et al., 1988; Nicolas and Boudier, 1995; Jousselin et al., 1998). Formation of the Ronda plagioclase tectonites decoupled from their overlying peridotite domains in high temperature asthenospheric flow is further inconsistent with: (i) the km-scale folding of high-*T* structures from the spinel to the plagioclase lherzolite facies (Fig. 6-2a) indicating that the S_0 compositional layering was folded upon cooling and decompression in a coherent lithospheric mantle section; (ii) subhorizontal lineations of the high-*T* plagioclase tectonite foliation with respect to the paleo-horizontal recrystallization front and the overlying spinel tectonite foliations that would represent the lithospheric domain; and (iii) the presence of low-*T* shear zones showing similar structures to the high-*T* plagioclase tectonites, which cannot occur in high temperature asthenospheric flow. Diapiric models neither account for the geochemical signatures of peridotites and pyroxenites in the different tectonic domains (Garrido and Bodinier, 1999) and the similar Re-Os ages of the different domains indicating a provenance from the same section of old subcontinental lithospheric mantle (Marchesi et al., 2010).

6.5. Geodynamic implications

The Alpine history of the Ronda Peridotite is related to strong Oligocene (Balanyá et al., 1997; Argles et al., 1999) thinning of the Alpujárride-Maláguide Eocene (Platt et al., 2005) orogenic wedge (Alborán crustal domain). Marchesi et al. (2012) showed that late Oligocene intrusive mantle pyroxenites in the Ronda massif were in equilibrium with andesite-like melts and have a geochemical signature similar to Neogene subduction-related lavas of the western and central Mediterranean. Rather than convective removal or delamination of a previously generated lithospheric root, these data support thinning of the Alborán Domain orogenic wedge and its convective thermal erosion induced by slab rollback in a backarc basin situated several hundred kilometers in a more easterly position (south of the Balearic Islands) during the Paleogene (Fig. 6-4a) (Lonergan and White, 1997; Rosenbaum et al., 2002; Faccenna et al., 2004; Booth-Rea et al., 2007; Garrido et al., 2011). In this setting, the 21-23 Ma intracrustal emplacement of the Ronda Peridotite (Priem et al., 1979; Esteban et al., 2011) occurred after the collision with the Maghrebian Passive Margin (*ca.* 23-25 Ma; Booth-Rea et al., 2005), providing a common origin for the peridotite bodies in the Betic-Rif and in the Kabylies in Algeria (Caby et al., 2001; Bruguier et al., 2009). Lonergan (1993) also proposed initial south directed migration of the Alborán Domain to explain the southward directed thrusting of the Maláguide-Alpujárride nappe-stack after undoing paleomagnetic rotations in the eastern Betics. During the early Miocene the system propagated westward producing the oblique collision with the South Iberian Passive Margin and the high-pressure metamorphism of the Nevado-Filábride units between 15-17 Ma (López Sánchez-Vizcaíno et al., 2001; Platt et al., 2006). All these time constraints are in correspondence with the 25±1 Ma Lu-Hf ages obtained for the formation of overlying garnet pyroxenites in the Beni Bousera massif, which is the counterpart to Ronda Peridotite in northern Morocco (Blichert-Toft et al., 1999; Pearson and Nowell 2004) as well as with the 19±5 Ma U-Pb ages of crystallization of late granites that crosscut the Ronda

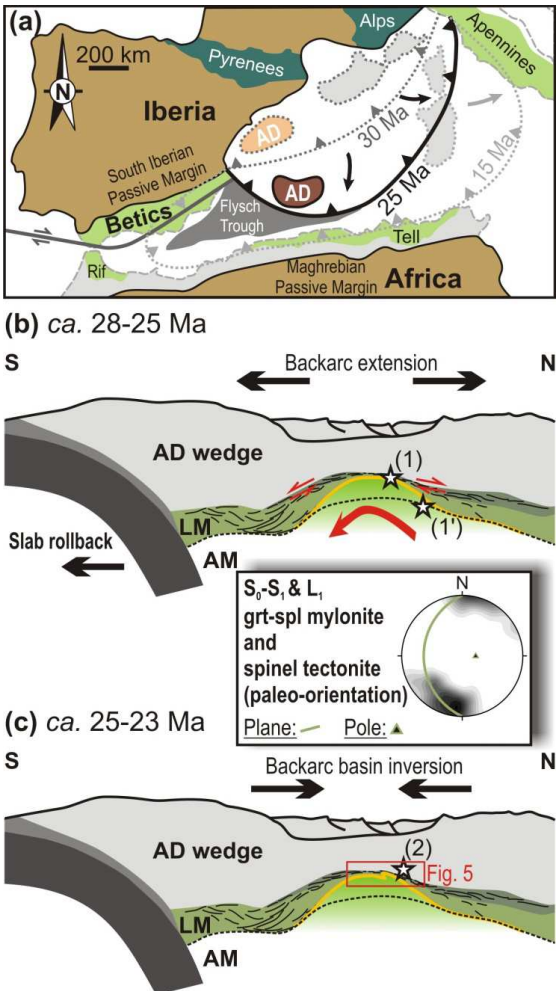

Figure 6-4. (a) Geodynamic reconstruction (modified after Booth-Rea et al., 2007 and Marchesi et al., 2012) showing the tectonic scenario proposed for the westernmost Mediterranean for the Late Oligocene-Early Miocene. AD: Alborán Domain including Ronda Peridotite. **(b)** N-S cross section for the Late Oligocene backarc extension (modified after Garrido et al., 2011). On the figure, (1) denotes the formation of grt-spl mylonites due to backarc extension and (1') refers to partial melting at the base of the lithosphere induced by asthenospheric upwelling. **(c)** N-S cross section for the Late Oligocene-Early Miocene backarc basin inversion that led to km-scale folding indicated by (2) and shown on Fig. 6-5 in details (outlined in red square). Color coding is the same as for Fig. 6-1b. AD wedge: Alborán crustal units; AM: asthenospheric mantle; LM: lithospheric mantle. Lower hemisphere, equal angle (Wulff) stereographic projection shows the paleo-orientation of the S_0 compositional layering and the S_1 tectonite foliation (simplified to a single plane being essentially parallel to each other) as a trace of plane and its pole, along with L_1 mineral lineation as grey shaded density contours (contours from 0.0 to 11.1) in the grt-sp mylonite and spinel tectonite domains of Ronda Peridotite (Darot, 1973; Van der Wal and Vissers, 1996; Precigout et al., 2007; Soustelle et al., 2009). The palaeo-orientation was approximated by undoing the late brittle rotations (tectonic tilting: García-Dueñas et al., 1992; paleomagnetic rotation: Villasante-Marcos et al., 2003).

Peridotite (Sánchez-Rodríguez and Gebauer, 2000). Garrido et al. (2011) have proposed a similar scenario to account for the poly-metamorphic, tectonic and igneous history of the Ronda Peridotite. For these authors, the Ronda grt-sp mylonite domain was formed in the Oligocene during decompression and cooling of garnet peridotites from 2.4-2.7 GPa at 1020-1100°C (*ca.* 85 km) to 2.0 GPa at 800-900°C (*ca.* 65 km) as a result of early exhumation and thinning of the Alborán Domain.

Structural and paleomagnetic studies have shown that after its emplacement the Ronda Peridotite underwent important brittle tectonic tilting: *ca.* 50° of anticlockwise rotation around a horizontal, N70°E-directed axis with respect to its present-day position; García-Dueñas et al., 1992; Crespo-Blanc and Campos, 2001) and *ca.* 35° of clockwise rotation around a vertical-axis (Villasante-Marcos et al., 2003). In order to discuss the kinematic evolution of the Ronda Peridotite in a geodynamic framework one should consider these brittle rotations and restore the present-day structures to their original paleo-orientation. Feinberg et al. (1996) and Villasante-Marcos et al. (2003) showed that the massif was already tilted when the paleomagnetic rotation took place in the middle-late Miocene. Consequently, we restored first the younger paleomagnetic rotation and then the older tectonic tilting of the massif by rotating the structural data anticlockwise 35° around a vertical axis (Villasante-Marcos et al., 2003) and then clockwise 50° around a horizontal N35°E axis, the latter one corresponding to the present-day N70°E horizontal axis (García-Dueñas et al., 1992; Crespo-Blanc and Campos, 2001) corrected for the later paleomagnetic rotation. The present-day WNW dipping S_0-S_1 planar structures and NE-SW trending L_1 lineation of the grt-sp mylonite and spinel tectonite domains (Fig. 6-1b) currently record top-to-the-N kinematics (Darot, 1973; Balanyá, 1991; Balanyá et al., 1993; Tubía, 1994). Undoing the late brittle rotations results in a palaeo-orientation of the S_0-S_1 planar structures dipping 25° to the W associated with a N-S trending L_1 lineation (Fig. 6-4b, stereogram) and subhorizontal north-directed kinematics. These kinematics and the decompressive p-T path of the grt-sp mylonite (Garrido et al., 2011) are consistent with late Paleogene thinning of a thick subcontinental lithospheric mantle in a backarc setting along an extensional detachment (Fig. 6-4b). This early thinning and exhumation was followed in the Late Oligocene-Early Miocene by heating and melting of the base of the extremely attenuated subcontinental lithosphere under spinel peridotite facies conditions (*ca.* 1.5 GPa; Lenoir et al., 2001).

Restoring the late brittle rotations for our structural data from the granular spinel peridotite and the younger plagioclase tectonite domains results in a subhorizontal, slightly inclined anticline with a fold axis plunging 5° to the NNW and a NE dipping axial surface (Fig. 6-5, stereogram). Our study shows that the high-*T* S_2 foliation already occurs in plagioclase-free spinel lherzolite (Fig. 6-3a) at the base of the granular spinel peridotites. The existence of the same high-*T* S_2 foliation in the underlying plagioclase tectonite domain (Fig. 6-2a) implies that the axial plane foliation developed continuously from the spinel to the plagioclase facies. These observations indicate that the fold started to form in the spinel lherzolite facies (Fig. 6-5a) in the deep, hottest part of the melted mantle domain below the recrystallization front (Fig. 6-2a), and developed a kilometer-scale anticline during progressive cooling and decompression at the base of the massif in the plagioclase tectonite domain (Fig. 6-5b-c). Folding further developed along a low-angle basal thrust-zone that continuously juxtaposed hot peridotite over colder metamorphic units during decompression (Fig. 6-5c). Upon cooling near the brittle-ductile peridotite transition, low-*T* shear zones (S_m), synkinematic to the high-*T* S_2 plagioclase tectonite foliation, developed in the reverse limb of the fold (Fig. 6-5c). This scenario resulted in a geometry where peridotites were conductively cooled from above and progressively cooled in the basal plagioclase tectonites with the hottest domain preserved in the center of the massif. This atop-and-below cooling would also account for the preservation of the metastable high-pressure grt-sp mylonites and the freezing of the melting

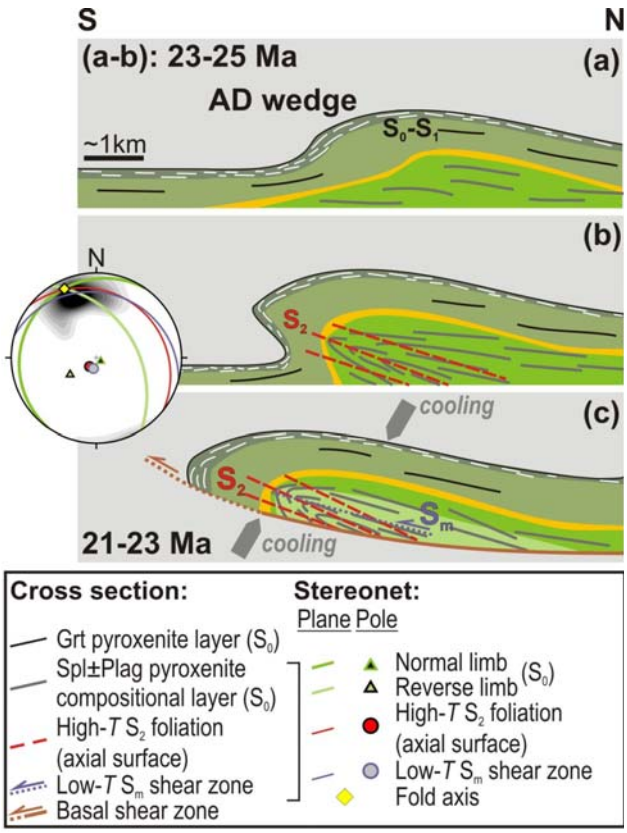

Figure 6-5. (a-c) Proposed scenario in N-S cross sections for the initiation and development of Late Oligocene massif-scale folding and Early Miocene intracrustal emplacement of Ronda Peridotite. Color coding is the same as for Fig. 6-1a. Lower hemisphere, equal angle (Wulff) stereographic projection shows the average paleo-orientations of normal and reverse limbs (S_0 compositional layering), S_2 tectonite foliation, S_m shear zone foliation as traces of planes and their poles along with subparallel stretching lineations of L_2 and L_m as grey shaded density contours (contours from 0.0 to 11.1) in the study area. The paleo-orientation was approximated by undoing the late brittle rotations (tectonic tilting: García-Dueñas et al., 1992; paleomagnetic rotation: Villasante-Marcos et al. 2003). See text for details on how the rotations were performed. Grt: garnet; Plag: plagioclase; Spl: spinel.

recrystallization front in the core of the Ronda Peridotite massif (Fig. 6-5c). Furthermore, restoring the shear sense to its paleo-orientation in the low-*T* structures – that are considered as formed synkinematic to folding – implies a top-to-the-south kinematics for the latest stages of the ductile evolution of the Ronda Peridotite, which is opposite to the higher-pressure northward directed kinematics of the overlying grt-sp mylonite and spinel tectonite domains (*cf.* Figs.6-4b and Fig. 6-5a, stereograms). This southward kinematics can be accounted for by an inversion from a backarc extension during slab rollback to a contractional basin during Late Oligocene-Early Miocene collision of the Alborán orogenic wedge with the Maghrebian Passive Margin (Fig. 6-4a,c). We propose that orogenic shortening and southward thrusting initiated a ductile fold recording the early Miocene intracrustal emplacement of the Ronda Peridotite (Fig. 6-4c, Fig. 6-5a-c).

6.6. Conclusions

The transition from the granular spinel peridotite to the plagioclase tectonite domain of the Ronda Peridotite records kilometer-scale folding and shearing at the base of the subcontinental lithospheric mantle section that initiated during decompression and cooling of the massif from spinel to plagioclase lherzolite facies. Newly developed foliation in plagioclase lherzolite from the plagioclase tectonite domain represents the axial plane foliation of an anticline. Synkinematic mylonitic-ultramylonitic shear zones were formed at the peridotite

plastic-brittle transition mainly in the reverse limb of this fold. Paleo-orientation of the present day structures, inferred from restoring the Miocene tectonic tilting and vertical axis clockwise paleomagnetic rotation of the massif, indicates a subhorizontal inclined anticline and a top-to-the-S sense of shear for the synkinematic shear zones. This geometry and the reconstructed kinematics suggest an Early Miocene inversion in the Alborán backarc extension prior to the intracrustal emplacement of the Ronda Peridotite massif. We propose a geodynamic model where folding and shearing of an attenuated mantle lithosphere occurred by backarc basin inversion during southward collision of the Alborán Domain with the paleo-Maghrebian Passive Margin (23-25 Ma), leading to the intracrustal emplacement of peridotites in the earlymost Miocene (21-23 Ma).

Part III - Summary & Conclusions

7. Conclusions and Perspectives

7.1. Conclusions

This study of the Beni Bousera peridotite massif contributed to providing new constraints on the natural deformation mechanisms of peridotites and pyroxenites deformed under subcontinental lithospheric and near-asthenospheric mantle conditions, and the mode of exhumation of subcontinental lithospheric mantle.

On the basis of the metamorphic facies and subfacies of peridotite defined by mineral assemblages of peridotites and host pyroxenite, we identified a continuous tectono-metamorphic zoning that we classified in four tectono-metamorphic domains, from top to bottom: (i) garnet-spinel mylonites, (ii) Ariègite subfacies fine-grained porphyroclastic peridotites (both enclosing garnet pyroxenites), (iii) Ariègite-Seiland transition, coarse porphyroclastic peridotites (enclosing garnet-spinel pyroxenites), and (iv) Seiland subfacies coarse porphyroclastic to coarse granular peridotites (enclosing spinel pyroxenites).

Field structural mapping revealed consistent kinematics across all domains with predominant shallowly SW-dipping foliations and NW-SE lineations, lacking any crosscut relationship. A change in kinematics is only observed in the lowermost Seiland domain peridotites, which show a gradual reorientation of the lineation towards a NNE-SSW strike and the presence of small areas bearing vertical lineations.

Microstructures and well-developed olivine and pyroxenes CPO of both peridotites and pyroxenites suggest that these rocks deformed dominantly by dislocation creep. Dislocation glide in olivine is consistent with simultaneous activation of [100](010) and [001](010) slip systems, whereas ortho-and clinopyroxenes glide on [001]{110} slip, both in peridotites as in pyroxenites. Yet, structurally downward increase of average recrystallized grain sizes and decreasing volume fractions in both rock types indicate deformation under decreasing work rates (stresses and most probably strain rates). Decreasing stresses are consistent with the continuous linear increase in synkinematic temperature ranging from 900-950°C in garnet-spinel mylonites to >1100-1150°C in the Seiland domain peridotites. Synkinematic pressures are moderate: 2.0 GPa in garnet-spinel mylonites and Ariègite domain peridotites, and 1.8 GPa for the Ariègite-Seiland and Seiland domain peridotites.

Careful analysis of olivine CPO patterns enabled to constrain deformation mechanisms and conditions. Axial-[010] olivine CPO in peridotites from all tectono-metamorphic are consistent with simultaneous activation of [100](010) and [001](010) slip, but their origin differ. In garnet-spinel mylonites and Ariègite domain peridotites, this is due to deformation under high stress, low temperature and moderate pressure. At the outrcrop scale, high stresses and low temperatures in these domains resulted in reduced (but not inversed) competence contrasts between garnet pyroxenite layers and host peridotite, whereas at thin section scale, high stresses allowed for ductile deformation of garnet in pyroxenites. In Ariègite-Seiland and Seiland domains, olivine axial-[010] patterns rather resulted from low-stress deformation (ca. 10 MPa) in the presence of melt, consistent with the high, near-solidus temperatures and extensive melt-rock reaction related textures. In this hot, partially molten (asthenospherized) lithospheric mantle, the small (ca. 100 -200 m) diapiric like zones in the Seiland domain peridotites represent gravitational instabilities developed due to local accumulation of high instantaneous melt fractions.

To account for the syn-to late kinematic character of all tectono-metamorphic domains, the large thermal gradient (ca. 200 °C) preserved across the 2 km thick section and the lineations subparallel to the metamorphic zoning, we conclude that Beni Bousera represents a single tectonic object: a transtensional mantle shear zone. To prevent thermal reequilibration in the low-temperature assemblages during deformation, high strain rates must have been sustained and subsequent rapid cooling when all domains reached 60 km depth. The latter could have been produced by further exhumation along another similar but more superficial extensional shear zone, or by inversion of the system from dominantly extensional to dominantly compressional, as recently proposed in the Ronda peridotite for the latest stages of exhumation from spinel- to plagioclase lherzolite facies peridotite.

7.2. Conclusiones

El estudio estructural y petrológico del macizo de peridotitas de Beni Bousera realizado en esta tesis doctoral ha permitido avanzar en la comprensión de los mecanismos que rigen la deformación dúctil de peridotitas y piroxenitas en el manto subcontinental litosférico a diferentes condiciones de presión y temperatura, así como de los procesos tectónicos involucrados en de exhumación, adelgazamiento y emplazamiento cortical de peridotitas subcontinentales.

La cartografía ha revelado la existencia de una zonación estructural y metamórfica en el macizo peridotítico de Beni Bousera. Esta zonación —que había sido identificada antes sólo en términos de facies metamórficas— muestra la existencia de una estrecha relación entre las facies petrológicas y la textura y microestructura de peridotitas y piroxenitas en este macizo. Desde el sudeste a noroeste, y desde el techo a la base del macizo, las zonas tectono-metamórficas identificas son: (i) un dominio superior de peridotitas con granate y espinela con peridotitas miloníticas de grano muy fino; (ii) un dominio de lherzolitas con espinela en subfacies Ariegita con clinopiroxenitas con granate y peridotitas con espinela con textura porfiroclásticas de grano fino a muy fino; (iii) una zona de transición de lherzolitas con espinela en subfacies Ariegita y Seiland con websteritas con espinela y granate, y peridotitas con espinela de textura porfiroclástica de grano grueso; y (iv) un dominio de lherzolitas con espinela en subfacies Seiland con websteritas con espinela y peridotitas con espinela con textura porfiroclástica o granular de grano grueso a muy grueso.

A pesar de la evolución polimetamórfica registrada por la secuencia de facies metamórficas, la cartografía estructural y microestructural muestra una gran coherencia cinemática de todos los dominios tectono-metamórficos, lo que apoya una evolución sincrónica. Todos los dominios poseen una foliación dúctil con buzamiento hacia el SO y lineaciones dúctiles definidas por el estiramiento mineral y la alineación de los ejes cristalográficos del olivino— alineadas según direcciones NO-SE. Sólo en la base del dominio de Seiland se observa un cambio en la cinemática dúctil; este cambio se caracteriza por una reorientación gradual de las lineaciones dúctiles hacia el NNE-SSO, en áreas hectométricas con lineaciones dúctiles verticales, que representan inestabilidades diapíricas producidas por una incipiente fusión parcial del manto litosférico en este dominio.

La microestructura y la excelente Orientaciones Cristalográficas Preferente (OCP) en los minerales de peridotitas y piroxenitas, indican que, en todos los dominios tectónicos, ambas litologías registran deformación dúctil por mecanismos de flujo por dislocaciones (“dislocation creep”). La deformación por flujo de dislocaciones en el olivino es consistente con la activación de los sistemas cristalinos de deslizamiento [100](010) y [001](010)

del olivino, y del [001]{110} en ortopiroxenos de peridotitas y piroxenitas. No obstante, el progresivo aumento del tamaño promedio de grano del olivino, unido a la disminución de la proporción de la matriz granoblástica hacia el dominio Seiland, indican una deformación en condiciones decrecientes de tasa de trabajo mecánico ("work rate") (i.e., del esfuerzo y, más probablemente, la tasa de deformación). El gradiente de la disminución del esfuerzo en la deformación es coherente con la variación de la temperatura de deformación desde los 900-950°C en las milonitas con granate y espinela, hasta temperaturas de 1100-1150°C en las peridotitas del dominio Seiland. Las presiones de deformación sincinemática varían entre los 2,0 GPa en las milonitas con espinela hasta unos 1,8 GPa en las peridotitas de los dominios transicional Ariegita-Seiland y Seiland.

El análisis meticuloso de los patrones de OCP del olivino nos ha permitido delimitar y desvelar los mecanismos y condiciones de la deformación plástica de las peridotitas y piroxenitas del macizo de Beni Bousera. Los patrones de OCP de olivino de tipo axial-[010] aparecen en las peridotitas de todos los dominios estructurales; este tipo de OCP indica la activación simultánea de los sistemas de deslizamiento intracristalino del olivino [100](010) y [001](010); sin embargo, la causa de la activación de este sistema de deslizamiento fue diferente en para los distintos dominios tectono-metamórficos. En los olivinos de las milonitas con granate y espinela y las peridotitas del domino Ariegita, la activación de estos sistemas de deslizamiento estuvo causada por la deformación en un régimen de altos esfuerzo (ca. 185 MPa) a baja temperatura y presiones moderadas. A escala de los afloramientos, estas condiciones de deformación causaron un fuerte contraste de la competencia de piroxenitas y peridotitas encajantes, produciendo boudinage y disgregación tectónica de la piroxenitas en las milonitas; a escala centimétrica, la deformación en un régimen de altos esfuerzo provocó la deformación dúctil del granate en las piroxenitas. En los dominios Ariegita-Seiland y Seiland, los patrones axial-[010] de la OCP del olivino se generó durante la deformación en un régimen de bajo esfuerzo (ca. 10 MPa) con la presencia de fundido; este régimen de deformación es coherente con las altas temperaturas —próximas al solidus hidratado de las peridotitas— en estos dominios, tal y como atestiguan las microestructura de las peridotitas y los cálculos geotermométricos. Estas observaciones indican que la transición Seiland-Ariegita y el dominio Seiland constituían una porción de manto litosférico de parcialmente fundida que se deformaba en condiciones cuasi-astenosféricas, pero que era mecánicamente solidaria con la litosfera mantélica suprayacente más fría. La presencia de pequeños dominios diapíricos en la transición Seiland-Ariegita atestiguan, sin embargo, el inicio de inestabilidades gravitacionales producidas por la acumulación local de fundidos en esta transición, representando localmente zonas de desacoplamiento mecánico producido por la erosión termo-mecánica de la litosfera mantélica subcontinental.

El carácter sincinemático de todos los dominios tectónicos, su evolución petrológica y microestructural y el alto gradiente térmico (ca. 200 ºC) registrado en el macizo de Beni Bousera pueden explicarse durante un estadio precoz de exhumación de unmanto continental litosférico espeso en una zona de cizalla transtensional, en un contexto de extensión y rifting asimétrico de la litosfera. Utilizando las lineaciones verticales de las inestabilidades diapíricas en el dominio Seiland como marcadores de la paleovertical, deducimos que la orientación actual de las estructuras deformacionales y la zonación tectono-metamórfica del macizo es similar a la de su posición estructural original en dicha zona de cizalla; por tanto, las milonitas con granate y espinela y el dominio Seiland constituían, respectivamente, el bloque de techo y el muro de la zona de cizalla. Inicialmente, ambos dominios procedieran de diferentes niveles litosfericos a lo largo de una misma geoterma y en el campo de estabilidad de lherzolitas con granate, pero el dominio Seiland provendría de los niveles más profundos, y por tanto, más calientes de la litosfera. El cizallamiento rápido —con tasas de deformación del orden de 10^{-11} s^{-1}— produjo la yuxtaposición mecánica, y en desequilibrio térmico, de niveles litosféricos procedentes de diferente

profundidades, hasta condiciones próximas a la transición de las facies Ariegita-Seiland (ca. 60 km, 1,8 GPa). En los dominios más superficiales y fríos, el cizallamiento diólugar a milonitas con granate y espinela; en este dominio la baja temperatura—y por tanto, una cinética de reacción lenta— y alto esfuerzos propiciaron la preservación metaestable de asociaciones minerales de alta presión y la localización de la deformación generando peridotitas milonitas con granate y espinela. Las edades de enfriamiento Lu-Hf preservadas en los pares granate-clinopiroxeno —con temperaturas de cierre del orden de los 850 ºC, próximas a la temperatura de deformación sin cinemática— en piroxenitas con granate del dominio de milonitas con granate yespinela indican que este evento tectónico ocurrió en torno a los 25 Ma. El domino Seiland, por el contrario, muestrearía los niveles más profundos y calientes de la litosfera en condiciones de muy alta temperatura (cuasi-astenosféricas, ca. 1100-1150 ºC); la alta temperatura de este domino produjo la fusión incipiente de este dominio al cruzar el sólidus hidratado de peridotitas. La combinación de alta temperatura y la presencia de pequeñas fracciones de fundidos, borró cualquier vestigio de asociaciones de peridotitas con granate, aunque la presencia de simplectitas con ortopiroxenos-clinopiroxeno-espinela en piroxenitas atestigua su derivación a partir de asociaciones con granate. La yuxtaposición en condiciones de un fuerte desequilibrio térmico de diferentes niveles litosféricos generó en una zona de cizalla de apenas 2 km de espesor un gradiente de 200ºC; la preservación de dicho gradiente térmico transitorio requirió que la exhumación de los diferentes niveles fuera lo suficientemente rápida para evitar que los diferentes niveles yuxtapuestos en la zona de cizalla se equilibraran térmicamente por conducción hasta la nuevas condiciones de temperatura más elevadas de la nueva geoterma generada por el fuerte adelgazamiento litosférico. Puesto que dicho equilibrio térmico se hubiera alcanzado en apenas $50x10^3$ años, la preservación de la zonación petrológica en el macizo implica que el emplazamiento final de las peridotitas tuvo que ocurrir al poco tiempo de este primer episodio de exhumación mantélica y adelgazamiento litosférico. Sin embargo, dicho evento tectónico no aparece registrado en el macizo de Beni Bousera, ya que las estructuras dúctiles de más baja presión en facies de lherzolitas con plagioclasa no afloran en este macizo.

El emplazamiento final de las peridotitas, desde facies Seiland a facies de lherzolitas con plagioclasa, está registrada, sin embargo, en las estructuras dúctiles en la transición del frente de recristalización y el dominio de plagioclasa en el macizo de Ronda (Cordillera Bética, S. España). En este macizo, el estudio estructural muestra que la peridotitas con plagioclasa presentan una foliación dúctil que constituye la superficie axial de cuyo sinforme cuyo flanco inverso está situado en la base del macizo. Los flancos de este pliegue están cortados por zonas de cizalla de peridotitas con plagioclasa miloníticas y ultramiloníticas con un sentido de cizallamiento de techo hacia el SO. La restauración de las estructuras—tras la corrección debida a las rotaciones de eje vertical y el basculamiento post-emplazamiento de edad Miocena— muestras que estas estructuras dúctiles registran una cinemática de emplazamiento hacia el sur. La geometría del pliegue y las asociaciones minerales en facies de lherzolita con plagioclasa de estructuras dúctiles son coherentes con el plegamiento y cizallamiento de una sección litosférica mantélica caliente y extremadamente atenuada. Este evento probablemente ocurrió por la inversión de una zona de rifting continental en un contexto de trasera de arco —situada en una posición más al este que su posición geográfica actual— y que estuvo implicada en la exhumación inicial desde las facies de Granate a Seiland. La inversión de dicha cuenca se produjo probablemente en el Oligoceno terminal (23-25 Ma) durante la colisión hacia el sur del dominio de Alborán con el paleo-margen pasivo Magrebí, produciendo la inversión del rift y el emplazamiento intracortical de la peridotitas en el Mioceno inferior (21-23Ma).

7.3. Perspectives

Our observations and interpretations bring, to our knowledge, the first natural evidence for shear zones penetrating deep (ca. 90 km) in subcontinental lithospheric mantle and the associated deformation mechanisms. Yet, the initial conditions of our model are largely based on the assumption that Seiland domain peridotites showing higher equilibration temperatures originated at higher pressure from the garnet stability field. Although there is petrologic evidence of former garnet, only locally preserved in the form of orthopyroxene-clinopyroxene-spinel symplectites, one possible way to verify this assumption thoroughly would be by careful investigation of cores of large Al-rich orthopyroxenes that would have been in equilibrium with garnet. Equilibrium of orthopyroxene with garnet could be tested by analysis of trace elements patterns showing HREE-depleted patterns. Subsequently, modeling of Al diffusion profiles in large orthopyroxene porphyroclasts as done by Ozawa (2004) in the Horoman peridotite in Japan might even further constrain uplift rates. Indeed, our first order calculations using peridotite thermal diffusivity indicate large uplift rates but they most probably represent an upper bound, as these are extremely high (ca $10^{-11}s^{-1}$). Yet, extreme geological conditions must have prevailed to account for the exhumation of the largest pieces of diamond facies subcontinental lithospheric mantle on Earth.

Microstructures typical of syn-to late kinematic melt percolation are present in all domains, though in variable extent and nature. In garnet-spinel mylonites peridotites, the lower synkinematic temperatures and the negative correlation between olivine CPO strength and clinopyroxene modal content could be related to the percolation of a Si-poor, Ca-rich magma, possibly carbonatitic, which interestingly mostly erupt in continental rift settings such as the East-African rift or the Rhine graben. On the other hand, microstructures and CPO in Ariègite-Seiland and Seiland domain peridotites rather suggest reactive melt transport either leading to pyroxene dissolution or crystallization at subsolidus temperatures. Another interesting issue would thus be to carry out a detailed geochemical analysis to better constrain the nature of the observed melt-rock reactions (e.g. refertilization processes) in the different tectono-metamorphic domains. Deformation in the presence of melt is one of the possible mechanisms that could account for reducing the viscosity of the subcontinental lithospheric mantle and hence reduce it strength during continental break-up. Whole rock geochemistry data and trace element concentrations in clinopyroxenes were for a large part gathered by the author, but not included in this work for a matter of consistency.

Finally, equilibrium thermomechanical models of lithospheric deformation, regardless of the geodynamic setting (rift, subduction, continental collision etc.) fail to reproduce high thermal gradients as observed in Beni Bousera peridotite because the computed scale of thermal reequilibration is too small. Future models should attempt to model disequilibrium heat transfer to account for the preservation of metastable high thermal gradients in both Beni Bousera and Ronda peridotite massifs.

Part IV - References

8. References

Abalos, B. (1997). Omphacite fabric variation in the Cabo Ortegal eclogite (NW Spain): relationships with strain symmetry during high-pressure deformation. *Journal of Structural Geology* **19**, 621-637.

Aerden, D.G.A.M. & Malavieille, J. (1999). Origin of a large-scale fold nappe in the Montagne Noire, Variscan belt, France. *Journal of Structural Geology* **21**, 1321-1333.

Afiri, A., Gueydan, F., Pitra, P., Essaifi, A. & Précigout, J. (2011). Oligo-Miocene exhumation of the Beni-Bousera peridotite through a lithosphere-scale extensional shear zone. *Geodinamica Acta* **24**(1), 49-60.

Agrusta, R., Arcay, D. Tommasi, A., Davaille, A., Ribe, N. & Gerya, T. (submitted). Small-scale convection in a plume-fed low viscosity layer beneath a moving plate. *Geophysical Journal International*.

Allègre, C. J. & Turcotte, D. L. (1986). Implications of a two-component marble-cake mantle. *Nature* **263**, 123–127.

Allken, V., Huismans, R. S. & Thieulot, C. (2011). Three-dimensional numerical modeling of upper crustal extensional systems. *Journal of Geophysical Research* **116**, B10409, doi:10.1029/2011JB008319.

Amiguet, E., Raterron, P., Cordier, P., Couvy, H. & Chen, J. (2009). Deformation of diopside single crystal at mantle pressure, 1: mechanical data. *Physics of the Earth and Planetary Interiors* **177**, 122–129.

Ando, J., Fujino, K. & Takeshita, T. (1993). Dislocation microstructures in naturally deformed silicate garnets. *Physics of the Earth Planetary Interiors* **80**, 105–116.

Argles, T.W., Platt, J.P. & Waters, D.J. (1999). Attenuation and excision of a crustal section during extensional exhumation: The Carratraca Massif, Betic Cordillera, southern Spain. *Journal of the Geological Society*, **156**, 149-162.

Austin, N.(2011). The microstructural and rheological evolution of shear zones. In: Prior, D. J., Rutter, E. H. & Tatham, D. J. (eds). Deformation Mechanisms, Rheology and Tectonics: Microstructures, Mechanics and Anisotropy. *Geological Society, London, Special Publications* **360**, 193–209. doi: 10.1144/SP360.11.

Austin, N. & Evans, B. (2007). Paleowattmeters: a scaling relation for dynamically recrystallized grain size. *Geology* **35**, 343-346.

Austin, N. & Evans, B. (2009). The kinetics of microstructural evolution during deformation of calcite. *Journal of Geophysical Research* **114**, B09402.

Avé Lallemant, H. G. (1967). Structural and petrological analysis of an 'Alpine-type' peridotite. The lherzolite of the French Pyrenees. *Leidse Geologische Mededelingen* **42**, 1-57.

Avé Lallemant, H.G. (1978). Experimental deformation of diopside and websterites. *Tectonophysics* **48**, 1-27.

Argles, T.W., Platt, J.P., & Waters, D.J. (1999). Attenuation and excision of a crustal section during extensional exhumation: The Carratraca Massif, Betic Cordillera, southern Spain. *Journal of the Geological Society* **156**, 149– 162, doi:10.1144/gsjgs.156.1.0149.

Bachmann, F., Hielscher, R. & Schaeben, H. (2010). Texture Analysis with MTEX - Free and Open Source Software Toolbox. *Solid State Phenomena* **160**, 63-68.

Bai, Q., Mackwell, S.J. & Kohlstedt, D.L (1991). High-temperature creep of olivine single crystals, 1, Mechanical results for buffered samples. *Journal of Geophysical Research* **96**, 2441-2463.

Bai, Q. & Kohlstedt, D.L. (1992). High-temperature creep of olivine single crystals. 2. Dislocation structures. *Tectonophysics* **206**, 1-29.

Balanyá, J.C. (1991). *Estructura del dominio de Alborán en la parte Norte del Arco de Gibraltar*. Ph.D. thesis, University of Granada.

Balanyá, J.C., Azañón, J.M., Sánchez-Gómez, M. & García-Dueñas, V. (1993). Pervasive ductile extension, isothermal decompression and thinning of the Jubrique unit in the Paleogene (Alpujárride Complex, western Betics Spain). *Comptes Rendus de l'Académie des Sciences Série II* **316**, 1595-1601.

Balanyá, J. C. & García-Dueñas, V. (1987). Les directions structurales dans le Domaine d'Alborán de part et d'autre du Détroit de Gibraltar. *Comptes Rendus de l'Académie des Sciences II* **304**, 929–932.

Balanyá, J.C., García-Dueñas, V., Azañón, J.M. & Sánchez-Gómez, M. (1997). Alternating contractional and extensional events in the Alpujarride Nappes of the Alboran domain (Betics, Gibraltar arc). *Tectonics* **16**, 226–238. doi:10.1029/96TC03871.

Barnhoorn, A., Bystricky, M., Nurlini, L. & Kunze, K. (2004). The role of recrystallisation on the deformation behaviour of calcite rocks: large strain torsion experiments on Carrara marble. *Journal of Structural Geology* **26**, 885-903.

Barranco, L. Ansorge, J. & Banda, E. (1990). Seismic refraction constraints on the geometry of the Ronda peridotitic massif (Betic Cordillera, Spain). *Tectonophysics* **184**, 379-392.

Bascou, J., Tommasi, A. & Mainprice, D. (2002). Plastic deformation and development of clinopyroxene lattice preferred orientations in eclogites. *Journal of Structural Geology* **24**, 1357-1368.

Bascou, J., Tommasi, A. & Mainprice, D. (2002). Plastic deformation and development of clinopyroxene lattice preferred orientations in eclogites. *Journal of Structural Geology* **24**, 1357-1368.

Beeman, M. L. & Kohlstedt, D. L. (1993). Deformation of fine- grained aggregates of olivine plus melt at high temperatures and pressures. *Journal of Geophysical Research* **98**, 6443-6452.

Bell, A.M. (1981). Vergence: an evaluation. *Journal of Structural Geology*, **3**, 197-202.

Bell, T.H. (1978). Progressive deformation and reorientation of fold axes in a ductile mylonite zone: the Woodroffe thrust. *Tectonophysics* **44**, 285-320.

Bell, T.H. & Etheridge, M.A. (1973). Microstructure of mylonites and their descriptive terminology. Lithos 6, 337-348.

Bellahsen, N., Faccenna,C., Funiciello, F., Daniel, J. & Jolivet, L. (2003). Why did Arabia separate from Africa? Insights from 3-D laboratory experiments. *Earth and Planetary Science Letters* **216**, 365–381.

Ben Ismail,W. & Mainprice, D. (1998). An olivine fabric database: an overview of upper mantle fabrics and seismic anisotropy. *Tectonophysics* **296**, 145-158.

Berger, E.T. & Weber, B.C. (1991). Dunitification of mantle lithosphere below the Society Archipelago: Evidence for magma-mantle thermal and chemical transfers through xenoliths from the Papenoo valley, Tahiti. *Journal of Geodynamics* **13**, 221-252

Berger, A., Herwegh, M., Schwarz. J.-O., & Putlitz, B. (2011). Quantitative analysis of crystal/grain sizes and their distributions in 2D and 3D. *Journal of Structural Geology* **33**, 1751-1763.

Bird, P. (1979). Continental delamination and the Colorado Plateau. *Journal of Geophysical Research* **84**, 7569–7571.

Bird, P. (2003). An updated digital model of plate boundaries. *Geochemistry, Geophysics, Geosystems* **4**, 1027. doi:10.1029/2001GC000252.

Blanco, M.J. & Spakman, W. (1993). The P-wave velocity structure of the mantle below the Iberian Peninsula: evidence for subducted lithosphere below southern Spain. *Tectonophysics* **221**, 13–34.

Blichert-Toft, J., Albarède, F. & Kornprobst, J. (1999a). Lu - Hf isotope systematics of garnet pyroxenites from Beni Bousera, Morocco: implications for basalt origin. *Science* **283**, 1303 - 1306.

Bodinier, J.-L., Guiraud, M., Fabriès, J., Dostal, J. & Dupuy, C. (1987). Petrogenesis of layered pyroxenites from the Lherz, Freychinède and Prades ultramafic bodies (Ariège, French Pyrenees). *Geochimica et Cosmochimica Acta* **51**, 279-290.

Bodinier, J.L., Garrido, C.J., Chanefo, I., Bruguier, O. & Gervilla, F. (2008). Origin of pyroxenite-peridotite veined mantle by refertilization reactions: Evidence from the Ronda peridotite (Southern Spain). *Journal of Petrology* **49**(5): 999-1025.

Bokelmann, G. & Maufroy, E. (2007). Mantle structure under Gibraltar constrained by dispersion of body waves. *Geophysical Research Letters*, **34**, 5.

Bokelmann, G., Maufroy, E., Buontempo, L., Morales, J. & Barruol, G. (2011). Testing oceanic subduction and convective removal models for the Gibraltar arc: Seismological constraints from dispersion and anisotropy. *Tectonophysics*, **502**, 28-37.

Boland, J.N. & Tullis, T.E. (1986). Deformation behavior of wet and dry clinopyroxenite in the brittle to ductile transition region. In: Hobbs, B.E., Heard, H.C. (Eds.), Mineral and Rock Deformation: Laboratory Studies. *American Geophysical Union Monograph* **36**, 35-49.

Booth-Rea, G., Azañon, J. M., Goffé, B., Vidal, O. & Martínez-Martínez, J. M. (2002). High-pressure, low-temperature metamorphism in the Alpujarride units outcropping in southeastern Betics (Spain). *Comptes Rendus de l'Académie des Sciences* **334**, 857–865.

Booth-Rea, G., García-Dueñas, V. & Azañón, J. M. (2002b). Extensional attenuation of the Malaguide and Alpujarride thrust sheets in a segment of the Alboran Basin folded during the Tortonian (Lorca area, eastern Betics). *Comptes Rendus Geosciences* **334**, 557 – 563.

Booth-Rea, G., Azañón, J.M., Martínez-Martínez, J.M., Vidal, O. & García-Dueñas, V. (2005). Contrasting structural and P-T evolution of tectonic units in the southeastern Betics: Key for understanding the exhumation of the Alboran Domain HP/LT crustal rocks (western Mediterranean). *Tectonics* **24**, TC2009, doi: 10.1029/2004TC001640.

Booth-Rea, G., Ranero, C.R., Martínez-Martínez, J.M., & Grevemeyer, I. (2007). Crustal types and Tertiary tectonic evolution of the Alboran sea, western Mediterranean: *Geochemistry Geophysics Geosystems* **8**, Q10005. doi:10.1029/2007GC001639.

Boudier, F. (1978). Structure and petrology of the Lanzo peridotite massif (Piedmont Alps). *Geological Society of America Bulletin* **89**, 1574-1591.

Boullier, A.M. (1975). Structure des peridotites en enclaves dans les kimberlites d'Afrique du Sud. PhD. Thesis, Université de Nantes, France, pp. 112.

Boullier, A.M. & Gueguen, Y. (1975). SP-mylonites - Origin of some mylonites by superplastic flow *Contributions to Mineralogy and Petrology* **50**, 93-104.

Boullier, A.M. & Nicolas, A. (1973). Texture and fabrics of peridotite nodules from kimberlite at Mothae, Theba Putsoa and Kimberley. In: Nixon, P.H. (ed). Lesotho Kimberlites, Cape and Transvaal, Cape Town, 57-66.

Boullier, A.M. & Nicolas, A. (1975). Classification of textures and fabrics of peridotite xenoliths from South African Kimberlites. Procedings of the 1rst International Kimberlite Conference. *Physics and Chemistry of the Earth* **9**, 467-475.

Bouybaouène, M. L. (1993). Etude pétrologique des métapélites des Sebtides supe´rieures (Rif inter, Maroc): Une évolution métamorphique de Haute Pression. Unpublished PhD Thesis, Université Mohamed V, Rabat, Morocco.

Bouybaouène, M. L., Goffé , B. & Michard, A. (1995). High-pressure, low-temperature metamorphism in the Sebtides nappes, northern Rif, Morocco. Geogaceta 17, 117–119.

Bouybaouène, M.L., Michard, A. & Goffé, B. (1998). High-pressure granulites on top of the Beni Bousera pridotites, Rif Belt, Morocco: a record of an ancient thickened crust in the Alboran domain. *Bulletin de la Societé Géologique de France* **2**, 153–162.

Brace, W.F. & Kohlstedt, D.L. (1980). Limits on lithospheric stress imposed by laboratory experiments. *Journal of Geophysical Research* **85**, 6248-6252.

Brey, G.P. & Köhler, T. (1990). Geothermobarometry in four-phase lherzolites. 2. New thermobarometers, and practical assessment of existing thermobarometers: *Journal of Petrology* **31**, 1353–1378.

Bruguier, O., Hammor, D., Bosch, D. & Caby, R. (2009). Miocene incorporation of peridotite into the Hercynian basement of the Maghrebides (Edough massif, NE Algeria): Implications for the geodynamic evolution of the Western Mediterranean. *Chemical Geology* **261**, 171-183.

Brune, S., Popov, A.A. & Sobolev, S.V. (2012). Modeling suggests that oblique extension facilitates rifting and continental break-up. *Journal of Geophysical Research* **117**, B08402. doi:10.1029/2011JB008860.

Buatier, M., Van Roermund, H.L.M., Drury M.R., Lardeaux, J.M. (1991). Deformation and recrystallization mechanisms in naturally deformed omphacites from the Sesia-Lanzo zone: geophysical consequences. *Tectonophysics* **195,** 11–27.

Buck, W. R. (2007). Dynamic processes in extensional and compressional settings - the dynamics of continental breakup and extension, in: Watts, A.B. (ed). Crust and Lithosphere Dynamics. *Treatise on Geophysics*. **6,** 335–376, Elsevier, New York.

Bunge, H. J. (1982). *Texture Analysis in Materials Sciences*. London: Butterworth.

Burchfiel, B.C. & Royden, L.H. (1985). North-South extension within the convergent Himalayan region. *Geology* **13**, 679-682.

Burov, E., Jolivet, L., Le Pourhiet, L. & Poliakov, A. (2001). A thermomechanical model of exhumation of high pressure (HP) and ultra-high pressure (UHP) metamorphic rocks in Alpine-type collision belts. *Tectonophysics* **342**, 113–136.

Byerlee, J.D. (1978). Friction of rocks. *Pure and Applied Geophysics* **116**, 615–626.

Bystricky, M.,Mackwell, S. (2001). Creep of dry clinopyroxene aggregates. *Journal of Geophysical Research* **106**, 13444–13454.

Burchfiel, B. C., Chen, Z., Hodges, K. V.,Yuping, L., Royden, L. H., Changrong, D. & Jiene, X.(1992). The south Tibetan detachment system, Himalayan orogen: Extension contemporaneous with and parallel to shortening in a collisional mountain belt: *Geological Society of America Special Paper* **269**, 41p.

Bystricky, M., Kuntze, K., Burlini, L. & Burg, J.-P. (2000). High shear strain of olivine aggregates: rheological and seismic consequences. *Science* **290**, 1564–1567.

Caby, R., Hammor, D. & Delor, C. 2001. Metamorphic evolution, partial melting and Miocene exhumation of lower crust in the Edough metamorphic core complex, west Mediterranean orogen, eastern Algeria. *Tectonophysics*, **342**, 239-273.

Calvert, A., Sandvol, E., Seber, D., Barazangi, M., Roecker, S., Mourabit, T., Vidal, F., Alguacil, G. & Jabour, N. 2000. Geodynamic evolution of the lithosphere and upper mantle beneath the Alboran region of the western Mediterranean: Constraints from travel time tomography. *Journal of Geophysical Research* **105**, 10871-10898.

Carminati, E., Wortel, M.J.R., Spakman, W. & Sabadini, R. (1998). The role of slab detachment processes in the opening of the western–central Mediterranean basins: some geological and geophysical evidence. *Earth and Planetary Science Letters* **160**, 651–665.

Carstens, H. (1969). Dislocation structures in pyropes from Norwegian and Czech garnet peridotites. *Contributions to Mineralogy and Petrology* **24**, 348–353.

Carstens, H. (1971). Plastic stress relaxation around solid inclusions in pyrope. *Contributions to Mineralogy and Petrology* **32**, 289–294.

Carter, N. L., Barker, D.W. & George, R. P., Jr (1972). Seismic anisotropy flow, and constitution of the upper mantle. In: Heard, H. C., Borg, I. Y., Carter, N. L. & Rayleigh, C. B. (eds) Flow and Fracture of Rocks. *AGU Geophysical Monograph* **16**, Washington, DC: American Geophysical Union, 167-190.

Castaing, R. (1951). Application des sondes électroniques à une méthode d'analyse ponctuelle chimique et cristallographique. PhD. Thesis, Université de Paris, France.

Ceuleneer, G., Nicolas, A. & Boudier, F. (1988). Mantle flow patterns at an oceanic spreading center - the Oman peridotites record. *Tectonophysics* **151**, 1-26.

Chalouan, A. & Michard, A. (1990). The Ghomarides nappes, Rif coastal Range, Morocco: a Variscan chip in the Alpine belt. *Tectonics* **9**, 1565–1583.

Chen, J., Wang, Q.C., Zhai, M.G., Ye, K. (1996). Plastic deformation of garnet in eclogite. *Science China Series D* **39**(1), 18–25.

Chen, S., Hiraga, T., Kohlstedt, D.L. (2006). Water weakening of clinopyroxene in the dislocation creep regime. *Journal of Geophysical Research* **111**, B08203, doi:10.1029/2005JB003885.

Chopra, P.N. & Paterson, M.S. (1981). The experimental deformation of dunite. *Tectonophysics* **78**, 453–473.

Chopra, P.N. & Paterson, M.S. (1984). The role of water in the deformation of dunite. *Journal of Geophysical Research* **86**, 7861–7876.

Comas,M.C., García-Dueñas,V. & Jurado, M.J. (1992). Neogene tectonic evolution of the Alboran Basin from MCS data. *GeoMarine Letters* **12**, 157–164.

Comas, M.C., Platt, J.P., Soto, J.I. & Watts, A.B. (1999). The origin and tectonic history of the Alboran Basin: Insights from Leg 161 results. In: R. Zahn, M.C. Comas and A. Klaus (Editors), *Proceedings of the Ocean Drilling Program*, Scientific Results, 555-580.

Connolly, J.A.D. (2009). The geodynamic equation of state: what and how. *Geochemistry Geophysics Geosystems* **10**, Q10014, doi:10.1029/2009GC002540.

Connolly, J.A.D. (2005). Computation of phase equilibria by linear programming: A tool for geodynamic modeling and its application to subduction zone decarbonation. *Earth and Planetary Science Letters* **236**, 524-541.

Corti, G., Bonini, M., Conticelli, S., Innocenti, F., Manetti, P. & Sokoutis, D. (2003). Analogue modelling of continental extension: A review focused on the relations between the patterns of deformation

and the presence of magma. *Earth Science Reviews* **63**, 169–247.

Couvy, H., Frost, D.J., Heidelbach, F., Nyilas, K., Ungar, T., Mackwell, S.J. & Cordier, P. (2004). Shear Deformation experiments of forsterite at 11 GPa – 1400°C in the multianvil apparatus. *European Journal of Mineralogy* **16**, 877–889.

Crespi, J.M., Chang Chan, Y. & Swaim, M.S. (1996). Synorogenic extension and exhumation of the Taiwan hinterland. *Geology* **24**, 247-250.

Crespo-Blanc, A. & Campos, J. (2001). Structure and kinematics of the South Iberian paleomargin and its relationship with the Flysch Trough units: extensional tectonics within the Gibraltar Arc fold-and-thrust belt (western Betics). *Journal of Structural Geology* **23**, 1615-1630.

Dalziel, I.W. & Bailey, S.W. (1968). Deformed garnets in a mylonitic rock from the Grenville front and their tectonic significance. *American Journal of Science* **266**, 542–562.

Darot, M. (1973). Méthodes d'analyse structurale et cinématique. Application á l'étude du massif ultrabasique de la Sierra Bermeja. Ph.D. Thesis, University of Nantes, France.

Darot, M. (1974). Cinématiques de l'extrusion, à partir du manteau, des péridotites de la Sierra Bermeja (Serrania de Ronda, Espagne). *Comptes Rendus de l'Académie des Sciences de Paris* **278**, 1673-1676.

Davies, G. (1980). Review of oceanic and global heat flow estimates. *Reviews of Geophysics* **18**, 718-722.

Davies, G. R., Nixon, P. H., Pearson, D. G. & Obata, M. (1993). Tectonic implications of graphitized diamonds from the Ronda peridotite massif, southern Spain. *Geology* **21**, 471-474.

De Bresser, J.H.P., Peach, C.J., Reijs, J.P.J. & Spiers, C.J. (1998). On dynamic recrystallization during solid state flow: effects of stress and temperature. *Geophysical Research Letters* **25**, 3457-3460.

Demouchy, S., Schneider, S.E., Mackwell, S.J., Zimmerman, M.E. & Kohlstedt, D.L., 2009. Experimental deformation of olivine single crystals at lithospheric temperatures. *Geophysical Research Letters* **36**, L04304.

Dercourt, J., Zonenshain, L.P., Ricou, L.E., Kazmin, V.G., Le Pichon, X., Knipper, A.L., Grandjacquet, C., Sbortshikov, I.M., Geyssant, J., Lepvrier, C., Pechersky, D.H., Boulin, J., Sibuet, J.-C., Savostin, L.A., Sorokhtin, O., Westphal, M., Bazhenov, M.L., Lauer, J.P. & Biju-Duval, B. (1986). Geological evolution of the Tethys belt from the Atlantic to the Pamirs since the Lias. *Tectonophysics* **123**, 241–315.

Dewey, J.F. & Bird, J.M. (1970). Mountain belts and the new global tectonics. *Journal of Geophysical Research* **75**, 2625–2647.

Dewey, J.F., Helman, M.L., Turco, E., Hutton, D.H.W. & Knott, S.D. (1989). Kinematics of the western Mediterranean. In: Coward, M.P., Dietrich, D., Park, R.G. (eds.). Alpine Tectonics. *Geological Society, London, Special Publication*, 265–283.

Dewey, J.F., Pitman, W.C., Ryan, W.B.F. & Bonnin, J. (1973). Plate tectonics and the evolution of the Alpine system. Geological Society of America Bulletin 84, 3137– 3180.

de Wit, M. J. (2003). Madagascar: Heads it's a continent, tails it's an island. *Annual Reviews of Earth Planetary Sciences* **31**, 213–248.

Di Leo, J.F., Wookey, J., Hammond, J.O., Yamashina, J.M. & Harjadi, P. (2012). Deformation and Mantle Flow beneath the Sangihe Subduction Zone from Seismic Anisotropy. *Physics of the Earth and Planetary Interiors* **194-195**, 38-54. doi: 10.1016/j.pepi.2012.01.008

Docherty, C. & Banda, E. (1995). Evidence for eastward migration of the Alboran Sea based on regional subsidence analysis: a case for basin formation by delamination of the subcrustal lithosphere? *Tectonics* **14**, 804–818.

Fallot, P. (1948). Les Cordillères bétiques. *Estudios Geoligicos* **8**, 83-172.

Dhont, D., Backé, G. & Hervouët, Y. (2005). Plio-Quaternary extension in the Venezuelan Andes: Mapping from SAR JERS imagery. *Tectonophysics* **399**, 293-312.

Doukhan, N., Sautter, V. & Doukhan, J.C. (1994). Ultradeep, ultramafic mantle xenoliths—transmission electron microscopy preliminary results. *Physics of the Earth Planetary Interiors* **82**, 195–207.

Dickey, J. S., Jr (1970). Partial fusion products in alpine-type peridotites: Serrania De La Ronda and other examples. *Mineralogical Society of America, Special Papers* **3**, 33–49.

Doblas, M. & Oyarzun, R. (1989b). "Mantle core complexes" and Neogene extensional detachment tectonics in the western Betic Cordilleras, Spain: an alternative model for the emplacement of the Ronda peridotite. *Earth and Planetary Science Letters* **93**, 76-84.

Doglioni, C., Carminati, E., Cuffaro, M. & Scrocca, D. (2007). Subduction kinematics and dynamic constraints. *Earth Science Reviews* **83**, 125–175.

Doukhan, N., Doukhan, J.C., FitzGerald, J.D., Chopra, P.N. & Paterson, M.S. (1984). A TEM microstructural study of experimentally deformed Anita Bay dunite. In: Tressler, R.E. & Bradt, R.C. (eds). Deformation of Ceramics II, 307-319, Plenum, New York.

Duggen, S., Hoernle, K., van den Bogaard, P., Rupke, L. & Phipps Morgan, J. (2003). Deep roots of the Messinian salinity crisis. *Nature* **422**, 602-606.

Durand-Delga, M., Rossi, P. Olivier, P. & Puglisi, D. (2000). Situation structurale et nature ophiolitique des roches basiques jurassiques associées aux flyschs maghrébins du Rif (Maroc) et de Sicile (Italie). *Comptes Rendus de l'Académie des Sciences II* **331**, 29–38.

Durham, W. B., & Goetze, C. (1977). Plastic flow of oriented single crystals of olivine: 1. Mechanical data. *Journal of Geophysical Research* **82**, 5737–5353. doi:10.1029/JB082i036p05737.

Durham, W.B., Goetze, G. & Blake, B. (1977). Plastic flow of oriented single crystals of olivine. 2. Observations and interpretations of the dislocation

structures. *Journal of Geophysical Research* **82**, 5755-5770.

Edwards, R. A., Whitmarsh, R. B. & Scrutton, R. A. (1997). The crustal structure across the transform continental margin off Ghana, eastern equatorial Atlantic. *Journal of Geophysical Research* **102**, 747–772, doi:10.1029/96JB02098.

El Atrassi, F., Brunet, F., Bouybaouene, M., Chopin, C. & Chazot, G. (2011). Melting textures and microdiamonds preserved in graphite pseudomorphs from the Beni Bousera peridotite massif, Morocco. *European Journal of Mineralogy* **23**(2), 157-168. doi: 10.1127/0935-1221/2011/0023-2094.

El Maz, A. & Guiraud, M. (2001). Paragenèse à faible variance dans les métapélites de la série de Filali (Rif interne marocain): description, interpretation et conséquences géodynamiques. *Bulletin de la Société Géologique de France* **172**, 469–485.

England, P. (1983). Constraints on extension of continental lithosphere. *Journal of Geophysical Research* **88**, 1145–1152.

Ernst, W.G. (2005). Alpine and Pacific styles of Phanerozoic mountain building: subduction-zone petrogenesis of continental crust. *Terra Nova* **17**, 165–188.

Esteban, J.J., Cuevas, J., Tubía, J.M., Liati, A., Seward, D. & Gebauer, D. (2007). Timing and origin of zircon-bearing chlorite schists in the Ronda peridotites (Betic Cordilleras, Southern Spain). *Lithos* **99**, 121-135.

Esteban, J.J., Cuevas, J., Tubía, J.M., Sergeev, S. & Larionov, A. (2011). A revised Aquitanian age for the emplacement of the Ronda peridotites (Betic Cordilleras, southern Spain). *Geological Magazine* **148**, 183-187.

Etheridge, M.A. (1975). Deformation and recrystallization of orthopyroxene from the Giles complex, Central Australia. *Tectonophysics* **25**, 87-114.

Etheridge, M.A. & Wilkie, J.C. (1979). Grainsize reduction, grain boundary sliding and the flow strength of mylonites. *Tectonophysics* **58**, 159-178.

Exner, H.E. (1972). Analysis of grain- and particle-size distributions in metallic materials. *International Metallica Reviews* **17**, 25-42.

Evans, B. & Goetze, C. (1979). The temperature variation of hardness of olivine and its implication for polycrystalline yield stress. *Journal of Geophysical Research* **84**, 5505–5524.

Faccenda, M., Burlini, L., Gerya, T., Mainprince, D. (2008). Fault-induced seismic anisotropy by hydration in subducting oceanic plates. *Nature* [E] **455**,Nature Publishing Group, London England, 1097-1100.

Faccenna C., Piromallo A., Crespo-Blanc A., Jolivet L. & Rossetti F. (2004). Lateral slab deformation and the origin of the Mediterranean arcs. *Tectonics* **23**, TC1012, 21 pp. doi:10.1029/2002TC001488.

Falus, G, Tommasi, A. & Soustelle, V. (2011) Effect of dynamic recrystallization on olivine crystal preferred orientations in mantle xenoliths deformed under varied stress conditions. *Journal of Structural Geology* **33**, 1528-1540. doi: 10.1016/j.jsg.2011.09.010.

Farr, T. G., et al. (2007). The Shuttle Radar Topography Mission. *Reviews in Geophysics* **45**, RG2004. doi:10.1029/2005RG000183.

Feinberg, H., Saddiqi, O. & Michard, A. (1996). New constraints on the bending of the Gibraltar Arc from paleomagnetism of the Ronda peridotites (Betic Cordilleras, Spain). *In:* Morris, A. & Tarling, D.H. (eds) Paleomagnetism and tectonics of the Mediterranean region. *Geological Society Special Publications* **105**, 43-52.

Féménias, O., Diot, H., Berza, T., Gauffriau, A. & Demaiffe, D. (2004). Asymmetrical to symmetrical magnetic of dikes: Paleo-flow orientations and Paleo-stresses recorded on feeder-bodies from the Motru Dike Swarm (Romania). *Journal od Structural Geology* **26**, 1401-1418.

Frets, E., Tommasi, A., Garrido, C.J., Padrón-Navarta, J.A., Amri, I. & Targuisti, K. (2012). Deformation processes and rheology of pyroxenites under lithospheric mantle conditions. *Journal of Structural Geology* **39**, 138-157, doi:10.1016/j.jsg.2012.02.019.

Galindo-Zaldívar, J., González-Lodeiro, F. & Jabaloy, A. (1989). Progressive extensional shear structures in a detachment contact in the western Sierra Nevada (Betic Cordilleras, Spain). *Geodinamica Acta* **3**, 73–85.

Gao, S., Davis, P.M., et al. (1997). SKS splitting beneath continental rift zones. *Journal of Geophysical Research* **102**, 22781-22797.

García-Dueñas, V., Balanyá, J.C. & Martínez-Martínez, J.M. (1992). Miocene extensional detachments in the outcropping basement of the northern Alboran Basin (Betics) and their tectonic implications. *Geo-Marine Letters* **12**, 88-95.

Garrido, C.J. & Bodinier, J.-L. (1999). Diversity of mafic rocks in the Ronda peridotite: evidence for pervasive melt/rock reaction during heating of subcontinental lithosphere by upwelling asthenosphere. *Journal of Petrology* **40**, 729-754.

Garrido, C. J., Kelemen, P. B. & Hirth, G. (2001). Variation of cooling rate with depth in lower crust formed at an oceanic spreading ridge: Plagioclase crystal size distributions in gabbros from the Oman ophiolite. *Geochemistry Geophysics Geosystems* **2**, 1041. doi:10.1029/2000GC000136.

Garrido, C.J., Gueydan, F., Booth-Rea, Precigout, J., Hidas, K., Padrón-Navarta, J.A. & Marchesi, C. (2011). Garnet lherzolite and garnet-spinel mylonite in the Ronda peridotite: Vestiges of Oligocene backarc mantle lithospheric extension in the western Mediterranean. *Geology* **39**, 927-930. doi:10.1130/G31760.1

Godard, G. & Van Roermund, H.L.M. (1995). Deformation-induced clinopyroxene from eclogites. *Journal of Structural Geology* **17**, 1425-1443.

Goetze, C. & Evans, B. (1979). Stress and temperature in the bending lithosphere as constrained by experimental rock mechanics. *Geophysical Journal of the Royal Astronomical Society* **59**, 463–478.

Goscombe, B.D., Passchier, C.W. & Hand, M. (2004). Boudinage classification: end-member boudin types

and modified boudin structures. *Journal of Structural Geology* **26**, 739-763.

Green D.H. & Ringwood, A.E. (1967b). The stability fields of aluminous pyroxene peridotite and garnet peridotite. *Earth and Planetary Science Letters* **3**, 151-160.

Green, H. W. & Radcliffe, S. V. (1972). Deformation processes in the upper mantle. In Heard, H. C.(ed). Flow and Fracture of Rocks. American Geophysical Union, Washington D.C., *Geophysical Monographs Series***16**, 139-156.

Green, H.W. & Radcliffe, S.V. (1972). Deformation processes in the upper mantle. In: Heard, H.C., Borg, L.Y., Carter, N.L., Raleigh, C.B.(eds). Flow and fracture of rocks. *American Geophysical Union*, Washington DC, 139-156.

Gueguen, Y. & Boullier, A.M. (1974). Evidence of superplasticity in mantle peridotites. Presentation at Nato Proceedings, Newcastle, England.

Gutscher, M.A., Malod, J., Rehault, J.P., Contrucci, I., Klingelhoefer, F., Mendes-Victor, L. & Spakman, W. (2002). Evidence for active subduction beneath Gibraltar. *Geology* **30**, 1071-1074.

Gysi, A.P., Jagoutz, O., Schmidt, M.W. & Targuisti, K. (2011). Petrogenesis of pyroxenites and melt infiltrations in the ultramafic complex of Beni Bousera, Northern Morocco. *Journal of Petrology* **52**, 1679-1735.

Haissen, F., García-Casco, A., Torres-Roldan, R.L. & Aghzer, A.M. (2004). Decompression reactions and P–T conditions in high-pressure granulites from Casares-Los Reales units of the Betic-Rif belt (S Spain and N Morocco). *Journal of African Earth Sciences* **39**, 375-383.

Handy, M.R., Hirth, G. & Bürgmann, R. (2007). Continental fault structure and rheology from the frictional-to-viscous transition downward. In: Handy, M.R., Hirth, G., Hovius, N. (Eds.), *Dahlem Workshop Reports*. The MIT Press, Cambridge, USA, 139–181.

Hauber, E., Grott, M. & Kronberg, P. (2010). Martian rifts: Structural geology and geophysics. *Earth and PLanetary Science Letters* **294**, 393-410.

Hempton, M. R. (1987). Constraints on Arabian plate motion and extensional history of the Red Sea. *Tectonics* **6**, 687–705.

Hidas, K., Booth-Rea, G., Garrido, C.J., Martínez-Martínez, J.M., Padrón-Navarta, J.A., Giaconia, F., Frets, E. & Marchesi, C. (in press). Backarc basin inversion and subcontinental mantle intracrustal emplacement: Kilometer-scale folding and shearing at the base of the proto-Alborán lithospheric mantle (Betic cordillera, South Spain). *Journal of the Geological Society of London.*

Hielscher, R. & Schaeben, H. (2008). A novel pole figure inversion method: specification of the MTEX algorithm. *Journal of Applied Crystallography* **41**, 1024 – 1037.

Higgie, K. & Tommasi, A. (submitted). Feedbacks between deformation and melt distribution in the crust-mantle transition zone of the Oman ophiolite. *Earth and Planetary Science Letters.*

Higgins, M.D. (1994). Numerical modeling of crystal shapes in thin-sections: estimation of crystal habit and true sizes. *American Mineralogist* **79**, 113-119.

Hillert, M. (1965). On the theory of normal and abnormal grain growth. *Acta Metallurgica* **13**, 227–238.

Hirschmann, M.M. & Stolper, E.M. (1996). A possible role for garnet pyroxenite in the origin of the "garnet signature" in MORB. *Contributions to Mineralogy and Petrology* **124**, 185-208.

Hirth, G. & Kohlstedt, D. L. (1995a). Experimental constraints on the dynamics of the partially molten upper mantle 2. Deformation in the dislocation creep regime. *Journal of Geophysical Research* **100** (B8), 15441-15449.

Hirth, G. & Kohlstedt, D. L. (1995b). Experimental constraints on the dynamics of the partially molten upper-mantle deformation in the diffusion creep regime. *Journal of Geophysical Research - Solid Earth* **100** (B2), 1981-2001.

Hirth, G. & Kohlstedt, D. (2003). Rheology of the upper mantle and the mantle wedge: A view from the experimentalists. In: Eiler, J. (Ed.). Inside the subduction factory: American Geophysical Union, *Geophysical monograph* **138**, 83–105.

Holland T.J.B. & Powell, R. (1996). Thermodynamics of order-disorder in minerals. 2. Symmetric formalism applied to solid solutions. *American Mineralogist* **81**, 1425-37.

Holland, T.J.B. & Powell, R. (1998). An internally consistent thermodynamic data set for phases of petrological interest. *Journal of Metamorphic Geology* **16**, 309-343.

Holtzman, B. K., Groebner, N. J., Zimmerman, M. E., Ginsberg, S. B. & Kohlstedt, D. L. (2003). Stress-driven melt segregation in partially molten rocks. *Geochemistry, Geophysics, Geosystems* **4**, 8607.

Houseman, G.A., McKenzie, D.P. & Molnar, P. (1981). Convective instability of a thickened boundary layer and its relevance for the thermal evolution of continental convergent belts. *Journal of Geophysical Research* **86**, 6115–6132.

Huismans, R.S. & Beaumont, C. (2002). Asymmetric lithospheric extension: the role of frictional-plastic strain softening inferred from numerical experiments. *Geology* **30**, 211-214.

Huismans, R.S. & Beaumont, C. (2003). Symmetric and Asymmetric lithospheric extension: Relative effects of frictional-plastic and viscous strain softening. *Journal of Geophysical Research* **108**, 2496. doi:10.1029/2002JB002026.

Huismans, R.S., Buiter, S.J.H. & Beaumont, C. (2005). The Effect of Plastic-Viscous Layering and Strain-Softening on Mode Selection During Lithospheric Extension. *Journal of Geophysical Research* **110**. doi:10.1029/2004JB003114.

Huismans, R.S. & Beaumont, C. (2007). Roles of lithospheric strain softening and heterogeneity in determining the geometry of rifts and continental margins. *Geological Society of London, Special Publications* **282**, 111-138. In: Karner, G. D., Manatschal, G. & Pinheiro, L. M. (eds). Imaging,

Mapping and Modelling Continental Lithosphere Extension and Breakup.

Huismans, R.S. & Beaumont, C. (2008). Complex rifted continental margins explained by dynamical models of depth-dependent lithospheric extension. *Geology* **36**, 163–166. doi: 10.1130/G24231A.1.

Humbert, M., Cey, N., Mullier, J. & Esling, C. (1996). Determination of mean orientation from a cloud of orientations. Application to electron backscatterring pattern measurements. *Journal of Applied Crystallography* **29**, 662–666.

Ingrin, J.; Doukhan, N., & Doukhan, J.C. (1992). Dislocation glide systems in diopside single crystals deformed at 800-900°C. *European Journal of Mineralogy* **4**, 1291-1302.

Isacks, B., Oliver, J. & Sykes, L.R. (1968). Seismology and the new global tectonics. *Journal of Geophysical Research* **73**, 5855–5899.

Humbert, M., Cey, N., Mullier, J. & Esling, C. (1996). Determination of mean orientation from a cloud of orientations. Application to electron backscatterring pattern measurements. *Journal of Applied Crystallography* **29**, 662-666.

Jackson, E. D. (1961). Primary textures and mineral associations in the ultramafic zone of the Stillwater complex, Montana. *US Geological Survey, Professional Papers* **358**.

Janots, E., Negro, F., Brunet, F., Goffé, B., Engi, M. & Bouybaouène, M.L. (2006). Evolution of the REE mineralogy in HP–LT metapelites of the Sebtide complex, Rif, Morocco: Monazite stability and geochronology. *Lithos* **87**, 214-234.

Jaoul, O. & Raterron, P. (1994). High-temperature of diopside crystal -3. Influences of pO_2 and SiO_2 precipitation. *Journal of Geophysical Research* **99**(B5), 9423-9439.

Jarvis. A., Reuter, H.I., Nelson, A. & Guevara, E. (2008). Hole-filled SRTM for the globe Version 4. Available from the CGIAR-SXI SRTM 90m database. http://srtm.csi.cgiar.org

Ji, S. & Martignole, J. (1994). Ductility of garnet as an indicator of extremely high temperature deformation. Journal of Structural Geology 16, 985–996.

Ji, S., Saruwatari, K., Mainprice, D., Wirth, R., Xu, Z. & Xia, B. (2003). Microstructures, petrofabrics and seismic properties of ultra high-pressure eclogites from Sulu region, China: implications for rheology of subducted continental crust and origin of mantle reflections. *Tectonophysics* **370**, 49–76.

Jolivet, L., Augier, R., Robin, C., Suc, J.P. & Rouchy, J.M. (2006). Lithosphericscale geodynamic context of the Messinian salinity crisis. *Sedimentary Geology* **188-189**, 9–33.

Jolivet, L., Faccenna, C., Goffé, B., Burov, E. & Agard, P. (2003). Subduction tectonics and exhumation of high-pressure metamorphic rocks in the Mediterranean orogens. *American Journal of Science* **303**, 353–409.

Jolivet, L., Faccenna, C.,et al. (1998). Midcrustal shear zones in postorogenic extension: example from the Tyrrhenian Sea. *Journal of Geophysical Research* **103**, 12123–12160.

Jolivet, L., Goffé, B., Bousquet, R., Oberhänsli,R. & Michard, A. (1998). Detachments in high pressure mountains belts. Tethyan examples. *Earth and Planetary Science Letters* **160**, 31–47.

Jolivet, L., Trotet, F., Monié, P., Vidal, O., Labrousse, L., Agard, P. & Ghorbal, B. (2010). Along-strike variations of P-T conditions in accretionary wedges and syn-orogenic extension, the HP-LT Phyllite-Quartzite Nappe in Crete and the Peloponnese. *Tectonophysics* **480**, 133-148.

Jousselin, D., Nicolas, A. & Boudier, F. (1998). Detailed mapping of a mantle diapir below a paleo-spreading center in the Oman ophiolite. *Journal of Geophysical Research* **103**, 153-170.

Jung, H., Katayama, I., Jiang, Z., Hiraga, T. & Karato, S. (2006). Effect of water and stress on the lattice-preferred orientation of olivine. *Tectonophysics* **421**, 1-22.

Kaczmarek, M.-A. & Tommasi, A. (2011). Anatomy of an extensional shear zone in the mantle (Lanzo massif, Italy). *Geochemistry, Geophysics Geosystems* **12**, Q0AG06. doi:10.1029/2011GC003627.

Karato, S., Toriumi, M. & Fujii, T. (1980). Dynamic recrystallization of olivine single crystals during high-temperature creep. *Geophysical Research Letters* **7**, 649–652.

Kelemen, P.B., Dick, H.J.B. & Quick, J.E. (1992). Formation of harzburgite by pervasive melt/rock reactions in the upper mantle. *Nature (London)* **358**, 635-641.

Kendall, J. M., Stuart, G.W., Ebinger, C. J., Bastow, I. D. & Keir, D. (2005). Magma-assisted rifting in Ethiopia. *Nature* **433**, 146-149.

Kirby, S.H. (1983). Rheology of the lithosphere. *Reviews in Geophysical Space Physics* **21**, 1458–1487.

Kleinschrodt, R. & McGrew, A.J. (2000). Garnet plasticity in the lower continental crust: implications for deformation mechanisms based on microstructures and SEM electron channeling pattern analysis. *Journal of Structural Geology* **22**, 795–809.

Kleinschrodt, R. & Duyster, J.P. (2002). HT-deformation of garnet: an EBSD study on granulites from Sri Lanka, India and the Ivrea Zone. *Journal of Structural Geology* **24**, 1829-1844.

Klemme, S. (2004). The influence of Cr on the garnet-spinel transition in the Earth's mantle: experiments in the system MgO-Cr_2O_3-SiO_2 and thermodynamic modelling. *Lithos* **77**, 639-646.

Klemme, S., Ivanic, T.J., Connolly, J.A.D. & Harte, B. (2009). Thermodynamic modelling of Cr-bearing garnets with implications for diamond inclusions and peridotite xenoliths. *Lithos* **112S**, 986-981.

Knoll, M., Tommasi, A., Logé, R.E. & Signorelli, J.W. (2009). A multiscale approach to model the anisotropic deformation of lithospheric plates. *Geochemistry, Geophysics, Geosystems* **10**, Q08009. http://dx.doi.org/10.1029/2009gc002423.

Kohlstedt, D.L. & Vandersande, J.B. (1973). Transmission electron microscopy investigation of the defect microstructure of four natural orthopyroxenes. *Contributions to Mineralogy and Petrology* **42**, 169-180.

Köhlstedt, D.L., Evans, B. & Mackwell, S.J. (1995). Strength of the lithosphere: constraints imposed by laboratory experiments. *Journal of Geophysical Research* **100**, 17587–17602.

Kollé, J., & Blacic, J. (1982). Deformation of Single-Crystal Clinopyroxenes: 1. Mechanical Twinning in Diopside and Hedenbergite. *Journal of Geophysical Research* **87**(B5), 4019-4034.

Kollé, J., & Blacic, J. (1983). Deformation of Single-Crystal Clinopyroxenes: 2. Dislocation-Controlled Flow Processes in Hedenbergite. *Journal of Geophysical Research* **88**(B3), 2381-2393.

Kornprobst, J. (1969). Le massif ultrabasique des Beni Bouchera (Rif Interne, Maroc): Etude des péridotites de haute température et de haute pression, et des pyroxénolites, à grenat ou sans grenat, qui leur sont associées. *Contributions to Mineralogy and Petrology* **23**, 283-322.

Kornprobst, J. (1970). Les péridotites et les pyroxénolites du massif ultrabasique des Beni Bouchera: une étude expérimentale entre 1100 et 1550°C, sous 15 à 30 kilobars de pression sèche. *Contributions to Mineralogy and Petrology* **29**, 290–309.

Kornprobst, J. (1974). Contribution a l'étude pétrographique et structurale de la zone interne du Rif (Maroc septentrional); petrography and structure of the Rif inner area, northern Morocco. *Notes et Mémoires du Service Géologique*, Rabat, 251 - 256.

Kornprobst, J., Piboule, M., Roden, M. & Tabit, A. (1990). Corundum-bearing garnet clinopyroxenites at Beni Bousera (Morocco): original plagioclase-rich gabbros recrystallized at depth within the mantle? *Journal of Petrology* **31**, 717—74.

Kornprobst, J. & Vielzeuf, D. (1984). Transcurrent crustal thinning; a mechanism for the uplift of deep continental crust/upper mantle associations, Kimberlites, II. The mantle and crust-mantle relationships. In: Third International Kimberlite Conference, Clermont-Ferrand, France, 347–359.

Kumazawa, M. & Anderson, O. L. (1969), Elastic moduli, pressure derivatives and temperature derivatives of single crystal olivine and single crystal forsterite. *Journal of Geophysical Research* **74**, 5961-5980.

Kusbach, V., Stanislav, U. & Schulmann, K. (2012). Ductile deformation and rheology of sub-continental mantle in a hot collisional orogeny: Example from the Bohemian Massif. *Journal of Geodynamics* **56-57**, 108-123.

Kushiro, I., Syono, Y. & Akimoto, S. (1968). Melting of a peridotite nodule at high pressures and high water pressures. *Journal of Geophysical Research* **73**:6023–6029.

Kusznir, N.J. & Park, R.G. (1984). Intraplate lithosphere deformation and the strength of the lithosphere. *Geophysical Journal of the Royal Astronomical Society* **79**, 513–538.

Lally, J.S., Fisher, R.M., Christie, J.M., Griggs, D.T., Nord, N.L. & Radcliffe, S.V. (1972). Electron petrography of Apollo 14 and 15 rocks. *Proceedings of the Lunar Scientific Conference* **3**rd, 401-22.

Lambart, S., Laporte, D. & Schiano, P. (2009). An experimental study of pyroxenite partial melts at 1 and 1.5 GPa: Implications for the major-element composition of Mid-Ocean Ridge Basalts. *Earth and Planetary Science Letters* **288**, 335-347.

Lavie, M.P. (1998). Déformation expérimentale du diopside polycristallin. Ph.D. thesis, Paris XI Orsay.

Lavier, L. & Manatschal, G. (2006). A mechanism to thin the continental lithosphere at magma-poor margins. *Nature* **440,** 324-329.

Lavier, L. L., Buck, W. R. & Poliakov, A. B. N. (1999). A self-consistent rolling-hinge model for the evolution of large-offset low-angle normal faults. *Geology* **27**, 1127-1130.

Lenoir, X., Garrido, C. J., Bodinier, J. L., Dautria, J. M. & Gervilla, F. (2001). The recrystallization front of the Ronda peridotite: Evidence for melting and thermal erosion of subcontinental lithospheric mantle beneath the Alboran basin. *Journal of Petrology* **42**, 141-158.

Le Roux, V., Bodinier, J.L, Tommasi, A., Alard, O., Dautria, J.M., Vauchez, A. & Riches, A. (2007) .The Lherz spinel-lherzolite: refertilized rather than pristine mantle. *Earth and Planetary Science Letters* **259**, 599-612. doi: 10.1016/j.epsl.2007.05.026

Le Roux, V., Tommasi, A. & Vauchez, A. (2008). Feedback between melt percolation and deformation in an exhumed lithosphere^asthenosphere boundary. *Earth and Planetary Science Letters* **274**, 401-413.

Li, Z.H. & Ribe, N. (2012). Dynamics of free subduction from 3-D Boundary- Element modeling. *Journal of Geophysical Research* **117**, B06408. doi:10.1029/2012JB009165.

Li, Z.H., Xu, Z.Q. & Gerya, T.V. (2011). Flat versus steep subduction: Contrasting modes for the formation and exhumation of high- to ultrahigh-pressure rocks in continental collision zones. Earth and Planetary Science Letters 301, 65-77. doi:10.1016/j.epsl.2010.10.014.

Li, Z.H., Xu, Z.Q. & Gerya, T.V. (2012). Numerical Geodynamic Modeling of Continental Convergent Margins. In: Dar, I.A. (Ed). Earth Sciences, Pub. InTech, 273-296.

Lister, G.S. (1974). The Theory of Deformation Fabrics. Ph.D. thesis, Australian National University, Canberra, Australia.

Loubet, M. & Allègre, C. J. (1982). Trace elements in orogenic lherzolites reveal the complex history of the upper mantle. *Nature* **298**, 809-814.

Loomis, T. P. (1972a). Contact metamorphism of pelitic rock by the Ronda ultramafic intrusion, southern Spain. *Geological Society of America Bulletin* **83**, 2449-2474.

Loomis, T.H. (1972b). Diapiric emplacement of the Ronda high-temperature ultramafic intrusion, southern Spain. *Geological Society of America Bulletin* **83**, 2475–2496.

Lonergan, L. 1993. Timing and kinematics of deformation in the Malaguide Complex, internal zone of the Betic Cordillera, southeast Spain. *Tectonics*, **12**, 460-476.

Lonergan, L. & White, N. (1997). Origin of the Betic-Rif mountain belt. *Tectonics*, **16**, 504-522.

López Sánchez-Vizcaíno, V., Rubatto, D., Gómez-Pugnaire, M.T., Trommsdorff, V. & Müntener, O. (2001). Middle Miocene high-pressure metamorphism and fast exhumation of the Nevado-Filábride Complex, SE Spain. *Terra Nova* **13**, 327-332.

Lundeen, M.T. (1978). Emplacement of the Ronda peridotite, Sierra Bermeja, Spain. *Geological Society of America Bulletin* **89**, 172–180.

Macdonald, D., et al. (2003). Mesozoic break-up of SW Gondwana: Implications for regional hydrocarbon potential of the southern South Atlantic. *Marine and Petroleum Geology* **20**, 287–308.

Mackwell, S.J., Kohlsted,D.L. & Paterson, M.S. (1985). Role of water in the deformation of olivine single-crystals. *Journal of Geophysical Research* **90**, 11319-11333.

Malavieille, J., Guihot, P., Costa, S., Lardeaux, J.-M. & Gardien, V. (1990). Collapse of the thickened crust in the French Massif Central: Mont Pilat extensional shear zone and St. Etienne Late Carboniferous basin. *Tectonophysics* **177**, 139–149.

Malinverno, A. & Ryan, W.F.B. (1986). Extension in the Tyrrhenian Sea and shortening in the Apennines as result of arc migration driven by sinking of the lithosphere. *Tectonics* **5**, 227-245.

Mainprice, D. (1990). A FORTRAN program to calculate seismic anisotropy from the lattice preferred orientation of minerals. *Computational Geosciences* **16**, 385– 393.

Mainprice, D., Bascou, J., Cordier, P. & Tommasi, A. (2004). Crystal preferred orientations of garnet: comparison between numerical simulations and electron back-scattered diffraction (EBSD) measurements in naturally deformed eclogites. *Journal of Structural Geology* **26**, 2089-2102.

Mainprice, D. & Humbert, M. (1994). Methods of calculating petrophysical properties from lattice preferred orientation data. *Surveys in Geophysics* **15**, 575–592.

Mainprice, D. & Silver, P.G. (1993). Interpretation of SKS-waves using samples from the subcontinental lithosphere. *Physics of the Earth and Planetary Interiors* **78**, 257–280.

Mainprice, D.; Tommasi A., Couvy, H., Cordier, P. & Frost, D.J. (2005). Pressure sensitivity of olivine slip systems and seismic anisotropy in the Earth's upper mantle. *Nature* **433,** 731-733. doi:10.1038/nature03266.

Marchesi, C., Griffin, W.L., Garrido, C.J., Bodinier, J.-L. & Pearson, N.J. (2010). Persistence of mantle lithospheric Re-Os signature during asthenospherization of the subcontinental lithospheric mantle: insights from in situ isotopic analysis of sulfides from the Ronda peridotite (Southern Spain). *Contributions to Mineralogy and Petrology* **159**, 315-330.

Marchesi, C., Garrido, C.J., Bosch, D., Bodinier, J.-L., Hidas, K., Padron-Navarta, J.A. & Gervilla, F. (2012). A Late Oligocene suprasubduction setting in the westernmost Mediterranean revealed by intrusive pyroxenite dikes in the Ronda peridotite (southern Spain). *The Journal of Geology* **120**, 237–247.

Marchesi, C., Griffin, W. L., Garrido, C. J., Bodinier, J.L., O'Reilly, S. Y. & Pearson, N. J. (2010). Persistence of mantle lithospheric Re-Os signature during asthenospherization of the subcontinental lithospheric mantle: insights from in situ isotopic analysis of sulfides from the Ronda peridotite (southern Spain). *Contributions to Mineralogy and Petrology* **159**, 315–330.

Mauler; A., Bystricky, M., Kunze, K. & Mackwell, S. (2000). Microstructures and lattice preferred orientation in experimentally deformed clinopyroxene aggregates. *Journal of Structural Geology* **22**, 1633-1648.

Mazzoli, S. & Martín Algarra, A. (2011). Deformation partitioning during transpressional emplacement of a 'mantle extrusion wedge': the Ronda peridotites, western Betic Cordillera, Spain. *Journal of the Geological Society*, **168**, 373-382.

McBride, J.H., Snyder, D.B., Tate, M.P., England, R.W. & Hobbs, R.W.(1995). Upper mantle reflector structure and origin beneath the Scottish Caledonides. *Tectonics* **14**, 1351–1367.

McGeary, S. & Warner, M.R. (1985). Seismic profiling the continental lithosphere. *Nature* **317**, 795–797.

McKenzie, D. (1969). Speculations on the consequences and causes of plate motions. *Geophysical Journal* **18**, 1–32.

McKenzie, D. (1978). Some remarks on the development of sedimentary basins. *Earth Planetary Science Leters* **40**, 25-32.

Mercier, J.C.(1972). Structure des phidotites en enclaves dans quelques basaltes d'Europe et d'Hawaï. Regards sur la constitution du manteau superieur. PhD. Thesis, Université de Nantes, France, pp. 229.

Mercier, J.C. & Nicolas, A. (1975). Textures and fabrics of upper-mantle peridotites as illustrated by xenoliths from basalts. *Journal of Petrology* **16**, 454-487.

Mercier, J.C., Anderson, D.A. & Carter, N.L. (1977). Stress in the lithosphere: Inferences from steady state flow of rocks. *Pure and Applied Geophysics* **115**, 199-226.

Michard, A., Goffé, B., Boubaouène, L. & Saddiqi, O. (1997). Hercyninan Mesozoic thinning in the Alboran Domain. Metamorphic data from the northern Rif, Morocco. *Terra Nova* **9**, 171-174.

Michard A., Saddiqi O., Chalouan A., Frizon de Lamotte, D. (2008). Continental Evolution: The Geology of Morocco. Structure, Stratigraphy, and Tectonics of the Africa- Atlantic-Mediterranean Triple Junction, Springer Verlag, Berlin, Heidelberg, 420 p.

Monié, P., Galindo-Zaldívar, J., González-Lodeiro, F., Goffé, B. & Jabaloy, A. (1991). 40Ar/39Ar geochronology of Alpine tectonism in the Betic Cordilleras (southern Spain). *Journal of the Geological Society of London* **148**, 289–297.

Monié, P., Torres-Roldán, R.-L. & García-Casco, A. (1994). Cooling and exhumation of the western Betic Cordilleras, 40Ar/39Ar thermochronological constraints on a collapsed terrane. *Tectonophysics* **238**, 353–379.

Montel, J.-M., Kornprobst, J. & Vielzeuf, D. (2000). Preservation of old U–Th–Pb ages in shielded monazite: example from the Beni Bousera Hercynian kinzigites (Morocco). *Journal of Metamorphic Geology* **18**, 335-342.

Morgan, D.J. & Jerram, D.A. (2006). On estimating crystal shape for crystal size distribution analysis. *Journal of Volcanic and Geothermal Research* **154**, 1-7.

Moulin, M., Aslanian, D. & Unternehr, P. (2010). A new starting point for the South and Equatorial Atlantic Ocean. *Earth Science Reviews* **98**, 1–37.

Muramoto, M., Michibayashi, K., Ando, J. & Kagi, H. (2011). Rheological contrast between garnet and clinopyroxene in the mantle wedge: An example from Higashi-akaishi peridotite mass, SW Japan. *Physics of the Earth and Planetary Interiors* **184**, 14-33.

Naze, L., Doukhan, J. C. & Latrons, K. (1987). A TEM study of lattice defects in naturally and experimentally deformed orthopyroxenes. *Bulletin de Minéralogie* **110**, 497-512.

Negro, F., Beyssac, O., Goffé, B., Saddiqi, O. & Bouybaouène, M.L. (2006). Thermal structure of the Alboran Domain in the Rif (northern Morocco) and the Western Betics (southern Spain). Constraints from Raman spectroscopy of carbonaceous material. *Journal Of Metamorphic Geology* **24**, 309–327.

Newton, R. C., Charlu, T. V. & Kleppa, O. J. (1980). Thermochemistry of the high structural state plagioclases.Geochimica et Cosmochimica Acta 44, 933-941.

Nickel, K. G. & Green, D. H. (1985). Empirical geothermobarometry for garnet peridotites and implications for the nature of the lithosphere, kimberlites and diamonds. *Earth and Planetary Science Letters* **73**, 158-170.

Nicolas, A., Achauer, U., & Daignieres, M. (1994). Rift initiation by lithospheric rupture. *Earth and Planetary Science Letters* **123**, 281-298.

Nicolas, A., Bouchez, J.L., Boudier, F. & Mercier, J.C. (1971). Textures, structures and fabrics due to solid state flow in some European lherzolites. *Tectonophysics* **12**, 55-86.

Nicolas, A., Bouchez, J.L. & Boudier, F. (1972). Interprétation cinématique des deformations plastiques dans le massif de lherzolite de Lanzo (Alpes piémontaises). Comparaison avec d'autres massifs. *Tectonophysics* **14**, 143-171.

Nicolas, A., Boudier, F. & Boullier, A.M. (1973). Mechanism of flow in naturally and experimentally deformed peridotites. *American Journal of Science* **273**, 853- 876.

Nicolas, A. & Boudier, F. (1975). Kinematic interpretation of folds in alpine-type peridotites. *Tectonophysics* **25**, 233-260.

Nicolas, A., & Poirier, J.P. (1976). Crystalline Plasticity and Solid State Flow in Metamorphic Rocks, John Wiley, London, pp. 444.

Nicolas, A. & Boudier, F. (1995). Mapping oceanic ridge segments Oman ophiolite. *Journal of Geophysical Research-Solid Earth* **100**, 6179-6197.

Nicolas, A. & Boudier, F. (2000). Large mantle upwellings and related variations in crustal thickness in the Oman ophiolite. *Geological Society of America Special Papers* **349**, 67-73, doi:10.1130/0-8137-2349-3.67

Nimis, P., & Taylor, W.R. (2000). Single clinopyroxene thermobarometry for garnet peridotites. Part I. Calibration and testing of a Cr-in-Cpx barometer and an enstatite-in-Cpx thermometer. *Contributions to Mineralogy and Petrology* **139**, 541–554. doi:10.1007/s004100000156.

Nimis, P. & Grütter, H. (2010). Internally consistent geothermometers for garnet peridotites and pyroxenites. *Contributions to Mineralogy and Petrology* **159**, 411-427.

Nürnberg, D., & Müller, R. D. (1991). The tectonic evolution of the South-Atlantic from late jurassic to present. *Tectonophysics* **191**, 27–53.

Obata, M. (1980). The Ronda peridotite: garnet-, spinel-, and plagioclase-lherzolite facies and the P–T trajectories of a high-temperature mantle intrusion. *Journal of Petrology* **21**, 533–572.

Obata, M. (1982). Reply to W. Schubert's comments on "The Ronda peridotite—Garnet-lherzolite, spinel-lherzolite, and plagioclase-lherzolite facies and the P-T trajectories of a high-temperature mantle intrusion". *Journal of Petrology* **23**, 296-298.

O'Hara, M. J. (1967). Mineral facies in ultramafic rocks. In: P. J. Wyllie (ed.) *Ultramafic and Related Rocks*. New York: John Wiley, 7-17.

Obata, M., & Ozawa, K. (2011). Topotaxic relationships between spinel and pyroxene in kelyphite after garnet in mantle-derived peridotites and their implications to reaction mechanism and kinetics. *Mineralogy and Petrology*. doi: 10.1007/s00710-011-0145-y.

Odashima, N., Morishita, T., Ozawa, K., Nagahara, H., Tsuchiyama, A., Nagashima, R., 2008. Formation and deformation of pyroxene-spinel symplectite in ascending mantle: An EBSD (electron backscatter diffraction) study in the Horoman peridotite complex, Japan. *Journal of Mineralogical and Petrological Sciences* **103**, 1-15.

Oldow, J.S., Bally, A.W. & Avé Lallemant, H.G. (1990). Transpression, orogenic float, and lithospheric balance. Geology 18, 991-994.

O'Neill, H.S.C. (1981). The transition between spinel lherzolite and garnet lherzolite, and its use as a geobarometer. *Contributions to Mineralogy and Petrology* **77**, 185–194. doi:10.1007/BF00636522.

Ozawa, K. (2004). Thermal history of the Horoman peridotite complex: a record of thermal perturbation in the lithospheric mantle. *Journal of Petrology* **45**, 253-273.

Padrón-Navarta, J.A. (2010). A coupled petrological and petrophysical study of high pressure dehydration reactions in subduction settings. PhD. Thesis, University of Granada, Spain.

Padrón-Navarta, J.A., Garrido, C.J., Sánchez-Navas, A., Tommasi, A., Sánchez-Vizcaíno, V.L., Gomez-Pugnaire, M.T. & Hussain, S.S. (2008). Oriented growth of garnet by topotactic reactions and epitaxy

in high-pressure, mafic garnet granulite formed by dehydration melting of metastable hornblende-gabbronorite (Jijal Complex, Kohistan Complex, north Pakistan). *Journal of Metamorphic Geology* **26**(8), 855-870.

Paterson, M.S. (1987). Problems in the extrapolation of laboratory rheological data. *Tectonophysics* **137**, 33–43.

Pearson, D. G., Davies, G. R., Nixon, P. H. & Milledge, H. J. (1989). Graphitized diamonds from a peridotite massif in Morocco and implications for anomalous diamond occurrences. *Nature* **338**, 60–62.

Pearson, D. G., Davies, G. R., Nixon, P. H., Greenwood, P. B. & Mattey, D. P. (1991). Oxygen isotope evidence for the origin of pyroxenites in the Beni Bousera peridotite massif, north Morocco: derivation from subducted oceanic lithosphere. *Earth and Planetary Science Letters* **102**, 289–301.

Pearson, D.G., Davies, G.R. & Nixon, P.H. (1992). Geochemical Constraints on the Petrogenesis of Diamond Facies Pyroxenites from the Beni Bousera Peridotite Massif, North Morocco. *Journal of Petrology* **34**(1), 125-172. doi: 10.1093/petrology/34.1.125.

Pearson, D. G., Davies, G. R. & Nixon, P. H. (1993). Geochemical constraints on the petrogenesis of diamond facies pyroxenites from the Beni Bousera peridotite massif, North Morocco. *Journal of Petrology* **34**, 125–172.

Pearson, D.G.& Nowell, G.M. (2004). Re-Os and Lu-Hf isotope constraints on the origin and age of pyroxenites from the Beni Bousera peridotite massif: implications for mixed peridotite-pyroxenite mantle sources. *Journal of Petrology* **45**, 439–455. doi:10.1093/petrology/egg102.

Phakey, P., Dollinger, G. & Christie, J. (1972). Transmission electron microscopy of experimentally deformed olivine crystals. In: Heard, H.C. et al. (eds). Flow and fracture of rocks. American Geophysical Union, Washington, D. C, *Geophyisical Monographs Series* **16**, 117-138.

Platt, J.P., Anczkiewicz, R., Soto, J.I., Kelley, S.P. & Thirlwall, M. (2006). Early Miocene continental subduction and rapid exhumation in the western Mediterranean. *Geology* **34**, 981-984.

Platt, J.P., Kelley, S.P., Carter, A. & Orozco, M. (2005). Timing of tectonic events in the Alpujárride Complex, Betic Cordillera, southern Spain. *Journal of the Geological Society* **162**, 451-462.

Platt, J. P., Soto, J. I. , Whitehouse, M. J., Hurford,A. J. & Kelley, S. P. (1998). Thermal evolution, rate of exhumation, and tectonic significance of metamorphic rocks from the floor of the Alborán Extensional Basin, western Mediterranean. Tectonics 17, 671–689.

Platt, J.P. & Vissers, R.L.M. (1989). Extensional collapse of thickened continental lithosphere: A working hypothesis for the Alboran Sea and Gibraltar arc. *Geology*, **17**, 540-543.

Platt, J.P., Whitehouse, M.J., Kelley, S.P., Carter, A. & Hollick, L. (2003). Simultaneous extensional exhumation across the Alboran Basin: Implications for the causes of late orogenic extension. *Geology* **31**, 251-254.

Platzman, G.W. (1984). Planetary energy balance for tidal dissipation. *Reviews of Geophysics* **22**, 73-84.

Poirier, J.P. (1985). Creep of crystals, Cambridge University Press, Cambridge.

Poirier J. P. (1995). Plastic rheology of crystals. In: Ahrens, T. J. (ed). Mineral physics and crystallography: A handbook of physical constants: American Geophysical Union, Washington D.C., 237–247.

Pollack, H.N., Hurter, S.J. & Johnson, J., R. (1993). Heat flow from the Earth's interior: analysis of the global data set. *Reviews of Geophysics* **31**, 267-280.

Polvé, M. & Allègre, C. J. (1980). Orogenic lherzolite complexes studied by 87Rb-87Sr: a clue to understand the mantle convection processes? *Earth and Planetary Science Letters* **51**, 71-93.

Précigout, J., Gueydan, F., Gapais, D., Garrido, C. J. & Essaifi, A. (2007). Strain localisation in the subcontinental mantle: a ductile alternative to the brittle mantle. *Tectonophysics* **445**, 318-336.

Priem, H.N.A., Boelrijk, N.A.I.M., Hebeda, E.H., Oen, I.S., Verdurmen, E.A.T. & Verschure, R.H. (1979). Isotopic dating of the emplacement of the ultramafic masses in the Serrania de Ronda, Southern Spain. *Contributions to Mineralogy and Petrology* **70**, 103-109.

Prior, D.J., Boyle, A.P., Brenker, F., Cheadle, M.C., Day, A., Lopez, G., Peruzzo, L., Potts, G.J., Reddy, S., Spiess, R., Timms, N.E., Trimby, P., Wheeler, J. & Zetterstrom, L. (1999). The application of electron backscatter diffraction and orientation contrast imaging in the SEM to textural problems in rocks. *American Mineralogist* **84**, 1741-1759.

Prior, D.J., Wheeler, J., Brenker, F.E., Harte, B. & Matthews, M. (2000). Crystal plasticity of natural garnet: new microstructural evidence. *Geology* **28**, 1003–1006.

Pusch, R. (1970). Microstructural changes in soft quick clay at failure. *Canadian Geotechnical Journal* **7**, 1-7. doi: 10.1139/t70-001.

Raleigh, C.B. (1965). Glide mechanisms in experimentally deformed minerals. *Science* **150**, 739-541.

Ranalli, G. (1986). Rheology of the Earth. Allen and Unwin, London, pp. 366.

Ranalli, G. & Murphy, D.C. (1987). Rheological stratification of the lithosphere. *Tectonophysics* **132**, 281–295.

Raterron, P., Chen, J., Li, L., Weidner, D. & Cordier,P. (2007). Pressure-induced slip-system transition in forsterite: Single-crystal rheological properties at mantle pressure and temperature. *American Mineralogist* **92**, 1436-1445. doi: 10.2138/am.2007.2474 0003004X

Raterron, P., Amiguet, E., Chen, J., Li, L. & Cordier, P. (2009). Experimental deformation of olivine single crystals at mantle pressure and temperature. *Physics of the Earth and Planetary Interiors* **172**, 74–83.

Raterron, P., Chen, J., Geenen, T. & Girard, J. (2011). Pressure effect on forsterite dislocation slip systems: Implications for upper-mantle LPO and low viscosity

zone. *Physics of the Earth and Planetary Interiors* **188**, 26-36. doi: 10.1016/j.pepi.2011.06.009.

Raterron, P., Girard, J. & Chen, J. (2012). Activities of olivine slip systems in the upper mantle. *Physics of the Earth and Planetary Interiors* **200-201**, 105-112. doi: 10.1016/j.pepi.2012.04.006.

Raterron, P. & Jaoul, O. (1991). High-temperature deformation of diopside single-crystal -1. Mechanical data. *Journal of Geophysical Research* **96**(B9), 14277-14286.

Regenauer-Lieb, K., Rosenbaum, G. & Weinberg, R.F. (2008). Strain localisation and weakening of the lithosphere during extension. *Tectonophysics* **458**, 96-104.

Reisberg, L., & Lorand, J.-P. (1995). Longevity of subcontinental mantle lithosphere from osmium isotope systematics in orogenic peridotite massifs. *Nature* **376**, 159–162.

Remaïdi, M. (1993). Etude pétrologique et géochimique d'une association péridotites refractaires–pyroxenites dans le Massif de Ronda(Espagne). Ph.D. Thesis, Université de Montpellier II, pp. 437.

Reston, T.J. (1990). Shear in the lower crust during extension: not so pure and simple. *Tectonophysics* **173**, 175–183.

Reuber, I., Michard, A., Chalouan, A., Juteau, T. & Jermoumi, B. (1982). Structure and emplacement of the Alpine-type peridotites from Beni Bousera, Rif, Morocco: A polyphase tectonic interpretation. *Tectonophysics* **82**, 231-251.

Reuter, H.I., Nelson, A. & Jarvis, A. (2007). An evaluation of void filling interpolation methods for SRTM data. *International Journal of Geographic and Informatic Sciences* **21**, 983–1008.

Rosenbaum, G., Lister, G.S. & Duboz, C. (2002). Relative motions of Africa, Iberia and Europe during Alpine orogeny. *Tectonophysics* **359**, 117-129.

Rolf, T., Coltice, C. & Tackley, P.J.. (accepted, 2012). Linking continental drift, plate tectonics and the thermal state of the Earth's mantle. *Earth and Planetary Science Letters*.

Rolf, T. & Tackley, P. (2011). Focussing of stress by continents in 3D spherical mantle convection with self-consistent plate tectonics. *Geophysical Research Letters* **38**, L18301. doi:10.1029/2011GL048677

Ross, J.V. (1973). Mylonitic rocks and flattened garnets in the southern Okanagan of British Columbia. *Canadian Journal of Earth Sciences* 10, 1–17.

Ross, J.V. & Nielsen, K.C. (1978). High-temperature flow of wet polycrystalline enstatite. *Tectonophysics* **44**, 233-261.

Rossetti, F., Theye, T., Lucci, F., Bouybaouène, M., Dini, A., Gerdes, A., Philips, D. & Cozzupoli D. (2010). Timing and modes of granite magmatism in the core of the Alboran Domain, Rif chain, northern Morocco. Implications for the Alpine evolution of the western Mediterranean. *Tectonics* **29**, 2017.

Royden, L.H. (1993). Evolution of retreating subduction boundaries formed during continental collision. *Tectonics*, **12**, 629-638.

Ruiz-Cruz, M.D. & de Galdeano, C.S. (2012). Diamond and coesite in ultrahigh-pressure, ultrahigh-temperature granulites from Ceuta, Northern Rif, northwest Africa. *Mineralogical Magazine* **76**, 683-705. doi: 10.1180/minmag.2012.076.3.17.

Saddiqi, O., Reuber, I. & Michard, A. (1988). Sur la tectonique de dénudation du manteau infracontinental dans les Beni Bousera, Rif septentrional, Maroc. *Comptes Rendus de l'Académie des Sciences, Série II*, **307**, 657–662.

Saddiqi, O. (1995). Exhumation des roches profondes, péridotites et roches métamorphiques HP-BT dans deux transects de la chaîne alpine: Arc de Gibraltar et Montagnes d'Oman. Unpublished PhD Thesis, Université Hassan II, Casablanca.

Sánchez-Gómez, M., Balanyá, J.C., García-Dueñas, V. & Azañón, J.M. (2002). Intracrustal tectonic evolution of large lithosphere mantle slabs in the western end of the Mediterranean orogen (Gibraltar arc). In: G. Rosenbaum and G.S. Lister (Editors), Reconstruction of the evolution of the Alpine-Himalayan orogen. *Journal of the Virtual Explorer* **8**, 23-34.

Sánchez-Rodríguez, L. & Gebauer, D. (2000). Mesozoic formation of pyroxenites and gabbros in the Ronda area (southern Spain), followed by Early Miocene subduction metamorphism and emplacement into the middle crust: U-Pb sensitive high-resolution ion microprobe dating of zircon. *Tectonophysics* **316**, 19-44.

Sandvol, E., Ni, J., Ozalaybey, S. & Schlue, J. (1992). Shear-wave splitting in the Rio Grande Rift. *Geophysical Research Letters* **19**, 2337- 2340.

Schellart, W.P. & Rawlinson, N. (2010). Convergent plate margin dynamics: new perspectives from structural geology, geophysics and geodynamic modelling. *Tectonophysics* **483**, 4–19.

Schmid, S.M., Paterson, M.S. & Boland, J.N. (1980). High temperature flow and dynamic recrystallisation in Carrarra marble. *Tectonophysics* **65**, 245–280.

Seber, D., Barazangi, M., Tadili, B.A., Ramdani, M., Ibenbrahim, A. & BenSari, D. (1996). Three-dimensional upper mantle structure beneath the intraplate atlas and interplate Rif mountains of Morocco. *Journal of Geophysical Research-Solid Earth* **101**, 3125-3138.

Skemer, P., Katayama, I., Jiang, Z. & Karato, S. (2005). The misorientation-index: development of a new method for calculating the strength of lattice-preferred orientation. *Tectonophysics* **411**, 157–167.

Sobolev, A.V., Hofmann, A.W., Sobolev, S.V. & Nikogosian, I.K. (2005). An olivine-free mantle source of Hawaiian shield basalts. *Nature* **434**, 590-597.

Soustelle, V., Tommasi, A., Bodinier, J.L, Vauchez, A. & Garrido, C.J.M. (2009). Deformation and reactive melt transport in the mantle lithosphere above a partial melting domain (Ronda peridotite massif, Spain). *Journal of Petrology* **50**, 1235-1266. doi:10.1093/petrology/egp032.

Soustelle, V., Tommasi, A., Demouchy, S. & Ionov, D.A. (2010). Deformation and Fluid–Rock Interaction in the Supra-subduction Mantle: Microstructures and

Water Contents in Peridotite Xenoliths from the Avacha Volcano, Kamchatka. *Journal of Petrology* **51**, 363-394. doi: 10.1093/petrology/egp085.

Spakman, W. & Wortel, R. (2004). A tomographic view on western Mediterranean geodynamics. In: Cavazza, W. Roure, F. Spakman, W. Stampfli, G.M. & Ziegler, P.A. (Editors). The TRANSMED atlas - The Mediterranean region from crust to mantle. Springer, pp. 31-52.

Stipp, M. & Tullis, J. (2003). The recrystallized grain size piezometer for quartz. *Geophysical Research Letters* **30**, 2088. doi:10.1029/2003 GL018444.

Storey, M., Mahoney, J. J., Saunders, A. D., Duncan, R. A., Kelley,S. P. & Coffin, M. F. (1995). Timing of hot spot-related volcanism and the break-up of Madagascar and India. *Science* **267**, 852–855.

Sue, C., Thouvenot, F., Fréchet, J., & Tricart, P. (1999). Widespread extension in the core of the Western Alps revealed by earthquake analysis: *Journal of Geophysical Research* **104**, 611– 622.

Suen, C. J & Frey, F. A. (1987). Origins of the mafic and ultramafic rocks in the Ronda peridotite. *Earth and Planetary Science Letters* **85**, 183-202.

Suter, G. (1980). Carte Géologique de la Chaîne Rifaine. Scale: 1/ 500 000. In: Editions du Service Géologique du Maroc, Notes et Mémoires), Rabat, Morocco.

Tabit, A., Kornprobst, J. &Woodland, A.B. (1997). The garnet peridotites of the Beni Bousera massif (Morocco): Tectonic mixing and iron-magnesium interdiffusion. *Comptes Rendus de l'Académie des Sciences* **325**, 665–670.

Takahashi, E. & Kushiro, I. (1983). Melting of a dry peridotite at high pressures and basalt magma genesis. *American Mineralogist* **68**, 859-879.

Takazawa, E., Frey, F., Shimizu, N. & Obata, M. (1996). Evolution of the Horoman peridotite (Hokkaido, Japan): implications from pyroxene compositions. *Chemical Geology* **134**, 3-26.

Targuisti, K. (1994). Petrología y geoquímica de los macizos ultramficos de Ojen (Andalucía) y de Béni Bousera (Rif Septentrional, Marruecos). *Unpublished PhD. thesis*, University of Granada.

Taylor, W. R. (1998). An experimental test of some geothermometer and geobarometer formulations for upper mantle peridotites with application to the thermobarometry of fertile lherzolite and garnet websterite. *Neues Jahrbuch für Mineralogie Abhandlugen* **172**, 381–408.

Thielmann, M. & Kaus, B.J.P. (submitted, in revision). Shear heating induced lithospheric-scale localization: Does it result in subduction? *Earth and Planetary Science Letters*.

Tikoff, B., Russo, R., Teyssier, C. & Tommasi, A (2004). Mantle-driven deformation of orogenic zones and clutch tectonics. In: Grocott, J., McCaffrey, K., Taylor G. & Tikoff, B. (eds) Vertical and horizontal decoupling in the lithosphere. *Geological Society of London Special Publications* **227**, 41-64.

Tikoff, B., Teyssier, C. & Waters, C.L. (2002). Clutch tectonics and partial attachment of lithospheric layers. *European Geophysical Union Special Publication Series* **1**, 93-117.

Tommasi, A., Gibert, B., Seipold, U. & Mainprice, D. (2001). Anisotropy of thermal diffusivity in the upper mantle. *Nature* **411**, 783-786.

Tommasi, A., Godard, M., Coromina, G., Dautria, J.-M. & Barsczus, H. (2004). Seismic anisotropy and compositionally induced velocity anomalies in the lithosphere above mantle plumes: a petrological and microstructural study of mantle xenoliths from French Polynesia. *Earth and Planetary Science Letters* **227** (3-4), 539-556.

Tommasi, A., Knoll, M., Vauchez, A., Signorelli, J. & Logé, R. (2009). Structural reactivation in plate tectonics controlled by olivine crystal anisotropy. *Nature Geoscience* **2**, 423–427.

Tommasi, A., Mainprice, D., Canova, G. & Chastel, Y. (2000). Viscoplastic self-consistent and equilibrium-based modeling of olivine lattice preferred orientations: Implications for the upper mantle seismic anisotropy. *Journal of Geophysical Research-Solid Earth* **105**(B4), 7893-7908.

Tommasi, A., Tikoff, B. & Vauchez, A. (1999). Upper mantle tectonics: three-dimensional deformation, olivine crystallographic fabrics and seismic properties. *Earth and Planetary Science Letters* **168**(1-2), 173-186.

Tommasi, A. & Vauchez, A. (2001). Continental rifting parallel to ancient collisional belts: an effect of the mechanical anisotropy of the lithospheric mantle. *Earth and Planetary Science Letters* **185**, 199–210.

Tommasi, A., Vauchez, A., Godard, M. & Belley, F. (2006). Deformation and melt transport in a highly depleted peridotite massif from the Canadian Cordillera: Implications to seismic anisotropy above subduction zones. *Earth and Planetary Science Letters* **252**, 245-259, doi:10.1016/j.epsl.2006.09.042

Tommasi A., Vauchez, A. & Ionov, D.A. (2008). Deformation, static recrystallization, and reactive melt transport in shallow subcontinental mantle xenoliths (Tok Cenozoic volcanic field, SE Siberia). *Earth and Planetary Science Letters* **272**, 65-77. doi: 10.1016/j.epsl.2008.04.020.

Torné, M., Banda, E., García-Dueñas, V. & Balanyá, J.C. (1992). Mantle-lithosphere bodies in the Alboran crustal domain (Ronda peridotites, Betic-Rif orogenic belt). *Earth and Planetary Science Letters* **110**, 163-171.

Torné, M., Fernàndez, M., Comas, M.C. & Soto, J.I. (2000). Lithospheric structure beneath the Alboran Basin: results from 3D gravity modeling and tectonic relevance. *Journal of Geophysical Research* **105**, 3209-3228.

Torres-Roldán, R. L., García-Casco, A. & García-Sánchez, P. A. (2000). CSpace: An integrated workplace for the graphical and algebraic analysis of phase assemblages on 32-bit Wintel platforms. *Computers and Geosciences* **26**, 779-793.

Torsvik, T. H., Rousse, S., Labails, C. & Smethurst, M. A. (2009). A new scheme for the opening of the South Atlantic Ocean and the dissection of an Aptian salt basin. *Geophysical Journal International* **177**, 1315–1333.

Toy, V. G., Newman, J., Lamb, W. & Tikoff, B. (2010). The role of pyroxenites in formation of shear instabilities in the mantle: Evidence from an

ultramafic ultramylonite, Twin Sisters Massif, Washington. *Journal of Petrology* **51**, 55-80.

Tubía, J.M. & Cuevas, J. (1986). High-temperature emplacement of the Los Reales peridotite nappe (Betic Cordillera, Spain) *Journal of Structural Geology* **8**, 473-482.

Tubía, J.M. & Cuevas, J. (1987). Structures et cinématique liées à la mise en place des péridotites de Ronda (Cordillères Bétiques, Espagne). *Geodinamica Acta* **1**, 59-69.

Tubía, J. M. (1994). The Ronda peridotites (Los Reales nappe): an example of the relationship between lithospheric thickening by oblique tectonics and late extensional deformation within the Betic Cordillera (Spain). *Tectonophysics* **238**, 381–398.

Tubía, J. M., Cuevas, J. & Esteban, J. J. (2004). Tectonic evidence in the Ronda peridotites, Spain, for mantle diapirism related to delamination. *Geology* **32**, 941–944.

Turner, F.J., Heard, H.C. & Griggs, D.T. & (1960). Experimental deformation of enstatite and accompanying inversion to clinoenstatite. Rpt 21st *International Geological Congres Copenhagen* **18**, 399-408.

Twiss, R. J. (1977). Theory and applicability of a recrystallized grain size paleopiezometer. *Pure and Applied Geophysics* **115**, 227-244.

Urai, J.L., Means, W.D. & Lister, G.S. (1986). Dynamic recrystallization of minerals. In: Hobbs, B.E. & Heard, H.C. (eds). Mineral and Rock Deformation: Laboratory Studies. American Geophysical Union, Washington, D. C., 161-199.

Vanderhaeghe, O. & Duchêne, S. (2010). Crustal-scale mass transfer, geotherm and topography at convergent plate boundaries. *Terra Nova* **22**, 315–323.

Van der Wal, D., Chopra, P.N., Drury, M.R. & FitzGerald, J.D. (1993). Relationships between dynamically recrystallised grainsize stress relationships in experimentally deformed olivine rocks. *Geophysical Research Letters* **20**, 1479-1482.

Van der Wal, D. & Vissers, R. L. M. (1993). Uplift and emplacement of upper mantle rocks in the western Mediterranean. *Geology* **21**, 1119-1122.

Van der Wal, D. & Bodinier, J.L. (1996). Origin of the recrystallisation front in the Ronda peridotite by km-scale pervasive porous melt flow. *Contributions to Mineralogy and Petrology* **122**, 387-405.

Van der Wal, D. & Vissers, R. L. M. (1996). Structural petrology of the Ronda peridotite, SW Spain: Deformation history. *Journal of Petrology* **37**(1), 23-43.

Van der Wal, D. & Vissers, R.L.M. (1997). Reply to Discussion by H.P: Zeck of "Structural petrology of the Ronda peridotite, SW Spain; Deformation history". *Journal of Petrology* **36**, 534–536.

Van Roermund, J. & Boland, H. (1981).The dislocation substructures of naturally deformed omphacites. *Tectonophysics* **78**, 403-418.

Van Roermund, H. (1983). Petrofabrics and microstructures of omphacites in a high temperature eclogite from the Swedish Caledonides. *Bulletin de Minéralogie* **106**, 709-713.

van Wijk, J. W. (2005). Role of weak zone orientation in continental lithosphere extension. *Geophysical Research Letters* **32**, L02303, doi:10.1029/2004GL022192.

Vauchez, A.; Barruol, G. & Tommasi, A. (1997). Why do continents break up parallel to ancient orogenic belts? *Terra Nova* **9**, 62-66.

Vauchez, A. & Garrido, C.J. (2001). Seismic properties of an asthenospherized lithospheric mantle: constraints from lattice preferred orientations in peridotite from the Ronda Massif. *Earth and Planetary Science Letters* **192**, 235–249.

Vauchez, A., Tommasi, A. & Barruol, G. (1998). Rheological heterogeneity, mechanical anisotropy and deformation of the continental lithosphere. Tectonophysics 296, 61-86.

Vauchez, A., Tommasi, A., Barruol, G. & Maumus, J. (2000). Upper mantle deformation and seismic amisotropy in continental rifts. *Physics and Chemistry of the Earth* **25**, 111-117.

Vauchez, A., Tommasi, A. & Mainprice, D. (2012). Faults (shear zones) in the Earth's mantle. *Tectonophysics* **558-559**, 1-27. doi:10.1016/j.tecto.2012.06.006.

Villasante-Marcos, V., Osete, M.L., Gervilla, F. & García-Dueñas, V. (2003). Palaeomagnetic study of the Ronda peridotites (Betic Cordillera, southern Spain). *Tectonophysics* **377**, 119-141.

Voegelé,V. (1998). Etude par microscopie électronique en transmission de la plasticité des grenats. Unpublished Ph.D. thesis, Université des Sciences et Technologie de Lille.

Voegelé, V., Ando, J.I., Cordier, P. & Liebermann, R.C. (1998a). Plastic deformation of silicate garnets: I. High-pressure experiments. *Physics of the Earth and Planetary Interiors* **108**, 305-318.

Voegelé, V., Cordier, P., Sautter, V., Sharp, T.G., Lardeaux, J.M. & Marques, F.O. (1998b). Plastic deformation of silicate garnets: II. Deformation microstructures in natural samples. *Physics of the Earth and Planetary Interiors* **108**, 319-338.

Vollmer, F.W. (1990). An application of eigenvalue methods to structural domain analysis. *Geological Society of America Bulletin* **102**, 786–791.

Warren, J.M. & Hirth, G. (2006). Grain size sensitive deformation mechanisms in naturally deformed peridotites. *Earth and Planetary Science Letters* **248**, 438–450.

Wasserburg, G.J., MacDonald, G.J.F., Hoyle, F. & Fowler, W.A. (1964). Relative contributions of uranium, thorium and potassium to heat production in the Earth. *Science* **143**, 465-467.

Webb, S.A.C., & Wood, B.J. (1986). Spinel-pyroxene-garnet relationships and their dependence on Cr/Al Ratio. *Contributions to Mineralogy and Petrology* **92**, 471–480. doi:10.1007/BF00374429.

Weber, M., et al. (2009). Anatomy of the Dead Sea transform from lithospheric to microscopic scale. *Reviews in Geophysics* **47**, RG2002, doi:10.1029/2008RG000264.

Weertman, J. (1978). Creep laws for the mantle of the Earth. *Philosophical Transactions of the Royal Society of London* **288**, 9–26.

Wenk, H.-R., Bennet, K., Canova, G.R. & Molinari, A. (1991). Modelling plastic deformation of peridotite with the self-consistent theory. *Journal of Geophysical Research* **96**, 8337–8349.

Wernicke, B. (1981). Low angle normal faults in Basin and Range province. Nappe tectonics in an extending orogen. *Nature* **291**, 645- 648.

Wernicke, B. (1985) Uniform-sense normal simple shear of the continental lithosphere, *Canadian Journal of Earth Sciences* **22**, 108-125.

White, S. (1977). Geological significance of recovery and recrystallization processes in quartz. *Tectonophysics* **39**, 143–170.

Whitney, D.L. & Evans, B.W. (2010). Abbreviations for names of rock-forming minerals. *American Mineralogist* **95**, 185-187.

Whittaker, J. M., Müller, R. D., Leitchenkov, G., Stagg,H., Sdrolias, M., Gaina, C. & Goncharov, A. (2007). Major Australian-Antarctic plate reorganization at Hawaiian-Emperor bend time. *Science* **318**, 83–86.

Wilks, K. & Carter, N.L. (1990). Rheology of some continental lower crustal rocks. *Tectonophysics* **182**, 57–77.

Wilson, J.T. (1966). Did the Atlantic close and then re-open? *Nature* **211**, 676–681.

Witt-Eickschen, G. & Seck, H.A. (1991). Solubility of Ca and Al in Ortho-pyroxene from spinel peridotite — an improved version of an empirical geothermometer. *Contributions to Mineralogy and Petrology* **106**, 431–439.

Wood., B. & Banno, S. (1973). Garnet-orthopyroxene and orthopyroxene-clinopyroxene relationships in simple and complex systems. *Contributions to Mineralogy and Petrology* **42**, 109-124.

Woodcock, N.H. & Naylor, M.A. (1983). Randomness testing in three-dimensional orientation data. *Journal of Structural Geology* **5**, 539-548.

Wortel, M.J.R. & Spakman, W. (2000). Subduction and Slab Detachment in the Mediterranean-Carpathian Region. *Science* **290**, 1910-1917.

Zeck, H.P. (1997). Discussion of 'Structural petrology of the Ronda peridotite, SW Spain: Deformation history' by Van der Wal, , D. & Vissers, R.L.M. *Journal of Petrology* **38**, 529– 531. doi:10.1093/petrology/38.4.529.

Zhang, J., Green, H.W. & Bozhilov, K. (2006). Rheology of omphacite at high temperature and pressure and significance of its lattice preferred orientations. *Earth and Planetary Science Letters* **246**, 432–443.

Zhang, S. & Karato, S. (1995). Lattice preferred orientation of olivine aggregates in simple shear. *Nature* **375**, 774-777.

Part V - Appendix

9. Field structural data and Sample location

Field structural data and Sample locations

Station	X(UTM)†	Y(UTM)†	Domain	Foliation		Lineation		Layering*		Shear sense	Sample
				Az	Dip	Az	Dip	Az	Dip		
2	324663	3910233	Grt-Sp Mylonites	96	35	150	30				
3	324754	3910128	Grt-Sp Mylonites	116	15						BB001
4	324769	3910124	Grt-Sp Mylonites	121	14						BB002
5	324727	3910165	Grt-Sp Mylonites	108	24						BB003
8	327408	3907716	Seiland	80	25	90	5				BB004
9b	329091	3901455	Grt-Sp Mylonites	257	8						
10	328999	3901421	Grt-Sp Mylonites	157	12						BB005
11	329096	3901021	Grt-Sp Mylonites	166	12						BB006
12	329375	3900747	Grt-Sp Mylonites	135	18						
13	329423	3900850	Arièǵite								BB007
13	329423	3900850	Arièǵite	110	16						BB008
14	329551	3900819	Arièǵite	116	57						
14b	329600	3900819	Arièǵite	270	62						
15	329620	3900818	Grt-Sp Mylonites	94	62						BB009
16	329656	3900848	Grt-Sp Mylonites	94	26						
17	329648	3900896	Arièǵite	144	17						
18	327931	3906525	Seiland	106	45			124	48		BB010
19	330688	3905527	Seiland	320	18			340	22		BB011
19	330688	3905527	Seiland								BB012
19b	330688	3905517	Seiland	150	20			280	20		
20	330591	3905475	Seiland	0	74			320	14		
21	330579	3905463	Seiland								BB013
22	330517	3905428	Seiland	280	70						
23	330478	3905284	Seiland	106	28			190	13		BB014
24	330508	3905274	Seiland								BB015
25	330342	3904928	Seiland								BB016
26	330173	3904753	Seiland	138	72						
27	330126	3904714	Arièǵite-Seiland					20	77		BB017
28	330215	3904771	Seiland								BB018
28	330215	3904771	Seiland								BB019
29	334740	3899108	Seiland	330	26						
31	335041	3898933	Arièǵite								BB020A
31	335041	3898933	Arièǵite								BB020B
31	335041	3898933	Arièǵite	324	56						BB020C
37	333873	3898027	Grt-Sp Mylonites	38	56						BB021
38	332542	3897444	Grt-Sp Mylonites	115	40						
41	332109	3897033	Grt-Sp Mylonites								BB022A
41	332109	3897033	Grt-Sp Mylonites								BB022B
42	332039	3897044	Grt-Sp Mylonites	96	85	97	2				BB023
44	331999	3897091	Grt-Sp Mylonites	94	20	130	12				
47	329866	3901073	Grt-Sp Mylonites	133	20						
48	329899	3900853	Grt-Sp Mylonites								BB028A
48	329899	3900853	Grt-Sp Mylonites								BB028B
48	329899	3900853	Grt-Sp Mylonites								BB028C
48	329899	3900853	Grt-Sp Mylonites								BB028D
48	329899	3900853	Grt-Sp Mylonites								BB028E
48	329899	3900853	Grt-Sp Mylonites								BB029A
48	329899	3900853	Grt-Sp Mylonites	116	20	160	14				BB029B
49	329941	3901050	Arièǵite	114	44						BB030
49b	329941	3901060	Arièǵite	112	57	150	44				
50	330030	3901047	Arièǵite	85	55	175	55				
51	330065	3901090	Arièǵite								BB031
52	330145	3901142	Grt-Sp Mylonites	58	58						BB032
53	330249	3901309	Arièǵite-Seiland	140	26						BB033
53	330249	3901309	Arièǵite-Seiland	140	26						BB034
54	330275	3901333	Arièǵite								BB035A
54	330275	3901333	Arièǵite								BB035B
54	330275	3901333	Arièǵite								BB035C
54	330275	3901333	Arièǵite	124	18						BB035D
56	330532	3901289	Arièǵite	90	26						
57	330684	3901307	Arièǵite	80	58	160	57				BB036
58	330075	3904515	Seiland	38	38			110	32		BB037
59	329893	3904515	Seiland	20	70			15	65		BB038
59	329893	3904515	Seiland	20	70			15	65		BB039
60	329857	3904494	Seiland					12	65		
61	329751	3904380	Seiland					184	40		
62	329717	3904335	Seiland					38	37		
62b	329647	3904265	Seiland					37	45		
63	329632	3904244	Seiland								BB040
63	329632	3904244	Seiland					40	38		BB041
65	329457	3904049	Seiland								BB042

Field structural data and Sample locations

Station	X(UTM)†	Y(UTM)†	Domain	Foliation		Lineation		Layering*		Shear sense	Sample
				Az	Dip	Az	Dip	Az	Dip		
67	332381	3904157	Seiland	35	49						BB043
67b	332370	3904140	Seiland	355	58						
68	332350	3904112	Seiland	354	88						BB044
70	332330	3904124	Seiland	354	89						BB045
70b	332295	3904090	Seiland	34	72						
71	332271	3903962	Seiland	4	70						BB046
72	332278	3903943	Seiland	18	58			22	68		
73	332293	3903897	Seiland	330	89			18	78		
74	332276	3903836	Seiland	184	68						BB047
75	332259	3903842	Seiland	344	74			18	68		BB048
76	332198	3903825	Seiland	175	15						BB049
78	332168	3903838	Seiland	193	23			14	51		BB050
78b	332150	3903825	Seiland					15	86		
79	332139	3903804	Seiland	324	13			7	82		BB051
80	332105	3903716	Seiland					190	82		
81	332117	3903706	Seiland					13	80		
82	332063	3903661	Seiland					16	77		BB052
83	332004	3903582	Seiland	14	41			12	66		BB053
84	331953	3903580	Seiland	207	48			180	66		BB054
85	331991	3903594	Seiland					10	87		
86	331921	3903485	Seiland	203	77			1	85		
87	331829	3903462	Seiland	165	83			25	67		
88	331817	3903480	Seiland	345	85						
89	331804	3903468	Seiland					17	69		BB055
90	331666	3903351	Seiland	20	70						
91	328599	3907351	Seiland	270	9						BB056
93	328107	3906719	Seiland	340	12						BB057
94	328050	3906763	Seiland								BB058
94	328050	3906763	Seiland								BB059a
94	328050	3906763	Seiland								BB059b
94	328050	3906763	Seiland	155	13			146	19		BB059c
95	328016	3906715	Seiland	325	22						
96	327985	3906690	Seiland								BB060
97	327944	3906681	Seiland								BB061
98	327921	3906618	Seiland	143	9						
99	327920	3906584	Seiland	159	30			88	15		BB062
100	327801	3906435	Seiland								BB063A
100	327801	3906435	Seiland	116	10	164	8				BB063B
101	327756	3906445	Seiland	74	18	174	17				
102	327687	3906431	Seiland	110	18	162	15				BB064
103	327735	3906409	Seiland	90	11						
104	327732	3906406	Seiland	148	23	198	18	68	16		BB065
104b	327732	3906401	Seiland	160	8			87	12		
104c	327732	3906391	Seiland	141	19			119	15		
105	327728	3906347	Seiland	173	45						BB066
106	327737	3906294	Seiland	135	21			124	30		
107	327686	3906237	Seiland					148	16		BB067
108	327706	3906212	Ariègite-Seiland								BB068
108	327706	3906212	Ariègite-Seiland					110	21		BB069
108b	327706	3906192	Ariègite-Seiland					100	19		
109	327593	3906167	Ariègite-Seiland								BB070
109	327593	3906167	Ariègite-Seiland								BB071
110	327543	3906181	Ariègite-Seiland					108	18		BB072
111	327483	3906093	Ariègite-Seiland	166	37			97	12		
111b	327470	3906080	Ariègite-Seiland					81	21		
112	327522	3906107	Ariègite-Seiland								BB073
112	327522	3906107	Ariègite-Seiland								BB074
112	327522	3906107	Ariègite-Seiland					102	23		BB075
113	327501	3905978	Ariègite-Seiland					124	10		
114	327564	3905953	Ariègite-Seiland								BB076A
114	327564	3905953	Ariègite-Seiland								BB076B
114	327564	3905953	Ariègite-Seiland	108	24			94	21		BB076C
115	327474	3905890	Ariègite-Seiland	32	31			347	15		
116b	327400	3905700	Ariègite-Seiland					94	27		
117	327511	3905673	Ariègite-Seiland	327	10						
118	327401	3905481	Ariègite-Seiland					100	38		
119	327378	3905454	Ariègite-Seiland					116	28		
120	327310	3905400	Ariègite-Seiland					163	51		
120b	327310	3905400	Ariègite-Seiland					98	19		
121	327271	3905311	Ariègite-Seiland	218	69			250	73		
122	327266	3905292	Ariègite-Seiland					90	29		

Field structural data and Sample locations

Station	X(UTM)†	Y(UTM)†	Domain	Foliation		Lineation		Layering*		Shear sense	Sample
				Az	Dip	Az	Dip	Az	Dip		
123	327245	3905256	Ariègite-Seiland	128	21						BB077
123	327245	3905256	Ariègite-Seiland								BB078
124	327254	3905188	Ariègite-Seiland	166	26			118	39		
124b	327254	3905168	Ariègite-Seiland					138	46		
124c	327254	3905148	Ariègite-Seiland					77	27		
125	327231	3905071	Ariègite-Seiland								BB079
125	327231	3905071	Ariègite-Seiland					120	33		BB080
125c	327210	3905020	Ariègite-Seiland					109	30		
126	327207	3905010	Ariègite-Seiland					99	31		
127	327192	3904983	Ariègite-Seiland					113	28		BB081
128	325814	3904596	Grt-Sp Mylonites	160	15	315	8				BB082
129	325674	3904914	Grt-Sp Mylonites	150	22	152	2				BB083
130	325819	3904610	Grt-Sp Mylonites								BB084
132	325918	3904335	Grt-Sp Mylonites	225	34						BB085
133	325970	3904390	Grt-Sp Mylonites	215	16	325	15				BB086
134	325990	3904408	Grt-Sp Mylonites	220	16						BB087
135	325976	3904448	Grt-Sp Mylonites								BB088A
135	325976	3904448	Grt-Sp Mylonites								BB088B
135	325976	3904448	Grt-Sp Mylonites								BB088C
135	325976	3904448	Grt-Sp Mylonites	223	20	270	15				BB088D
136	326014	3904494	Grt-Sp Mylonites	236	13	330	13				BB089
137	326046	3904548	Grt-Sp Mylonites	238	22						BB090
138	326041	3904564	Grt-Sp Mylonites								BB091
138	326041	3904564	Grt-Sp Mylonites	240	18						BB092
139	326057	3904591	Grt-Sp Mylonites								BB093A
139	326057	3904591	Grt-Sp Mylonites	254	14						BB093B
140	326082	3904597	Ariègite	144	30			133	20		BB094
141	326093	3904628	Ariègite	106	32			132	36		
142	326128	3904636	Ariègite	132	30						BB095
143	326192	3904635	Seiland	155	30			130	20		BB096
144	326354	3904684	Grt-Sp Mylonites	144	33						BB097
145	326393	3904700	Grt-Sp Mylonites	127	40						
146	326446	3904704	Ariègite	140	22			115	28		
147	326425	3904698	Ariègite	120	37						
149	326496	3904706	Ariègite					132	32		BB098
150	326527	3904712	Seiland	138	43			133	34		BB099
150b	326532	3904713	Seiland	118	34			280	67		
151	326536	3904757	Ariègite	130	26			108	22		
152	326548	3904762	Seiland	150	28			140	30		BB100
153	326558	3904757	Seiland	140	24						
154	326627	3904772	Seiland	134	30			131	38		
155	326663	3904814	Seiland	120	18						BB101
156	326686	3904823	Ariègite-Seiland					104	26		
157	326724	3904828	Ariègite-Seiland					124	25		BB102
159	327211	3904978	Ariègite-Seiland								BB103A
159	327211	3904978	Ariègite-Seiland	160	16			115	25		BB103B
160	327199	3904932	Ariègite-Seiland					100	23		
161	328631	3908118	Ariègite					110	22		BB104
162	328418	3908218	Ariègite								BB105
163	328423	3908245	Ariègite					141	25		BB106
164	326565	3908666	Ariègite	120	38						BB107
165	327055	3908734	Ariègite	114	38						BB108
166	327108	3908723	Ariègite	118	35						
167	327119	3908705	Ariègite								BB109A
167	327119	3908705	Ariègite	129	40			122	35		BB109B
168	326895	3908767	Ariègite	92	24						BB110
169	327721	3906353	Ariègite	90	20						
170	327495	3906096	Ariègite	139	27						BB111
171	327489	3906086	Ariègite								BB112A
171	327489	3906086	Ariègite								BB112B
171	327489	3906086	Ariègite								BB112C
171	327489	3906086	Ariègite	109	19						BB112D
173	327508	3905909	Seiland					130	18		BB113
174	327508	3905914	Ariègite	154	17			115	17		BB114
175	327146	3905079	Seiland	120	26						BB115
176	327160	3905019	Seiland	108	28						BB116
177	327130	3905030	Seiland								BB117A
177	327130	3905030	Seiland	110	24						BB117B
178	327102	3905052	Seiland								BB118A
178	327102	3905052	Seiland								BB118B
178	327102	3905052	Seiland	110	25						BB118C

Field structural data and Sample locations

Station	X(UTM)†	Y(UTM)†	Domain	Foliation		Lineation		Layering*		Shear sense	Sample
				Az	Dip	Az	Dip	Az	Dip		
180	327108	3902567	Grt-Sp Mylonites								BB119M1
180	327108	3902567	Grt-Sp Mylonites								BB119M2
180	327108	3902567	Grt-Sp Mylonites								BB119M3
180	327108	3902567	Grt-Sp Mylonites								BB119M4
180	327108	3902567	Grt-Sp Mylonites	122	22						
181	327344	3902604	Grt-Sp Mylonites	168	25						
182	327425	3902551	Grt-Sp Mylonites	226	25						BB120
183	327391	3902480	Grt-Sp Mylonites								BB121A
183	327391	3902480	Grt-Sp Mylonites								BB121B
183	327391	3902480	Grt-Sp Mylonites	195	25						BB121C
184	327496	3902553	Ariègite	180	26	340	10				BB122
185	327528	3902512	Grt-Sp Mylonites								BB123A
185	327528	3902512	Grt-Sp Mylonites	195	30	325	24				BB123B
186	327581	3902480	Grt-Sp Mylonites	185	20						BB124
187	327583	3902456	Grt-Sp Mylonites	160	20	320	8				
188	327605	3902345	Grt-Sp Mylonites	145	13	320	2			Top SE	BB125A
188	327605	3902345	Grt-Sp Mylonites								BB125B
189	327155	3903470	Ariègite	150	30	180	16				BB126
191	327238	3903320	Ariègite	133	31						BB127
192	327252	3903332	Ariègite	142	40			120	40		
193	327259	3903345	Ariègite	120	40						BB128
195	327228	3903404	Ariègite	134	40						BB129
196	327267	3903449	Ariègite	140	31						
197	327280	3903477	Seiland	132	42						
198	327295	3903510	Seiland	139	35						BB130
199	327217	3903521	Ariègite								BB131
201	327119	3903671	Ariègite								BB132
202	327181	3903744	Seiland	144	30	320	3				BB133
203	327206	3903780	Seiland	127	19						BB134
204	331975	3903592	Seiland	232	25			203	33		BB135
205	331971	3903577	Seiland	0	42			12	83		BB136
206	331727	3903421	Seiland	143	50			178	72		
207	331731	3903398	Seiland	34	37						
208	331590	3903253	Seiland					79	79		BB137
209	331543	3903187	Seiland	138	70						BB138
210	331530	3903195	Seiland								BB139
211	331524	3903186	Seiland	50	75	200	62				BB140
213	331306	3903057	Seiland					75	75		BB141
214	331258	3903052	Seiland								BB142A
214	331258	3903052	Seiland								BB142B
214	331258	3903052	Seiland	100	24			50	36		BB142C
215	331159	3903040	Seiland					55	26		
216	326567	3908689	Ariègite	120	25						BB143
217	326558	3908709	Ariègite								BB144A
217	326558	3908709	Ariègite	128	30	250	26	170	40	top NE	BB144B
218	326567	3908674	Ariègite	120	25	190	24				
219	326556	3908613	Ariègite	139	26						BB145
220	326397	3907931	Ariègite	110	17			140	14		BB146
222	330069	3904577	Seiland								BB147
223	330018	3904572	Seiland					12	51		
224	329991	3904571	Seiland					0	60		
225	329954	3904557	Seiland	135	50			190	58		BB148
226	329875	3904483	Seiland					20	70		BB149
227	329856	3904480	Seiland					172	20		
228	329792	3904428	Seiland					185	50		BB150
229	329765	3904390	Seiland					22	22		
230	329724	3904341	Seiland					30	15		BB151
231	329689	3904292	Seiland					50	35		
232	329625	3904245	Seiland					45	34		BB152
233	331460	3903238	Seiland	30	55						BB153
234	331392	3903259	Seiland								BB154
234	331392	3903259	Seiland	20	80			68	78		BB155
235	331342	3903252	Seiland								BB156
236	331283	3903282	Seiland					320	25		BB157
237	331237	3903306	Seiland					45	39		BB158
238	331134	3903297	Seiland	47	30	180	23	185	30		BB159
239	331096	3903316	Seiland	28	32						BB160
240	331080	3903288	Seiland								BB161
240	331080	3903288	Seiland	130	15			20	30		BB162
241	331033	3903317	Seiland	90	25						
242	331024	3903333	Seiland	128	18						BB163

Field structural data and Sample locations

Station	X(UTM)†	Y(UTM)†	Domain	Foliation		Lineation		Layering*		Shear sense	Sample
				Az	Dip	Az	Dip	Az	Dip		
244	328670	3901560	Grt-Sp Mylonites	40	23						BB164
245	328688	3901576	Grt-Sp Mylonites	10	17						BB165
246	328707	3901602	Grt-Sp Mylonites	112	6						BB166
247	328656	3901589	Grt-Sp Mylonites								BB167
248	328720	3901898	Grt-Sp Mylonites								BB168
249	328762	3901994	Grt-Sp Mylonites								BB169
249	328762	3901994	Grt-Sp Mylonites	35	19						BB170
250	328800	3902043	Grt-Sp Mylonites	115	26						BB171
251	328797	3902068	Grt-Sp Mylonites	90	29						BB172
252	328821	3902125	Grt-Sp Mylonites	112	28			105	20		
253	328865	3902241	Grt-Sp Mylonites	94	22						BB173
254	328882	3902271	Grt-Sp Mylonites	90	17						
255	329408	3903952	Seiland	50	33						BB174
256	329388	3903915	Seiland	342	27			42	30		
257	329339	3903833	Seiland	10	28			40	26		BB175
258	329328	3903799	Seiland	38	30						BB176
259	329345	3903700	Ariègite-Seiland								BB177A
259	329345	3903700	Ariègite-Seiland	38	21						BB177B
260	329397	3903651	Seiland								BB178
260	329397	3903651	Seiland					32	19		BB179
261	329425	3903484	Ariègite-Seiland					20	12		BB180
262	326303	3908333	Seiland	62	23						BB181
263	326287	3908305	Seiland	321	42						BB182
264	326259	3908311	Ariègite-Seiland					122	22		
265	326248	3908294	Ariègite	150	31						BB183
266	326164	3908210	Ariègite	90	20						
267	326135	3908176	Ariègite	145	30						BB184
268	326094	3908139	Seiland					140	35		BB185
269	325990	3908016	Ariègite	160	12						BB186
270	325772	3908080	Ariègite	162	27						BB187
271	325761	3908102	Grt-Sp Mylonites	162	20	170	3				BB188
272	325740	3908106	Grt-Sp Mylonites	230	20						BB189
273	325690	3908160	Grt-Sp Mylonites	164	23						BB190
274	325654	3908164	Grt-Sp Mylonites	140	21						BB191
275	325624	3908181	Grt-Sp Mylonites	170	25	320	13				BB192
276	325521	3908250	Grt-Sp Mylonites	173	32	147	10				BB193
277	325411	3908265	Grt-Sp Mylonites	163	29	330	8				BB194
278	325448	3908258	Grt-Sp Mylonites	172	29						BB195
279	325431	3908266	Grt-Sp Mylonites	180	25						BB196
280	325397	3908293	Grt-Sp Mylonites	251	24						BB197A
280	325397	3908293	Grt-Sp Mylonites								BB197B
282	325326	3908359	Grt-Sp Mylonites	275	24						BB198
282	325326	3908359	Grt-Sp Mylonites								BB199
283	325308	3908403	Grt-Sp Mylonites								BB200
283	325308	3908403	Grt-Sp Mylonites	206	22						BB201
284	325260	3908360	Grt-Sp Mylonites	160	23						BB202X
286	325443	3908165	Grt-Sp Mylonites	160	10						
287	328786	3901523	Grt-Sp Mylonites	182	24						
288	328749	3901524	Grt-Sp Mylonites	230	28						
289	328742	3901553	Grt-Sp Mylonites	80	20	130	15				BB202
290	328911	3902317	Ariègite	177	13			139	13		BB203
291	328905	3902332	Ariègite-Seiland	205	10	305	8	154	15		BB204
292	328910	3902394	Ariègite-Seiland	119	19						BB205
293	328921	3902481	Ariègite-Seiland					163	8		
294	328970	3902560	Ariègite-Seiland	70	13						BB206
295	329012	3902621	Ariègite-Seiland	135	11						BB207
296	329044	3902640	Ariègite-Seiland	90	18						
297	329093	3902674	Ariègite-Seiland								BB208
297	329093	3902674	Ariègite-Seiland	95	18						BB209
298	329706	3903304	Seiland	19	18						BB210
299	329138	3902872	Seiland	130	29			168	38		BB211
300	329086	3902778	Seiland	85	29						
301	329105	3902781	Seiland	200	15						BB212
302	329239	3902905	Seiland	160	22						BB213
303	329292	3902984	Seiland	85	80			87	55		BB214A
304	329320	3903063	Seiland					90	72		BB214B
305	329330	3903076	Seiland					85	71		BB215
306	329369	3903106	Ariègite	95	82						BB216
306	329369	3903106	Ariègite								BB217
307	329415	3903199	Seiland	98	64						BB218

Field structural data and Sample locations

Station	X(UTM)†	Y(UTM)†	Domain	Foliation		Lineation		Layering*		Shear sense	Sample
				Az	Dip	Az	Dip	Az	Dip		
308	329414	3903270	Seiland	70	15			0	33		BB219
309	329418	3903325	Seiland					90	12		
310	329421	3903412	Seiland	46	13						
311	329413	3903509	Seiland	5	18						BB220
313	334524	3899525	Seiland	350	42						BB221
314	334395	3899607	Ariègite-Seiland								BB222A
314	334395	3899607	Ariègite-Seiland					0	64		BB222B
315	334315	3899627	Ariègite-Seiland	0	80						
316	334346	3899733	Grt-Sp Mylonites	352	70	170	7				BB223
317	334287	3899795	Seiland	350	63						BB224
318	334230	3899858	Seiland	310	66			335	50		BB225
319	334089	3900007	Ariègite	0	55						BB226
320	334010	3900025	Ariègite	0	63						
321	333949	3900003	Ariègite					208	30		
322	333809	3900057	Seiland								BB227A
322	333809	3900057	Seiland					302	30		BB227B
323	327371	3907788	Seiland	20	12			40	30		BB228
324	327934	3906760	Seiland								BB229A
324	327934	3906760	Seiland	171	22			185	13		BB229B
325	330643	3905829	Seiland	235	78			215	49		BB230A
325	330643	3905829	Seiland								BB230B
326	330512	3905799	Seiland	285	9	25	10	215	60		BB231
328	332976	3903895	Seiland					245	37		BB232
332	332105	3897043	Grt-Sp Mylonites	119	45	130	10			Top SE	
333	332026	3897111	Grt-Sp Mylonites	116	38	145	20				
334	332027	3897126	Grt-Sp Mylonites	123	23	130	3				
335	332016	3897234	Grt-Sp Mylonites	106	35	130	15				
336	332013	3897252	Grt-Sp Mylonites	120	46	137	17				BB233
337	332014	3897353	Grt-Sp Mylonites	122	30	122	0				BB234
338	331986	3897430	Grt-Sp Mylonites	120	40	140	16				
339	332056	3897544	Grt-Sp Mylonites	130	33	145	10				BB235
340	331861	3897911	Grt-Sp Mylonites	130	35	160	19				BB236
342	327444	3902557	Grt-Sp Mylonites	197	30	315	27				BB237
343	327477	3902587	Grt-Sp Mylonites	164	20	320	15				BB238
345	327445	3902638	Grt-Sp Mylonites	134	21						
346	327428	3902655	Seiland	130	23						BB239
347	327415	3902662	Seiland	135	30	310	3				
348	327400	3902683	Ariègite								BB240
349	327392	3902713	Seiland	120	31	120	0				BB241
350	327381	3902770	Grt-Sp Mylonites	128	36						BB242
351	333715	3900132	Seiland					55	57		BB243
351	333715	3900132	Seiland								BB244
352	333715	3900132	Ariègite								BB245
353	333565	3900098	Seiland					28	70		BB246
354	333512	3900119	Seiland	248	55			40	59		
355	333490	3900155	Seiland					37	58		BB247
356	333466	3900214	Seiland					50	60		
357	333432	3900239	Seiland	30	67						BB248
358	331179	3905372	Seiland					90	50		
359	331074	3905290	Seiland					76	50		
361	330873	3904797	Seiland					35	49		
362	330872	3904751	Seiland					40	35		BB249
363	330861	3904865	Seiland					21	31		
364	330752	3904625	Seiland					26	35		
365	330706	3904552	Seiland	150	30			45	36		BB250
366	330661	3904556	Seiland					8	25		
367	330603	3904525	Seiland					336	60		
368	330433	3904488	Seiland					345	40		
369	330347	3904375	Seiland					352	20		BB251
370	330404	3904175	Seiland					45	36		BB252
371	330310	3904072	Seiland					26	30		
372	330281	3904063	Seiland					1	49		BB253
373	330204	3904127	Seiland	105	47			45	32		
374	329995	3904048	Seiland					26	29		
375	329947	3903967	Seiland					27	20		BB254
376	329855	3903927	Seiland					32	33		
377	329733	3903820	Seiland					26	35		BB255
378	329969	3903696	Seiland	40	20						BB256
379	330012	3903794	Seiland	20	28						BB257
380	330029	3903687	Seiland	10	30			22	22		

Field structural data and Sample locations

Station	X(UTM)†	Y(UTM)†	Domain	Foliation		Lineation		Layering*		Shear sense	Sample
				Az	Dip	Az	Dip	Az	Dip		
381	330064	3903694	Seiland	16	20						BB258
382	329988	3903571	Seiland					32	12		BB259
383	329790	3903244	Seiland								BB260
383	329790	3903244	Seiland					88	70		BB261
384	333404	3900261	Seiland					50	53		
385	333316	3900281	Seiland	32	66	174	54				BB262
386	333287	3900321	Seiland								BB263
386	333287	3900321	Seiland								BB264
387	333127	3900356	Seiland	50	45						
388	333068	3900390	Seiland					42	54		BB265
389	333200	3900317	Arièrgite-Seiland					175	79		BB266
390	333390	3900340	Seiland	60	49						BB267
390	333390	3900340	Seiland								BB268
393	329889	3903041	Seiland	50	32						BB269
394	329921	3902976	Seiland	248	14			85	22		BB270
395	329603	3902837	Seiland	250	73						BB271
396	329457	3902630	Seiland	295	52						
397	329294	3902444	Seiland	175	75						BB272
398	329278	3902404	Seiland	205	70	0	50				BB273
398	329278	3902404	Seiland								BB273
399	329286	3902329	Seiland	65	18						BB274
400	329176	3902392	Arièrgite	55	15						BB275

†UTM coordinates, Zone 30 (6°W-0°W) using WGS84 datum
*In case the layering is not parallel to the foliation or the foliation is not visible.
Right hand convention for dip of planes

10. Microstructures and CPO of peridotites

Sample location, tectono-metamorphic domain, rock type, microstructure and CPO characteristics

Sample	Lat. (°N)	Long. (°W)	Domain	Rock type	Micro-structure	Distance to contact (m)	Mean ol grain size (µm)	Symmetry of olivine fabric	J-index of olivine	mod. vol. of cpx (%)
BB001W	35°19'08.5"	4°55'40.3"	Grt-Sp Myl.	cpx-rich lhz.	Mylonitic	31	-	Ax [010]	2.96	14
BB005AE	35°14'28.7"	4°52'45.7"	Grt-Sp Myl.	cpx-rich lhz.	Mylonitic	10	-	Ax [010]	3.75	13
BB006AW	35°14'15.7"	4°52'41.6"	Grt-Sp Myl.	lherzolite	Mylonitic	118	-	Ax [010]	3.54	7
BB009W	35°14'09.5"	4°52'20.7"	Grt-Sp Myl.	cpx-rich lhz.	Mylonitic	281	-	Ax [010]	3.68	12
BB083E	35°16'19.9"	4°54'59.9"	Grt-Sp Myl.	cpx-rich lhz.	Mylonitic	5	127	Ax [010]	2.76	10
BB084BE	35°16'10.2"	4°54'53.9"	Grt-Sp Myl.	cpx-rich lhz.	Mylonitic	103	93	Ax [010]	2.65	13
BB085W	35°16'01.3"	4°54'49.8"	Grt-Sp Myl.	lherzolite	Mylonitic	131	118	Ax [010]	2.78	7
BB087E	35°16'03.7"	4°54'47.0"	Grt-Sp Myl.	harzburgite	Mylonitic	165	-	Ax [010]	3.55	4
BB088BW	35°16'05.0"	4°54'47.6"	Grt-Sp Myl.	lherzolite	Mylonitic	169	158	Ax [010]	6.13	7
BB119M3W	35°15'04.7"	4°54'01.4"	Grt-Sp Myl.	lherzolite	Mylonitic	8	-	Ax [010]	3.02	6
BB120W	35°15'04.4"	4°53'48.8"	Grt-Sp Myl.	cpx-rich lhz.	Fine porph.	105	-	Ax [010]	4.47	10
BB123BE	35°15'03.2"	4°53'44.7"	Grt-Sp Myl.	cpx-rich lhz.	Mylonitic	99	-	Ax [010]	2.71	8
BB165E	35°14'33.5"	4°52'58.1"	Grt-Sp Myl.	lherzolite	Mylonitic	58	138	Ax [010]	4.22	7
BB171AW	35°14'48.7"	4°52'54.1"	Grt-Sp Myl.	harzburgite	Mylonitic	317	157	Ax [010]	10.04	5
BB201E	35°18'12.9"	4°55'17.0"	Grt-Sp Myl.	cpx-rich lhz.	Mylonitic	4	-	Ax [010]	6.53	9
BB237W	35°15'04.6"	4°53'48.1"	Grt-Sp Myl.	harzburgite	Mylonitic	115	-	Ortho	9.87	4
BB242E	35°15'11.4"	4°53'50.7"	Grt-Sp Myl.	dunite	Fine porph.	209	-	Ax [010]	12.69	1
BB004E	35°17'51.9"	4°53'53.4"	Ar	harzburgite	Fine porph.	1138	-	Ax [010]	4.83	4
BB008E	35°14'10.4"	4°52'28.5"	Ar	harzburgite	Fine porph.	237	-	Ax [010]	7.06	3
BB026W	35°14'17.9"	4°52'11.2"	Ar	harzburgite	Fine porph.	306	-	Ax [001]	3.9	4
BB029AE	35°14'10.8"	4°52'09.7"	Ar	lherzolite	Fine porph.	381	-	Ax [001]	4.25	6
BB032W	35°14'20.3"	4°52'00.2"	Ar	harzburgite	Fine porph.	314	-	Ortho	8.96	2
BB035DW	35°14'26.6"	4°51'55.2"	Ar	harzburgite	Fine porph.	327	-	Ax [010]	8.36	2
BB036W	35°14'26.0"	4°51'39.0"	Ar	cpx-rich lhz.	Fine porph.	378	-	Ax [010]	5.37	10
BB095AW	35°16'11.2"	4°54'41.7"	Ar	cpx-rich lhz.	Fine porph.	260	198	Ax [010]	7.52	9
BB098E	35°16'13.7"	4°54'27.2"	Ar	lherzolite	Fine porph.	426	235	Ax [010]	6.58	6
BB102E	35°16'17.8"	4°54'18.3"	Ar	lherzolite	Fine porph.	555	-	Ax [001]	3.92	6
BB127W	35°15'29.2"	4°53'56.8"	Ar	lherzolite	Fine porph.	458	-	Ax [010]	6.97	7
BB146W	35°17'58.3"	4°54'33.6"	Ar	harzburgite	Fine porph.	561	-	Ax [010]	7.44	3
BB182E	35°18'10.3"	4°54'38.2"	Ar	harzburgite	Fine porph.	606	-	Ax [010]	5.99	4
BB183AW	35°18'09.9"	4°54'39.8"	Ar	cpx-rich lhz.	Fine porph.	583	-	Ax [010]	3.03	10
BB184W	35°18'06.0"	4°54'44.1"	Ar	cpx-rich lhz.	Fine porph.	504	-	Ax [010]	4.49	10
BB187AW	35°18'02.7"	4°54'58.4"	Ar	lherzolite	Fine porph.	271	-	Ax [010]	4.87	8
BB191E	35°18'05.4"	4°55'03.2"	Ar	cpx-rich lhz.	Fine porph.	225	-	Ax [010]	9.91	8
BB192AW	35°18'05.9"	4°55'04.4"	Ar	harzburgite	Fine porph.	212	-	Ax [010]	8.6	4
BB195AW	35°18'08.3"	4°55'11.4"	Ar	harzburgite	Fine porph.	103	-	Ax [010]	14.46	4
BB204W	35°14'58.2"	4°52'50.1"	Ar	cpx-rich lhz.	Fine porph.	490	188	Ax [010]	5.16	11
BB207W	35°15'07.6"	4°52'46.1"	Ar	lherzolite	Fine porph.	666	263	Ortho	7.38	7
BB235W	35°12'24.7"	4°50'42.0"	Ar	harzburgite	Fine porph.	228	-	Ax [001]	6.53	5
BB236W	35°12'36.5"	4°50'50.0"	Ar	cpx-rich lhz.	Fine porph.	350	-	Ax [010]	7.81	10
BB069E	35°17'03.3"	4°53'40.5"	Ar-Se	dunite	Coarse porph.	1185	-	Ortho	4.95	1
BB070E	35°17'01.8"	4°53'44.9"	Ar-Se	harzburgite	Coarse porph.	1139	-	Ax [001]	6.69	2
BB071W	35°17'01.8"	4°53'44.9"	Ar-Se	harzburgite	Coarse porph.	1139	313	Ax [001]	5.99	3
BB072W	35°17'02.2"	4°53'46.9"	Ar-Se	harzburgite	Coarse porph.	1126	-	Ax [010]	4.31	2
BB076A-BE	35°16'54.8"	4°53'45.9"	Ar-Se	harzburgite	Coarse porph.	1084	325	Ax [001]	8.29	2
BB076C-BE	35°16'54.8"	4°53'45.9"	Ar-Se	cpx-rich lhz.	Coarse porph.	1084	250	Ax [010]	5.24	8
BB079E	35°16'26.0"	4°53'58.4"	Ar-Se	cpx-rich lhz.	Coarse porph.	872	-	Ax [010]	3.4	10
BB103BE	35°16'23.0"	4°53'59.1"	Ar-Se	harzburgite	Coarse porph.	844	280	Ax [010]	3.02	5
BB133E	35°15'42.9"	4°53'59.4"	Ar-Se	harzburgite	Fine porph.	653	-	Ax [010]	6.16	2
BB163W	35°15'31.9"	4°51'27.1"	Ar-Se	cpx-rich lhz.	Coarse porph.	1012	-	Ax [010]	4.12	13
BB211E	35°15'15.8"	4°52'41.3"	Ar-Se	cpx-rich lhz.	Fine porph.	815	192	Ax [001]	8.19	9
BB216E	35°15'23.6"	4°52'32.4"	Ar-Se	lherzolite	Coarse porph.	1012	263	Ax [010]	6.37	8
BB254E	35°15'51.8"	4°52'10.1"	Ar-Se	cpx-rich lhz.	Coarse porph.	1326	-	Ortho	7.1	8
BB256E	35°15'43.1"	4°52'09.1"	Ar-Se	lherzolite	Coarse porph.	1159	-	Ortho	3.73	7
BB259E	35°15'39.0"	4°52'08.2"	Ar-Se	harzburgite	Coarse porph.	1113	-	Ortho	4.03	5
BB011AW	35°16'42.9"	4°51'42.0"	Se	lherzolite	Coarse gran.	2209	-	Ortho	5.45	6
BB012E	35°16'42.9"	4°51'42.°"	Se	lherzolite	Coarse gran.	2209	-	Ax [010]	6.07	6
BB013BW	35°16'40.8"	4°51'46.2"	Se	cpx-rich lhz.	Coarse porph.	2182	-	Ax [010]	4.52	13
BB014W	35°16'34.9"	4°51'50.1"	Se	harzburgite	Coarse porph.	2102	-	Ax [010]	5.55	2
BB017E	35°16'16.2"	4°52'03.6"	Se	cpx-rich lhz.	Coarse porph.	1849	-	Ax [010]	6.18	11

Sample location, tectono-metamorphic domain, rock type, microstructure and CPO characteristics

Sample	Lat. (°N)	Long. (°W)	Domain	Rock type	Micro-structure	Distance to contact (m)	Mean ol grain size (µm)	Symmetry of olivine fabric	J-index of olivine	mod. vol. of cpx (%)
BB019E	35°16'18.1"	4°52'00.1"	Se	harzburgite	Coarse gran.	1888	396	Ax [010]	6.5	2
BB021W	35°12'41.5"	4°49'30.5"	Se	lherzolite	Coarse porph.	250	-	Ax [010]	6.59	5
BB039W	35°16'09.6"	4°52'12.7"	Se	harzburgite	Coarse porph.	1736	622	Ax [010]	4.13	2
BB041E	35°16'00.6"	4°52'22.8"	Se	lherzolite	Coarse porph.	1597	480	Ortho	5.41	8
BB042W	35°15'54.2"	4°52'29.6"	Se	lherzolite	Coarse porph.	1597	-	Ax [010]	4.72	6
BB046W	35°15'53.1"	4°50'38.2"	Se	lherzolite	Coarse porph.	1744	700	Ax [001]	7.89	7
BB049W	35°15'48.6"	4°50'41.0"	Se	harzburgite	Coarse gran.	1614	528	Ax [001]	7.89	4
BB050CW	35°15'49.0"	4°50'42.2"	Se	cpx-bearing dunite	Coarse porph.	1599	-	Ax [001]	11.3	3
BB052BW	35°15'43.2"	4°50'46.2"	Se	cpx-rich lhz.	Coarse porph.	1577	-	Ax [001]	5.26	11
BB053W	35°15'40.6"	4°50'48.5"	Se	lherzolite	Coarse porph.	1456	363	Ortho	7.14	8
BB055W	35°15'36.8"	4°50'56.3"	Se	cpx-rich lhz.	Coarse porph.	1385	-	Ax [001]	5.49	12
BB056W	35°17'40.8"	4°53'06.0"	Se	cpx-rich lhz.	Coarse porph.	1586	353	Ax [001]	5.96	11
BB057E	35°17'20.0"	4°53'25.0"	Se	cpx-rich lhz.	Coarse porph.	1371	594	Ax [010]	3.03	12
BB059CW	35°17'21.4"	4°53'27.3"	Se	lherzolite	Coarse porph.	1362	-	Ax [010]	4.08	8
BB061W	35°17'18.7"	4°53'31.4"	Se	lherzolite	Coarse porph.	1315	-	Ax [010]	3.81	6
BB062W	35°17'15.5"	4°53'32.3"	Se	cpx-rich lhz.	Coarse porph.	1309	-	Ax [010]	3.68	12
BB063AW	35°17'10.6"	4°53'36.9"	Se	lherzolite	Coarse porph.	1247	-	Ax [010]	3.91	7
BB066E	35°17'07.7"	4°53'39.7"	Se	cpx-rich lhz.	Coarse porph.	1215	-	Ortho	3.11	19
BB107E	35°18'22.2"	4°54'27.5"	Se	cpx-rich lhz.	Coarse porph.	827	-	Ax [010]	3.91	12
BB108W	35°18'24.7"	4°54'08.2"	Se	lherzolite	Coarse porph.	1079	-	Ax [010]	3.71	7
BB135W	35°15'40.9"	4°50'49.6"	Se	dunite	Coarse porph.	1456	-	Ortho	6.72	1
BB138W	35°15'29.7"	4°51'04.6"	Se	lherzolite	Coarse gran.	1253	209	Ax [001]	9.5	6
BB141E	35°15'23.2"	4°51'15.7"	Se	cpx-rich lhz.	Coarse gran.	1104	402	Ax [001]	5.1	12
BB142A-AW	35°15'23.0"	4°51'17.6"	Se	harzburgite	Coarse porph.	1086	-	Ax [001]	9.1	1
BB142B-BW	35°15'23.0"	4°51'17.6"	Se	harzburgite	Coarse porph.	1086	-	Ax [001]	7.06	2
BB159E	35°15'30.8"	4°51'22.7"	Se	cpx-rich lhz.	Coarse porph.	1063	-	Ax [010]	5.33	15
BB178BE	35°15'41.3"	4°52'31.7"	Se	lherzolite	Coarse porph.	1301	312	Ax [010]	7.36	8
BB180E	35°15'35.9"	4°52'30.4"	Se	cpx-rich lhz.	Coarse porph.	1221	249	Ax [001]	5.87	10
BB214AE	35°15'19.6"	4°52'35.3"	Se	harzburgite	Coarse porph.	935	317	Ortho	7.4	1
BB231E	35°16'51.6"	4°51'49.2"	Se	cpx-rich lhz.	Coarse porph.	2246	-	Ortho	7.31	11
BB244W	35°13'49.7"	4°49'38.3"	Se	cpx-rich lhz.	Coarse porph.	607	-	Ax [001]	6.79	15
BB246AS	35°13'48.5"	4°49'44.2"	Se	cpx-rich lhz.	Coarse gran.	726	-	Ortho	4.71	13
BB249E	35°16'17.8"	4°51'34.1"	Se	harzburgite	Coarse porph.	1735	-	Ortho	6.69	4
BB252AW	35°15'58.9"	4°51'52.2"	Se	dunite	Coarse porph.	1442	-	Ortho	5.33	1
BB260W	35°15'28.3"	4°52'15.8"	Se	cpx-rich lhz.	Coarse gran.	986	-	Ax [010]	3.58	8
BB262E	35°13'54.3"	4°49'54.2"	Se	cpx-rich lhz.	Coarse gran.	900	-	Ax [001]	9.09	10
BB266E	35°13'57.7"	4°50'04.1"	Se	lherzolite	Coarse porph.	1059	-	Ax [001]	6.92	6
BB270W	35°15'19.7"	4°52'10.4"	Se	harzburgite	Coarse porph.	828	-	Ax [010]	6.84	3
BB272E	35°15'02.0"	4°52'34.8"	Se	harzburgite	Coarse porph.	559	-	Ax [010]	4.61	3

11. Mineral Chemistry (major elements) data used for thermobarometric calculations

Major element compositions (wt. %) of minerals used for geothermobarometry

Sample	BB001W										BB006AW										BB083E									
Locality	Beach										Aarkob										Yahia1									
Domain	Myl										Myl										Myl									
Microstruct.	Mylonitic										Mylonitic										Mylonitic									
Dcontact (m)	31										118										5									
Rock type	Cpx rich lhz.										Lherzolite										Cpx rich lhz.									
Mineral	ol		opx		cpx		sp		grt		ol		opx		cpx		sp		grt		ol		opx		cpx		sp		grt	
core / rim	c	r	c	r	c	r	c	r	c	r	c	r	c	r	c	r	c	r	c	r	c	r	c	r	c	r	c	r	c	r
SiO_2	40.5		55.5		50.7		0.08		41.7		41.19	41.0	54.9	54.9	51.9	52.2	0.15	0.16	42.2	42.3	40.49	40.5	54.5	55.3	51.5	51.5	b.d.l.	b.d.l.	42.0	
TiO_2	b.d.l.		0.13		0.73		0.10		0.16		b.d.l.	b.d.l.	0.24	0.14	0.78	0.82	0.16	0.08	0.19	0.22	b.d.l.	b.d.l.	0.17	0.14	0.61	0.61	0.16	0.09	0.24	
Al_2O_3	b.d.l.		3.52		7.15		55.1		23.6		b.d.l.	b.d.l.	5.45	3.66	7.21	6.3	50.0	48.2	23.4	23.6	b.d.l.	b.d.l.	4.66	3.56	7.78	7.8	46.2	50.8	22.6	
Cr_2O_3	b.d.l.		0.29		0.91		14.0		1.14		b.d.l.	b.d.l.	0.56	0.36	1.00	0.96	19.2	21.3	1.17	1.08	b.d.l.	b.d.l.	0.51	0.42	0.99	0.99	21.0	17.3	1.22	
FeO	10.8		6.96		2.86		12.7		8.62		10.7	10.4	6.75	6.57	2.92	3.03	13.6	14.0	9.01	9.24	10.7	10.7	6.96	6.94	2.78	2.78	14.9	13.0	8.09	
MnO	0.22		0.17		0.07		0.20		0.40		0.15	0.13	0.13	0.12	0.10	0.06	0.16	0.13	0.37	0.40	0.16	0.16	0.13	0.08	0.12	0.12	0.20	0.19	0.36	
NiO	0.39		0.07		b.d.l.		0.29		b.d.l.		0.42	0.40	0.09	0.11	0.05	0.06	0.28	0.23	b.d.l.	b.d.l.	0.39	0.39	0.09	0.10	0.10	0.10	0.31	0.26	b.d.l.	
MgO	47.7		32.8		14.2		17.8		19.7		47.4	47.2	31.1	32.7	13.6	14.5	16.9	16.0	19.7	19.5	48.1	48.1	32.4	32.9	13.4	13.4	16.6	18.0	20.2	
CaO	b.d.l.		0.45		20.4		b.d.l.		5.35		b.d.l.	b.d.l.	0.45	0.48	20.0	19.9	b.d.l.	0.06	4.90	5.08	b.d.l.	b.d.l.	0.45	0.40	19.5	19.5	b.d.l.	b.d.l.	5.04	
Na_2O	b.d.l.		b.d.l.		2.04		b.d.l.		b.d.l.		b.d.l.	b.d.l.	b.d.l.	0.07	2.36	1.98	b.d.l.	b.d.l.	b.d.l.	b.d.l.	b.d.l.	b.d.l.	b.d.l.	b.d.l.	2.46	2.46	b.d.l.	b.d.l.	b.d.l.	
K_2O	0.68		b.d.l.		b.d.l.		b.d.l.		b.d.l.		b.d.l.	b.d.l.	b.d.l.	b.d.l.	b.d.l.	b.d.l.	0.3	b.d.l.	b.d.l.	b.d.l.	b.d.l.	b.d.l.	b.d.l.	b.d.l.	b.d.l.	b.d.l.	b.d.l.	b.d.l.	b.d.l.	
Total	100.4		99.9		99.1		100.2		100.6		100.0	99.2	99.7	99.2	100.0	99.8	101.0	100.0	101.0	101.0	99.9	99.9	100.0	99.8	99.2	99.2	99.4	99.8	99.8	
O†	4		6		6		4		12		4	4	6	6	6	6	4	4	12	12	4	4	6	6	6	6	4	4	12	
Si	1.000		1.922		1.859		0.002		2.945		1.013	1.015	1.902	1.916	1.882	1.894	0.004	0.004	2.979	2.976	0.999	0.999	1.891	1.917	1.878	1.878	0.001	0.001	2.992	
Ti	0.000		0.003		0.020		0.002		0.008		0.000	0.000	0.006	0.004	0.021	0.022	0.003	0.002	0.010	0.011	0.000	0.000	0.004	0.004	0.017	0.017	0.003	0.002	0.013	
Altot	0.001		0.144		0.309		1.711		1.966		0.000	0.000	0.223	0.150	0.308	0.270	1.585	1.549	1.946	1.957	0.000	0.000	0.191	0.146	0.334	0.334	1.507	1.612	1.895	
^{IV}Al			0.078		0.141								0.098	0.084	0.118	0.106							0.109	0.083	0.122	0.122				
^{VI}Al			0.066		0.167								0.125	0.066	0.190	0.164							0.082	0.063	0.212	0.212				
Cr	0.000		0.008		0.026		0.291		0.064		0.000	0.000	0.015	0.010	0.029	0.028	0.407	0.458	0.065	0.060	0.000	0.000	0.014	0.011	0.029	0.029	0.459	0.369	0.069	
Fe_{tot}*	0.222		0.202		0.087		0.280		0.510		0.221	0.216	0.195	0.192	0.088	0.092	0.307	0.318	0.533	0.544	0.222	0.222	0.202	0.201	0.085	0.085	0.344	0.292	0.482	
Fe^{2+}‡					0.009				0.447						0.054	0.078			0.523	0.535					0.050	0.050			0.456	
Fe^{3+}‡					0.078				0.063						0.034	0.014			0.010	0.009					0.035	0.035			0.026	
Mn	0.005		0.005		0.002		0.005		0.024		0.003	0.003	0.004	0.004	0.003	0.002	0.004	0.003	0.022	0.024	0.003	0.003	0.004	0.002	0.004	0.004	0.005	0.004	0.022	
Mg	1.753		1.695		0.777		0.698		2.078		1.740	1.742	1.606	1.702	0.736	0.784	0.676	0.649	2.074	2.045	1.768	1.768	1.676	1.700	0.727	0.727	0.685	0.722	2.142	
Ca	0.000		0.017		0.799		0.000		0.405		0.001	0.001	0.017	0.018	0.777	0.772	0.000	0.002	0.371	0.383	0.000	0.000	0.017	0.015	0.760	0.760	0.000	0.000	0.385	
Na	0.000		0.001		0.145		0.000				0.000	0.000	0.003	0.005	0.166	0.139	0.000	0.000			0.000	0.000	0.001	0.002	0.174	0.174	0.000	0.000		
K	0.021		0.000		0.000		0.000				0.000	0.000	0.000	0.000	0.000	0.000	0.010	0.000			0.000	0.000	0.001	0.001	0.001	0.001	0.000	0.001		
Ni	0.008		0.002		0.001		0.006				0.008	0.008	0.003	0.003	0.002	0.002	0.006	0.005			0.008	0.008	0.003	0.003	0.003	0.003	0.007	0.006		
Total	3.010		3.999		4.026		2.995		8.000		2.986	2.985	3.974	4.003	4.011	4.005	3.002	2.991	8.000	8.000	3.001	3.001	4.003	4.002	4.011	4.011	3.013	3.008	8.000	
X_{Mg}**	0.887		0.894		0.899		0.714		0.823		0.887	0.890	0.891	0.899	0.893	0.895	0.688	0.671	0.799	0.793	0.889	0.889	0.892	0.894	0.896	0.896	0.666	0.712	0.825	
Cr#**							0.146										0.204	0.228									0.234	0.186		
CaTs					0.127										0.088	0.067									0.102	0.102				
Ac					0.078										0.035	0.014									0.035	0.035				
Jd					0.067										0.132	0.127									0.140	0.140				
X_{Prp}									0.706										0.697	0.688									0.718	
X_{Alm}									0.152										0.176	0.180									0.153	
X_{Grs}									0.071										0.084	0.091									0.078	
X_{Sps}									0.008										0.007	0.008									0.007	
X_{Adr}									0.063										0.035	0.032									0.044	

† Number of oxygens for which cations are calculated.

*FeO and Fe calculated as total iron.

‡ Fe^{2+} and Fe^{3+} based on garnet and clinopyroxene stoichiometry.

** X_{Mg} = Mg / (Mg + Fe^{2+}). Fe_{tot} was used for orthopyroxene, olivine and spinel. Cr# = Cr / (Cr + Al).

Ac = Fe^{3+}, CaTs = CrCaTs+AlCaTS, CrCaTs = Cr, AlCaTs = ^{VI}AlJd, Jd = NaAc (if NaAc < ^{VI}Al), Jd=^{VI}Al (if NaAc ≥ ^{VI}Al).

Major element compositions (wt. %) of minerals used for geothermobarometry

Sample	BB085W										BB087E									
Locality	Yahia1										Yahia1									
Domain	Myl										Myl									
Microstruct.	Mylonitic										Mylonitic									
Dcontact (m)	131										165									
Rock type	Lherzolite										Harzburgite									
Mineral	ol		opx		cpx		sp		grt		ol		opx		cpx		sp			
core / rim	c	r	c	r	c	r	c	r	c	r	c	r	c	r	c	r	c	r		
SiO_2	41.12		55.5		52.3		0.08		43.1		40.93	40.9	54.1	55.6	51.5	51.5	0.14	0.13		
TiO_2	b.d.l.		0.11		0.46		0.11		0.14		b.d.l.	b.d.l.	0.13	0.12	0.59	0.75	0.09	b.d.l.		
Al_2O_3	b.d.l.		3.91		5.67		55.8		23.9		b.d.l.	b.d.l.	6.23	4.23	7.83	7.90	55.5	60.3		
Cr_2O_3	b.d.l.		0.48		0.89		13.9		1.03		b.d.l.	b.d.l.	0.50	0.25	0.83	0.76	14.0	9.2		
FeO	9.823		6.38		2.46		12.0		8.29		10.4	10.4	6.48	6.72	2.69	2.45	11.7	10.4		
MnO	0.17		0.14		0.07		0.16		0.40		0.17	0.17	0.13	0.16	0.09	0.05	0.14	0.12		
NiO	0.35		0.10		b.d.l.		0.29		b.d.l.		0.39	0.39	0.11	0.08	b.d.l.	b.d.l.	0.32	0.38		
MgO	48.2		32.6		14.8		18.8		19.8		47.9	47.9	31.6	32.7	13.7	14.1	18.3	19.7		
CaO	b.d.l.		0.59		21.7		b.d.l.		5.08		b.d.l.	b.d.l.	0.38	0.49	20.3	20.7	b.d.l.	b.d.l.		
Na_2O	b.d.l.		0.06		1.67		b.d.l.		b.d.l.		b.d.l.	b.d.l.	0.05	0.07	2.14	2.00	b.d.l.	b.d.l.		
K_2O	b.d.l.		b.d.l.		b.d.l.		b.d.l.		b.d.l.		b.d.l.	b.d.l.	b.d.l.	b.d.l.	b.d.l.	b.d.l.	b.d.l.	b.d.l.		
Total	99.8		99.9		100.1		101.1		101.7		99.9	99.9	99.8	100.3	99.7	100.2	100.2	100.3		
O†	4		6		6		4		12		4	4	6	6	6	6	4	4		
Si	1.010		1.920		1.897		0.002		3.012		1.007	1.007	1.874	1.914	1.868	1.858	0.004	0.003		
Ti	0.000		0.003		0.012		0.002		0.007		0.000	0.000	0.003	0.003	0.016	0.020	0.002	0.000		
Altot	0.000		0.159		0.242		1.711		1.969		0.000	0.000	0.254	0.172	0.335	0.337	1.713	1.819		
^{IV}Al			0.080		0.103								0.126	0.086	0.132	0.142				
^{VI}Al			0.079		0.139								0.128	0.085	0.203	0.195				
Cr	0.000		0.013		0.025		0.285		0.057		0.000	0.000	0.014	0.007	0.024	0.022	0.291	0.187		
Fe_{tot}*	0.202		0.184		0.074		0.260		0.485		0.213	0.213	0.187	0.194	0.082	0.074	0.257	0.223		
Fe^{2+}‡					0.027				0.485						0.047	0.037				
Fe^{3+}‡					0.047				0.000						0.034	0.037				
Mn	0.003		0.004		0.002		0.003		0.024		0.004	0.004	0.004	0.005	0.003	0.002	0.003	0.003		
Mg	1.766		1.681		0.801		0.727		2.065		1.759	1.759	1.633	1.678	0.743	0.758	0.717	0.751		
Ca	0.000		0.022		0.843		0.000		0.381		0.001	0.001	0.014	0.018	0.789	0.801	0.000	0.000		
Na	0.001		0.004		0.117		0.000				0.001	0.001	0.003	0.005	0.151	0.140	0.000	0.000		
K	0.000		0.000		0.000		0.000				0.000	0.000	0.000	0.000	0.000	0.000	0.000	0.000		
Ni	0.007		0.003		0.001		0.006				0.008	0.008	0.003	0.002	0.001	0.001	0.007	0.008		
Total	2.991		3.993		4.015		2.998		8.000		2.993	2.993	3.990	3.996	4.011	4.012	2.993	2.994		
X_{Mg}**	0.897		0.901		0.915		0.736		0.810		0.892	0.892	0.897	0.896	0.901	0.911	0.736	0.771		
Cr#**							0.143										0.145	0.093		
CaTs					0.094										0.111	0.114				
Ac					0.047										0.034	0.037				
Jd					0.070										0.117	0.104				
X_{Prp}									0.702											
X_{Alm}									0.165											
X_{Grs}									0.098											
X_{Sps}									0.008											
X_{Adr}									0.027											

Sample	BB088b										BB122BW									
Locality	Yahia1										Yahia2									
Domain	Myl										Myl									
Microstruct.	Mylonitic										Mylonitic									
Dcontact (m)	169										116									
Rock type	Lherzolite										Lherzolite									
Mineral	ol		opx		cpx		sp				ol		opx		cpx		sp			
core / rim	c	r	c	r	c	r	c	r			c	r	c	r	c	r	c	r		
SiO_2	41.33		54.4	55.8	51.9	53.0	0.08				40.78		55.4	54.8	52.7	52.7	0.17	0.14		
TiO_2	b.d.l.		0.09	b.d.l.	0.37	0.40	0.14				b.d.l.		0.13	0.14	0.45	0.45	0.17	0.13		
Al_2O_3	b.d.l.		6.04	4.41	7.43	5.94	53.2				b.d.l.		4.17	4.65	4.66	4.66	54.2	51.9		
Cr_2O_3	b.d.l.		0.65	0.49	1.12	0.79	15.0				b.d.l.		0.47	0.53	0.71	0.71	16.3	16.9		
FeO	9.609		6.08	6.13	2.45	2.39	12.4				9.51		6.28	6.36	2.42	2.42	12.0	12.0		
MnO	0.14		0.16	0.15	0.08	0.09	0.12				0.14		0.14	0.16	0.09	0.09	0.12	0.10		
NiO	0.39		0.08	0.09	b.d.l.	b.d.l.	0.29				0.38		0.08	0.12	0.05	0.05	0.27	0.25		
MgO	48.5		31.6	32.5	14.0	14.6	18.8				48.4		33.1	32.4	15.6	15.6	18.0	18.4		
CaO	b.d.l.		0.52	0.41	20.5	21.1	b.d.l.				b.d.l.		0.52	0.41	21.8	21.8	b.d.l.	b.d.l.		
Na_2O	b.d.l.		0.05	b.d.l.	2.04	1.78	b.d.l.				b.d.l.		b.d.l.	b.d.l.	1.41	1.41	b.d.l.	b.d.l.		
K_2O	b.d.l.		b.d.l.	b.d.l.	b.d.l.	b.d.l.	b.d.l.				b.d.l.		b.d.l.	b.d.l.	b.d.l.	b.d.l.	b.d.l.	b.d.l.		
Total	100.0		99.7	100.1	100.0	100.0	100.1				99.2		100.3	99.7	99.9	99.9	101.2	99.8		
O†	4		6	6	6	6	4				4		6	6	6	6	4	4		
Si	1.011		1.883	1.921	1.878	1.914	0.002				1.006		1.908	1.901	1.914	1.914	0.005	0.004		
Ti	0.000		0.002	0.001	0.010	0.011	0.003				0.000		0.003	0.004	0.012	0.012	0.003	0.003		
Altot	0.000		0.246	0.179	0.317	0.253	1.662				0.000		0.169	0.190	0.199	0.199	1.672	1.630		
^{IV}Al			0.117	0.079	0.122	0.086							0.092	0.099	0.086	0.086				
^{VI}Al			0.129	0.099	0.195	0.167							0.077	0.091	0.113	0.113				
Cr	0.000		0.018	0.013	0.032	0.023	0.315				0.000		0.013	0.015	0.020	0.020	0.337	0.357		
Fe_{tot}*	0.197		0.176	0.176	0.074	0.072	0.275				0.196		0.181	0.184	0.073	0.073	0.262	0.267		
Fe^{2+}‡					0.047	0.072									0.031	0.031				
Fe^{3+}‡					0.027	0.000									0.042	0.042				
Mn	0.003		0.005	0.004	0.002	0.003	0.003				0.003		0.004	0.005	0.003	0.003	0.003	0.002		
Mg	1.770		1.631	1.669	0.757	0.784	0.740				1.779		1.696	1.676	0.843	0.843	0.700	0.732		
Ca	0.001		0.019	0.015	0.795	0.816	0.000				0.000		0.019	0.015	0.849	0.849	0.000	0.000		
Na	0.000		0.004	0.002	0.143	0.125	0.000				0.000		0.003	0.002	0.099	0.099	0.000	0.000		
K	0.000		0.000	0.000	0.000	4.607	0.000				0.000		0.000	0.000	0.000	0.000	0.000	0.000		
Ni	0.008		0.002	0.003	0.001	0.001	0.006				0.007		0.002	0.003	0.001	0.001	0.006	0.005		
Total	2.989		3.985	3.983	4.009	4.000	3.006				2.994		4.000	3.995	4.014	4.014	2.988	3.000		
X_{Mg}**	0.900		0.903	0.904	0.911	0.916	0.729				0.901		0.904	0.901	0.920	0.920	0.728	0.732		
Cr#**							0.159										0.168	0.180		
CaTs					0.111	0.065									0.076	0.076				
Ac					0.027	0.000									0.042	0.042				
Jd					0.116	0.126									0.057	0.057				

† Number of oxygens for which cations are calculated.

*FeO and Fe calculated as total iron.

‡ Fe^{2+} and Fe^{3+} based on garnet and clinopyroxene stoichiometry.

** $X_{Mg} = Mg / (Mg + Fe^{2+})$. Fe_{tot} was used for orthopyroxene, olivine and spinel. Cr# = Cr / (Cr + Al).

Ac = Fe^{3+}, CaTs = CrCaTs+AlCaTS. CrCaTs = Cr, AlCaTs = ^{VI}AlJd, Jd = NaAc (if NaAc < ^{VI}Al), Jd=^{VI}Al (if NaAc ≥ ^{VI}Al).

Major element compositions (wt. %) of minerals used for geothermobarometry

Sample	BB171AW										BB201E										BB026W										BB035DW									
Locality	Nich1										Amaziten										Aarkob										Aarkob									
Domain	Myl										Myl										Ar										Ar									
Microstruct.	Mylonitic										Mylonitic										Fine porph.										Fine porph.									
Dcontact (m)	317										1										306										327									
Rock type	Harzburgite										Cpx rich lhz.										Harzburgite										Harzburgite									
Mineral	ol		opx		cpx		sp		grt		ol		opx		cpx		sp		ol		opx		cpx		sp		ol		opx		cpx		sp			
core / rim	c	r	c	r	c	r	c	r	c	r	c	r	c	r	c	r	c	r	c	r	c	r	c	r	c	r	c	r	c	r	c	r	c	r	c	r		
SiO_2	41.19	41.6	56.2	56.2	52.6	52.6	0.13	0.11	43.1	42.6	41.23		55.6	56.2	53.4	53.4	0.13	0.13	41.42		55.2	55.2	52.4	53.4	0.10	0.10	41.07	41.2	56.2	56.7	52.9	56.8	0.15	0.12		
TiO_2	b.d.l.	b.d.l.	0.06	0.09	0.88	0.75	0.16	0.14	0.23	0.17	b.d.l.		0.05	b.d.l.	0.11	0.11	b.d.l.	b.d.l.	b.d.l.		b.d.l.	b.d.l.	0.14	0.13	b.d.l.	b.d.l.	b.d.l.	b.d.l.	b.d.l.	b.d.l.	0.08	b.d.l.	0.15	0.15		
Al_2O_3	b.d.l.	b.d.l.	4.08	4.04	6.58	6.32	50.9	53.8	24.1	23.9	b.d.l.		3.93	3.18	4.00	4.00	49.5	49.5	b.d.l.		5.10	4.97	5.28	4.87	56.3	56.3	b.d.l.	b.d.l.	2.28	1.92	2.14	1.88	21.9	21.9		
Cr_2O_3	b.d.l.	b.d.l.	0.26	0.25	0.48	0.50	17.5	16.0	0.55	0.48	b.d.l.		0.57	0.29	0.90	0.90	20.4	20.4	b.d.l.		0.67	0.55	0.88	0.76	13.7	13.7	b.d.l.	b.d.l.	0.72	0.54	0.88	0.50	43.6	43.1		
FeO	10.62	10.56	6.85	6.79	3.23	3.34	14.0	12.7	8.39	8.65	9.962		6.04	6.38	2.41	2.41	12.3	12.3	9.563		6.13	6.25	2.29	2.37	11.3	11.3	8.70	8.76	5.62	5.81	2.20	5.82	22.2	22.8		
MnO	0.14	0.16	0.14	0.14	0.06	0.08	0.13	0.14	0.29	0.34	0.12		0.11	0.14	0.07	0.07	0.17	0.17	0.13		0.13	0.16	0.08	0.07	0.11	0.11	0.12	0.11	0.15	0.14	0.08	0.14	0.24	0.31		
NiO	0.39	0.39	0.09	0.06	0.06	b.d.l.	0.30	0.3	b.d.l.	b.d.l.	0.40		0.10	0.09	b.d.l.	b.d.l.	0.21	0.21	0.40		0.11	0.08	b.d.l.	b.d.l.	0.28	0.28	0.42	0.42	0.08	0.08	b.d.l.	0.06	0.12	0.10		
MgO	47.7	48.0	32.2	32.0	14.2	14.5	17.0	17.6	19.8	19.7	48.7		32.8	33.7	16.0	16.0	17.6	17.6	48.3		32.0	32.2	15.4	16.0	18.6	18.6	49.4	49.0	33.6	33.8	16.6	33.8	12.1	11.9		
CaO	b.d.l.	b.d.l.	0.40	0.37	20.4	20.7	b.d.l.	b.d.l.	4.76	4.74	b.d.l.		1.06	0.43	21.6	21.6	b.d.l.	b.d.l.	b.d.l.		0.48	0.62	22.3	21.9	b.d.l.	b.d.l.	b.d.l.	b.d.l.	0.59	0.49	23.8	0.47	b.d.l.	b.d.l.		
Na_2O	b.d.l.	b.d.l.	b.d.l.	b.d.l.	1.61	1.38	b.d.l.	b.d.l.	b.d.l.	b.d.l.	b.d.l.		b.d.l.	b.d.l.	1.14	1.14	b.d.l.	b.d.l.	b.d.l.		b.d.l.	b.d.l.	1.06	1.03	b.d.l.	b.d.l.	b.d.l.	b.d.l.	b.d.l.	b.d.l.	0.58	b.d.l.	b.d.l.	b.d.l.		
K_2O	b.d.l.	b.d.l.	b.d.l.	b.d.l.	b.d.l.	b.d.l.	b.d.l.	b.d.l.	b.d.l.	b.d.l.	b.d.l.		b.d.l.	b.d.l.	b.d.l.	b.d.l.	b.d.l.	b.d.l.	b.d.l.		b.d.l.	b.d.l.	b.d.l.	b.d.l.	b.d.l.	b.d.l.	b.d.l.	b.d.l.	b.d.l.	b.d.l.	b.d.l.	b.d.l.	b.d.l.	b.d.l.		
Total	100.1	100.7	100.3	100.0	100.1	100.1	100.0	100.7	101.3	100.7	100.4		100.2	100.5	99.7	99.7	100.4	100.4	99.8		99.8	100.1	99.9	100.6	100.4	100.4	99.7	99.5	99.2	99.4	99.3	99.6	100.3	100.4		
O†	4	4	6	6	6	6	4	4	12	12	4		6	6	6	6	4	4	4		6	6	6	6	4	4	4	4	6	6	6	6	4	4		
Si	1.012	1.014	1.934	1.934	1.901	1.900	0.003	0.003	3.026	3.009	1.007		1.915	1.930	1.937	1.937	0.003	0.003	1.015		1.905	1.903	1.903	1.919	0.003	0.003	1.005	1.009	1.950	1.962	1.941	1.964	0.005	0.004		
Ti	0.000	0.000	0.001	0.001	0.024	0.021	0.003	0.003	0.012	0.009	0.000		0.001	0.001	0.003	0.003	0.001	0.001	0.000		0.001	0.001	0.004	0.004	0.000	0.000	0.000	0.000	0.001	0.000	0.002	0.001	0.004	0.004		
Altot	0.001	0.000	0.166	0.166	0.280	0.269	1.615	1.673	1.991	1.990	0.000		0.160	0.129	0.171	0.171	1.567	1.567	0.000		0.207	0.202	0.226	0.206	1.730	1.730	0.000	0.000	0.093	0.078	0.093	0.076	0.807	0.810		
^{IV}Al			0.066	0.066	0.099	0.100							0.085	0.070	0.063	0.063					0.095	0.097	0.097	0.081					0.050	0.038	0.059	0.036				
^{VI}Al			0.100	0.100	0.181	0.169							0.075	0.059	0.109	0.109					0.113	0.105	0.129	0.125					0.043	0.040	0.033	0.040				
Cr	0.000	0.001	0.007	0.007	0.014	0.014	0.373	0.334	0.031	0.027	0.000		0.015	0.008	0.026	0.026	0.434	0.434	0.000		0.018	0.015	0.025	0.022	0.283	0.283	0.000	0.000	0.020	0.015	0.025	0.014	1.080	1.070		
Fe_{tot}*	0.218	0.215	0.197	0.197	0.098	0.101	0.314	0.279	0.492	0.511	0.203		0.174	0.183	0.073	0.073	0.277	0.277	0.196		0.177	0.180	0.069	0.071	0.246	0.246	0.178	0.180	0.163	0.168	0.067	0.169	0.580	0.598		
Fe^{2+}‡					0.098	0.101			0.492	0.511					0.070	0.070							0.054	0.071							0.011	0.169				
Fe^{3+}‡					0.000	0.000			0.000	0.000					0.003	0.003							0.016	0.000							0.057	0.000				
Mn	0.003	0.003	0.004	0.004	0.002	0.002	0.003	0.003	0.017	0.020	0.003		0.003	0.004	0.002	0.002	0.004	0.004	0.003		0.004	0.005	0.003	0.002	0.002	0.002	0.002	0.002	0.004	0.004	0.003	0.004	0.006	0.008		
Mg	1.745	1.745	1.651	1.651	0.763	0.781	0.682	0.691	2.073	2.076	1.772		1.684	1.727	0.867	0.867	0.703	0.703	1.764		1.647	1.656	0.832	0.857	0.721	0.721	1.800	1.791	1.737	1.743	0.910	1.743	0.563	0.555		
Ca	0.000	0.000	0.015	0.015	0.790	0.801	0.000	0.000	0.358	0.359	0.000		0.039	0.016	0.841	0.841	0.001	0.001	0.000		0.018	0.023	0.867	0.844	0.000	0.000	0.000	0.001	0.022	0.018	0.936	0.017	0.000	0.000		
Na	0.001	0.000	0.001	0.001	0.112	0.096	0.000	0.000			0.000		0.003	0.001	0.080	0.080	0.000	0.000	0.000		0.001	0.002	0.075	0.072	0.000	0.000	0.001	0.001	0.000	0.002	0.041	0.001	0.000	0.001		
K	0.000	0.000	0.000	0.000	0.000	0.000	0.000	0.000			0.000		0.000	0.000	0.000	0.000	0.000	0.000	0.000		0.000	0.000	0.000	0.000	0.000	0.000	0.000	0.000	0.000	0.000	0.000	0.000	0.000	0.000		
Ni	0.008	0.008	0.002	0.002	0.002	0.001	0.006	0.006			0.008		0.003	0.003	0.001	0.001	0.005	0.005	0.008		0.003	0.002	0.001	0.001	0.006	0.006	0.008	0.008	0.002	0.002	0.001	0.002	0.003	0.003		
Total	2.988	2.986	3.979	3.979	3.985	3.987	3.000	2.991	8.000	8.000	2.993		3.997	4.001	4.001	4.001	2.995	2.995	2.985		3.982	3.989	4.005	3.999	2.991	2.991	2.996	2.992	3.993	3.992	4.019	3.991	3.048	3.053		
X_{Mg}**	0.889	0.890	0.893	0.893	0.886	0.885	0.685	0.712	0.808	0.803	0.897		0.906	0.904	0.922	0.922	0.717	0.717	0.900		0.903	0.902	0.923	0.923	0.746	0.746	0.910	0.909	0.914	0.912	0.931	0.912	0.492	0.481		
Cr#**							0.187	0.166									0.217	0.217							0.140	0.140							0.572	0.569		
CaTs					0.084	0.088									0.058	0.058							0.095	0.075							0.073	0.053				
Ac					0.000	0.000									0.003	0.003							0.016	0.000							0.041	0.000				
Jd					0.115	0.098									0.077	0.077							0.059	0.072							0.000	0.001				
X_{Prp}									0.709	0.703																										
X_{Alm}									0.168	0.173																										
X_{Grs}									0.104	0.105																										
X_{Sps}									0.006	0.007																										
X_{Adr}									0.013	0.011																										

† Number of oxygens for which cations are calculated.

*FeO and Fe calculated as total iron.

‡ Fe^{2+} and Fe^{3+} based on garnet and clinopyroxene stoichiometry.

** $X_{Mg} = Mg / (Mg + Fe^{2+})$. Fe_{tot} was used for orthopyroxene, olivine and spinel. Cr# = Cr / (Cr + Al).

Ac = Fe^{3+}, CaTs = CrCaTs+AlCaTS, CrCaTs = Cr, AlCaTs = ^{VI}AlJd, Jd = NaAc (if NaAc < ^{VI}Al), Jd=^{VI}Al (if NaAc ≥ ^{VI}Al).

Major element compositions (wt. %) of minerals used for geothermobarometry

Sample	BB095AW								BB098E								BB102E								BB183AW							
Locality	Yahia1								Yahia1								Yahia1								Amaziten							
Domain	Ar								Ar								Ar								Ar							
Microstruct.	Fine porph.								Fine porph.								Fine porph.								Fine porph.							
Dcontact (m)	260								426								555								583							
Rock type	Cpx rich lhz.								Lherzolite								Lherzolite								Cpx rich lhz.							
Mineral	ol		opx		cpx		sp		ol		opx		cpx		sp		ol		opx		cpx		sp		ol		opx		cpx		sp	
core / rim	c	r	c	r	c	r	c	r	c	r	c	r	c	r	c	r	c	r	c	r	c	r	c	r	c	r	c	r	c	r	c	r
SiO_2	40.73		54.1		51.7		0.06		41.21		54.8	56.8	52.4	53.0	0.08	0.08	41.2	41.24	54.0	54.1	51.9	52.5	0.02		41.0		55.2	55.8	51.7		0.03	
TiO_2	b.d.l.		0.13		0.45		0.10		b.d.l.		0.14	0.11	0.54	0.56	0.18	0.20	b.d.l.	b.d.l.	0.09	0.11	0.29	0.35	0.11		b.d.l.		0.14	0.13	0.54		b.d.l.	
Al_2O_3	b.d.l.		6.00		7.42		56.5		b.d.l.		5.33	2.51	7.07	6.27	52.4	51.9	b.d.l.	b.d.l.	5.74	4.69	6.84	5.49	54.5		b.d.l.		4.78	3.94	7.82		56.6	
Cr_2O_3	b.d.l.		0.62		0.97		11.0		b.d.l.		0.73	0.26	1.44	1.14	15.6	16.8	0.063	b.d.l.	0.73	0.53	1.16	0.80	14.6		b.d.l.		0.40	0.32	0.95		12.6	
FeO	11.0		6.89		2.49		11.5		9.86		6.16	6.43	2.46	2.39	12.7	13.2	9.206	9.233	5.82	6.09	2.35	2.16	11.1		10.31		6.36	6.54	2.62		11.7	
MnO	0.12		0.15		0.08		0.12		0.14		0.13	0.16	0.08	0.09	0.13	0.14	0.127	0.125	0.11	0.18	0.09	0.06	0.14		0.149		0.14	0.16	0.10		0.13	
NiO	0.37		0.08		0.06		0.37		0.38		0.07	0.09	b.d.l.	b.d.l.	0.32	0.31	0.355	0.364	0.08	0.11	b.d.l.	b.d.l.	0.30		0.39		0.11	0.09	b.d.l.		0.35	
MgO	48.0		31.6		14.0		19.4		48.4		32.0	33.3	14.2	14.3	18.5	17.1	49.0	48.77	32.1	32.1	14.6	15.0	19.3		48.3		32.1	32.7	13.7		19.0	
CaO	b.d.l.		0.58		20.4		b.d.l.		b.d.l.		0.51	0.44	19.8	20.9	b.d.l.	b.d.l.	b.d.l.	b.d.l.	0.61	0.93	20.5	21.4	b.d.l.		b.d.l.		0.74	0.44	20.1		b.d.l.	
Na_2O	b.d.l.		0.06		1.90		b.d.l.		b.d.l.		0.07	b.d.l.	2.20	1.88	b.d.l.	b.d.l.	b.d.l.	b.d.l.	b.d.l.	0.05	1.66	1.49	b.d.l.		b.d.l.		0.10	b.d.l.	2.01		b.d.l.	
K_2O	b.d.l.		b.d.l.		b.d.l.		b.d.l.		b.d.l.		b.d.l.	b.d.l.	b.d.l.	b.d.l.	b.d.l.	b.d.l.	b.d.l.	b.d.l.	b.d.l.	b.d.l.	b.d.l.	b.d.l.	b.d.l.		b.d.l.		b.d.l.	b.d.l.	b.d.l.		b.d.l.	
Total	100.4		100.3		99.5		99.1		100.1		100.0	100.2	100.3	100.6	99.9	99.7	100.0	99.78	99.3	98.9	99.4	99.4	100.1		100.2		100.1	100.1	99.5		100.4	
O†	4	4	6	6	6	6	4	4	4	4	6	6	6	6	4	4	4	4	6	6	6	6	4		4		6	6	6		4	
Si	1.001	1.001	1.871	1.871	1.879	1.879	0.002	0.002	1.009	1.009	1.893	1.956	1.888	1.906	0.002	0.002	1.007	1.010	1.875	1.893	1.886	1.912	0.000		1.005		1.905	1.922	1.875		0.001	
Ti	0.000	0.000	0.003	0.003	0.012	0.012	0.002	0.002	0.000	0.000	0.004	0.003	0.015	0.015	0.004	0.004	0.000	0.000	0.002	0.003	0.008	0.010	0.002		0.000		0.004	0.003	0.015		0.000	
Altot	0.000	0.000	0.245	0.245	0.318	0.318	1.749	1.749	0.001	0.001	0.217	0.102	0.300	0.266	1.645	1.642	0.000	0.000	0.235	0.194	0.293	0.235	1.686		0.000		0.194	0.160	0.334		1.738	
^{IV}Al			0.129	0.129	0.121	0.121					0.107	0.044	0.112	0.094					0.125	0.107	0.114	0.088					0.095	0.078	0.125			
^{VI}Al			0.115	0.115	0.197	0.197					0.110	0.057	0.188	0.172					0.110	0.086	0.179	0.147					0.100	0.082	0.209			
Cr	0.000	0.000	0.017	0.017	0.028	0.028	0.229	0.229	0.000	0.000	0.020	0.007	0.041	0.032	0.330	0.357	0.001	0.000	0.020	0.015	0.033	0.023	0.303		0.000		0.011	0.009	0.027		0.259	
Fe_{tot}*	0.226	0.226	0.199	0.199	0.075	0.075	0.254	0.254	0.202	0.202	0.178	0.185	0.074	0.072	0.283	0.296	0.188	0.189	0.169	0.178	0.071	0.066	0.244		0.212		0.184	0.189	0.079		0.254	
Fe^{2+}‡					0.068	0.068							0.063	0.072							0.068	0.059							0.079			
Fe^{3+}‡					0.007	0.007							0.012	0.000							0.003	0.007							0.000			
Mn	0.003	0.003	0.004	0.004	0.003	0.003	0.003	0.003	0.003	0.003	0.004	0.005	0.003	0.003	0.003	0.003	0.003	0.003	0.003	0.005	0.003	0.002	0.003		0.003		0.004	0.005	0.003		0.003	
Mg	1.761	1.761	1.630	1.630	0.757	0.757	0.761	0.761	1.767	1.767	1.646	1.711	0.765	0.765	0.733	0.683	1.786	1.780	1.665	1.673	0.792	0.813	0.757		1.766		1.653	1.683	0.744		0.738	
Ca	0.000	0.000	0.021	0.021	0.794	0.794	0.000	0.000	0.001	0.001	0.019	0.016	0.763	0.804	0.000	0.000	0.000	0.000	0.023	0.035	0.797	0.836	0.000		0.001		0.028	0.016	0.780		0.000	
Na	0.000	0.000	0.004	0.004	0.134	0.134	0.000	0.000	0.000	0.000	0.005	0.001	0.154	0.131	0.000	0.000	0.001	0.000	0.003	0.003	0.117	0.105	0.000		0.000		0.007	0.001	0.142		0.000	
K	0.001	0.001	0.001	0.001	0.001	0.001	0.000	0.000	0.000	0.000	0.000	0.000	0.000	0.000	0.000	0.000	0.000	0.000	0.000	0.000	0.000	0.000	0.000		0.000		0.000	0.000	0.000		0.000	
Ni	0.007	0.007	0.002	0.002	0.002	0.002	0.008	0.008	0.007	0.007	0.002	0.002	0.001	0.001	0.007	0.007	0.007	0.007	0.002	0.003	0.000	0.001	0.006		0.008		0.003	0.003	0.001		0.007	
Total	2.999	2.999	3.998	3.998	4.002	4.002	3.008	3.008	2.990	2.990	3.987	3.988	4.004	3.995	3.007	2.994	2.993	2.990	3.997	4.002	4.001	4.002	3.003		2.995		3.992	3.991	4.000		3.000	
X_{Mg}**	0.886	0.886	0.891	0.891	0.909	0.909	0.750	0.750	0.897	0.897	0.902	0.902	0.912	0.914	0.722	0.698	0.905	0.904	0.908	0.904	0.917	0.925	0.756		0.893		0.900	0.899	0.904		0.744	
Cr#**							0.116	0.116							0.167	0.179							0.152								0.130	
CaTs					0.100	0.100							0.088	0.074							0.100	0.072							0.096			
Ac					0.008	0.008							0.012	0.000							0.003	0.007							0.000			
Jd					0.127	0.127							0.143	0.132							0.114	0.099							0.143			

† Number of oxygens for which cations are calculated.

*FeO and Fe calculated as total iron.

‡ Fe^{2+} and Fe^{3+} based on clinopyroxene stoichiometry.

** $X_{Mg} = Mg / (Mg + Fe^{2+})$. Fe_{tot} was used for orthopyroxene, olivine and spinel. Cr# = Cr / (Cr + Al).

Ac = Fe^{3+}, CaTs = CrCaTs+AlCaTS, CrCaTs = Cr, AlCaTs = ^{VI}AlJd, Jd = NaAc (if NaAc < ^{VI}Al), Jd=^{VI}Al (if NaAc ≥ ^{VI}Al).

Major element compositions (wt. %) of minerals used for geothermobarometry

Sample	BB187AW								BB191E							
Locality	Amaziten								Amaziten							
Domain	Ar								Ar							
Microstruct.	Fine porph.								Fine porph.							
Dcontact (m)	271								225							
Rock type	Lherzolite								Cpx rich lhz.							
Mineral	ol		opx		cpx		sp		ol		opx		cpx		sp	
core / rim	c	r	c	r	c	r	c	r	c	r	c	r	c	r	c	r
SiO_2	40.7		55.0		52.0		0.05		40.9		55.8		51.7		0.05	
TiO_2	b.d.l.		0.09		0.56		0.09		b.d.l.		b.d.l.		0.23		0.06	
Al_2O_3	b.d.l.		4.15		7.30		56.5		b.d.l.		3.52		6.67		55.3	
Cr_2O_3	b.d.l.		0.34		1.01		12.5		b.d.l.		0.32		1.03		14.1	
FeO	10.23		6.76		2.63		11.8		9.437		6.51		2.30		11.3	
MnO	0.152		0.12		0.10		0.12		0.165		0.17		0.10		0.13	
NiO	0.375		0.06		b.d.l.		0.38		0.382		0.10		b.d.l.		0.32	
MgO	48.9		32.8		14.1		19.3		49.0		33.4		14.8		19.3	
CaO	b.d.l.		0.5		19.7		b.d.l.		b.d.l.		0.43		21.4		b.d.l.	
Na_2O	b.d.l.		0.05		2.45		b.d.l.		b.d.l.		b.d.l.		1.53		b.d.l.	
K_2O	b.d.l.		b.d.l.		b.d.l.		b.d.l.		b.d.l.		b.d.l.		b.d.l.		b.d.l.	
Total	100.3		99.9		99.8		100.7		100.0		100.3		99.8		100.5	
O†	4		6		6		4		4		6		6		4	
Si	0.997		1.905		1.883		0.001		1.002		1.922		1.877		0.001	
Ti	0.000		0.002		0.015		0.002		0.000		0.001		0.006		0.001	
Altot	0.000		0.170		0.312		1.729		0.000		0.143		0.285		1.701	
^{IV}Al			0.095		0.117						0.078		0.123			
^{VI}Al			0.075		0.195						0.065		0.162			
Cr	0.000		0.009		0.029		0.256		0.000		0.009		0.030		0.290	
Fe_{tot}*	0.210		0.196		0.079		0.256		0.193		0.187		0.070		0.246	
Fe^{2+}‡					0.027								0.030			
Fe^{3+}‡					0.052								0.040			
Mn	0.003		0.004		0.003		0.003		0.003		0.005		0.003		0.003	
Mg	1.786		1.695		0.760		0.749		1.790		1.715		0.801		0.752	
Ca	0.000		0.019		0.763		0.000		0.000		0.016		0.833		0.000	
Na	0.000		0.004		0.172		0.000		0.000		0.000		0.107		0.000	
K	0.000		0.000		0.000		0.000		0.000		0.000		0.000		0.000	
Ni	0.007		0.002		0.001		0.008		0.008		0.003		0.001		0.007	
Total	3.003		4.005		4.017		3.004		2.998		4.001		4.013		3.002	
X_{Mg}**	0.895		0.896		0.905		0.745		0.903		0.901		0.920		0.754	
Cr#**							0.129								0.146	
CaTs					0.104								0.124			
Ac					0.052								0.039			
Jd					0.120								0.068			

Sample	BB204W								BB207W							
Locality	Nich1								Nich1							
Domain	Ar								Ar							
Microstruct.	Fine porph.								Fine porph.							
Dcontact (m)	490								666							
Rock type	Cpx rich lhz.								Lherzolite							
Mineral	ol		opx		cpx		sp		ol		opx		cpx		sp	
core / rim	c	r	c	r	c	r	c	r	c	r	c	r	c	r	c	r
SiO_2	41.2	41.1	53.8	54.9	51.7	51.7	0.10	0.06	41.6	41.6	55.5	56.0	52.0	51.7	0.10	0.09
TiO_2	b.d.l.	b.d.l.	0.20	0.13	0.56	0.55	0.06	0.09	b.d.l.	b.d.l.	b.d.l.	b.d.l.	0.17	0.55	0.06	b.d.l.
Al_2O_3	b.d.l.	b.d.l.	6.46	5.42	7.47	7.12	58.5	58.5	b.d.l.	b.d.l.	4.52	3.86	6.42	7.12	54.1	56.9
Cr_2O_3	b.d.l.	b.d.l.	0.52	0.43	0.78	0.66	9.72	10.2	b.d.l.	b.d.l.	0.45	0.34	1.17	0.66	14.3	12.1
FeO	10.31	10.19	6.30	6.50	2.88	2.75	12.4	12.6	9.411	9.411	6.19	6.18	2.77	2.75	12.6	11.7
MnO	0.146	0.121	0.13	0.16	0.06	0.10	0.10	0.12	0.114	0.114	0.14	0.15	0.08	0.10	0.15	0.14
NiO	0.389	0.347	0.12	0.10	b.d.l.	b.d.l.	0.35	0.37	0.394	0.394	0.09	0.09	b.d.l.	b.d.l.	0.34	0.33
MgO	47.6	48.0	30.5	31.9	13.6	14.0	19.3	18.6	48.4	48.4	32.3	32.7	14.5	14.0	18.8	19.5
CaO	b.d.l.	b.d.l.	1.97	0.52	20.5	20.6	b.d.l.	b.d.l.	b.d.l.	b.d.l.	0.65	0.47	21.2	20.6	b.d.l.	b.d.l.
Na_2O	b.d.l.	b.d.l.	0.20	0.06	1.92	1.91	b.d.l.	b.d.l.	b.d.l.	b.d.l.	b.d.l.	b.d.l.	1.46	1.91	b.d.l.	b.d.l.
K_2O	b.d.l.	b.d.l.	b.d.l.	b.d.l.	b.d.l.	b.d.l.	b.d.l.	b.d.l.	b.d.l.	b.d.l.	b.d.l.	b.d.l.	b.d.l.	b.d.l.	b.d.l.	b.d.l.
Total	99.7	99.83	100.1	100.1	99.5	99.5	100.6	100.6	99.9	99.95	99.9	99.9	99.8	99.5	100.4	100.8
O†	4	4	6	6	6	6	4	4	4	4	6	6	6	6	4	4
Si	1.014	1.010	1.938	1.865	1.881	1.880	0.003	0.002	1.017	1.017	1.915	1.931	1.891	1.880	0.003	0.002
Ti	0.000	0.000	0.002	0.005	0.015	0.015	0.001	0.002	0.000	0.000	0.001	0.001	0.005	0.015	0.001	0.001
Altot	0.000	0.000	0.164	0.264	0.320	0.306	1.782	1.786	0.000	0.000	0.184	0.157	0.275	0.306	1.679	1.737
^{IV}Al			0.062	0.135	0.119	0.120					0.085	0.069	0.109	0.120		
^{VI}Al			0.102	0.129	0.202	0.186					0.099	0.088	0.166	0.186		
Cr	0.001	0.000	0.007	0.014	0.023	0.019	0.199	0.209	0.000	0.000	0.012	0.009	0.034	0.019	0.299	0.248
Fe_{tot}*	0.212	0.209	0.196	0.183	0.088	0.084	0.269	0.273	0.192	0.192	0.179	0.178	0.084	0.084	0.278	0.254
Fe^{2+}‡					0.088	0.054							0.078	0.054		
Fe^{3+}‡					0.000	0.030							0.006	0.030		
Mn	0.003	0.003	0.004	0.004	0.002	0.003	0.002	0.003	0.002	0.002	0.004	0.004	0.003	0.003	0.003	0.003
Mg	1.748	1.760	1.647	1.574	0.736	0.762	0.743	0.717	1.763	1.763	1.664	1.683	0.783	0.762	0.737	0.752
Ca	0.000	0.000	0.014	0.073	0.798	0.805	0.000	0.000	0.000	0.000	0.024	0.017	0.824	0.805	0.000	0.000
Na	0.000	0.000	0.001	0.013	0.136	0.135	0.000	0.000	0.001	0.001	0.003	0.001	0.103	0.135	0.000	0.000
K	0.000	0.000	0.000	0.000	0.000	0.000	0.000	0.000	0.000	0.000	0.000	0.000	0.000	0.000	0.000	0.000
Ni	0.008	0.007	0.002	0.003	0.001	0.001	0.007	0.008	0.008	0.008	0.002	0.003	0.001	0.001	0.007	0.007
Total	2.986	2.990	3.975	3.998	4.000	4.010	3.006	2.999	2.983	2.983	3.988	3.986	4.002	4.010	3.007	3.004
X_{Mg}**	0.892	0.894	0.894	0.896	0.894	0.901	0.734	0.724	0.902	0.902	0.903	0.904	0.903	0.901	0.726	0.747
Cr#**							0.100	0.105							0.151	0.125
CaTs					0.089	0.100							0.103	0.100		
Ac					0.000	0.030							0.006	0.030		
Jd					0.137	0.106							0.097	0.106		

† Number of oxygens for which cations are calculated.

*FeO and Fe calculated as total iron.

‡ Fe^{2+} and Fe^{3+} based on clinopyroxene stoichiometry.

** $X_{Mg} = Mg / (Mg + Fe^{2+})$. Fe_{tot} was used for orthopyroxene, olivine and spinel. Cr# = Cr / (Cr + Al).

Ac = Fe^{3+}, CaTs = CrCaTs+AlCaTS, CrCaTs = Cr, AlCaTs = ^{VI}AlJd, Jd = NaAc (if NaAc < ^{VI}Al), Jd=^{VI}Al (if NaAc ≥ ^{VI}Al).

Major element compositions (wt. %) of minerals used for geothermobarometry

Sample	BB070E								BB076CBE								BB078W								BB079E							
Locality	Yahia1								Yahia1								Yahia1								Yahia1							
Domain	ArSe								ArSe								ArSe								ArSe							
Microstruct.	Coarse porph.								Coarse porph.								Coarse porph.								Coarse porph.							
Dcontact (m)	1139								1084								903								872							
Rock type	Harzburgite								Cpx rich lhz.								Lherzolite								Cpx rich lhz.							
Mineral	ol		opx		cpx		sp		ol		opx		cpx		sp		ol		opx		cpx		sp		ol		opx		cpx		sp	
core / rim	c	r	c	r	c	r	c	r	c	r	c	r	c	r	c	r	c	r	c	r	c	r	c	r	c	r	c	r	c	r	c	r
SiO_2	41.0	40.9	55.3	56.2	52.8	52.6	0.04	0.04	41.6	40.8	54.2	54.5	51.6	52	0.09	0.10	41.7	41.1	53.8	56.1	49.7	50	0.23	0.08	41.4	41.7	55.0	55.0	51.7	52.1	0.07	0.06
TiO_2	b.d.l.	b.d.l.	0.06	b.d.l.	0.10	0.17	0.11	0.07	b.d.l.	b.d.l.	0.15	0.17	0.59	0.60	0.08	0.08	b.d.l.	b.d.l.	0.11	b.d.l.	0.36	0.37	0.06	b.d.l.	b.d.l.	b.d.l.	0.17	0.14	0.49	0.43	0.05	0.08
Al_2O_3	b.d.l.	b.d.l.	3.61	2.53	4.07	3.94	36.5	45.4	b.d.l.	b.d.l.	6.45	5.02	7.97	7.68	57.6	58.6	b.d.l.	b.d.l.	5.90	2.79	7.51	7.13	53.7	55.0	b.d.l.	b.d.l.	6.40	6.18	7.79	8.01	57.9	59.6
Cr_2O_3	b.d.l.	b.d.l.	0.86	0.47	1.56	1.48	31.1	21.7	b.d.l.	b.d.l.	0.55	0.44	0.92	0.90	10.8	10.2	b.d.l.	b.d.l.	0.78	0.32	1.28	1.16	14.9	14.6	b.d.l.	b.d.l.	0.65	0.59	1.08	1.11	11.7	9.9
FeO	9.169	9.184	5.97	6.25	3.49	2.56	16.0	14.0	11.37	11.08	7.16	7.47	3.04	3.03	12.1	12.3	9.459	9.624	5.90	6.18	2.31	2.49	11.2	11.1	9.686	9.806	6.22	6.29	2.49	2.41	11.2	10.8
MnO	0.164	0.169	0.14	0.17	0.09	0.08	0.29	0.20	0.163	0.151	0.17	0.15	0.10	0.11	0.12	0.12	0.134	0.134	0.11	0.14	0.09	0.09	0.15	0.12	0.15	0.143	0.12	0.16	0.07	0.11	0.13	0.09
NiO	0.384	0.354	0.10	0.10	0.06	b.d.l.	0.09	0.21	0.355	0.339	0.07	0.07	b.d.l.	b.d.l.	0.34	0.33	0.37	0.376	0.08	0.08	b.d.l.	0.06	0.35	0.32	0.405	0.378	0.08	0.10	b.d.l.	b.d.l.	0.36	0.39
MgO	48.8	49.0	32.7	33.3	20.6	16.6	15.0	17.2	47.0	47.3	30.8	31.8	13.6	13.9	18.8	18.4	47.8	48.5	31.7	33.5	13.5	14.2	19.1	19.1	48.1	47.9	30.6	31.3	13.7	13.5	19.3	20.0
CaO	b.d.l.	b.d.l.	0.87	0.56	15.8	20.7	b.d.l.	b.d.l.	b.d.l.	b.d.l.	0.72	0.69	20.1	19.9	b.d.l.	b.d.l.	b.d.l.	b.d.l.	0.66	0.34	19.5	19.2	b.d.l.	b.d.l.	b.d.l.	b.d.l.	1.67	1.06	20.8	20.6	b.d.l.	b.d.l.
Na_2O	b.d.l.	b.d.l.	b.d.l.	b.d.l.	0.62	0.91	b.d.l.	b.d.l.	b.d.l.	b.d.l.	0.09	b.d.l.	2.13	2.01	b.d.l.	b.d.l.	b.d.l.	b.d.l.	0.06	b.d.l.	1.97	1.83	b.d.l.	b.d.l.	b.d.l.	b.d.l.	0.09	0.10	1.81	2.03	b.d.l.	b.d.l.
K_2O	b.d.l.	b.d.l.	b.d.l.	b.d.l.	b.d.l.	b.d.l.	b.d.l.	b.d.l.	b.d.l.	b.d.l.	b.d.l.	b.d.l.	b.d.l.	b.d.l.	b.d.l.	0.18	b.d.l.	b.d.l.	b.d.l.	b.d.l.	b.d.l.	b.d.l.	b.d.l.	b.d.l.	b.d.l.	b.d.l.	b.d.l.	b.d.l.	b.d.l.	b.d.l.	b.d.l.	b.d.l.
Total	99.6	99.65	99.8	99.6	99.3	99.2	99.1	99.0	100.5	99.74	100.4	100.3	100.0	100.2	99.9	100.3	99.4	99.87	99.1	99.5	96.4	96.6	99.6	100.4	99.8	100.0	101.0	100.9	100.0	100.4	100.7	100.9
O†	4	4	6	6	6	6	4	4	4	4	6	6	6	6	4	4	4	4	6	6	6	6	4	4	4	4	6	6	6	6	4	4
Si	1.007	1.004	1.918	1.947	1.908	1.921	0.001	0.001	1.019	1.009	1.873	1.888	1.869	1.878	0.002	0.003	1.023	1.009	1.874	1.943	1.867	1.872	0.006	0.002	1.015	1.021	1.884	1.883	1.870	1.877	0.002	0.002
Ti	0.000	0.000	0.002	0.001	0.003	0.005	0.002	0.001	0.000	0.000	0.004	0.004	0.016	0.016	0.002	0.001	0.000	0.000	0.003	0.001	0.010	0.010	0.001	0.001	0.000	0.000	0.004	0.004	0.013	0.012	0.001	0.002
Altot	0.000	0.000	0.148	0.103	0.173	0.170	1.250	1.487	0.000	0.000	0.263	0.205	0.340	0.327	1.769	1.791	0.000	0.000	0.242	0.114	0.332	0.314	1.672	1.697	0.000	0.000	0.259	0.249	0.332	0.340	1.760	1.796
^{IV}Al			0.082	0.053	0.092	0.079					0.127	0.112	0.131	0.122					0.126	0.057	0.133	0.128					0.116	0.117	0.130	0.123		
^{VI}Al			0.065	0.050	0.082	0.090					0.136	0.092	0.209	0.204					0.116	0.057	0.199	0.186					0.142	0.133	0.202	0.216		
Cr	0.000	0.000	0.024	0.013	0.044	0.043	0.713	0.477	0.000	0.001	0.015	0.012	0.026	0.026	0.222	0.208	0.000	0.000	0.021	0.009	0.038	0.034	0.311	0.302	0.000	0.000	0.017	0.016	0.031	0.032	0.239	0.199
Fe_{tot}*	0.188	0.189	0.173	0.181	0.105	0.078	0.388	0.326	0.233	0.229	0.207	0.216	0.092	0.092	0.265	0.267	0.194	0.197	0.172	0.179	0.072	0.078	0.248	0.243	0.199	0.201	0.178	0.180	0.075	0.073	0.243	0.230
Fe^{2+}‡					0.099	0.075							0.071	0.090							0.044	0.048							0.075	0.073		
Fe^{3+}‡					0.006	0.003							0.021	0.001							0.028	0.030							0.000	0.000		
Mn	0.003	0.004	0.004	0.005	0.003	0.003	0.007	0.005	0.003	0.003	0.005	0.004	0.003	0.003	0.003	0.003	0.003	0.003	0.003	0.004	0.003	0.003	0.003	0.003	0.003	0.003	0.003	0.005	0.002	0.003	0.003	0.002
Mg	1.786	1.792	1.691	1.720	1.108	0.906	0.649	0.714	1.717	1.742	1.585	1.641	0.732	0.749	0.730	0.713	1.748	1.773	1.648	1.729	0.756	0.793	0.751	0.744	1.758	1.745	1.561	1.599	0.739	0.723	0.741	0.761
Ca	0.000	0.000	0.032	0.021	0.611	0.810	0.000	0.000	0.001	0.000	0.027	0.026	0.778	0.769	0.000	0.000	0.001	0.001	0.025	0.012	0.786	0.771	0.001	0.001	0.001	0.001	0.061	0.039	0.807	0.796	0.000	0.000
Na	0.000	0.000	0.002	0.001	0.044	0.064	0.001	0.001	0.000	0.000	0.006	0.003	0.150	0.141	0.000	0.001	0.000	0.001	0.004	0.001	0.143	0.133	0.000	0.000	0.000	0.001	0.006	0.007	0.127	0.142	0.000	0.000
K	0.000	0.000	0.001	0.000	0.001	0.001	0.000	0.000	0.000	0.000	0.000	0.000	0.000	0.000	0.000	0.006	0.000	0.000	0.000	0.000	0.000	0.000	0.000	0.000	0.000	0.000	0.000	0.000	0.000	0.000	0.000	0.000
Ni	0.008	0.007	0.003	0.003	0.002	0.001	0.002	0.005	0.007	0.007	0.002	0.002	0.001	0.001	0.007	0.007	0.007	0.007	0.002	0.002	0.001	0.002	0.007	0.007	0.008	0.007	0.002	0.003	0.001	0.001	0.008	0.008
Total	2.993	2.996	3.997	3.994	4.002	4.001	3.015	3.016	2.981	2.991	3.987	4.001	4.007	4.000	3.000	3.000	2.977	2.992	3.994	3.995	4.009	4.010	3.001	2.998	2.984	2.979	3.977	3.984	3.999	3.997	2.997	2.999
X_{Mg}**	0.905	0.905	0.907	0.905	0.913	0.921	0.626	0.687	0.880	0.884	0.885	0.884	0.888	0.891	0.734	0.727	0.900	0.900	0.906	0.906	0.913	0.911	0.752	0.754	0.899	0.897	0.898	0.899	0.908	0.909	0.753	0.768
Cr#**							0.363	0.243							0.112	0.104							0.157	0.151							0.120	0.100
CaTs					0.089	0.072							0.107	0.092							0.122	0.118							0.107	0.107		
Ac					0.006	0.003							0.021	0.001							0.028	0.030							0.000	0.000		
Jd					0.038	0.062							0.129	0.141							0.116	0.103							0.128	0.143		

† Number of oxygens for which cations are calculated.

*FeO and Fe calculated as total iron.

‡ Fe^{2+} and Fe^{3+} based on clinopyroxene stoichiometry.

** X_{Mg} = Mg / (Mg + Fe^{2+}). Fe_{tot} was used for orthopyroxene, olivine and spinel. Cr# = Cr / (Cr + Al).

Ac = Fe^{3+}, CaTs = CrCaTs+AlCaTS, CrCaTs = Cr, AlCaTs = ^{VI}AlJd, Jd = NaAc (if NaAc < ^{VI}Al), Jd=^{VI}Al (if NaAc ≥ ^{VI}Al).

Major element compositions (wt. %) of minerals used for geothermobarometry

Sample	BB163W								BB211E								BB216E								BB254E					
Locality	Aarkob								Nich1								Nich1								Nich2					
Domain	ArSe								ArSe								ArSe								ArSe					
Microstruct.	Coarse porph.								Fine porph.								Coarse porph.								Coarse porph.					
Dcontact (m)	1012								815								1012								1326					
Rock type	Cpx rich lhz.								Cpx rich lhz.								Lherzolite								Cpx rich lhz.					
Mineral	ol		opx		cpx		sp		ol		opx		cpx		sp		ol		opx		cpx		sp		ol		opx		cpx		sp	
core / rim	c	r	c	r	c	r	c	r	c	r	c	r	c	r	c	r	c	r	c	r	c	r	c	r	c	r	c	r	c	r	c	r
SiO_2	40.8	40.8	54.3	54.4	52.5	52.2	0.05	0.06	41.6	42.0	56.0	55.6	52.7	52.7	0.08	0.08	41.5	41.3	57.2	55.4	52.2	52.7	0.11	0.10	41.2	41.0	54.4	55.4	51.4	52.2	0.07	0.05
TiO_2	b.d.l.	b.d.l.	0.18	0.14	0.66	0.62	0.11	0.09	b.d.l.	b.d.l.	0.05	0.08	0.33	0.35	0.06	0.09	b.d.l.	b.d.l.	b.d.l.	0.09	0.42	0.35	b.d.l.	b.d.l.	b.d.l.	b.d.l.	0.13	0.1	0.55	0.41	0.07	0.08
Al_2O_3	b.d.l.	b.d.l.	5.68	5.71	7.83	7.22	60.0	60.9	b.d.l.	b.d.l.	3.93	4.85	6.48	6.67	54.2	54.6	b.d.l.	b.d.l.	2.34	5.31	7.24	6.06	51.1	52.2	b.d.l.	b.d.l.	5.79	4.58	7.39	6.46	55.7	54.7
Cr_2O_3	b.d.l.	b.d.l.	0.39	0.42	0.78	0.65	8.76	8.9	b.d.l.	b.d.l.	0.39	0.52	1.01	1.02	14.7	14.7	b.d.l.	b.d.l.	0.28	0.65	1.47	1.27	18.4	17.3	b.d.l.	b.d.l.	0.69	0.45	1.08	0.90	13.1	12.8
FeO	10.82	10.8	6.96	7.08	2.59	2.89	11.5	11.5	9.562	9.42	6.28	6.41	2.42	2.08	11.8	11.6	9.406	9.403	6.44	6.17	2.55	3.32	12.0	12.0	9.583	9.549	5.93	6.19	2.59	2.54	11.9	12.0
MnO	0.155	0.15	0.16	0.17	0.09	0.11	0.13	0.08	0.144	0.152	0.15	0.15	0.11	0.09	0.14	0.14	0.128	0.123	0.16	0.14	0.08	0.10	0.18	0.15	0.111	0.132	0.14	0.14	0.08	0.09	0.12	0.13
NiO	0.347	0.35	0.07	0.05	b.d.l.	b.d.l.	0.36	0.39	0.392	0.413	0.08	0.07	b.d.l.	b.d.l.	0.31	0.30	0.40	0.412	0.07	0.11	b.d.l.	0.06	0.28	0.34	0.365	0.384	0.08	0.09	0.06	b.d.l.	0.33	0.31
MgO	48.1	48.3	31.8	31.8	13.7	14.6	19.6	19.4	48.3	47.8	32.7	32.3	14.4	14.2	18.9	18.5	48.6	48.6	33.4	32.4	14.3	16.1	18.0	18.4	48.9	48.9	32.0	32.7	14.3	14.6	19.5	19.6
CaO	b.d.l.	b.d.l.	0.67	0.52	20.7	20.2	b.d.l.	b.d.l.	b.d.l.	b.d.l.	0.59	0.48	20.9	20.8	b.d.l.	b.d.l.	b.d.l.	b.d.l.	0.41	0.34	19.6	18.4	b.d.l.	b.d.l.	b.d.l.	b.d.l.	0.78	1.03	20.5	20.9	b.d.l.	b.d.l.
Na_2O	b.d.l.	b.d.l.	b.d.l.	0.06	2.16	1.93	b.d.l.	b.d.l.	b.d.l.	b.d.l.	0.05	b.d.l.	1.64	1.86	b.d.l.	b.d.l.	b.d.l.	b.d.l.	b.d.l.	b.d.l.	2.03	1.65	b.d.l.	b.d.l.	b.d.l.	b.d.l.	0.25	b.d.l.	1.78	1.65	b.d.l.	b.d.l.
K_2O	b.d.l.	b.d.l.	b.d.l.	b.d.l.	b.d.l.	b.d.l.	b.d.l.	b.d.l.	b.d.l.	b.d.l.	b.d.l.	b.d.l.	b.d.l.	b.d.l.	b.d.l.	b.d.l.	b.d.l.	b.d.l.	b.d.l.	b.d.l.	b.d.l.	b.d.l.	b.d.l.	b.d.l.	b.d.l.	b.d.l.	b.d.l.	b.d.l.	b.d.l.	b.d.l.	b.d.l.	b.d.l.
Total	100.2	100.4	100.2	100.4	101.0	100.5	100.5	101.4	99.9	99.8	100.3	100.5	100.0	99.7	100.3	100.1	100.1	99.81	100.4	100.6	100.0	100.0	100.2	100.5	100.2	100.0	100.2	100.7	99.7	99.8	100.7	99.7
O†	4	4	6	6	6	6	4	4	4	4	6	6	6	6	4	4	4	4	6	6	6	6	4	4	4	4	6	6	6	6	4	4
Si	1.003	1.001	1.879	1.878	1.878	1.879	0.001	0.001	1.016	1.027	1.927	1.910	1.903	1.906	0.002	0.002	1.014	1.011	1.963	1.898	1.887	1.900	0.003	0.003	1.007	1.003	1.876	1.900	1.866	1.892	0.002	0.001
Ti	0.000	0.000	0.005	0.004	0.018	0.017	0.002	0.002	0.000	0.000	0.001	0.002	0.009	0.009	0.001	0.002	0.000	0.000	0.001	0.002	0.011	0.010	0.001	0.001	0.000	0.000	0.003	0.003	0.015	0.011	0.001	0.001
Altot	0.000	0.000	0.231	0.232	0.330	0.306	1.813	1.823	0.000	0.000	0.159	0.196	0.276	0.284	1.682	1.694	0.000	0.000	0.095	0.215	0.308	0.257	1.609	1.631	0.000	0.000	0.235	0.185	0.316	0.276	1.711	1.700
^{IV}Al			0.121	0.122	0.122	0.121					0.073	0.090	0.097	0.094					0.037	0.102	0.113	0.100					0.124	0.100	0.134	0.108		
^{VI}Al			0.110	0.111	0.208	0.185					0.086	0.106	0.179	0.190					0.057	0.113	0.194	0.157					0.111	0.086	0.182	0.167		
Cr	0.000	0.000	0.011	0.011	0.022	0.019	0.178	0.179	0.000	0.000	0.011	0.014	0.029	0.029	0.306	0.306	0.000	0.000	0.008	0.018	0.042	0.036	0.389	0.363	0.000	0.000	0.019	0.012	0.031	0.026	0.269	0.266
Fe_{tot}*	0.222	0.221	0.201	0.205	0.077	0.087	0.247	0.244	0.196	0.193	0.181	0.184	0.073	0.063	0.261	0.255	0.192	0.193	0.185	0.177	0.077	0.100	0.269	0.266	0.196	0.196	0.171	0.178	0.078	0.077	0.258	0.265
Fe^{2+}‡					0.067	0.059							0.073	0.063							0.077	0.096							0.053	0.063		
Fe^{3+}‡					0.011	0.027							0.000	0.000							0.000	0.004							0.026	0.013		
Mn	0.003	0.003	0.005	0.005	0.003	0.003	0.003	0.002	0.003	0.003	0.004	0.004	0.003	0.003	0.003	0.003	0.003	0.003	0.005	0.004	0.003	0.003	0.004	0.003	0.002	0.003	0.004	0.004	0.003	0.003	0.003	0.003
Mg	1.760	1.766	1.637	1.638	0.732	0.782	0.749	0.736	1.760	1.742	1.678	1.653	0.774	0.764	0.741	0.727	1.770	1.773	1.712	1.654	0.768	0.867	0.716	0.726	1.779	1.786	1.646	1.675	0.774	0.791	0.755	0.771
Ca	0.001	0.001	0.025	0.019	0.792	0.781	0.000	0.000	0.000	0.000	0.022	0.018	0.810	0.805	0.000	0.001	0.000	0.000	0.015	0.012	0.760	0.711	0.000	0.000	0.001	0.001	0.029	0.038	0.798	0.812	0.000	0.000
Na	0.000	0.001	0.002	0.004	0.150	0.135	0.000	0.000	0.000	0.000	0.003	0.001	0.115	0.131	0.000	0.000	0.000	0.000	0.002	0.001	0.142	0.115	0.000	0.000	0.000	0.000	0.017	0.002	0.126	0.116	0.000	0.000
K	0.000	0.000	0.000	0.000	0.000	0.000	0.000	0.000	0.000	0.000	0.000	0.000	0.000	0.000	0.000	0.000	0.000	0.000	0.000	0.000	0.000	0.000	0.000	0.000	0.000	0.000	0.000	0.000	0.000	0.000	0.000	0.000
Ni	0.007	0.007	0.002	0.001	0.001	0.001	0.008	0.008	0.008	0.008	0.002	0.002	0.001	0.000	0.007	0.006	0.008	0.008	0.002	0.003	0.001	0.002	0.005	0.007	0.007	0.008	0.002	0.002	0.002	0.001	0.007	0.007
Total	2.997	3.000	3.997	3.998	4.003	4.009	3.001	2.996	2.984	2.973	3.989	3.984	3.993	3.994	3.003	2.996	2.986	2.988	3.986	3.984	3.998	4.001	2.997	3.000	2.993	2.996	4.002	3.999	4.008	4.004	3.007	3.014
X_{Mg}**	0.888	0.889	0.891	0.889	0.904	0.900	0.752	0.751	0.900	0.900	0.903	0.900	0.914	0.924	0.740	0.740	0.902	0.902	0.903	0.903	0.909	0.896	0.727	0.732	0.901	0.901	0.906	0.904	0.908	0.912	0.745	0.744
Cr#**							0.089	0.090							0.154	0.153							0.195	0.182							0.136	0.135
CaTs					0.091	0.097							0.094	0.089							0.095	0.083							0.114	0.091		
Ac					0.011	0.027							0.000	0.000							0.000	0.004							0.026	0.014		
Jd					0.141	0.108							0.116	0.132							0.143	0.112							0.100	0.103		

† Number of oxygens for which cations are calculated.

*FeO and Fe calculated as total iron.

‡ Fe^{2+} and Fe^{3+} based on clinopyroxene stoichiometry.

** X_{Mg} = Mg / (Mg + Fe^{2+}). Fe_{tot} was used for orthopyroxene, olivine and spinel. Cr# = Cr / (Cr + Al).

Ac = Fe^{3+}, CaTs = CrCaTs+AlCaTS, CrCaTs = Cr, AlCaTs = ^{VI}AlJd, Jd = NaAc (if NaAc < ^{VI}Al), Jd=^{VI}Al (if NaAc ≥ ^{VI}Al).

Major element compositions (wt. %) of minerals used for geothermobarometry

Sample	BB256AE								BB259E								BB014W								BB017E							
Locality	Nich2								Nich2								Nich1								Nich1							
Domain	ArSe								ArSe								Se								Se							
Microstruct.	Coarse porph.								Coarse porph.								Coarse porph.								Coarse porph.							
Dcontact (m)	1159								1113								2102								1849							
Rock type	Lherzolite								Harzburgite								Harzburgite								Cpx rich lhz.							
Mineral	ol		opx		cpx		sp		ol		opx		cpx		sp		ol		opx		cpx		sp		ol		opx		cpx		sp	
core / rim	c	r	c	r	c	r	c	r	c	r	c	r	c	r	c	r	c	r	c	r	c	r	c	r	c	r	c	r	c	r	c	r
SiO_2	41.6	41.7	55.0	55.7	50.4	50.3	0.02	0.18	41.7	41.8	55.8	56.2	52.7	53.3	0.07	0.09	40.9	40.7	55.1	55.4	52.4	52.6	0.03	0.04	41.0	41.3	54.7	56.2	51.8	52.1	0.01	0.04
TiO_2	b.d.l.	b.d.l.	0.45	0.34	2.03	1.96	0.36	0.35	b.d.l.	b.d.l.	0.09	0.1	0.24	0.25	0.18	0.17	b.d.l.	b.d.l.	0.05	0.07	0.15	0.16	0.07	0.05	b.d.l.	b.d.l.	0.15	0.06	0.33	0.36	0.06	0.05
Al_2O_3	b.d.l.	b.d.l.	4.90	3.82	7.26	7.27	47.9	42.5	b.d.l.	b.d.l.	3.97	3.49	5.01	4.26	38.3	41.9	b.d.l.	b.d.l.	3.99	3.35	4.78	4.02	39.6	43.3	b.d.l.	b.d.l.	5.49	3.45	7.86	6.89	55.2	43.3
Cr_2O_3	b.d.l.	b.d.l.	0.75	0.52	1.36	1.34	20.1	20.5	b.d.l.	b.d.l.	0.85	0.73	1.56	1.11	30.3	27.2	b.d.l.	b.d.l.	0.97	0.75	1.68	1.46	28.4	24.7	b.d.l.	b.d.l.	0.66	0.29	1.26	1.08	14.1	24.7
FeO	10.1	9.89	6.44	6.63	2.67	2.69	14.9	17.9	8.639	8.563	5.65	5.60	2.34	2.28	14.9	13.5	9.249	9.538	6.03	6.00	2.41	2.21	14.4	13.8	9.428	9.36	5.88	6.37	2.35	2.60	11.1	13.8
MnO	0.13	0.13	0.14	0.15	0.07	0.08	0.15	0.20	0.13	0.12	0.17	0.15	0.11	0.09	0.22	0.16	0.12	0.11	0.14	0.12	0.08	0.13	0.23	0.17	0.158	0.13	0.15	0.13	0.09	0.09	0.12	0.17
NiO	0.361	0.394	0.11	0.08	b.d.l.	0.06	0.30	0.26	0.384	0.392	0.09	0.09	b.d.l.	b.d.l.	0.17	0.22	0.41	0.347	0.12	0.07	0.06	0.06	0.13	0.24	0.383	0.43	0.09	0.08	b.d.l.	b.d.l.	0.35	0.24
MgO	47.9	47.5	31.8	32.4	13.9	14.0	17.5	16.2	49.3	49.1	33.1	33.2	15.2	15.6	16.2	16.7	48.9	49.1	32.3	32.8	15.4	15.5	16.4	17.0	49.2	48.9	31.4	32.9	13.8	17.0	19.4	17.0
CaO	b.d.l.	b.d.l.	0.91	0.64	20.4	20.7	b.d.l.	b.d.l.	b.d.l.	b.d.l.	0.74	0.59	21.8	21.8	b.d.l.	b.d.l.	b.d.l.	b.d.l.	0.93	0.79	20.4	21.5	b.d.l.	b.d.l.	b.d.l.	b.d.l.	1.61	0.52	20.6	19.3	b.d.l.	b.d.l.
Na_2O	b.d.l.	b.d.l.	0.06	b.d.l.	1.72	1.59	b.d.l.	b.d.l.	b.d.l.	b.d.l.	b.d.l.	b.d.l.	1.21	1.09	b.d.l.	b.d.l.	b.d.l.	b.d.l.	0.09	b.d.l.	1.54	1.40	b.d.l.	b.d.l.	b.d.l.	b.d.l.	0.14	b.d.l.	1.90	1.74	b.d.l.	b.d.l.
K_2O	b.d.l.	b.d.l.	b.d.l.	b.d.l.	b.d.l.	b.d.l.	b.d.l.	b.d.l.	b.d.l.	b.d.l.	b.d.l.	b.d.l.	b.d.l.	b.d.l.	b.d.l.	b.d.l.	b.d.l.	b.d.l.	b.d.l.	b.d.l.	b.d.l.	b.d.l.	b.d.l.	b.d.l.	b.d.l.	b.d.l.	b.d.l.	b.d.l.	b.d.l.	b.d.l.	b.d.l.	b.d.l.
Total	100.2	99.69	100.5	100.3	99.8	100.1	101.2	98.1	100.2	100.0	100.5	100.2	100.2	99.9	100.3	100.1	99.8	99.94	99.7	99.5	99.1	99.1	99.2	99.3	100.2	100.2	100.2	100.0	100.0	101.1	100.3	99.3
O†	4	4	6	6	6	6	4	4	4	4	6	6	6	6	4	4	4	4	6	6	6	6	4	4	4	4	6	6	6	6	4	4
Si	1.018	1.024	1.894	1.920	1.834	1.829	0.001	0.005	1.013	1.017	1.915	1.932	1.908	1.931	0.002	0.002	1.004	0.999	1.911	1.911	1.916	1.927	0.001	0.001	1.001	1.008	1.887	1.938	1.871	1.858	0.000	0.001
Ti	0.000	0.001	0.012	0.009	0.056	0.054	0.007	0.008	0.000	0.000	0.002	0.003	0.007	0.007	0.004	0.003	0.000	0.000	0.001	0.001	0.004	0.004	0.002	0.001	0.000	0.000	0.004	0.002	0.009	0.010	0.001	0.001
Altot	0.000	0.000	0.199	0.155	0.311	0.312	1.526	1.433	0.000	0.000	0.160	0.141	0.214	0.182	1.282	1.377	0.000	0.000	0.163	0.163	0.206	0.174	1.327	1.425	0.000	0.000	0.224	0.140	0.335	0.290	1.701	1.425
^{IV}Al			0.106	0.080	0.166	0.171					0.085	0.068	0.092	0.069					0.089	0.089	0.084	0.073					0.113	0.062	0.129	0.142		
^{VI}Al			0.092	0.075	0.146	0.140					0.076	0.073	0.122	0.113					0.074	0.074	0.123	0.101					0.111	0.079	0.206	0.148		
Cr	0.000	0.000	0.021	0.014	0.039	0.039	0.430	0.463	0.000	0.000	0.023	0.020	0.045	0.032	0.679	0.600	0.000	0.000	0.027	0.027	0.049	0.042	0.639	0.546	0.000	0.001	0.018	0.008	0.036	0.031	0.291	0.546
Fe_{tot}*	0.207	0.203	0.185	0.191	0.081	0.082	0.337	0.427	0.176	0.174	0.162	0.161	0.071	0.069	0.352	0.315	0.190	0.196	0.175	0.175	0.074	0.068	0.342	0.321	0.193	0.191	0.170	0.184	0.071	0.077	0.243	0.321
Fe^{2+}‡					0.081	0.082							0.071	0.069							0.052	0.036							0.066	0.000		
Fe^{3+}‡					0.000	0.000							0.000	0.000							0.022	0.032							0.005	0.097		
Mn	0.003	0.003	0.004	0.004	0.002	0.002	0.004	0.005	0.003	0.002	0.005	0.004	0.003	0.003	0.005	0.004	0.002	0.002	0.004	0.004	0.003	0.004	0.005	0.004	0.003	0.003	0.004	0.004	0.003	0.003	0.003	0.004
Mg	1.747	1.737	1.632	1.667	0.753	0.760	0.703	0.692	1.786	1.780	1.691	1.698	0.819	0.845	0.685	0.697	1.791	1.796	1.669	1.669	0.843	0.846	0.694	0.707	1.793	1.779	1.614	1.689	0.745	0.906	0.756	0.707
Ca	0.001	0.000	0.033	0.024	0.796	0.808	0.000	0.000	0.001	0.000	0.027	0.022	0.847	0.847	0.000	0.001	0.000	0.001	0.035	0.035	0.800	0.844	0.000	0.000	0.001	0.000	0.060	0.019	0.798	0.737	0.000	0.000
Na	0.000	0.000	0.004	0.002	0.122	0.112	0.000	0.001	0.000	0.000	0.002	0.003	0.085	0.077	0.000	0.000	0.000	0.000	0.006	0.006	0.109	0.099	0.000	0.001	0.000	0.000	0.009	0.000	0.133	0.121	0.000	0.001
K	0.000	0.000	0.000	0.000	0.000	0.000	0.000	0.000	0.000	0.000	0.000	0.000	0.000	0.000	0.000	0.000	0.000	0.000	0.001	0.001	0.001	0.001	0.000	0.001	0.000	0.000	0.000	0.000	0.000	0.001	0.000	0.001
Ni	0.007	0.008	0.003	0.002	0.001	0.002	0.007	0.006	0.008	0.008	0.002	0.003	0.001	0.001	0.004	0.005	0.008	0.007	0.003	0.003	0.002	0.002	0.003	0.005	0.008	0.008	0.003	0.002	0.001	0.001	0.007	0.005
Total	2.982	2.976	3.987	3.988	3.996	3.999	3.014	3.040	2.986	2.983	3.991	3.986	3.999	3.993	3.014	3.005	2.996	3.001	3.996	3.996	4.007	4.011	3.015	3.013	2.999	2.992	3.993	3.986	4.002	4.032	3.003	3.013
X_{Mg}**	0.894	0.895	0.898	0.897	0.903	0.903	0.676	0.618	0.910	0.911	0.913	0.913	0.920	0.924	0.660	0.688	0.904	0.902	0.905	0.905	0.920	0.926	0.670	0.688	0.903	0.903	0.905	0.902	0.913	0.922	0.757	0.688
Cr#**							0.220	0.244							0.346	0.304							0.325	0.277							0.146	0.277
CaTs					0.065	0.069							0.082	0.069							0.084	0.076							0.114	0.154		
Ac					0.000	0.000							0.000	0.000							0.022	0.032							0.005	0.096		
Jd					0.126	0.115							0.086	0.077							0.087	0.067							0.129	0.023		

† Number of oxygens for which cations are calculated.

*FeO and Fe calculated as total iron.

‡ Fe^{2+} and Fe^{3+} based on clinopyroxene stoichiometry.

** $X_{Mg} = Mg / (Mg + Fe^{2+})$. Fe_{tot} was used for orthopyroxene, olivine and spinel. Cr# = Cr / (Cr + Al).

Ac = Fe^{3+}, CaTs = CrCaTs+AlCaTS, CrCaTs = Cr, AlCaTs = ^{VI}AlJd, Jd = NaAc (if NaAc < ^{VI}Al), Jd=^{VI}Al (if NaAc ≥ ^{VI}Al).

Major element compositions (wt. %) of minerals used for geothermobarometry

Sample	BB019W								BB039W								BB041E								BB042W					
Locality	Nich1								Nich1								Nich1								Nich1					
Domain	Se								Se								Se								Se					
Microstruct.	Coarse gran.								Coarse porph.								Coarse porph.								Coarse porph.					
Dcontact (m)	1888								1736								1597								1597					
Rock type	Harzburgite								Harzburgite								Lherzolite								Lherzolite					
Mineral	ol		opx		cpx		sp		ol		opx		cpx		sp		ol		opx		cpx		sp		ol		opx		cpx		sp	
core / rim	c	r	c	r	c	r	c	r	c	r	c	r	c	r	c	r	c	r	c	r	c	r	c	r	c	r	c	r	c	r	c	r
SiO_2	41.2	41.0	54.1	55.4	51.2	50.8	0.04	0.04	41.1	40.9	56.0	55.4	53.2	53	0.03	0.02	41.3	41.6	54.6	56.1	52.4	52.1	0.01	0.26	40.8	40.8	54.1	54.9	50.5	51.8	0.02	0.03
TiO_2	b.d.l.	b.d.l.	0.22	0.12	0.80	0.78	0.16	0.20	b.d.l.	b.d.l.	0.06	0.08	0.21	0.25	0.10	0.11	b.d.l.	b.d.l.	0.10	0.06	0.35	0.49	0.09	0.08	b.d.l.	b.d.l.	0.16	0.10	0.58	0.48	0.07	0.06
Al_2O_3	b.d.l.	b.d.l.	5.27	3.49	7.08	7.1	48.6	44.8	b.d.l.	b.d.l.	3.95	4.04	5.51	5.44	43.6	46.3	b.d.l.	b.d.l.	5.96	3.59	6.97	6.60	55.0	54.2	b.d.l.	b.d.l.	5.77	4.45	8.00	6.55	56.1	59.7
Cr_2O_3	b.d.l.	b.d.l.	0.90	0.66	1.52	1.54	20.5	24.9	b.d.l.	b.d.l.	0.87	0.83	1.64	1.78	26.3	24.5	b.d.l.	b.d.l.	0.69	0.73	1.12	0.96	14.5	13.6	b.d.l.	b.d.l.	0.63	0.41	1.08	0.95	11.5	7.8
FeO	9.50	9.582	5.91	6.21	2.52	2.34	12.4	13.5	9.071	9.237	5.71	5.78	2.50	2.25	13.4	13.2	9.688	9.628	6.14	5.94	2.34	2.32	11.3	12.2	10.2	9.954	6.22	6.43	2.51	2.50	11.2	11.0
MnO	0.149	0.14	0.11	0.11	0.09	0.09	0.15	0.18	0.089	0.114	0.12	0.11	0.08	0.08	0.19	0.18	0.136	0.13	0.13	0.17	0.08	0.08	0.11	0.12	0.128	0.143	0.11	0.14	0.05	0.06	0.15	0.14
NiO	0.356	0.359	0.10	0.07	b.d.l.	b.d.l.	0.23	0.2	0.361	0.398	0.09	0.12	b.d.l.	b.d.l.	0.19	0.19	0.354	0.376	0.10	0.07	b.d.l.	b.d.l.	0.31	0.31	0.377	0.387	0.16	0.08	0.08	0.06	0.35	0.40
MgO	49.1	48.5	32.1	33.3	14.3	14.1	17.9	16.4	49.0	49.2	32.8	32.3	15.7	14.8	16.8	16.5	49.0	48.5	31.6	33.1	14.5	14.8	19.3	19.1	48.4	48.3	31.4	32.3	14.1	14.3	19.9	20.0
CaO	b.d.l.	b.d.l.	1.04	0.60	20.1	20.4	b.d.l.	b.d.l.	b.d.l.	b.d.l.	0.63	1.63	20.0	20.7	b.d.l.	b.d.l.	b.d.l.	b.d.l.	0.79	0.48	20.9	21.6	b.d.l.	b.d.l.	b.d.l.	b.d.l.	1.11	0.51	19.7	20.8	b.d.l.	b.d.l.
Na_2O	b.d.l.	b.d.l.	0.08	0.06	2.09	2.1	b.d.l.	b.d.l.	b.d.l.	b.d.l.	b.d.l.	0.14	1.60	1.71	b.d.l.	b.d.l.	b.d.l.	b.d.l.	0.09	b.d.l.	1.66	1.47	b.d.l.	b.d.l.	b.d.l.	b.d.l.	0.10	b.d.l.	1.96	1.59	b.d.l.	b.d.l.
K_2O	b.d.l.	b.d.l.	b.d.l.	b.d.l.	b.d.l.	b.d.l.	b.d.l.	b.d.l.	b.d.l.	b.d.l.	b.d.l.	b.d.l.	b.d.l.	b.d.l.	b.d.l.	b.d.l.	b.d.l.	b.d.l.	b.d.l.	0.15	b.d.l.	b.d.l.	b.d.l.	b.d.l.	b.d.l.	b.d.l.	b.d.l.	b.d.l.	b.d.l.	b.d.l.	b.d.l.	b.d.l.
Total	100.3	99.62	99.9	100.0	99.7	99.3	100	100.2	99.7	99.87	100.2	100.4	100.4	100.0	100.6	101.1	100.5	100.3	100.2	100.4	100.3	100.4	100.6	99.9	100.1	99.75	99.8	99.4	98.6	99.1	99.3	99.1
O†	4	4	6	6	6	6	4	4	4	4	6	6	6	6	4	4	4	4	6	6	6	6	4	4	4	4	6	6	6	6	4	4
Si	1.004	1.008	1.875	1.915	1.861	1.857	0.001	0.001	1.008	1.001	1.924	1.909	1.911	1.916	0.001	0.001	1.005	1.014	1.883	1.928	1.888	1.879	0.000	0.007	1.002	1.005	1.877	1.909	1.854	1.891	0.000	0.001
Ti	0.000	0.000	0.006	0.003	0.022	0.021	0.003	0.004	0.000	0.000	0.002	0.002	0.006	0.007	0.002	0.002	0.000	0.000	0.003	0.001	0.009	0.013	0.002	0.002	0.000	0.000	0.004	0.003	0.016	0.013	0.001	0.001
Altot	0.000	0.000	0.215	0.142	0.304	0.306	1.549	1.454	0.000	0.000	0.160	0.164	0.234	0.232	1.416	1.482	0.000	0.000	0.242	0.145	0.296	0.280	1.694	1.686	0.000	0.000	0.236	0.182	0.346	0.282	1.736	1.824
^{IV}Al			0.125	0.085	0.139	0.143					0.076	0.091	0.089	0.084					0.117	0.072	0.112	0.121					0.123	0.091	0.146	0.109		
^{VI}Al			0.090	0.057	0.165	0.163					0.084	0.073	0.145	0.148					0.125	0.073	0.184	0.159					0.113	0.091	0.200	0.173		
Cr	0.000	0.000	0.025	0.018	0.044	0.045	0.439	0.543	0.000	0.000	0.024	0.023	0.047	0.051	0.572	0.528	0.000	0.000	0.019	0.020	0.032	0.027	0.299	0.283	0.000	0.001	0.017	0.011	0.031	0.027	0.238	0.159
Fe_{tot}*	0.194	0.197	0.171	0.179	0.076	0.071	0.279	0.311	0.186	0.189	0.164	0.167	0.075	0.068	0.310	0.301	0.197	0.196	0.177	0.171	0.071	0.070	0.247	0.269	0.210	0.205	0.181	0.187	0.077	0.076	0.246	0.238
Fe^{2+}‡					0.026	0.009							0.075	0.068							0.071	0.053							0.043	0.076		
Fe^{3+}‡					0.050	0.062							0.000	0.000							0.000	0.017							0.034	0.000		
Mn	0.003	0.003	0.003	0.003	0.003	0.003	0.003	0.004	0.002	0.002	0.004	0.003	0.002	0.003	0.004	0.004	0.003	0.003	0.004	0.005	0.002	0.002	0.003	0.003	0.003	0.003	0.003	0.004	0.002	0.002	0.003	0.003
Mg	1.786	1.776	1.660	1.715	0.776	0.769	0.720	0.673	1.788	1.797	1.679	1.660	0.842	0.798	0.692	0.670	1.781	1.764	1.622	1.694	0.777	0.794	0.750	0.752	1.775	1.773	1.625	1.674	0.770	0.779	0.779	0.773
Ca	0.001	0.001	0.039	0.022	0.783	0.798	0.000	0.000	0.001	0.000	0.023	0.060	0.770	0.801	0.000	0.000	0.001	0.001	0.029	0.017	0.806	0.835	0.000	0.000	0.001	0.001	0.041	0.019	0.773	0.813	0.000	0.000
Na	0.000	0.000	0.005	0.004	0.147	0.149	0.000	0.001	0.000	0.000	0.002	0.009	0.111	0.120	0.000	0.000	0.000	0.000	0.006	0.003	0.116	0.103	0.001	0.001	0.000	0.000	0.007	0.002	0.139	0.112	0.000	0.000
K	0.000	0.000	0.000	0.000	0.000	0.000	0.000	0.000	0.000	0.000	0.000	0.000	0.000	0.000	0.000	0.000	0.000	0.000	0.000	0.007	0.000	0.000	0.000	0.000	0.000	0.000	0.001	0.001	0.001	0.000	0.000	0.000
Ni	0.007	0.007	0.003	0.002	0.001	0.001	0.005	0.005	0.007	0.008	0.002	0.003	0.000	0.001	0.004	0.004	0.007	0.007	0.003	0.002	0.000	0.001	0.006	0.006	0.007	0.008	0.004	0.002	0.002	0.002	0.007	0.008
Total	2.996	2.992	4.002	4.004	4.017	4.020	3.001	2.997	2.992	2.998	3.984	4.000	3.999	3.996	3.003	2.992	2.995	2.985	3.987	3.993	3.997	4.006	3.002	3.008	2.998	2.995	3.996	3.993	4.011	3.998	3.011	3.007
X_{Mg}**	0.902	0.900	0.906	0.905	0.910	0.915	0.720	0.684	0.906	0.905	0.911	0.909	0.918	0.921	0.691	0.690	0.900	0.900	0.902	0.909	0.917	0.919	0.752	0.737	0.894	0.896	0.900	0.900	0.909	0.911	0.760	0.765
Cr#**							0.221	0.272							0.288	0.262							0.150	0.144							0.121	0.080
CaTs					0.112	0.121							0.081	0.079							0.100	0.101							0.127	0.088		
Ac					0.051	0.062							0.000	0.000							0.000	0.017							0.034	0.000		
Jd					0.098	0.087							0.112	0.121							0.117	0.086							0.106	0.114		

† Number of oxygens for which cations are calculated.

*FeO and Fe calculated as total iron.

‡ Fe^{2+} and Fe^{3+} based on clinopyroxene stoichiometry.

** $X_{Mg} = Mg / (Mg + Fe^{2+})$. Fe_{tot} was used for orthopyroxene, olivine and spinel. Cr# = Cr / (Cr + Al).

Ac = Fe^{3+}, CaTs = CrCaTs+AlCaTS, CrCaTs = Cr, AlCaTs = ^{VI}AlJd, Jd = NaAc (if NaAc < ^{VI}Al), Jd=^{VI}Al (if NaAc ≥ ^{VI}Al).

Major element compositions (wt. %) of minerals used for geothermobarometry

Sample	BB044AT								BB055W								BB056W								BB059CW							
Locality	Aarkob								Aarkob								Yahia1								Yahia1							
Domain	Se								Se								Se								Se							
Microstruct.	Coarse gran.								Coarse porph.								Coarse porph.								Coarse porph.							
Dcontact (m)	1767								1385								1586								1362							
Rock type	Cpx rich lhz.								Cpx rich lhz.								Cpx rich lhz.								Lherzolite							
Mineral	ol		opx		cpx		sp		ol		opx		cpx		sp		ol		opx		cpx		sp		ol		opx		cpx		sp	
core / rim	c	r	c	r	c	r	c	r	c	r	c	r	c	r	c	r	c	r	c	r	c	r	c	r	c	r	c	r	c	r	c	r
SiO_2	41.3	41.2	54.4	54.6	51.8	51.9	0.08	0.06	40.7	41.0	53.9	55.4	51.6	51.6	0.05	0.05	41.4	41.0	53.7	54.3	50.7	51.4	0.11	0.12	40.8	40.6	53.6	53.5	51.4	51.3	0.04	0.02
TiO_2	b.d.l.	b.d.l.	0.24	0.27	0.74	0.59	b.d.l.	b.d.l.	b.d.l.	b.d.l.	0.11	0.10	0.46	0.49	b.d.l.	0.07	b.d.l.	b.d.l.	0.14	0.09	0.44	0.48	b.d.l.	b.d.l.	b.d.l.	b.d.l.	0.18	0.12	0.58	0.63	0.10	0.09
Al_2O_3	b.d.l.	b.d.l.	6.36	5.61	8.40	7.64	57.0	56.8	b.d.l.	b.d.l.	6.15	4.12	7.65	7.56	57.9	56.4	b.d.l.	b.d.l.	6.14	5.09	7.33	6.55	56.7	56.3	b.d.l.	b.d.l.	6.24	6.53	7.57	6.94	57.4	53.3
Cr_2O_3	b.d.l.	b.d.l.	0.59	0.56	1.05	1.09	12.1	11.4	b.d.l.	b.d.l.	0.65	0.42	1.11	1.08	12.4	13.5	b.d.l.	b.d.l.	0.58	0.51	1.01	0.88	12.4	12.2	b.d.l.	b.d.l.	0.55	0.56	0.82	0.80	9.92	14.4
FeO	10.3	10.3	6.61	6.39	2.75	2.93	12.3	11.8	9.86	9.84	6.33	6.33	2.26	2.34	10.3	10.3	9.77	9.763	6.16	6.35	2.55	2.48	11.3	11.3	10.6	10.35	6.74	7.19	2.76	2.73	11.7	12.1
MnO	0.13	0.12	0.15	0.15	0.11	0.09	0.13	0.13	0.12	0.14	0.12	0.14	0.10	0.10	0.12	0.12	0.13	0.145	0.14	0.18	0.09	0.11	0.12	0.12	0.19	0.134	0.13	0.15	0.07	0.12	0.11	0.16
NiO	0.36	0.34	0.11	0.09	0.05	0.05	0.33	0.34	0.37	0.35	0.10	0.07	b.d.l.	b.d.l.	0.33	0.27	0.37	0.366	0.08	0.11	b.d.l.	0.06	0.37	0.36	0.41	0.367	0.06	0.09	b.d.l.	b.d.l.	0.40	0.30
MgO	48.0	48.7	30.8	30.2	13.1	14.5	18.8	19.3	49.2	49.1	32.4	33.3	14.4	14.1	20.2	19.7	48.1	48.1	31.4	31.2	14.0	14.5	19.1	19.3	48.1	48.1	31.1	31.6	13.6	14.1	19.7	18.9
CaO	b.d.l.	b.d.l.	1.00	2.24	20.1	19.3	b.d.l.	b.d.l.	b.d.l.	b.d.l.	0.67	0.65	21.3	21.0	b.d.l.	b.d.l.	b.d.l.	b.d.l.	0.76	0.69	20.7	20.9	b.d.l.	b.d.l.	b.d.l.	b.d.l.	0.98	0.42	20.7	21.3	b.d.l.	b.d.l.
Na_2O	b.d.l.	b.d.l.	0.09	0.20	2.05	1.94	b.d.l.	b.d.l.	b.d.l.	b.d.l.	b.d.l.	b.d.l.	1.73	1.87	b.d.l.	b.d.l.	b.d.l.	b.d.l.	0.07	b.d.l.	1.55	1.49	b.d.l.	b.d.l.	b.d.l.	b.d.l.	0.08	b.d.l.	1.77	1.43	b.d.l.	b.d.l.
K_2O	b.d.l.	b.d.l.	b.d.l.	b.d.l.	b.d.l.	b.d.l.	b.d.l.	b.d.l.	b.d.l.	b.d.l.	b.d.l.	b.d.l.	b.d.l.	b.d.l.	b.d.l.	b.d.l.	b.d.l.	b.d.l.	0.14	b.d.l.	b.d.l.	b.d.l.	b.d.l.	b.d.l.	b.d.l.	b.d.l.	b.d.l.	b.d.l.	b.d.l.	b.d.l.	b.d.l.	b.d.l.
Total	100.1	100.6	100.4	100.3	100.1	100.1	100.8	99.9	100.2	100.6	100.4	100.5	100.6	100.1	101.3	100.5	99.8	99.43	99.3	98.6	98.3	98.8	100.1	99.8	100.2	99.72	99.7	100.2	99.4	99.3	99.4	99.3
O†	4	4	6	6	6	6	4	4	4	4	6	6	6	6	4	4	4	4	6	6	6	6	4	4	4	4	6	6	6	6	4	4
Si	1.013	1.005	1.876	1.876	1.869	1.874	0.002	0.002	0.996	1.001	1.857	1.905	1.857	1.866	0.001	0.001	1.015	1.011	1.870	1.902	1.867	1.882	0.003	0.003	1.003	1.002	1.865	1.854	1.874	1.872	0.001	0.001
Ti	0.000	0.000	0.006	0.006	0.020	0.016	0.000	0.000	0.000	0.000	0.003	0.002	0.013	0.013	0.001	0.001	0.000	0.000	0.004	0.002	0.012	0.013	0.001	0.001	0.000	0.000	0.005	0.003	0.016	0.017	0.002	0.002
Altot	0.000	0.000	0.258	0.258	0.358	0.325	1.744	1.748	0.000	0.000	0.250	0.167	0.325	0.322	1.746	1.723	0.000	0.000	0.252	0.210	0.318	0.283	1.740	1.736	0.000	0.000	0.256	0.267	0.325	0.299	1.768	1.673
^{IV}Al			0.124	0.124	0.131	0.126					0.143	0.095	0.143	0.134					0.130	0.098	0.133	0.118					0.135	0.146	0.126	0.128		
^{VI}Al			0.135	0.135	0.227	0.199					0.107	0.072	0.182	0.189					0.122	0.113	0.185	0.165					0.121	0.121	0.199	0.171		
Cr	0.000	0.000	0.016	0.016	0.030	0.031	0.249	0.235	0.000	0.000	0.018	0.011	0.031	0.031	0.251	0.278	0.000	0.000	0.016	0.014	0.029	0.026	0.256	0.252	0.000	0.001	0.015	0.015	0.024	0.023	0.205	0.303
Fe_{tot}*	0.211	0.209	0.191	0.191	0.083	0.088	0.267	0.258	0.202	0.201	0.183	0.182	0.068	0.071	0.220	0.223	0.200	0.201	0.179	0.186	0.078	0.076	0.246	0.248	0.219	0.213	0.196	0.208	0.084	0.083	0.256	0.271
Fe^{2+}‡					0.083	0.088							0.030	0.043							0.071	0.066							0.084	0.083		
Fe^{3+}‡					0.000	0.000							0.038	0.028							0.008	0.010							0.000	0.001		
Mn	0.003	0.003	0.004	0.004	0.003	0.003	0.003	0.003	0.003	0.003	0.004	0.004	0.003	0.003	0.003	0.003	0.003	0.003	0.004	0.005	0.003	0.004	0.003	0.003	0.004	0.003	0.004	0.004	0.002	0.004	0.002	0.004
Mg	1.752	1.770	1.585	1.585	0.703	0.778	0.730	0.752	1.795	1.786	1.663	1.705	0.771	0.758	0.771	0.762	1.759	1.766	1.631	1.632	0.766	0.792	0.741	0.752	1.763	1.770	1.613	1.630	0.738	0.766	0.768	0.749
Ca	0.001	0.001	0.037	0.037	0.778	0.747	0.000	0.001	0.001	0.001	0.025	0.024	0.823	0.813	0.000	0.001	0.001	0.001	0.028	0.026	0.817	0.820	0.000	0.000	0.000	0.000	0.036	0.016	0.809	0.832	0.000	0.000
Na	0.001	0.000	0.006	0.006	0.143	0.136	0.000	0.000	0.000	0.000	0.003	0.001	0.121	0.131	0.001	0.000	0.000	0.001	0.005	0.002	0.111	0.106	0.000	0.000	0.000	0.000	0.006	0.001	0.125	0.101	0.000	0.000
K	0.000	0.000	0.000	0.000	0.000	0.000	0.000	0.000	0.000	0.000	0.000	0.000	0.000	0.000	0.000	0.000	0.000	0.000	0.006	0.000	0.000	0.000	0.000	0.000	0.000	0.001	0.001	0.001	0.001	0.000	0.001	0.000
Ni	0.007	0.007	0.003	0.003	0.001	0.002	0.007	0.007	0.007	0.007	0.003	0.002	0.001	0.001	0.007	0.006	0.007	0.007	0.002	0.003	0.001	0.002	0.008	0.007	0.008	0.007	0.002	0.003	0.001	0.001	0.008	0.007
Total	2.987	2.995	3.983	3.983	3.989	4.000	3.001	3.007	3.004	2.999	4.008	4.004	4.013	4.009	3.000	2.997	2.985	2.990	3.998	3.984	4.002	4.003	2.998	3.002	2.997	2.998	3.998	4.003	3.999	4.000	3.011	3.009
X_{Mg}**	0.892	0.894	0.893	0.893	0.894	0.898	0.732	0.745	0.899	0.899	0.901	0.904	0.919	0.915	0.778	0.774	0.898	0.898	0.901	0.898	0.907	0.913	0.751	0.752	0.890	0.892	0.892	0.887	0.898	0.902	0.750	0.735
Cr#**							0.125	0.119							0.126	0.139							0.128	0.127							0.104	0.153
CaTs					0.115	0.095							0.131	0.117							0.112	0.095							0.098	0.094		
Ac					0.000	0.000							0.038	0.028							0.008	0.010							0.000	0.001		
Jd					0.146	0.137							0.083	0.103							0.104	0.097							0.127	0.102		

† Number of oxygens for which cations are calculated.

*FeO and Fe calculated as total iron.

‡ Fe^{2+} and Fe^{3+} based on clinopyroxene stoichiometry.

** $X_{Mg} = Mg / (Mg + Fe^{2+})$. Fe_{tot} was used for orthopyroxene, olivine and spinel. Cr# = Cr / (Cr + Al).

Ac = Fe^{3+}, CaTs = CrCaTs+AlCaTS, CrCaTs = Cr, AlCaTs = ^{VI}AlJd, Jd = NaAc (if NaAc < ^{VI}Al), Jd=^{VI}Al (if NaAc ≥ ^{VI}Al).

Major element compositions (wt. %) of minerals used for geothermobarometry

Sample	BB062W								BB063AW								BB108W								BB138W							
Locality	Yahia1								Yahia1								Amaziten								Aarkob							
Domain	Se								Se								Se								Se							
Microstruct.	Coarse porph.								Coarse porph.								Coarse porph.								Coarse gran.							
Dcontact (m)	1309								1247								1079								1253							
Rock type	Cpx rich lhz.								Lherzolite								Lherzolite								Lherzolite							
Mineral	ol		opx		cpx		sp		ol		opx		cpx		sp		ol		opx		cpx		sp		ol		opx		cpx		sp	
core / rim	c	r	c	r	c	r	c	r	c	r	c	r	c	r	c	r	c	r	c	r	c	r	c	r	c	r	c	r	c	r	c	r
SiO_2	40.5	41.2	53.6	54.4	51.2	51.3	0.02	0.02	40.8	40.8	54.2	55.2	51.2	51.2	0.02	0.01	40.9	40.9	53.9	55.0	51.5	51.5	0.07	0.07	40.6	41.3	55.3	55.1	52.1	52.5	0.08	0.05
TiO_2	b.d.l.	b.d.l.	0.16	0.11	0.52	0.52	b.d.l.	b.d.l.	b.d.l.	b.d.l.	0.16	0.08	0.58	0.63	0.08	b.d.l.	b.d.l.	b.d.l.	0.20	0.15	0.50	0.50	b.d.l.	b.d.l.	b.d.l.	b.d.l.	b.d.l.	0.11	0.23	0.31	0.12	0.07
Al_2O_3	b.d.l.	b.d.l.	6.10	5.39	7.33	7.01	56.4	57.6	b.d.l.	b.d.l.	5.58	3.83	7.85	7.64	57.5	59.7	b.d.l.	b.d.l.	6.45	5.19	7.94	7.94	58.6	58.6	b.d.l.	b.d.l.	3.96	4.07	5.28	4.81	38.9	39.4
Cr_2O_3	b.d.l.	b.d.l.	0.53	0.49	0.9	0.87	11.1	10.2	b.d.l.	b.d.l.	0.48	0.26	0.9	0.82	9.58	7.7	b.d.l.	b.d.l.	0.59	0.44	0.91	0.91	9.92	9.9	b.d.l.	b.d.l.	0.93	0.98	1.84	1.79	31.4	31.0
FeO	9.98	10.22	6.52	6.59	3.15	2.56	12.3	12.1	10.33	10.36	6.87	6.88	3.09	2.96	11.9	11.5	10.3	10.33	6.18	6.53	2.64	2.64	11.1	11.1	9.39	9.39	6.01	6.03	2.21	1.82	14.2	14.0
MnO	0.12	0.162	0.16	0.13	0.09	0.11	0.14	0.13	0.146	0.158	0.15	0.11	0.10	0.07	0.19	0.14	0.16	0.165	0.13	0.15	0.10	0.10	0.11	0.11	0.15	0.10	0.13	0.16	0.12	0.09	0.21	0.21
NiO	0.38	0.387	0.09	0.10	0.07	b.d.l.	0.36	0.35	0.40	0.373	0.08	0.10	0.09	b.d.l.	0.40	0.41	0.39	0.388	0.10	0.09	0.05	0.05	0.39	0.39	0.39	0.36	0.13	0.08	b.d.l.	0.05	0.16	0.15
MgO	48.2	47.9	31.1	31.9	14.5	13.7	19.6	19.9	48.2	48.2	31.7	32.7	14.1	13.8	19.8	19.9	48.6	48.6	30.3	32.5	14.0	14.0	19.6	19.6	49.5	49.3	33.1	32.9	14.6	15.4	15.9	15.8
CaO	b.d.l.	b.d.l.	0.85	0.29	19.5	21.1	b.d.l.	b.d.l.	b.d.l.	b.d.l.	0.89	0.44	19.5	20.0	b.d.l.	b.d.l.	b.d.l.	b.d.l.	2.56	0.48	20.5	20.5	b.d.l.	b.d.l.	b.d.l.	b.d.l.	0.63	0.84	21.2	22	b.d.l.	b.d.l.
Na_2O	b.d.l.	b.d.l.	0.10	b.d.l.	1.68	1.66	b.d.l.	b.d.l.	b.d.l.	b.d.l.	0.10	b.d.l.	1.91	1.95	b.d.l.	b.d.l.	b.d.l.	b.d.l.	0.31	0.05	2.04	2.04	b.d.l.	b.d.l.	b.d.l.	b.d.l.	0.06	0.07	1.66	1.46	b.d.l.	b.d.l.
K_2O	b.d.l.	b.d.l.	b.d.l.	b.d.l.	b.d.l.	b.d.l.	b.d.l.	b.d.l.	b.d.l.	b.d.l.	b.d.l.	b.d.l.	b.d.l.	b.d.l.	b.d.l.	b.d.l.	b.d.l.	b.d.l.	b.d.l.	b.d.l.	b.d.l.	b.d.l.	b.d.l.	b.d.l.	b.d.l.	b.d.l.	b.d.l.	b.d.l.	b.d.l.	b.d.l.	b.d.l.	b.d.l.
Total	99.3	99.89	99.2	99.5	99.0	99.0	100.0	100.3	100.1	99.92	100.2	99.6	99.3	99.3	99.5	99.5	100.3	100.3	100.8	100.6	100.2	100.2	99.8	99.8	100.1	100.6	100.3	100.3	99.2	100.3	101.0	100.7
O†	4	4	6	6	6	6	4	4	4	4	6	6	6	6	4	4	4	4	6	6	6	6	4	4	4	4	6	6	6	6	4	4
Si	1.002	1.012	1.871	1.891	1.873	1.880	0.001	0.001	1.004	1.004	1.876	1.917	1.865	1.871	0.000	0.000	1.001	1.001	1.862	1.889	1.861	1.861	0.002	0.002	0.995	1.005	1.907	1.901	1.904	1.902	0.002	0.001
Ti	0.000	0.000	0.004	0.003	0.014	0.014	0.001	0.001	0.000	0.000	0.004	0.002	0.016	0.017	0.001	0.000	0.000	0.000	0.005	0.004	0.014	0.014	0.000	0.000	0.000	0.000	0.001	0.003	0.006	0.008	0.003	0.001
Altot	0.000	0.000	0.251	0.220	0.316	0.303	1.739	1.760	0.000	0.000	0.228	0.157	0.337	0.329	1.770	1.822	0.000	0.000	0.263	0.210	0.338	0.338	1.788	1.788	0.000	0.000	0.161	0.166	0.227	0.205	1.290	1.307
^{IV}Al			0.129	0.109	0.127	0.120					0.124	0.083	0.135	0.129					0.138	0.111	0.139	0.139					0.093	0.099	0.096	0.098		
^{VI}Al			0.122	0.111	0.189	0.183					0.104	0.073	0.202	0.200					0.124	0.099	0.199	0.199					0.068	0.067	0.132	0.107		
Cr	0.000	0.000	0.015	0.013	0.026	0.025	0.229	0.210	0.000	0.000	0.013	0.007	0.026	0.024	0.198	0.158	0.000	0.000	0.016	0.012	0.026	0.026	0.203	0.203	0.000	0.000	0.025	0.027	0.053	0.051	0.698	0.690
Fe_{tot}*	0.206	0.210	0.190	0.191	0.096	0.078	0.269	0.262	0.212	0.213	0.199	0.200	0.094	0.090	0.260	0.248	0.212	0.212	0.178	0.188	0.079	0.079	0.240	0.240	0.192	0.191	0.173	0.174	0.067	0.055	0.335	0.329
Fe^{2+}‡					0.091	0.076							0.078	0.077							0.034	0.034							0.044	0.017		
Fe^{3+}‡					0.005	0.003							0.016	0.014							0.045	0.045							0.023	0.038		
Mn	0.003	0.003	0.005	0.004	0.003	0.003	0.003	0.003	0.003	0.003	0.004	0.003	0.003	0.002	0.004	0.003	0.003	0.003	0.004	0.004	0.003	0.003	0.002	0.002	0.003	0.002	0.004	0.005	0.004	0.003	0.005	0.005
Mg	1.779	1.754	1.618	1.652	0.788	0.749	0.764	0.769	1.768	1.768	1.635	1.694	0.765	0.750	0.772	0.768	1.774	1.774	1.558	1.667	0.755	0.755	0.758	0.758	1.805	1.789	1.699	1.690	0.795	0.830	0.665	0.662
Ca	0.001	0.000	0.032	0.011	0.764	0.828	0.000	0.000	0.001	0.001	0.033	0.016	0.761	0.781	0.000	0.000	0.001	0.001	0.095	0.018	0.793	0.793	0.000	0.000	0.001	0.001	0.023	0.031	0.832	0.854	0.000	0.000
Na	0.000	0.000	0.006	0.003	0.119	0.118	0.000	0.000	0.000	0.000	0.006	0.001	0.135	0.138	0.000	0.001	0.000	0.000	0.021	0.003	0.143	0.143	0.000	0.000	0.000	0.000	0.004	0.005	0.117	0.103	0.000	0.000
K	0.000	0.000	0.001	0.001	0.001	0.001	0.000	0.001	0.000	0.000	0.001	0.000	0.001	0.001	0.000	0.001	0.000	0.000	0.000	0.000	0.000	0.000	0.000	0.000	0.000	0.000	0.000	0.000	0.000	0.000	0.000	0.000
Ni	0.007	0.008	0.003	0.003	0.002	0.001	0.008	0.007	0.008	0.007	0.002	0.003	0.003	0.000	0.008	0.009	0.008	0.008	0.003	0.002	0.001	0.001	0.008	0.008	0.008	0.007	0.004	0.002	0.001	0.002	0.004	0.003
Total	2.998	2.988	3.996	3.991	4.002	4.001	3.015	3.014	2.996	2.996	4.003	4.000	4.005	4.004	3.014	3.010	2.999	2.999	4.004	3.998	4.015	4.015	3.002	3.002	3.005	2.995	4.001	4.003	4.008	4.013	3.001	2.999
X_{Mg}**	0.896	0.893	0.895	0.896	0.891	0.905	0.739	0.746	0.893	0.892	0.891	0.895	0.890	0.892	0.748	0.756	0.893	0.893	0.897	0.899	0.905	0.905	0.759	0.759	0.904	0.904	0.907	0.907	0.922	0.938	0.665	0.668
Cr#**							0.116	0.106							0.101	0.080							0.102	0.102							0.351	0.345
CaTs					0.101	0.094							0.110	0.100							0.127	0.127							0.091	0.094		
Ac					0.005	0.003							0.016	0.014							0.045	0.045							0.023	0.038		
Jd					0.115	0.116							0.120	0.126							0.098	0.098							0.094	0.064		

† Number of oxygens for which cations are calculated.

*FeO and Fe calculated as total iron.

‡ Fe^{2+} and Fe^{3+} based on clinopyroxene stoichiometry.

** $X_{Mg} = Mg / (Mg + Fe^{2+})$. Fe_{tot} was used for orthopyroxene, olivine and spinel. Cr# = Cr / (Cr + Al).

Ac = Fe^{3+}, CaTs = CrCaTs+AlCaTS, CrCaTs = Cr, AlCaTs = ^{VI}AlJd, Jd = NaAc (if NaAc < ^{VI}Al), Jd=^{VI}Al (if NaAc ≥ ^{VI}Al).

Major element compositions (wt. %) of minerals used for geothermobarometry

Sample	BB142BAW								BB159E								BB180E								BB214AE							
Locality	Aarkob								Aarkob								Nich1								Nich1							
Domain	Se								Se								Se								Se							
Microstruct.	Coarse porph.								Coarse porph.								Coarse porph.								Coarse porph.							
Dcontact (m)	1086								1063								1221								935							
Rock type	Harzburgite								Cpx rich lhz.								Cpx rich lhz.								Harzburgite							
Mineral	ol		opx		cpx		sp		ol		opx		cpx		sp		ol		opx		cpx		sp		ol		opx		cpx		sp	
core / rim	c	r	c	r	c	r	c	r	c	r	c	r	c	r	c	r	c	r	c	r	c	r	c	r	c	r	c	r	c	r	c	r
SiO_2	41.7	41.5	56.1	56.7	53.3	53.2	0.08	0.08	41.2	41.1	54.4	54.7	51.7	51.8	0.08	0.08	41.1	41.7	54.1	55.9	51.8	53.7	0.03	0.05	40.9	40.9	55.8	56.0	52.6	53.3	0.05	0.04
TiO_2	b.d.l.	b.d.l.	0.07	0.07	0.32	0.39	0.27	0.23	b.d.l.	b.d.l.	0.16	0.19	0.63	0.67	0.09	0.07	b.d.l.	b.d.l.	0.22	0.13	0.65	0.44	b.d.l.	b.d.l.	b.d.l.	b.d.l.	0.09	0.08	0.21	0.20	0.24	0.21
Al_2O_3	b.d.l.	b.d.l.	3.71	2.43	4.77	4.15	34.5	36.5	b.d.l.	b.d.l.	6.44	5.96	8.74	8.21	59.8	60.1	b.d.l.	b.d.l.	6.37	4.00	8.55	6.71	62.0	60.4	b.d.l.	b.d.l.	2.74	2.67	4.27	3.94	30.5	36.4
Cr_2O_3	b.d.l.	b.d.l.	0.98	0.67	1.79	1.47	34.5	32.4	b.d.l.	b.d.l.	0.47	0.35	0.8	0.76	8.33	7.85	b.d.l.	b.d.l.	0.55	0.27	0.85	0.84	7.71	9.3	b.d.l.	b.d.l.	0.69	0.64	1.78	1.83	39.0	32.8
FeO	8.70	8.97	5.76	5.83	2.29	2.13	15.7	15.6	11.0	10.89	6.99	7.00	2.95	2.74	12.0	11.8	10.5	10.41	6.55	6.82	2.41	3.11	10.9	11.8	8.69	8.60	5.61	5.61	2.13	2.17	15.8	14.4
MnO	0.08	0.14	0.15	0.13	0.09	0.06	0.23	0.25	0.15	0.17	0.15	0.17	0.12	0.10	0.10	0.11	0.14	0.13	0.15	0.13	0.11	0.12	0.10	0.11	0.12	0.14	0.13	0.13	0.10	0.08	0.23	0.20
NiO	0.40	0.39	0.11	0.10	b.d.l.	b.d.l.	0.14	0.16	0.36	0.36	0.10	0.10	b.d.l.	b.d.l.	0.40	0.38	0.35	0.37	0.13	0.08	b.d.l.	b.d.l.	0.38	0.36	0.38	0.39	0.10	0.08	0.06	b.d.l.	0.14	0.16
MgO	49.3	49.1	33	33.8	15.2	15.5	14.8	14.8	47.2	47.5	30.9	31.3	13.6	13.7	19.5	19.8	47.9	47.8	30.6	32.5	13.3	16.6	19.4	18.6	50.1	50.4	34	34.2	15.8	15.9	14.8	16.0
CaO	b.d.l.	b.d.l.	0.60	0.45	21.3	21.6	b.d.l.	b.d.l.	b.d.l.	b.d.l.	0.75	0.61	19.7	20.1	b.d.l.	b.d.l.	b.d.l.	b.d.l.	1.61	0.58	20.6	17.0	b.d.l.	b.d.l.	b.d.l.	b.d.l.	0.83	0.79	20.6	20.9	b.d.l.	b.d.l.
Na_2O	b.d.l.	b.d.l.	b.d.l.	b.d.l.	1.51	1.48	b.d.l.	b.d.l.	b.d.l.	b.d.l.	0.10	0.06	2.24	2.18	b.d.l.	b.d.l.	b.d.l.	b.d.l.	0.12	b.d.l.	2.02	1.61	b.d.l.	b.d.l.	b.d.l.	b.d.l.	b.d.l.	0.12	1.74	1.63	b.d.l.	b.d.l.
K_2O	b.d.l.	b.d.l.	b.d.l.	b.d.l.	b.d.l.	b.d.l.	b.d.l.	b.d.l.	b.d.l.	b.d.l.	b.d.l.	b.d.l.	b.d.l.	b.d.l.	b.d.l.	b.d.l.	b.d.l.	b.d.l.	b.d.l.	b.d.l.	b.d.l.	b.d.l.	b.d.l.	b.d.l.	b.d.l.	b.d.l.	b.d.l.	b.d.l.	b.d.l.	b.d.l.	b.d.l.	b.d.l.
Total	100.2	100.1	100.5	100.2	100.6	100.1	100.2	100.1	99.9	100.1	100.4	100.5	100.6	100.4	100.3	100.2	100.0	100.4	100.5	100.4	100.2	100.2	100.5	100.6	100.3	100.5	100.0	100.3	99.3	100.0	100.7	100.2
O†	4	4	6	6	6	6	4	4	4	4	6	6	6	6	4	4	4	4	6	6	6	6	4	4	4	4	6	6	6	6	4	4
Si	1.014	1.010	1.924	1.948	1.920	1.927	0.002	0.002	1.015	1.011	1.877	1.886	1.858	1.866	0.002	0.002	1.009	1.018	1.870	1.924	1.864	1.914	0.001	0.001	0.996	0.994	1.924	1.926	1.919	1.930	0.001	0.001
Ti	0.000	0.000	0.002	0.002	0.009	0.011	0.006	0.005	0.000	0.000	0.004	0.005	0.017	0.018	0.002	0.001	0.000	0.000	0.006	0.003	0.018	0.012	0.001	0.001	0.000	0.000	0.002	0.002	0.006	0.006	0.005	0.004
Altot	0.000	0.001	0.150	0.098	0.203	0.177	1.178	1.239	0.000	0.001	0.262	0.242	0.370	0.348	1.814	1.822	0.000	0.000	0.259	0.162	0.363	0.282	1.858	1.826	0.001	0.000	0.112	0.108	0.183	0.168	1.056	1.226
^{IV}Al			0.076	0.052	0.080	0.073					0.123	0.114	0.142	0.134					0.130	0.076	0.136	0.086					0.076	0.074	0.081	0.070		
^{VI}Al			0.073	0.047	0.122	0.104					0.139	0.128	0.228	0.215					0.129	0.086	0.227	0.196					0.036	0.035	0.102	0.098		
Cr	0.000	0.000	0.027	0.018	0.051	0.042	0.792	0.738	0.000	0.000	0.013	0.010	0.023	0.022	0.169	0.160	0.000	0.000	0.015	0.007	0.024	0.024	0.155	0.190	0.000	0.000	0.019	0.017	0.051	0.052	0.906	0.743
Fe_{tot}*	0.177	0.183	0.165	0.168	0.069	0.064	0.380	0.376	0.226	0.224	0.202	0.202	0.088	0.082	0.259	0.253	0.216	0.213	0.189	0.196	0.073	0.093	0.231	0.252	0.177	0.175	0.162	0.161	0.065	0.066	0.387	0.345
Fe^{2+}‡					0.069	0.051							0.068	0.063							0.073	0.093							0.007	0.031		
Fe^{3+}‡					0.000	0.013							0.020	0.020							0.000	0.000							0.058	0.034		
Mn	0.002	0.003	0.004	0.004	0.003	0.002	0.006	0.006	0.003	0.004	0.004	0.005	0.004	0.003	0.002	0.002	0.003	0.003	0.004	0.004	0.003	0.004	0.002	0.002	0.002	0.003	0.004	0.004	0.003	0.002	0.006	0.005
Mg	1.785	1.784	1.689	1.733	0.816	0.838	0.641	0.635	1.733	1.741	1.586	1.607	0.729	0.737	0.747	0.757	1.755	1.741	1.577	1.666	0.714	0.885	0.735	0.710	1.819	1.826	1.750	1.754	0.861	0.861	0.646	0.682
Ca	0.001	0.001	0.022	0.017	0.821	0.839	0.000	0.000	0.001	0.000	0.028	0.023	0.760	0.776	0.000	0.001	0.001	0.000	0.060	0.021	0.794	0.652	0.000	0.000	0.001	0.000	0.031	0.029	0.807	0.811	0.000	0.000
Na	0.000	0.000	0.002	0.002	0.106	0.104	0.000	0.001	0.001	0.000	0.007	0.004	0.156	0.152	0.000	0.000	0.000	0.000	0.008	0.001	0.141	0.112	0.000	0.000	0.000	0.000	0.003	0.008	0.123	0.115	0.001	0.000
K	0.000	0.000	0.000	0.000	0.000	0.000	0.000	0.000	0.000	0.000	0.000	0.000	0.000	0.000	0.000	0.000	0.000	0.000	0.000	0.000	0.000	0.000	0.000	0.000	0.000	0.000	0.000	0.000	0.000	0.000	0.000	0.000
Ni	0.008	0.008	0.003	0.003	0.001	0.001	0.003	0.004	0.007	0.007	0.003	0.003	0.001	0.001	0.008	0.008	0.007	0.007	0.003	0.002	0.001	0.001	0.008	0.007	0.007	0.008	0.003	0.002	0.002	0.001	0.003	0.004
Total	2.986	2.989	3.987	3.993	3.998	4.004	3.007	3.005	2.985	2.988	3.985	3.985	4.007	4.006	3.004	3.006	2.991	2.982	3.992	3.989	3.995	3.978	2.992	2.990	3.004	3.006	4.010	4.013	4.019	4.011	3.013	3.010
X_{Mg}**	0.910	0.907	0.911	0.912	0.922	0.929	0.628	0.628	0.885	0.886	0.887	0.889	0.892	0.899	0.743	0.750	0.890	0.891	0.893	0.895	0.907	0.905	0.761	0.738	0.911	0.913	0.915	0.916	0.930	0.929	0.625	0.664
Cr#**							0.402	0.373							0.085	0.081							0.077	0.094							0.462	0.377
CaTs					0.068	0.056							0.116	0.105							0.112	0.111							0.088	0.070		
Ac					0.000	0.013							0.020	0.020							0.000	0.000							0.058	0.034		
Jd					0.107	0.091							0.137	0.134							0.143	0.114							0.065	0.080		

† Number of oxygens for which cations are calculated.

*FeO and Fe calculated as total iron.

‡ Fe^{2+} and Fe^{3+} based on clinopyroxene stoichiometry.

** X_{Mg} = Mg / (Mg + Fe^{2+}). Fe_{tot} was used for orthopyroxene, olivine and spinel. Cr# = Cr / (Cr + Al).

Ac = Fe^{3+}, CaTs = CrCaTs+AlCaTS, CrCaTs = Cr, AlCaTs = ^{VI}AlJd, Jd = NaAc (if NaAc < ^{VI}Al), Jd=^{VI}Al (if NaAc ≥ ^{VI}Al).

Major element compositions (wt. %) of minerals used for geothermobarometry

Sample	BB231E								BB246AS								BB244W							
Locality	Nich1								Aarkob								Aarkob							
Domain	Se								Se								Se							
Microstruct.	Coarse porph.								Coarse gran.								Coarse porph.							
Dcontact (m)	2246								726								607							
Rock type	Cpx rich lhz.								Cpx rich lhz.								Cpx rich lhz.							
Mineral	ol		opx		cpx		sp		ol		opx		cpx		sp		ol		opx		cpx		sp	
core / rim	c	r	c	r	c	r	c	r	c	r	c	r	c	r	c	r	c	r	c	r	c	r	c	r
SiO_2	41.6	41.5	54.8	54.7	52.0	b.d.l.	0.09	0.10	40.9	41.1	53.8	55.4	51.8	51.8	0.04	0.05	41.0	40.6	53.2	54.2	51.5	50.9	0.05	0.06
TiO_2	b.d.l.	b.d.l.	0.10	0.07	0.33	b.d.l.	b.d.l.	b.d.l.	b.d.l.	b.d.l.	0.14	0.12	0.34	0.37	b.d.l.	b.d.l.	b.d.l.	b.d.l.	0.18	0.14	0.58	0.66	b.d.l.	0.06
Al_2O_3	b.d.l.	b.d.l.	6.18	5.87	7.64	b.d.l.	59.8	60.9	b.d.l.	b.d.l.	6.15	4.83	7.71	6.67	55.2	55.5	b.d.l.	b.d.l.	6.31	5.61	8.62	8.35	61.6	61.7
Cr_2O_3	b.d.l.	b.d.l.	0.52	0.48	0.85	b.d.l.	9.41	8.92	b.d.l.	b.d.l.	0.74	0.54	1.12	1.02	14.5	13.80	b.d.l.	b.d.l.	0.42	0.41	0.69	0.70	7.75	7.47
FeO	9.94	9.93	6.29	6.45	2.64	b.d.l.	10.4	10.4	10.1	10.2	6.11	6.71	2.61	2.50	11.3	11.1	11.1	11.5	7.14	7.18	2.86	2.72	11.0	10.9
MnO	0.14	0.17	0.15	0.16	0.10	b.d.l.	0.10	0.08	0.13	0.14	0.15	0.17	0.10	0.09	0.11	0.11	0.16	0.15	0.14	0.17	0.06	0.09	0.11	0.10
NiO	0.39	0.36	0.08	0.08	b.d.l.	b.d.l.	0.41	0.40	0.37	0.38	0.10	0.05	b.d.l.	b.d.l.	0.31	0.33	0.38	0.39	0.10	0.08	b.d.l.	b.d.l.	0.42	0.35
MgO	48.2	48.1	31.2	31.7	14.1	b.d.l.	20.1	20.1	48.5	48.5	30.9	32.9	14.1	14.5	19.0	19.6	47.5	47.6	31.0	31.2	13.4	13.6	19.6	20.0
CaO	b.d.l.	b.d.l.	1.13	0.75	21.0	b.d.l.	b.d.l.	b.d.l.	b.d.l.	b.d.l.	1.89	0.42	20.9	21.3	b.d.l.	b.d.l.	b.d.l.	b.d.l.	0.73	0.59	20.5	20.6	b.d.l.	b.d.l.
Na_2O	b.d.l.	b.d.l.	0.07	b.d.l.	1.59	b.d.l.	b.d.l.	b.d.l.	b.d.l.	b.d.l.	0.12	b.d.l.	1.83	1.61	b.d.l.	b.d.l.	b.d.l.	b.d.l.	b.d.l.	b.d.l.	2.03	1.93	b.d.l.	b.d.l.
K_2O	b.d.l.	b.d.l.	b.d.l.	b.d.l.	b.d.l.	b.d.l.	b.d.l.	b.d.l.	b.d.l.	b.d.l.	b.d.l.	b.d.l.	b.d.l.	b.d.l.	b.d.l.	b.d.l.	b.d.l.	b.d.l.	b.d.l.	b.d.l.	b.d.l.	b.d.l.	b.d.l.	b.d.l.
Total	100.3	100.1	100.6	100.4	100.4	b.d.l.	100.3	101.0	100.0	100.4	100.1	101.1	100.5	99.9	100.5	100.5	100.2	100.2	99.3	99.6	100.2	99.7	100.5	100.6
O†	4	4	6	6	6		4	4	4	4	6	6	6	6	4	4	4	4	6	6	6	6	4	4
Si	1.016	1.015	1.883	1.885	1.874		0.002	0.003	1.005	1.005	1.864	1.894	1.867	1.879	0.001	0.001	1.008	1.001	1.862	1.887	1.858	1.851	0.001	0.002
Ti	0.000	0.000	0.002	0.002	0.009		0.000	0.001	0.000	0.000	0.004	0.003	0.009	0.010	0.000	0.000	0.000	0.000	0.005	0.004	0.016	0.018	0.000	0.001
Altot	0.000	0.000	0.250	0.238	0.325		1.804	1.821	0.000	0.000	0.251	0.195	0.327	0.285	1.701	1.705	0.000	0.000	0.260	0.230	0.367	0.358	1.849	1.848
^{IV}Al			0.117	0.115	0.126						0.136	0.106	0.133	0.121					0.138	0.113	0.142	0.149		
^{VI}Al			0.134	0.123	0.199						0.115	0.089	0.194	0.164					0.122	0.117	0.225	0.209		
Cr	0.000	0.000	0.014	0.013	0.024		0.191	0.179	0.000	0.000	0.020	0.015	0.032	0.029	0.299	0.283	0.000	0.000	0.011	0.011	0.020	0.020	0.156	0.150
Fe_{tot}*	0.203	0.203	0.181	0.186	0.080		0.223	0.221	0.207	0.209	0.177	0.192	0.078	0.076	0.247	0.242	0.228	0.237	0.209	0.209	0.086	0.083	0.235	0.231
Fe^{2+}‡					0.080								0.053	0.045							0.074	0.053		
Fe^{3+}‡					0.000								0.025	0.031							0.012	0.030		
Mn	0.003	0.003	0.004	0.005	0.003		0.002	0.002	0.003	0.003	0.004	0.005	0.003	0.003	0.002	0.002	0.003	0.003	0.004	0.005	0.002	0.003	0.002	0.002
Mg	1.753	1.754	1.600	1.628	0.758		0.769	0.761	1.772	1.769	1.599	1.678	0.756	0.787	0.742	0.763	1.742	1.750	1.615	1.617	0.721	0.736	0.744	0.757
Ca	0.001	0.001	0.042	0.028	0.813		0.000	0.000	0.001	0.001	0.070	0.015	0.807	0.828	0.000	0.000	0.001	0.000	0.027	0.022	0.791	0.804	0.000	0.000
Na	0.000	0.000	0.005	0.003	0.111		0.000	0.001	0.000	0.000	0.008	0.001	0.128	0.113	0.000	0.000	0.000	0.000	0.003	0.002	0.142	0.136	0.000	0.000
K	0.000	0.000	0.000	0.000	0.000		#####	0.000	0.000	0.000	0.000	0.000	0.000	0.000	0.000	0.000	0.000	0.000	0.000	0.000	0.000	0.000	0.000	0.000
Ni	0.008	0.007	0.002	0.002	0.001		0.008	0.008	0.007	0.007	0.003	0.001	0.001	0.001	0.006	0.007	0.008	0.008	0.003	0.002	0.001	0.001	0.009	0.007
Total	2.984	2.984	3.984	3.989	3.998		3.000	2.997	2.995	2.995	4.001	3.999	4.008	4.010	2.999	3.004	2.991	2.999	3.999	3.990	4.004	4.010	2.996	2.998
X_{Mg}**	0.896	0.896	0.898	0.898	0.905		0.775	0.775	0.896	0.894	0.900	0.897	0.906	0.912	0.750	0.759	0.884	0.881	0.885	0.886	0.893	0.899	0.760	0.766
Cr#**							0.096	0.090							0.150	0.143							0.078	0.075
CaTs					0.113								0.124	0.111							0.115	0.123		
Ac					0.000								0.025	0.031							0.012	0.030		
Jd					0.112								0.103	0.082							0.131	0.107		

† Number of oxygens for which cations are calculated.

*FeO and Fe calculated as total iron.

‡ Fe^{2+} and Fe^{3+} based on clinopyroxene stoichiometry.

** $X_{Mg} = Mg / (Mg + Fe^{2+})$. Fe_{tot} was used for orthopyroxene, olivine and spinel. Cr# = Cr / (Cr + Al).

Ac = Fe^{3+}, CaTs = CrCaTs+AlCaTS, CrCaTs = Cr, AlCaTs = ^{VI}AlJd, Jd = NaAc (if NaAc < ^{VI}Al), Jd=^{VI}Al (if NaAc ≥ ^{VI}Al).

Major element compositions (wt. %) of minerals used for geothermobarometry

Sample	BB249E								BB252AW								BB260W							
Locality	Nich2								Nich2								Nich2							
Domain	Se								Se								Se							
Microstruct.	Coarse porph.								Coarse porph.								Coarse gran.							
Dcontact (m)	1735								1442								986							
Rock type	Harzburgite								Dunite								Cpx rich lhz.							
Mineral	ol		opx		cpx		sp		ol		opx		cpx		sp		ol		opx		cpx		sp	
core / rim	c	r	c	r	c	r	c	r	c	r	c	r	c	r	c	r	c	r	c	r	c	r	c	r
SiO_2	41.4	42.1	b.d.l.	b.d.l.	52.4	52.5	0.04	0.05	41.4	41.4	54.2	54.6	51.1	51.8	0.02	0.04	41.0	40.7	54.0	55.0	51.7	51.3	0.07	0.08
TiO_2	b.d.l.	b.d.l.	b.d.l.	b.d.l.	0.41	0.46	b.d.l.	b.d.l.	b.d.l.	b.d.l.	0.12	0.12	0.47	0.42	0.06	b.d.l.	b.d.l.	b.d.l.	0.14	0.10	0.59	0.59	0.07	0.12
Al_2O_3	b.d.l.	b.d.l.	54.30	58.20	7.08	6.83	54.3	58.2	b.d.l.	b.d.l.	6.20	5.16	7.63	7.22	56.7	54.3	b.d.l.	b.d.l.	6.24	4.46	7.19	7.56	59.5	57.6
Cr_2O_3	b.d.l.	b.d.l.	15.50	11.6	1.34	1.25	15.5	11.60	b.d.l.	b.d.l.	0.74	0.54	1.20	1.10	12.6	15.50	b.d.l.	b.d.l.	0.56	0.34	0.88	0.92	10.2	12.20
FeO	9.47	9.32	11.60	11.20	2.54	2.63	11.6	11.2	9.50	9.39	6.15	6.09	2.79	2.70	11.9	11.6	9.85	9.878	6.17	6.42	2.35	2.45	10.0	10.4
MnO	0.13	0.13	0.14	0.13	0.10	0.11	0.14	0.13	0.12	0.11	0.12	0.14	0.08	0.10	0.10	0.14	0.14	0.14	0.14	0.13	0.10	0.10	0.10	0.14
NiO	0.39	0.40	0.27	0.35	b.d.l.	b.d.l.	0.27	0.35	0.39	0.39	0.08	0.11	b.d.l.	b.d.l.	0.34	0.27	0.37	0.41	0.09	0.08	b.d.l.	b.d.l.	0.34	0.30
MgO	48.0	48.2	18.6	18.9	14.9	15.4	18.6	18.9	48.9	48.8	32.4	32.8	15.2	16.0	18.8	18.6	48.6	48.8	32.1	33	14.3	14.2	20.1	19.8
CaO	b.d.l.	b.d.l.	b.d.l.	b.d.l.	20.0	19.6	b.d.l.	b.d.l.	b.d.l.	b.d.l.	0.64	0.62	19.6	19.3	b.d.l.	b.d.l.	b.d.l.	b.d.l.	0.72	0.47	21.1	20.8	b.d.l.	0.05
Na_2O	b.d.l.	b.d.l.	b.d.l.	b.d.l.	1.68	1.64	b.d.l.	b.d.l.	b.d.l.	b.d.l.	0.05	0.06	1.72	1.5	b.d.l.	b.d.l.	b.d.l.	b.d.l.	0.06	b.d.l.	1.71	1.78	b.d.l.	b.d.l.
K_2O	b.d.l.	b.d.l.	b.d.l.	b.d.l.	b.d.l.	b.d.l.	b.d.l.	b.d.l.	b.d.l.	b.d.l.	b.d.l.	b.d.l.	b.d.l.	b.d.l.	b.d.l.	b.d.l.	b.d.l.	b.d.l.	b.d.l.	b.d.l.	b.d.l.	b.d.l.	b.d.l.	b.d.l.
Total	99.5	100.2	100.5	100.5	100.4	100.6	100.5	100.5	100.3	100.1	100.6	100.2	99.8	100.2	100.4	100.5	100.1	100.0	100.2	100.0	99.9	99.8	100.4	100.6
O†	4	4	4	4	6	6	4	4	4	4	6	6	6	6	4	4	4	4	6	6	6	6	4	4
Si	1.018	1.025	0.001	0.001	1.883	1.884	0.001	0.001	1.008	1.010	1.861	1.882	1.852	1.865	0.000	0.001	1.005	0.999	1.862	1.900	1.873	1.862	0.002	0.002
Ti	0.000	0.000	0.001	0.001	0.011	0.012	0.001	0.001	0.000	0.000	0.003	0.003	0.013	0.011	0.001	0.001	0.000	0.000	0.004	0.003	0.016	0.016	0.001	0.002
Altot	0.000	0.000	1.681	1.774	0.300	0.289	1.681	1.774	0.001	0.000	0.251	0.210	0.326	0.306	1.740	1.681	0.000	0.000	0.254	0.181	0.307	0.323	1.797	1.750
^{IV}Al					0.117	0.116					0.139	0.118	0.148	0.135					0.138	0.100	0.127	0.138		
^{VI}Al					0.183	0.173					0.112	0.092	0.178	0.171					0.116	0.081	0.180	0.185		
Cr	0.000	0.000	0.323	0.237	0.038	0.035	0.323	0.237	0.000	0.000	0.020	0.015	0.034	0.031	0.260	0.323	0.000	0.000	0.015	0.009	0.025	0.026	0.206	0.249
Fe_{tot}*	0.194	0.190	0.255	0.242	0.077	0.079	0.255	0.242	0.194	0.192	0.177	0.176	0.084	0.081	0.259	0.255	0.202	0.203	0.178	0.186	0.071	0.074	0.213	0.223
Fe^{2+}‡					0.077	0.079							0.037	0.059							0.058	0.044		
Fe^{3+}‡					0.000	0.000							0.047	0.022							0.013	0.030		
Mn	0.003	0.003	0.003	0.003	0.003	0.003	0.003	0.003	0.002	0.002	0.004	0.004	0.003	0.003	0.002	0.003	0.003	0.003	0.004	0.004	0.003	0.003	0.002	0.003
Mg	1.758	1.748	0.727	0.727	0.796	0.825	0.727	0.727	1.777	1.776	1.657	1.686	0.819	0.859	0.729	0.727	1.776	1.788	1.652	1.698	0.772	0.770	0.767	0.760
Ca	0.001	0.001	0.000	0.000	0.769	0.755	0.000	0.000	0.000	0.001	0.023	0.023	0.762	0.745	0.000	0.000	0.001	0.001	0.027	0.017	0.817	0.809	0.000	0.001
Na	0.000	0.000	0.000	0.000	0.117	0.114	0.000	0.000	0.000	0.000	0.004	0.004	0.121	0.105	0.000	0.000	0.000	0.000	0.004	0.002	0.120	0.125	0.000	0.000
K	0.000	0.000	0.000	0.000	0.000	0.000	0.000	0.000	0.000	0.000	0.000	0.000	0.000	0.000	0.000	0.000	0.000	0.000	0.000	0.000	0.000	0.000	0.000	0.000
Ni	0.008	0.008	0.006	0.007	0.001	0.001	0.006	0.007	0.008	0.008	0.002	0.003	0.001	0.001	0.007	0.006	0.007	0.008	0.003	0.002	0.000	0.000	0.007	0.006
Total	2.982	2.975	2.996	2.993	3.995	3.998	2.996	2.993	2.991	2.989	4.002	4.005	4.015	4.007	2.999	2.996	2.994	3.001	4.002	4.003	4.004	4.010	2.996	2.996
X_{Mg}**	0.900	0.902	0.740	0.750	0.912	0.913	0.740	0.750	0.902	0.903	0.904	0.906	0.907	0.914	0.738	0.740	0.898	0.898	0.903	0.901	0.916	0.912	0.783	0.773
Cr#**			0.161	0.118			0.161	0.118							0.130	0.161							0.103	0.124
CaTs					0.105	0.096							0.138	0.120							0.100	0.116		
Ac					0.000	0.000							0.047	0.022							0.013	0.030		
Jd					0.118	0.115							0.074	0.083							0.107	0.096		

† Number of oxygens for which cations are calculated.

*FeO and Fe calculated as total iron.

‡ Fe^{2+} and Fe^{3+} based on clinopyroxene stoichiometry.

** $X_{Mg} = Mg / (Mg + Fe^{2+})$. Fe_{tot} was used for orthopyroxene, olivine and spinel. Cr# = Cr / (Cr + Al).

Ac = Fe^{3+}, CaTs = CrCaTs+AlCaTS, CrCaTs = Cr, AlCaTs = ^{VI}AlJd, Jd = NaAc (if NaAc < ^{VI}Al), Jd=^{VI}Al (if NaAc ≥ ^{VI}Al).

Major element compositions (wt. %) of minerals used for geothermobarometry

Sample	BB262E								BB270W								BB272E							
Locality	Aarkob								Nich2								Nich2							
Domain	Se								Se								Se							
Microstruct.	Coarse gran.								Coarse porph.								Coarse porph.							
Dcontact (m)	900								828								559							
Rock type	Cpx rich lhz.								Harzburgite								Harzburgite							
Mineral	ol		opx		cpx		sp		ol		opx		cpx		sp		ol		opx		cpx		sp	
core / rim	c	r	c	r	c	r	c	r	c	r	c	r	c	r	c	r	c	r	c	r	c	r	c	r
SiO_2	41.0	41.1	54.0	54.4	51.5	52.8	0.04	0.06	41.4	41.5	54.9	55.5	52.0	52.7	0.14	0.02	41.5	41.5	55.4	55.8	57.2	0.12	0.12	
TiO_2	b.d.l.	b.d.l.	0.16	0.12	0.32	0.39	0.06	0.06	b.d.l.	b.d.l.	b.d.l.	0.06	0.14	0.13	0.06	b.d.l.	b.d.l.	b.d.l.	0.08	b.d.l.	b.d.l.	0.08	0.08	
Al_2O_3	b.d.l.	b.d.l.	6.65	5.85	7.69	6.08	58.9	58.6	b.d.l.	b.d.l.	5.03	4.06	5.36	5.20	47.2	40.8	b.d.l.	b.d.l.	4.52	3.71	2.56	45.7	45.7	
Cr_2O_3	b.d.l.	b.d.l.	0.71	0.59	1.13	0.77	11.0	11.80	b.d.l.	b.d.l.	0.97	0.77	1.58	1.55	23.9	29.20	b.d.l.	b.d.l.	0.78	0.55	0.32	21.7	21.70	
FeO	9.87	9.56	5.85	6.10	2.52	2.18	10.4	10.4	9.34	8.936	5.81	5.91	2.05	2.20	12.1	13.4	9.19	9.21	5.74	5.94	6.15	14.5	14.5	
MnO	0.11	0.13	0.15	0.15	0.08	0.09	0.13	0.12	0.14	0.11	0.11	0.13	0.09	0.09	0.15	0.23	0.13	0.13	0.10	0.10	0.14	0.14	0.14	
NiO	0.36	0.36	0.10	0.08	b.d.l.	0.06	0.34	0.34	0.35	0.38	0.10	0.09	b.d.l.	b.d.l.	0.22	0.16	0.38	0.39	0.06	0.09	0.08	0.24	0.24	
MgO	48.6	48.9	30.9	32	14.9	15.1	20.0	19.7	48.2	48.5	31.7	32.1	14.9	15.0	17.1	15.8	48.9	49.0	32.0	33.0	33.5	17.2	17.2	
CaO	b.d.l.	b.d.l.	1.83	1.06	19.1	21.5	b.d.l.	b.d.l.	b.d.l.	b.d.l.	0.82	0.89	22.0	22.1	b.d.l.	b.d.l.	b.d.l.	b.d.l.	0.92	0.54	0.42	b.d.l.	b.d.l.	
Na_2O	b.d.l.	b.d.l.	0.22	0.10	1.78	1.61	b.d.l.	b.d.l.	b.d.l.	b.d.l.	b.d.l.	b.d.l.	1.18	1.15	b.d.l.	b.d.l.	b.d.l.	b.d.l.	0.14	b.d.l.	b.d.l.	b.d.l.	b.d.l.	
K_2O	b.d.l.	b.d.l.	b.d.l.	b.d.l.	b.d.l.	b.d.l.	b.d.l.	b.d.l.	b.d.l.	b.d.l.	b.d.l.	b.d.l.	b.d.l.	b.d.l.	b.d.l.	b.d.l.	b.d.l.	b.d.l.	b.d.l.	b.d.l.	b.d.l.	b.d.l.	b.d.l.	
Total	100.0	100.1	100.6	100.5	99.1	100.6	100.9	101.0	99.4	99.45	99.5	99.6	99.4	100.1	100.9	99.7	100.1	100.3	99.7	99.8	100.4	99.6	99.6	
O†	4	4	6	6	6	6	4	4	4	4	6	6	6	6	4	4	4	4	6	6	6	4	4	
Si	1.006	1.006	1.861	1.873	1.871	1.897	0.001	0.001	1.017	1.017	1.903	1.923	1.899	1.907	0.004	0.001	1.012	1.011	1.916	1.927	1.959	0.003	0.003	
Ti	0.000	0.000	0.004	0.003	0.009	0.011	0.001	0.001	0.000	0.000	0.001	0.001	0.004	0.003	0.001	0.001	0.000	0.000	0.002	0.001	0.001	0.002	0.002	
Altot	0.000	0.000	0.270	0.237	0.330	0.258	1.776	1.769	0.000	0.000	0.205	0.166	0.230	0.222	1.502	1.354	0.000	0.000	0.184	0.151	0.104	1.486	1.486	
^{IV}Al			0.139	0.127	0.129	0.103					0.097	0.077	0.101	0.093					0.084	0.073	0.041			
^{VI}Al			0.131	0.111	0.201	0.155					0.109	0.089	0.129	0.129					0.100	0.078	0.063			
Cr	0.000	0.001	0.019	0.016	0.032	0.022	0.223	0.238	0.000	0.000	0.027	0.021	0.045	0.044	0.510	0.650	0.000	0.000	0.021	0.015	0.009	0.473	0.473	
Fe_{tot}*	0.202	0.196	0.168	0.176	0.077	0.065	0.223	0.223	0.192	0.183	0.169	0.171	0.063	0.067	0.273	0.316	0.188	0.188	0.166	0.171	0.177	0.335	0.335	
Fe^{2+}‡					0.070	0.040							0.060	0.067							0.177			
Fe^{3+}‡					0.007	0.025							0.002	0.000							0.000			
Mn	0.002	0.003	0.004	0.004	0.002	0.003	0.003	0.003	0.003	0.002	0.003	0.004	0.003	0.003	0.003	0.005	0.003	0.003	0.003	0.003	0.004	0.003	0.003	
Mg	1.775	1.781	1.585	1.642	0.810	0.811	0.763	0.752	1.763	1.773	1.637	1.659	0.810	0.811	0.688	0.665	1.777	1.778	1.646	1.698	1.712	0.709	0.709	
Ca	0.001	0.001	0.067	0.039	0.746	0.828	0.000	0.000	0.000	0.000	0.031	0.033	0.862	0.856	0.001	0.000	0.001	0.000	0.034	0.020	0.016	0.000	0.000	
Na	0.000	0.000	0.015	0.007	0.126	0.112	0.000	0.000	0.000	0.000	0.002	0.002	0.084	0.081	0.001	0.000	0.000	0.000	0.009	0.002	0.002	0.000	0.000	
K	0.000	0.000	0.000	0.000	0.000	0.000	0.000	0.000	0.000	0.000	0.000	0.000	0.000	0.000	0.000	0.000	0.000	0.000	0.000	0.000	0.000	0.000	0.000	
Ni	0.007	0.007	0.003	0.002	0.000	0.002	0.007	0.007	0.007	0.008	0.003	0.002	0.001	0.001	0.005	0.004	0.007	0.008	0.002	0.002	0.002	0.005	0.005	
Total	2.994	2.994	3.997	4.000	4.002	4.008	2.998	2.994	2.982	2.983	3.981	3.983	4.001	3.996	2.989	2.996	2.988	2.988	3.984	3.990	3.985	3.016	3.016	
X_{Mg}**	0.898	0.901	0.904	0.903	0.914	0.925	0.774	0.771	0.902	0.906	0.907	0.907	0.928	0.924	0.716	0.678	0.905	0.905	0.909	0.908	0.906	0.679	0.679	
Cr#**							0.112	0.119							0.254	0.324						0.241	0.241	
CaTs					0.115	0.090							0.094	0.094							0.070			
Ac					0.007	0.025							0.002	0.000							0.000			
Jd					0.119	0.088							0.081	0.081							0.002			

† Number of oxygens for which cations are calculated.

*FeO and Fe calculated as total iron.

‡ Fe^{2+} and Fe^{3+} based on clinopyroxene stoichiometry.

** $X_{Mg} = Mg / (Mg + Fe^{2+})$. Fe_{tot} was used for orthopyroxene, olivine and spinel. Cr# = Cr / (Cr + Al).

Ac = Fe^{3+}, CaTs = CrCaTs+AlCaTS, CrCaTs = Cr, AlCaTs = ^{VI}AlJd, Jd = NaAc (if NaAc < ^{VI}Al), Jd=^{VI}Al (if NaAc ≥ ^{VI}Al).

12. Calculated temperatures in Beni Bousera peridotites

Calculated equilibrium temperatures for Beni Bousera peridotites

Sample	valley	Domain	Latitude	Longitude	Rock type	Microstructure	$D_{contact}$ (m)	$d_{ol.}$ (µm)	†P (Gpa) c	†P (Gpa) r	$T_{cpx-opx}$ (ºC) c	$T_{cpx-opx}$ (ºC) r	T_{ca-opx} (ºC) c	T_{ca-opx} (ºC) r	$T_{ca-opx-mod}$ (ºC) c	$T_{ca-opx-mod}$ (ºC) r	$T_{Cr-Al-opx}$ (ºC) c	$T_{Cr-Al-opx}$ (ºC) r
BB191	Amaziten	Ar	35°18'05.4"	4°55'03.2"	Cpx-rich lhz.	Fine porph.	225	-	1.8	1.8	-	787	-	879	-	840	-	901
BB187A	Amaziten	Ar	35°18'02.7"	4°54'58.4"	Lherzolite	Fine porph.	271	-	1.8	1.8	-	800	-	910	-	879	-	940
BB183A	Amaziten	Ar	35°18'09.9"	4°54'39.8"	Cpx-rich lhz.	Fine porph.	583	-	1.8	1.8	859	838	997	882	983	844	986	915
BB026	Azarhar	Ar	35°14'17.9"	4°52'11.2"	Harzburgite	Fine porph.	306	-	1.8	1.8	836	940	900	954	867	933	1099	1050
BB035D	Azarhar	Ar	35°14'26.6"	4°51'55.2"	Harzburgite	Fine porph.	327	-	1.8	1.8	602	1350	946	908	923	876	1000	919
BB207	Nich1	Ar	35°15'07.6"	4°52'46.1"	Lherzolite	Fine porph.	666	263	1.8	1.8	864	777	965	895	946	861	995	924
BB095A	Yahia1	Ar	35°16'11.2"	4°54'41.7"	Cpx-rich lhz.	Fine porph.	260	198	1.8	1.8	871	794	940	928	916	902	1116	1029
BB098	Yahia1	Ar	35°16'13.7"	4°54'27.2"	Lherzolite	Fine porph.	426	235	1.8	1.8	894	785	915	882	885	844	1129	835
BB102	Yahia1	Ar	35°16'17.8"	4°54'18.3"	Lherzolite	Fine porph.	555	-	1.8	1.8	930	827	953	1054	932	1048	1151	1033
BB204	Nich1	Ar-Se	35°14'58.2"	4°52'50.1"	Cpx-rich lhz.	Fine porph.	490	188	1.8	1.8	868	808	1274	916	1272	887	1106	1023
BB163	Aarkob	Ar-Se	35°15'31.9"	4°51'27.1"	Cpx-rich lhz.	Coarse porph.	1012	-	1.8	1.8	792	902	973	919	955	891	1015	1030
BB211	Nich1	Ar-Se	35°15'15.8"	4°52'41.3"	Cpx-rich lhz.	Fine porph.	815	192	1.8	1.8	857	832	943	902	920	869	947	1028
BB216	Nich1	Ar-Se	35°15'23.6"	4°52'32.4"	Lherzolite	Coarse porph.	1012	263	1.8	1.8	950	1108	1054	834	1048	782	1048	1095
BB259	Nich2	Ar-Se	35°15'39.0"	4°52'08.2"	Harzburgite	Coarse porph.	1113	-	1.8	1.8	857	891	994	943	981	920	1111	1049
BB256A	Nich2	Ar-Se	35°15'43.1"	4°52'09.1"	Lherzolite	Coarse porph.	1159	-	1.8	1.8	837	805	1043	961	1037	941	1101	972
BB254	Nich2	Ar-Se	35°15'51.8"	4°52'10.1"	Cpx-rich lhz.	Coarse porph.	1326	-	1.8	1.8	882	860	1008	1074	997	1071	1148	991
BB079	Yahia1	Ar-Se	35°16'26.0"	4°53'58.4"	Cpx-rich lhz.	Coarse porph.	872	-	1.8	1.8	858	831	1216	1083	1218	1081	1139	1110
BB078	Yahia1	Ar-Se	35°16'32.4"	4°53'58.0"	Lherzolite	Coarse porph.	903	250	1.8	1.8	861	882	970	835	952	783	1176	873
BB076C	Yahia1	Ar-Se	35°16'54.8"	4°53'45.9"	Cpx-rich lhz.	Coarse porph.	1084	325	1.8	1.8	866	901	988	981	974	965	1110	1007
BB070	Yahia1	Ar-Se	35°17'01.8"	4°53'44.9"	Harzburgite	Coarse porph.	1139	-	1.8	1.8	1283	1006	1036	932	1028	906	1107	916
BB201	Amaziten	Myl	35°18'12.9"	4°55'17.0"	Cpx-rich lhz.	Mylonitic	1	-	*2.2	*2.1	926	903	914	892	1103	856	1035	876
BB006A	Azarhar	Myl	35°14'15.7"	4°52'41.6"	Lherzolite	Mylonitic	118	-	*2.1	*2.1	798	887	904	917	871	884.4	1066	923
BB001	Beach	Myl	35°19'08.5"	4°55'40.3"	Cpx-rich lhz.	Mylonitic	31	-	1.8	1.8		746		892		857		889
BB171A	Nich1	Myl	35°14'48.7"	4°52'54.1"	Harzburgite	Mylonitic	317	157	*2.0	*1.9	909	930	871	857	829	812	902	896
BB083	Yahia1	Myl	35°16'19.9"	4°54'59.9"	Cpx-rich lhz.	Mylonitic	5	127	*2.4	*2.1	821	791	915	882	886	843	1016	938
BB085	Yahia1	Myl	35°16'01.3"	4°54'49.8"	Lherzolite	Mylonitic	131	118	*2.1	-	708	-	958	-	937	-	977	-
BB087	Yahia1	Myl	35°16'03.7"	4°54'47.0"	Harzburgite	Mylonitic	165	-	*1.9	*1.9	814	768	861	910	816	879	1084	908
BB088B	Yahia1	Myl	35°16'05.0"	4°54'47.6"	Lherzolite	Mylonitic	169	158	1.8	1.8	831	808	920	870	891	828	1131	1004
BB122B	Yahia2	Myl	35° 15'04.5"	4° 53'46.0"	Lherzolite	Mylonitic	116	-	*2.0	*2.0	790	799	928	880	901	842	981	1026
BB159	Aarkob	Se	35°15'30.8"	4°51'22.7"	Cpx-rich lhz.	Coarse porph.	1063	-	1.8	1.8	895	848	997	952	984	931	1079	1012

†P=1.8 Gpa for temperature calculation (from Frets et al., 2012)

*P in garnet-spinel mylonites calculated applying the geobarometer calibration of the Grt-Sp lherzolite transition in the CMAS-Cr system (Webb & Wood, 1986), corrected for the effect of FeO in olivine (O'Neill, 1981)

Calculated equilibrium temperatures for Beni Bousera peridotites

Sample	valley	Domain	Latitude	Longitude	Rock type	Microstructure	$D_{contact}$ (m)	$d_{ol.}$ (µm)	†P (Gpa) c	†P (Gpa) r	$T_{cpx-opx}$ (ºC) c	$T_{cpx-opx}$ (ºC) r	T_{ca-opx} (ºC) c	T_{ca-opx} (ºC) r	$T_{ca-opx-mod}$ (ºC) c	$T_{ca-opx-mod}$ (ºC) r	$T_{Cr-Al-opx}$ (ºC) c	$T_{Cr-Al-opx}$ (ºC) r
BB142B	Aarkob	Se	35°15'23.0"	4°51'17.6"	Harzburgite	Coarse porph.	1086	-	1.8	1.8	871	787	948	888	925	851	1149	983
BB138	Aarkob	Se	35°15'29.7"	4°51'04.6"	Lherzolite	Coarse gran.	1253	209	1.8	1.8	771	747	958	1024	937	1015	1148	1168
BB055	Aarkob	Se	35°15'36.8"	4°50'56.3"	Cpx-rich lhz.	Coarse porph.	1385	-	1.8	1.8	806	762	972	964	955	945	1136	962
BB044A	Aarkob	Se	35°15'8.0"	4°50'35.2"	Cpx-rich lhz.	Coarse gran.	1767	-	1.8	1.8	879	1007	1070	1320	1066	1313	1100	1080
BB108	Amaziten	Se	35°18'24.7"	4°54'08.2"	Lherzolite	Coarse porph.	1079	-	1.8	1.8	830	807	903	902	870	869	1137	1011
BB244	Mter	Se	35°13'49.7"	4°49'38.3"	Cpx-rich lhz.	Coarse porph.	607	-	1.8	1.8	837	793	996	947	982	925	1056	1022
BB246A	Mter	Se	35°13'48.5"	4°49'44.2"	Cpx-rich lhz.	Coarse gran.	726	-	1.8	1.8	862	806	1260	874	1259	834	1173	1032
BB262	Mter	Se	35°13'54.3"	4°49'54.2"	Cpx-rich lhz.	Coarse gran.	900	-	1.8	1.8	1061	845	1246	1085	1246	1083	1186	1103
BB214a	Nich1	Se	35°15'19.6"	4°52'35.3"	Harzburgite	Coarse porph.	935	317	1.8	1.8	852	869	1022	1011	1012	1000	1006	988
BB180	Nich1	Se	35°15'35.9"	4°52'30.4"	Cpx-rich lhz.	Coarse porph.	1221	249	1.8	1.8	841	1161	1207	940	1208	916	1105	900
BB041	Nich1	Se	35°16'00.6"	4°52'22.8"	Lherzolite	Coarse porph.	1597	480	1.8	1.8	903	799	1009	899	998	865	1142	1056
BB042	Nich1	Se	35°15'54.2"	4°52'29.6"	Lherzolite	Coarse porph.	1597	-	1.8	1.8	912	859	1099	914	1098	884	1116	975
BB039	Nich1	Se	35°16'09.6"	4°52'12.7"	Harzburgite	Coarse porph.	1736	622	1.8	1.8	1001	900	957	1210	937	1211	1123	1117
BB017	Nich1	Se	35°16'16.2"	4°52'03.6"	Cpx-rich lhz.	Coarse porph.	1849	-	1.8	1.8	856	1016	1206	917	1208	888	1115	887
BB019	Nich1	Se	35°16'18.1"	4°52'00.1"	Harzburgite	Coarse gran.	1888	396	1.8	1.8	845	735	1081	947	1079	924	1187	1024
BB014	Nich1	Se	35°16'34.9"	4°51'50.1"	Harzburgite	Coarse porph.	2102	-	1.8	1.8	941	813	1052	1012	1047	1001	1170	1059
BB231	Nich1	Se	35°16'51.6"	4°51'49.2"	Cpx-rich lhz.	Coarse porph.	2246	-	1.8	1.8	895	891	1101	999	1100	986	1089	1059
BB272	Nich2	Se	35°15'02.0"	4°52'34.8"	Harzburgite	Coarse porph.	559	-	1.8	1.8	-	-	1049	925	1043	897	1123	997
BB270	Nich2	Se	35°15'19.7"	4°52'10.4"	Harzburgite	Coarse porph.	828	-	1.8	1.8	820	840	1022	1041	1012	1034	1210	1094
BB260	Nich2	Se	35°15'28.3"	4°52'15.8"	Cpx-rich lhz.	Coarse gran.	986	-	1.8	1.8	840	803	989	899	975	865	1105	947
BB252A	Nich2	Se	35°15'58.9"	4°51'52.2"	Dunite	Coarse porph.	1442	-	1.8	1.8	1002	1061	960	953	940	932	1166	1050
BB249	Nich2	Se	35°16'17.8"	4°51'34.1"	Harzburgite	Coarse porph.	1735	-	1.8	1.8	991	1024	983	1026	967.6	1017	1139	1072
BB063A	Yahia1	Se	35°17'10.6"	4°53'36.9"	Lherzolite	Coarse porph.	1247	-	1.8	1.8	952	842	1041	886	1035	848	1108	894
BB062	Yahia1	Se	35°17'15.5"	4°53'32.3"	Cpx-rich lhz.	Coarse porph.	1309	-	1.8	1.8	1004	784	1032	810	1024	750	1093	1045
BB059C	Yahia1	Se	35°17'21.4"	4°53'27.3"	Lherzolite	Coarse porph.	1362	-	1.8	1.8	847	856	1065	878	1061	839	1102	1116
BB056	Yahia1	Se	35°17'40.8"	4°53'06.0"	Cpx-rich lhz.	Coarse porph.	1586	-	1.8	1.8	877	871	1004	981	992	965	1114	1045

†P=1.8 Gpa for temperature calculation (from Frets et al., 2012)

*P in garnet-spinel mylonites calculated applying the geobarometer calibration of the Grt-Sp lherzolite transition in the CMAS-Cr system (Webb andWood, 1986), corrected for the effect of FeO in olivine (O'Neill, 1981)

13. Synthetic EBSD sheets of peridotite samples

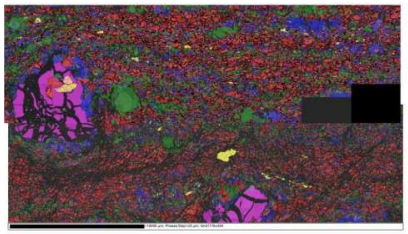

step=35μm

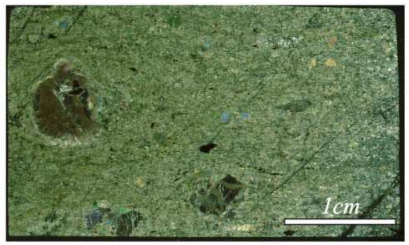

Geographic coordinates (1 point per grain)

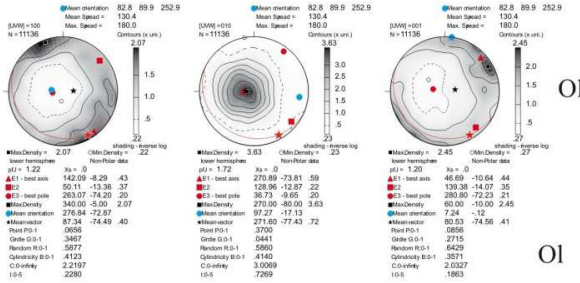

Ol

Ol

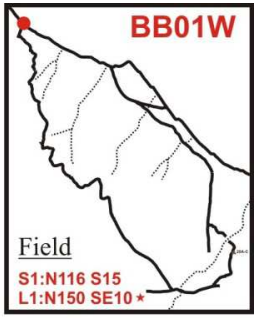

Sample coordinates (raw data)

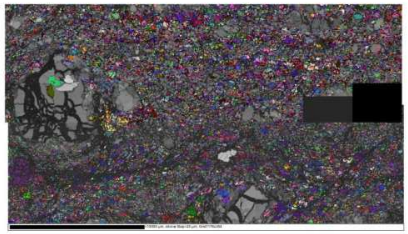

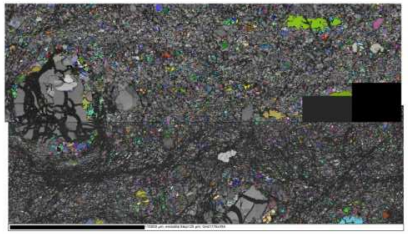

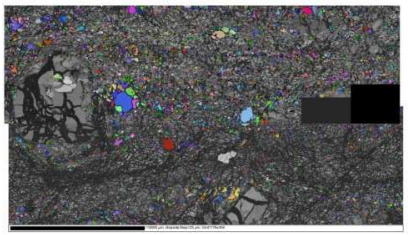

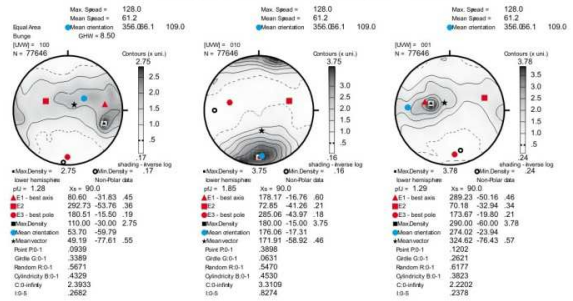

Ol

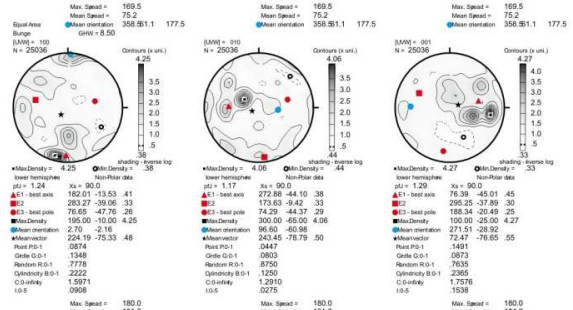

Opx

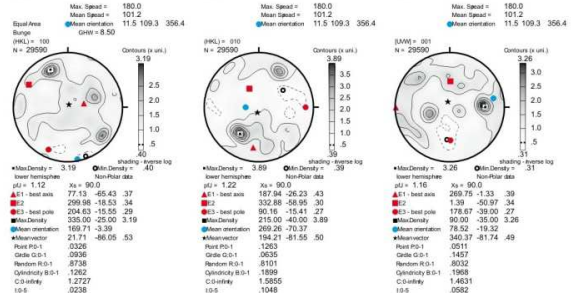

Cpx

Sample coordinates (1 point per grain)

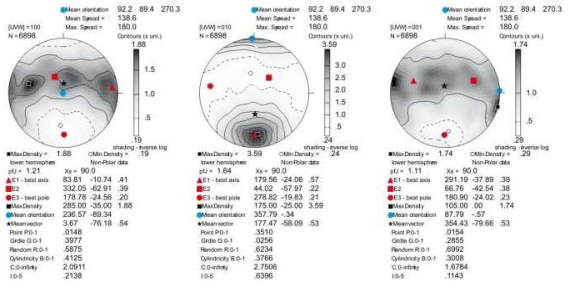

Ol

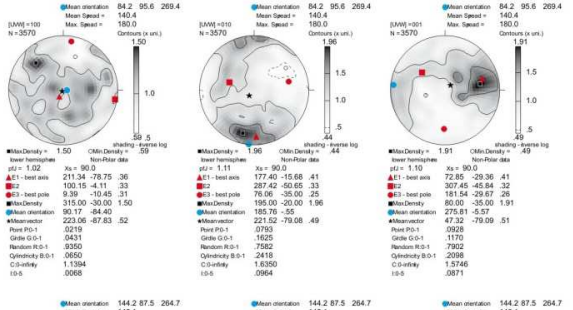

Opx

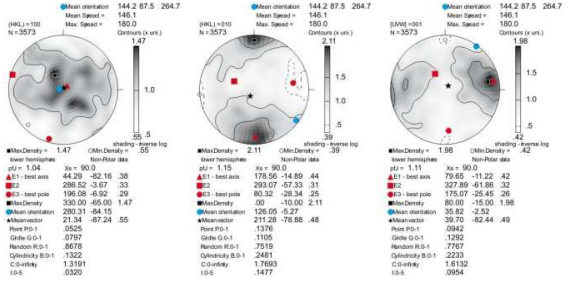

Cpx

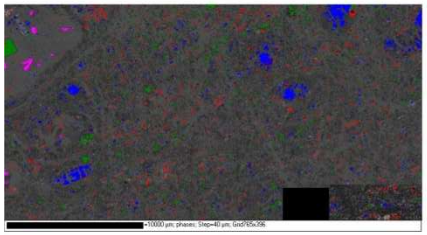

step=40μm

Geographic coordinates (1 point per grain)

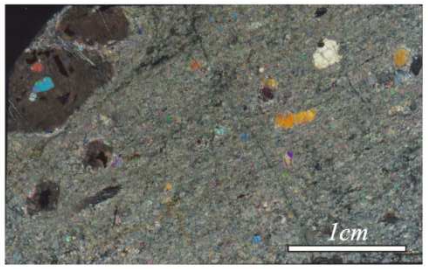

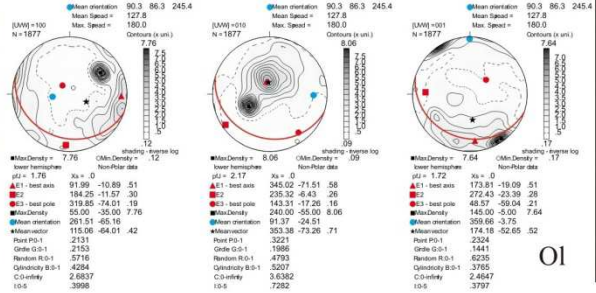

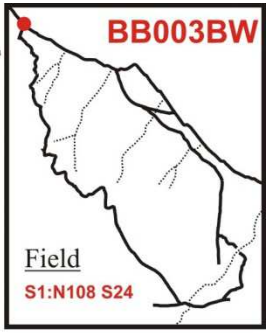

Ol

Sample coordinates (raw data)

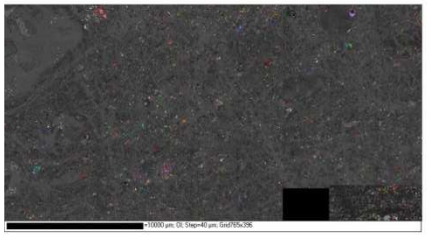

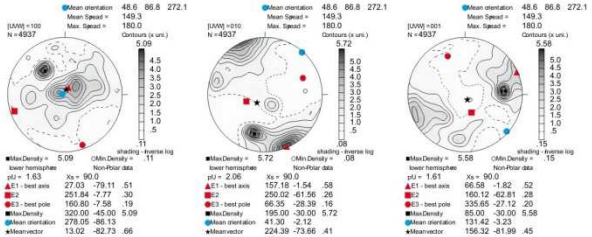

Ol

Sample coordinates (1 point per grain)

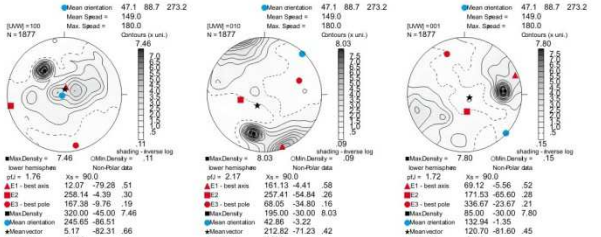

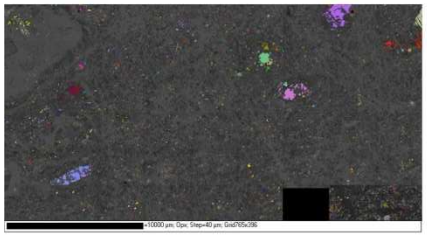

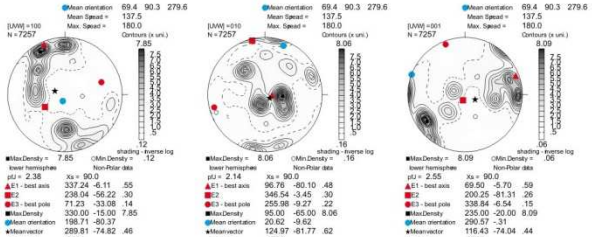

Opx

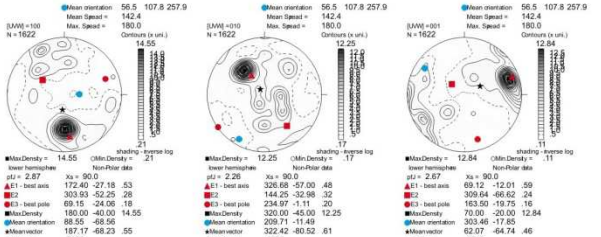

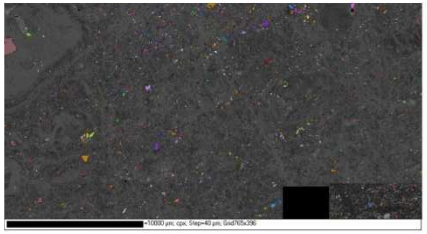

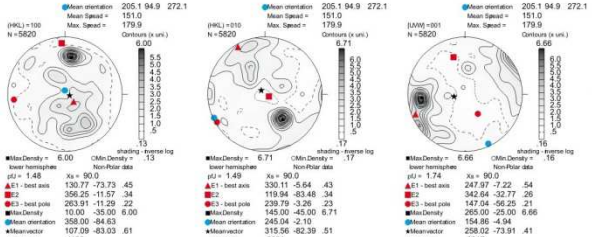

Cpx

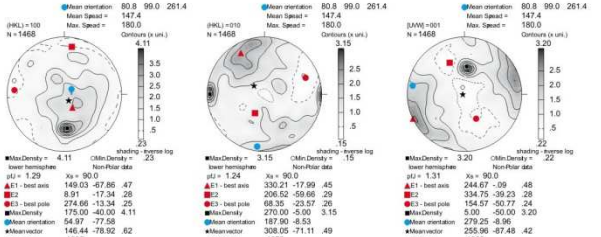

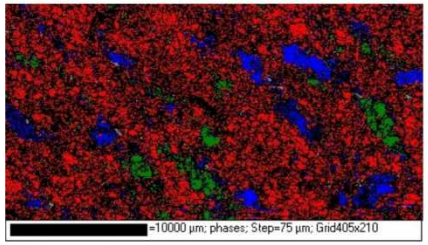

step=75µm

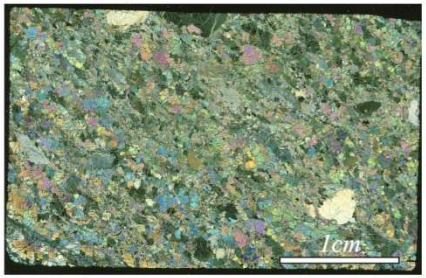

Geographic coordinates (1 point per grain)

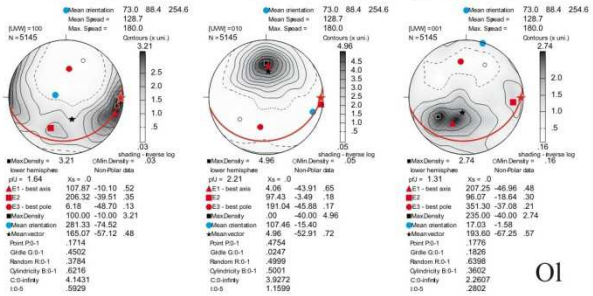

Ol

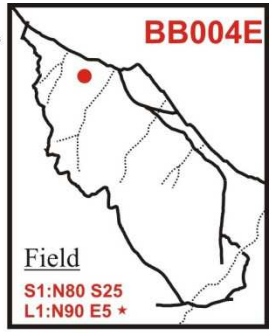

Sample coordinates (raw data)

Sample coordinates (1 point per grain)

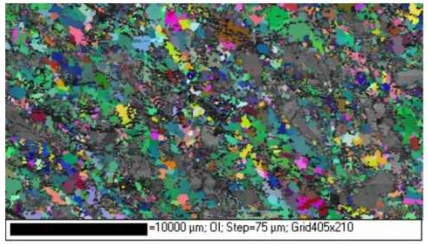

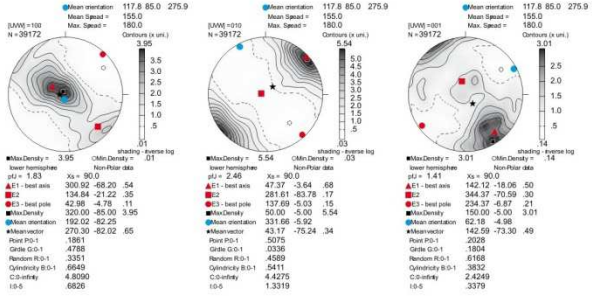

Ol

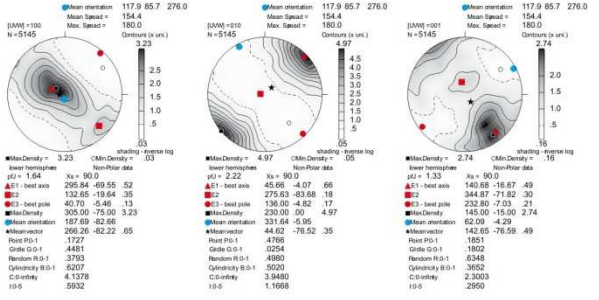

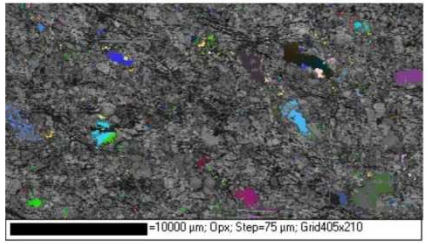

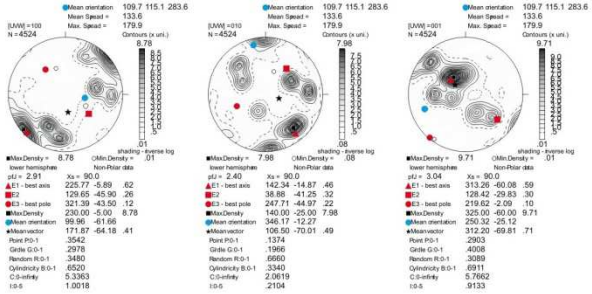

Opx

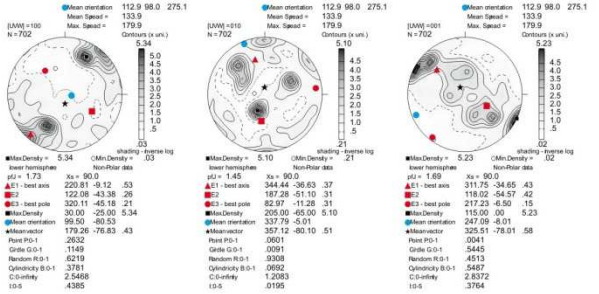

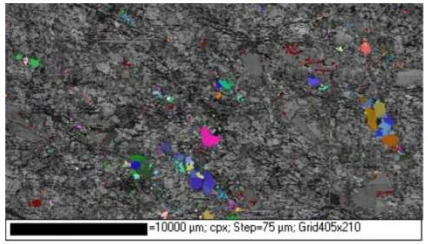

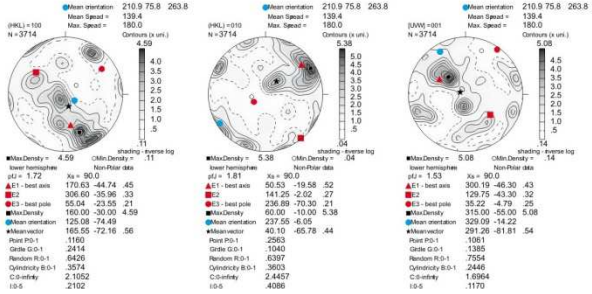

Cpx

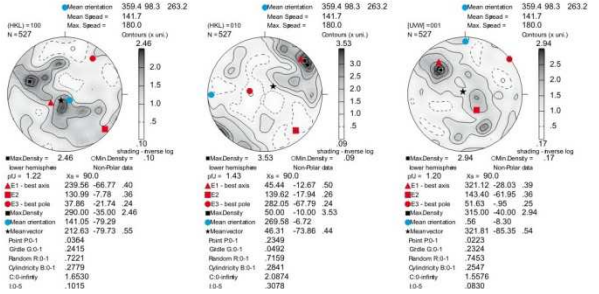

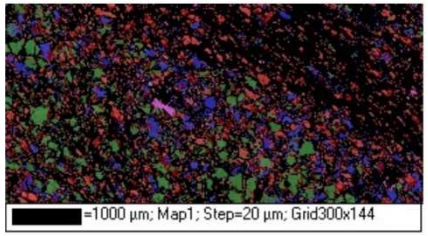

step=75µm

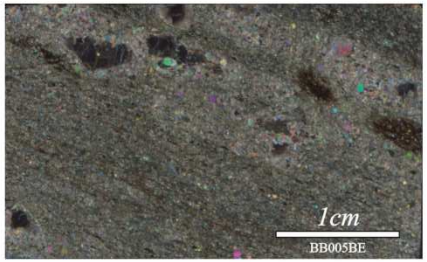

Geographic coordinates (1 point per grain)

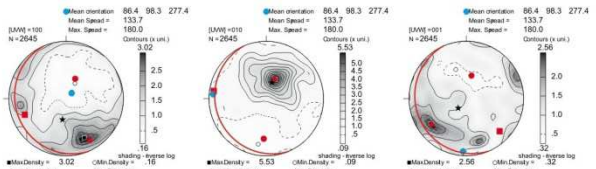

Ol

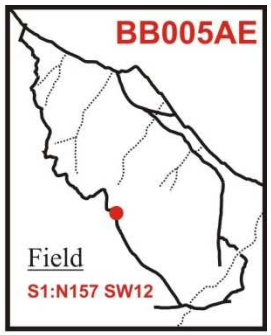

Sample coordinates (raw data)

Sample coordinates (1 point per grain)

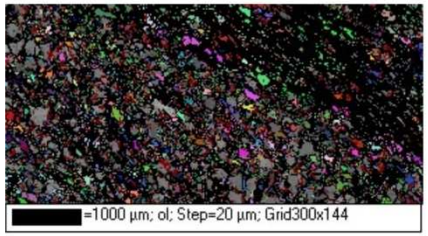

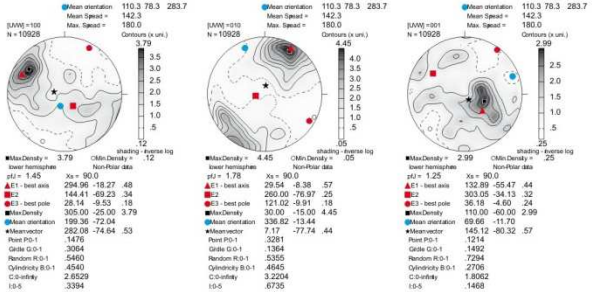

Ol

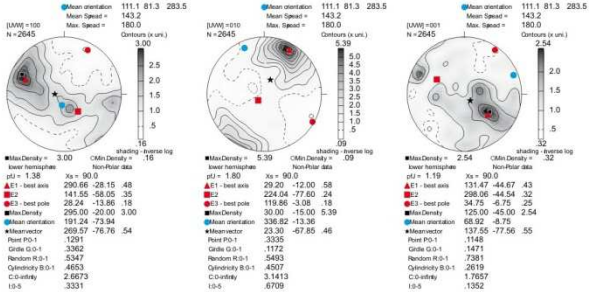

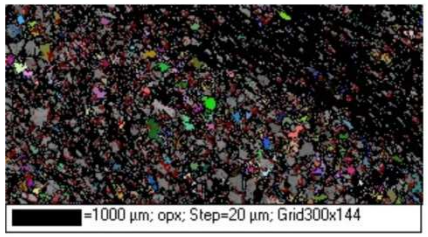

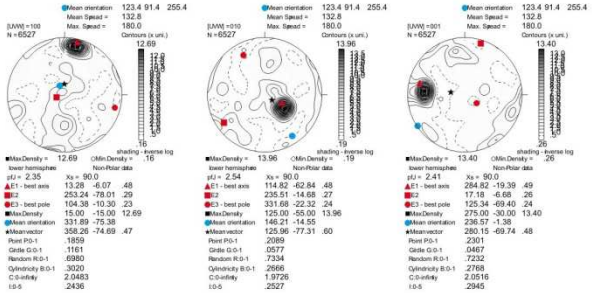

Opx

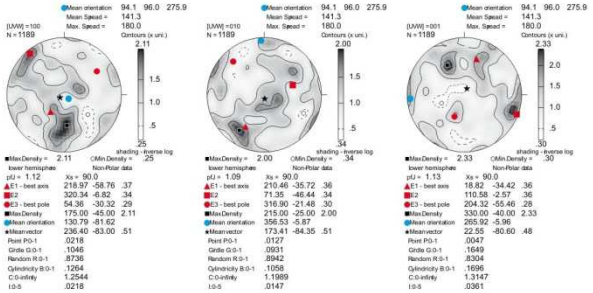

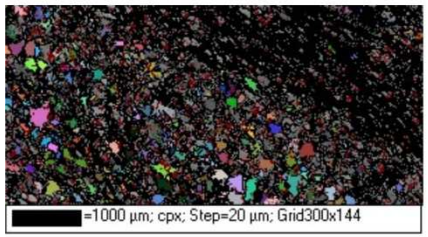

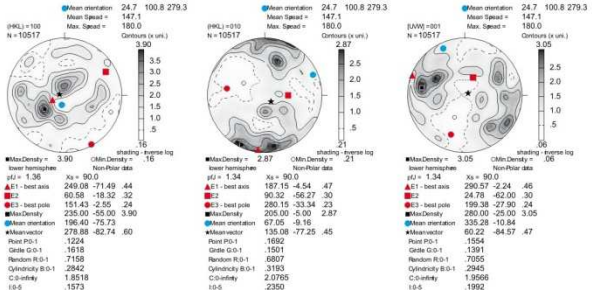

Cpx

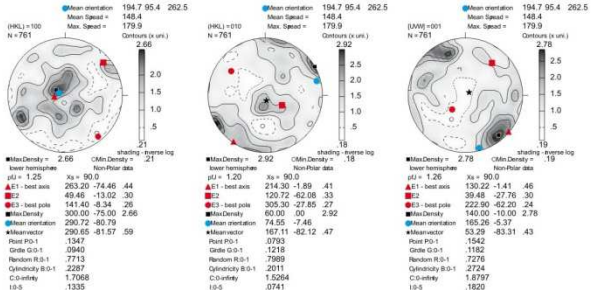

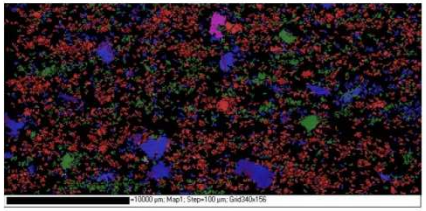

step=100µm

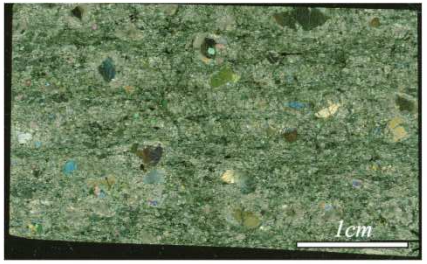

Geographic coordinates (1 point per grain)

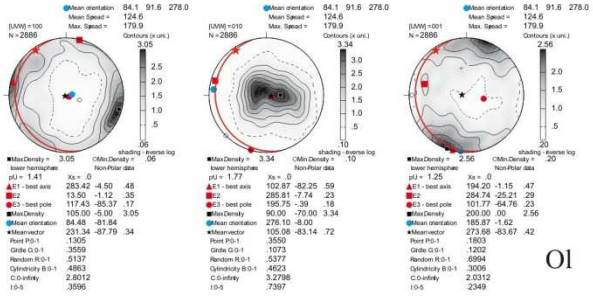

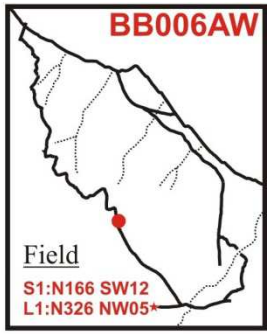

Ol

Sample coordinates (raw data)

Sample coordinates (1 point per grain)

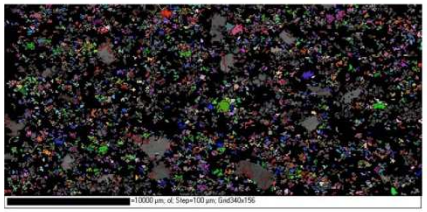

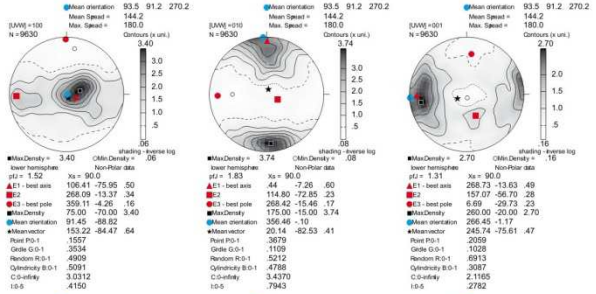

Ol

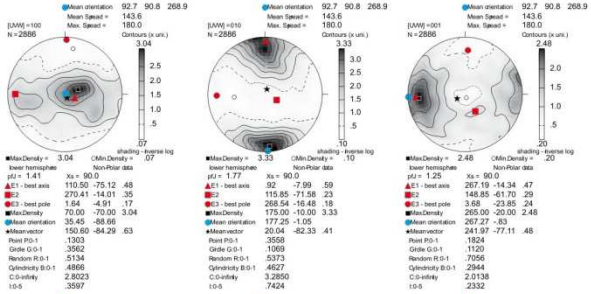

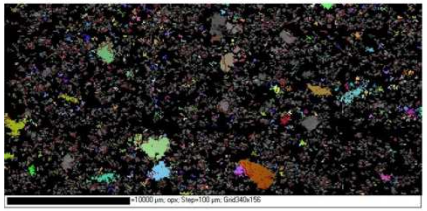

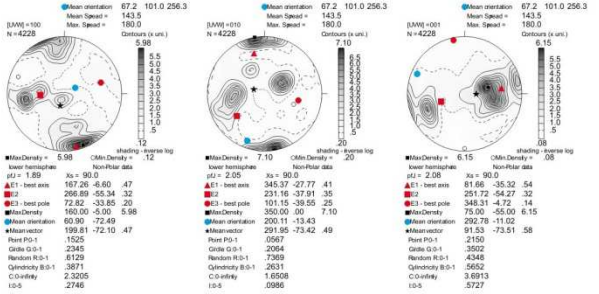

Opx

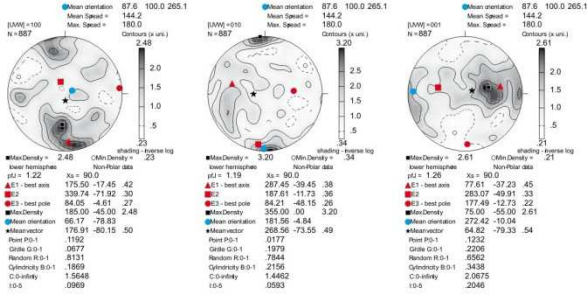

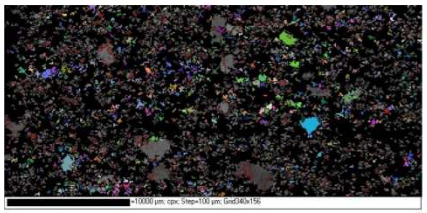

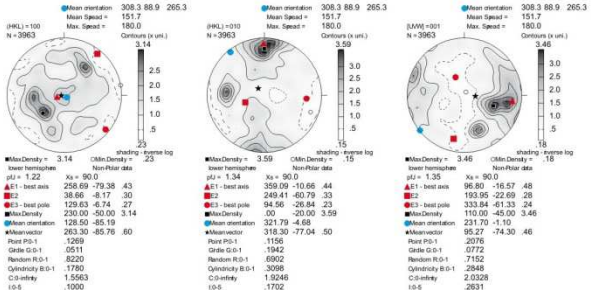

Cpx

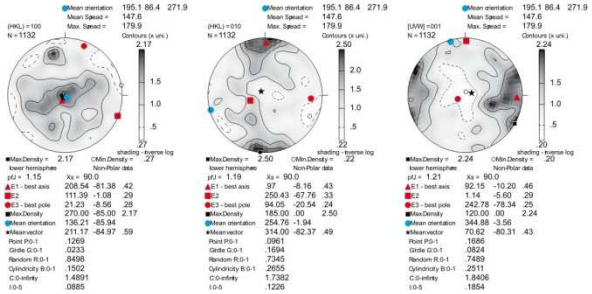

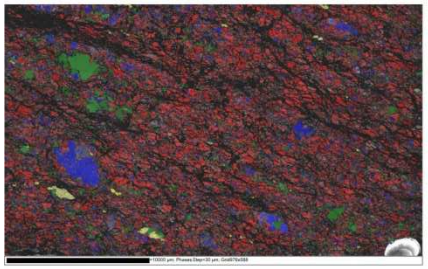

step=30µm

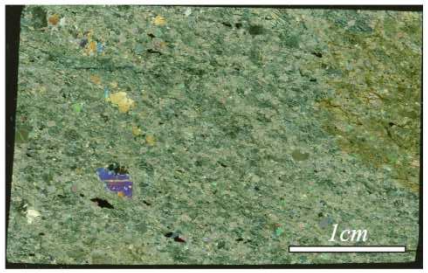

Geographic coordinates (1 point per grain)

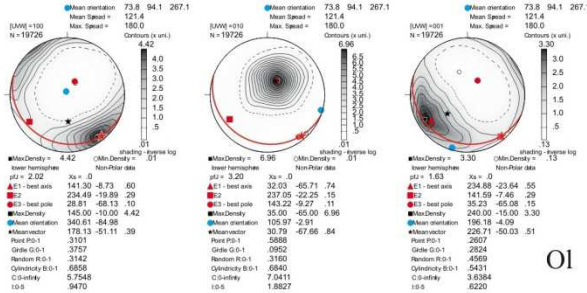

Ol

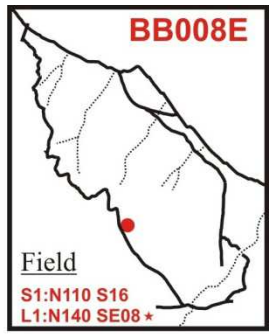

Sample coordinates (raw data)

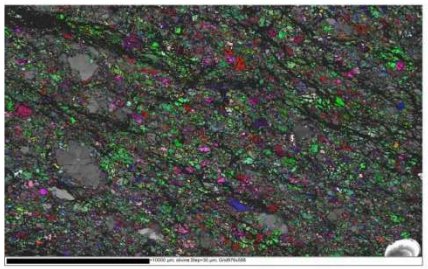

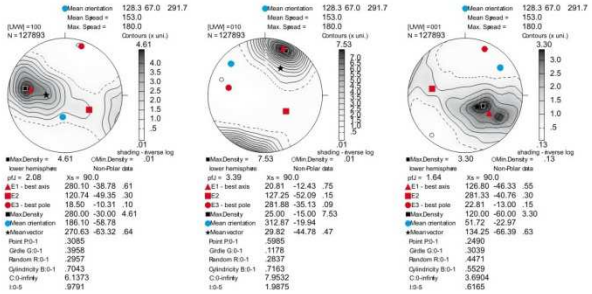

Ol

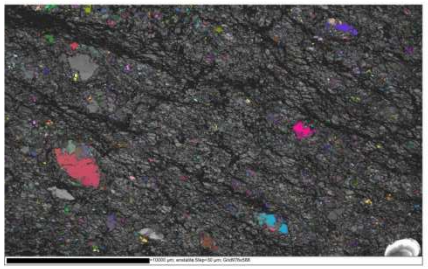

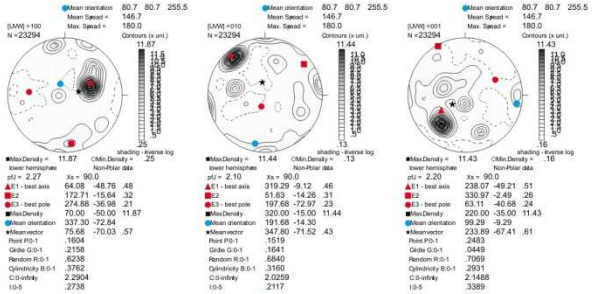

Opx

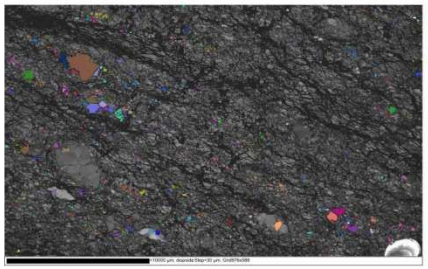

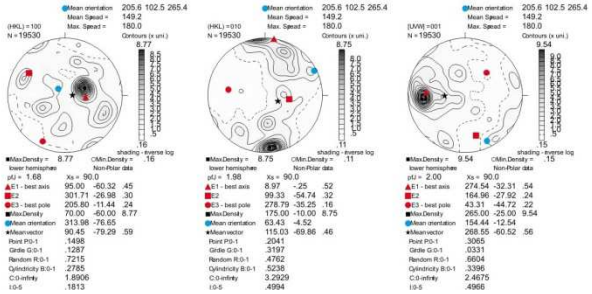

Cpx

Sample coordinates (1 point per grain)

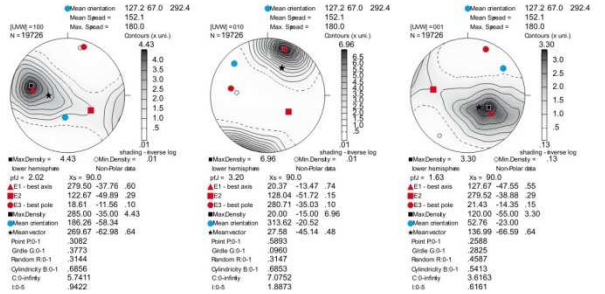

Ol

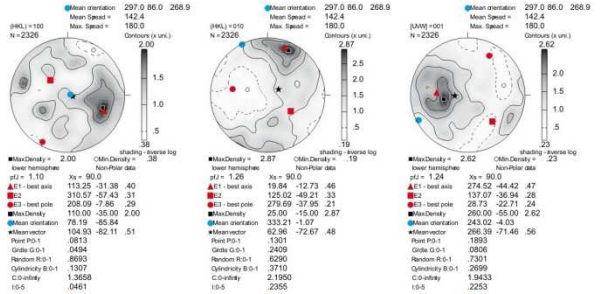

Opx

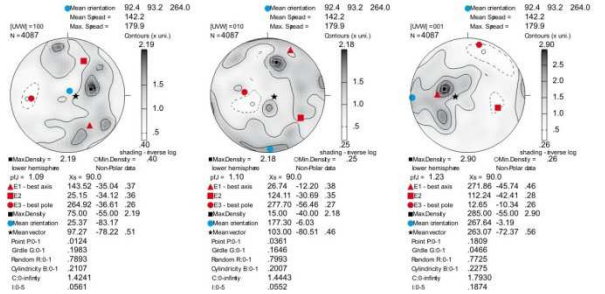

Cpx

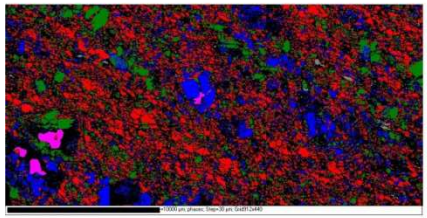

step=30µm

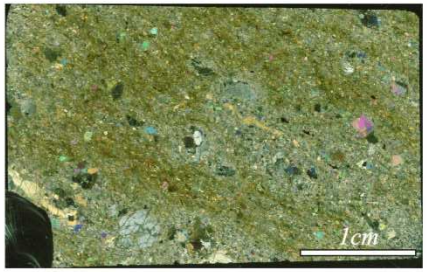

Geographic coordinates (1 point per grain)

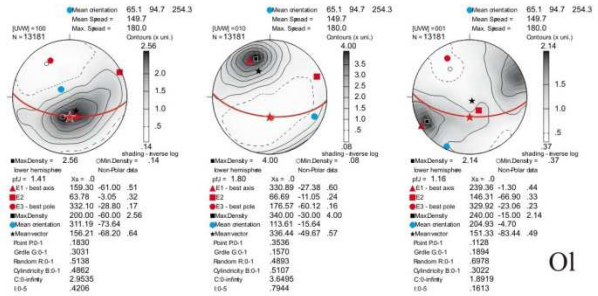

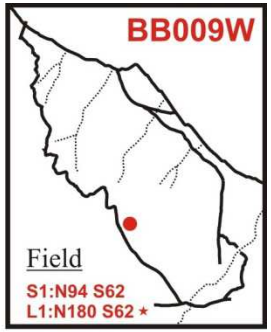

Ol

Sample coordinates (raw data)

Sample coordinates (1 point per grain)

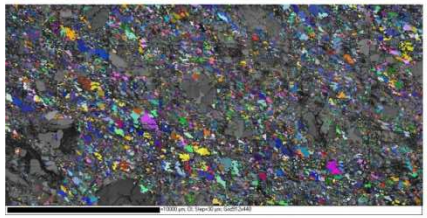

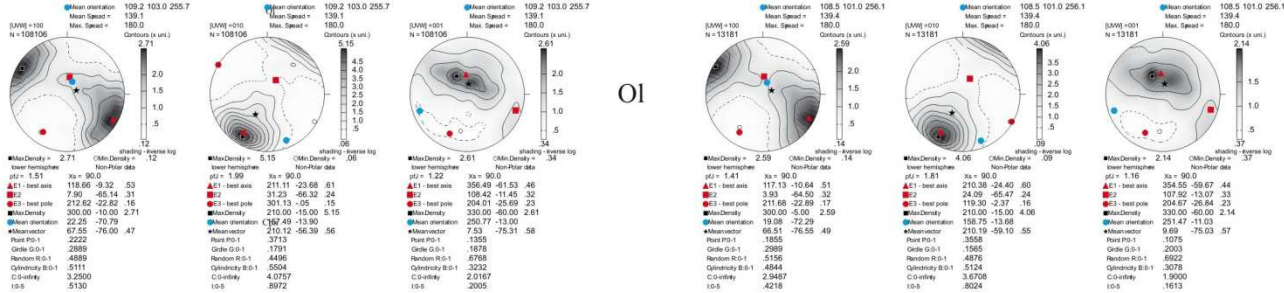

Ol

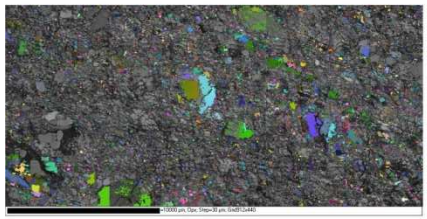

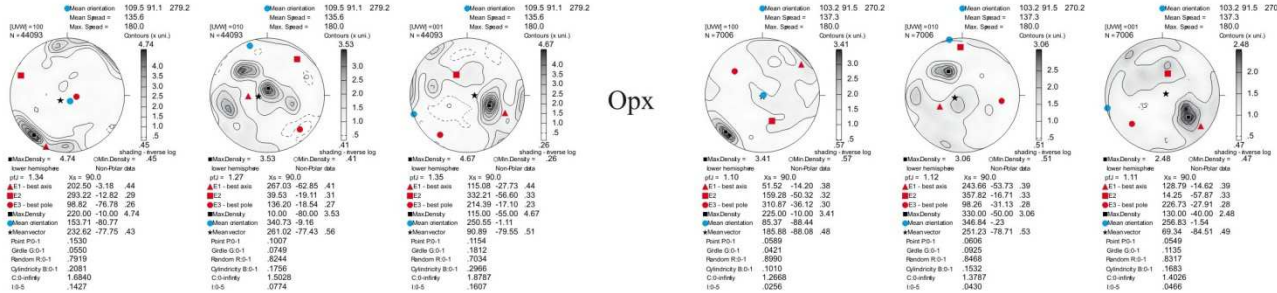

Opx

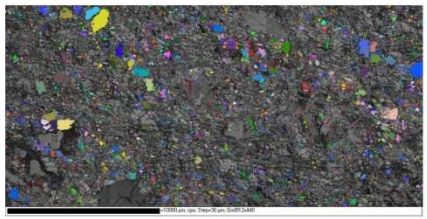

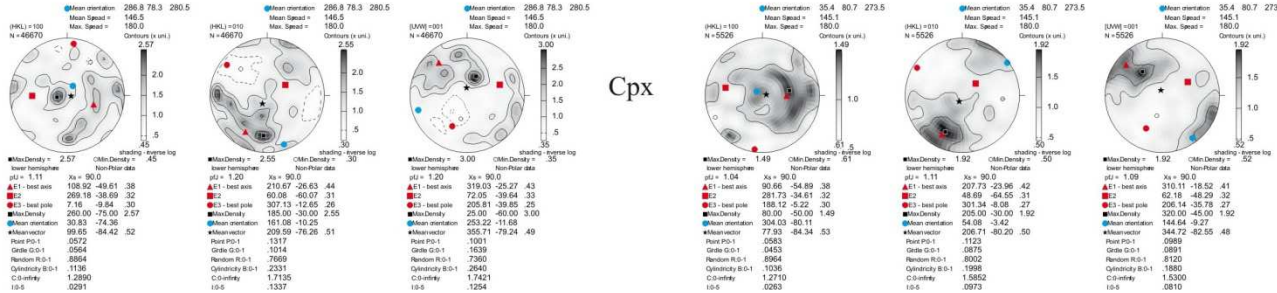

Cpx

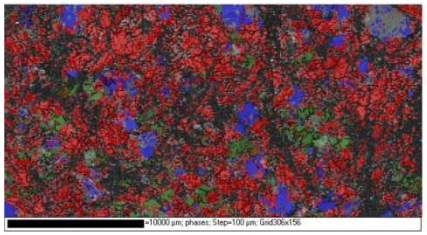

step=100µm

Geographic coordinates (1 point per grain)

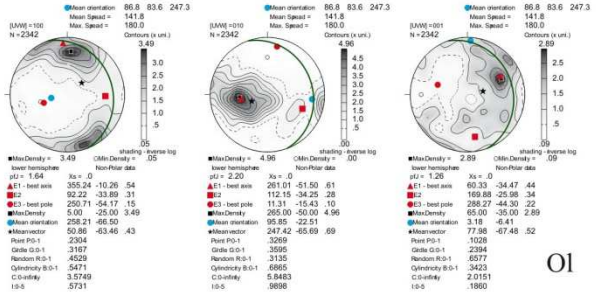

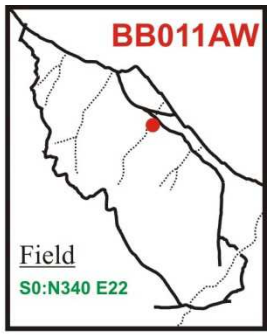

Ol

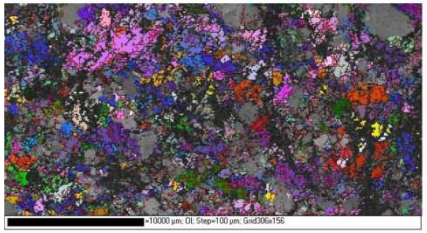

Sample coordinates (raw data)

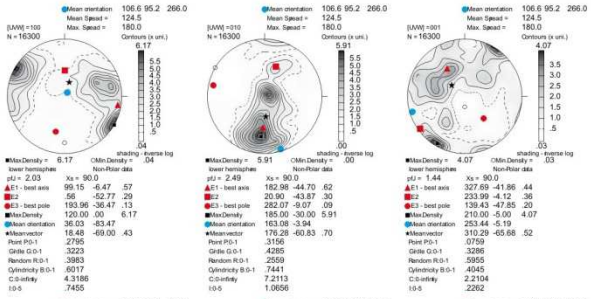

Sample coordinates (1 point per grain)

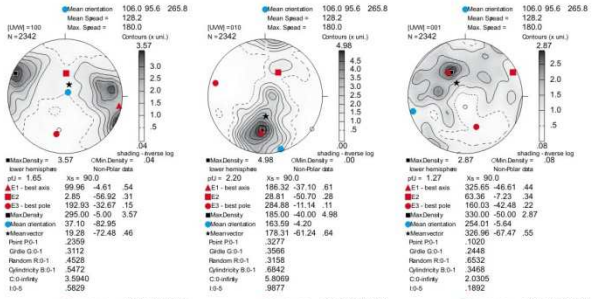

Ol

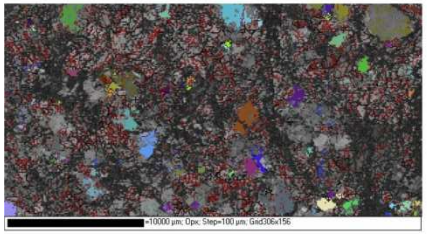

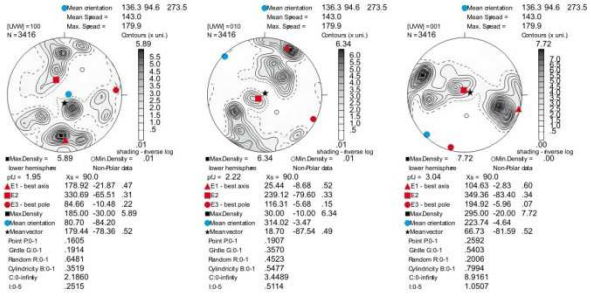

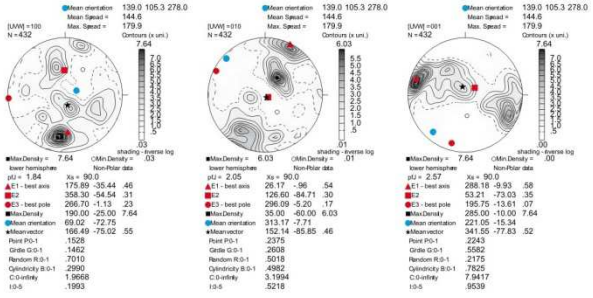

Opx

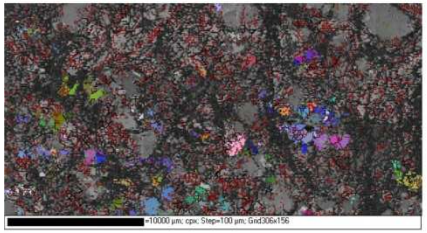

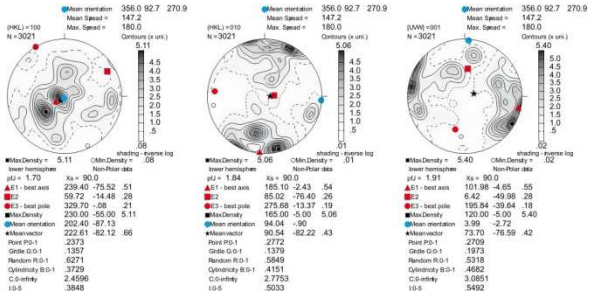

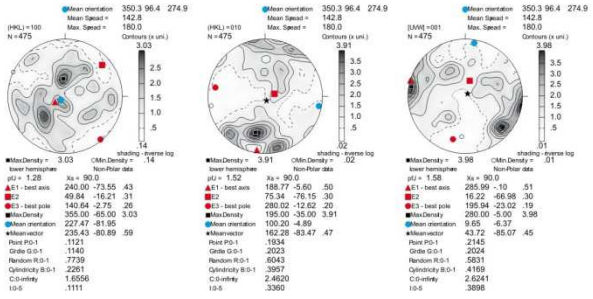

Cpx

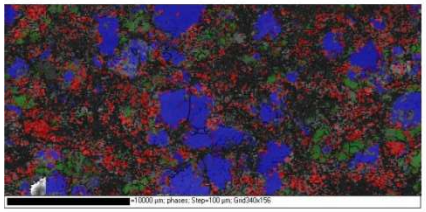

step=100µm

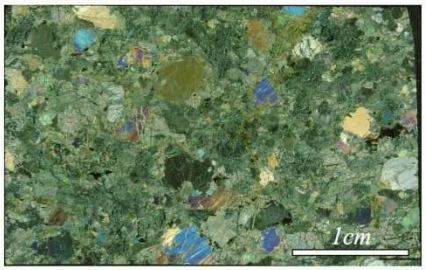

Geographic coordinates (1 point per grain)

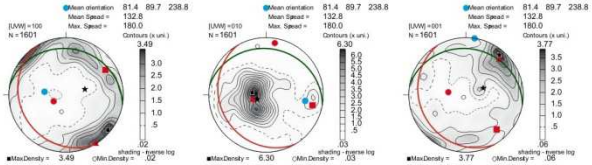

Ol

Sample coordinates (raw data)

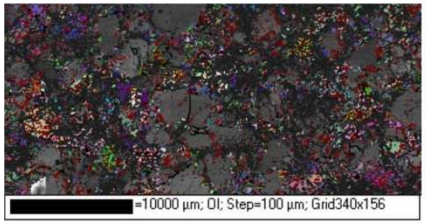

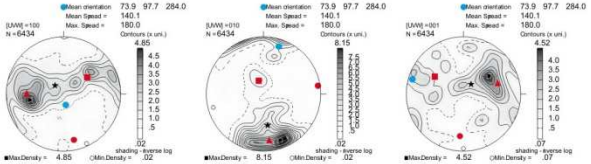

Ol

Sample coordinates (1 point per grain)

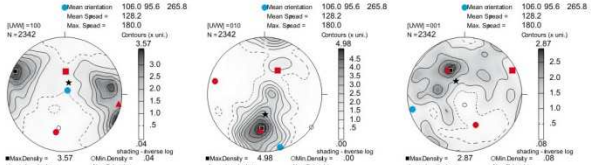

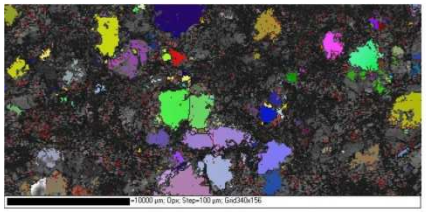

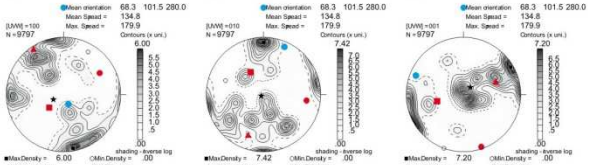

Opx

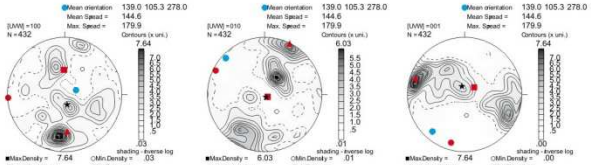

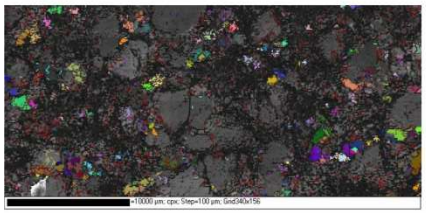

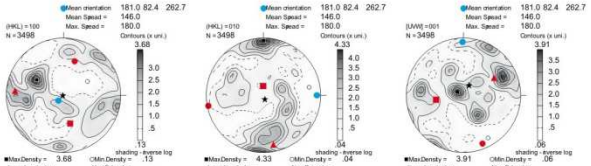

Cpx

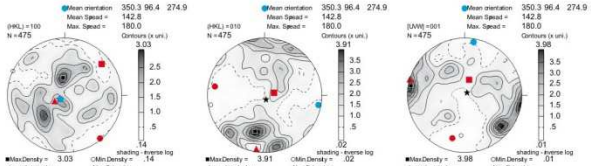

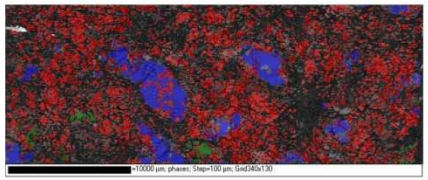

step=100µm

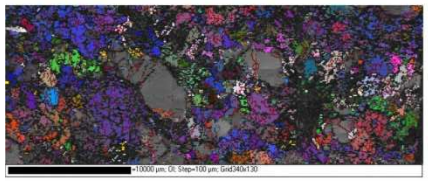

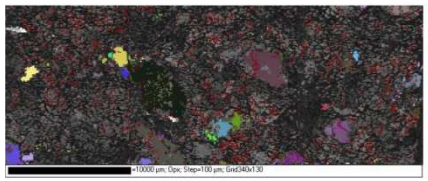

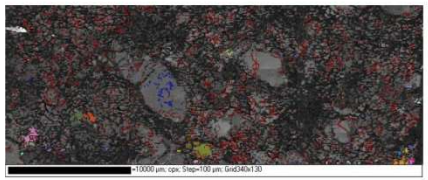

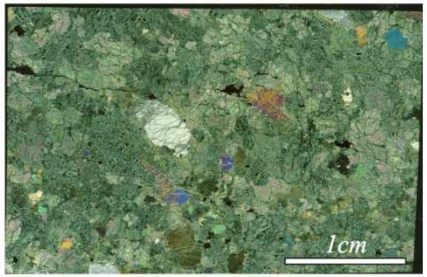

Geographic coordinates (1 point per grain)

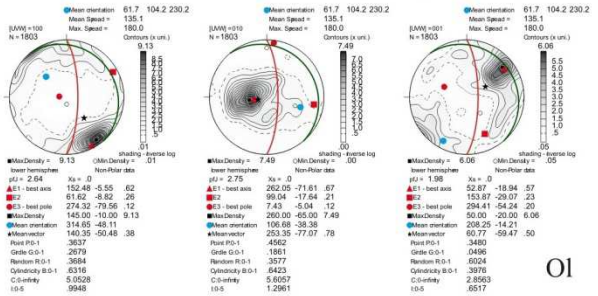

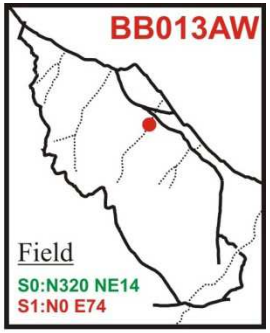

Ol

Sample coordinates (raw data)

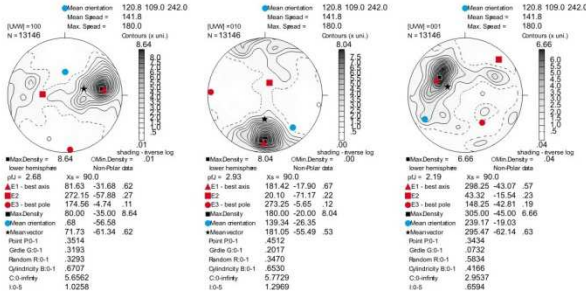

Ol

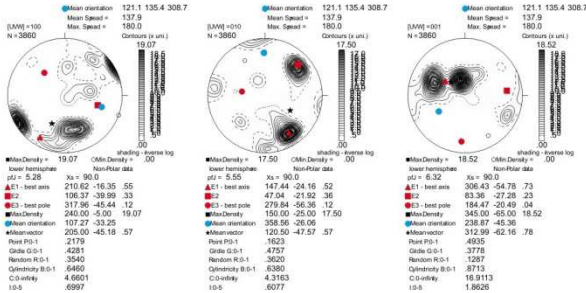

Opx

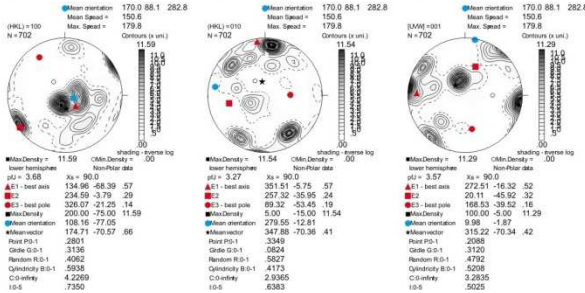

Cpx

Sample coordinates (1 point per grain)

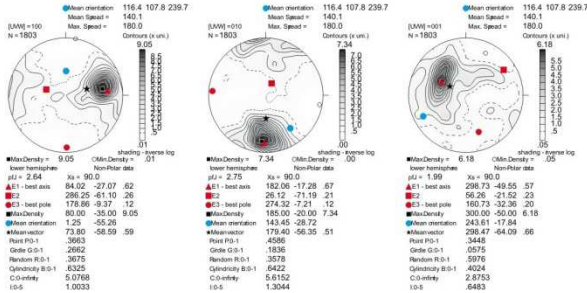

Ol

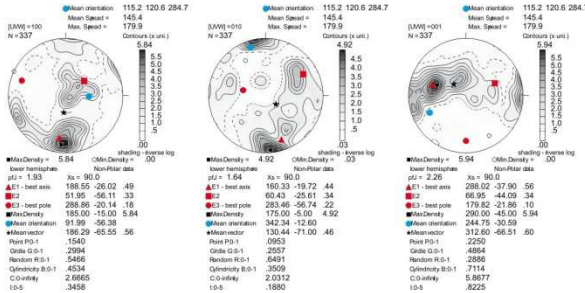

Opx

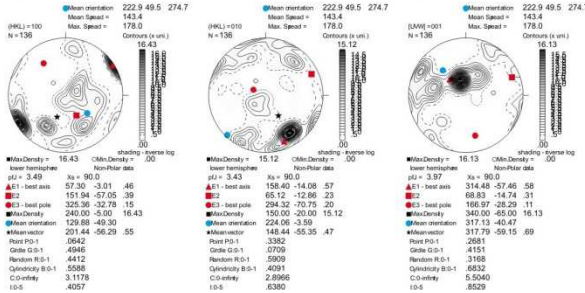

Cpx

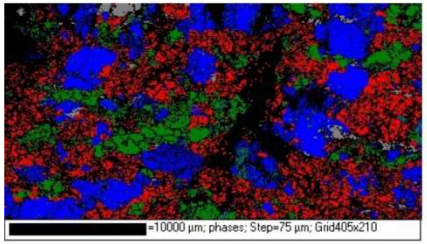

step=75µm

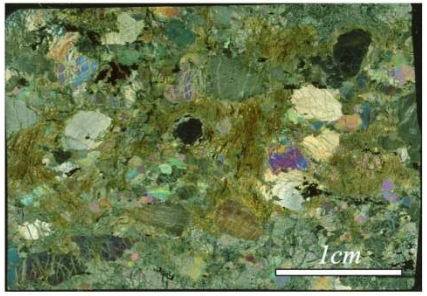

Geographic coordinates (1 point per grain)

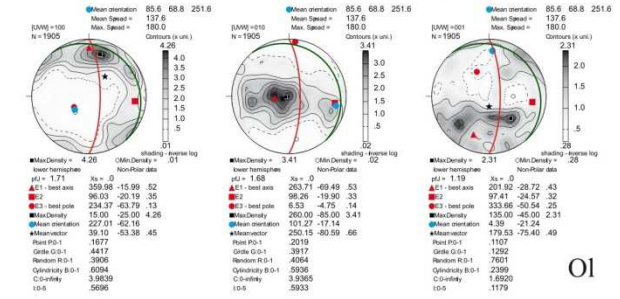

Ol

Sample coordinates (raw data)

Sample coordinates (1 point per grain)

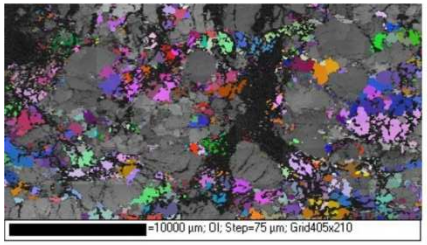

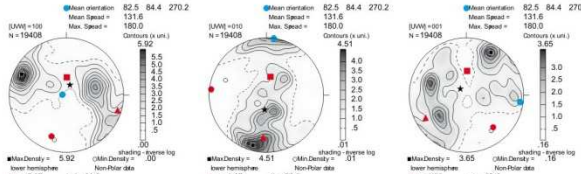

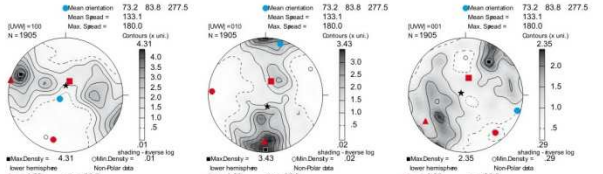

Opx

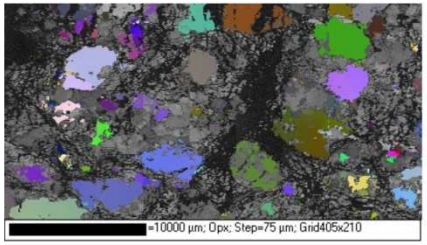

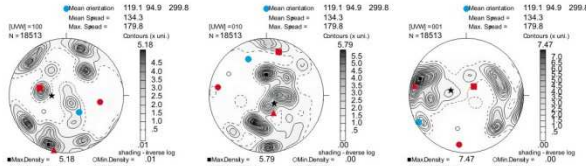

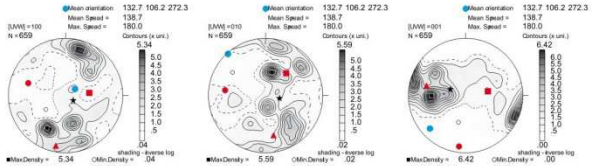

Cpx

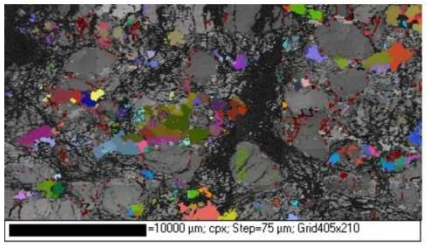

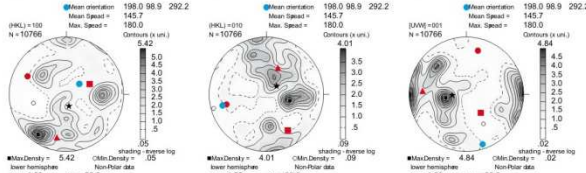

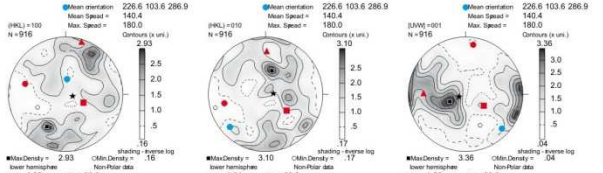

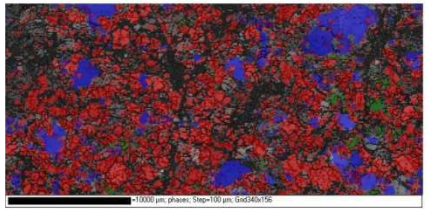

step=100µm

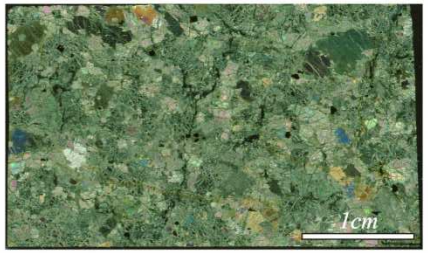

Geographic coordinates (1 point per grain)

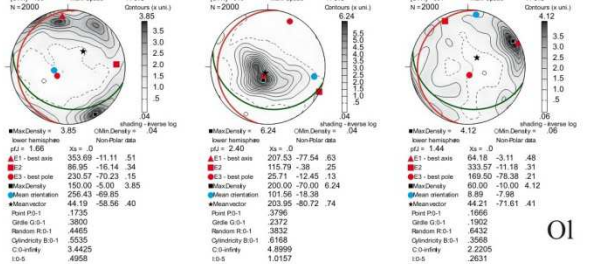

Ol

Sample coordinates (raw data)

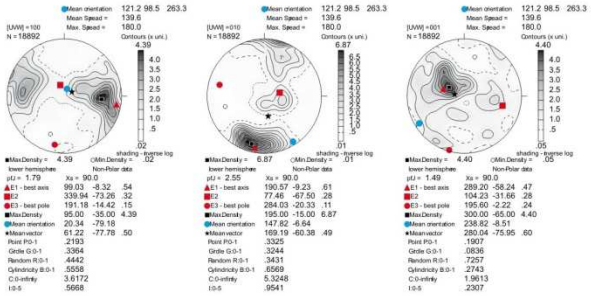

Ol

Sample coordinates (1 point per grain)

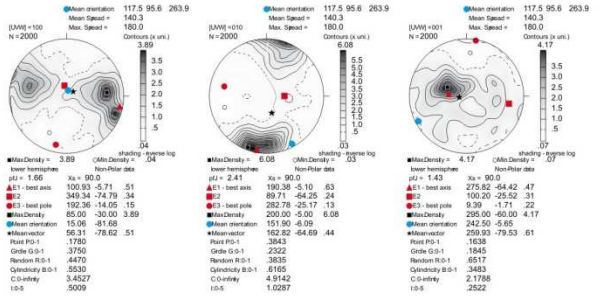

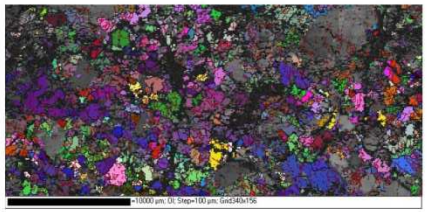

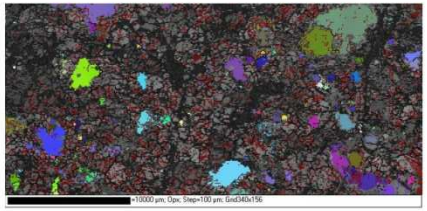

Opx

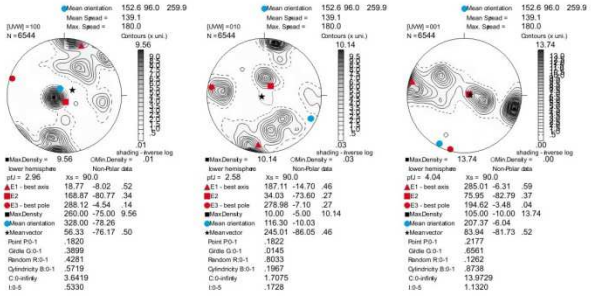

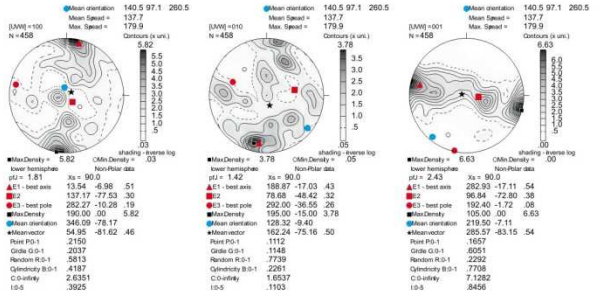

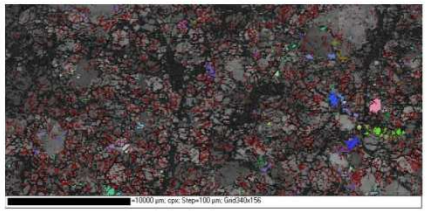

Cpx

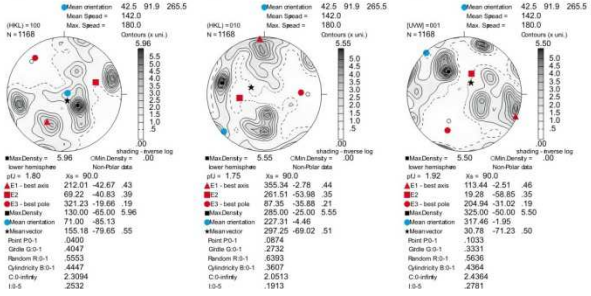

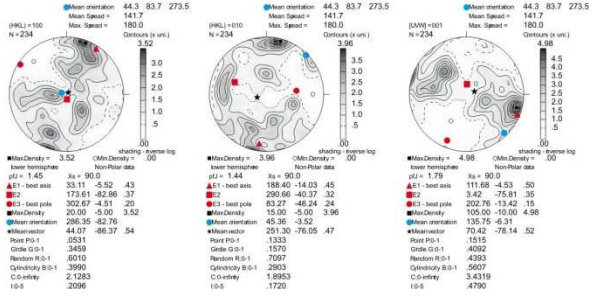

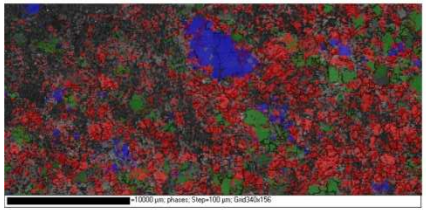

step=100µm

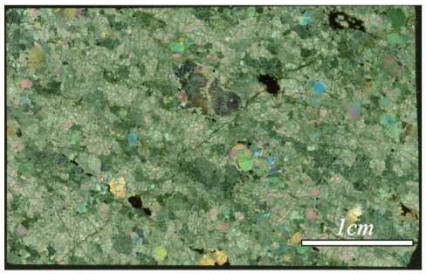

Geographic coordinates (1 point per grain)

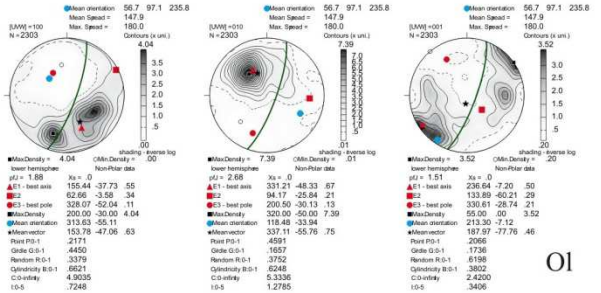

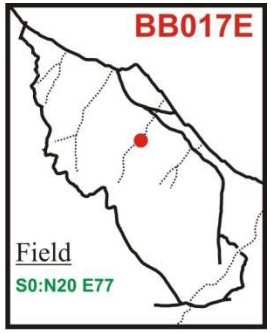

Ol

Sample coordinates (raw data)

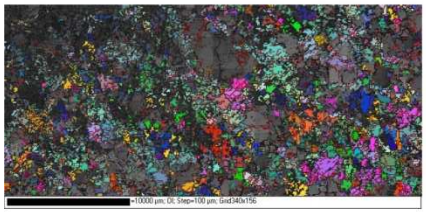

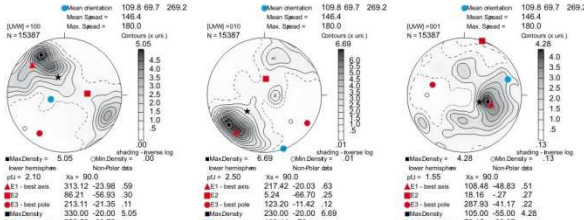

Ol

Sample coordinates (1 point per grain)

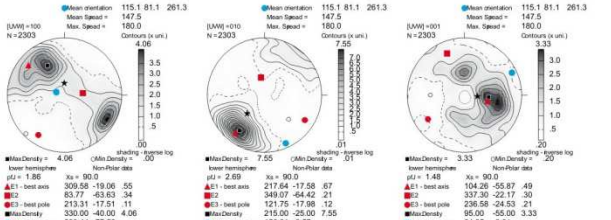

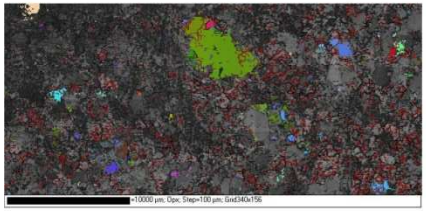

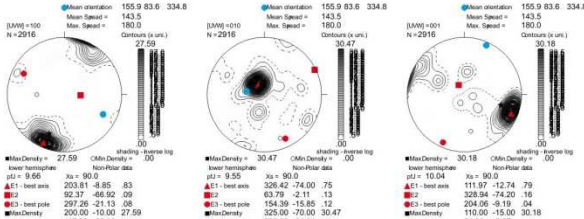

Opx

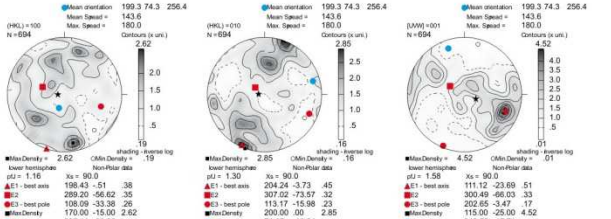

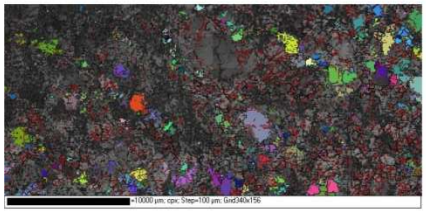

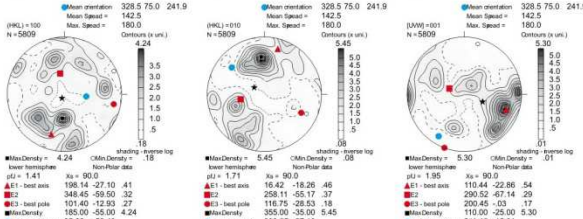

Cpx

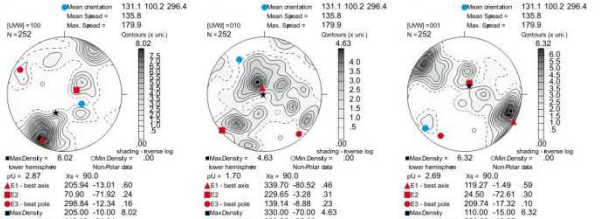

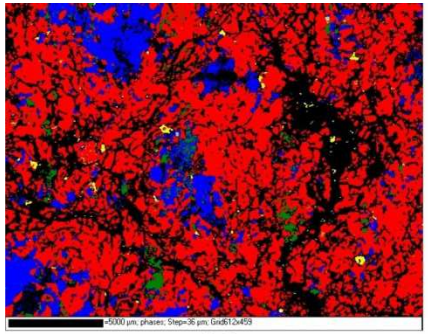

step=36µm

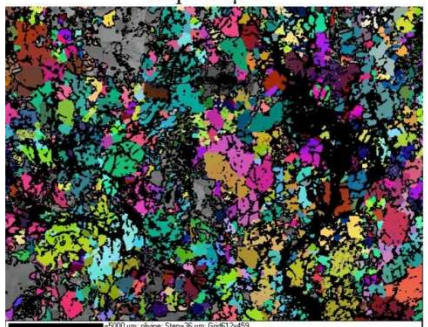

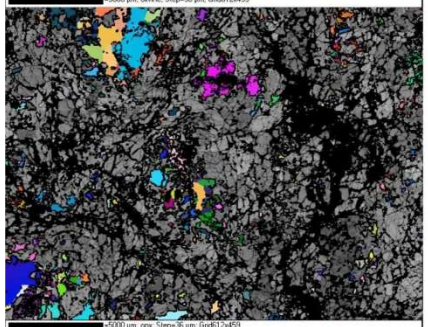

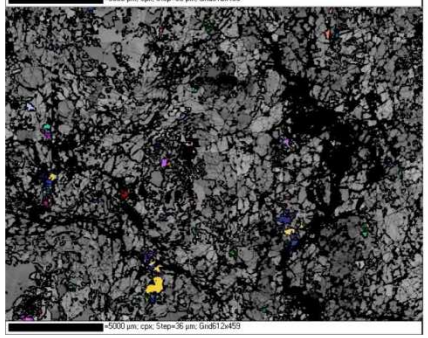

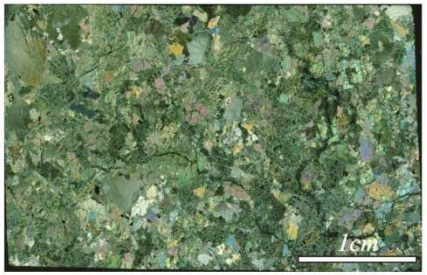

Geographic coordinates (1 point per grain)

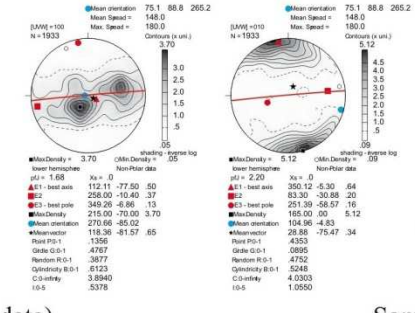

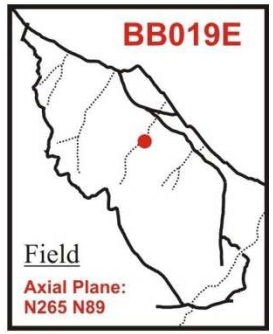

Ol

Sample coordinates (raw data)

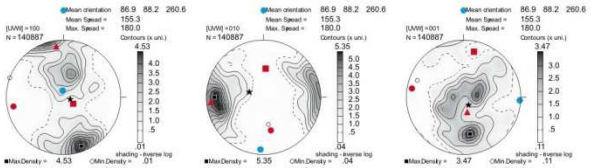

Ol

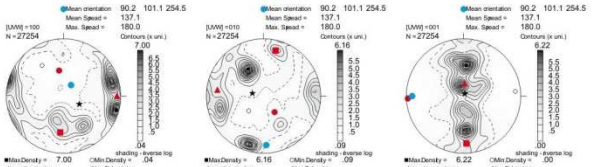

Opx

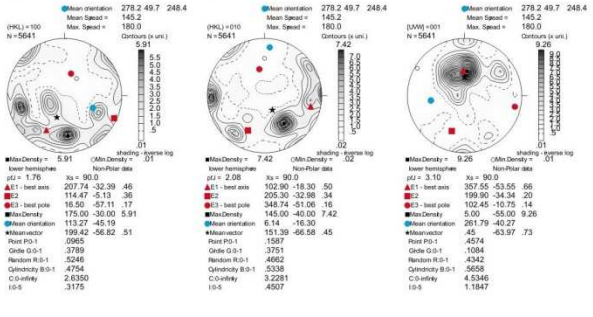

Cpx

Sample coordinates (1 point per grain)

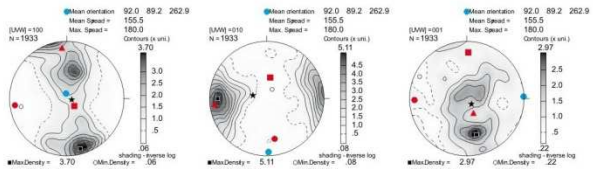

Ol

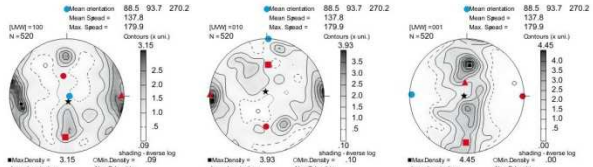

Opx

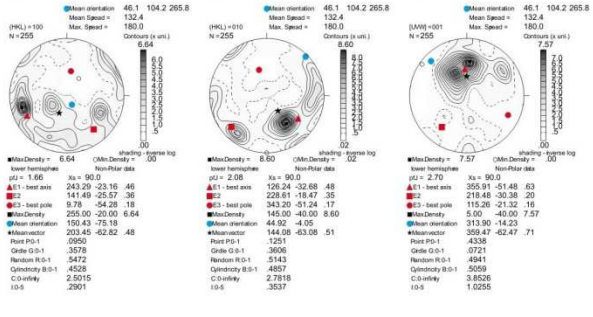

Cpx

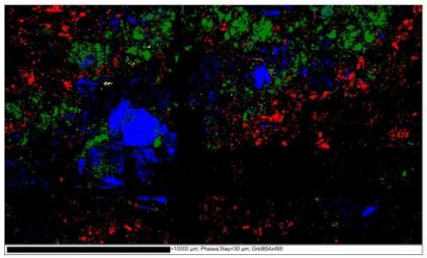

step=30μm

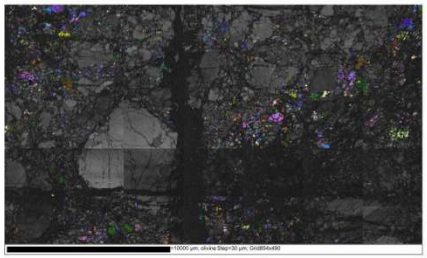

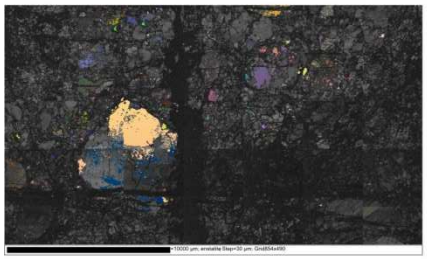

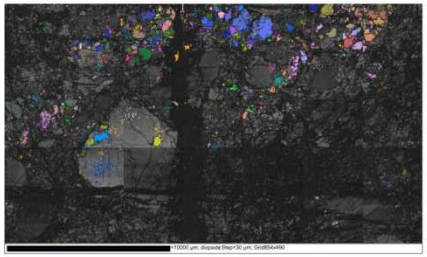

Geographic coordinates (1 point per grain)

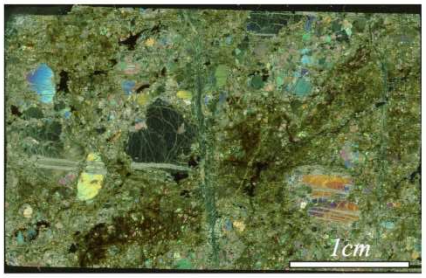

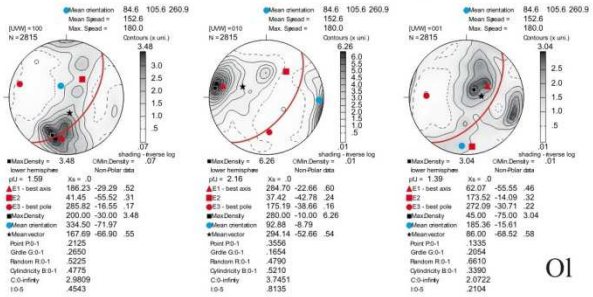

Ol

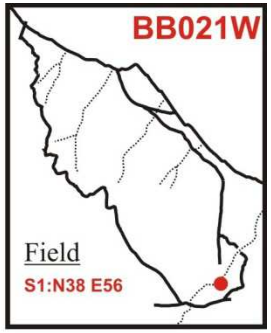

Sample coordinates (raw data)

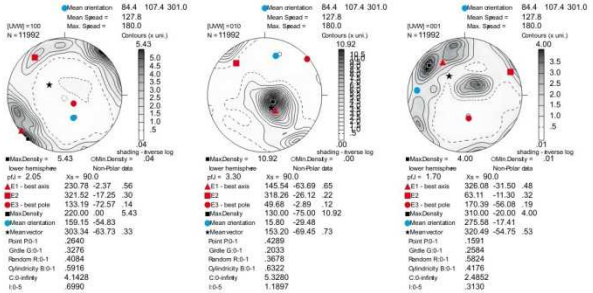

Ol

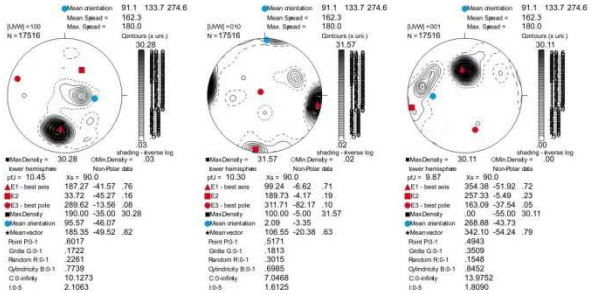

Opx

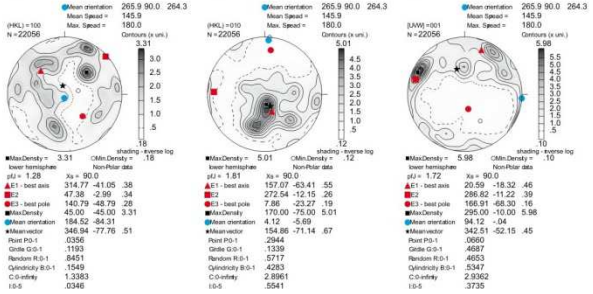

Cpx

Sample coordinates (1 point per grain)

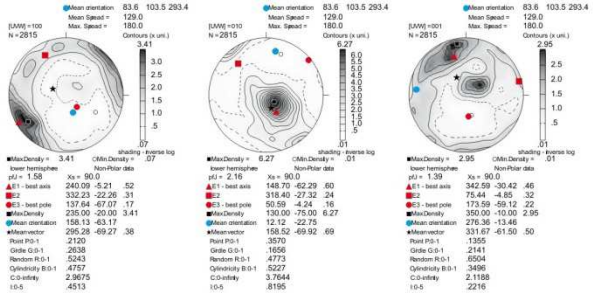

Ol

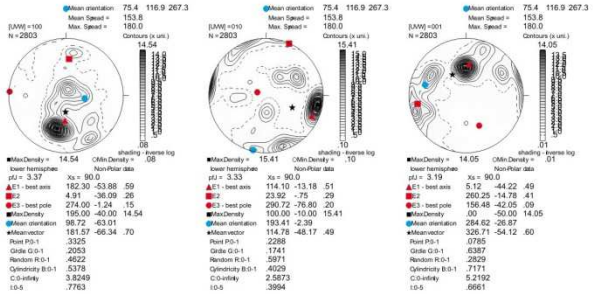

Opx

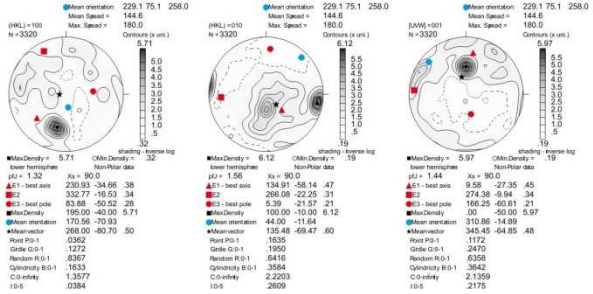

Cpx

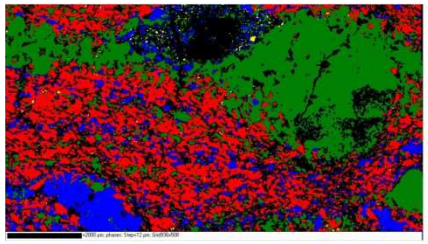

step=12µm

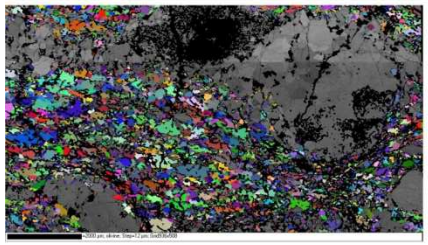

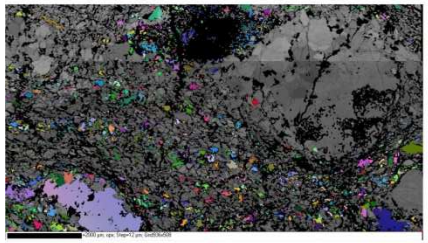

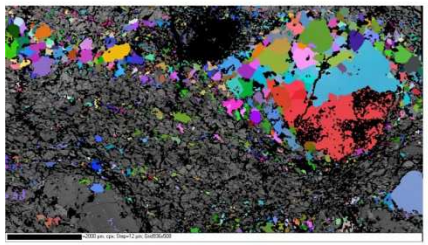

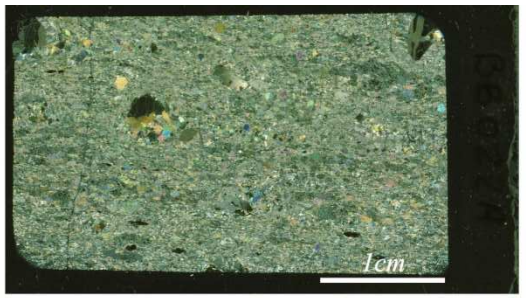

Sample coordinates (raw data)

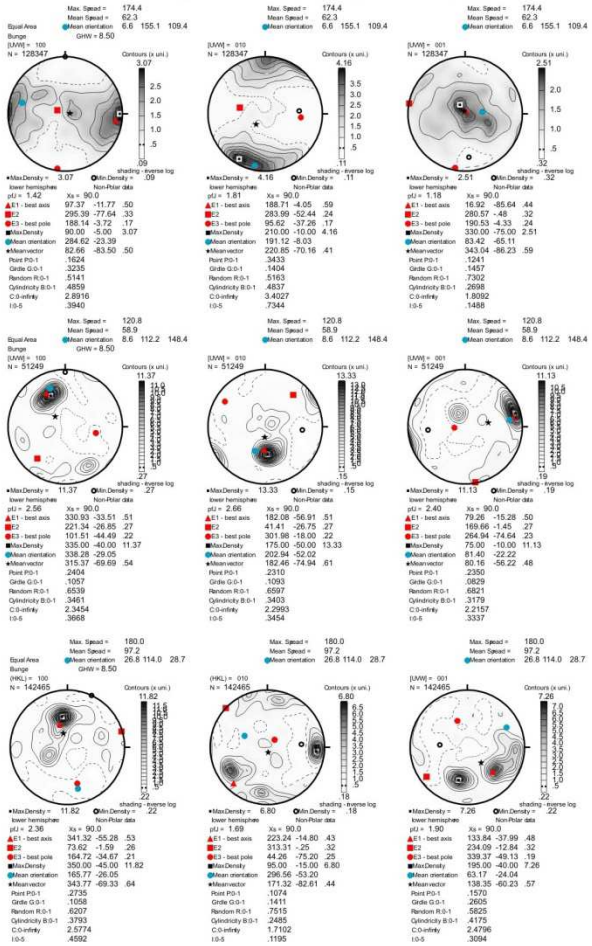

Sample coordinates (1 point per grain)

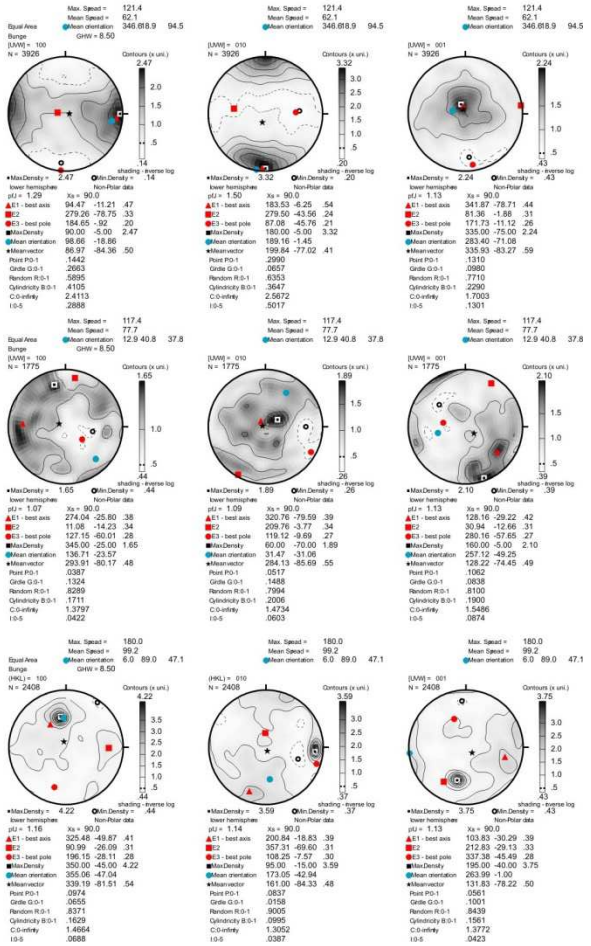

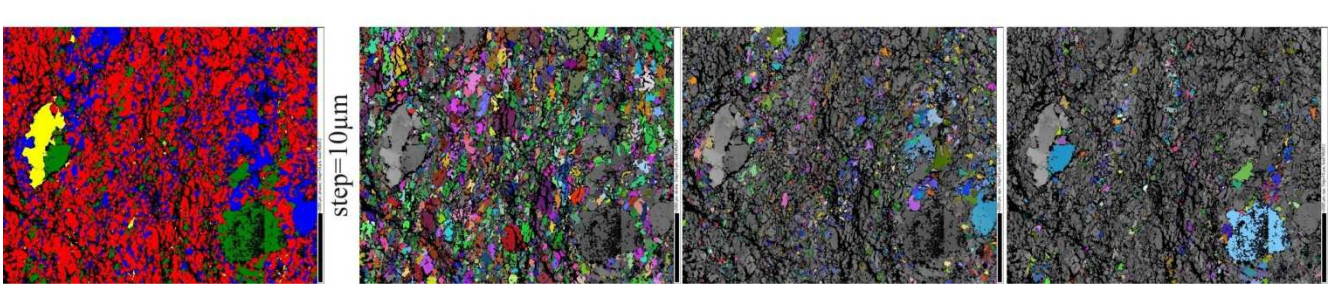
step=10μm

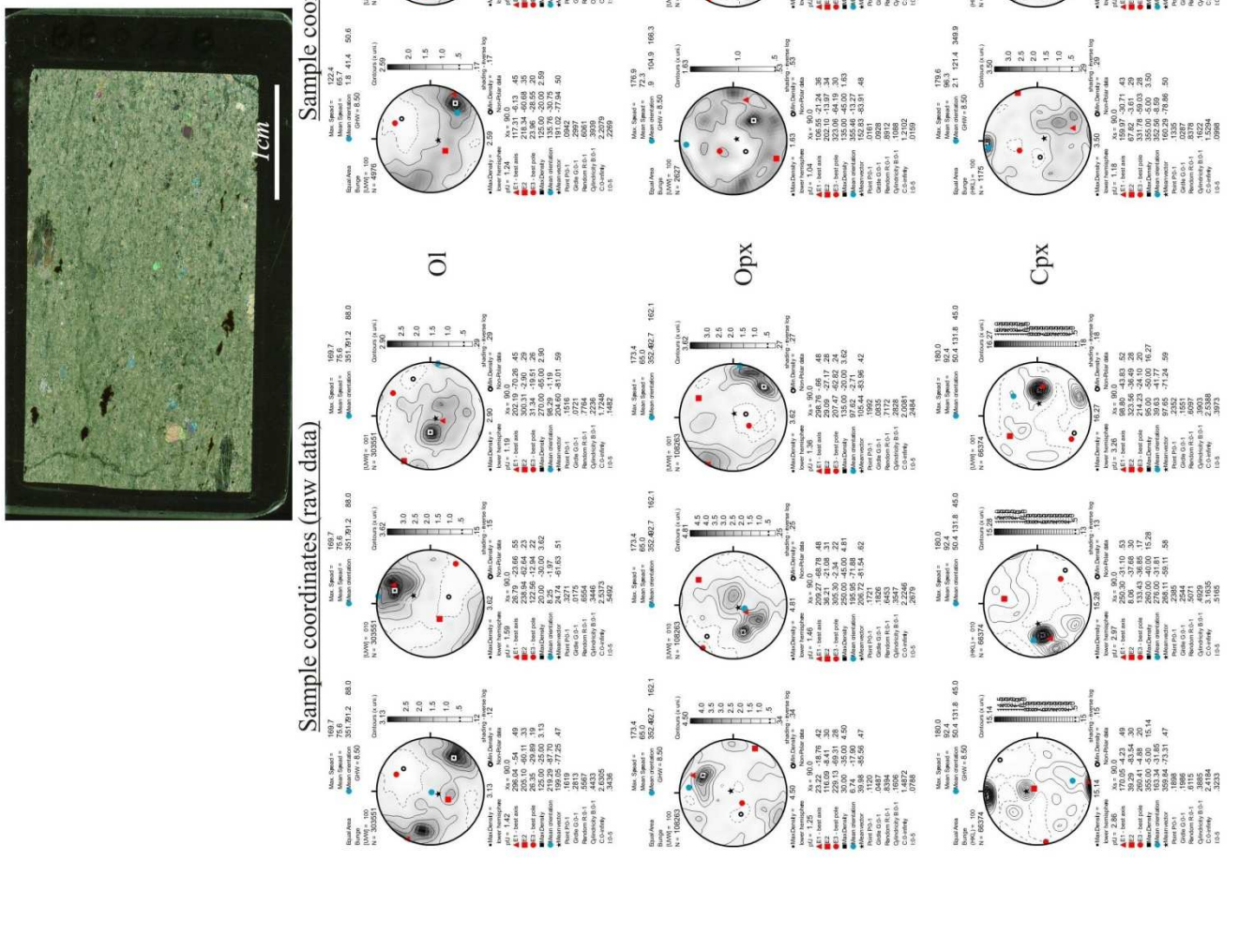
1cm
Sample coordinates (raw data)
Sample coordinates (1 point per grain)
Ol
Opx
Cpx

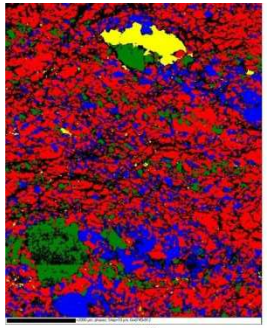

step=10μm

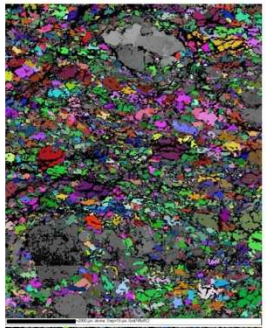

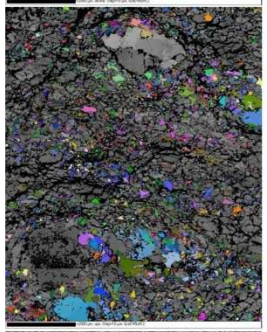

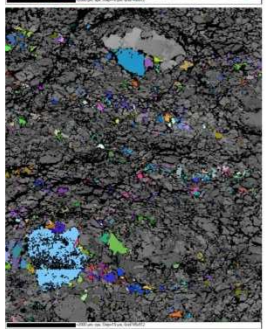

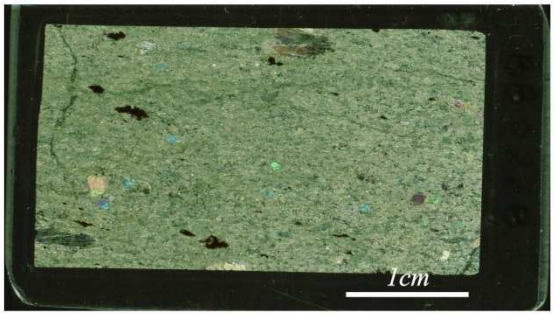

Sample coordinates (raw data)

Sample coordinates (1 point per grain)

Ol

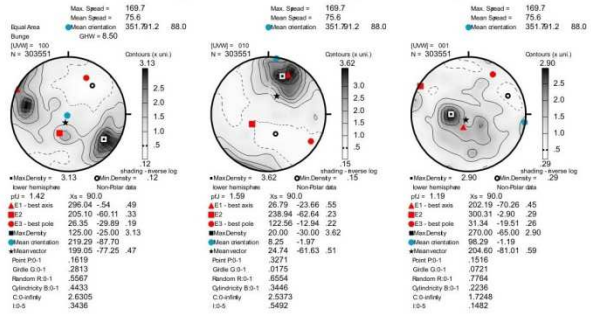

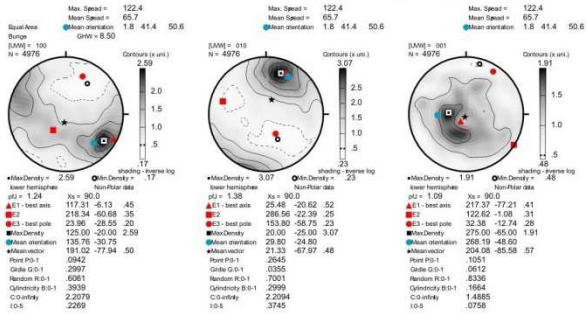

Opx

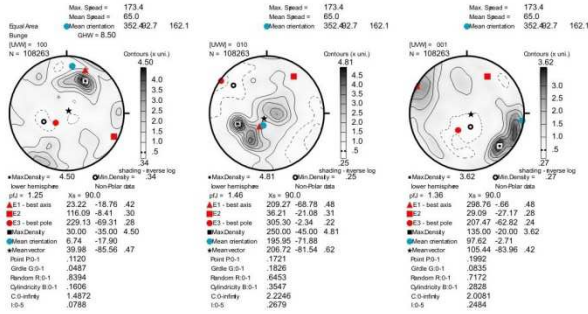

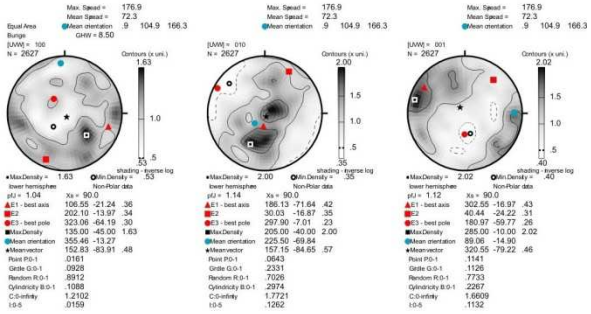

Cpx

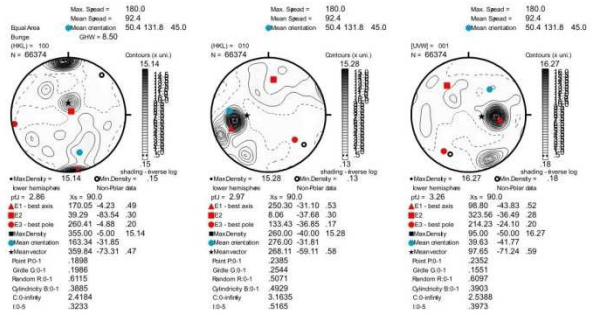

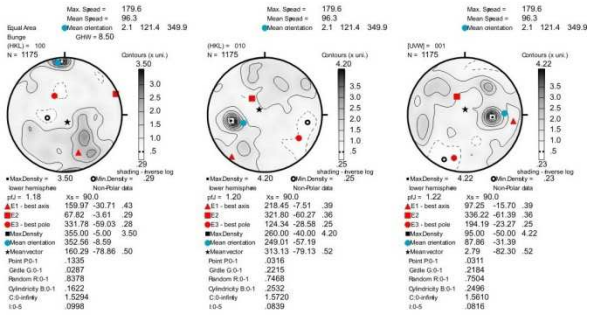

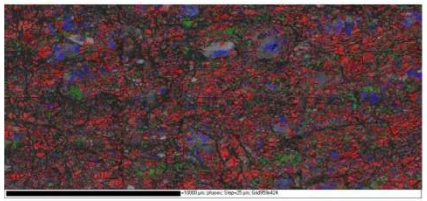

step=25µm

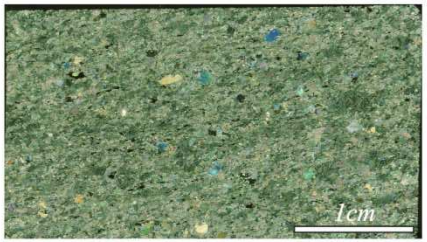

Geographic coordinates (1 point per grain)

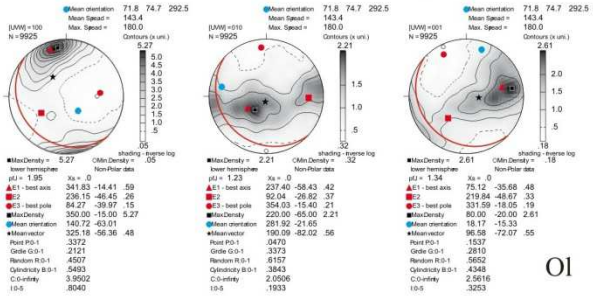

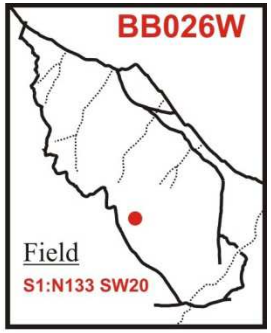

Ol

Sample coordinates (raw data)

Sample coordinates (1 point per grain)

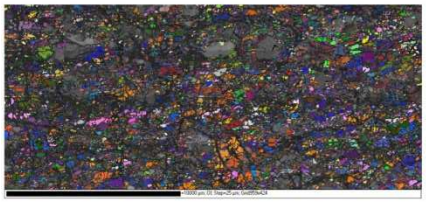

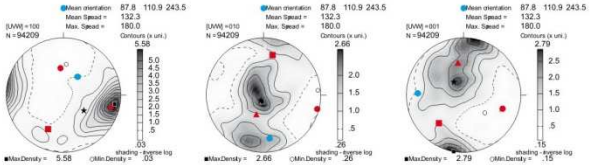

Ol

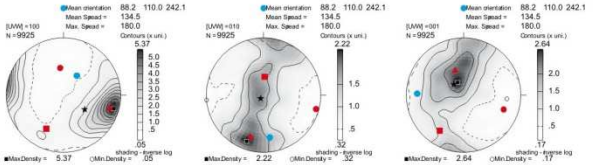

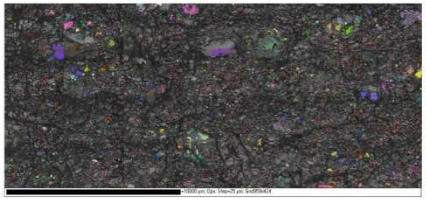

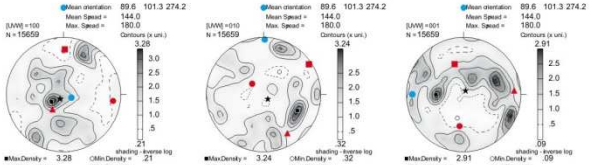

Opx

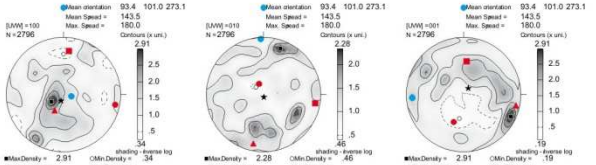

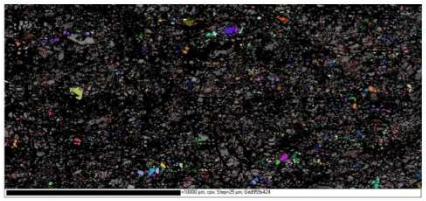

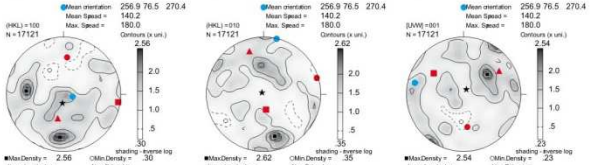

Cpx

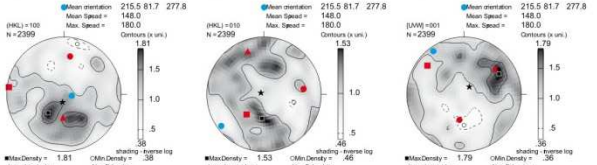

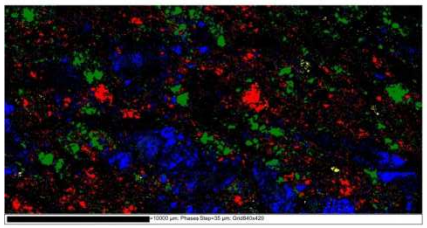

step=35µm

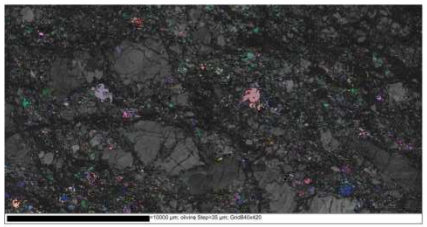

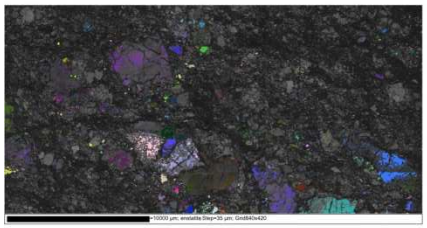

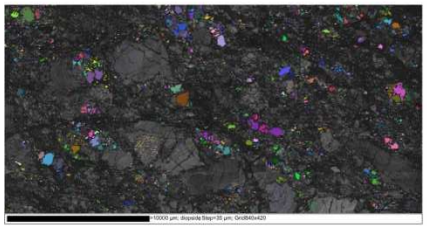

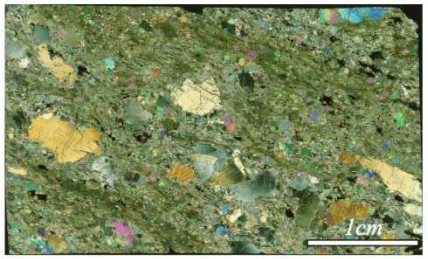

Geographic coordinates (1 point per grain)

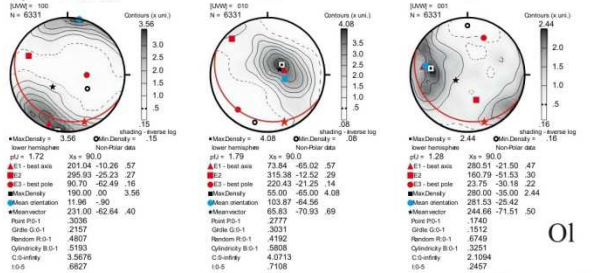

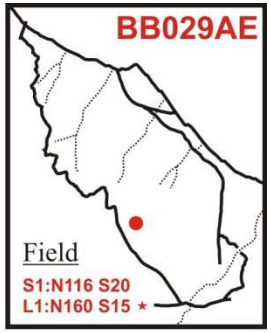

Ol

Sample coordinates (raw data)

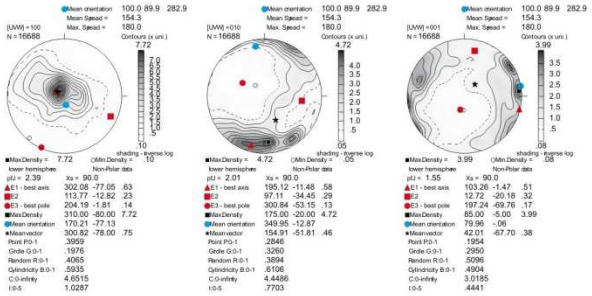

Ol

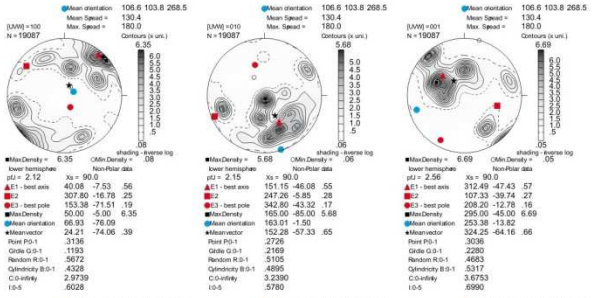

Opx

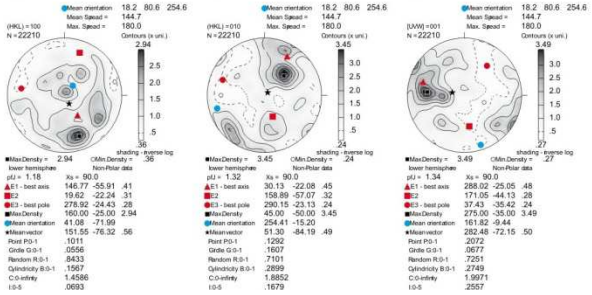

Cpx

Sample coordinates (1 point per grain)

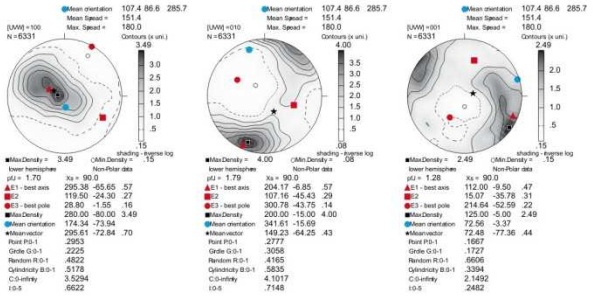

Ol

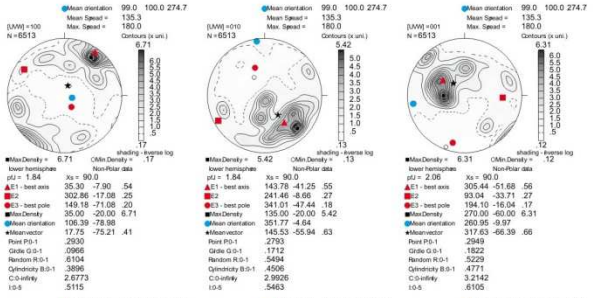

Opx

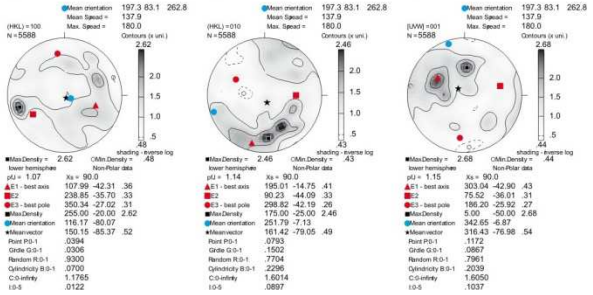

Cpx

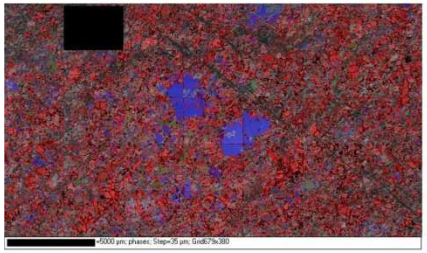

step=35µm

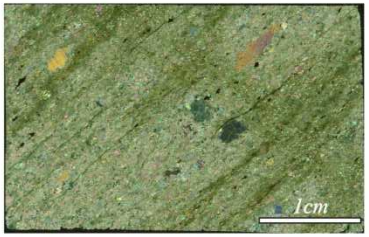

Geographic coordinates (1 point per grain)

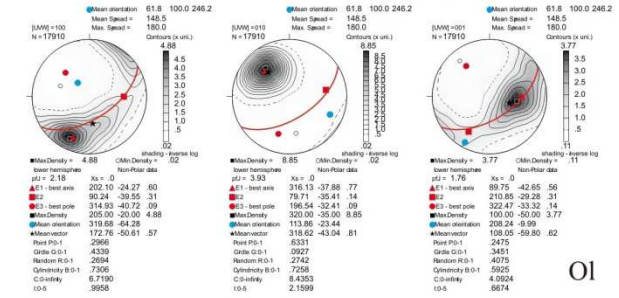

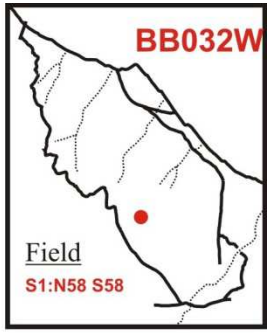

Ol

Sample coordinates (raw data)

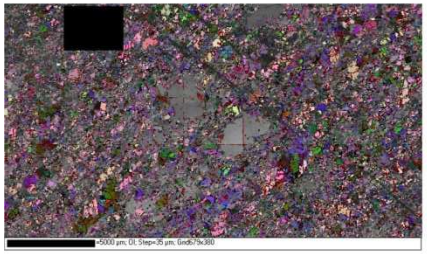

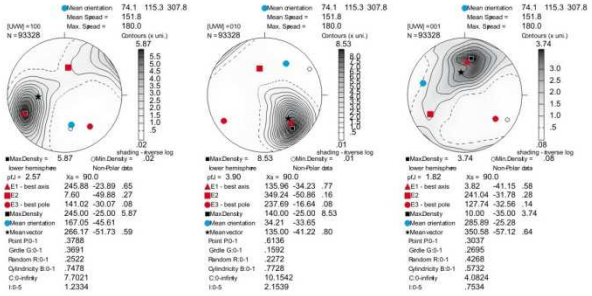

Ol

Sample coordinates (1 point per grain)

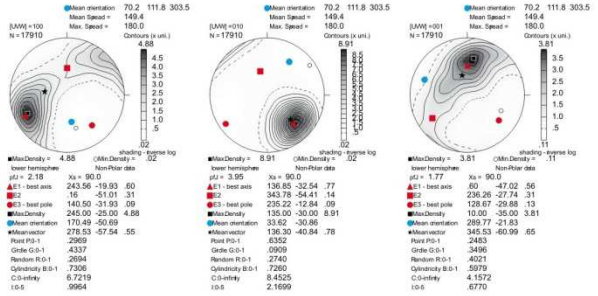

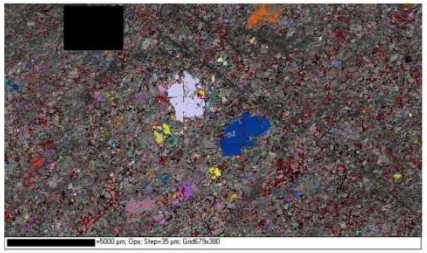

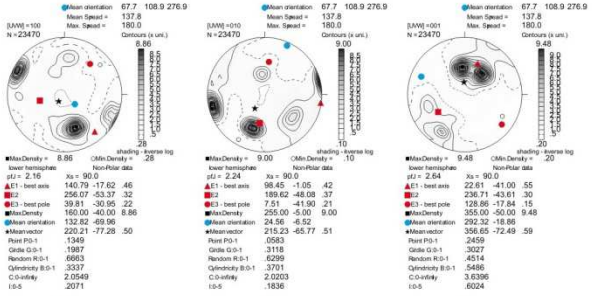

Opx

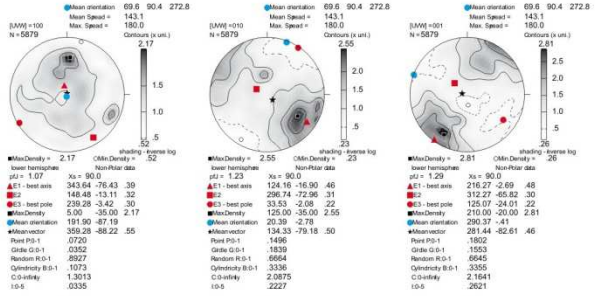

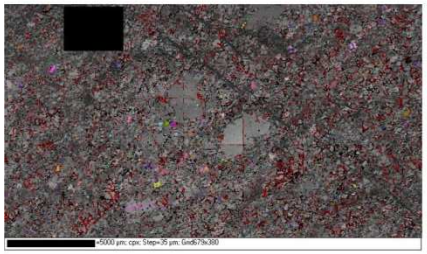

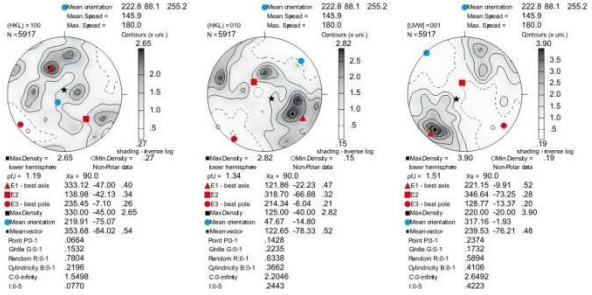

Cpx

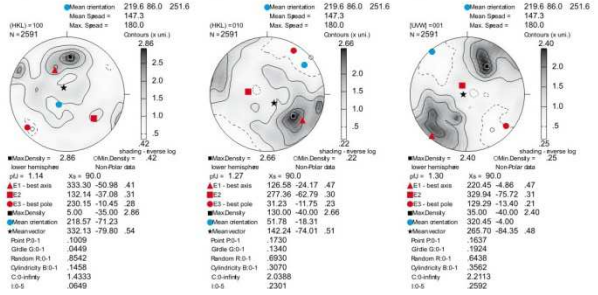

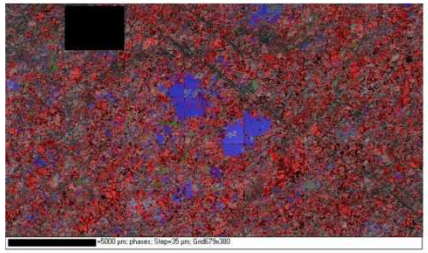

step=35μm

Geographic coordinates (1 point per grain)

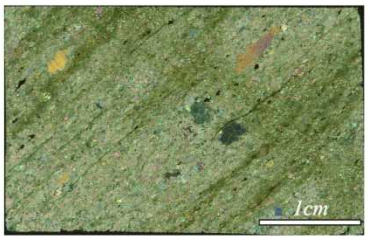

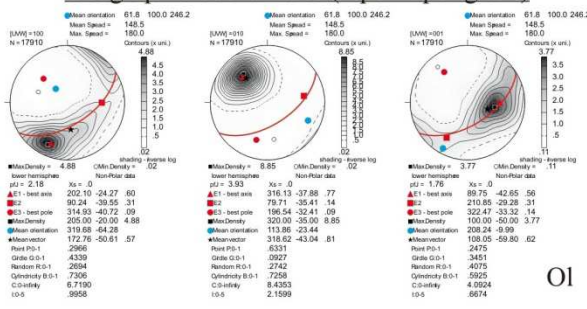

Ol

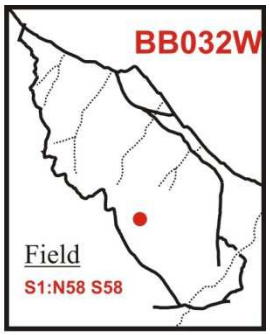

Sample coordinates (raw data)

Sample coordinates (1 point per grain)

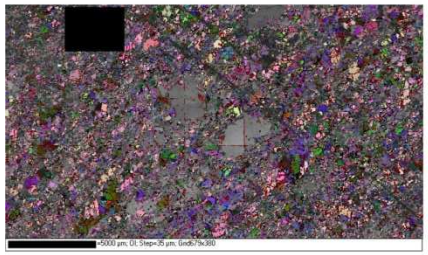

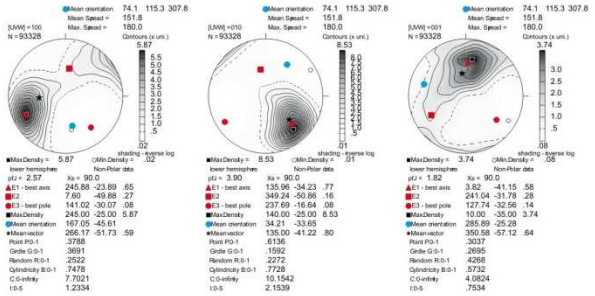

Ol

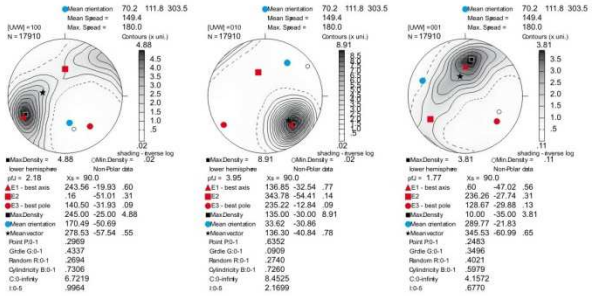

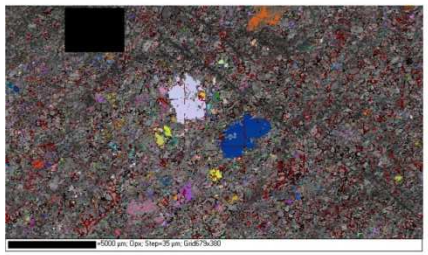

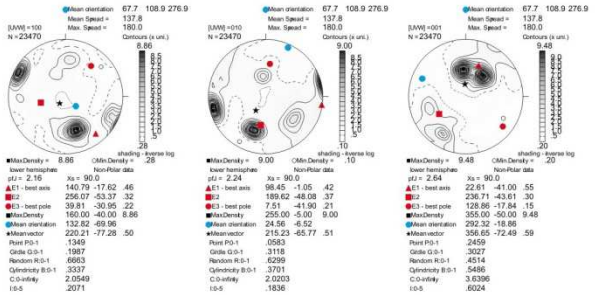

Opx

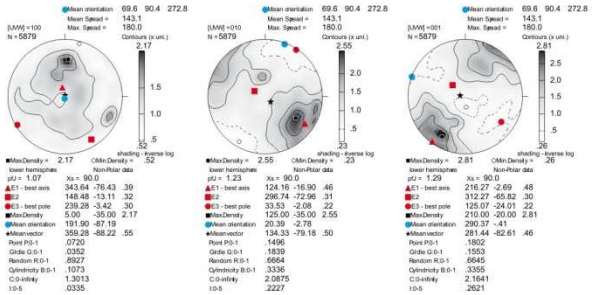

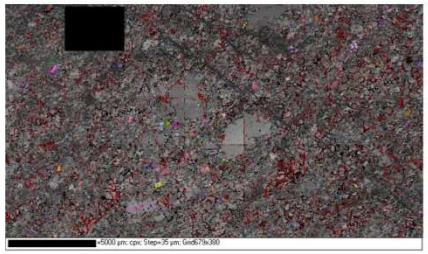

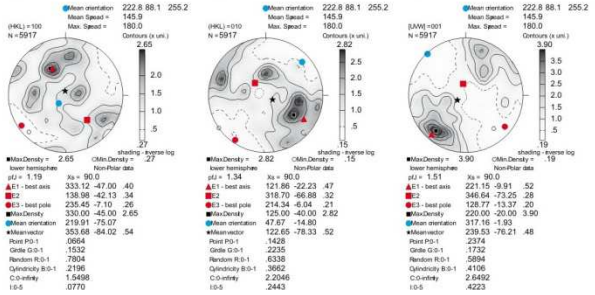

Cpx

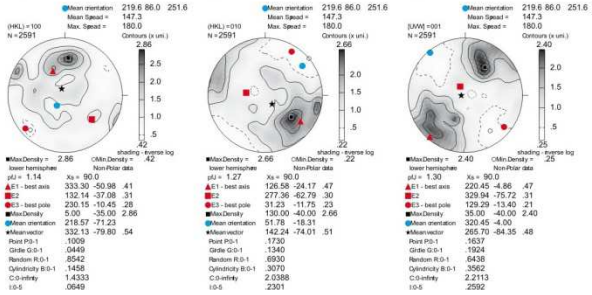

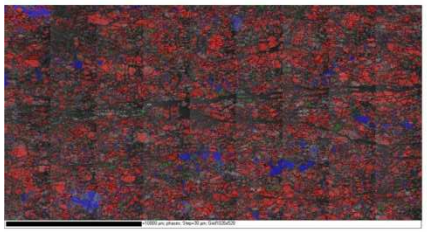

step=30µm

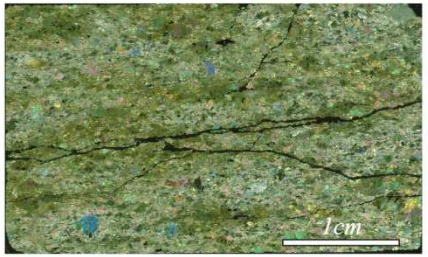

Geographic coordinates (1 point per grain)

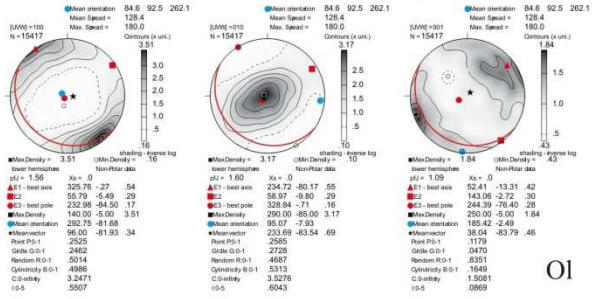

Ol

Sample coordinates (raw data)

Sample coordinates (1 point per grain)

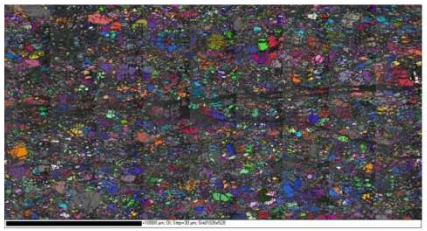

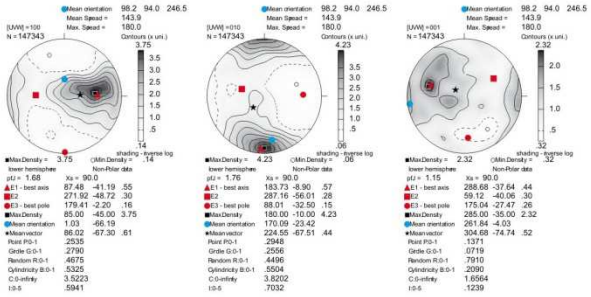

Ol

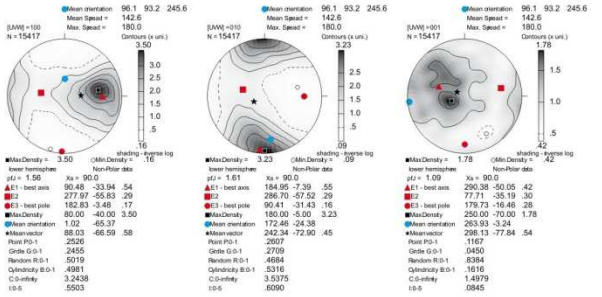

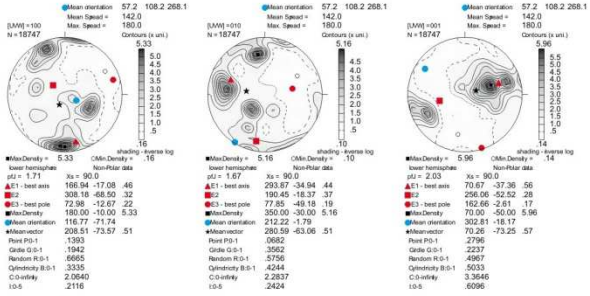

Opx

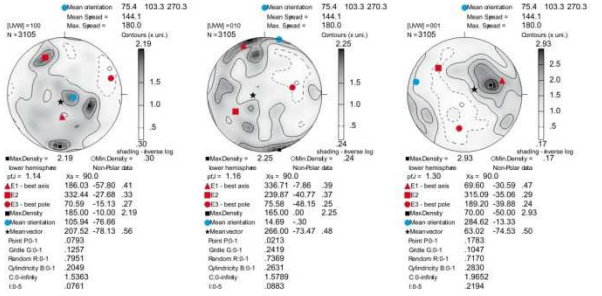

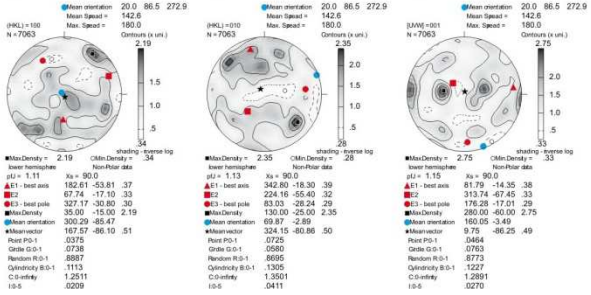

Cpx

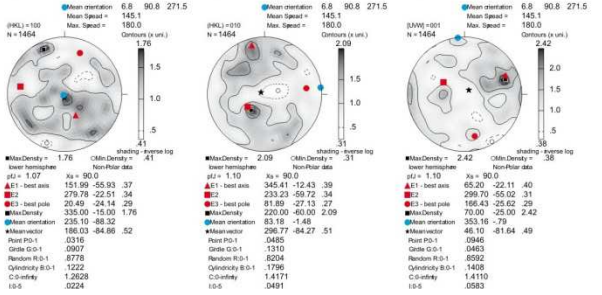

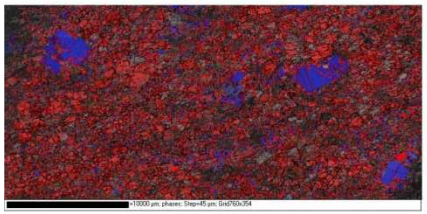

step=45µm

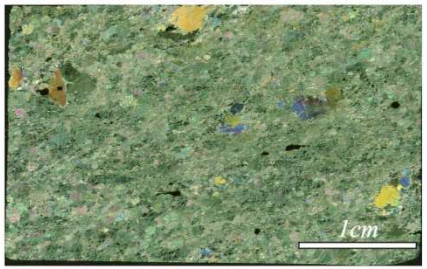

Geographic coordinates (1 point per grain)

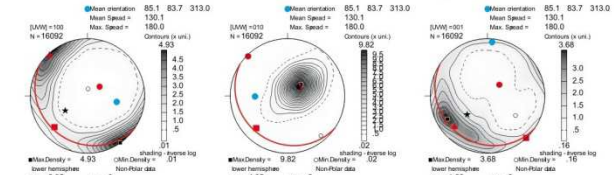

Ol

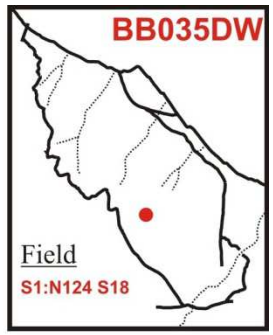

Sample coordinates (raw data)

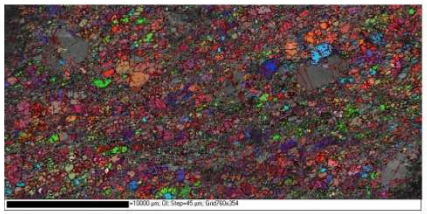

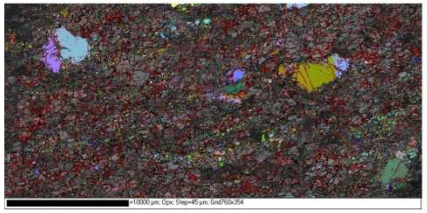

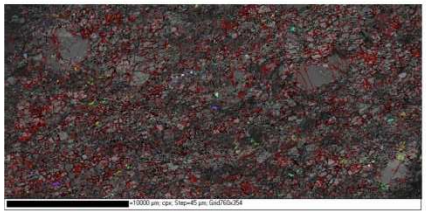

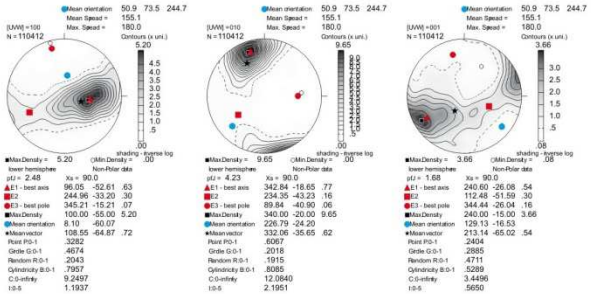

Ol

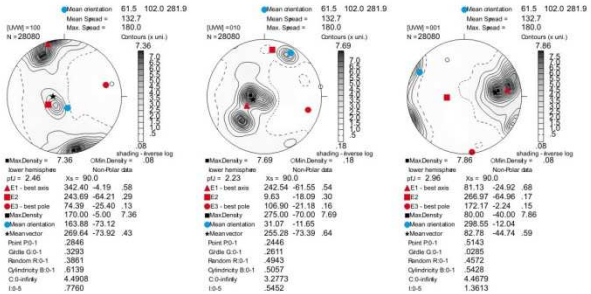

Opx

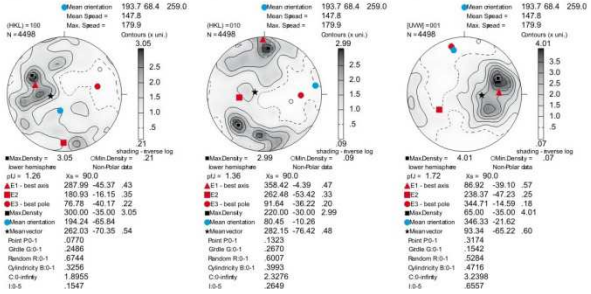

Cpx

Sample coordinates (1 point per grain)

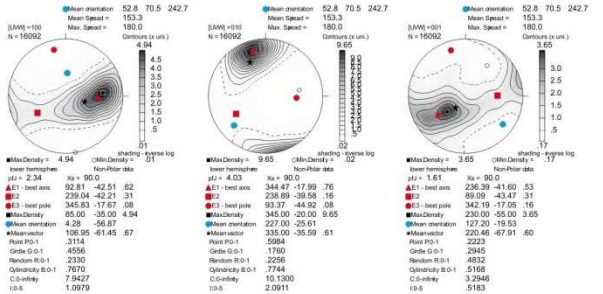

Ol

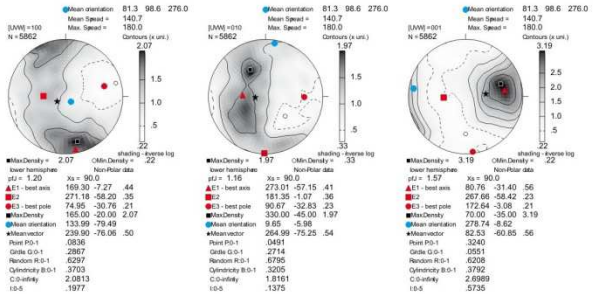

Opx

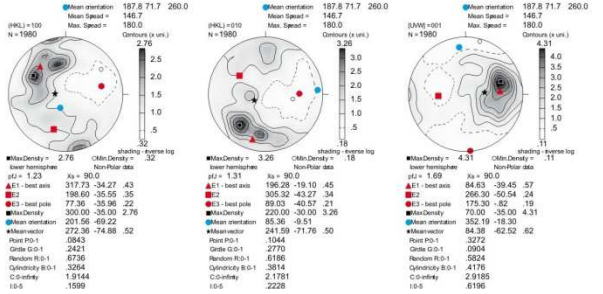

Cpx

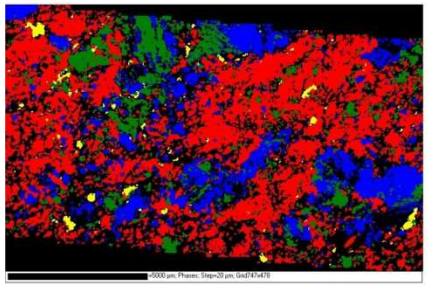

step=20μm

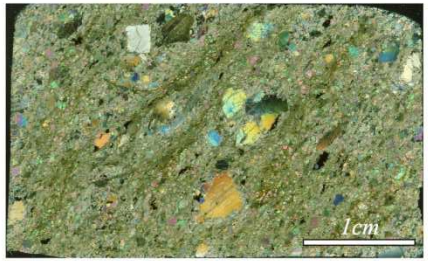

Geographic coordinates (1 point per grain)

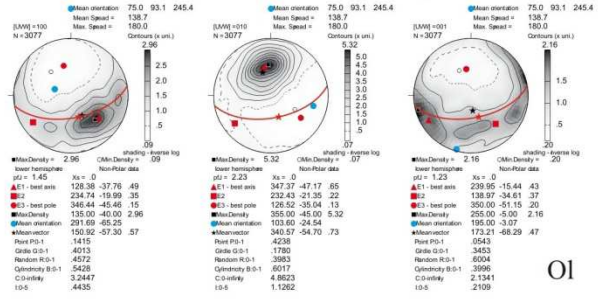

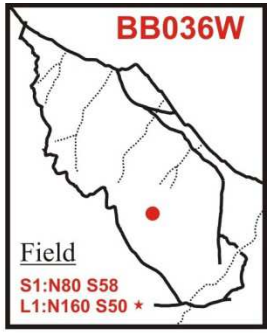

Ol

Sample coordinates (raw data)

Sample coordinates (1 point per grain)

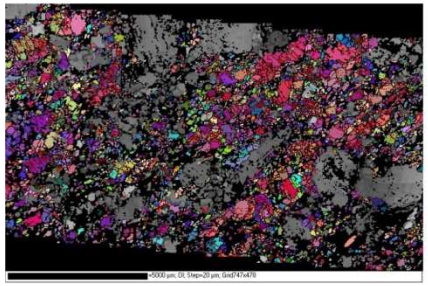

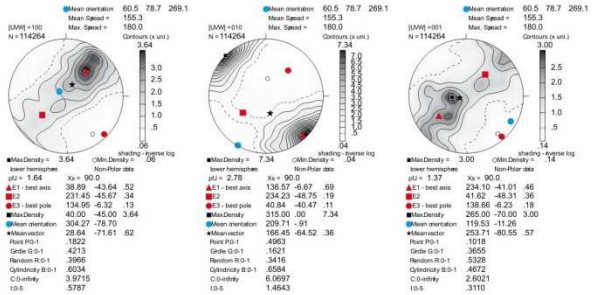

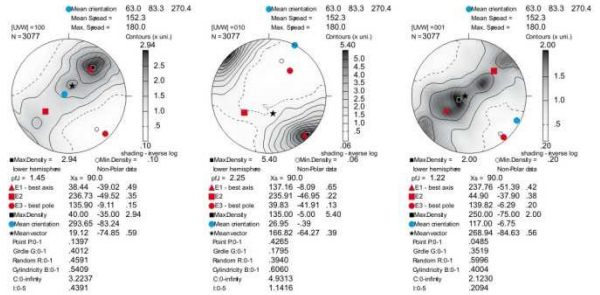

Opx

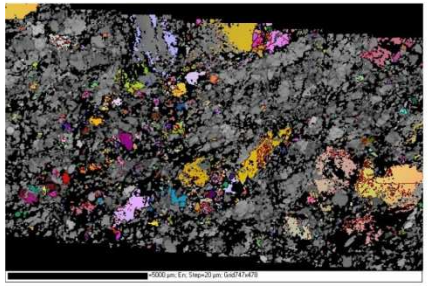

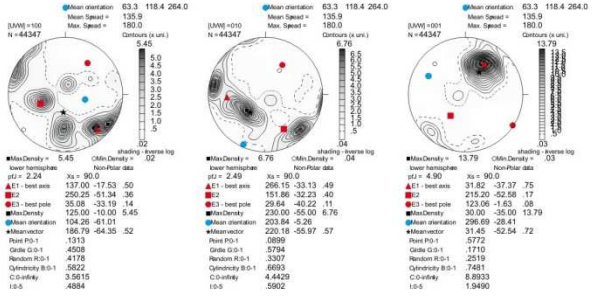

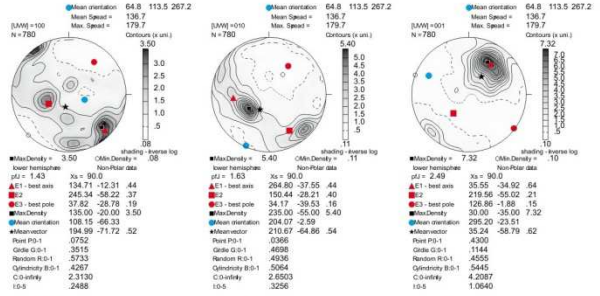

Cpx

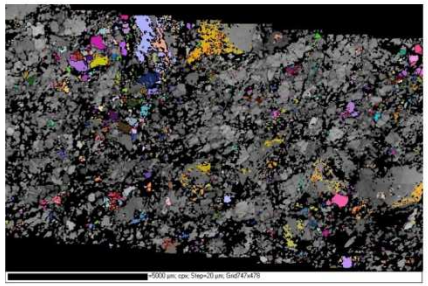

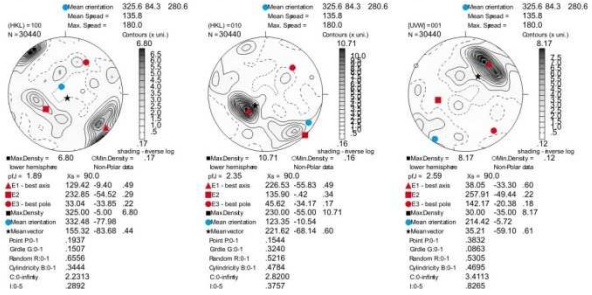

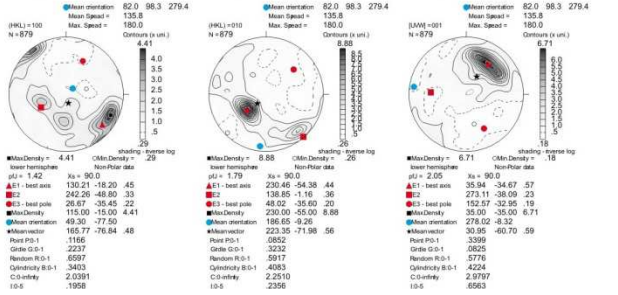

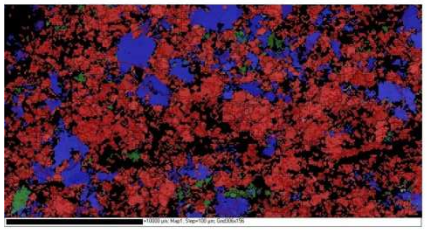

step=100μm

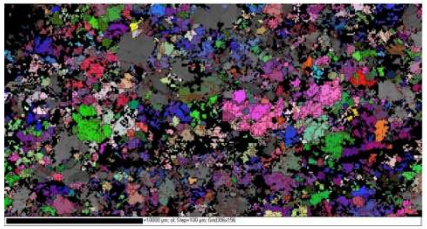

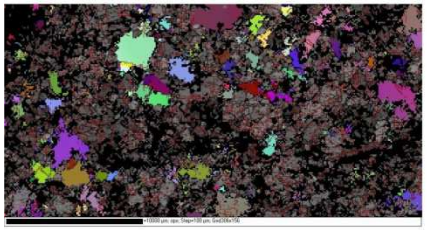

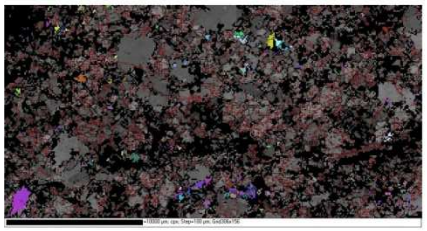

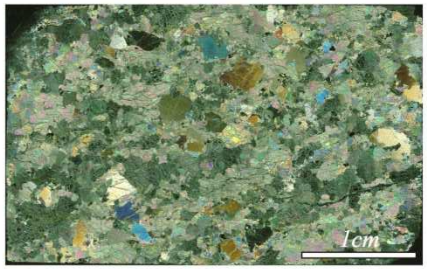

Geographic coordinates (1 point per grain)

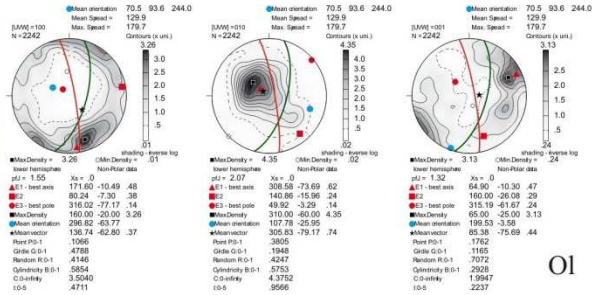

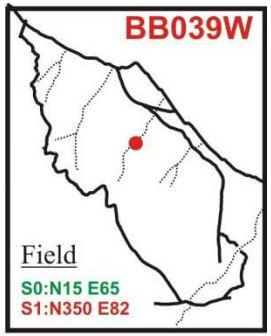

Ol

Sample coordinates (raw data)

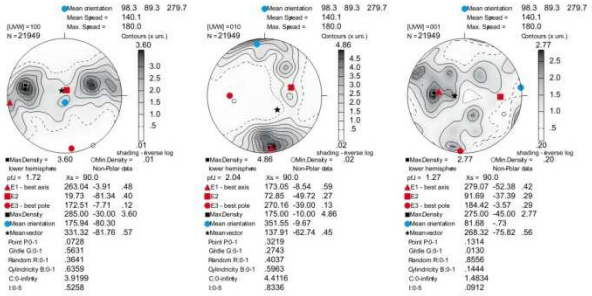

Ol

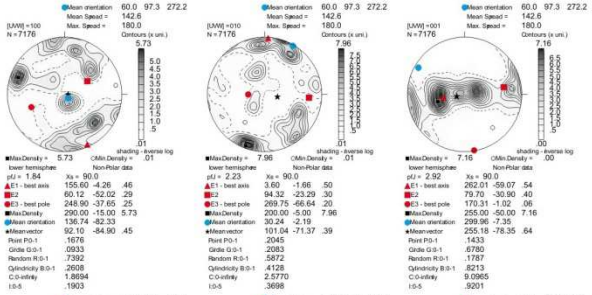

Opx

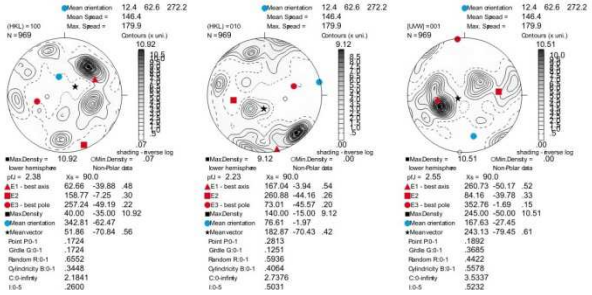

Cpx

Sample coordinates (1 point per grain)

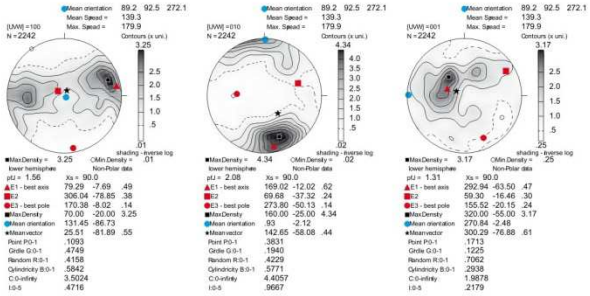

Ol

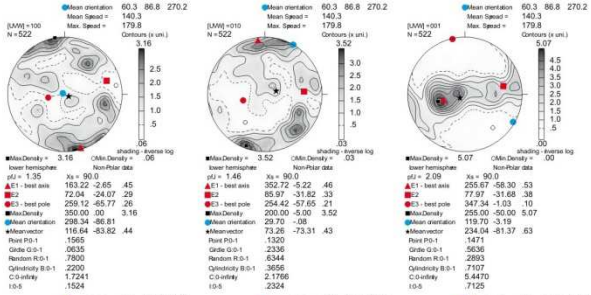

Opx

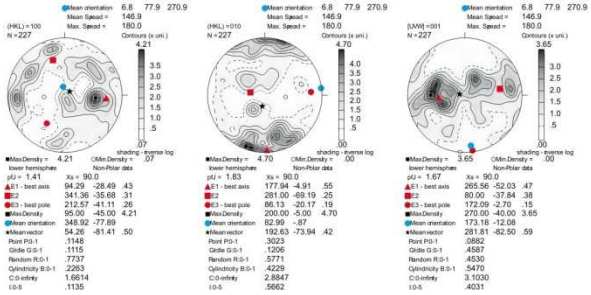

Cpx

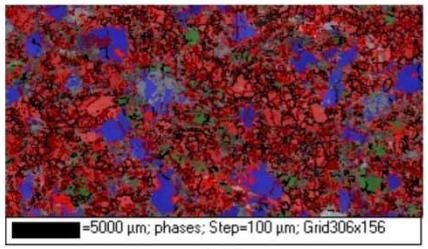

step=100µm

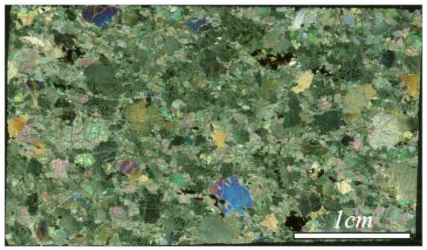

Geographic coordinates (1 point per grain)

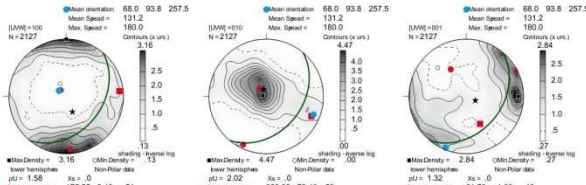

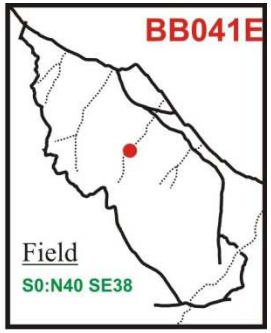

Ol

Sample coordinates (raw data)

Sample coordinates (1 point per grain)

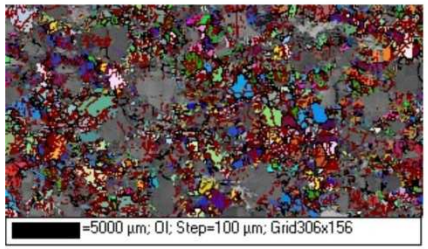

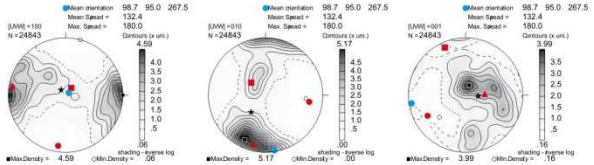

Ol

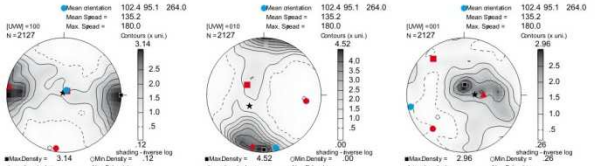

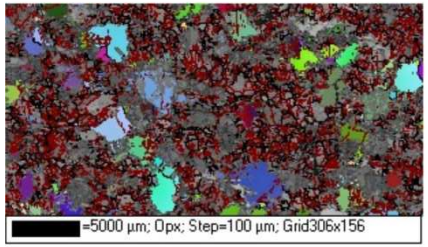

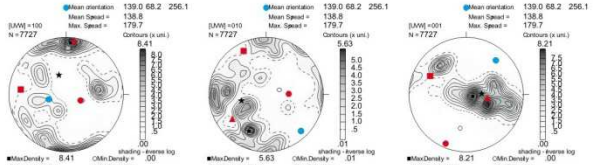

Opx

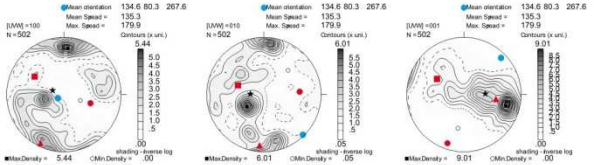

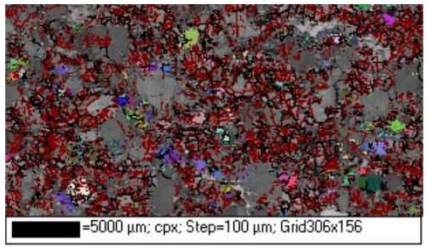

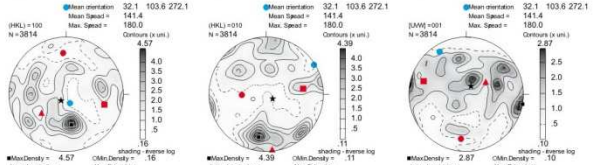

Cpx

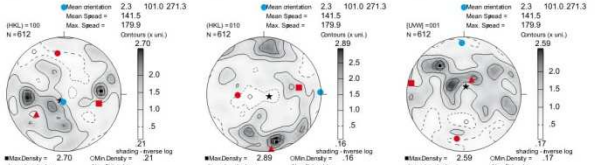

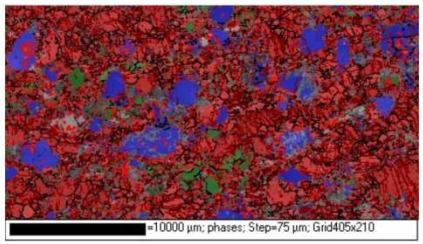

step=75µm

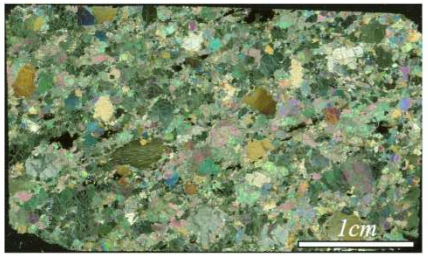

Geographic coordinates (1 point per grain)

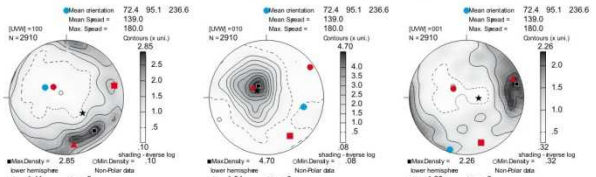

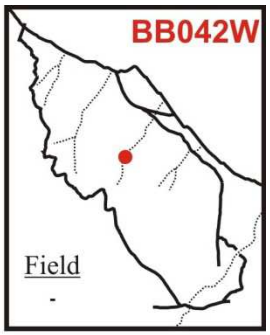

Ol

Sample coordinates (raw data)

Sample coordinates (1 point per grain)

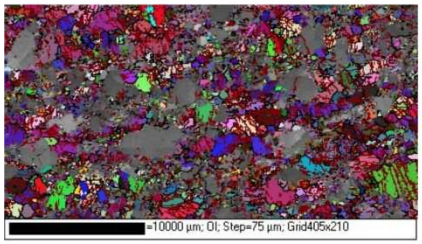

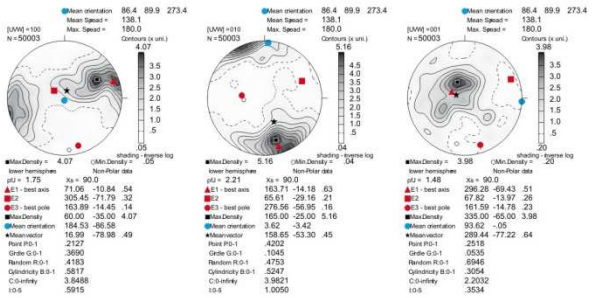

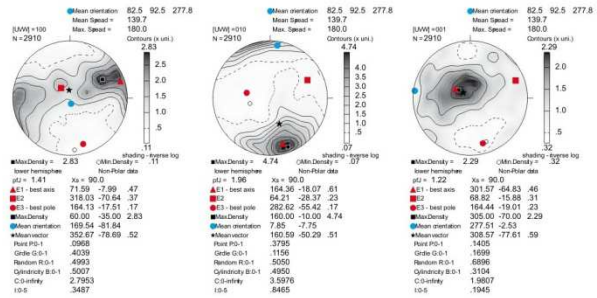

Ol

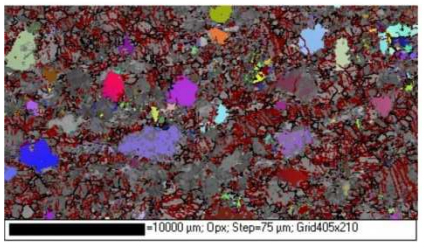

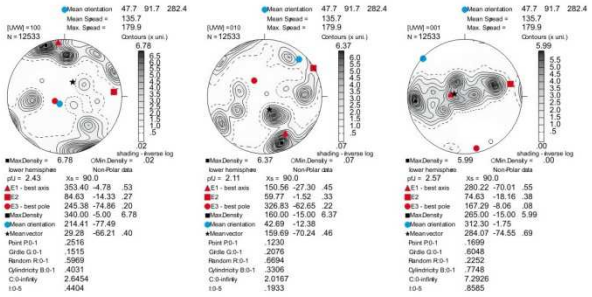

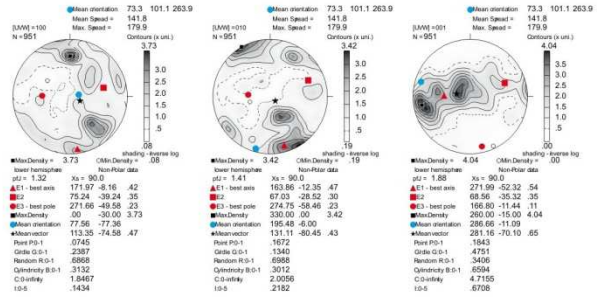

Opx

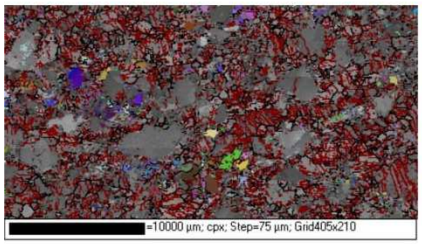

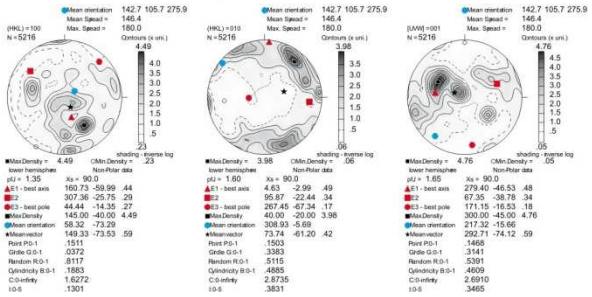

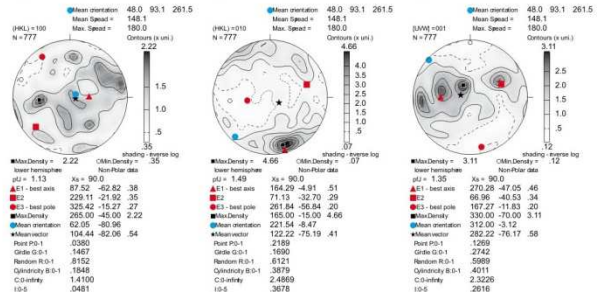

Cpx

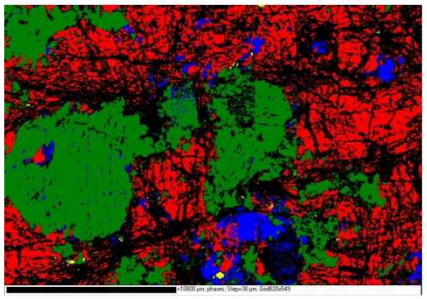

step=30μm

Geographic coordinates (1 point per grain)

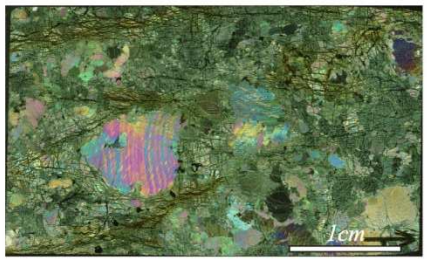

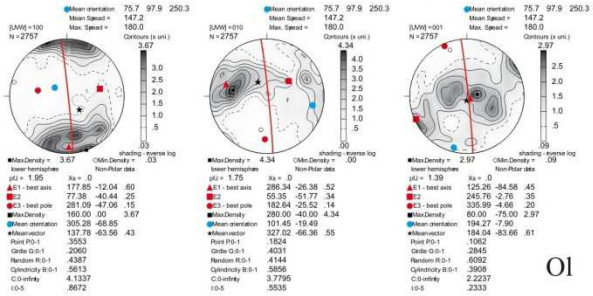

Ol

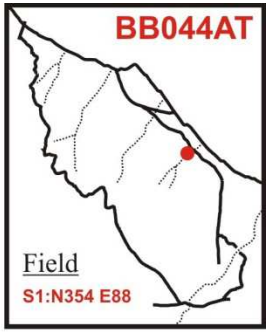

Sample coordinates (raw data)

Sample coordinates (1 point per grain)

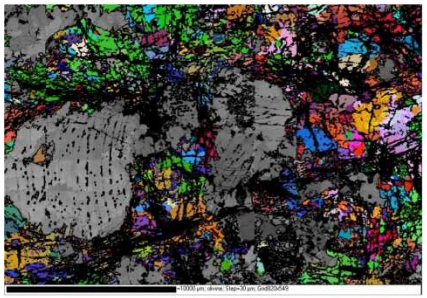

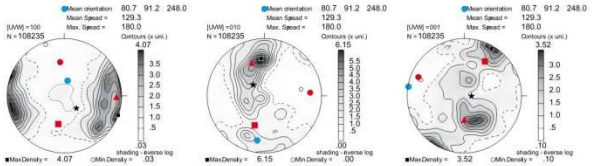

Ol

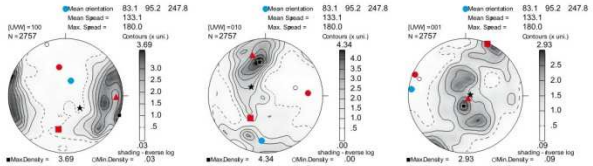

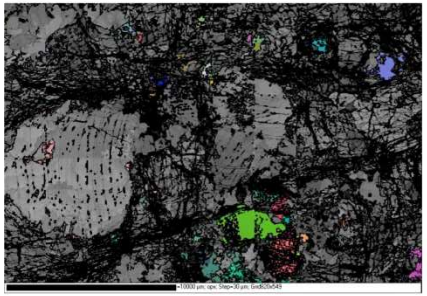

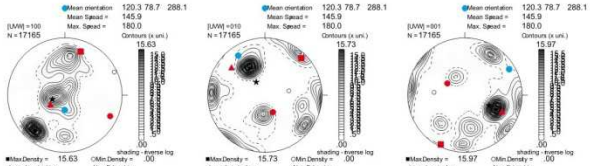

Opx

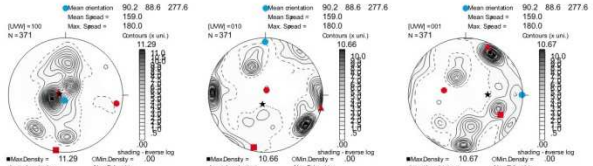

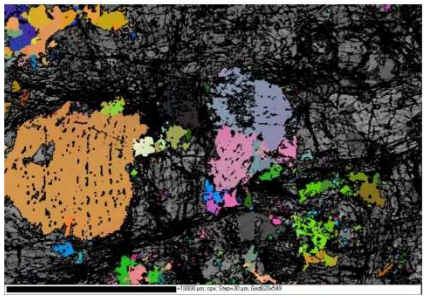

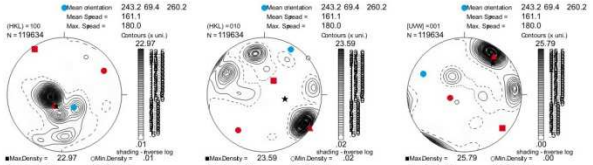

Cpx

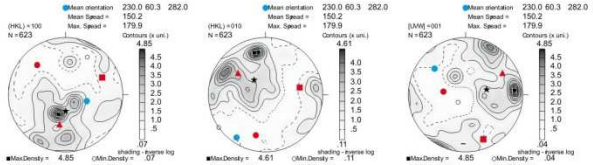

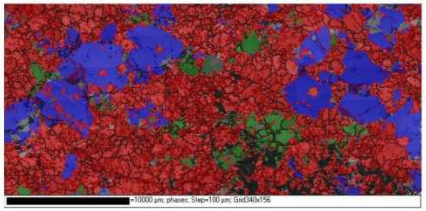

step=100µm

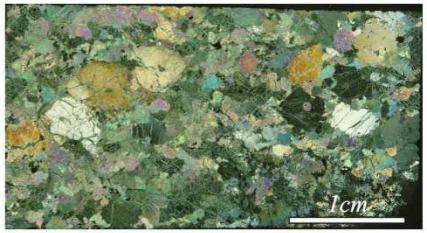

Geographic coordinates (1 point per grain)

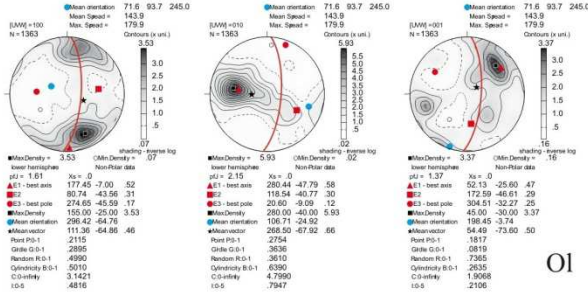

Ol

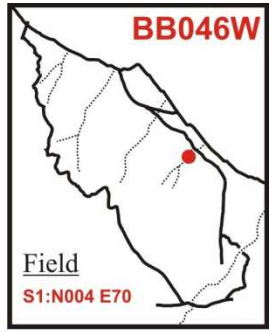

Sample coordinates (raw data)

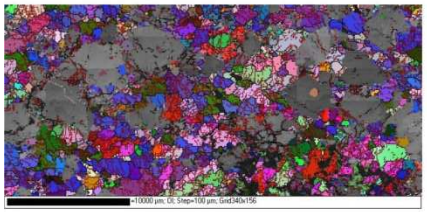

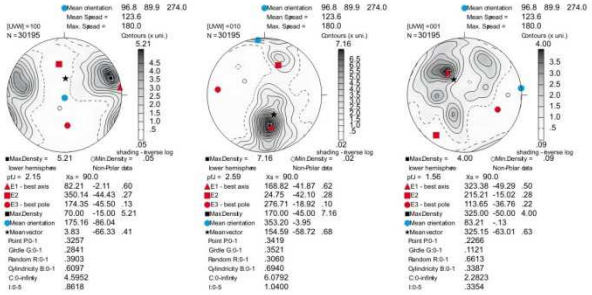

Ol

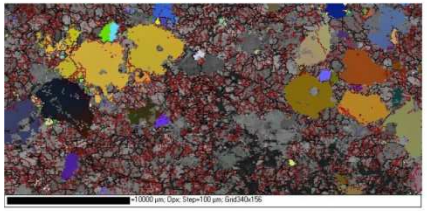

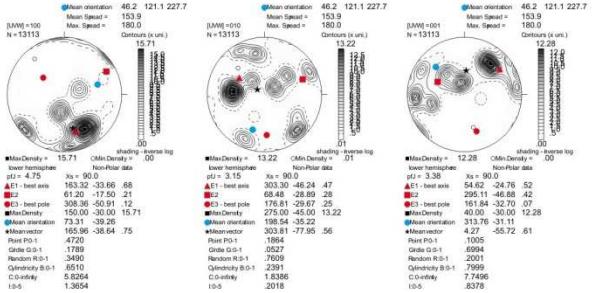

Opx

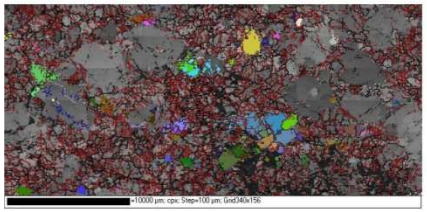

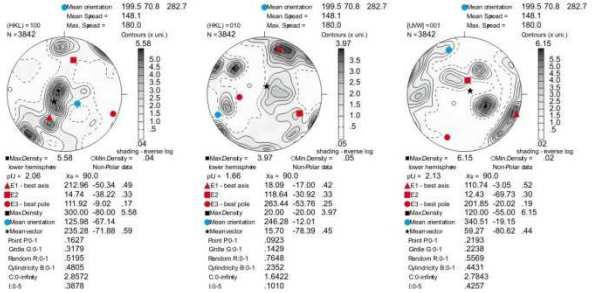

Cpx

Sample coordinates (1 point per grain)

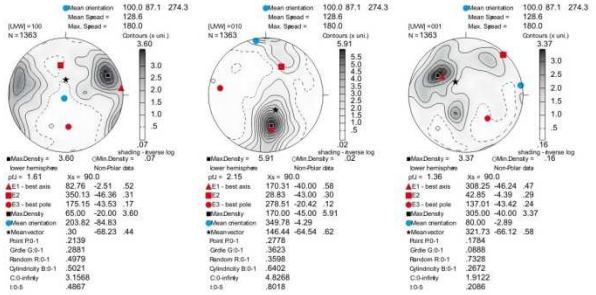

Ol

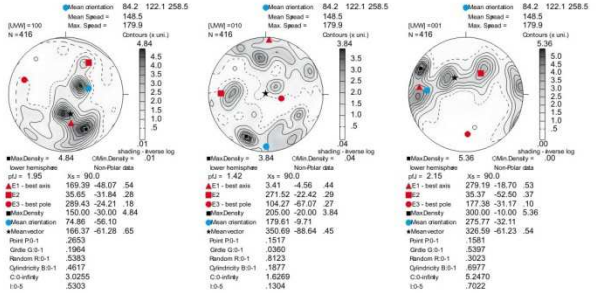

Opx

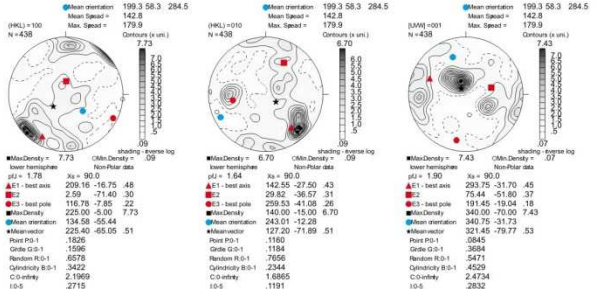

Cpx

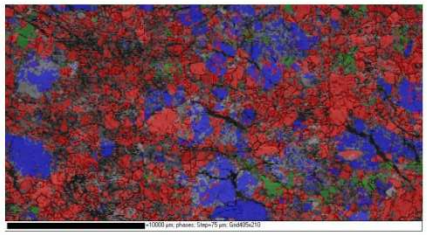

step=75µm

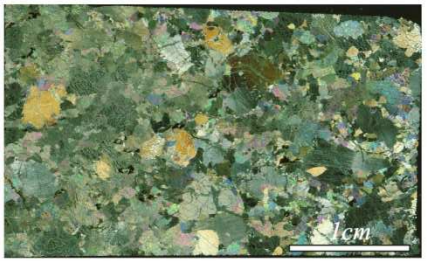

Geographic coordinates (1 point per grain)

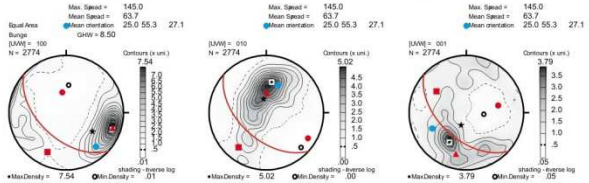

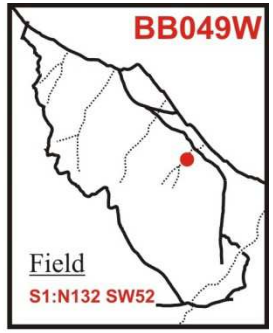

Ol

Sample coordinates (raw data)

Sample coordinates (1 point per grain)

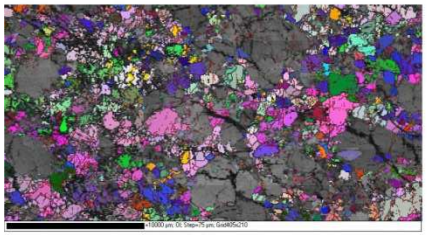

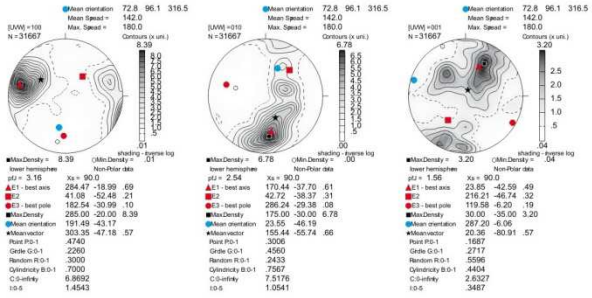

Ol

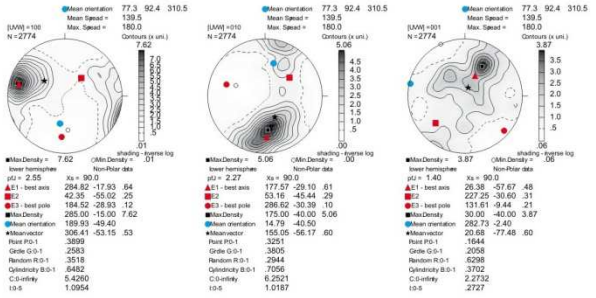

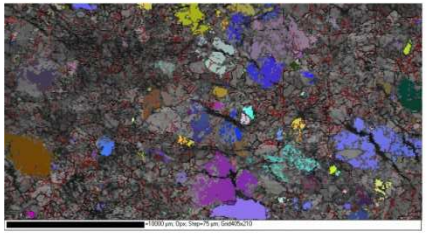

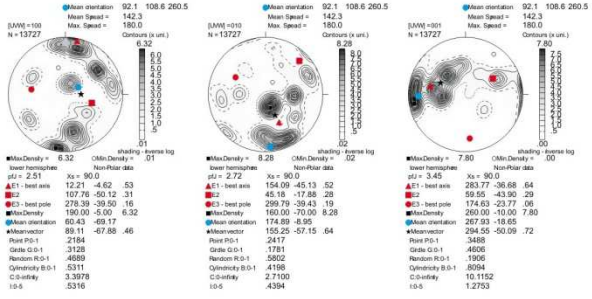

Opx

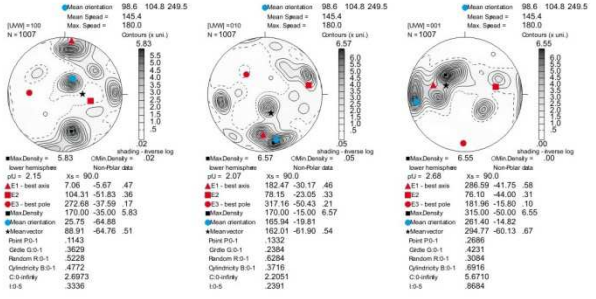

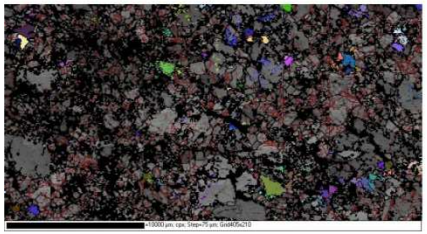

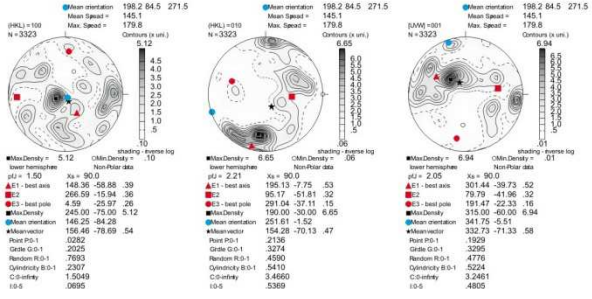

Cpx

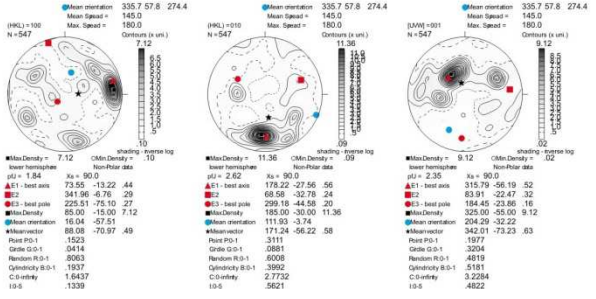

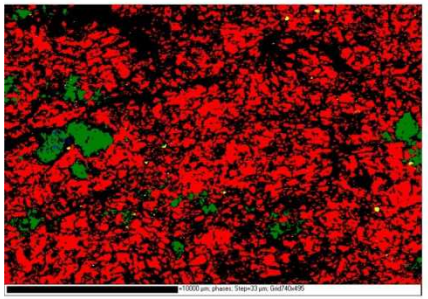

step=33µm

Geographic coordinates (1 point per grain)

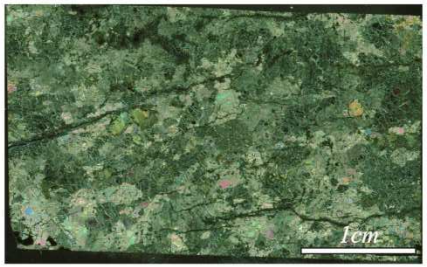

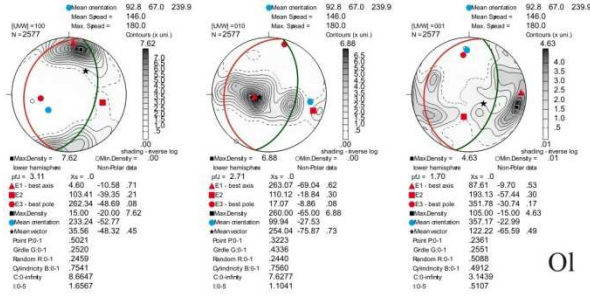

Sample coordinates (raw data)

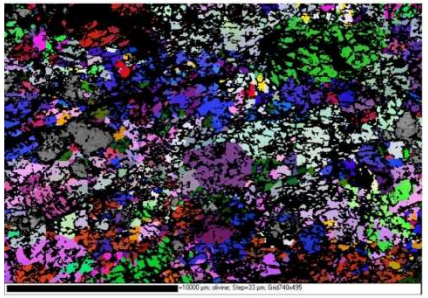

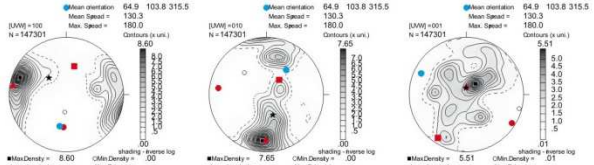

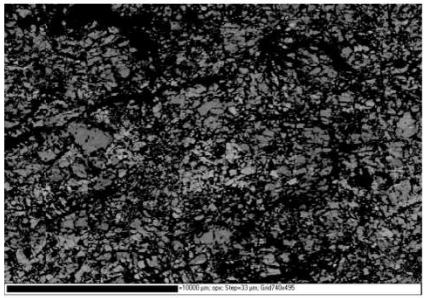

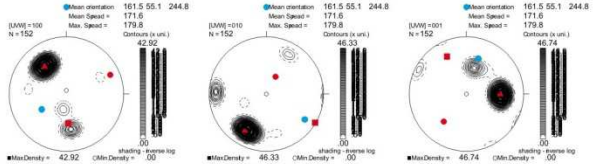

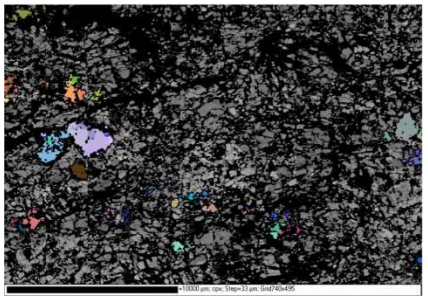

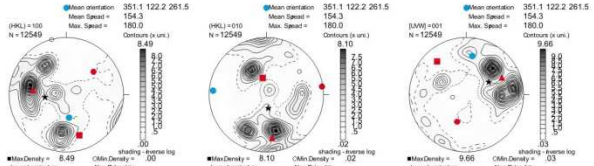

Sample coordinates (1 point per grain)

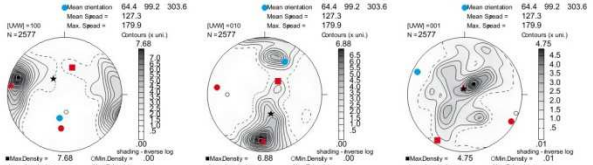

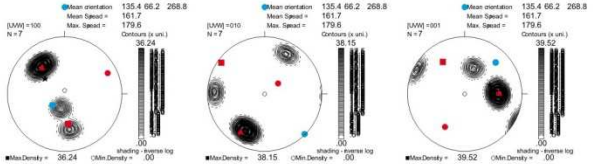

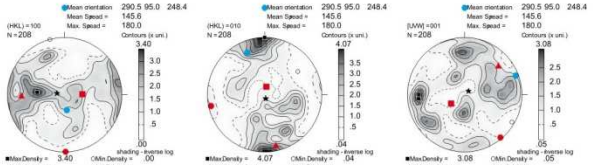

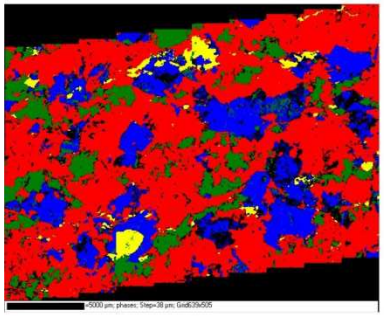

step=38µm

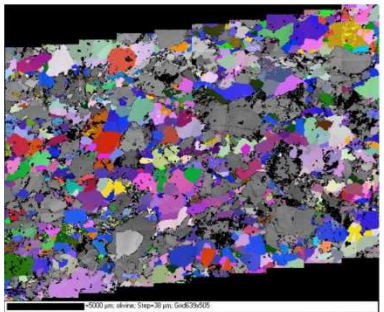

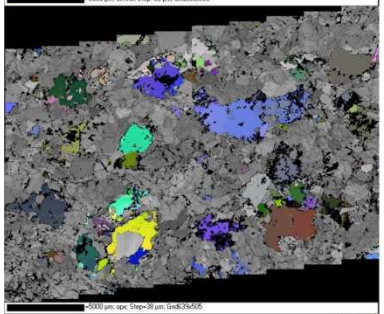

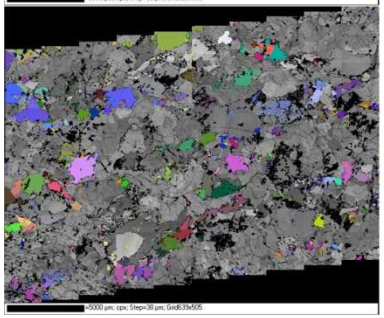

Geographic coordinates (1 point per grain)

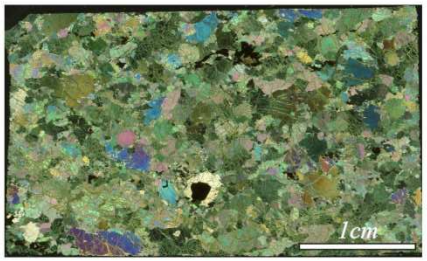

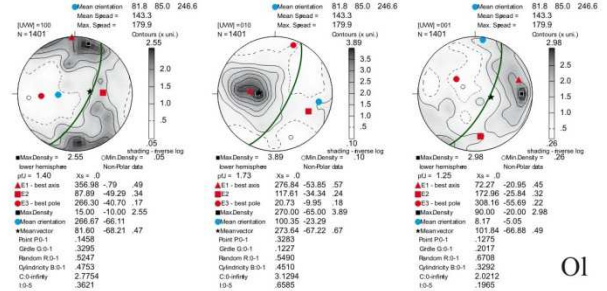

Ol

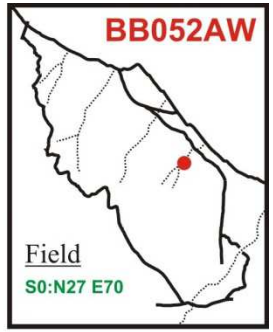

Sample coordinates (raw data)

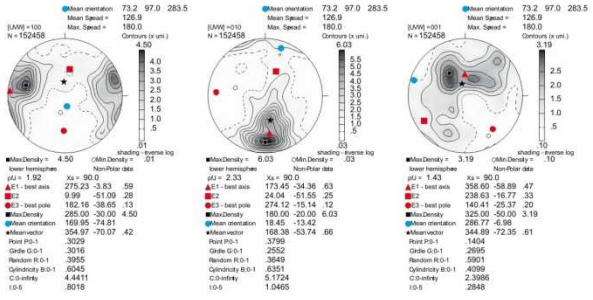

Ol

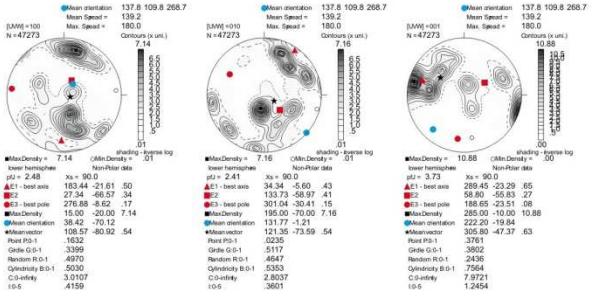

Opx

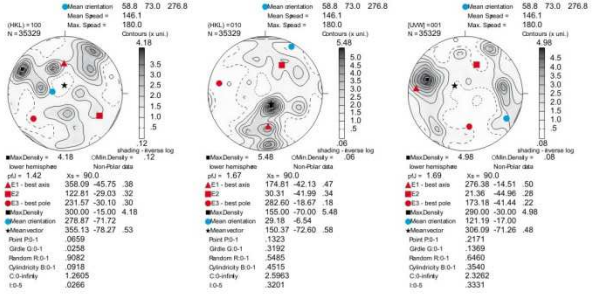

Cpx

Sample coordinates (1 point per grain)

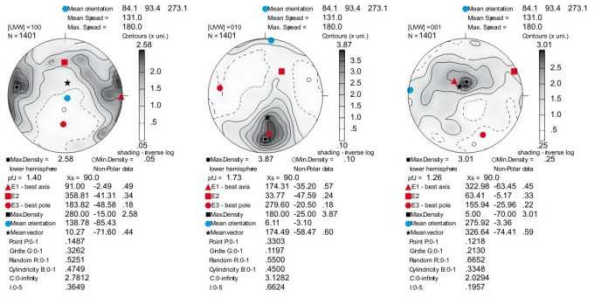

Ol

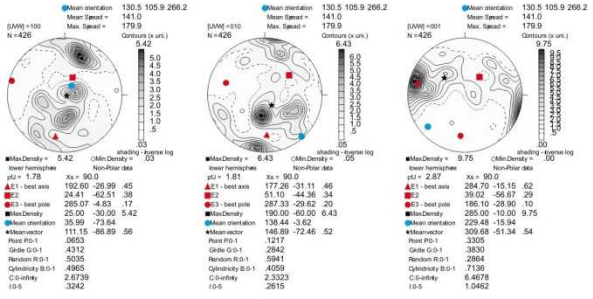

Opx

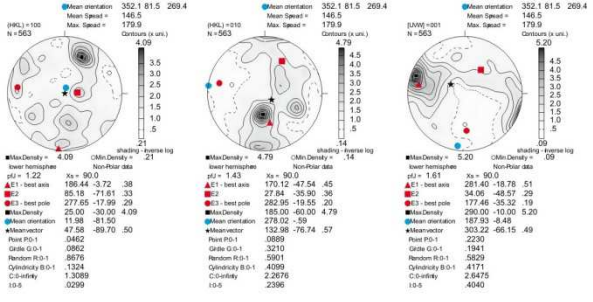

Cpx

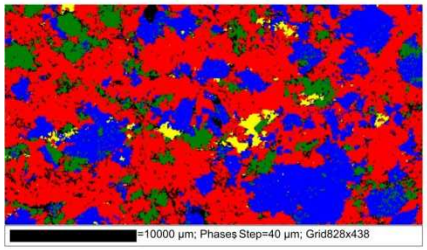

step=40µm

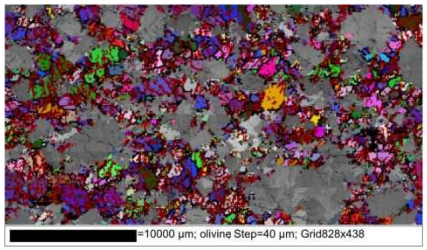

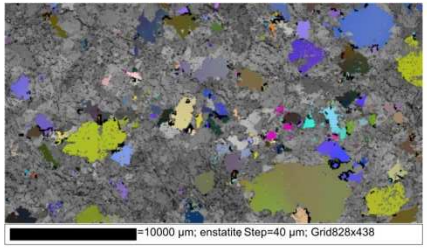

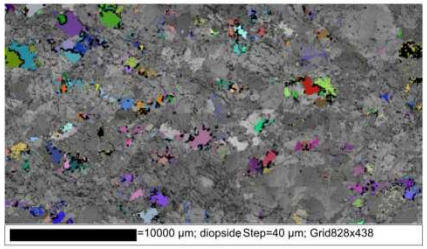

Geographic coordinates (1 point per grain)

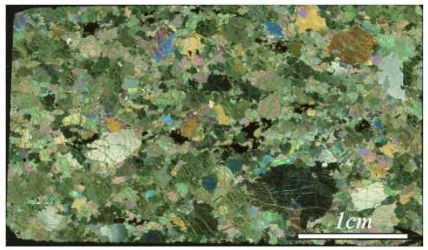

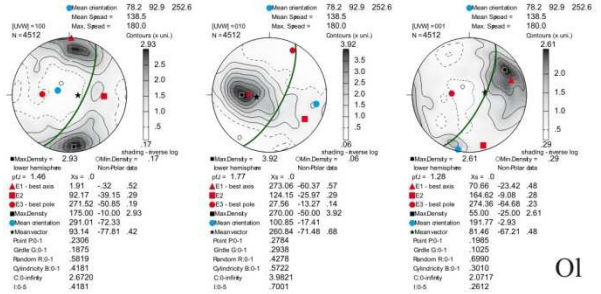

Ol

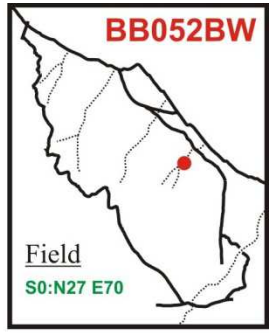

Sample coordinates (raw data)

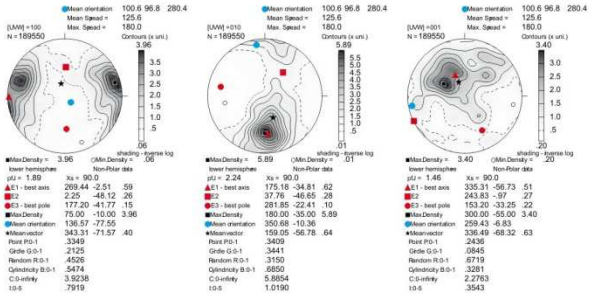

Ol

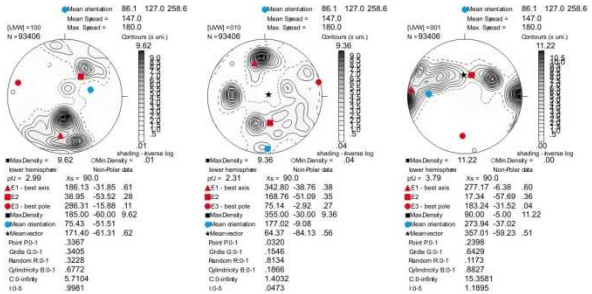

Opx

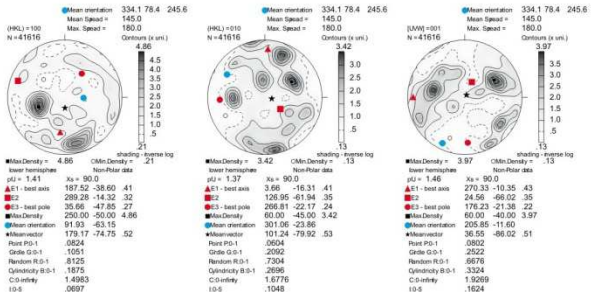

Cpx

Sample coordinates (1 point per grain)

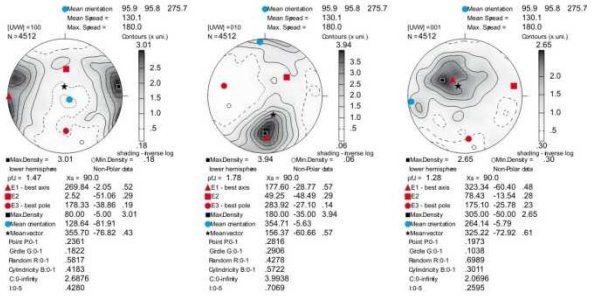

Ol

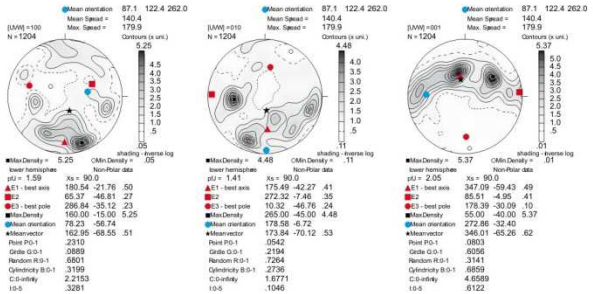

Opx

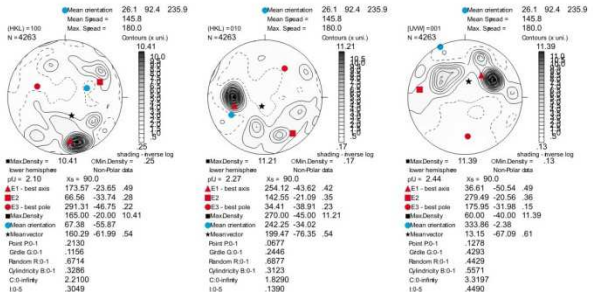

Cpx

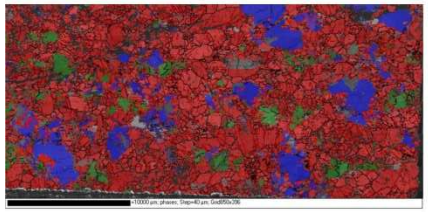

step=40μm

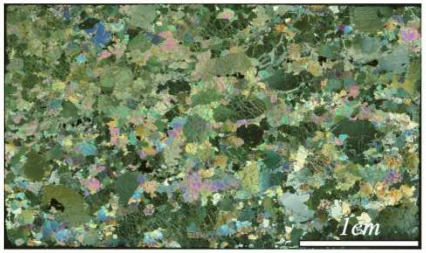

Geographic coordinates (1 point per grain)

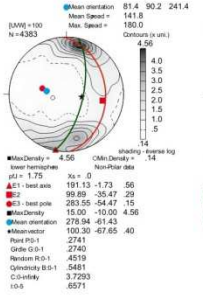

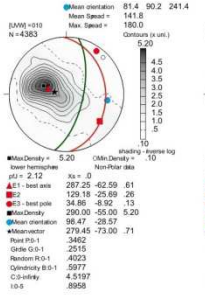

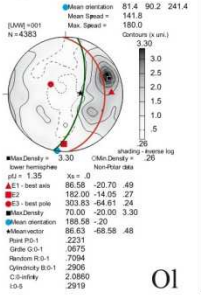

Ol

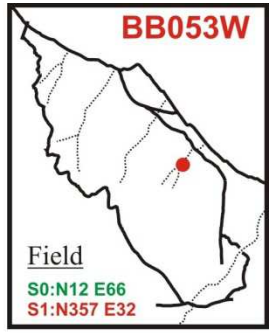

Sample coordinates (raw data)

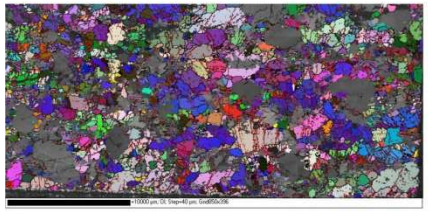

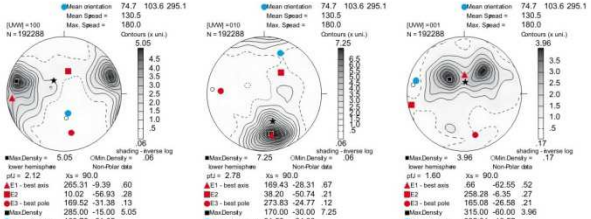

Ol

Sample coordinates (1 point per grain)

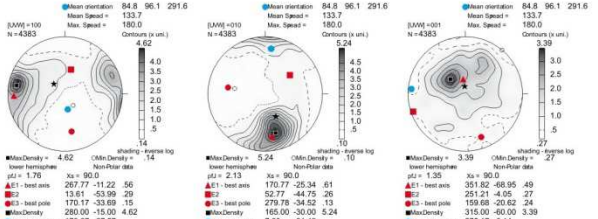

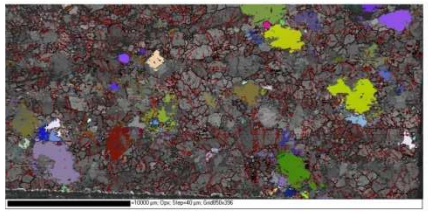

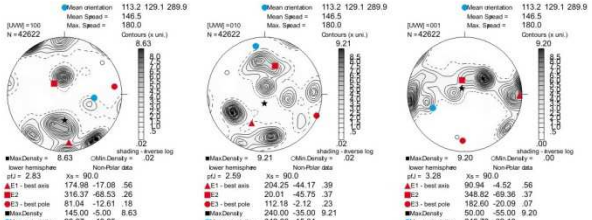

Opx

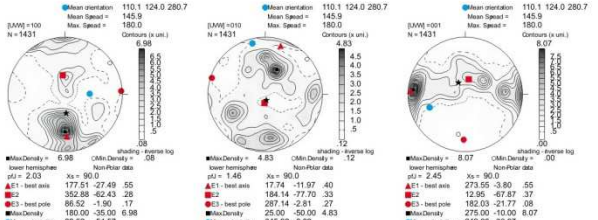

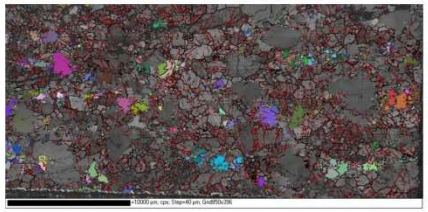

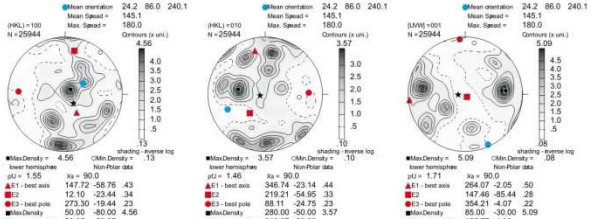

Cpx

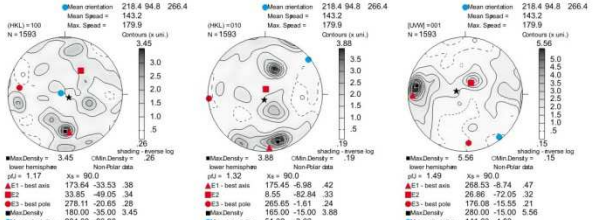

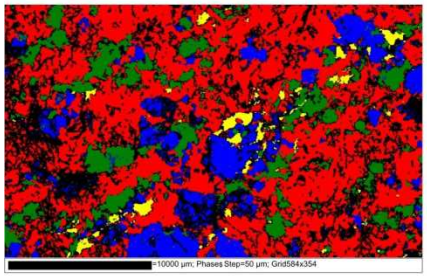

step=50µm

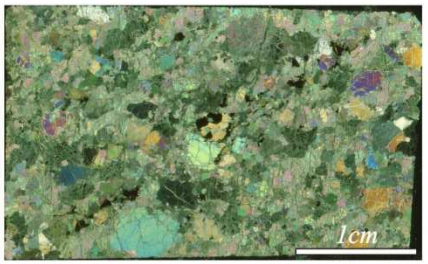

Geographic coordinates (1 point per grain)

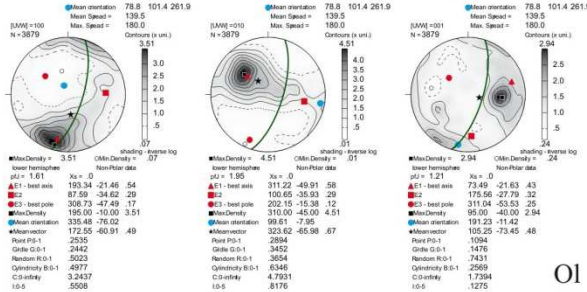

Ol

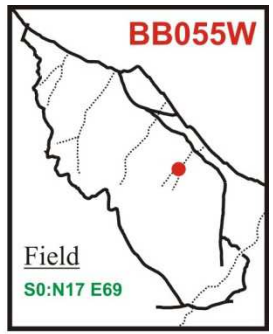

Sample coordinates (raw data)

Sample coordinates (1 point per grain)

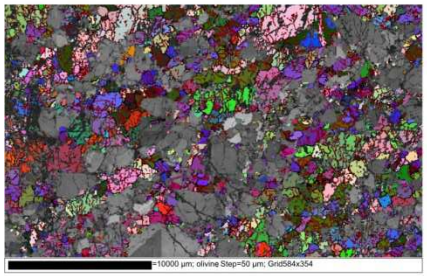

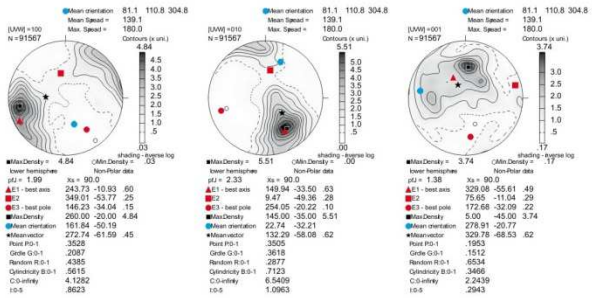

Ol

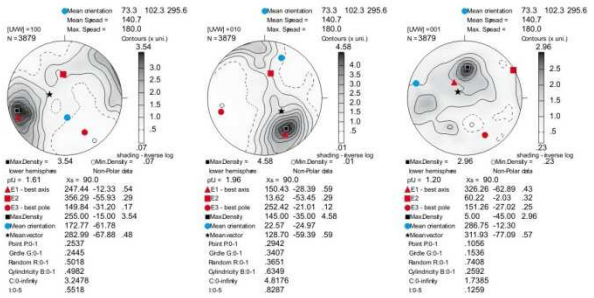

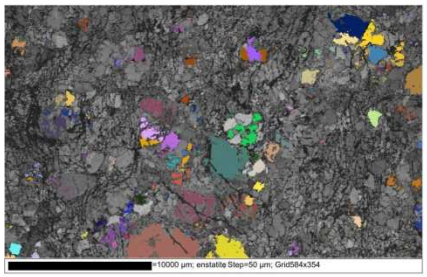

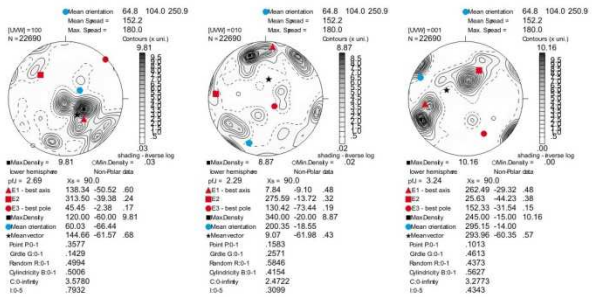

Opx

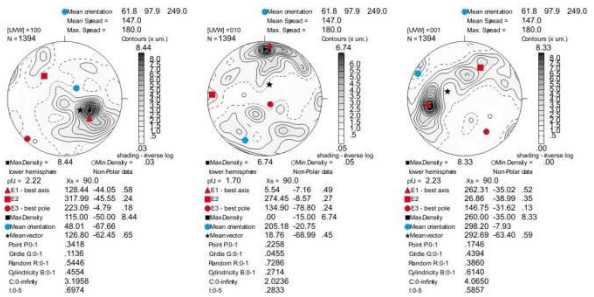

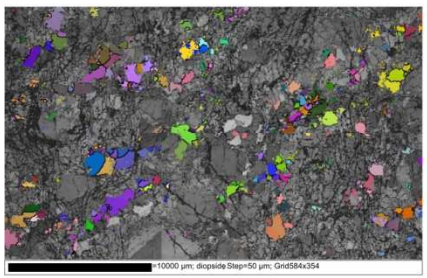

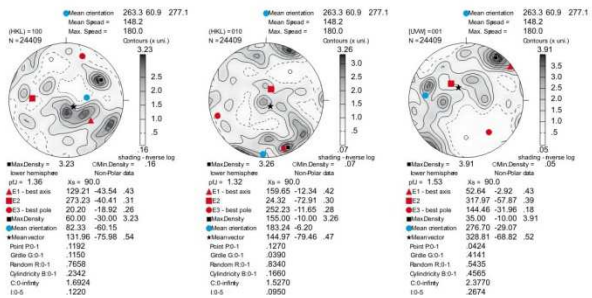

Cpx

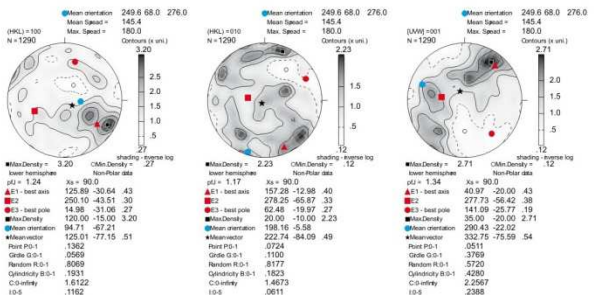

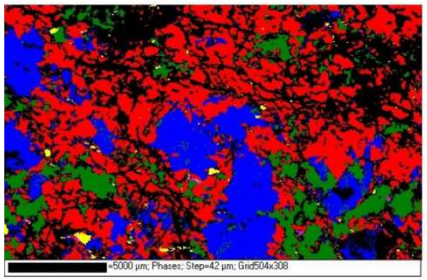

step=42µm

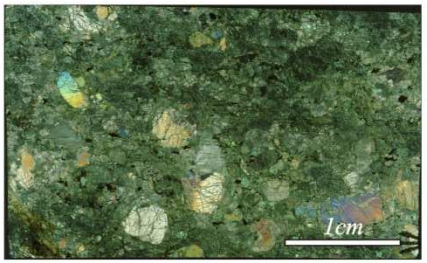

Geographic coordinates (1 point per grain)

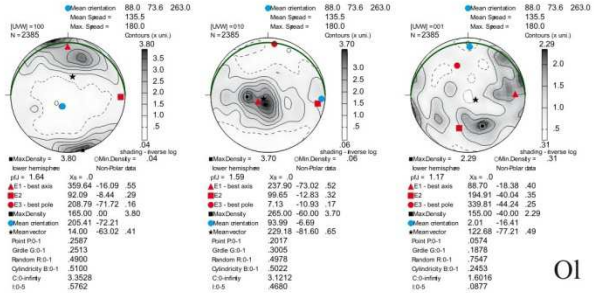

Ol

Sample coordinates (raw data)

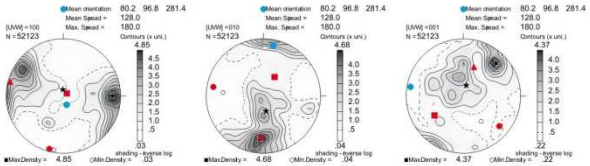

Ol

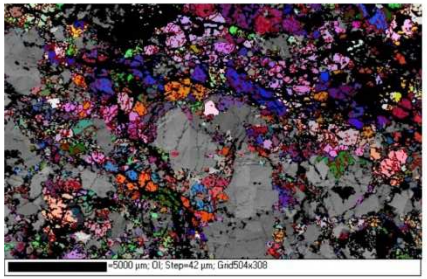

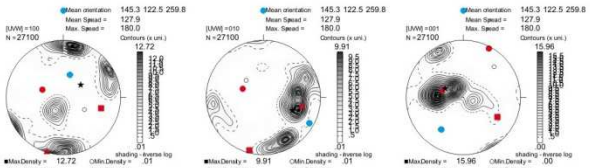

Opx

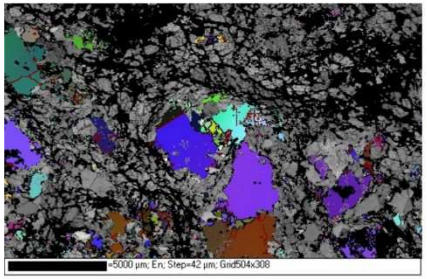

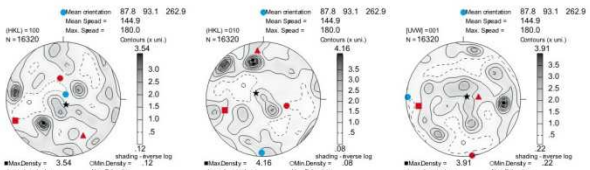

Cpx

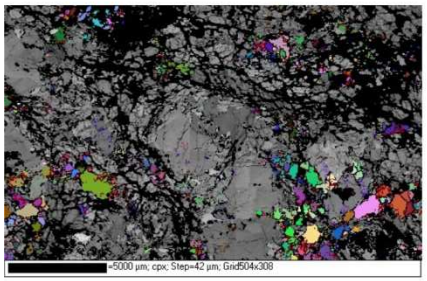

Sample coordinates (1 point per grain)

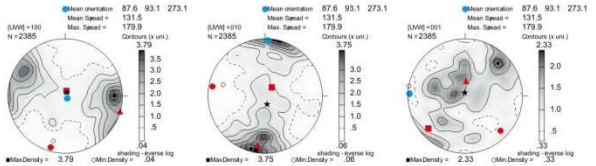

Ol

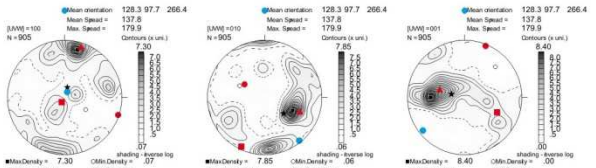

Opx

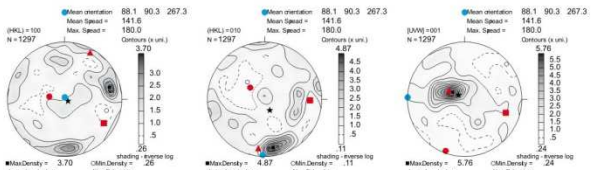

Cpx

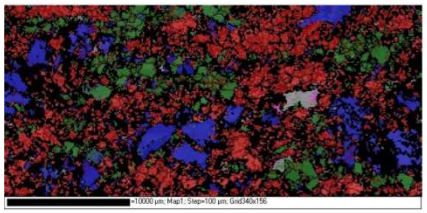

step=100µm

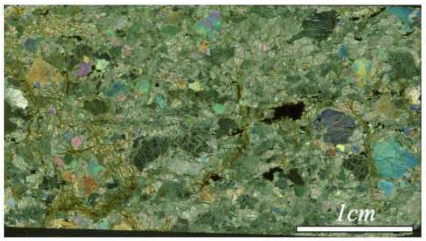

Geographic coordinates (1 point per grain)

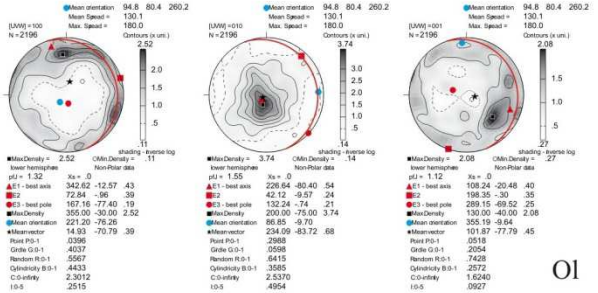

Ol

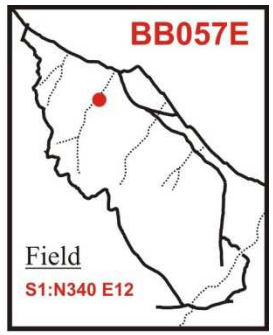

Sample coordinates (raw data)

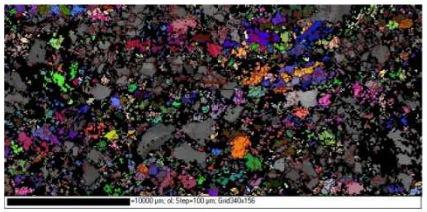

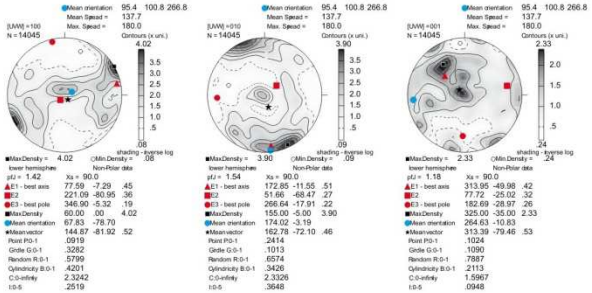

Ol

Sample coordinates (1 point per grain)

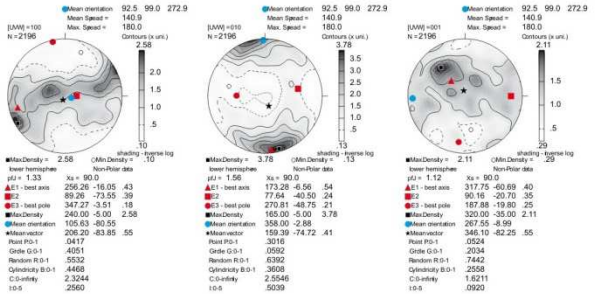

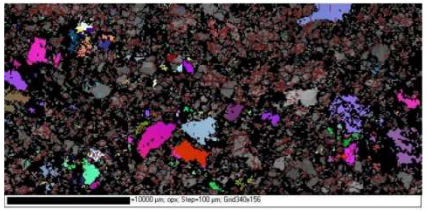

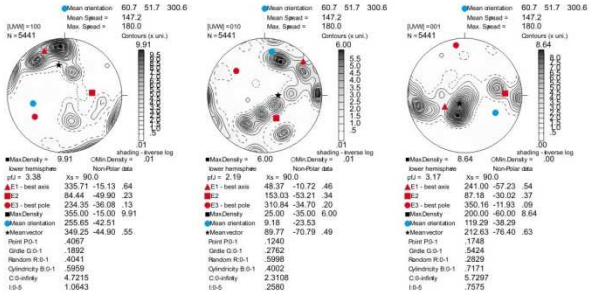

Opx

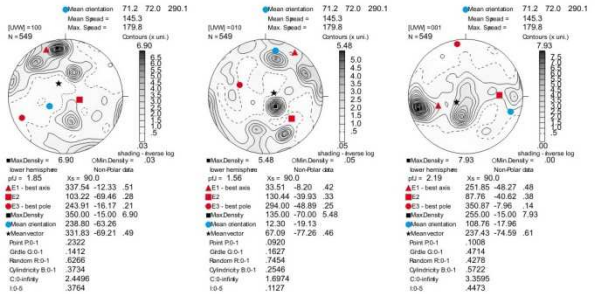

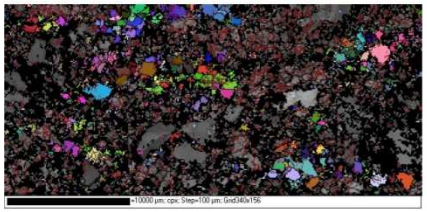

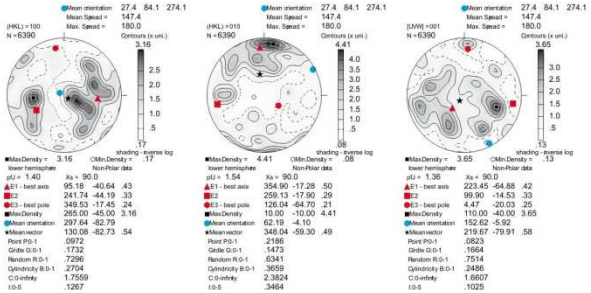

Cpx

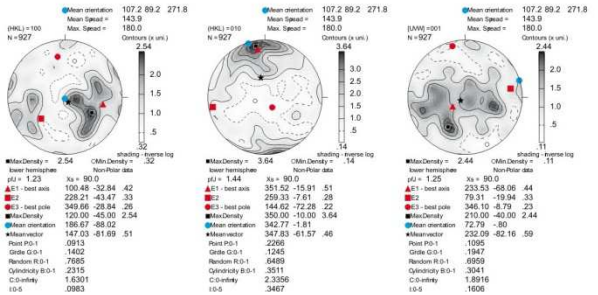

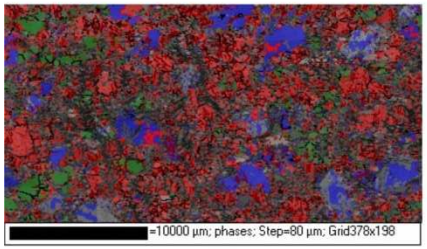

step=80µm

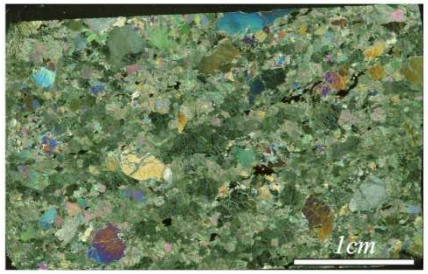

Geographic coordinates (1 point per grain)

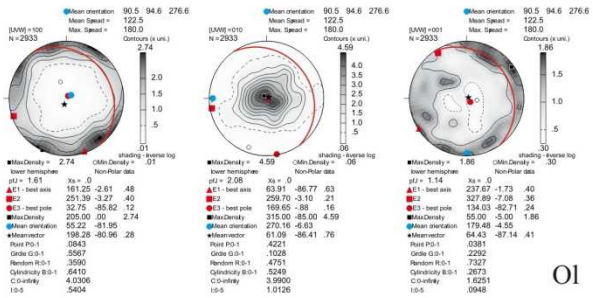

Ol

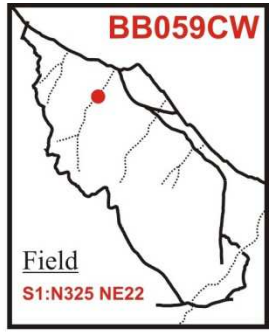

Sample coordinates (raw data)

Sample coordinates (1 point per grain)

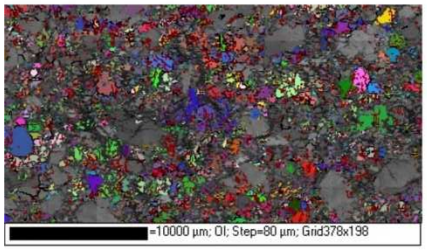

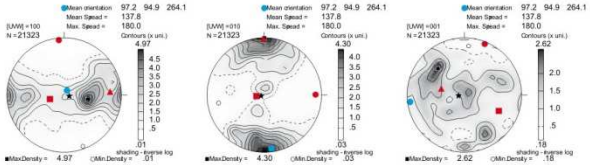

Ol

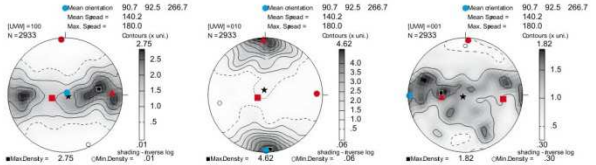

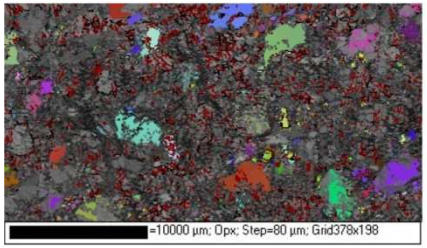

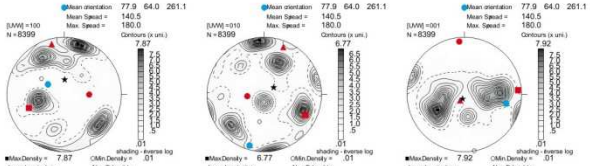

Opx

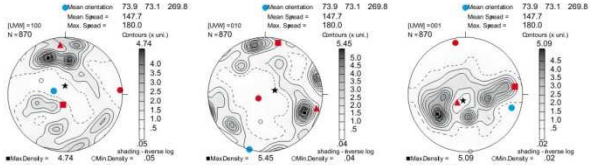

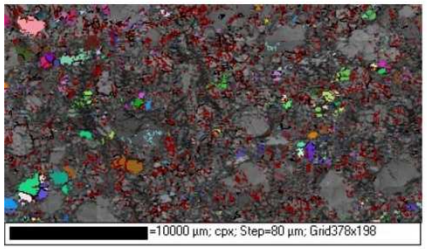

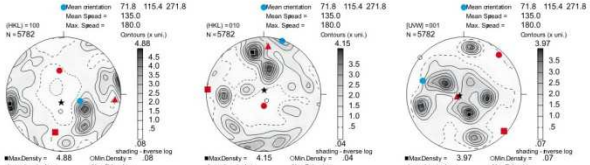

Cpx

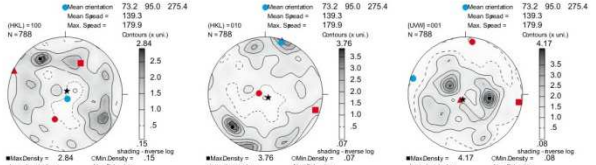

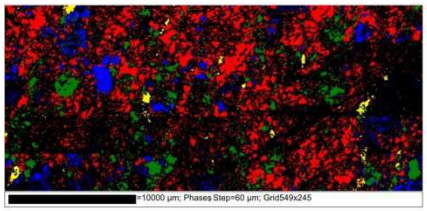

step=60µm

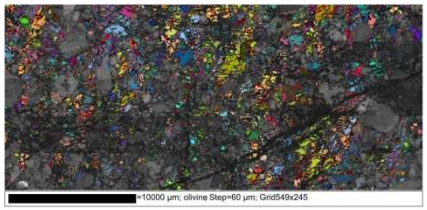

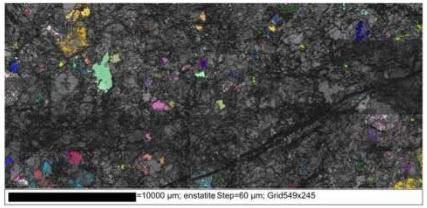

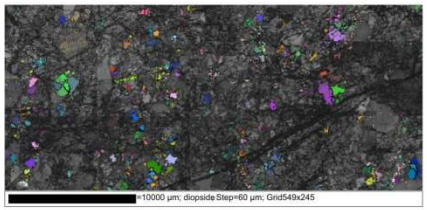

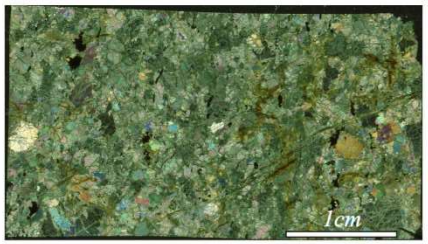

Geographic coordinates (1 point per grain)

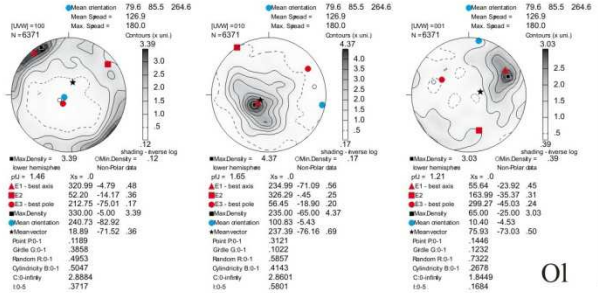

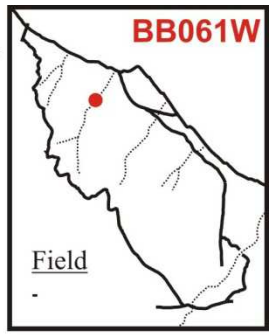

Ol

Sample coordinates (raw data)

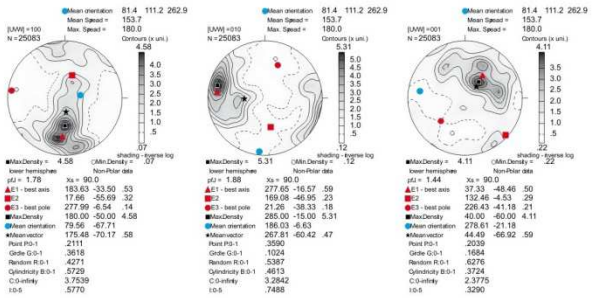

Ol

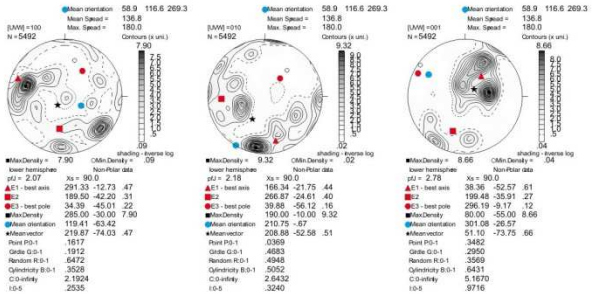

Opx

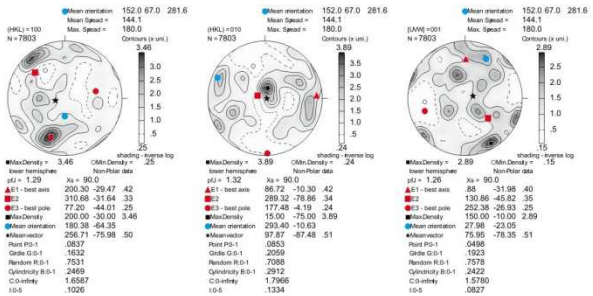

Cpx

Sample coordinates (1 point per grain)

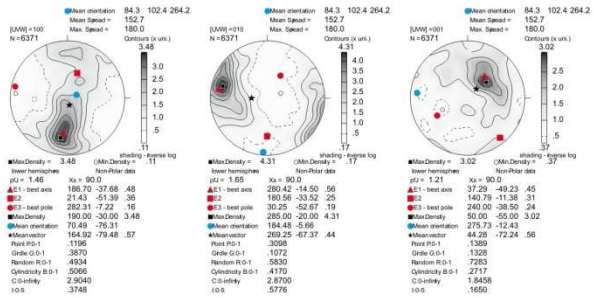

Ol

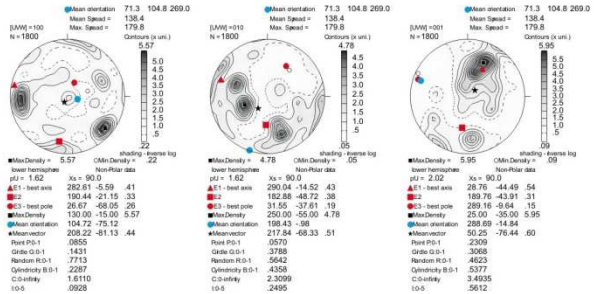

Opx

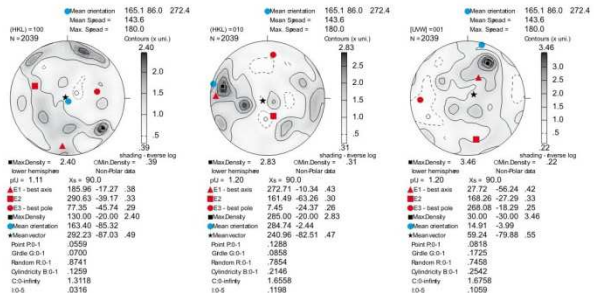

Cpx

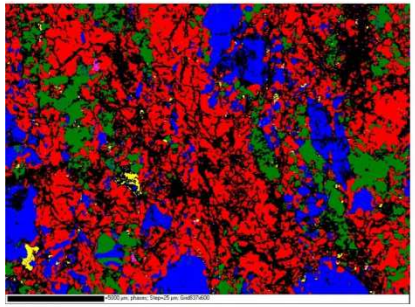

step=25µm

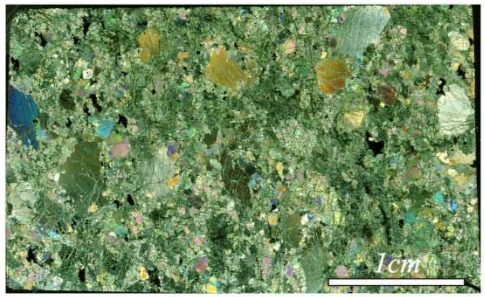

Geographic coordinates (1 point per grain)

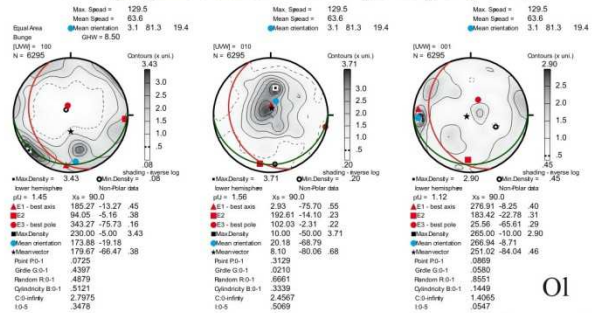

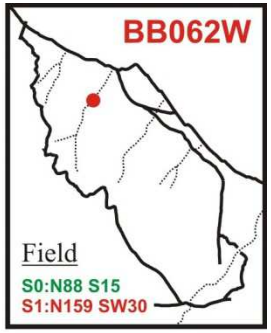

Ol

Sample coordinates (raw data)

Sample coordinates (1 point per grain)

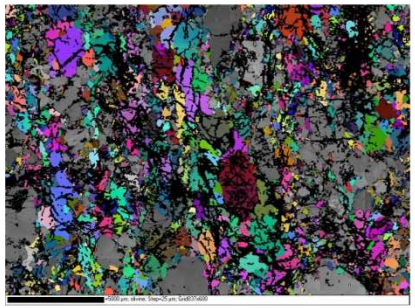

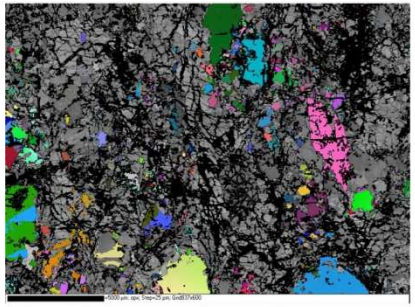

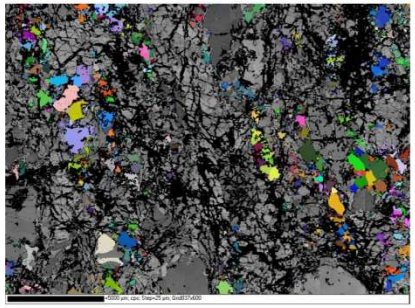

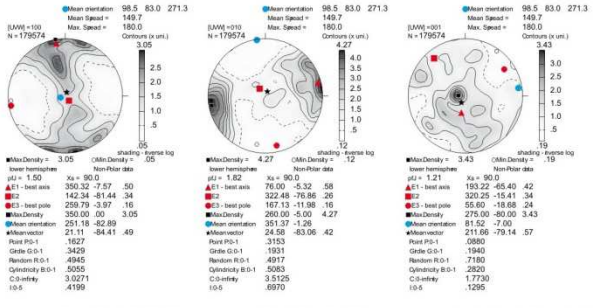

Ol

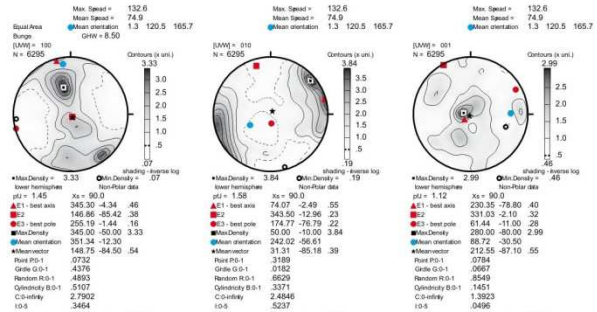

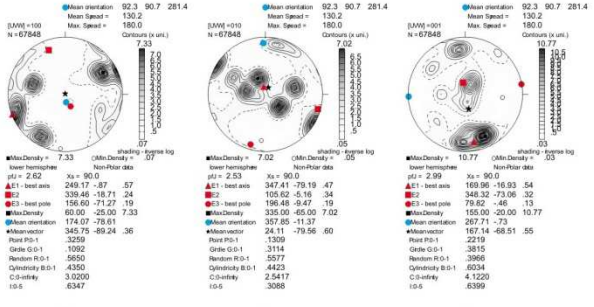

Opx

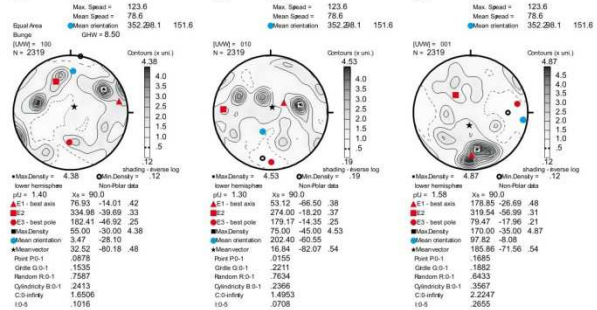

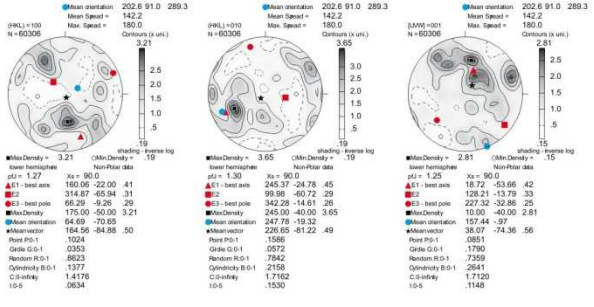

Cpx

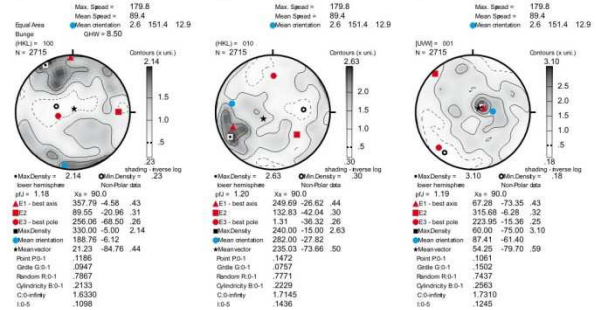

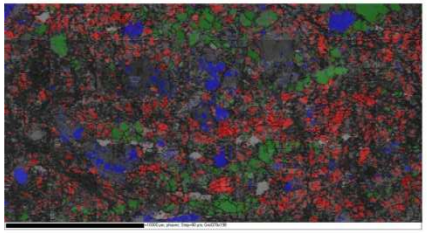

step=80μm

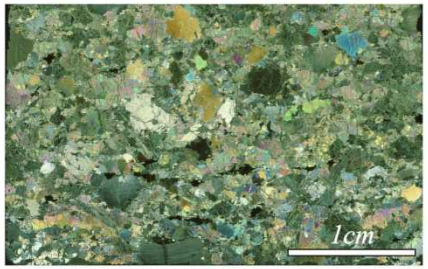

Geographic coordinates (1 point per grain)

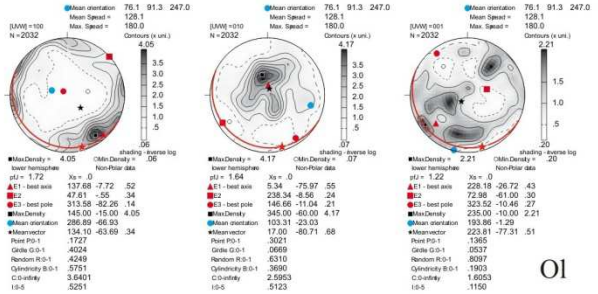

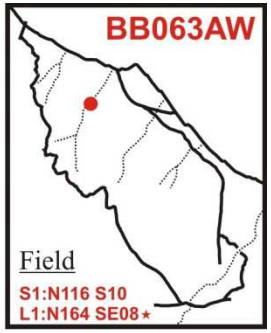

Ol

Sample coordinates (raw data)

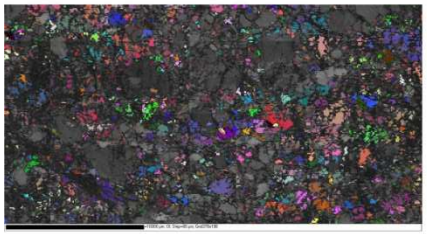

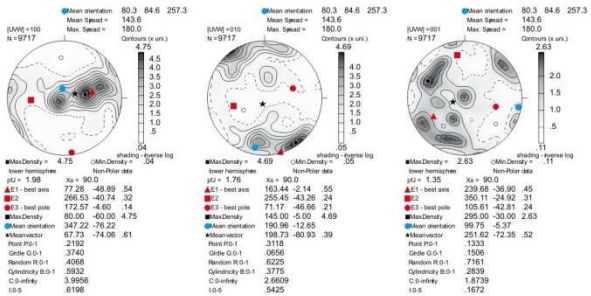

Ol

Sample coordinates (1 point per grain)

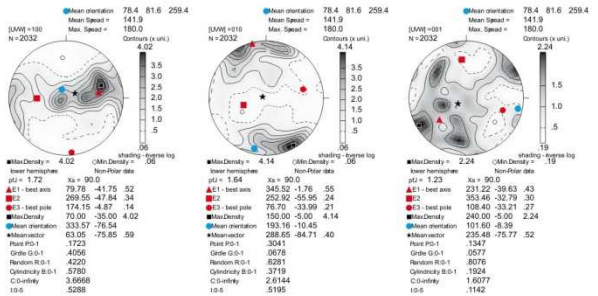

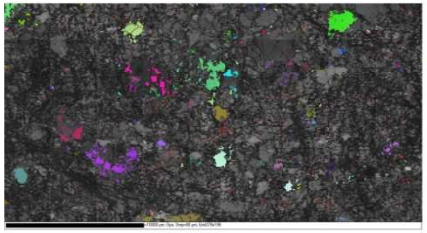

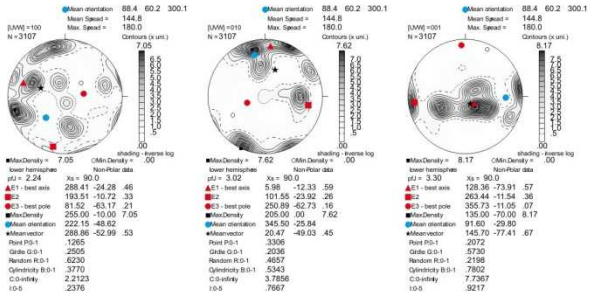

Opx

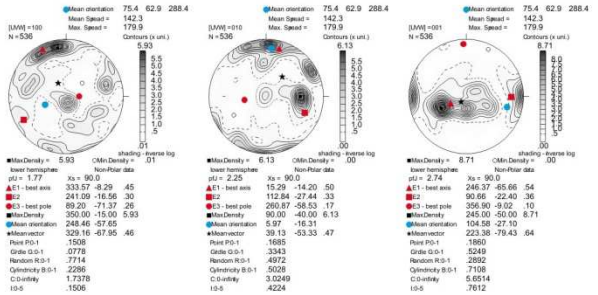

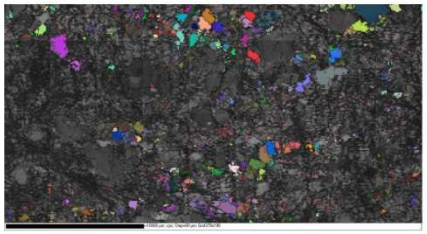

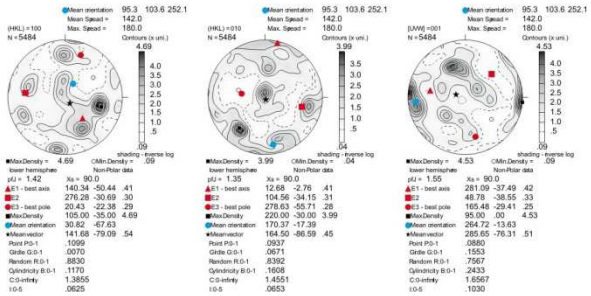

Cpx

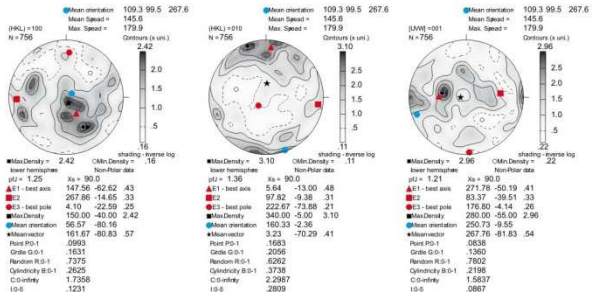

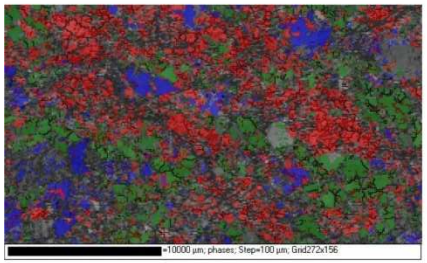

step=100µm

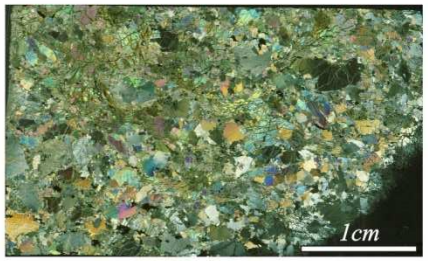

Geographic coordinates (1 point per grain)

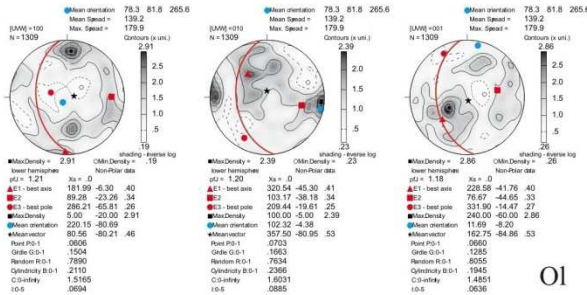

Ol

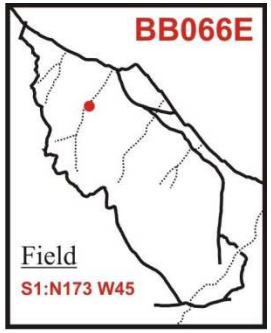

Sample coordinates (raw data)

Sample coordinates (1 point per grain)

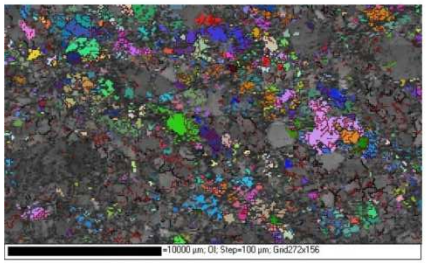

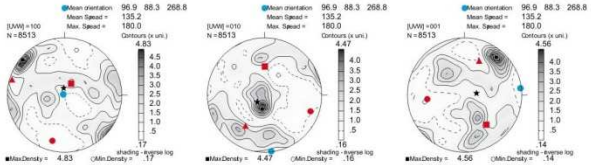

Ol

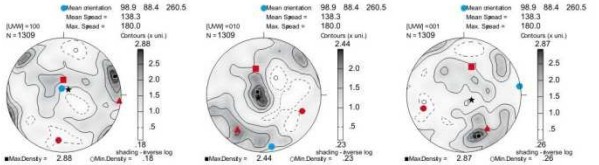

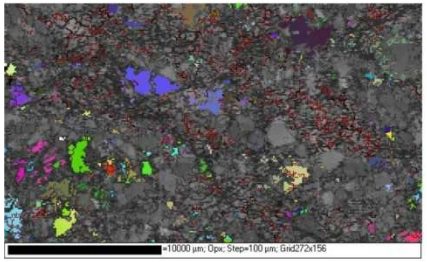

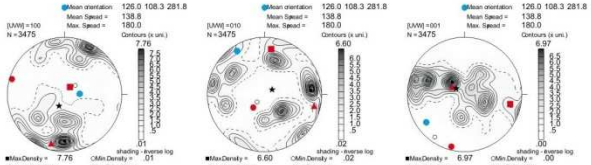

Opx

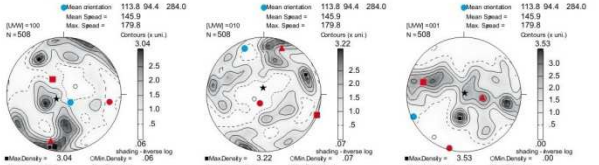

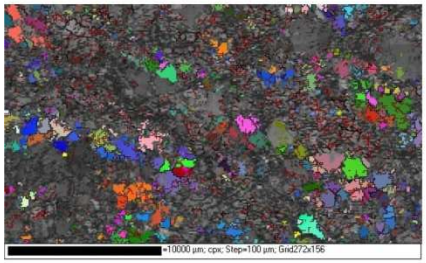

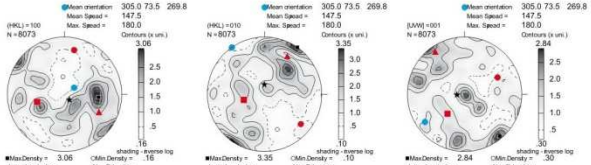

Cpx

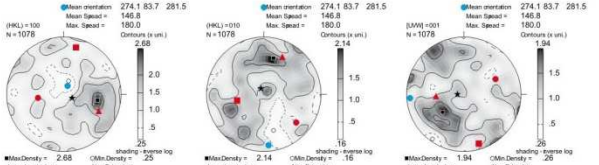

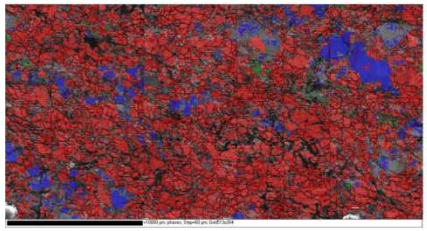

step=60µm

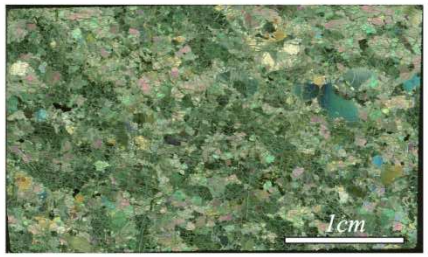

Geographic coordinates (1 point per grain)

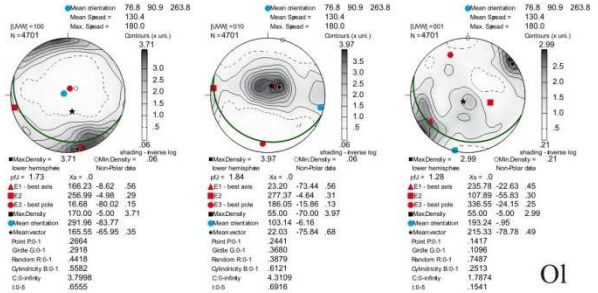

Ol

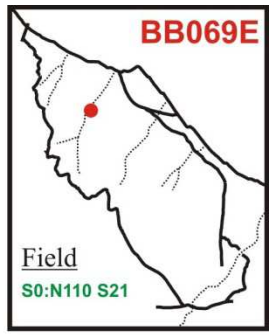

Sample coordinates (raw data)

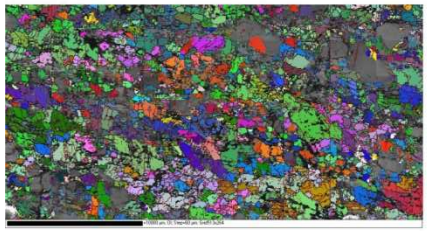

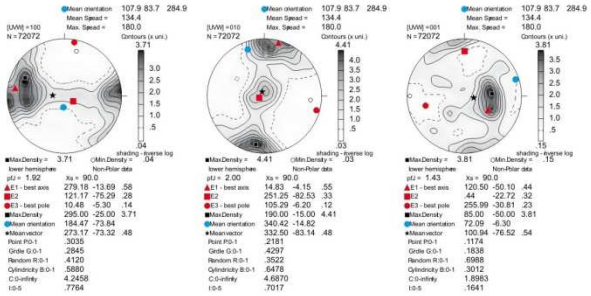

Ol

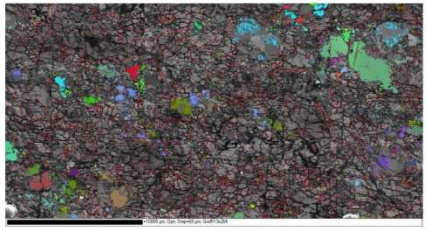

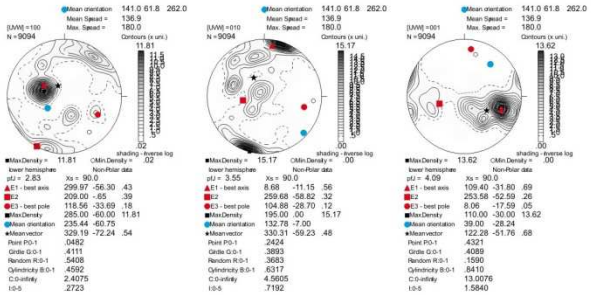

Opx

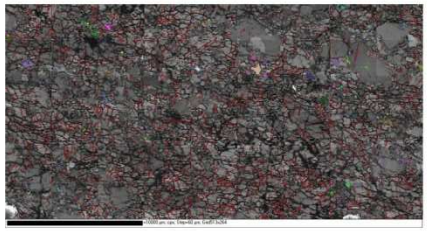

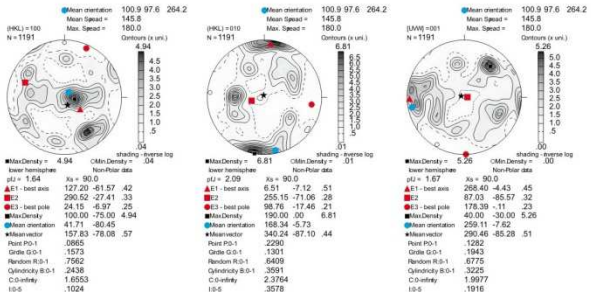

Cpx

Sample coordinates (1 point per grain)

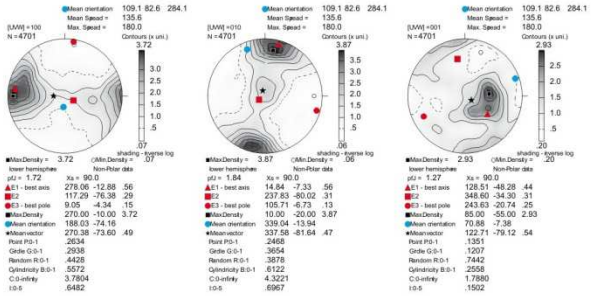

Ol

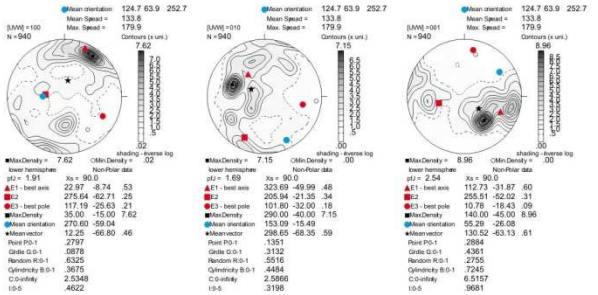

Opx

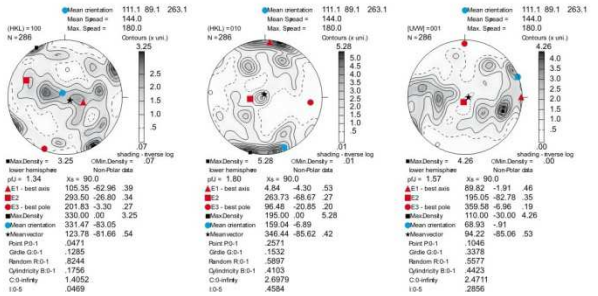

Cpx

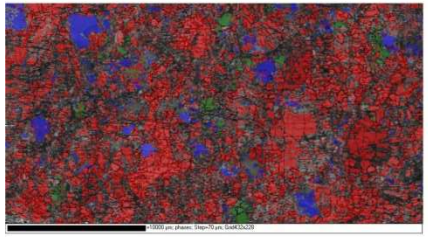

step=70µm

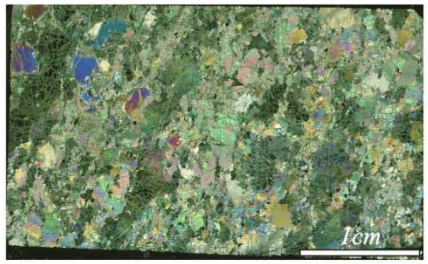

Geographic coordinates (1 point per grain)

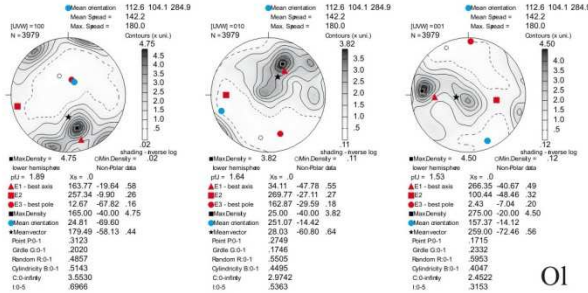

Ol

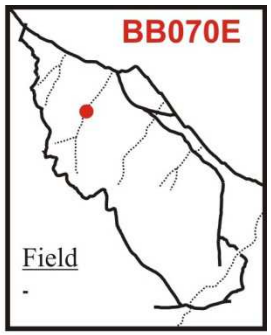

Sample coordinates (raw data)

Sample coordinates (1 point per grain)

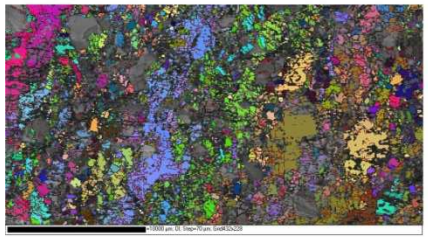

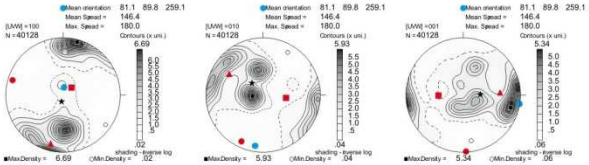

Ol

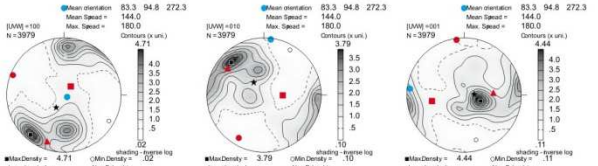

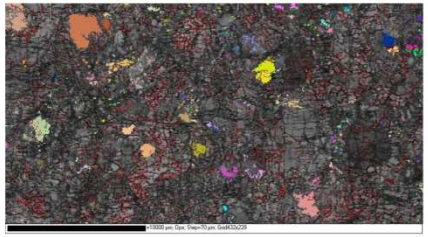

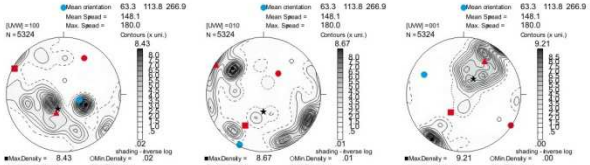

Opx

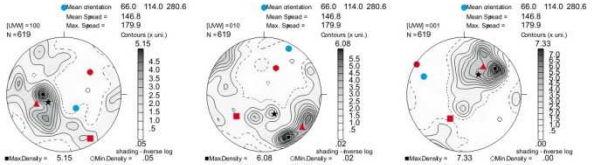

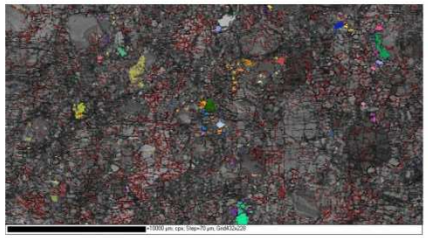

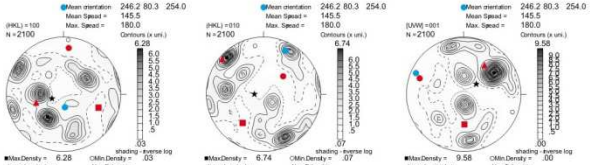

Cpx

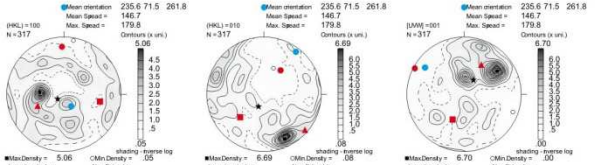

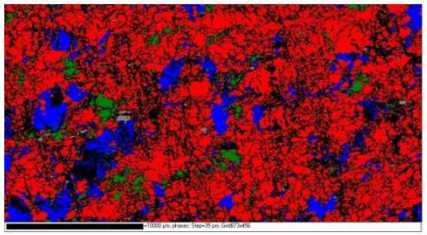

step=35μm

Geographic coordinates (1 point per grain)

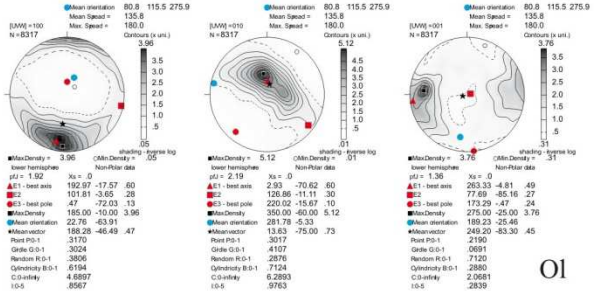

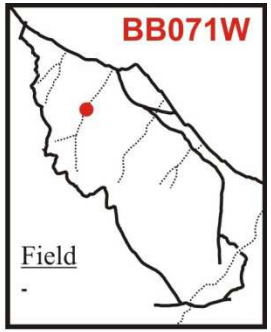

Ol

Sample coordinates (raw data)

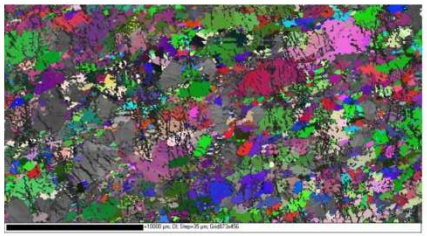

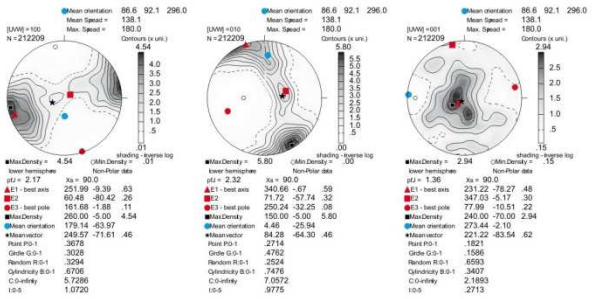

Ol

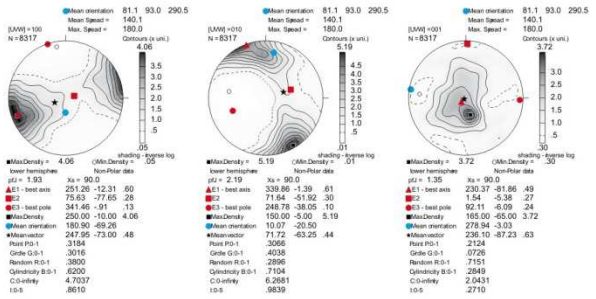

Sample coordinates (1 point per grain)

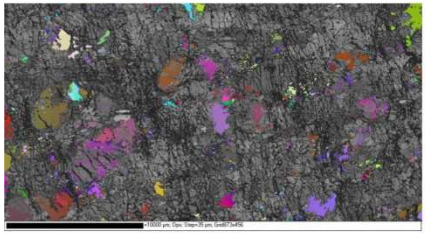

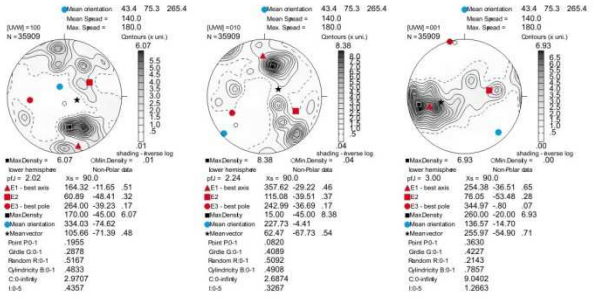

Opx

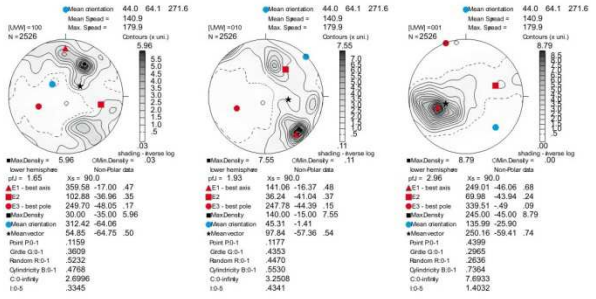

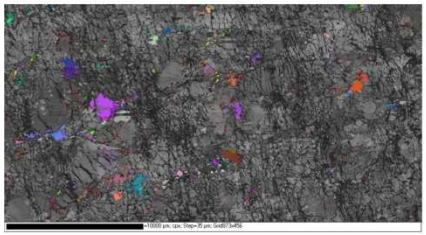

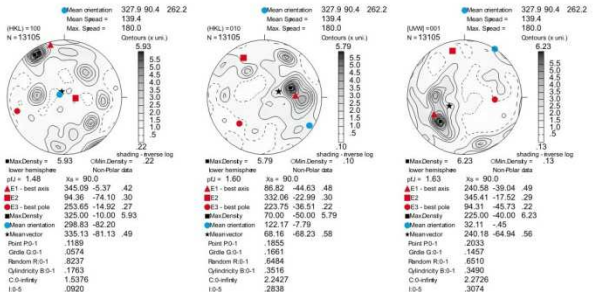

Cpx

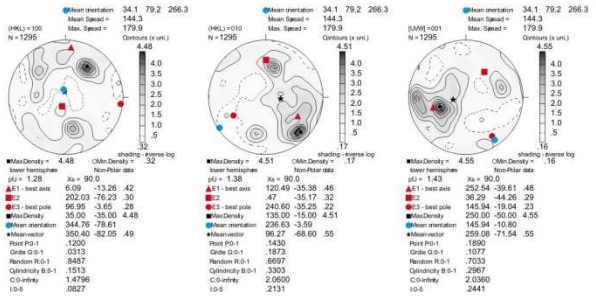

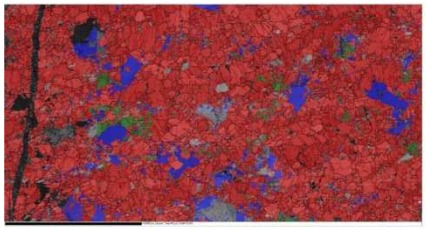

step=50μm

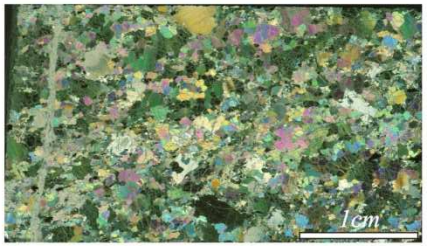

Geographic coordinates (1 point per grain)

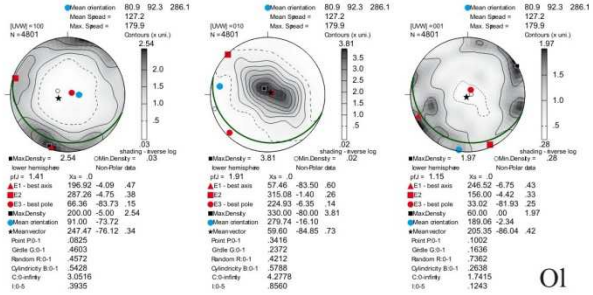

Ol

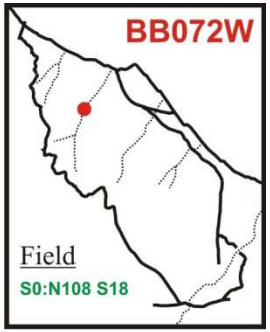

Sample coordinates (raw data)

Sample coordinates (1 point per grain)

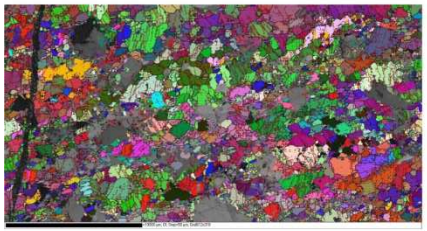

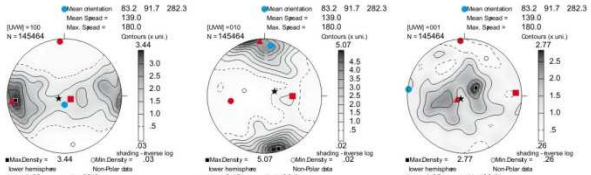

Ol

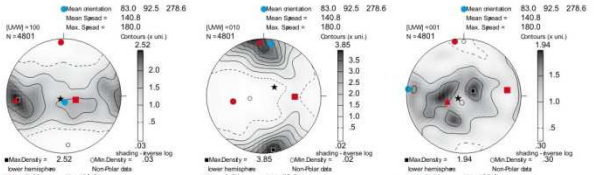

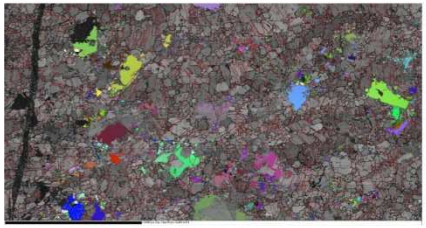

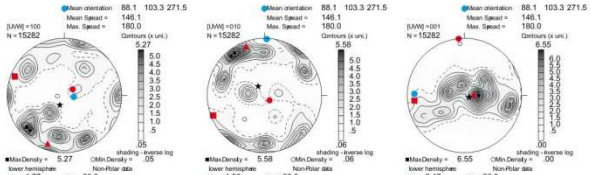

Opx

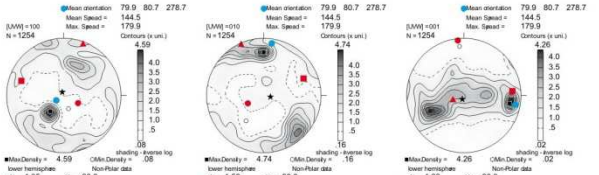

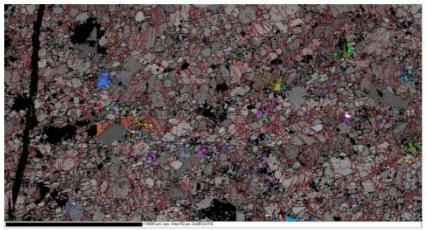

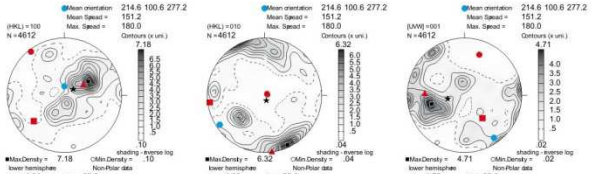

Cpx

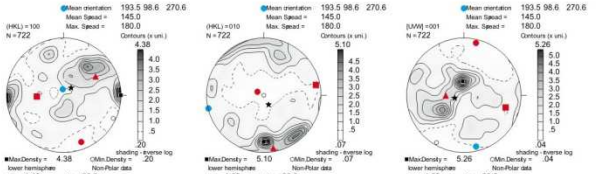

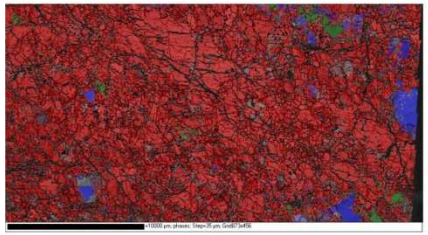

step=35µm

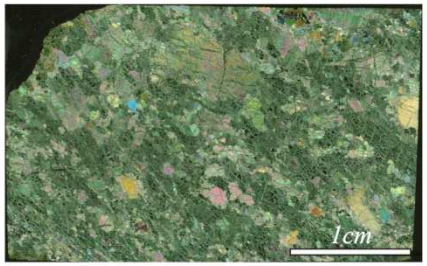

Geographic coordinates (1 point per grain)

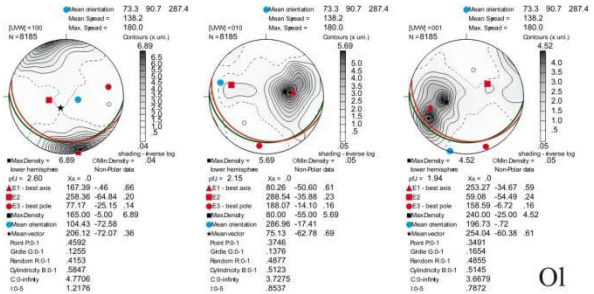

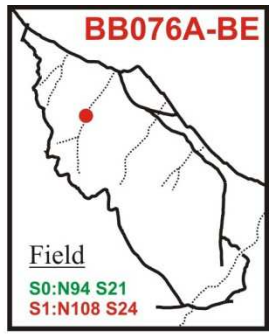

Ol

Sample coordinates (raw data)

Sample coordinates (1 point per grain)

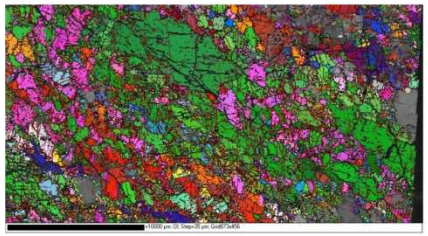

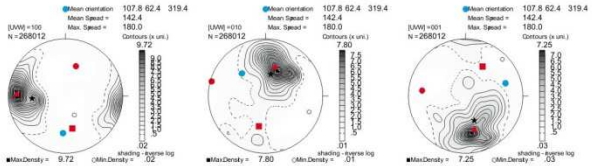

Ol

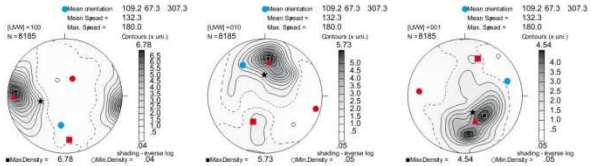

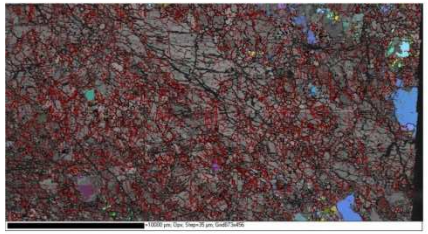

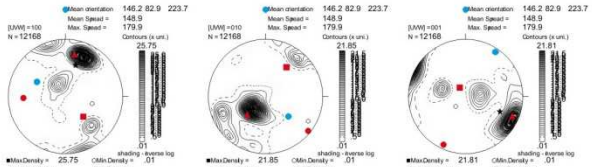

Opx

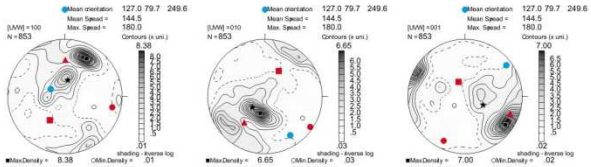

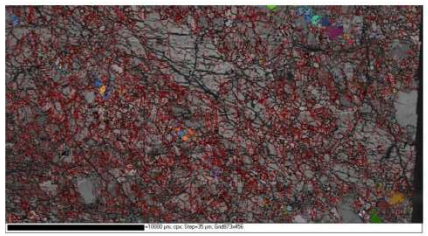

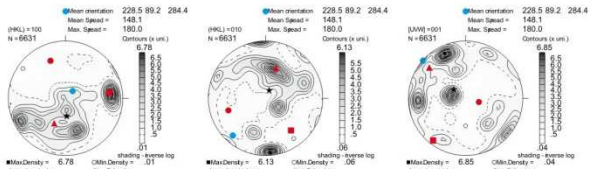

Cpx

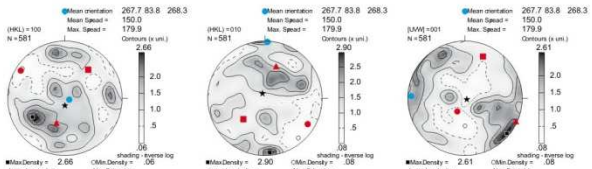

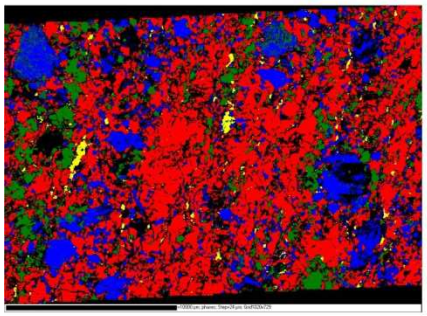

step=24µm

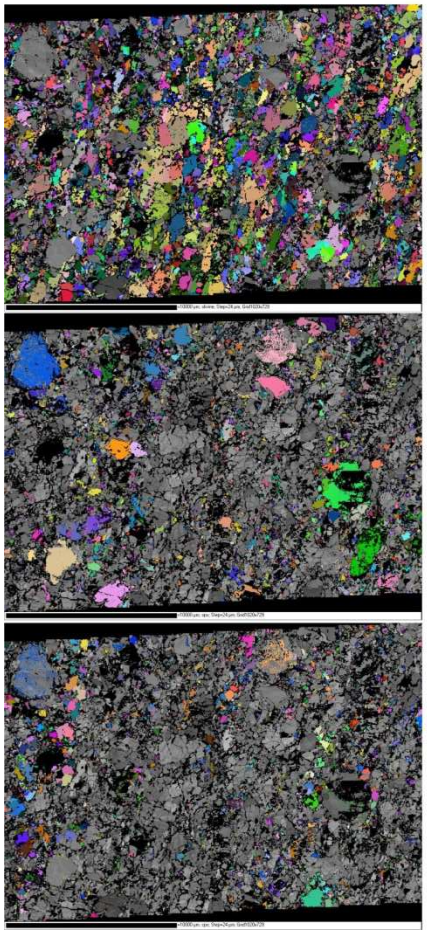

Geographic coordinates (1 point per grain)

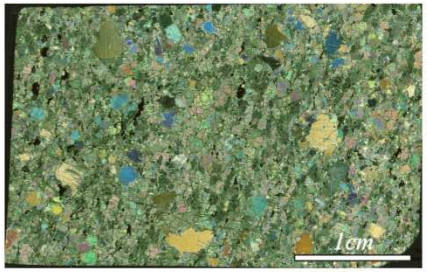

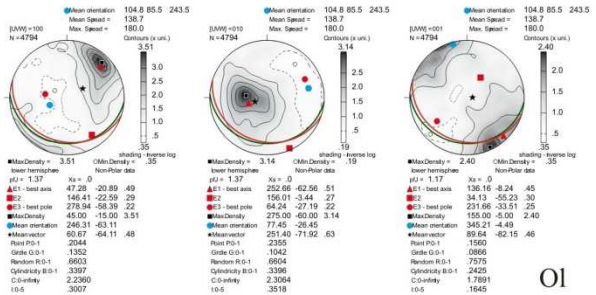

Ol

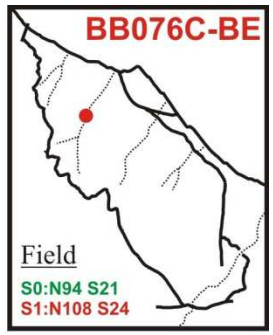

Sample coordinates (raw data)

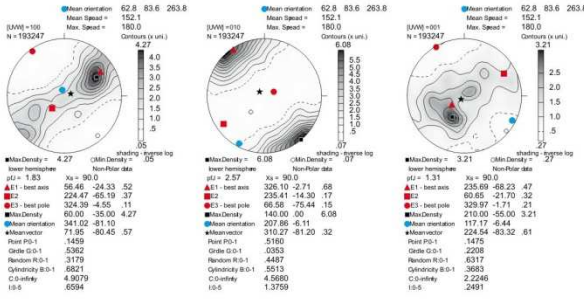

Ol

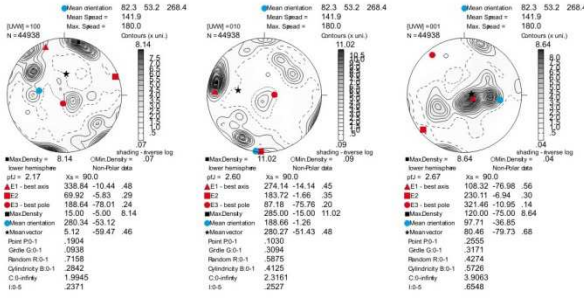

Opx

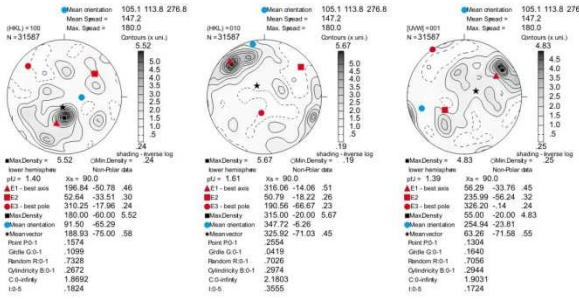

Cpx

Sample coordinates (1 point per grain)

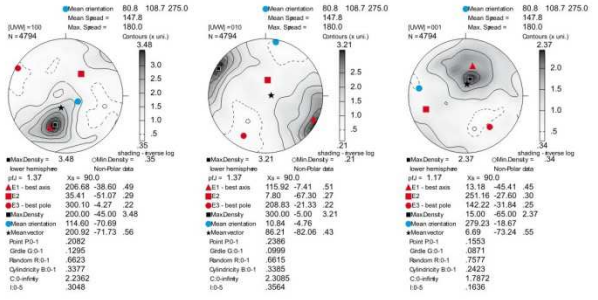

Ol

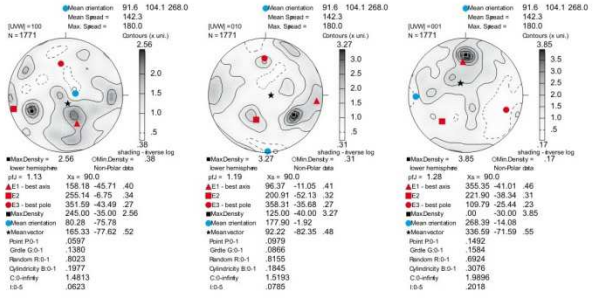

Opx

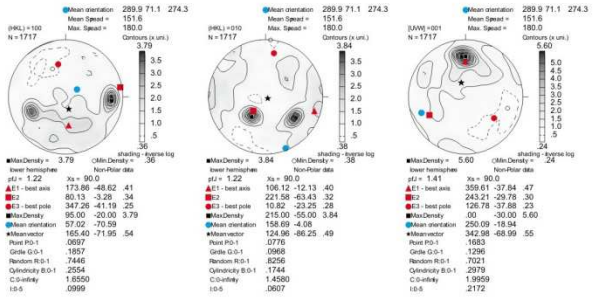

Cpx

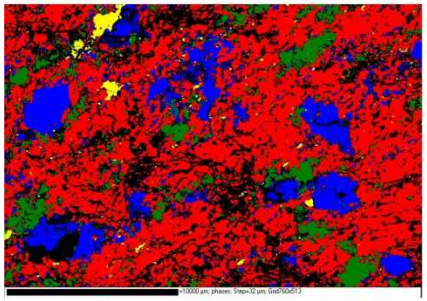

step=32µm

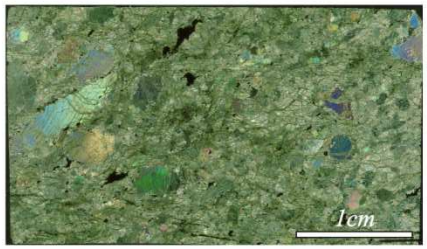

Geographic coordinates (1 point per grain)

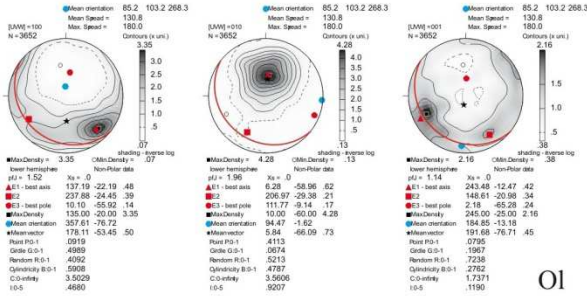

Ol

Sample coordinates (raw data)

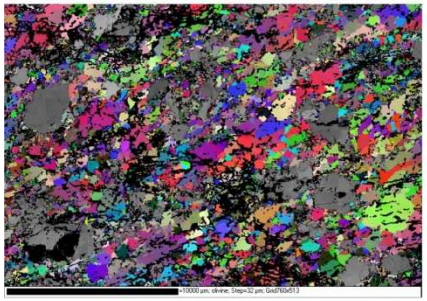

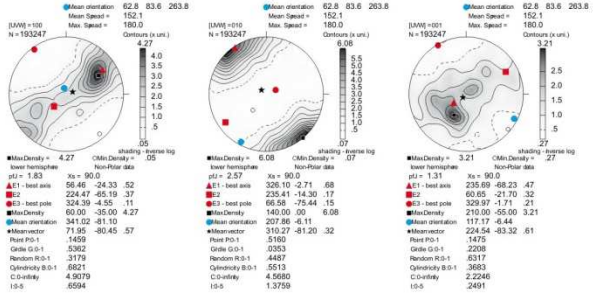

Ol

Sample coordinates (1 point per grain)

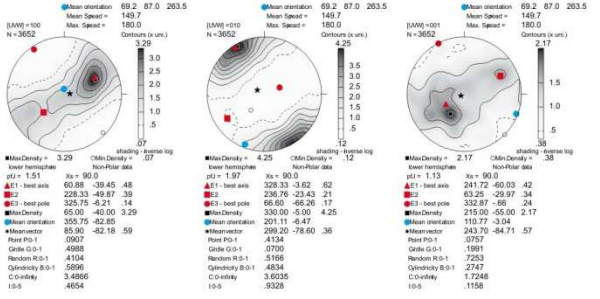

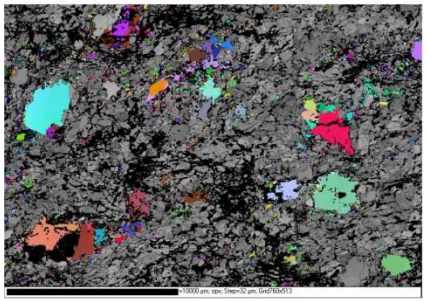

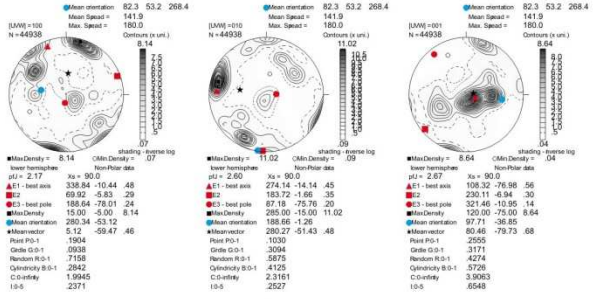

Opx

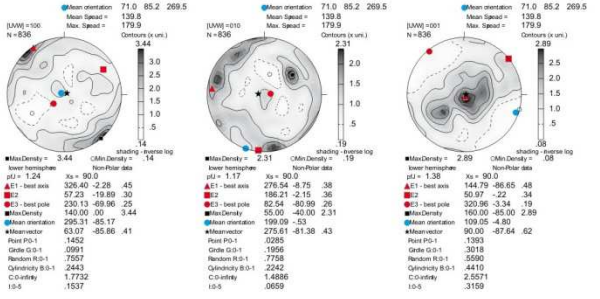

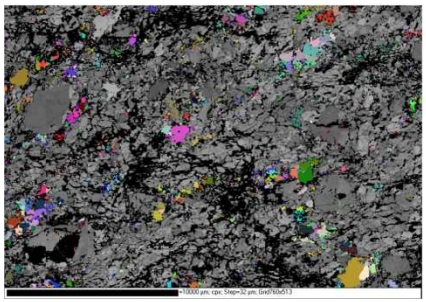

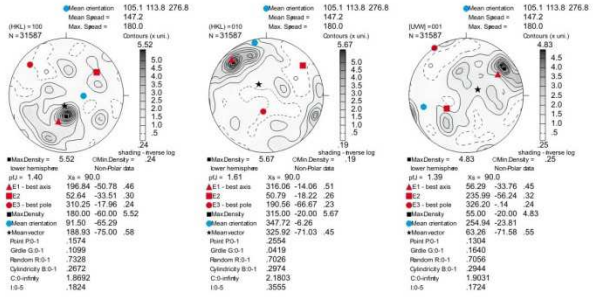

Cpx

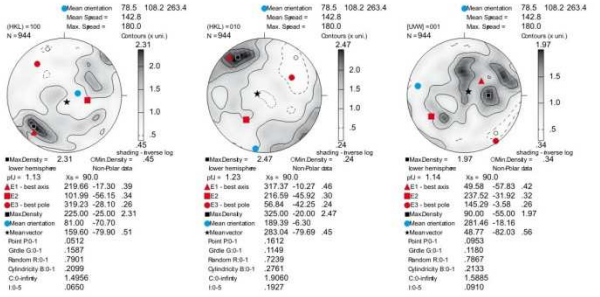

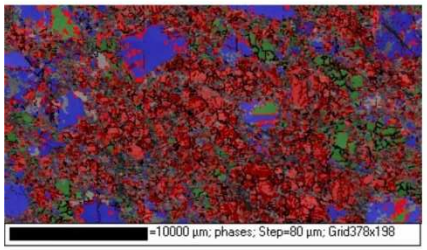

step=80µm

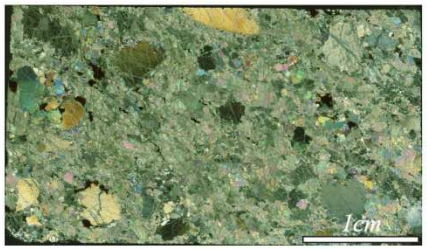

Geographic coordinates (1 point per grain)

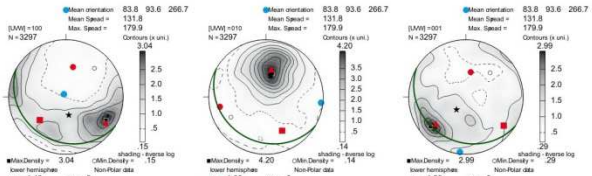

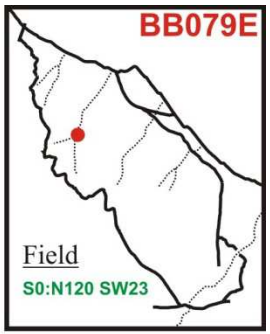

Ol

Sample coordinates (raw data)

Sample coordinates (1 point per grain)

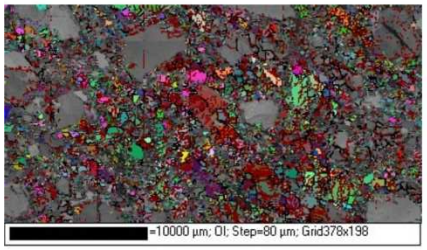

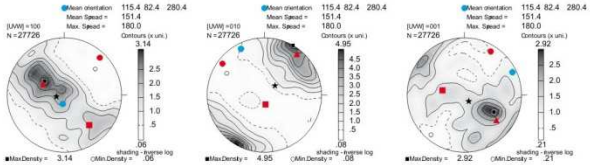

Ol

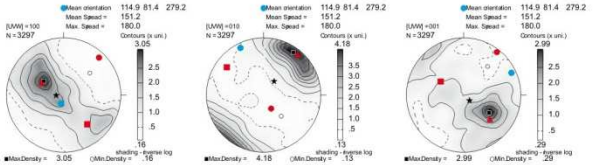

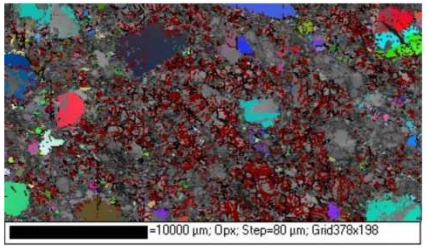

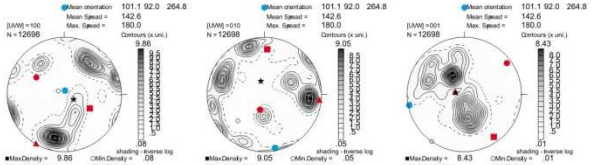

Opx

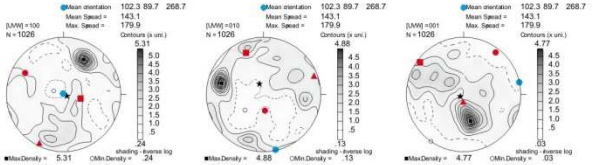

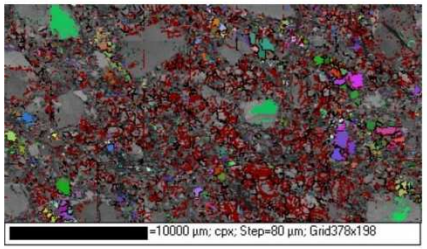

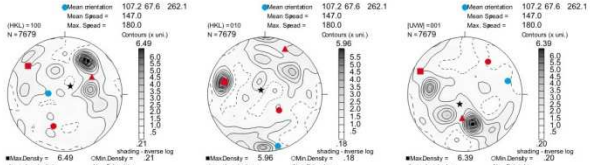

Cpx

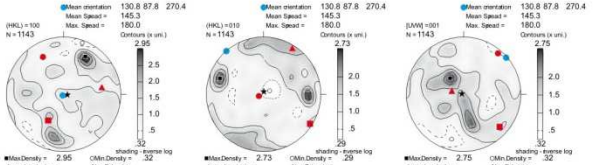

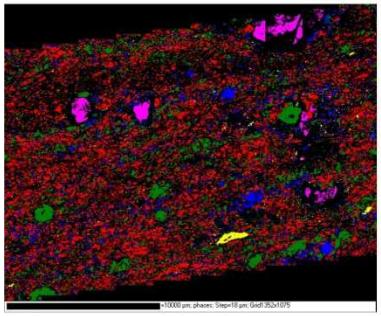

step=18µm

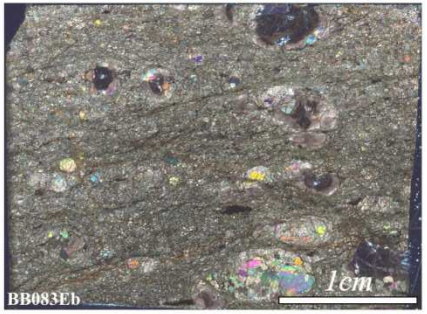

Geographic coordinates (1 point per grain)

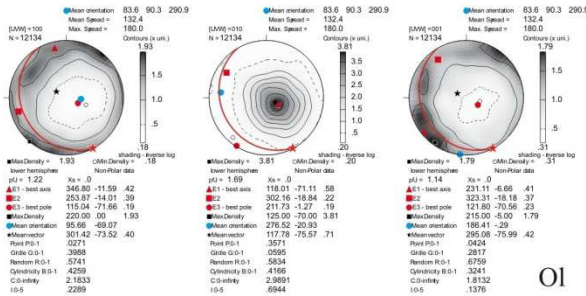

Ol

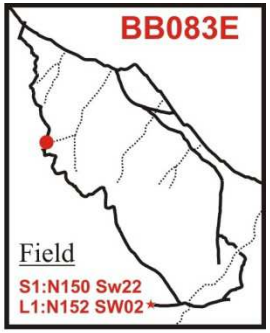

Sample coordinates (raw data)

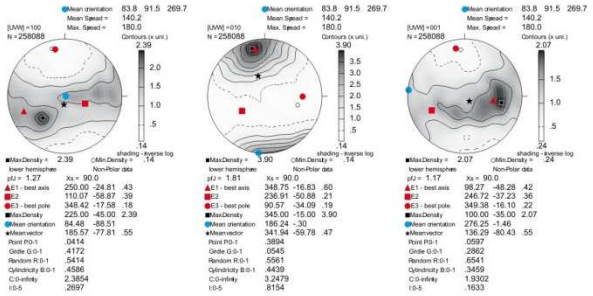

Ol

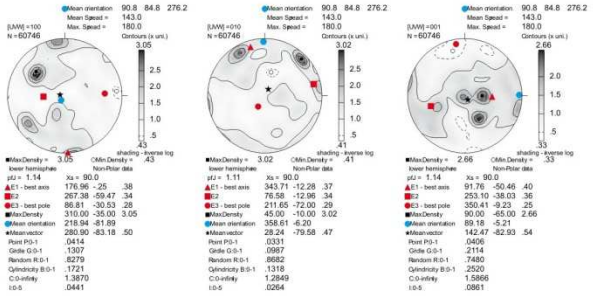

Opx

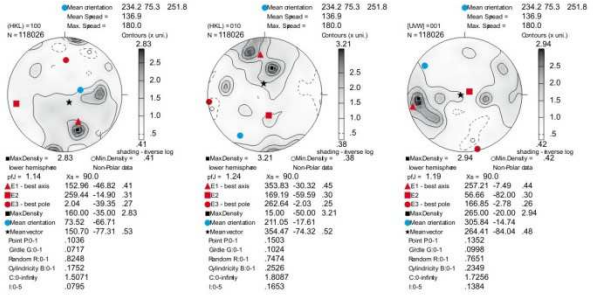

Cpx

Sample coordinates (1 point per grain)

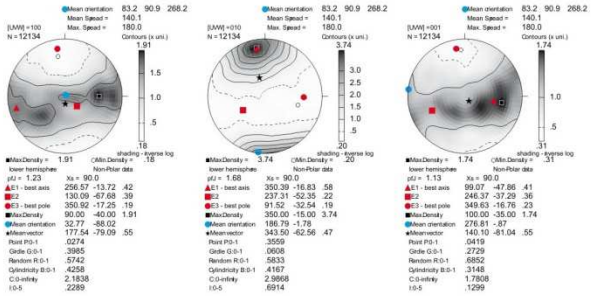

Ol

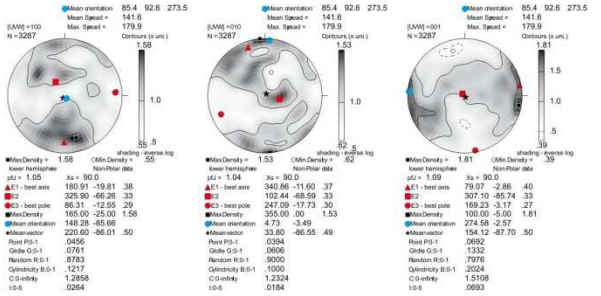

Opx

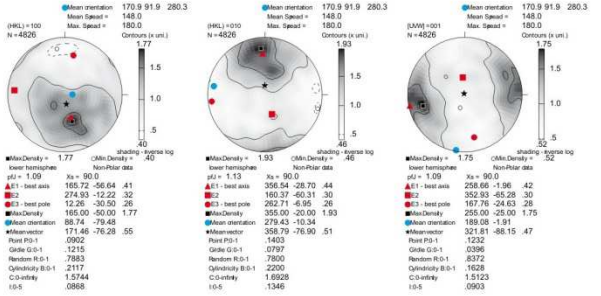

Cpx

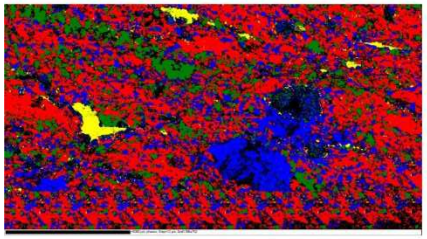

step=12µm

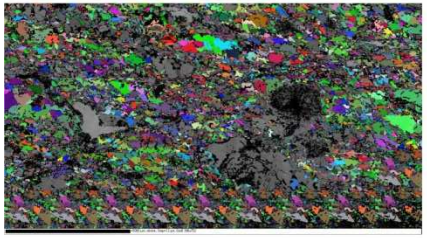

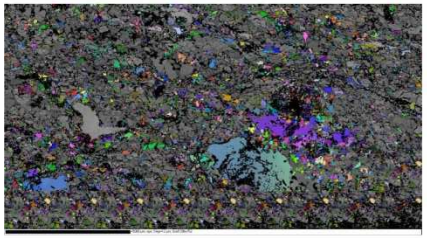

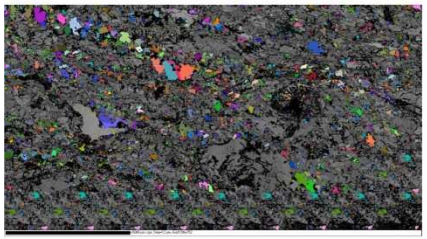

Geographic coordinates (1 point per grain)

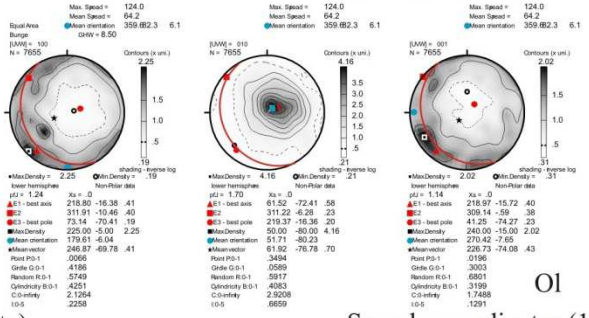

Ol

Sample coordinates (raw data)

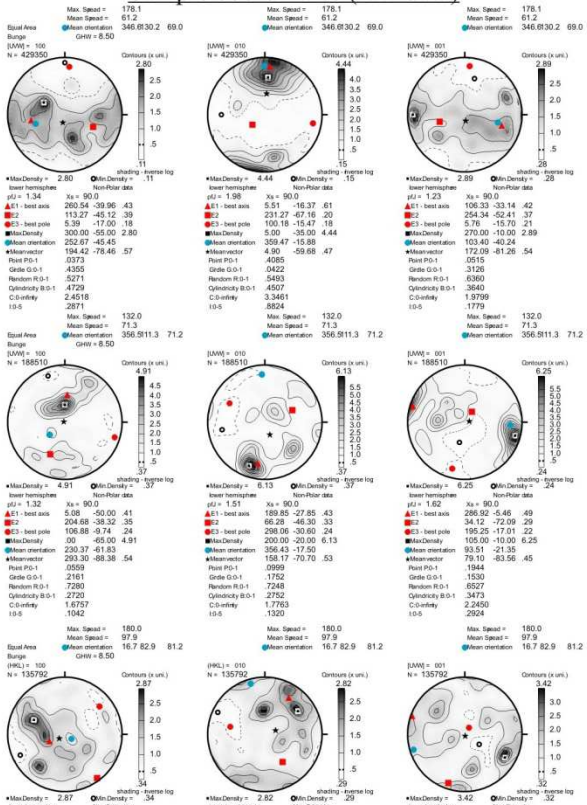

Ol

Opx

Cpx

Sample coordinates (1 point per grain)

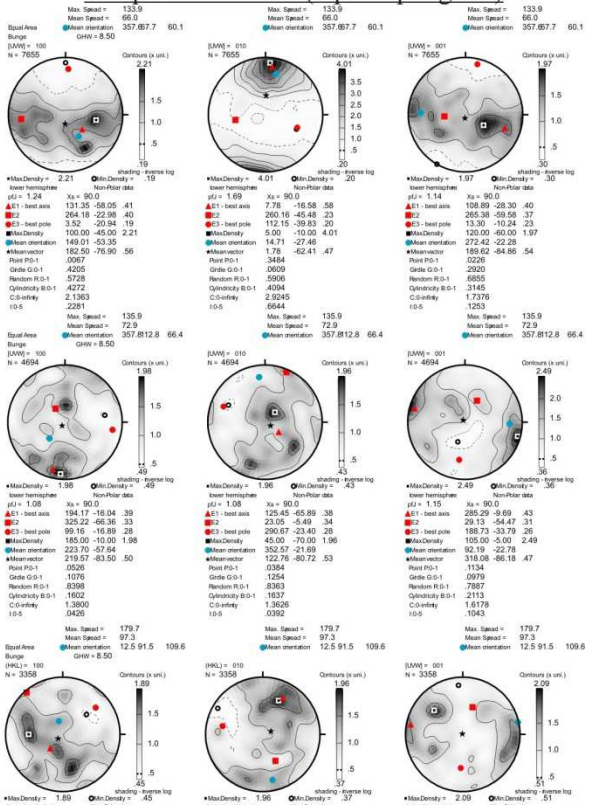

Ol

Opx

Cpx

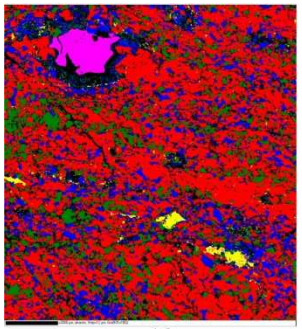

step=12µm

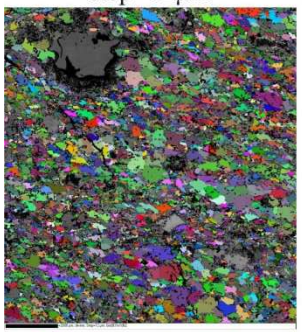

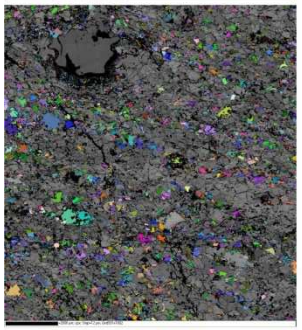

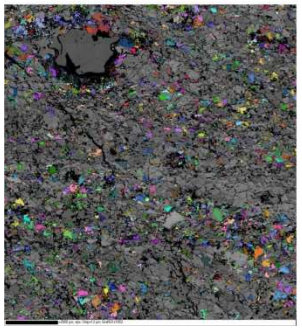

Geographic coordinates (1 point per grain)

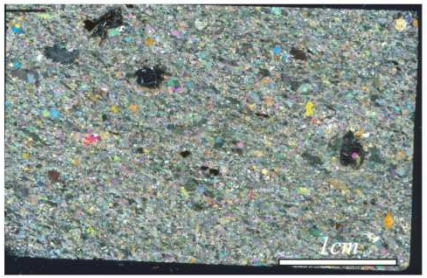

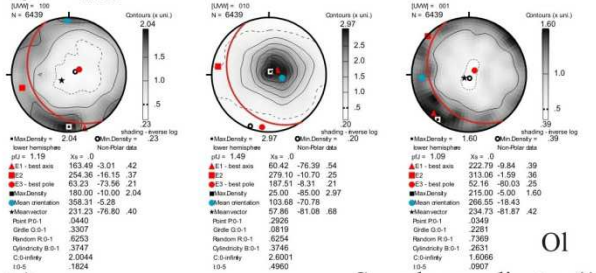

Ol

Sample coordinates (raw data)

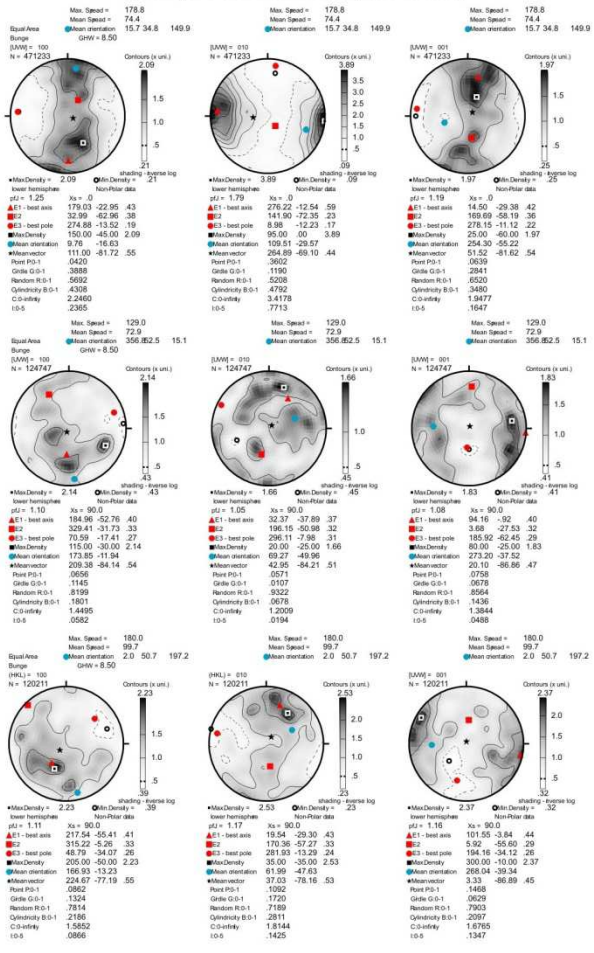

Sample coordinates (1 point per grain)

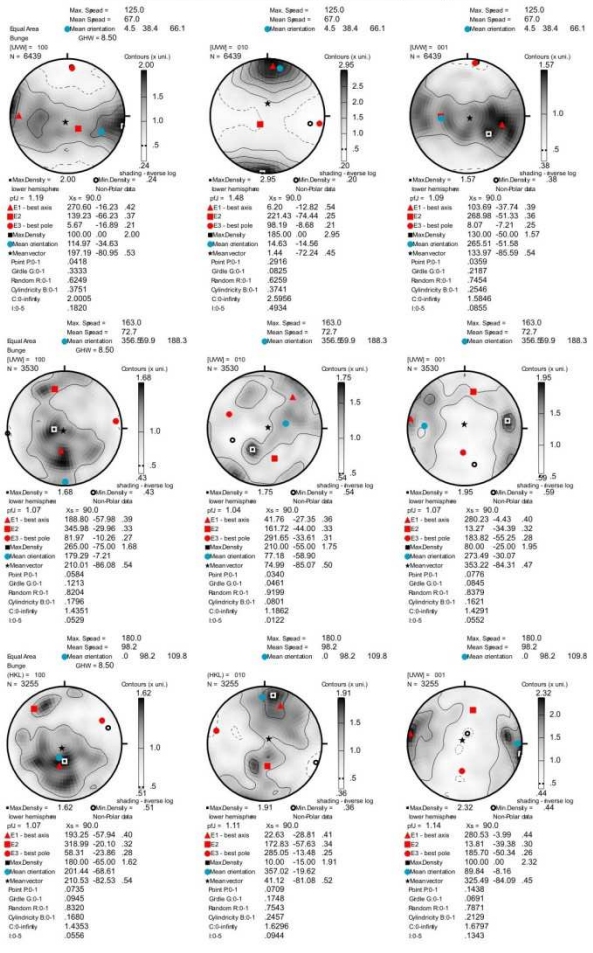

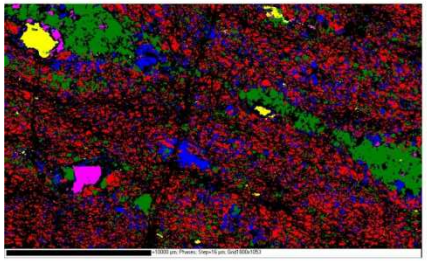

step=16µm

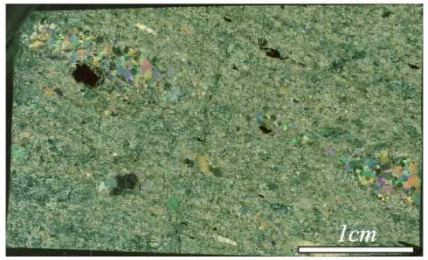

Geographic coordinates (1 point per grain)

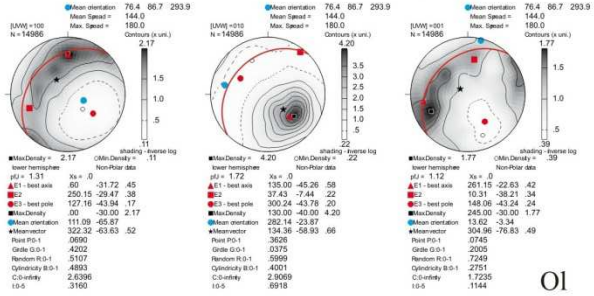

Ol

Sample coordinates (raw data)

Sample coordinates (1 point per grain)

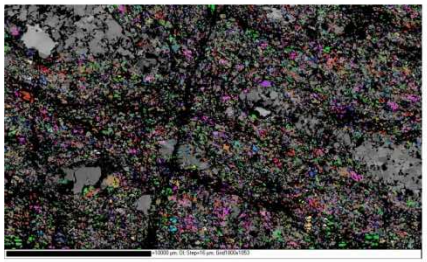

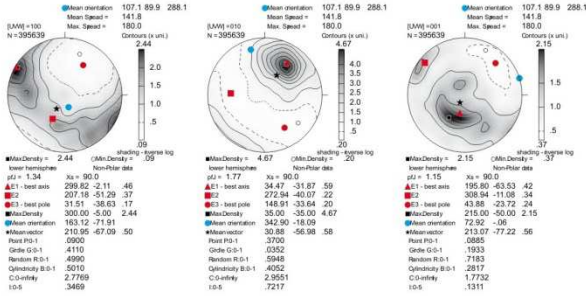

Ol

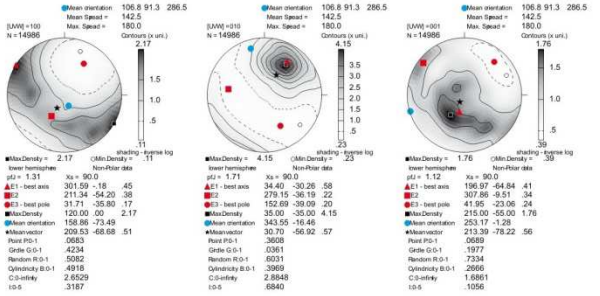

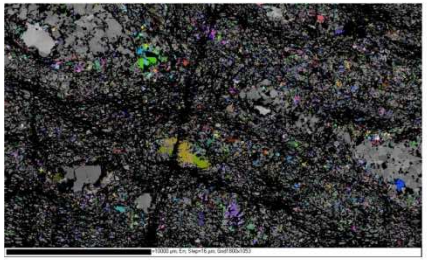

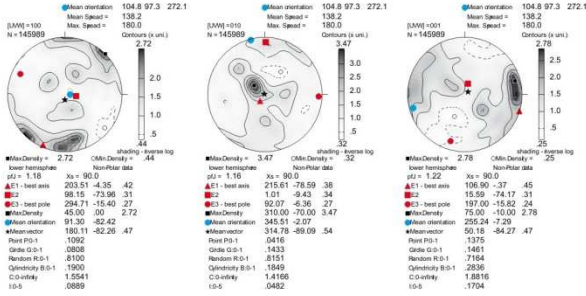

Opx

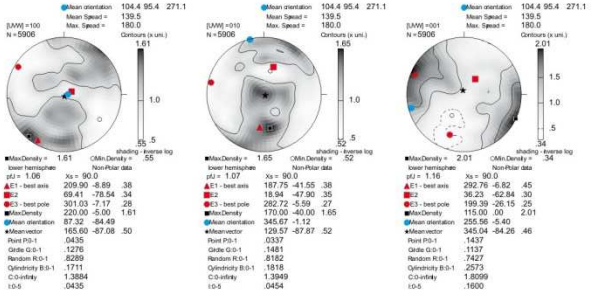

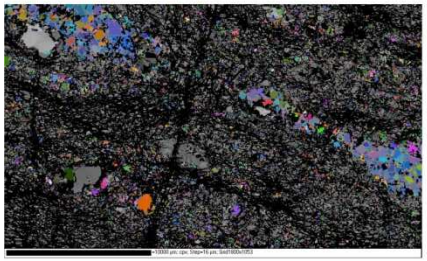

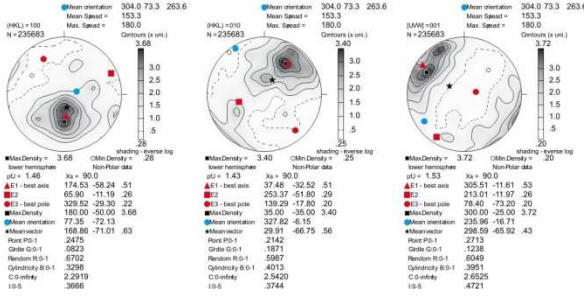

Cpx

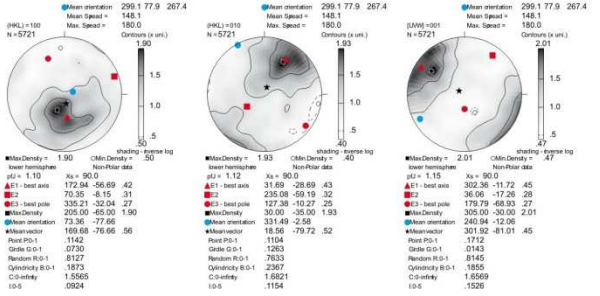

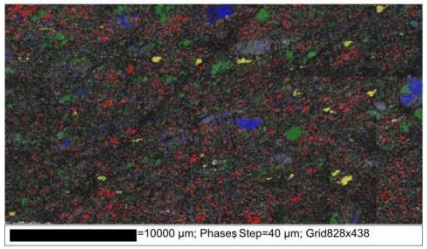

step=40µm

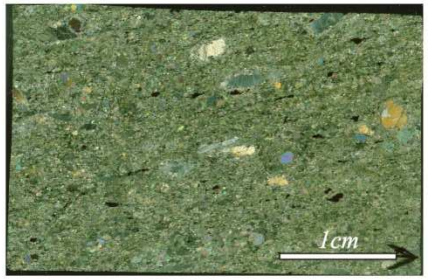

Geographic coordinates (1 point per grain)

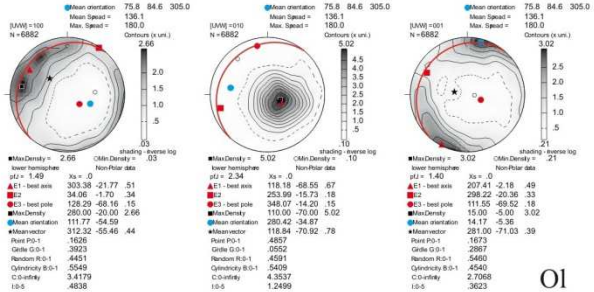

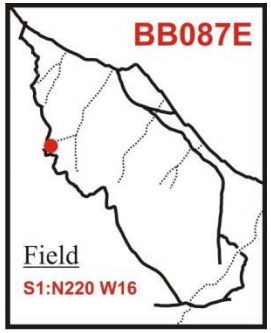

Ol

Sample coordinates (raw data)

Sample coordinates (1 point per grain)

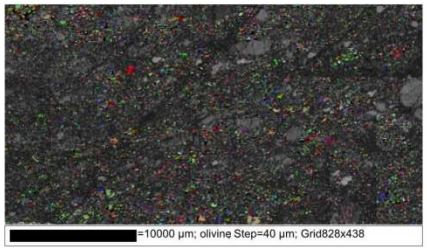

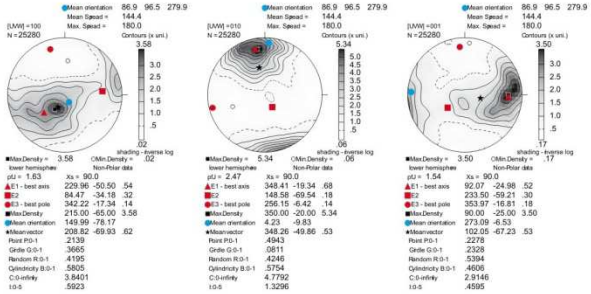

Ol

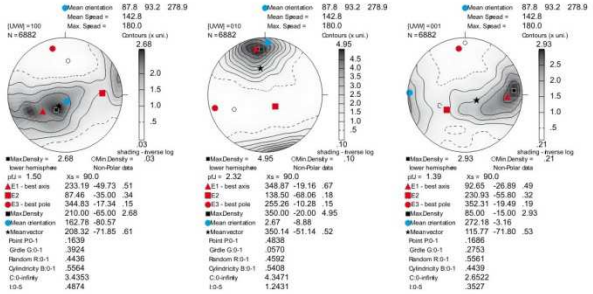

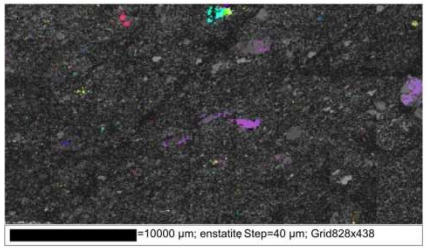

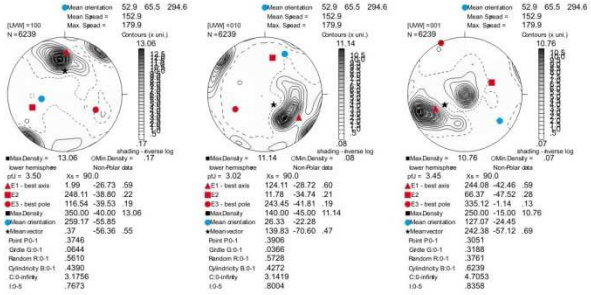

Opx

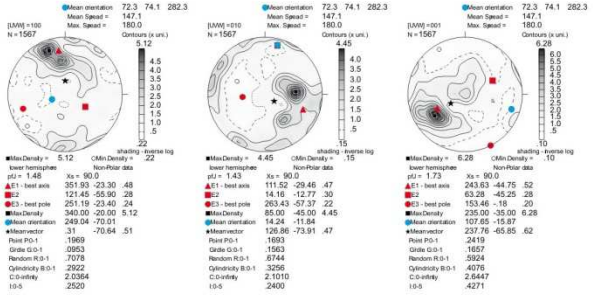

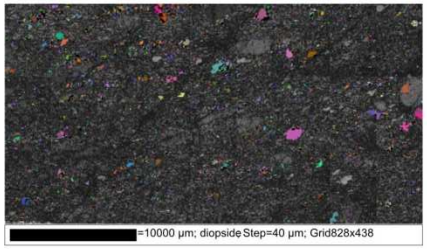

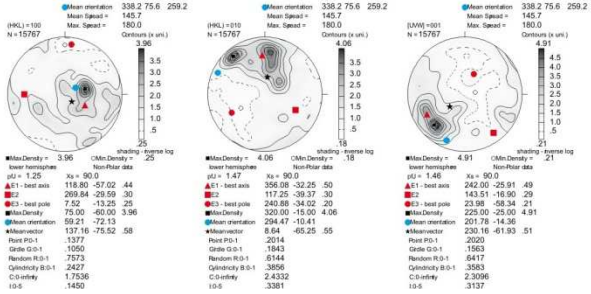

Cpx

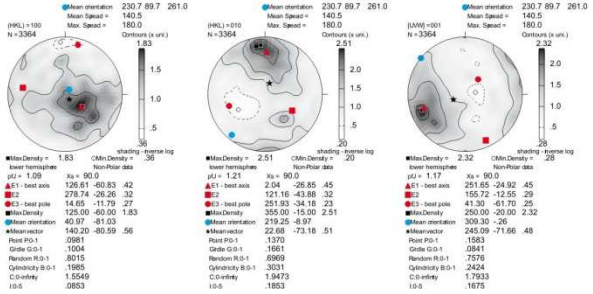

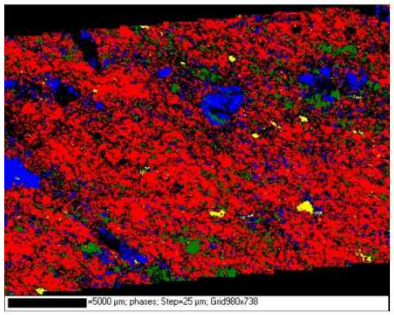

step=25µm

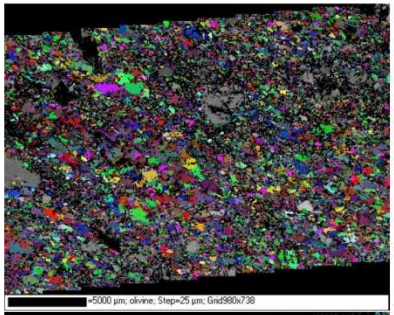

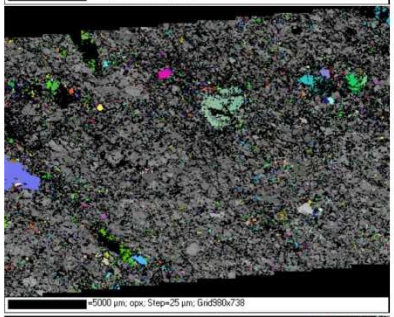

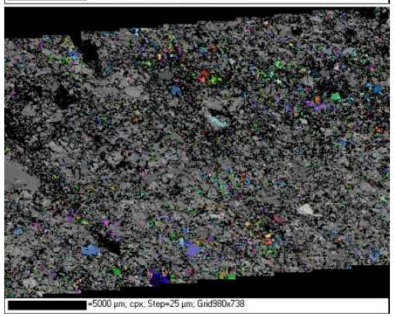

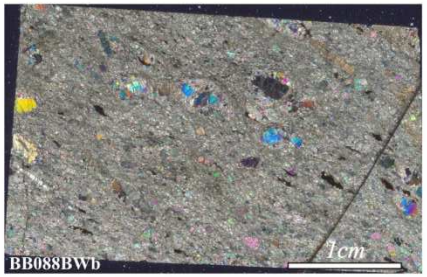

Geographic coordinates (1 point per grain)

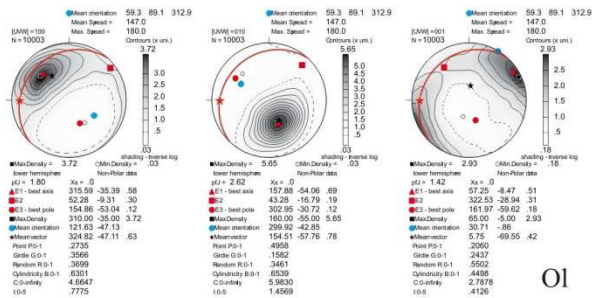

Ol

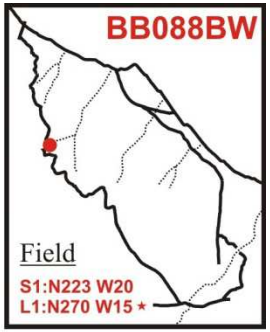

Sample coordinates (raw data)

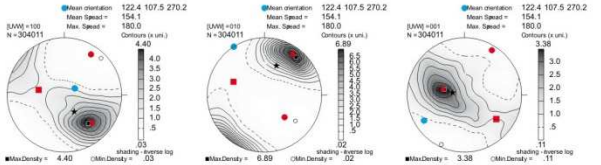

Ol

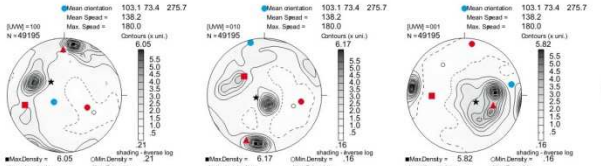

Opx

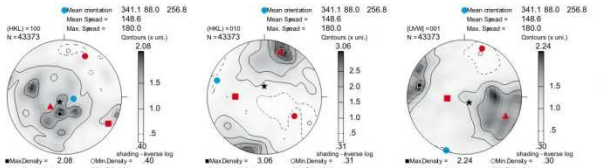

Cpx

Sample coordinates (1 point per grain)

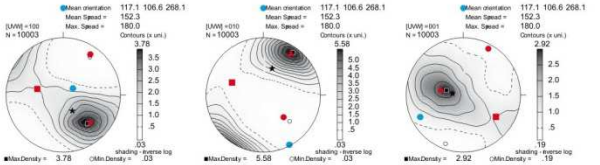

Ol

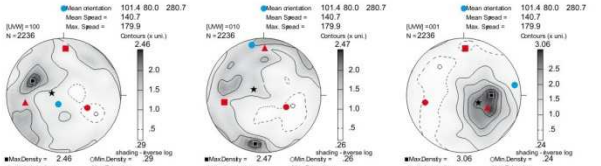

Opx

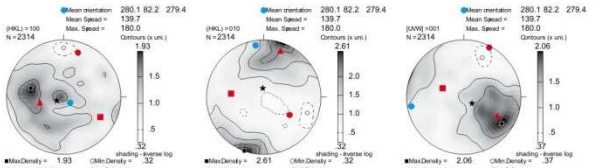

Cpx

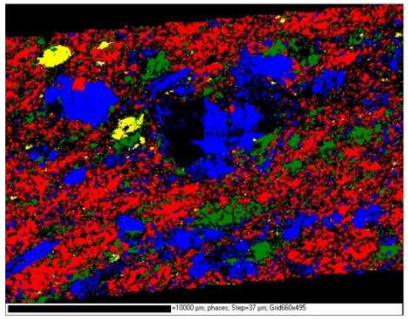

step=37µm

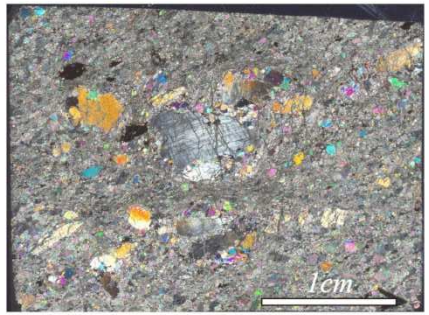

Geographic coordinates (1 point per grain)

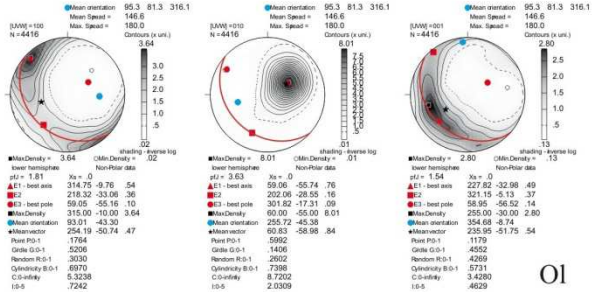

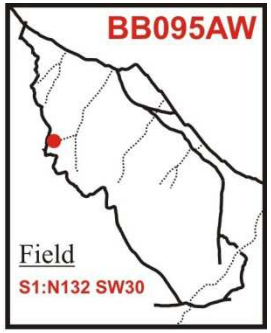

Ol

Sample coordinates (raw data)

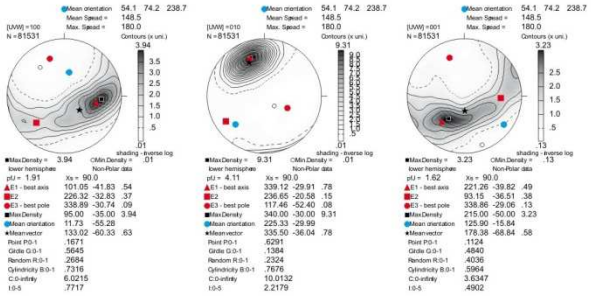

Sample coordinates (1 point per grain)

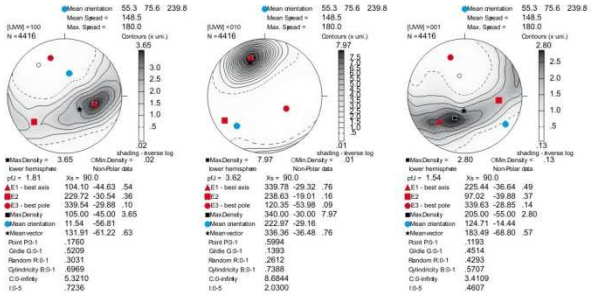

Ol

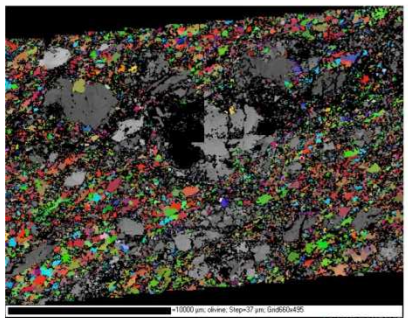

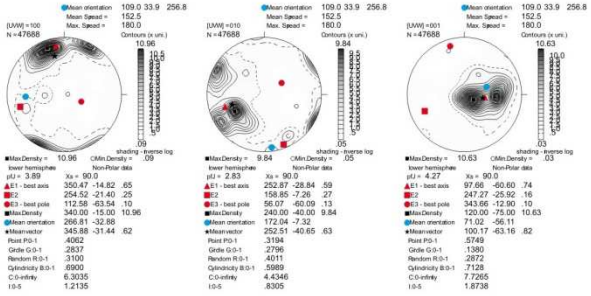

Opx

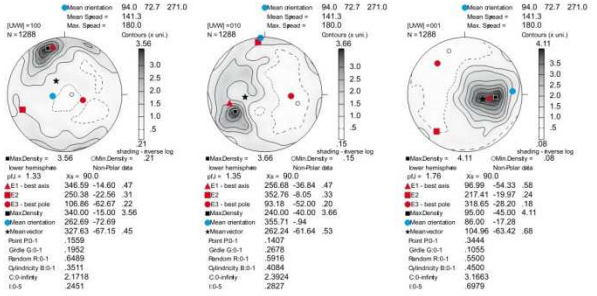

Opx

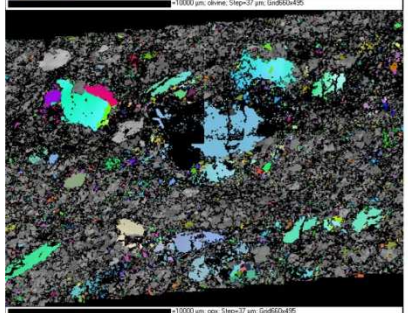

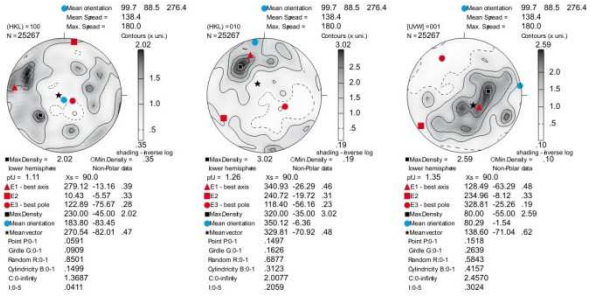

Cpx

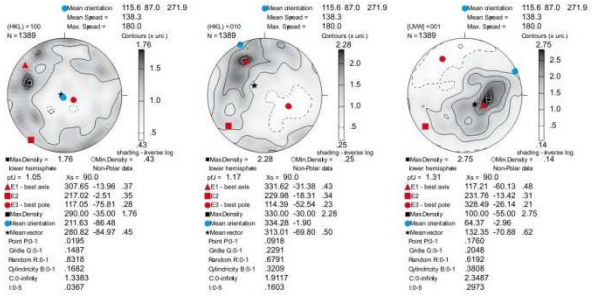

Cpx

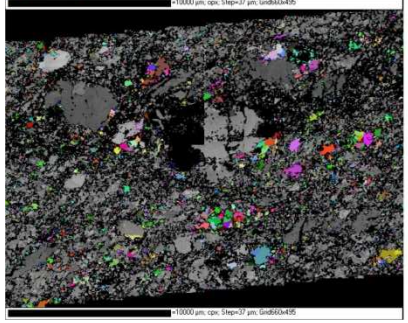

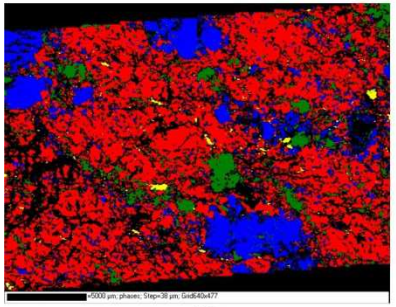

step=38µm

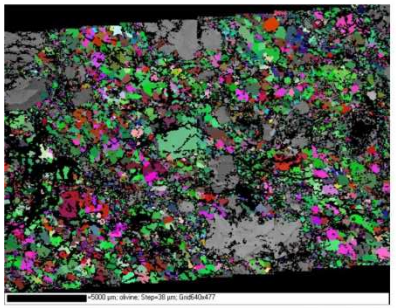

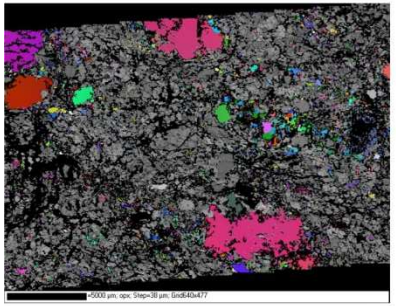

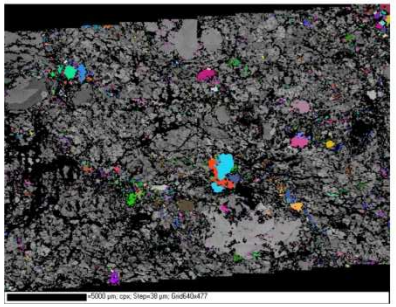

Geographic coordinates (1 point per grain)

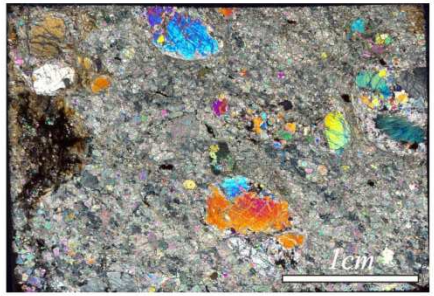

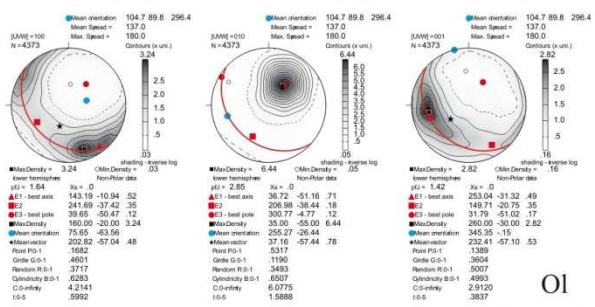

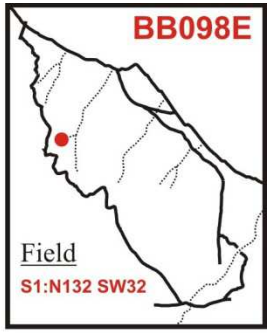

Ol

Sample coordinates (raw data)

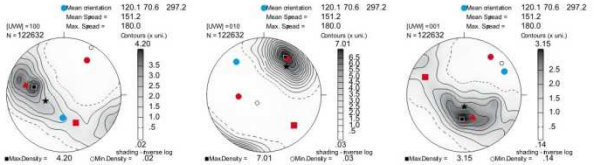

Ol

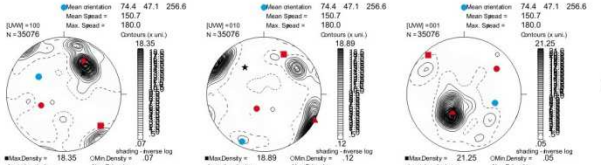

Opx

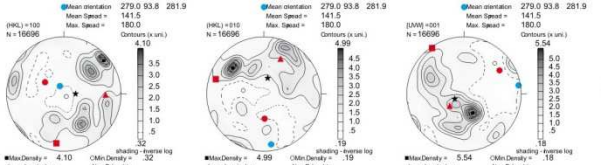

Cpx

Sample coordinates (1 point per grain)

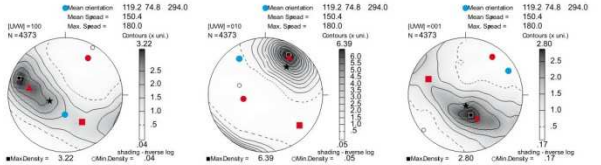

Ol

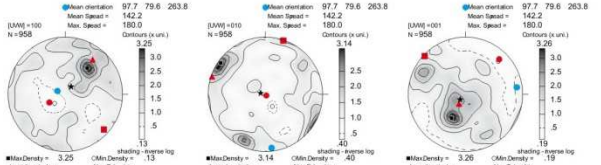

Opx

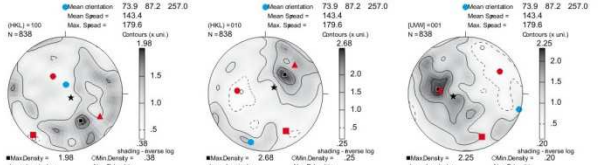

Cpx

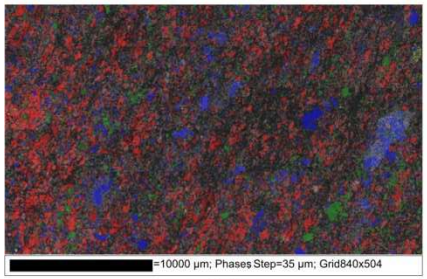

step=35µm

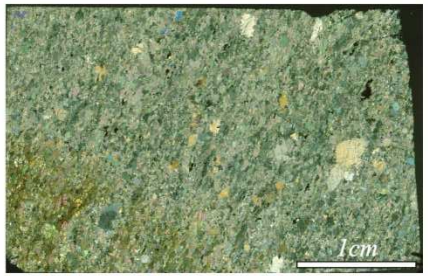

Geographic coordinates (1 point per grain)

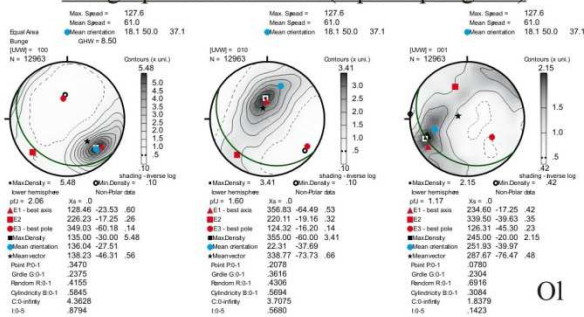

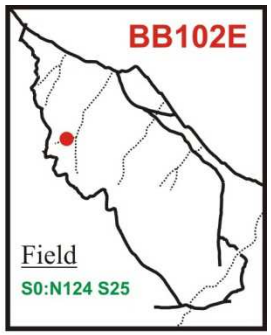

Ol

Sample coordinates (raw data)

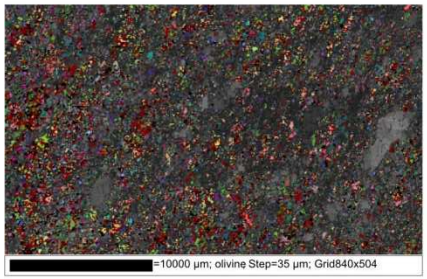

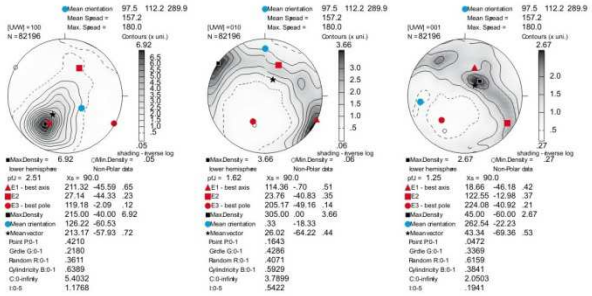

Ol

Sample coordinates (1 point per grain)

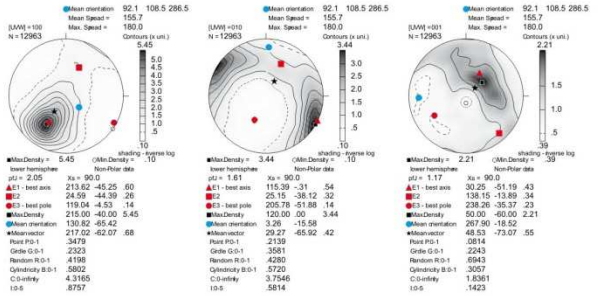

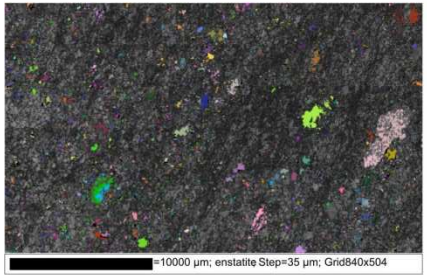

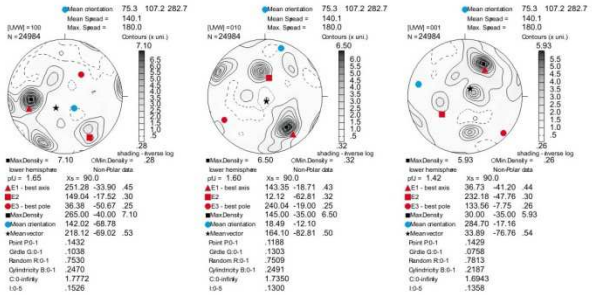

Opx

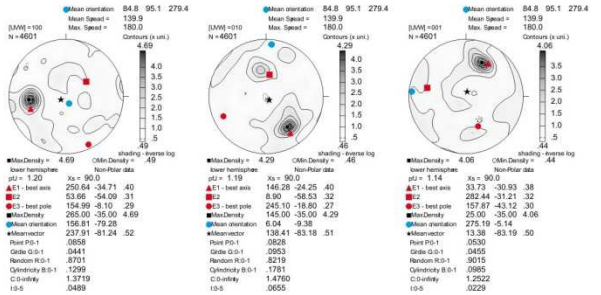

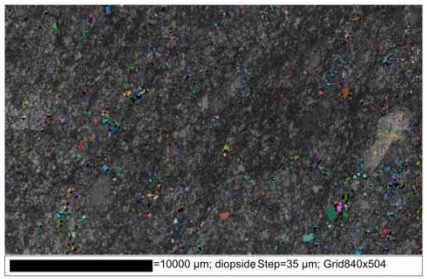

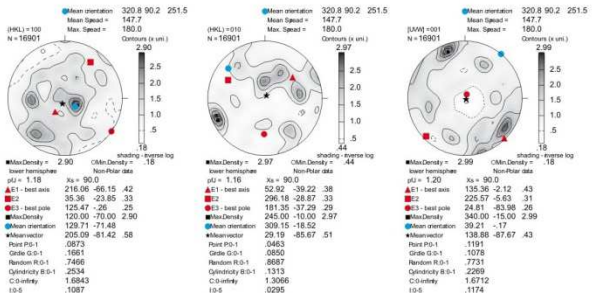

Cpx

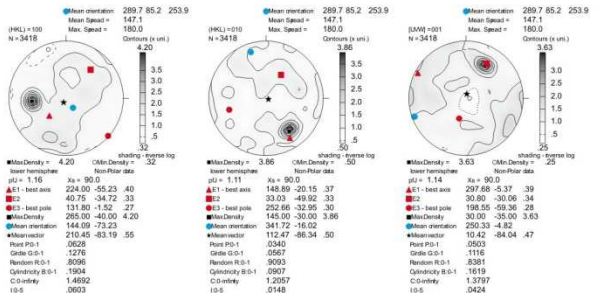

Geographic coordinates (1 point per grain)

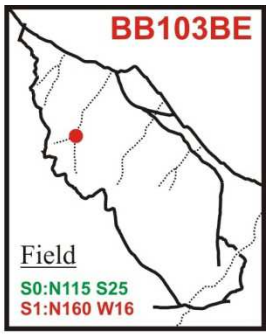

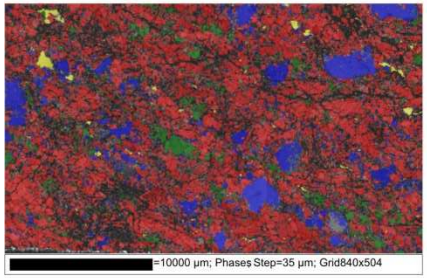

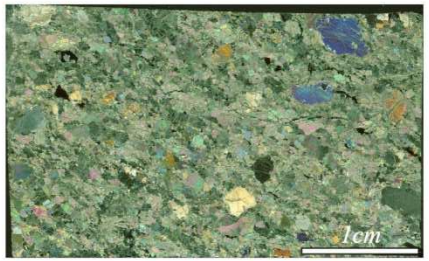

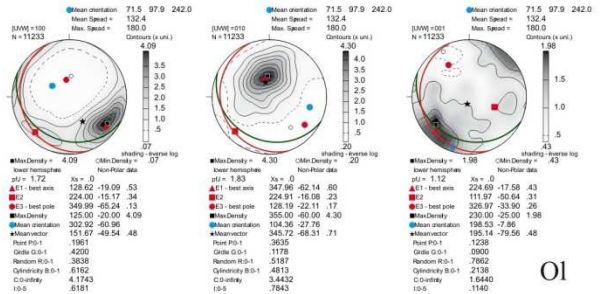

Ol

step=35µm

Sample coordinates (raw data)

Sample coordinates (1 point per grain)

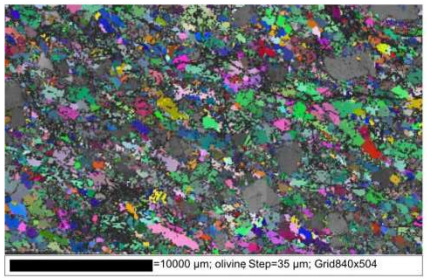

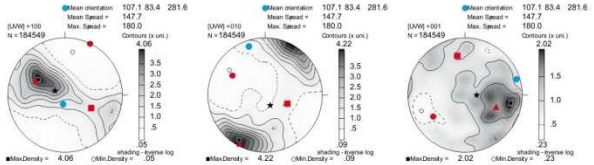

Ol

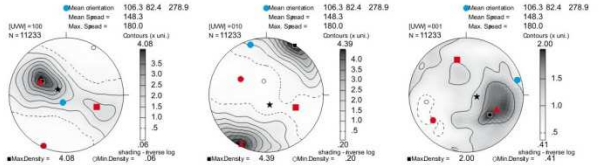

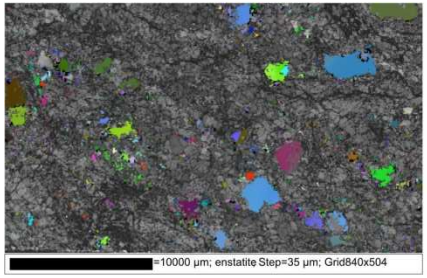

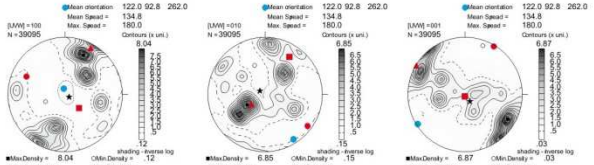

Opx

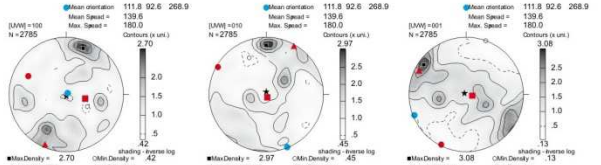

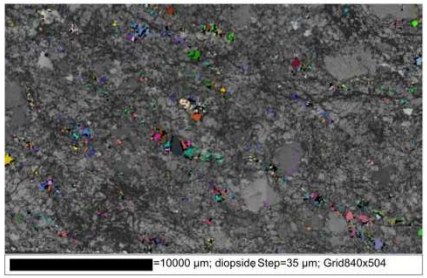

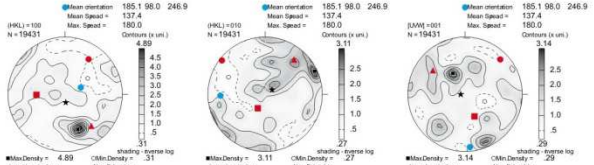

Cpx

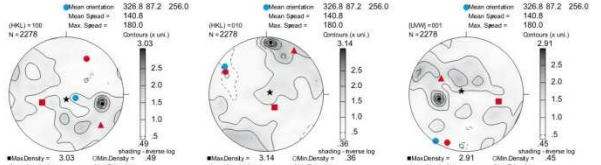

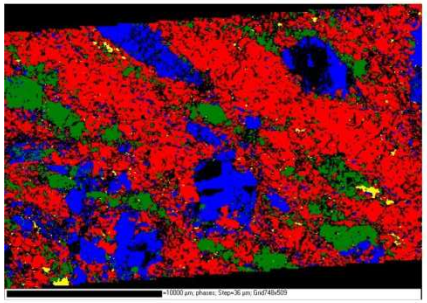

step=36µm

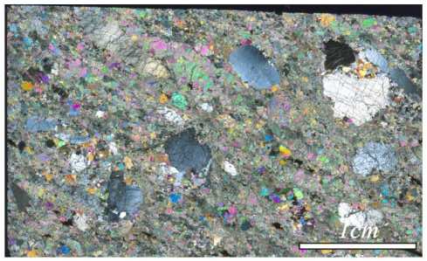

Geographic coordinates (1 point per grain)

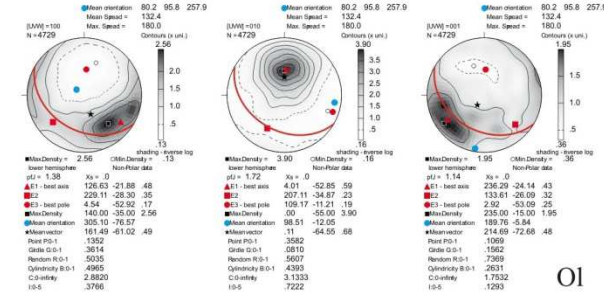

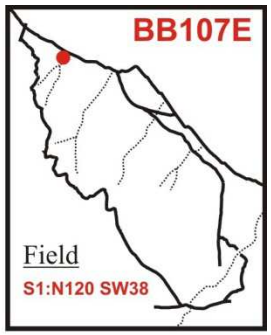

Ol

Sample coordinates (raw data)

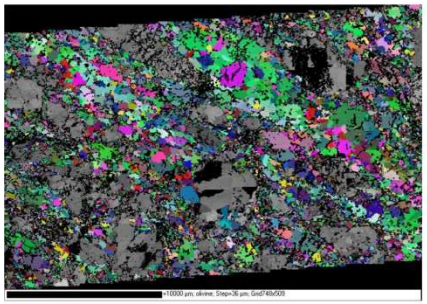

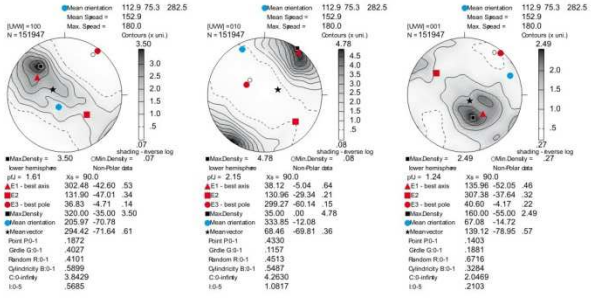

Sample coordinates (1 point per grain)

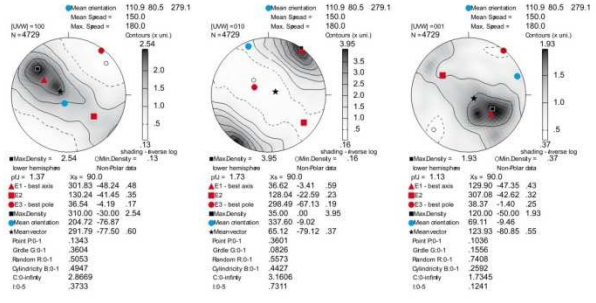

Ol

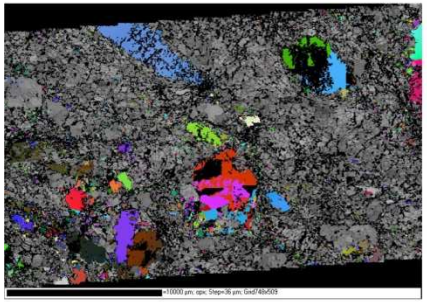

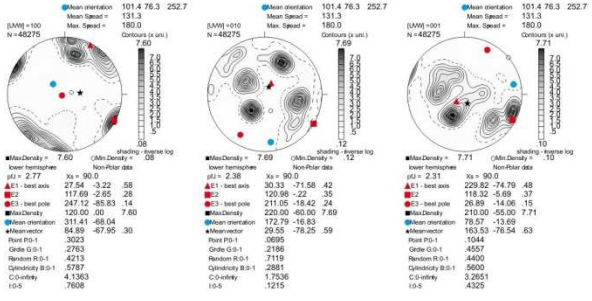

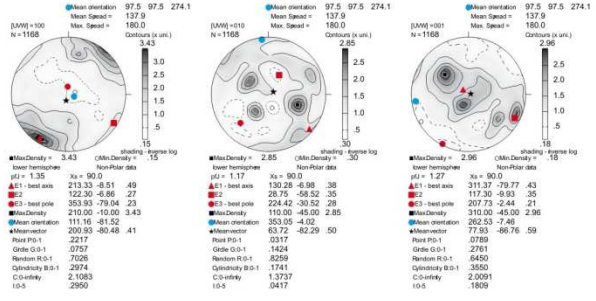

Opx

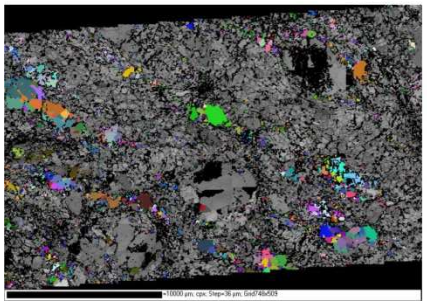

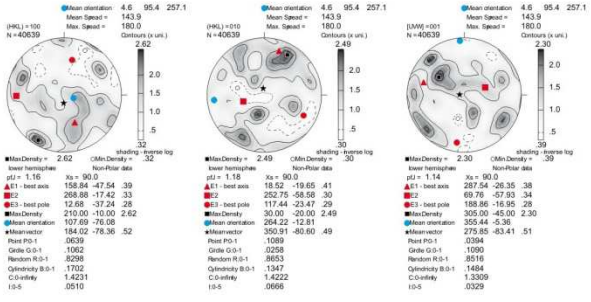

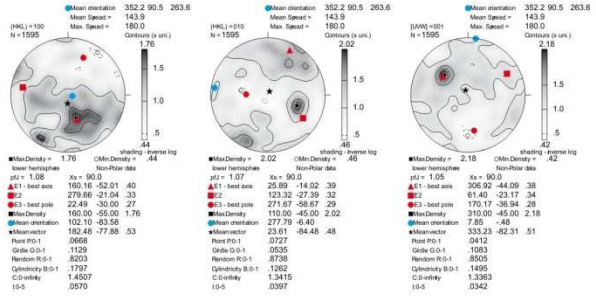

Cpx

Geographic coordinates (1 point per grain)

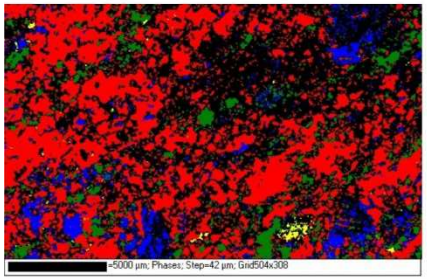

step=42µm

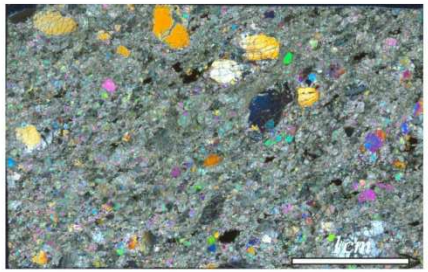

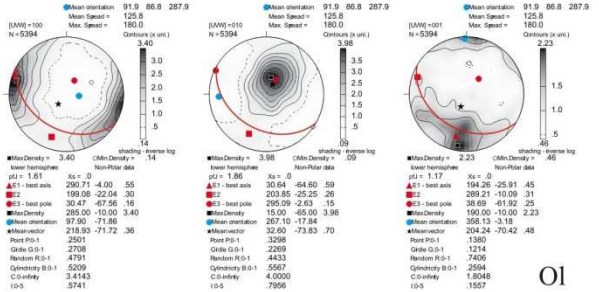

Ol

Sample coordinates (raw data)

Sample coordinates (1 point per grain)

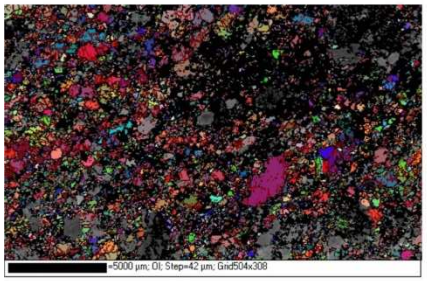

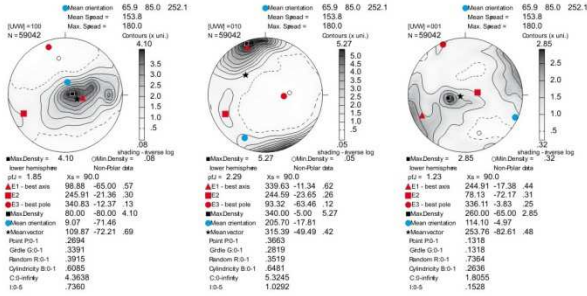

Ol

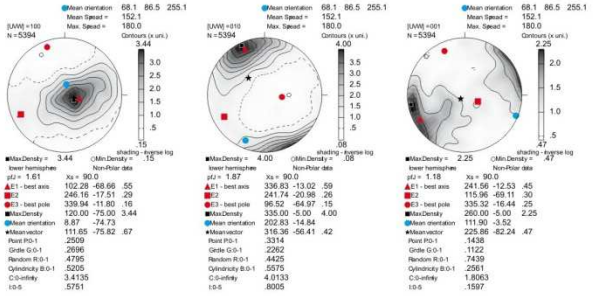

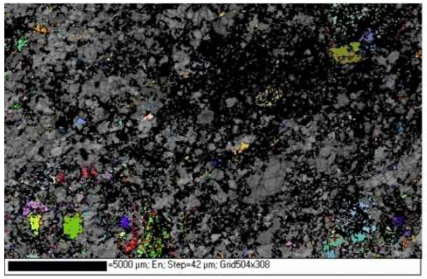

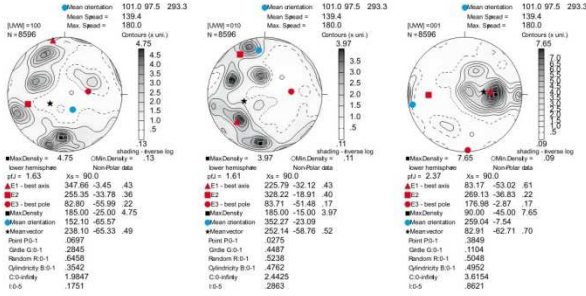

Opx

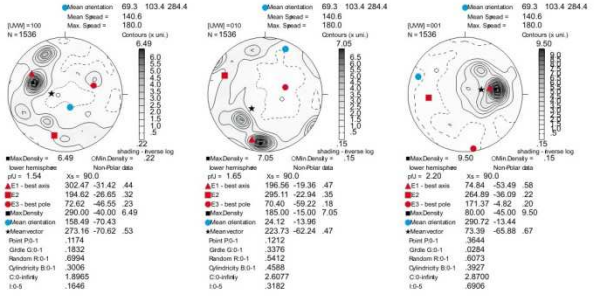

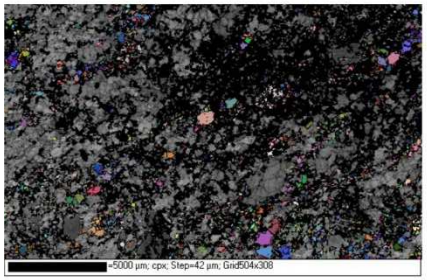

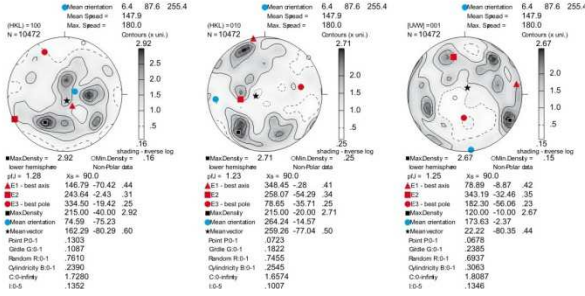

Cpx

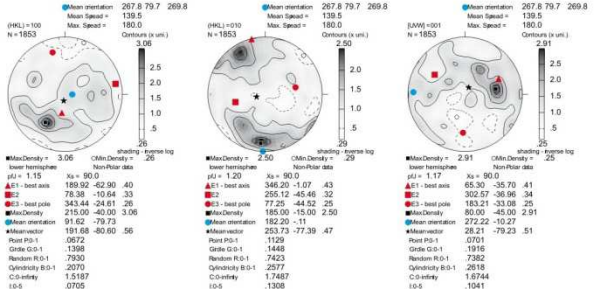

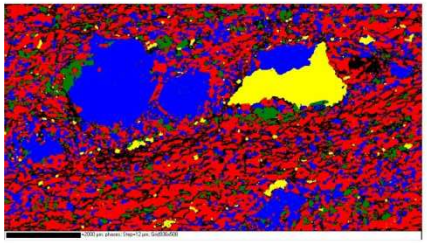

step=12µm

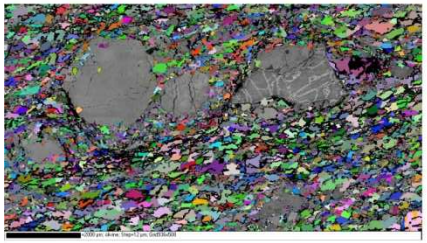

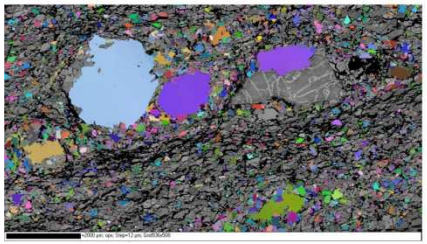

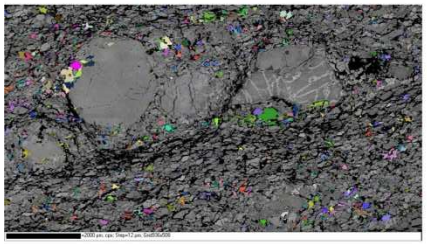

Geographic coordinates (1 point per grain)

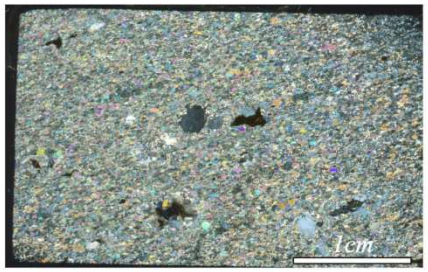

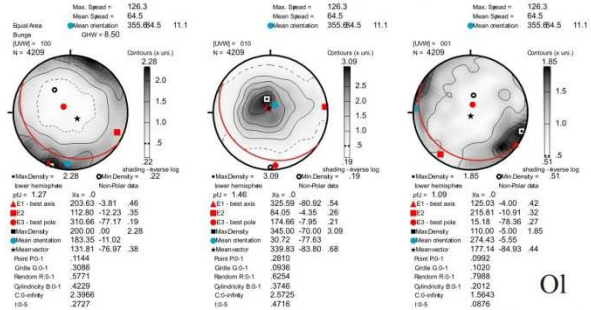

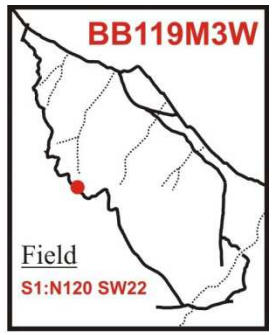

Ol

Sample coordinates (raw data)

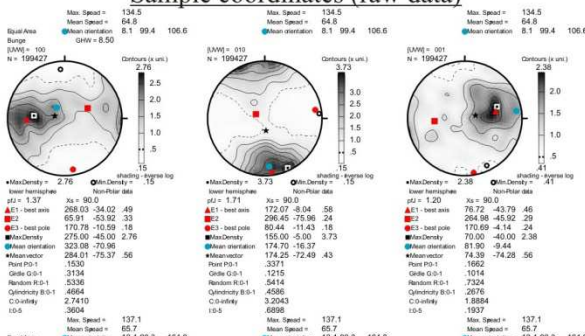

Ol

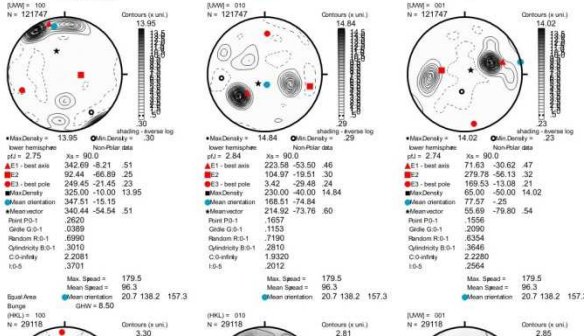

Opx

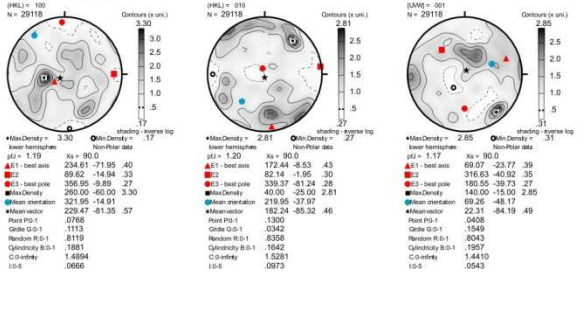

Cpx

Sample coordinates (1 point per grain)

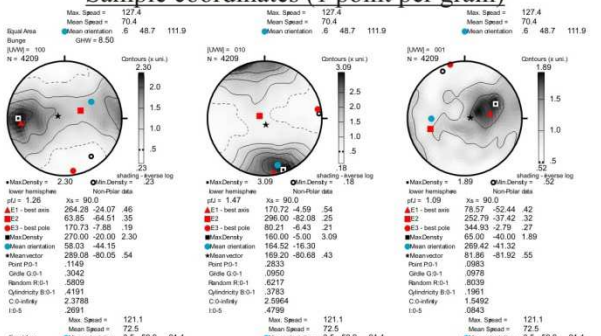

Ol

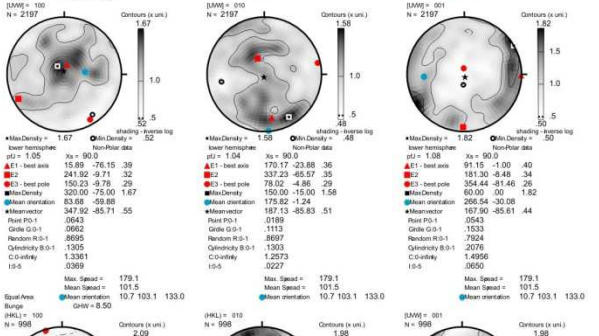

Opx

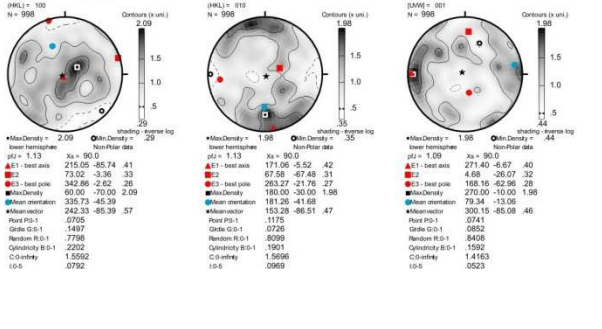

Cpx

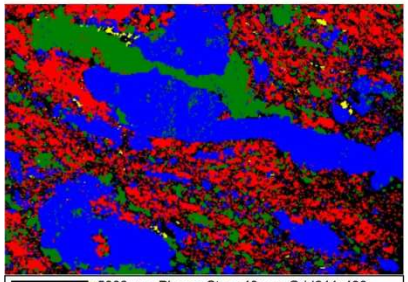

[redacted]=5000 µm; Phases Step=40 µm; Grid644x438

step=40µm

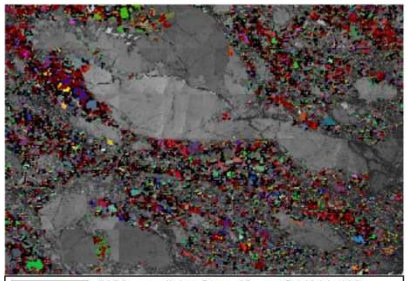

[redacted]=5000 µm; olivine Step=40 µm; Grid644x438

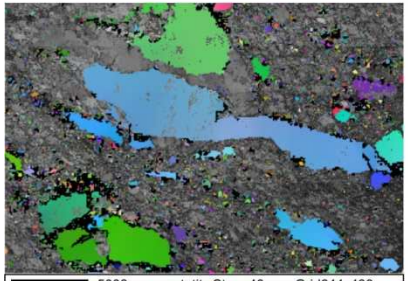

[redacted]=5000 µm; enstatite Step=40 µm; Grid644x438

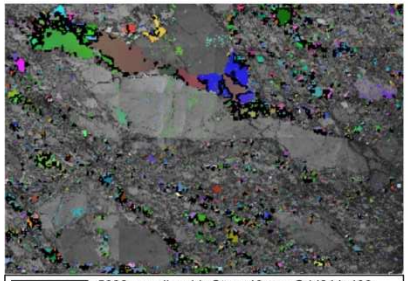

[redacted]=5000 µm; diopside Step=40 µm; Grid644x438

Geographic coordinates (1 point per grain)

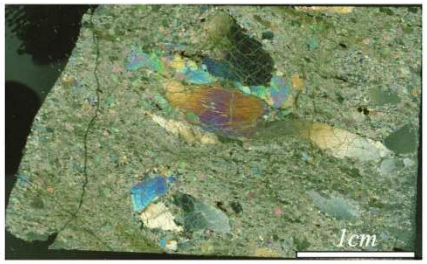

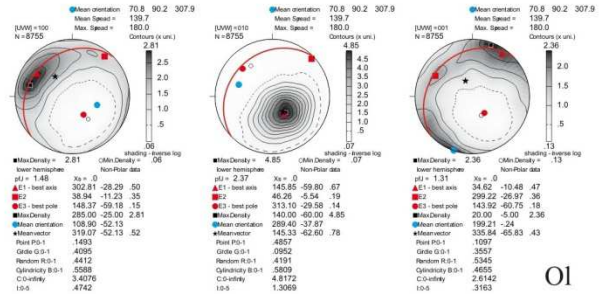

Ol

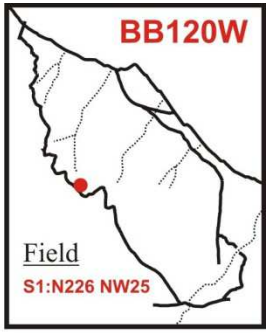

Sample coordinates (raw data)

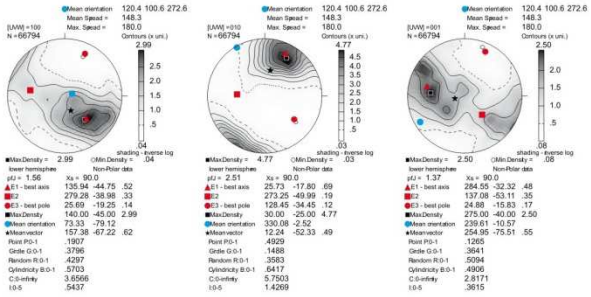

Ol

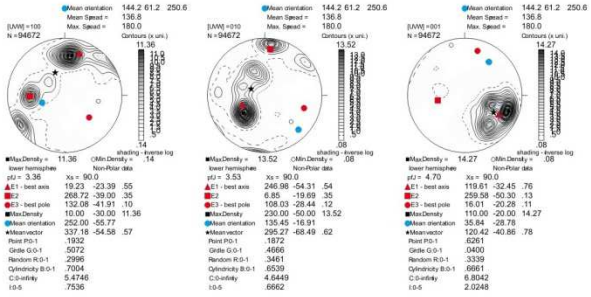

Opx

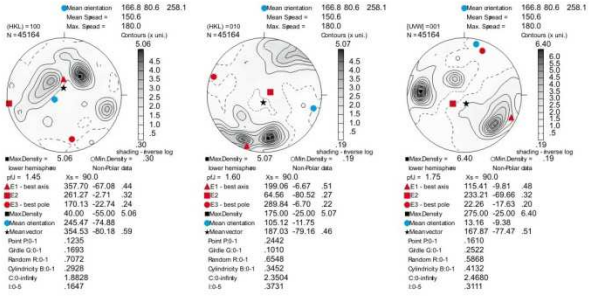

Cpx

Sample coordinates (1 point per grain)

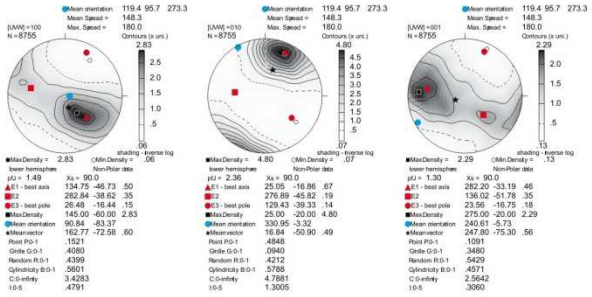

Ol

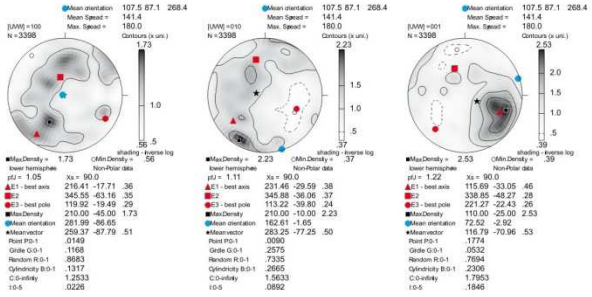

Opx

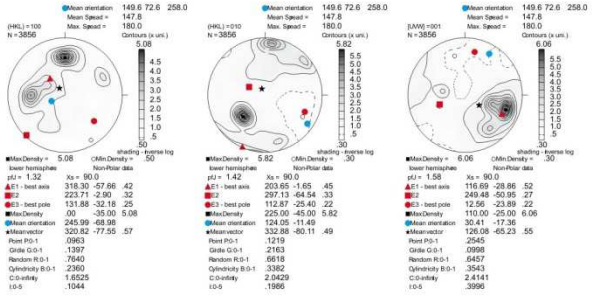

Cpx

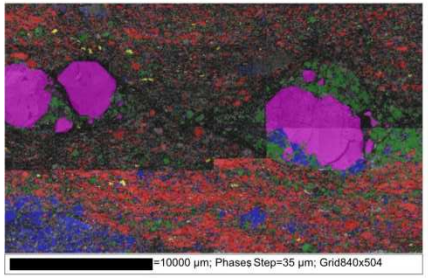

step=35µm

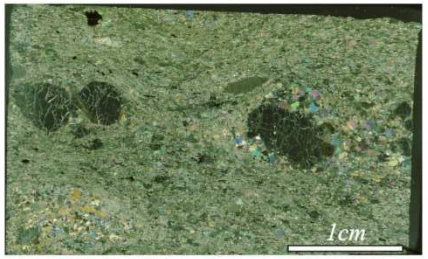

Geographic coordinates (1 point per grain)

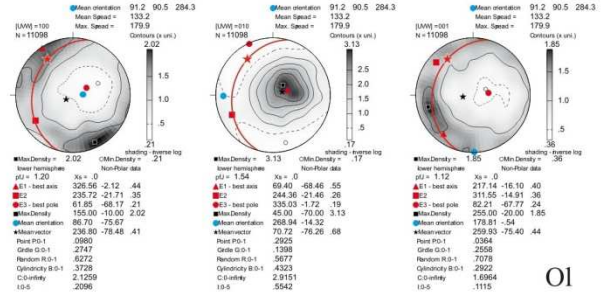

Ol

Sample coordinates (raw data)

Sample coordinates (1 point per grain)

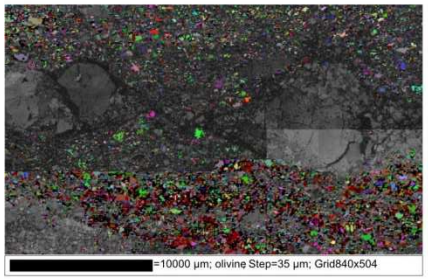

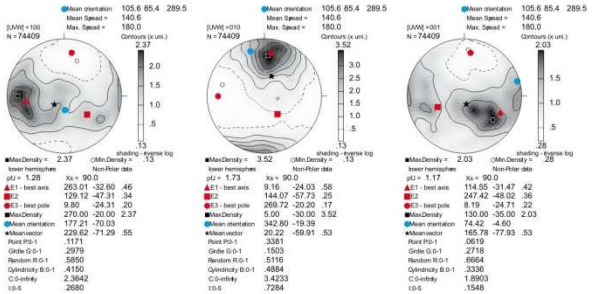

Ol

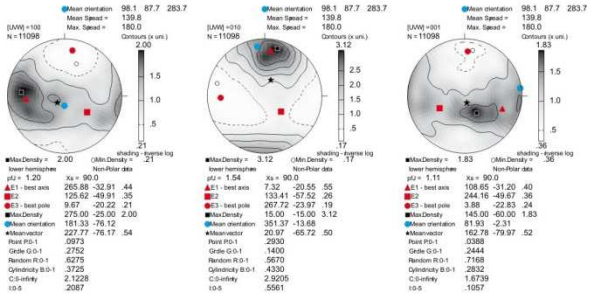

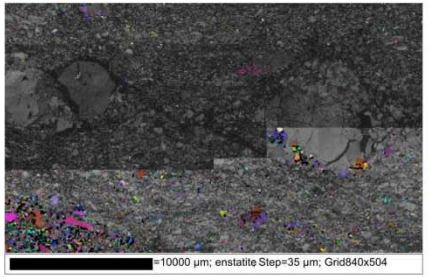

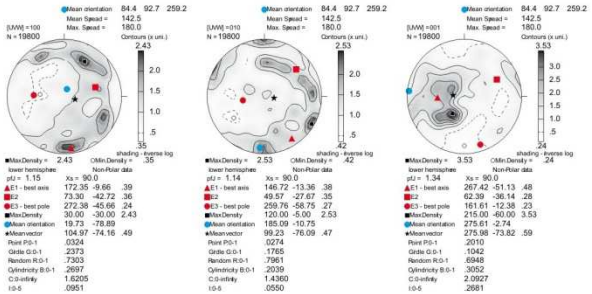

Opx

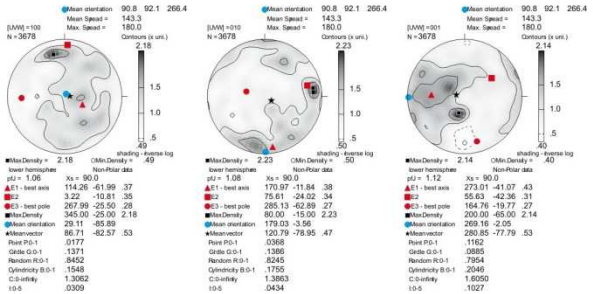

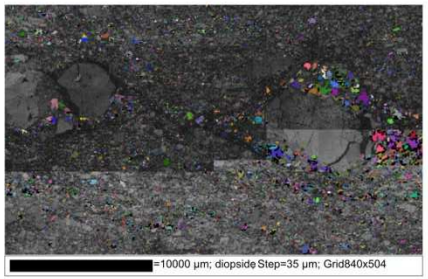

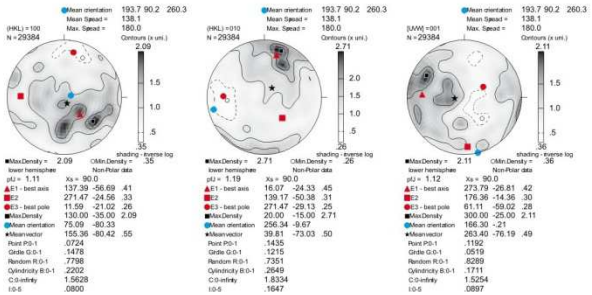

Cpx

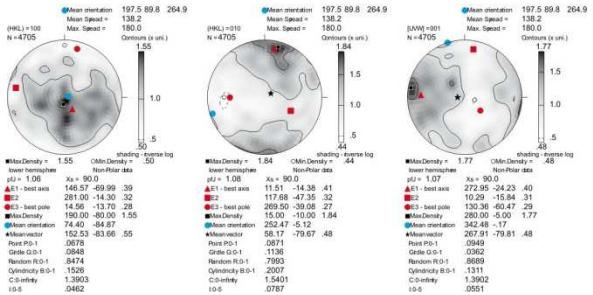

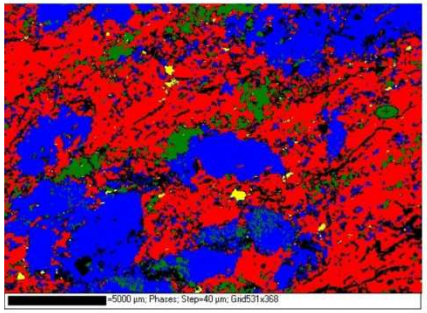

step=40µm

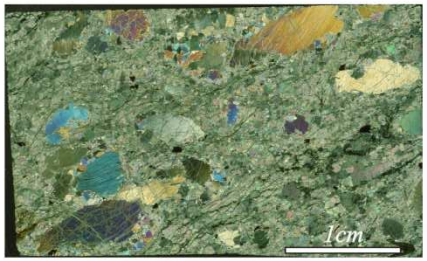

Geographic coordinates (1 point per grain)

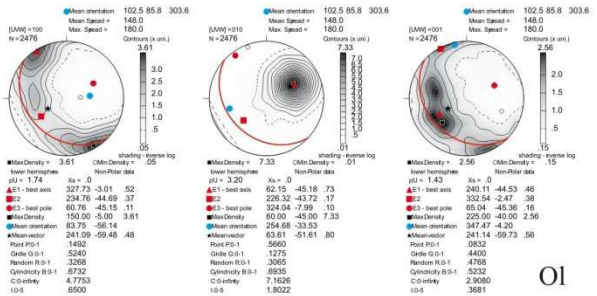

Ol

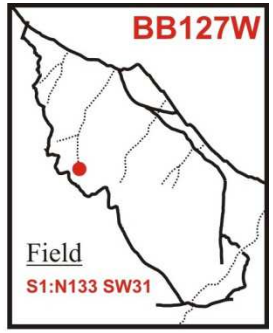

Sample coordinates (raw data)

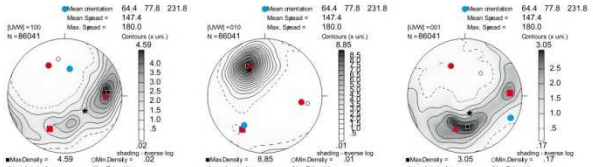

Ol

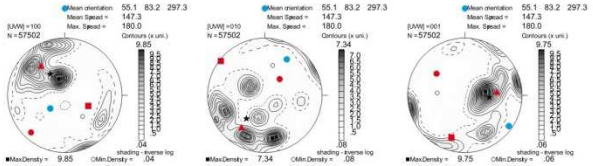

Opx

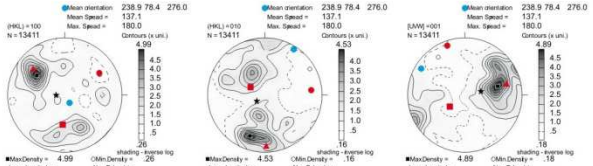

Cpx

Sample coordinates (1 point per grain)

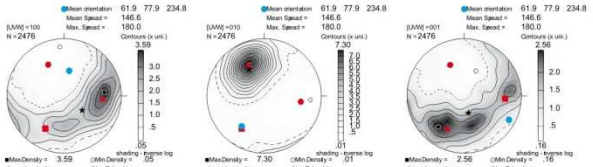

Ol

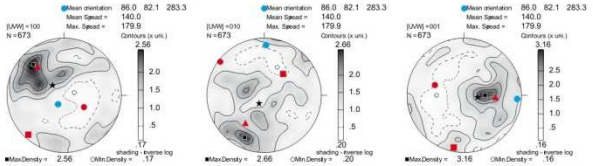

Opx

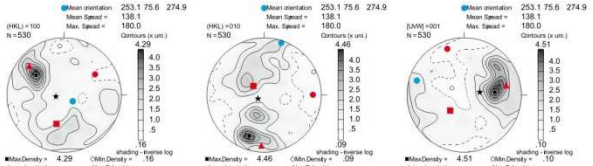

Cpx

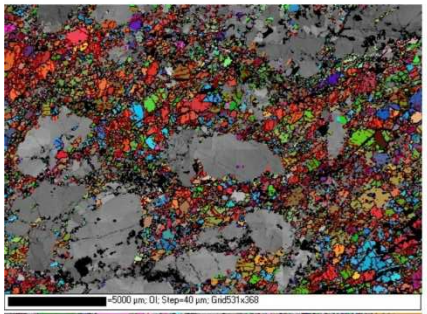

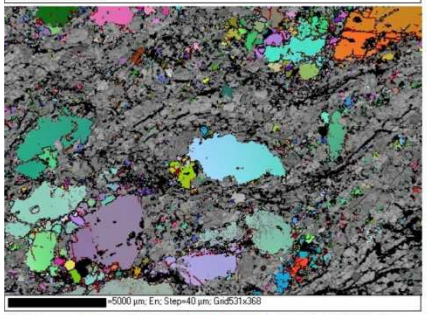

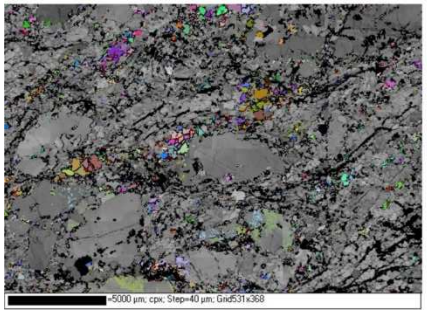

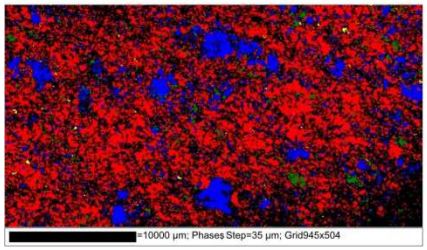

step=35µm

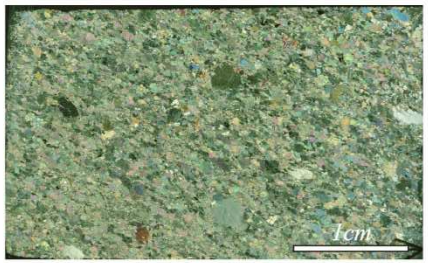

Geographic coordinates (1 point per grain)

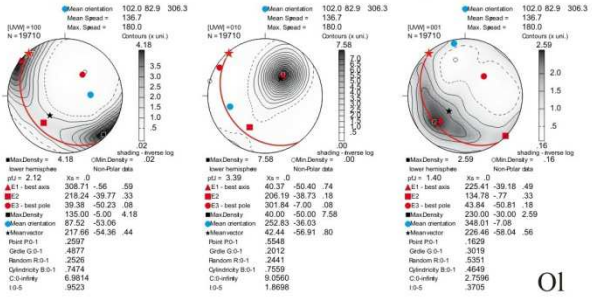

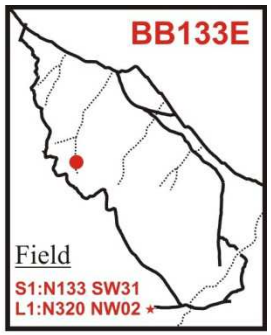

Ol

Sample coordinates (raw data)

Sample coordinates (1 point per grain)

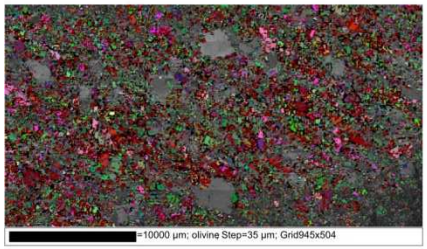

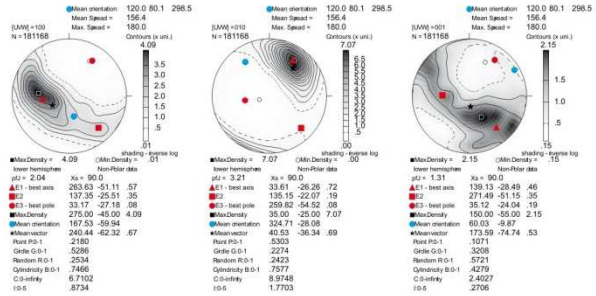

Ol

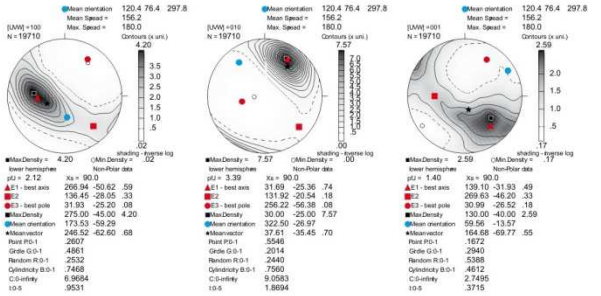

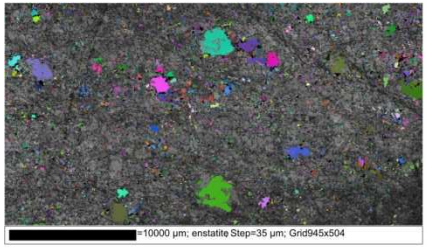

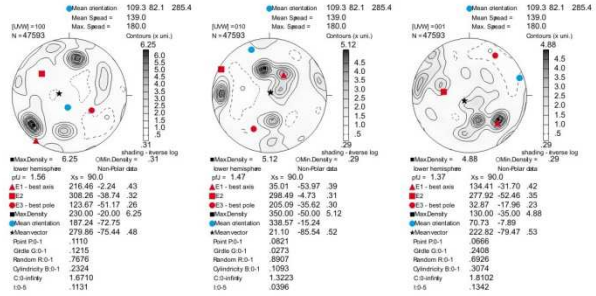

Opx

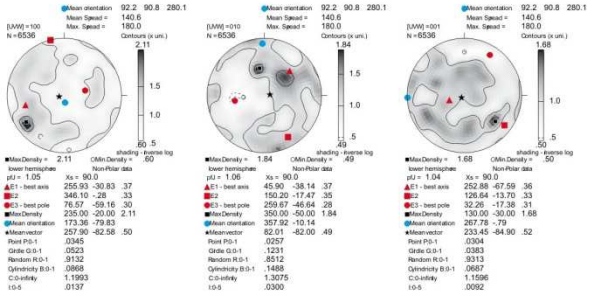

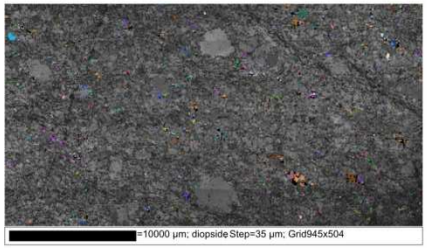

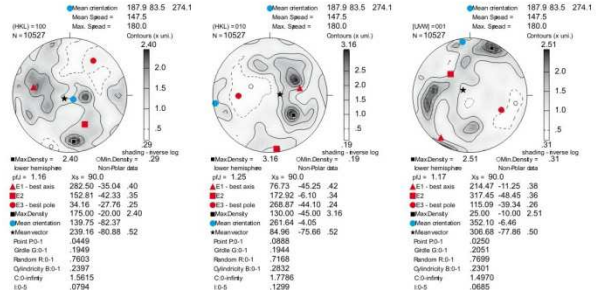

Cpx

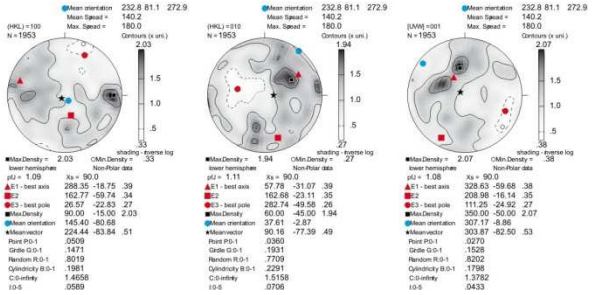

Geographic coordinates (1 point per grain)

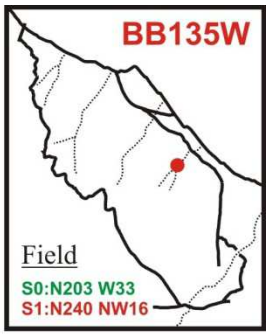

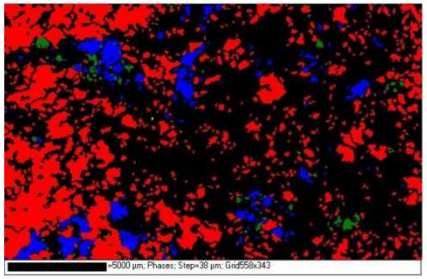

step=38µm

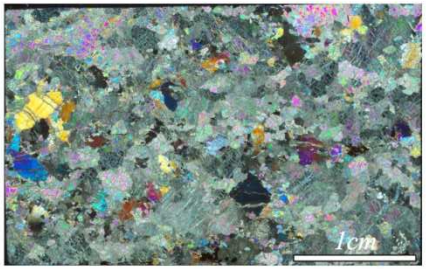

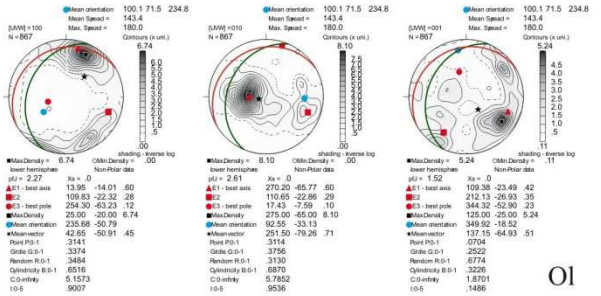

Ol

Sample coordinates (raw data)

Sample coordinates (1 point per grain)

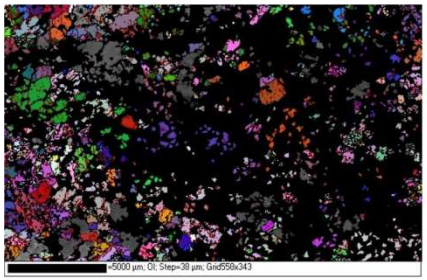

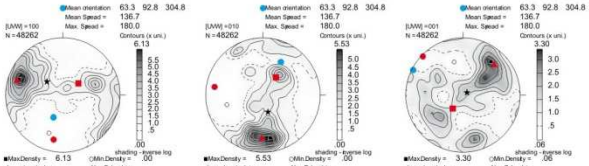

Ol

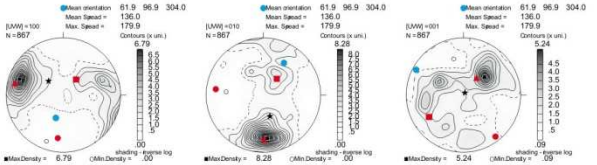

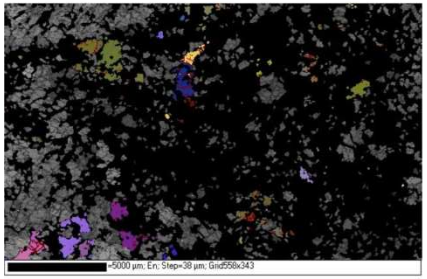

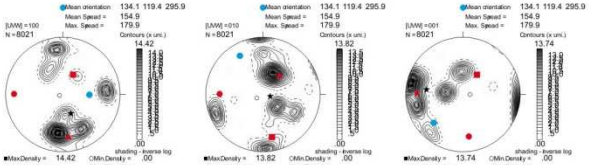

Opx

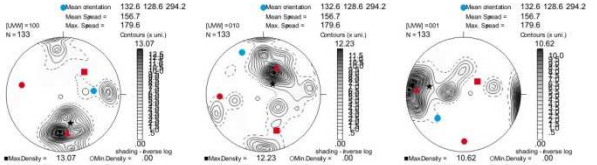

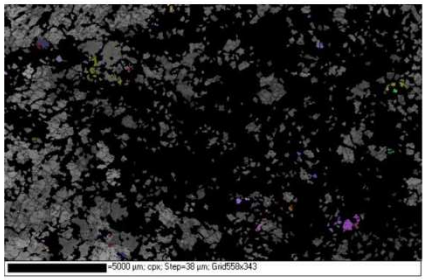

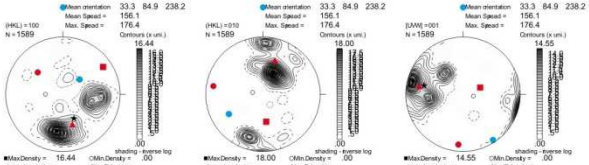

Cpx

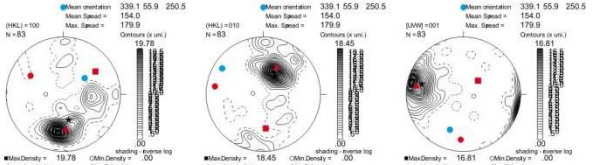

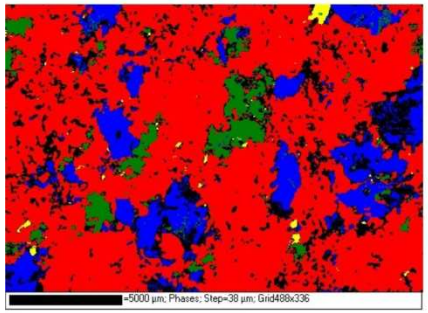

step=38µm

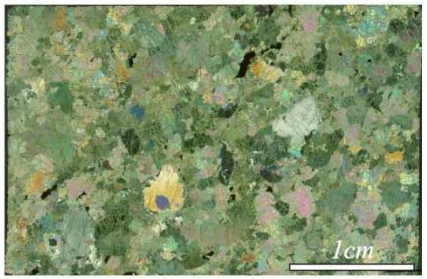

Geographic coordinates (1 point per grain)

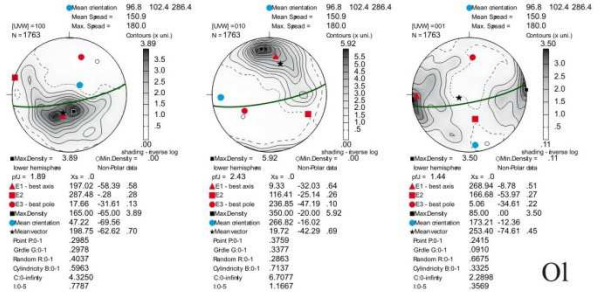

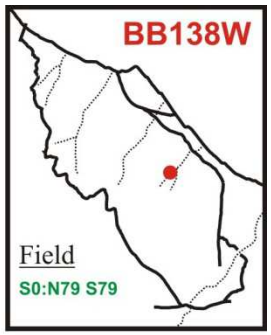

Ol

Sample coordinates (raw data)

Sample coordinates (1 point per grain)

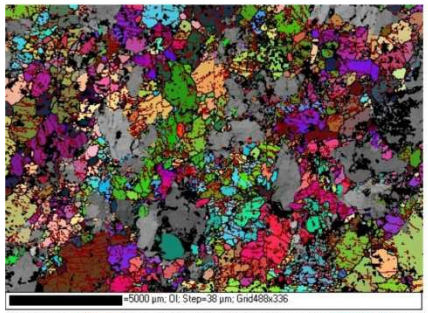

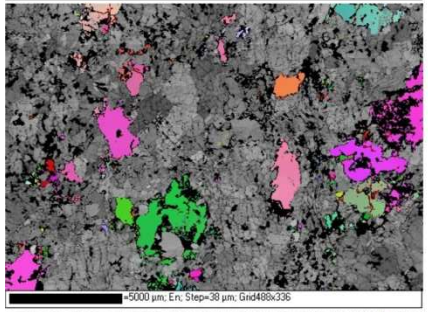

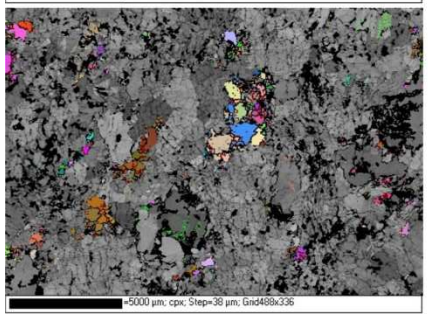

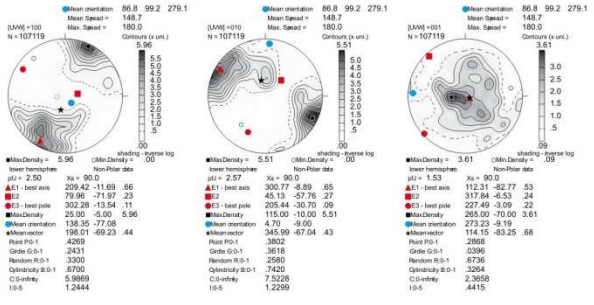

Ol

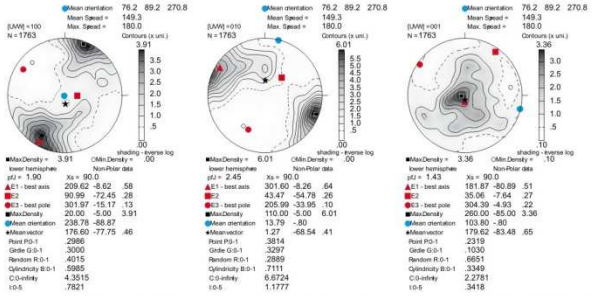

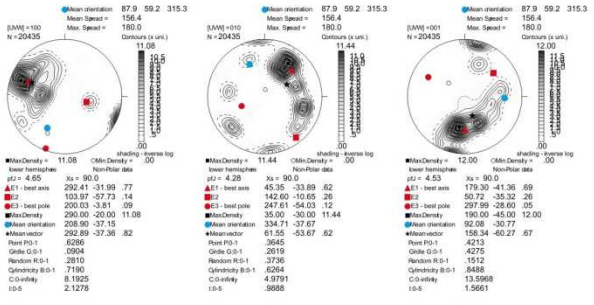

Opx

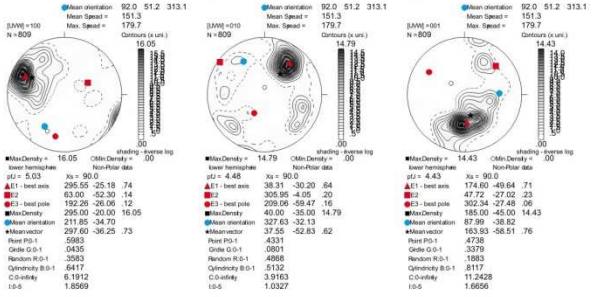

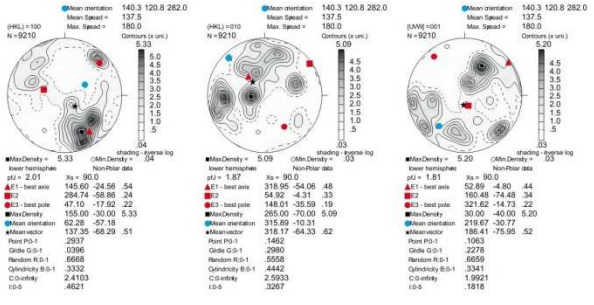

Cpx

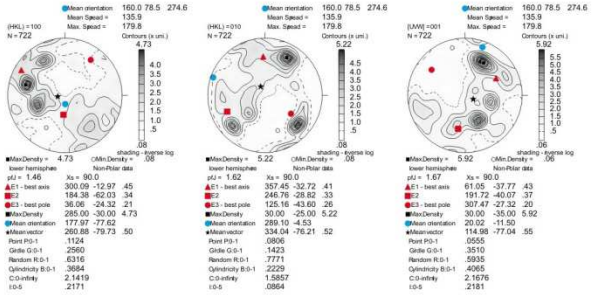

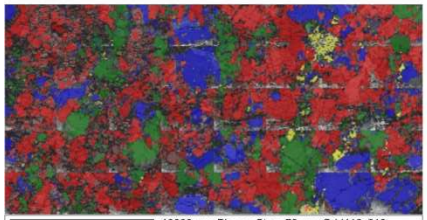

step=70µm

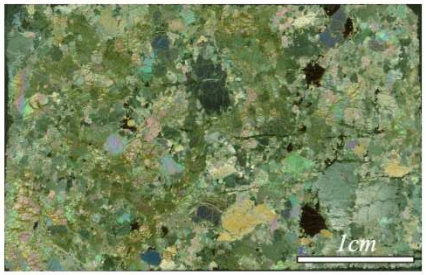

Geographic coordinates (1 point per grain)

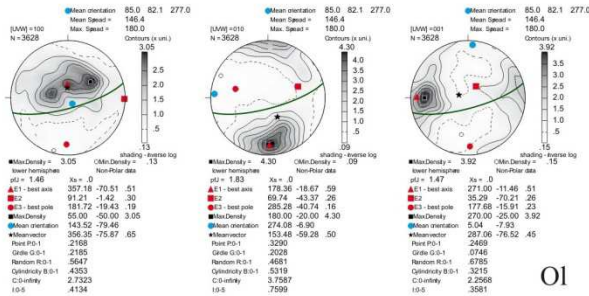

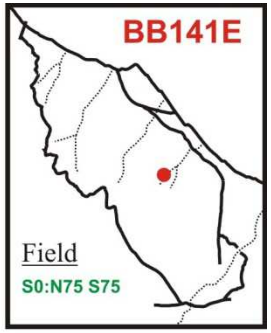

Ol

Sample coordinates (raw data)

Sample coordinates (1 point per grain)

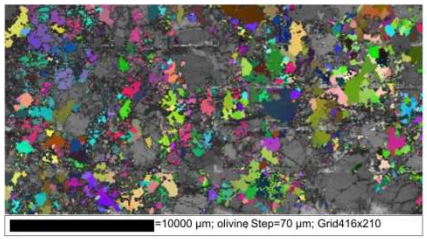

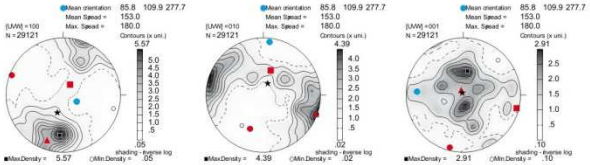

Ol

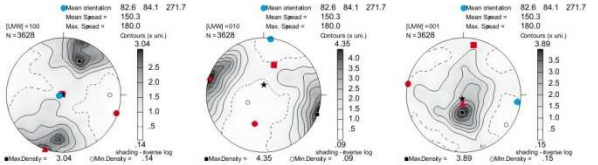

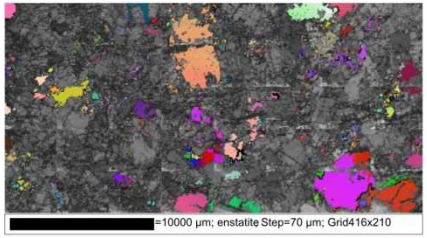

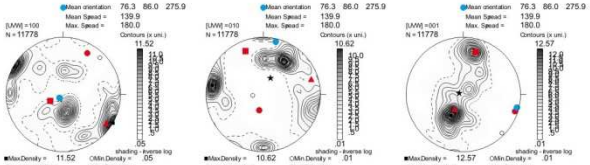

Opx

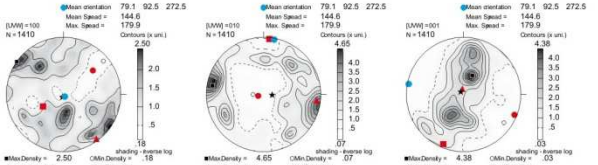

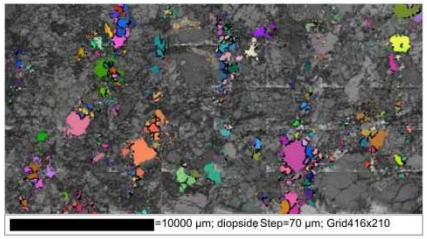

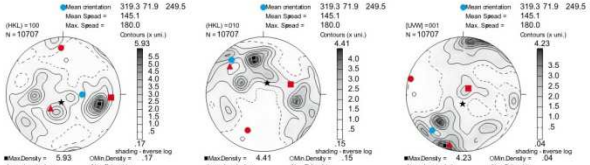

Cpx

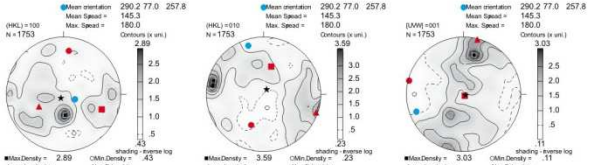

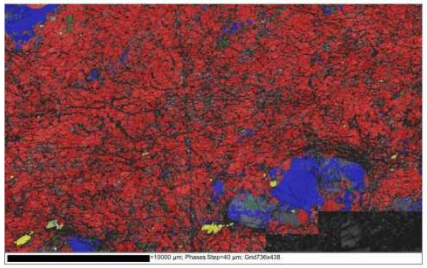

step=40μm

Geographic coordinates (1 point per grain)

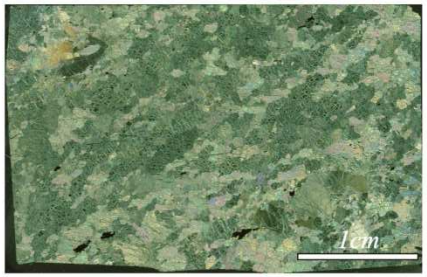

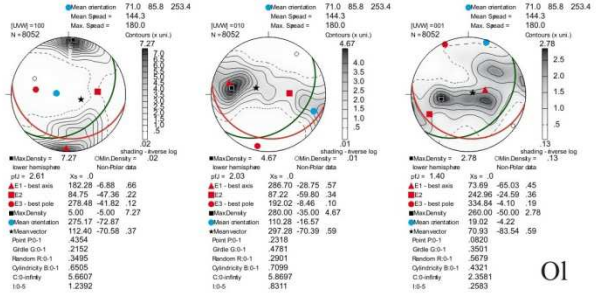

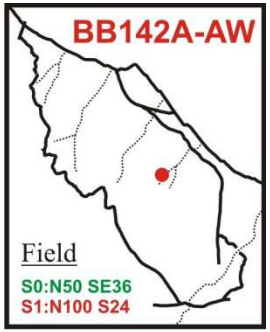

Ol

Sample coordinates (raw data)

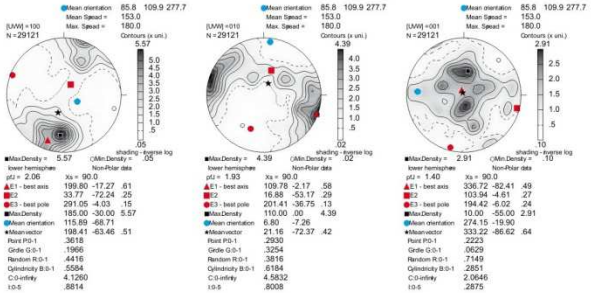

Ol

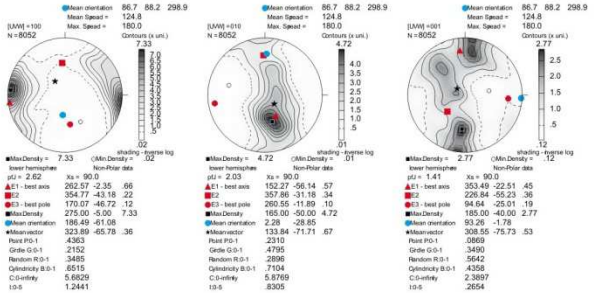

Sample coordinates (1 point per grain)

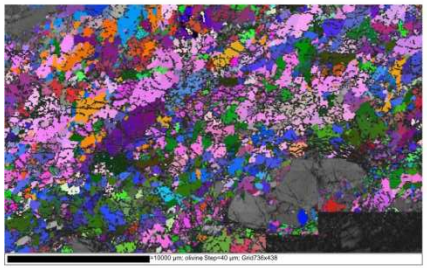

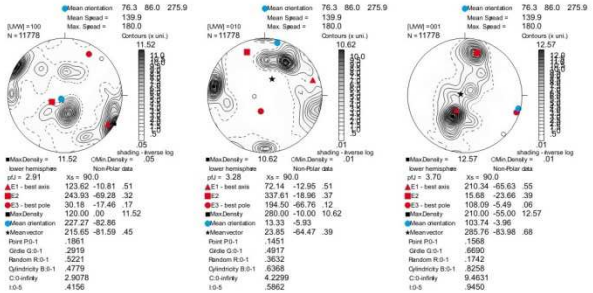

Opx

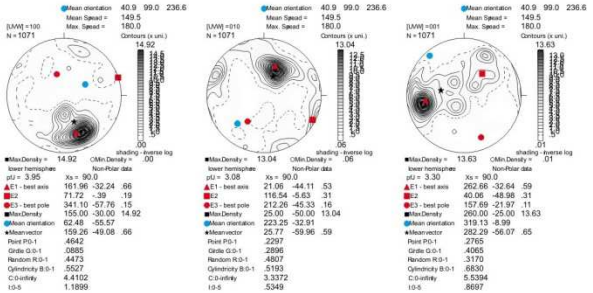

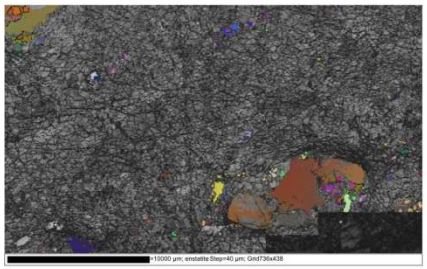

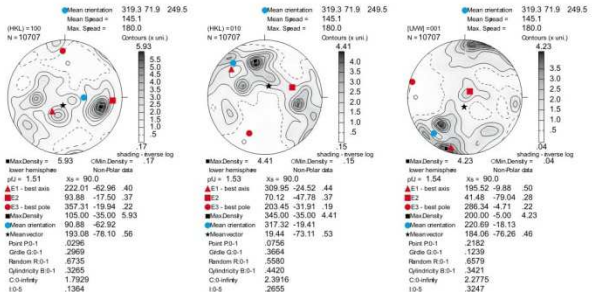

Cpx

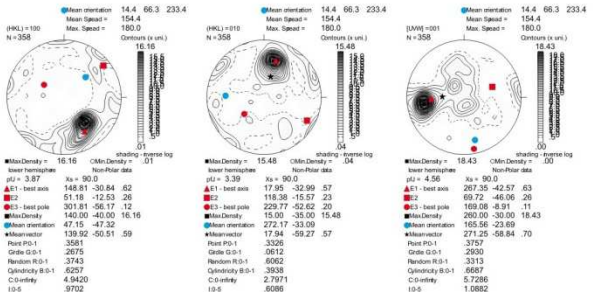

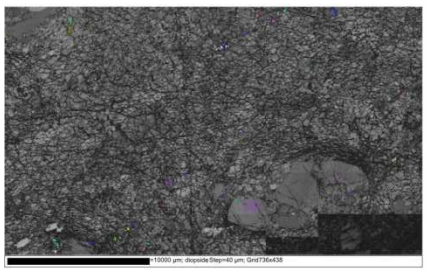

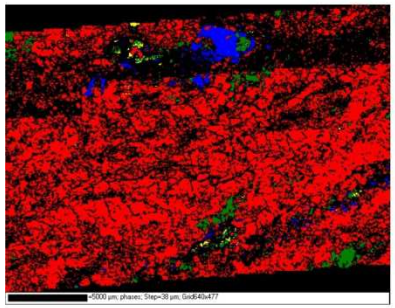

step=38μm

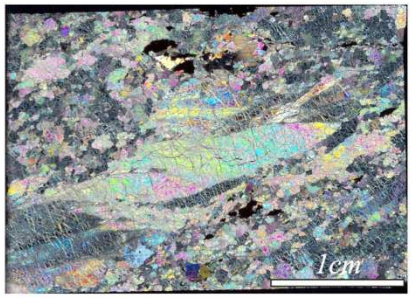

Geographic coordinates (1 point per grain)

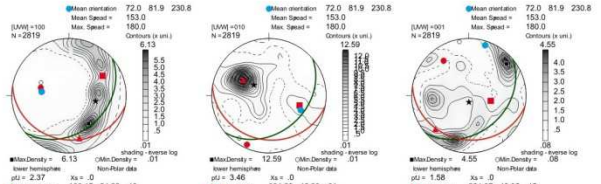

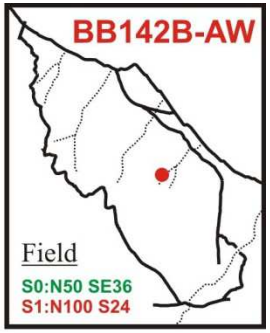

Ol

Sample coordinates (raw data)

Sample coordinates (1 point per grain)

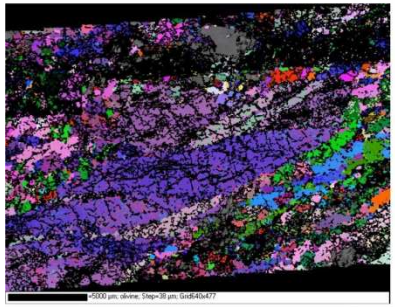

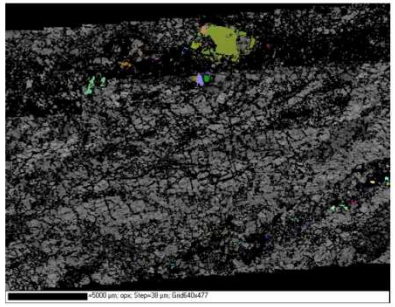

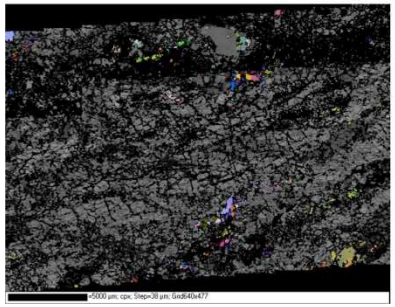

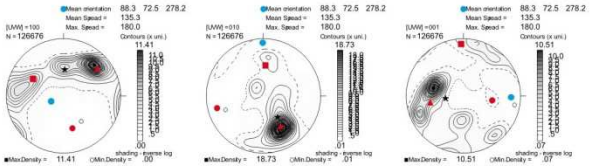

Ol

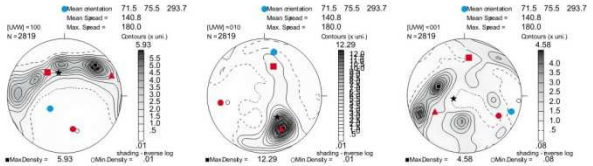

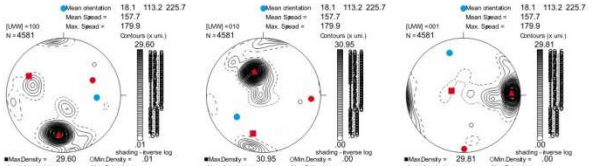

Opx

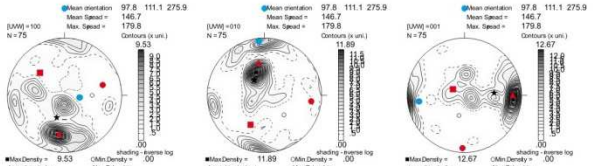

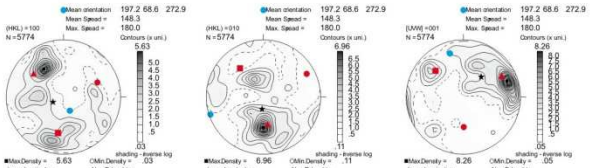

Cpx

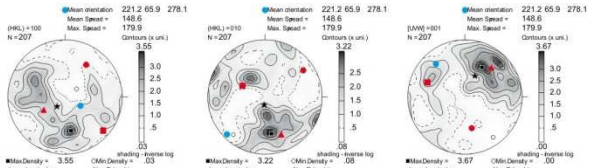

Geographic coordinates (1 point per grain)

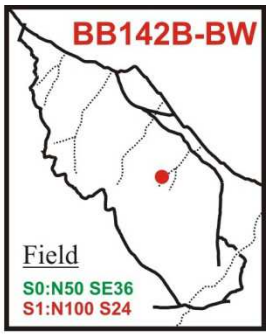

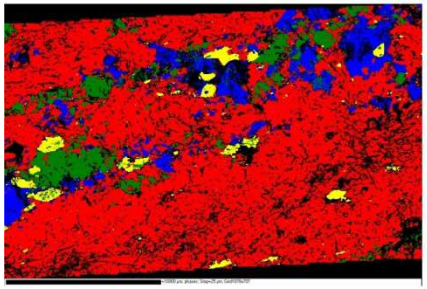

step=25µm

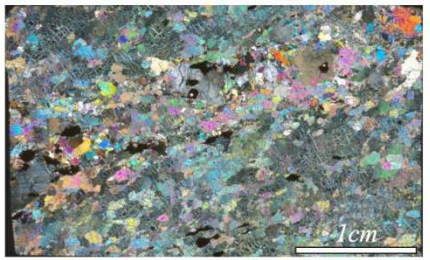

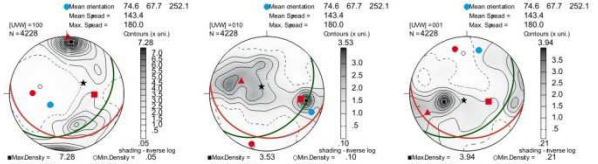

Ol

Sample coordinates (raw data)

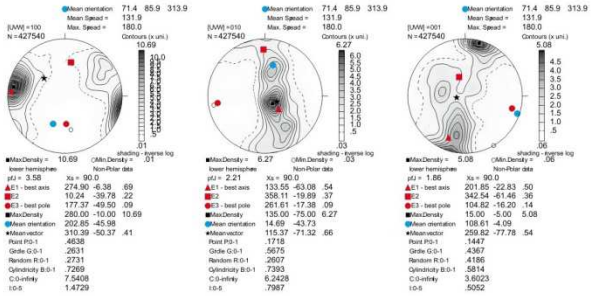

Sample coordinates (1 point per grain)

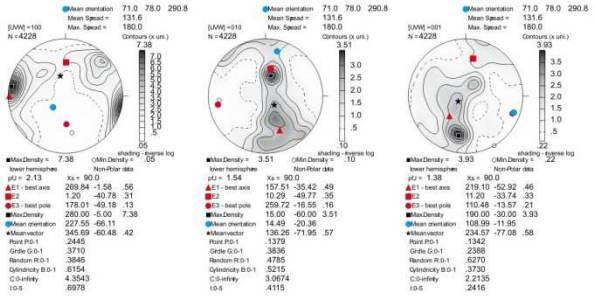

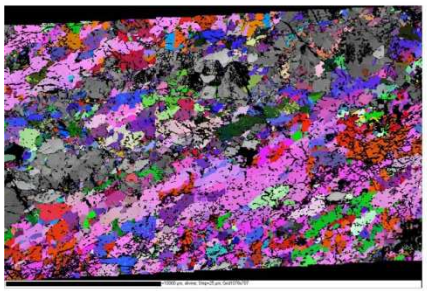

Opx

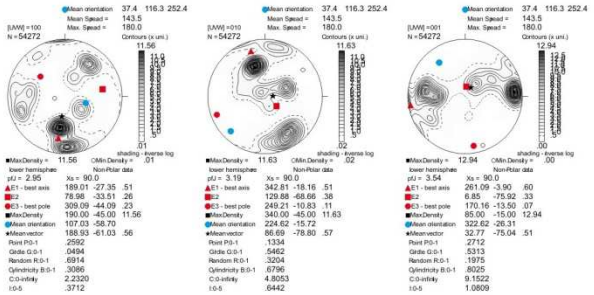

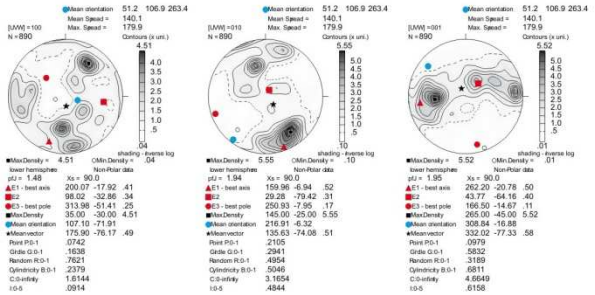

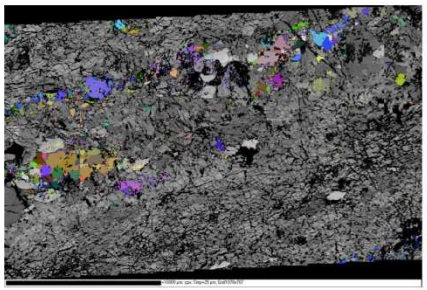

Cpx

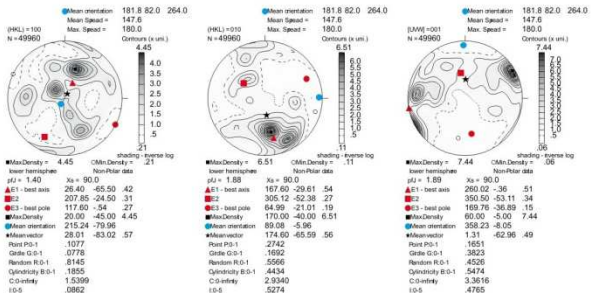

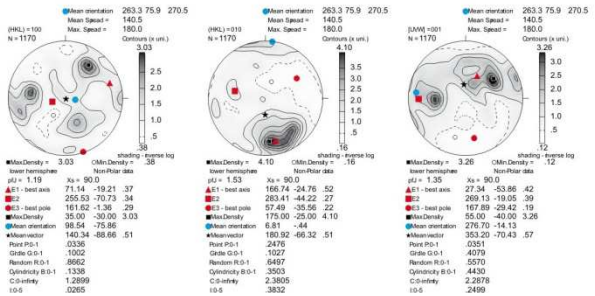

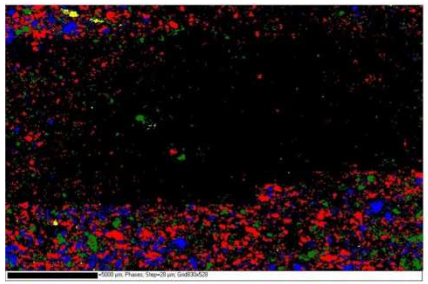

step=28µm

Geographic coordinates (1 point per grain)

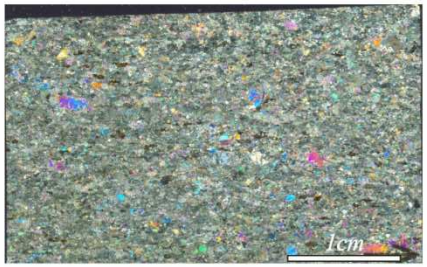

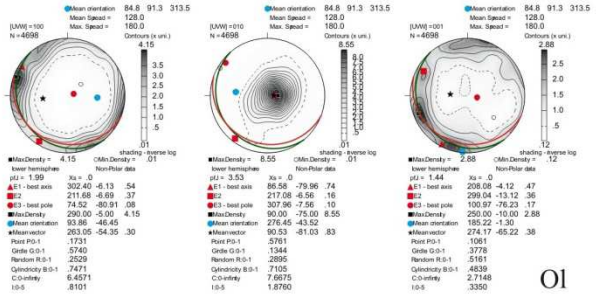

Ol

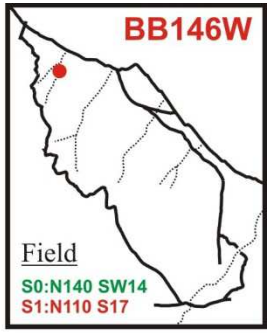

Sample coordinates (raw data)

Sample coordinates (1 point per grain)

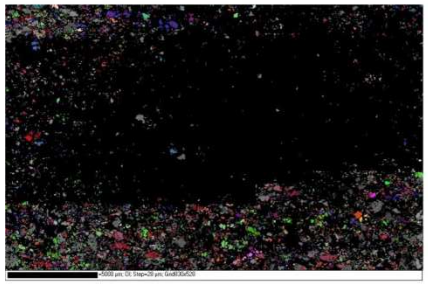

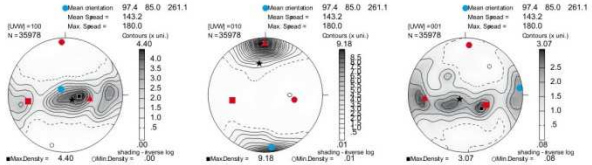

Ol

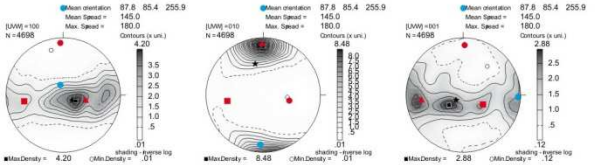

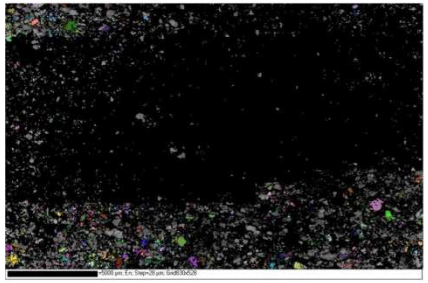

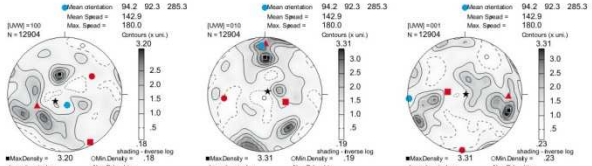

Opx

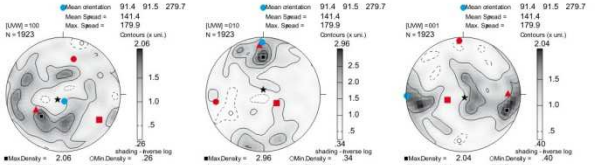

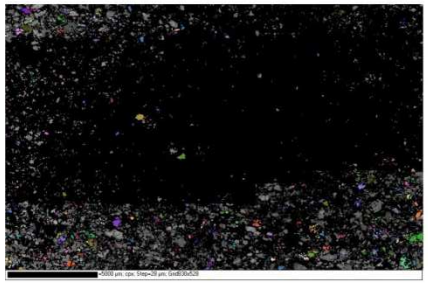

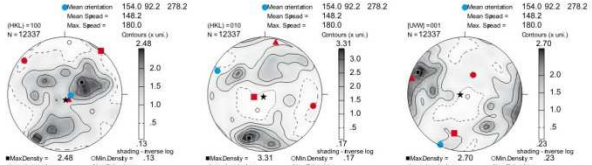

Cpx

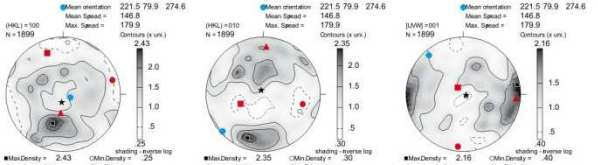

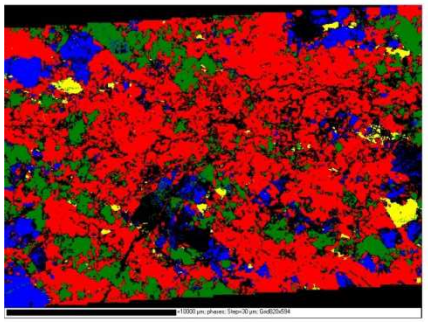

step=30µm

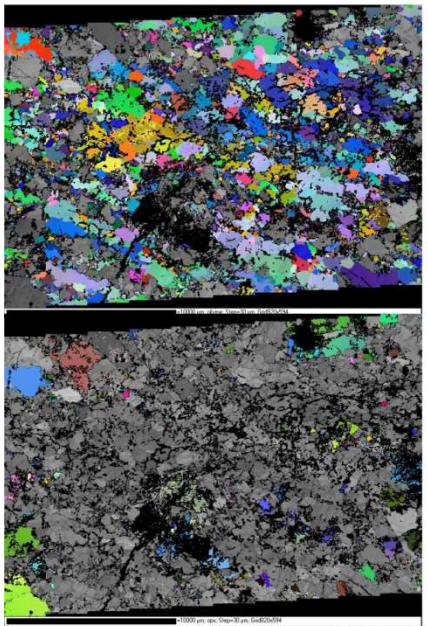

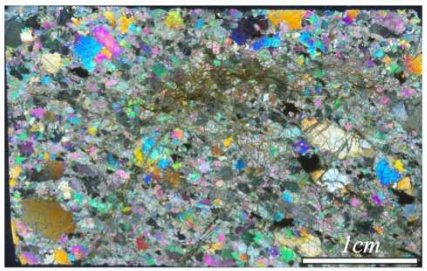

Geographic coordinates (1 point per grain)

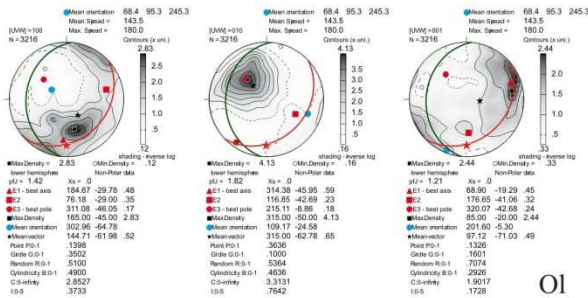

Ol

Sample coordinates (raw data)

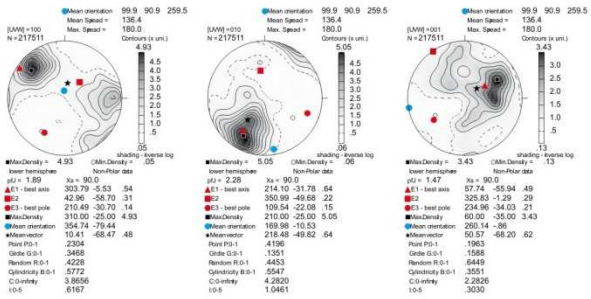

Ol

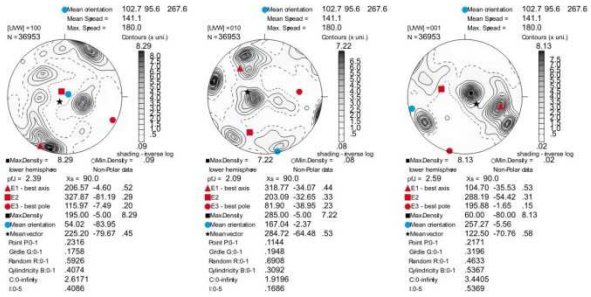

Opx

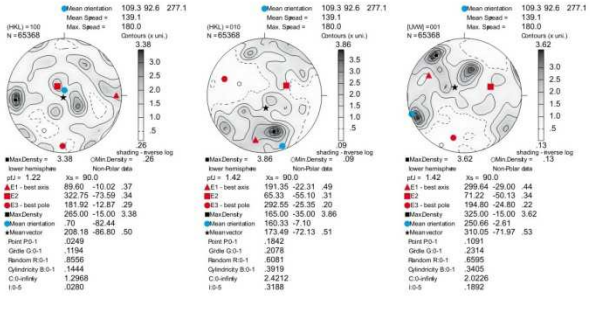

Cpx

Sample coordinates (1 point per grain)

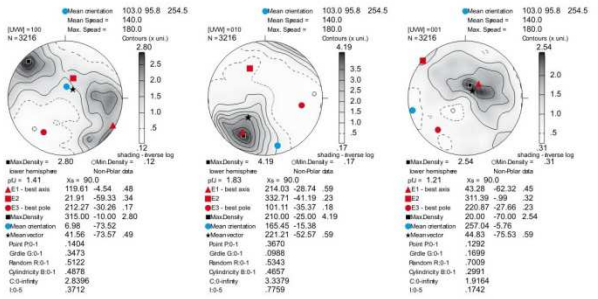

Ol

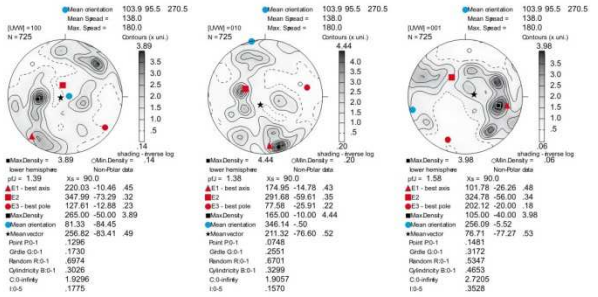

Opx

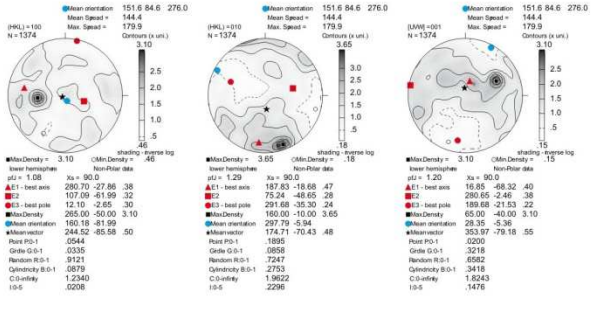

Cpx

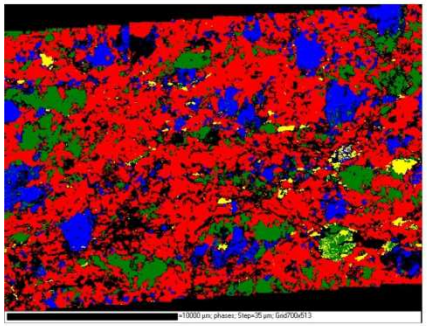

step=35µm

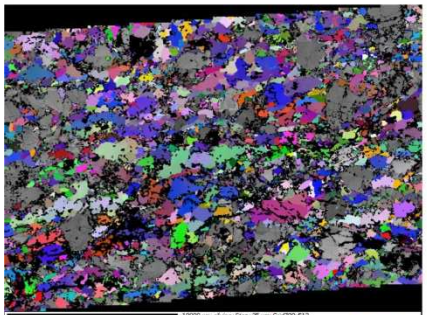

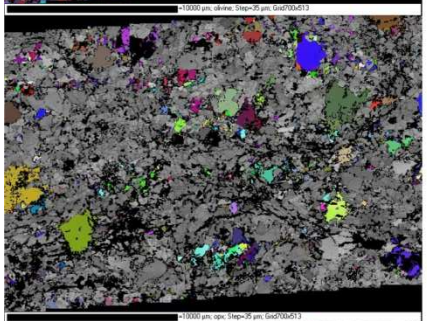

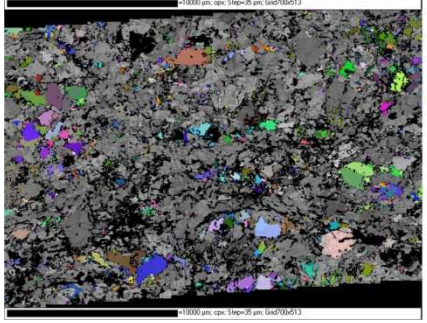

Geographic coordinates (1 point per grain)

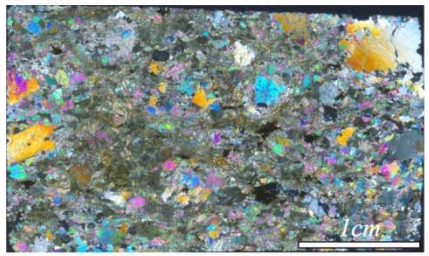

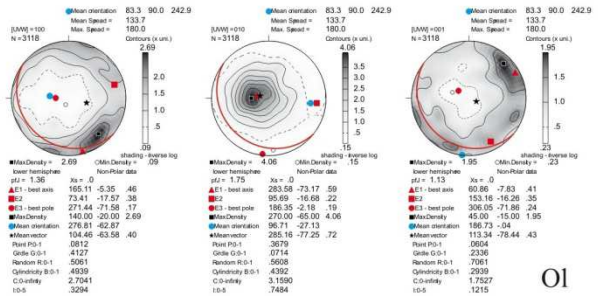

Ol

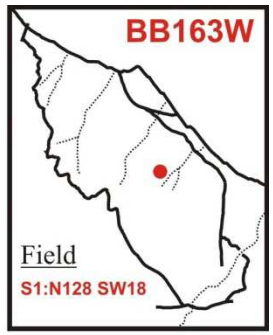

Sample coordinates (raw data)

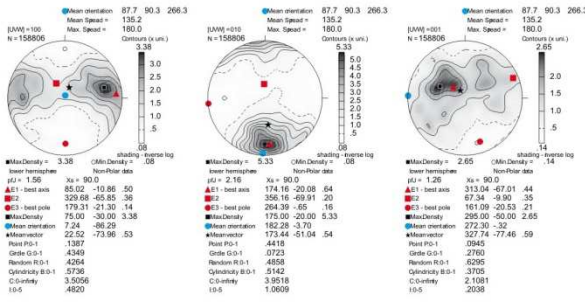

Ol

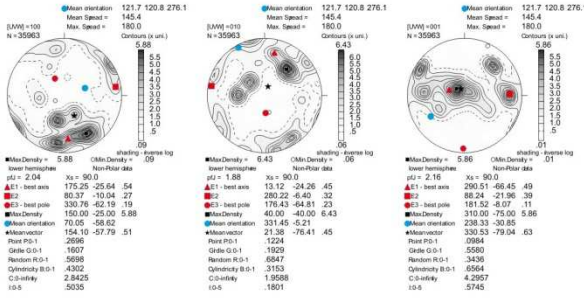

Opx

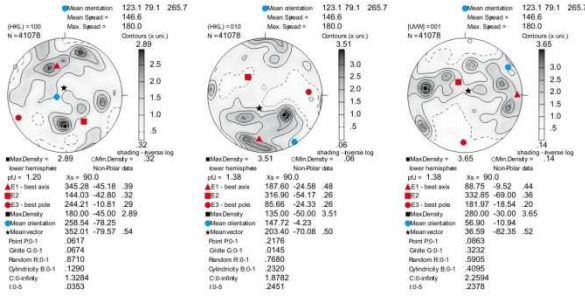

Cpx

Sample coordinates (1 point per grain)

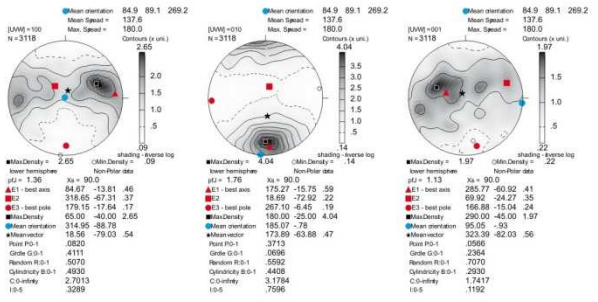

Ol

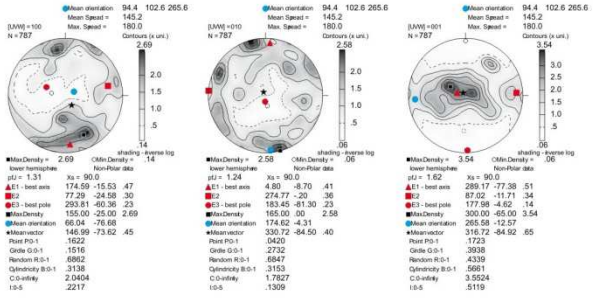

Opx

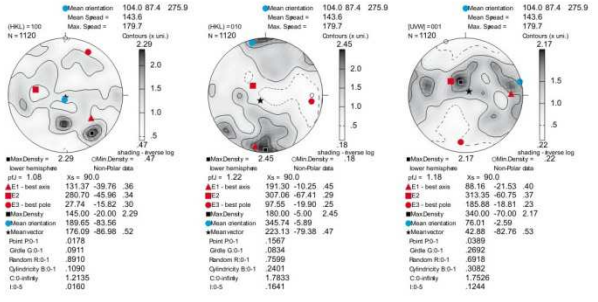

Cpx

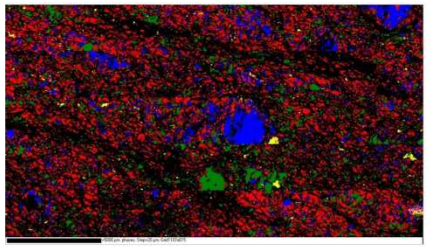

step=20μm

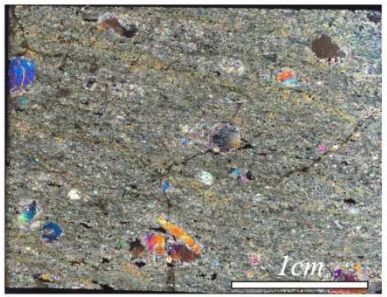

Geographic coordinates (1 point per grain)

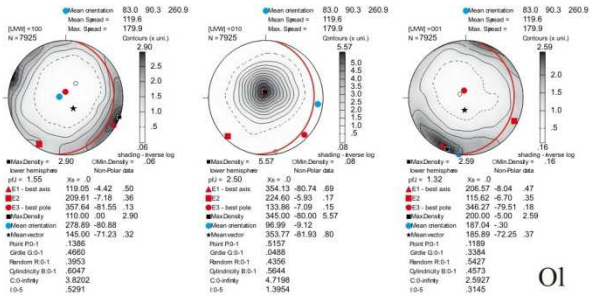

Ol

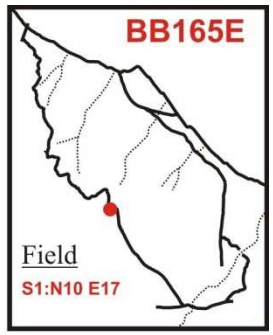

Sample coordinates (raw data)

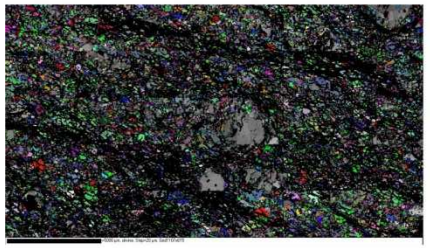

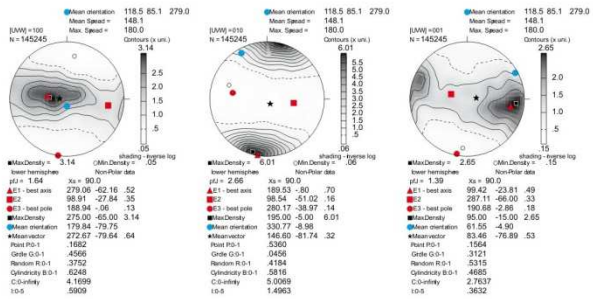

Ol

Sample coordinates (1 point per grain)

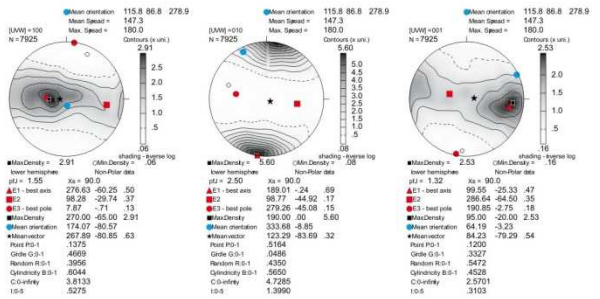

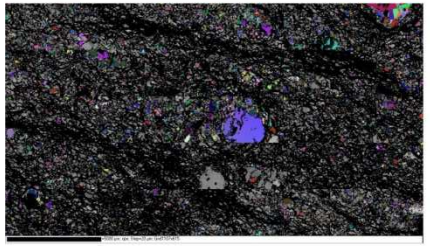

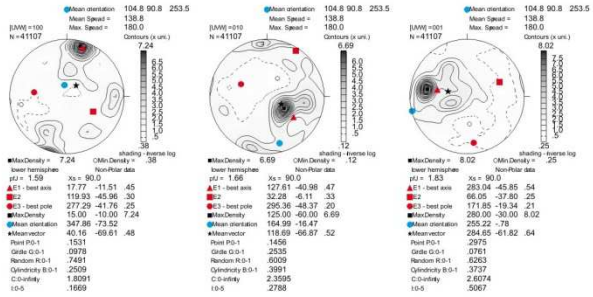

Opx

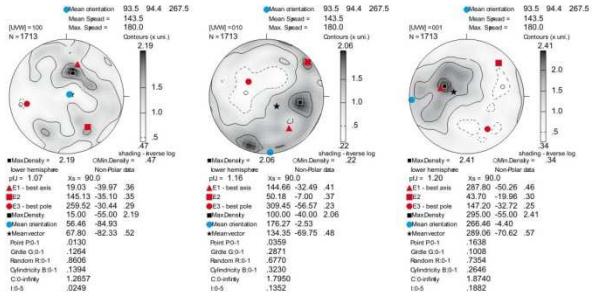

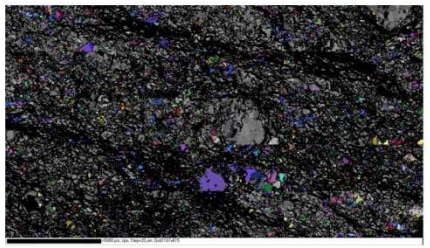

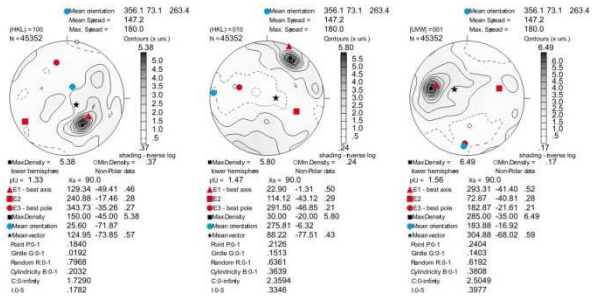

Cpx

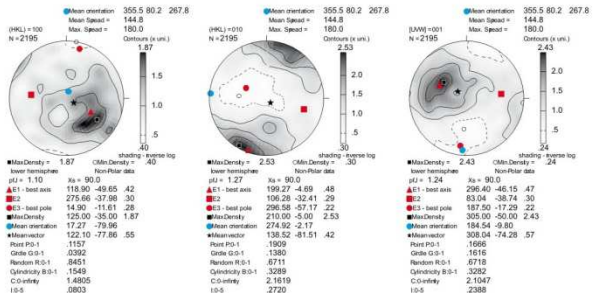

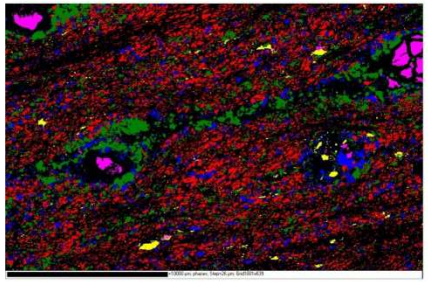

step=26µm

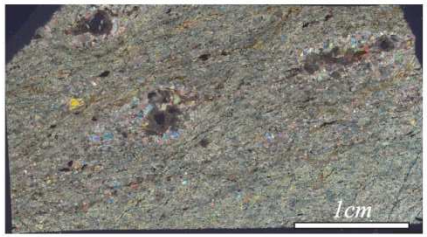

Geographic coordinates (1 point per grain)

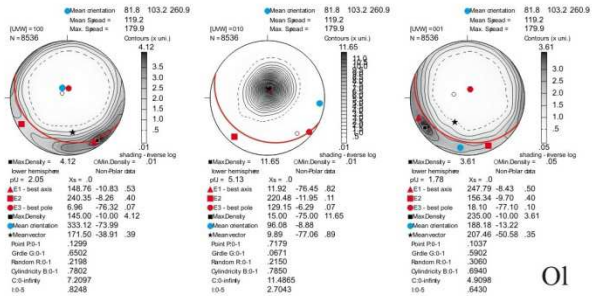

Ol

Sample coordinates (raw data)

Sample coordinates (1 point per grain)

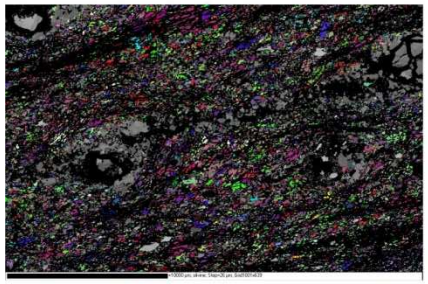

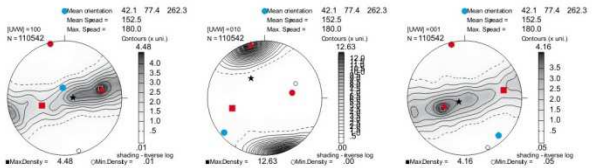

Ol

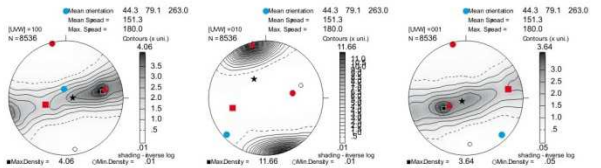

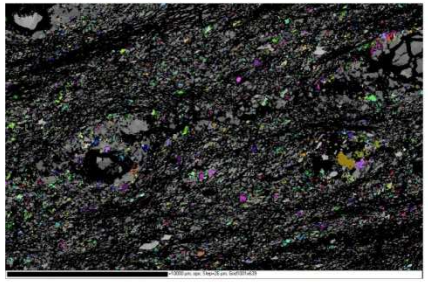

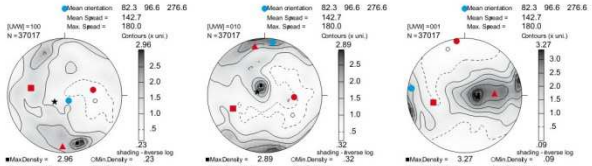

Opx

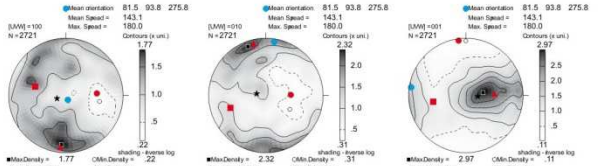

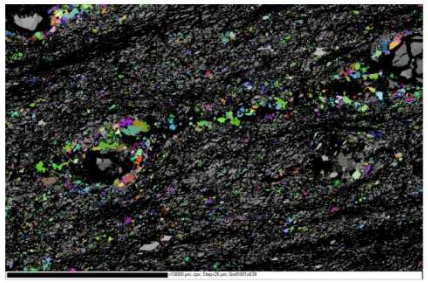

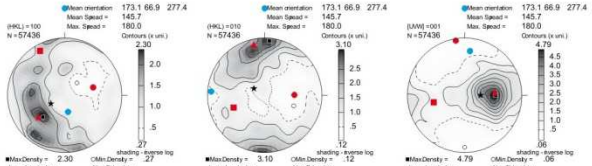

Cpx

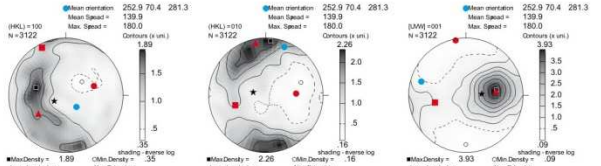

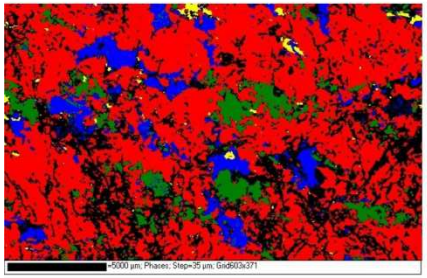

step=35µm

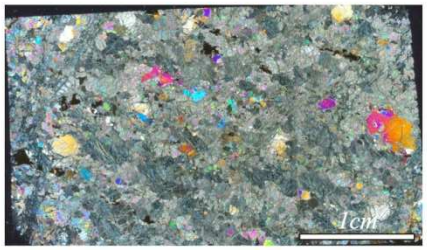

Geographic coordinates (1 point per grain)

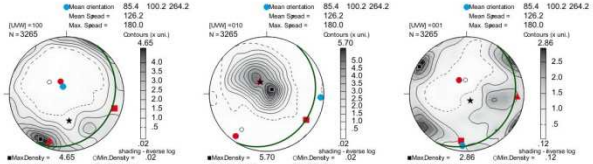

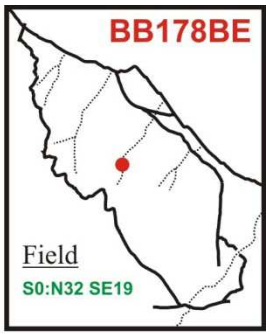

Ol

Sample coordinates (raw data)

Sample coordinates (1 point per grain)

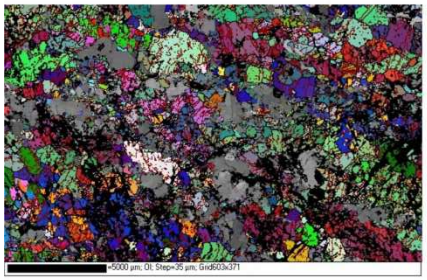

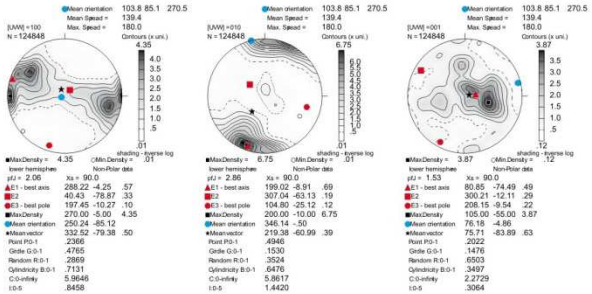

Ol

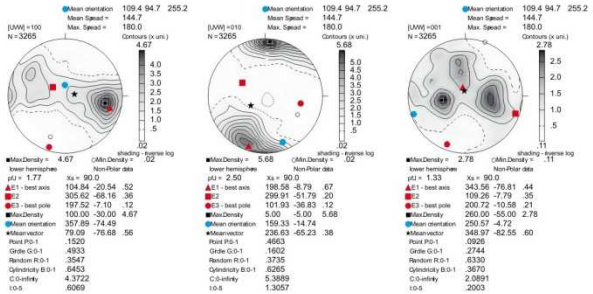

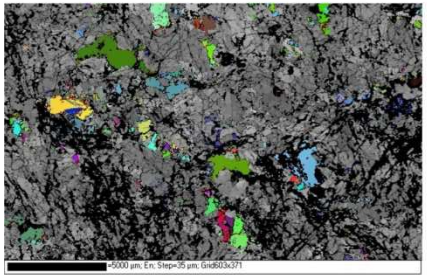

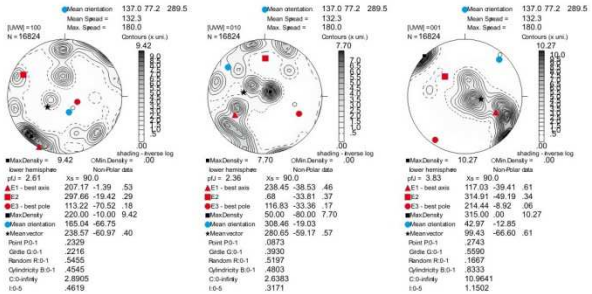

Opx

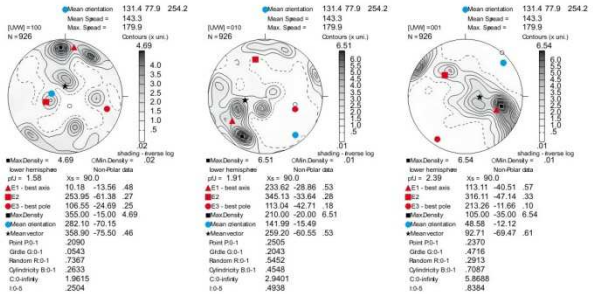

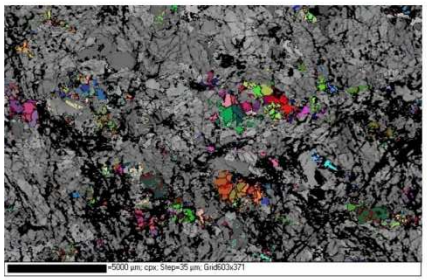

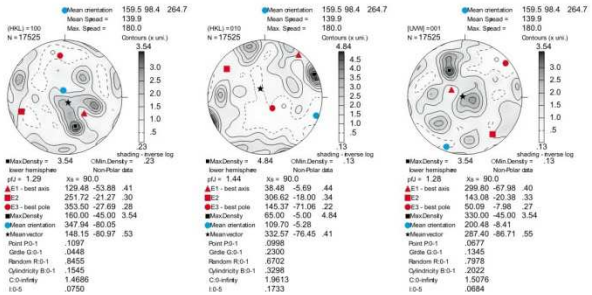

Cpx

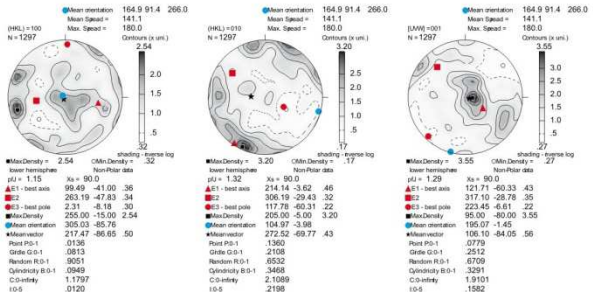

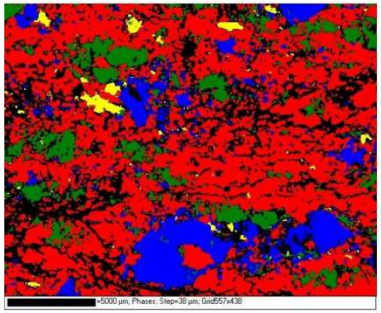

step=38µm

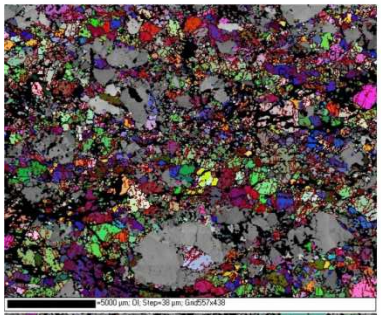

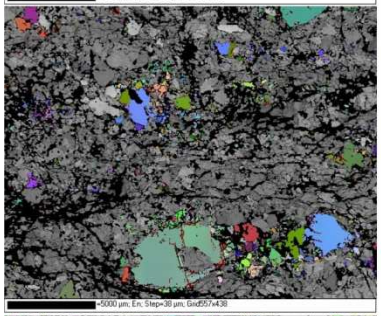

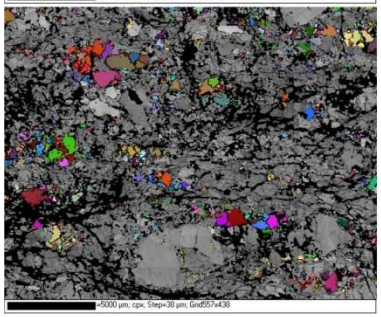

Geographic coordinates (1 point per grain)

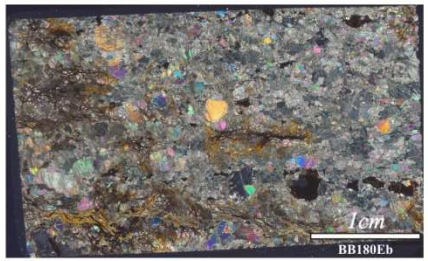

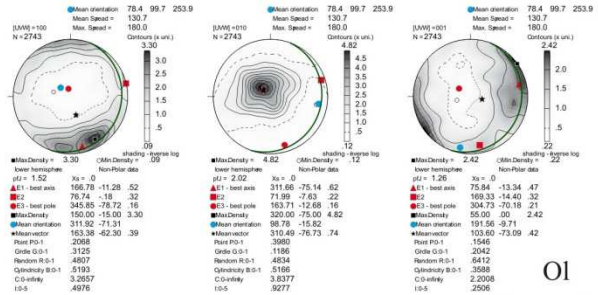

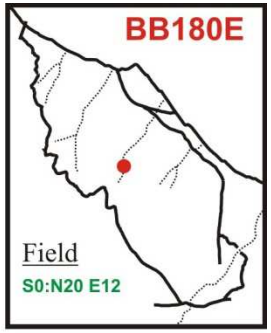

Ol

Sample coordinates (raw data)

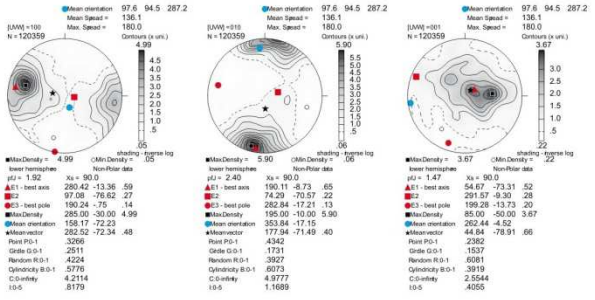

Ol

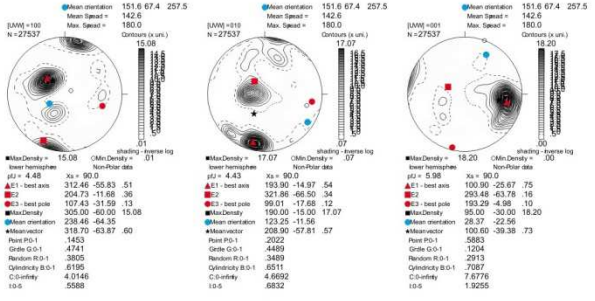

Opx

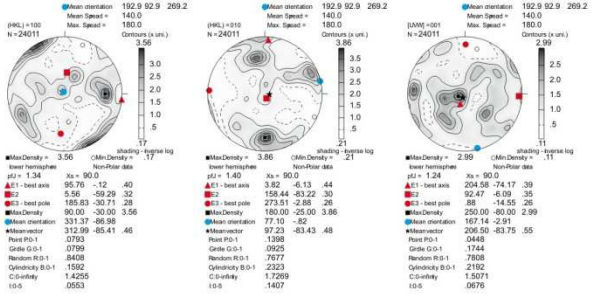

Cpx

Sample coordinates (1 point per grain)

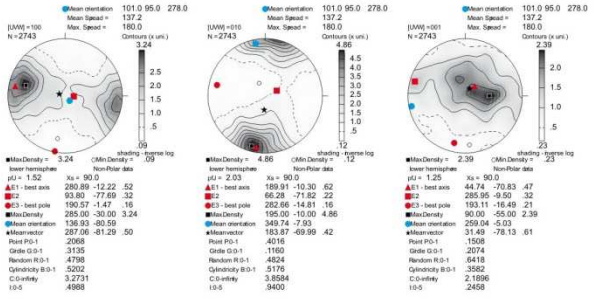

Ol

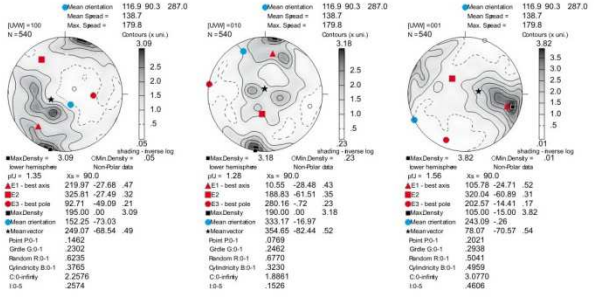

Opx

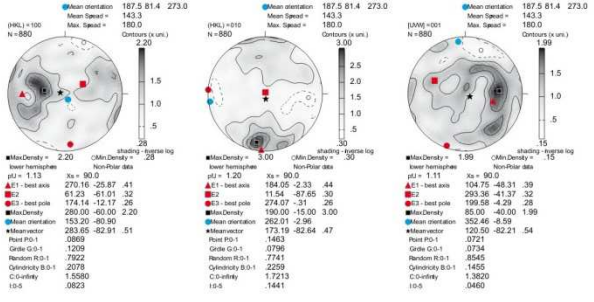

Cpx

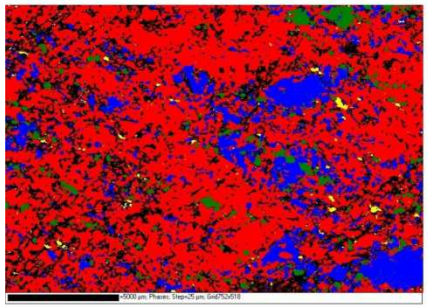

step=25µm

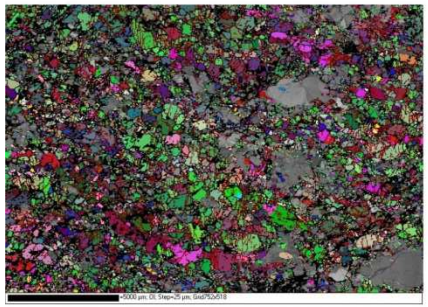

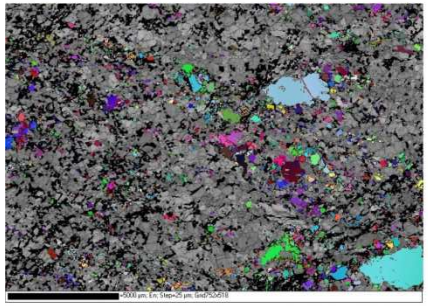

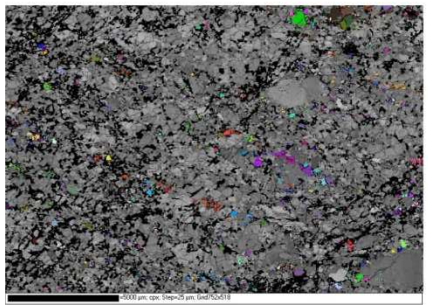

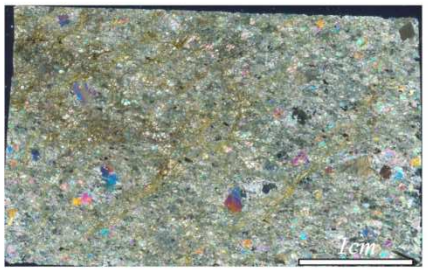

Geographic coordinates (1 point per grain)

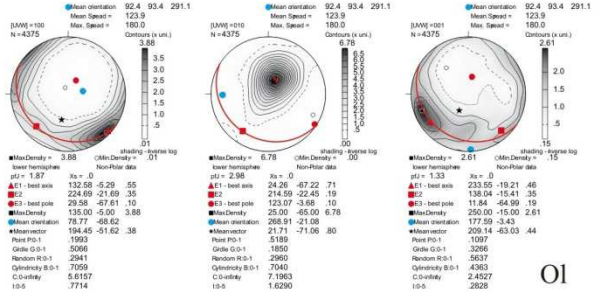

Ol

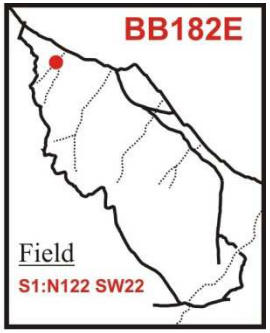

Sample coordinates (raw data)

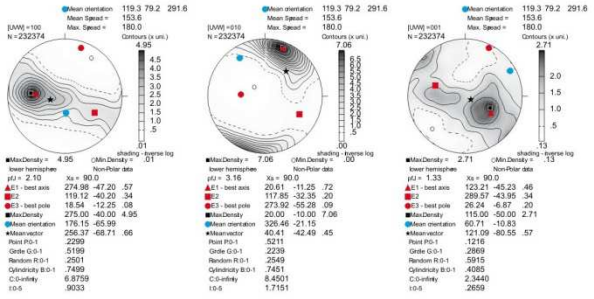

Ol

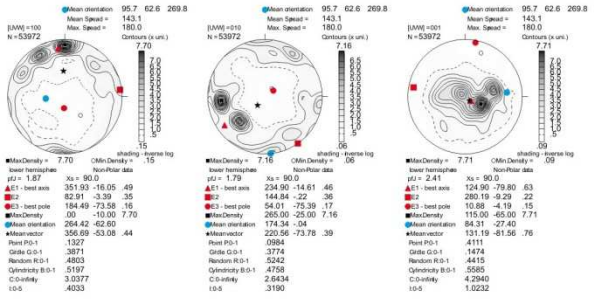

Opx

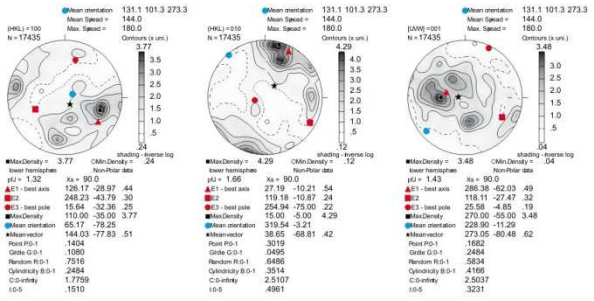

Cpx

Sample coordinates (1 point per grain)

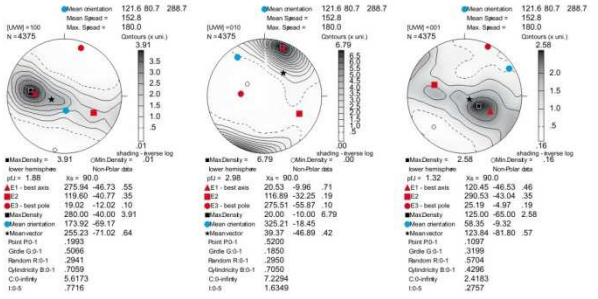

Ol

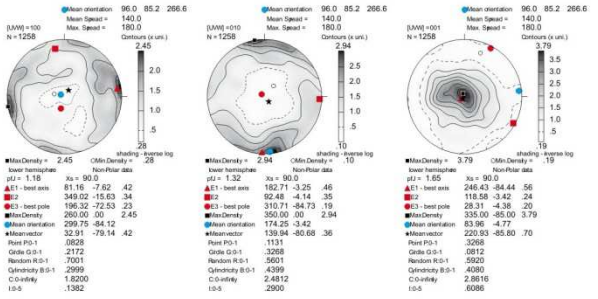

Opx

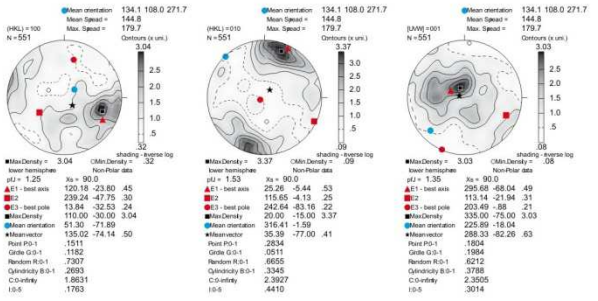

Cpx

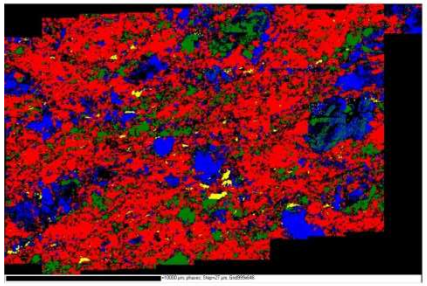

step=27μm

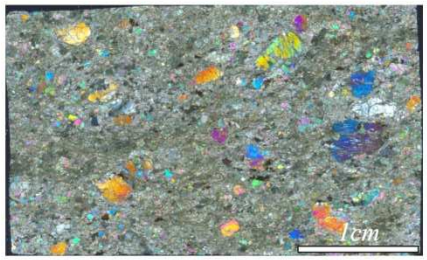

Geographic coordinates (1 point per grain)

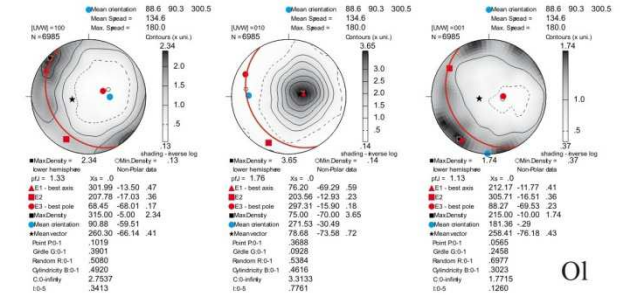

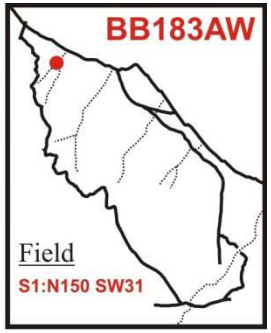

Ol

Sample coordinates (raw data)

Sample coordinates (1 point per grain)

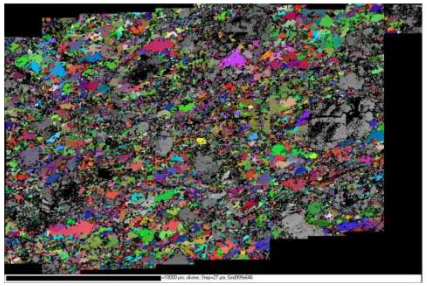

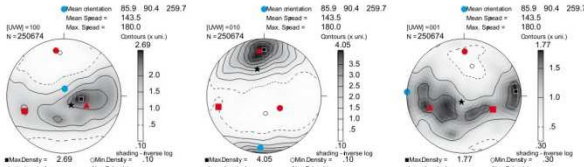

Ol

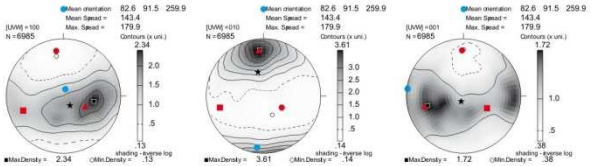

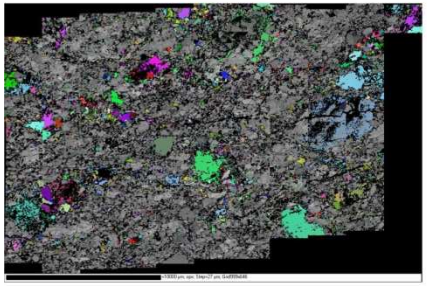

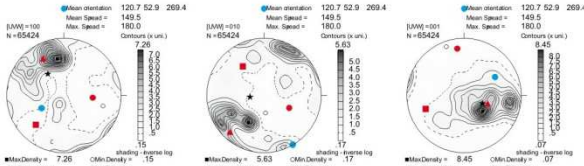

Opx

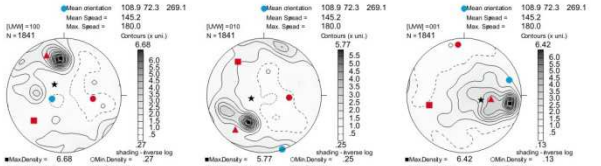

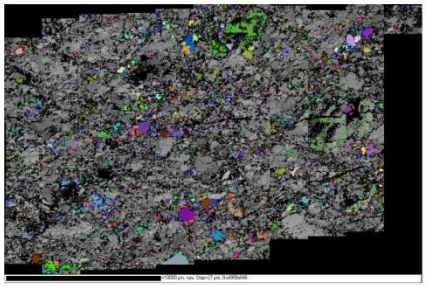

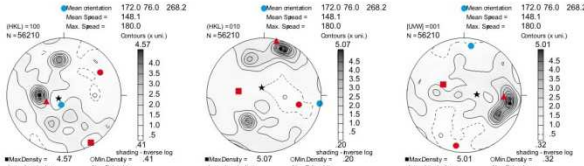

Cpx

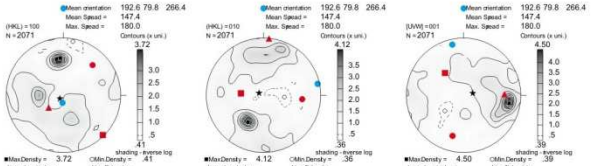

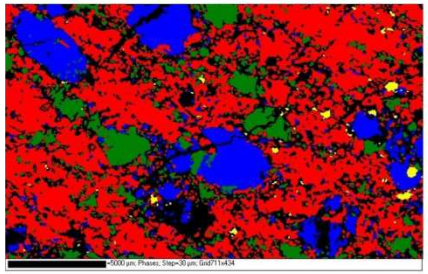

step=30μm

Geographic coordinates (1 point per grain)

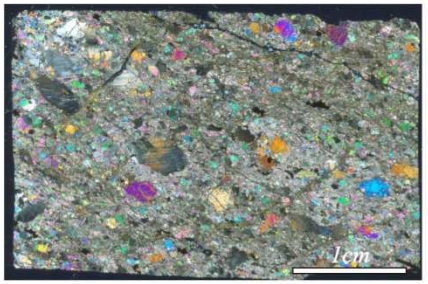

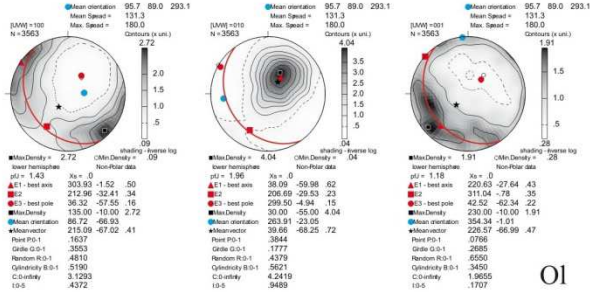

Ol

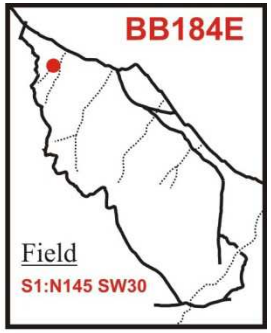

Sample coordinates (raw data)

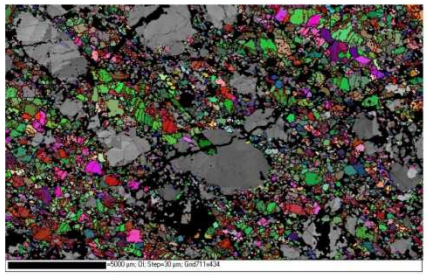

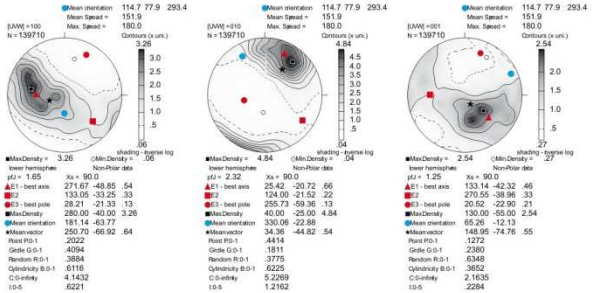

Ol

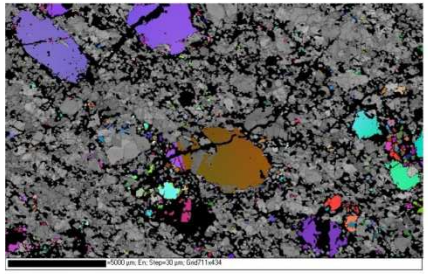

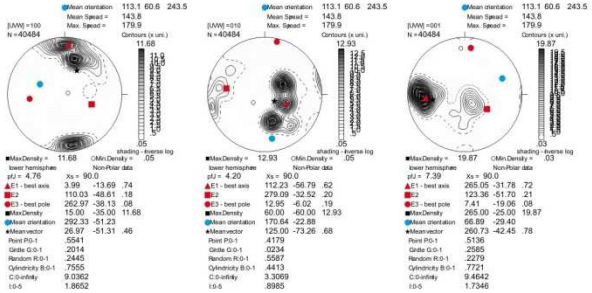

Opx

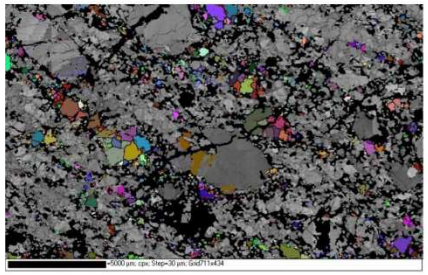

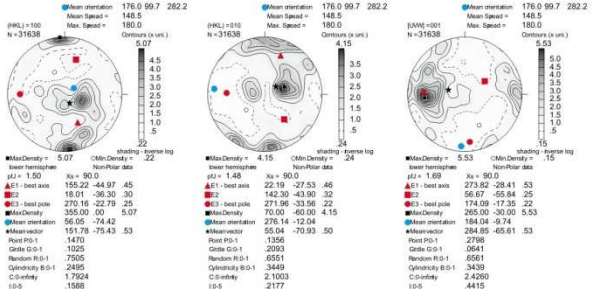

Cpx

Sample coordinates (1 point per grain)

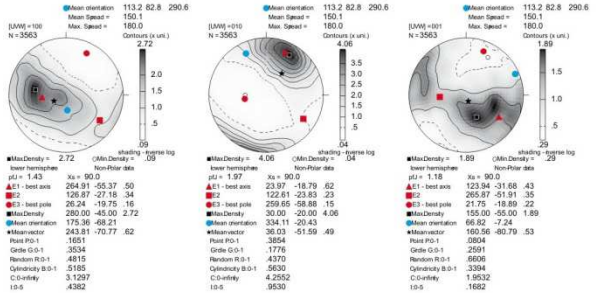

Ol

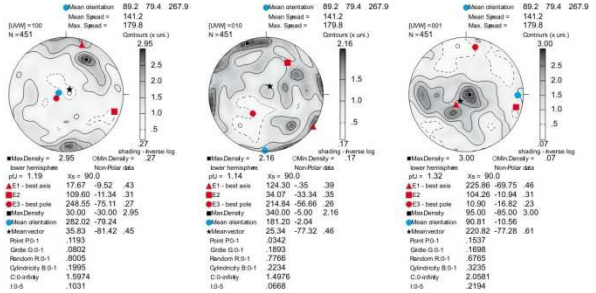

Opx

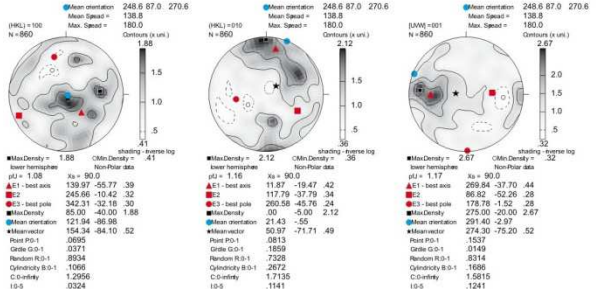

Cpx

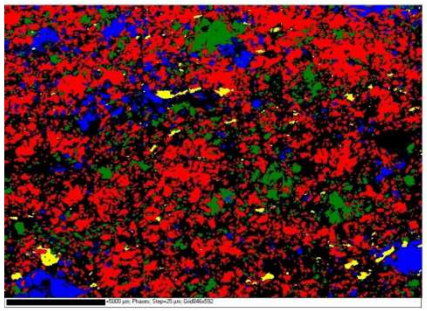

step=25µm

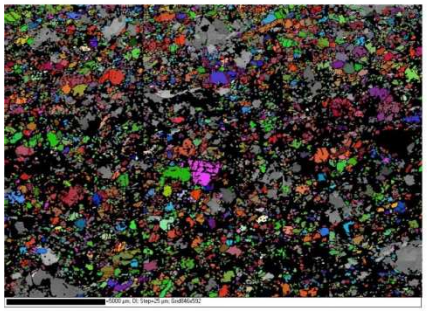

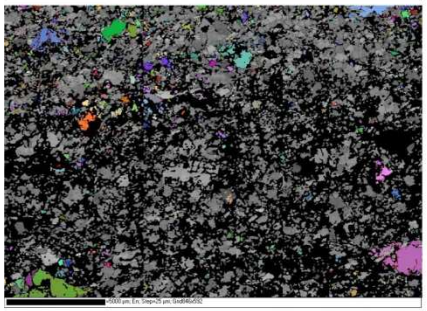

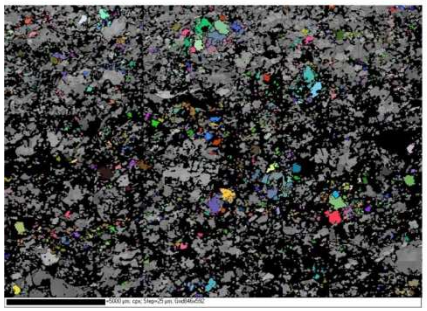

Geographic coordinates (1 point per grain)

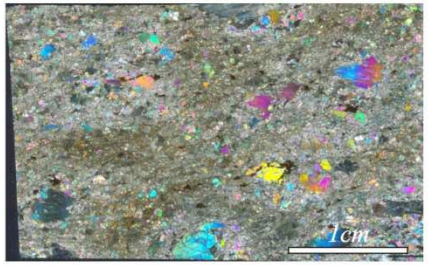

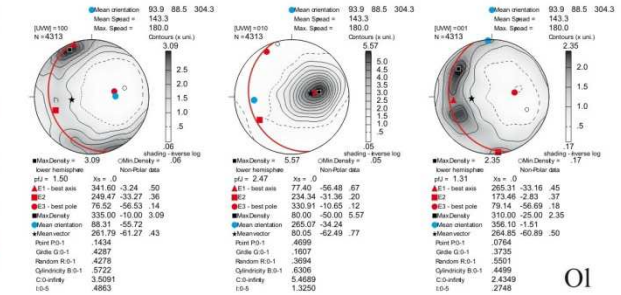

Ol

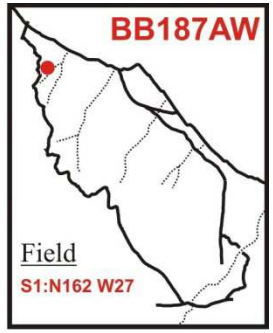

Sample coordinates (raw data)

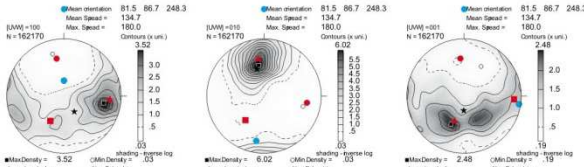

Ol

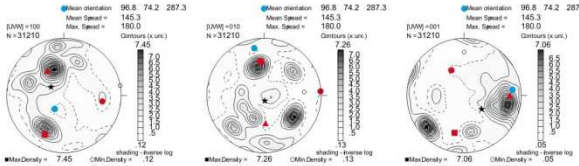

Opx

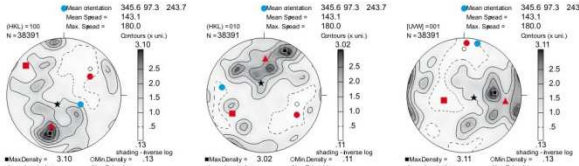

Cpx

Sample coordinates (1 point per grain)

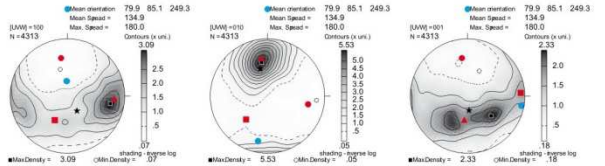

Ol

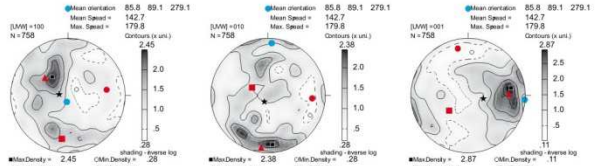

Opx

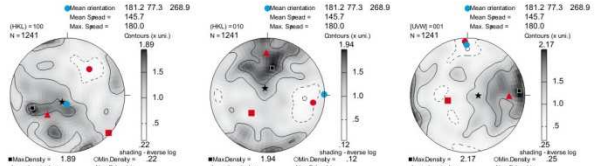

Cpx

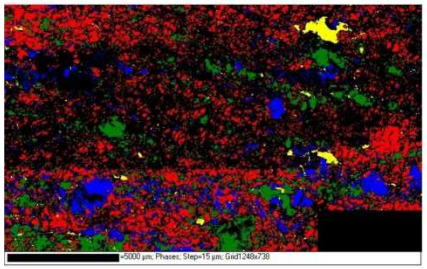

step=15µm

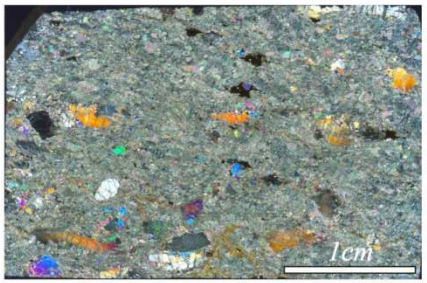

Geographic coordinates (1 point per grain)

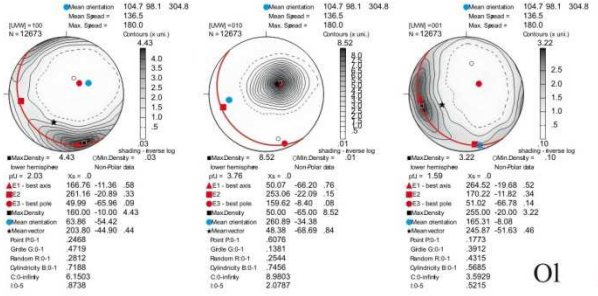

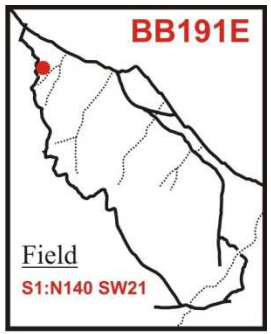

Ol

Sample coordinates (raw data)

Sample coordinates (1 point per grain)

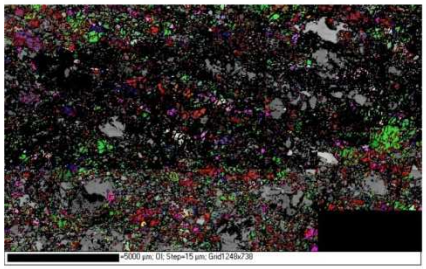

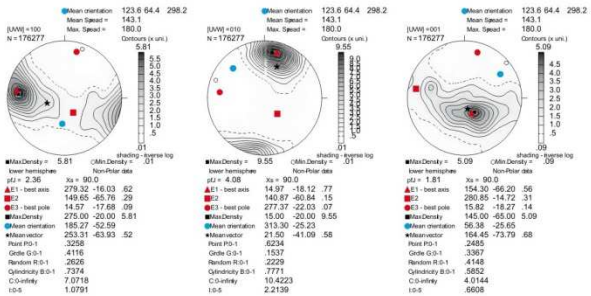

Ol

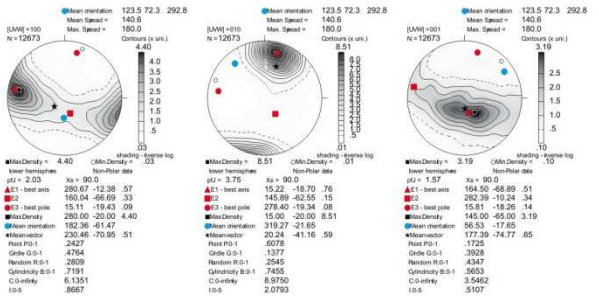

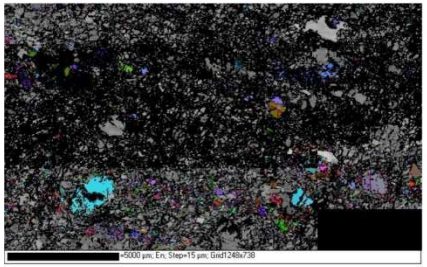

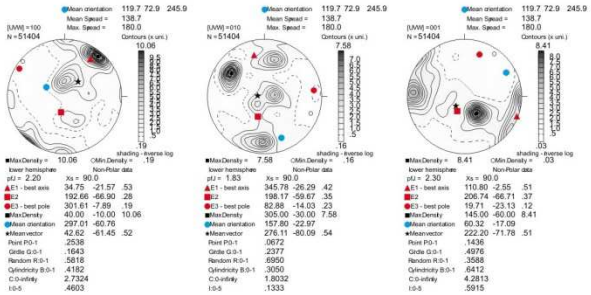

Opx

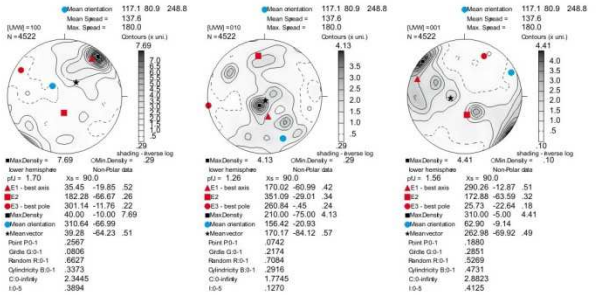

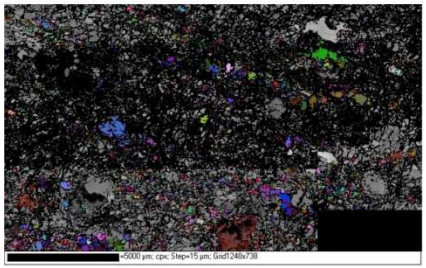

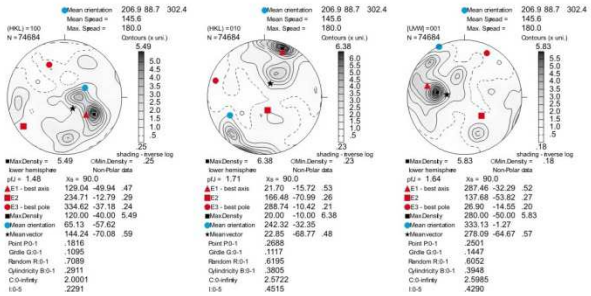

Cpx

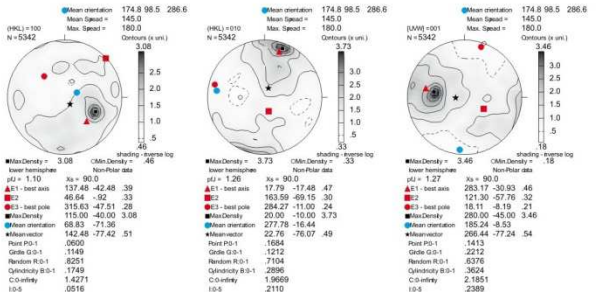

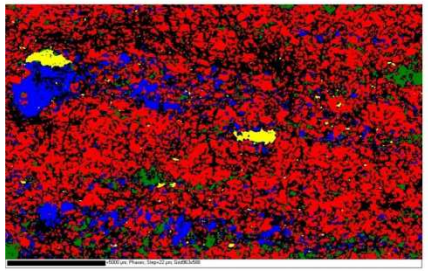

step=22μm

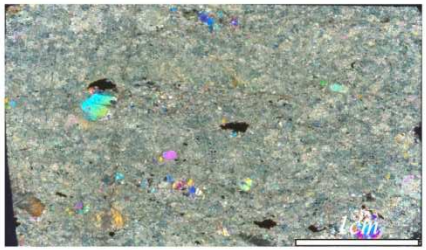

Geographic coordinates (1 point per grain)

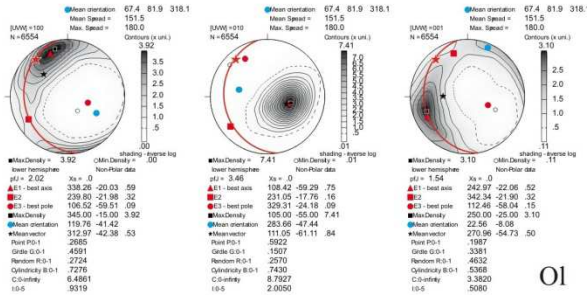

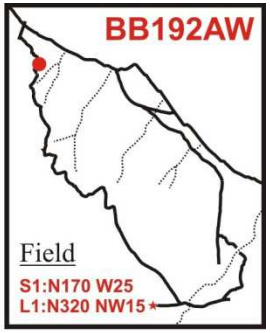

Ol

Sample coordinates (raw data)

Sample coordinates (1 point per grain)

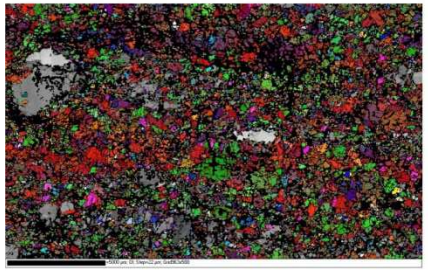

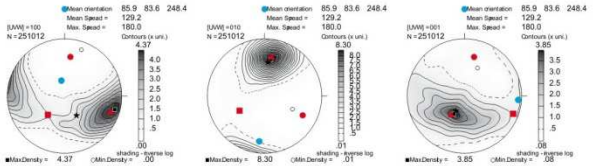

Ol

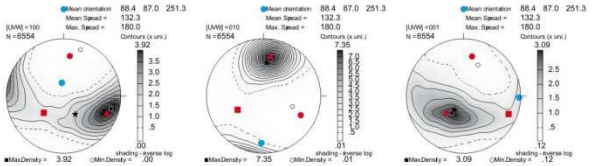

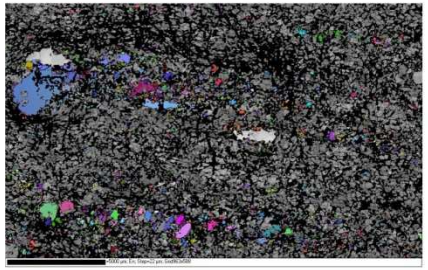

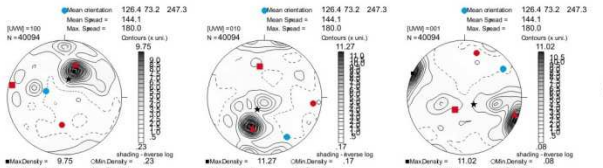

Opx

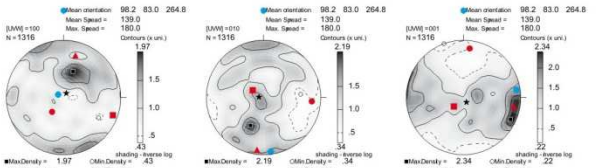

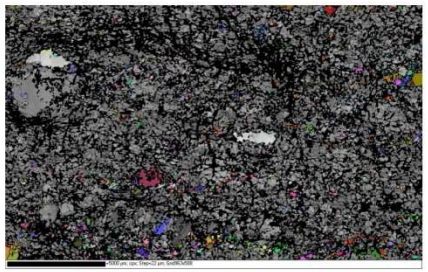

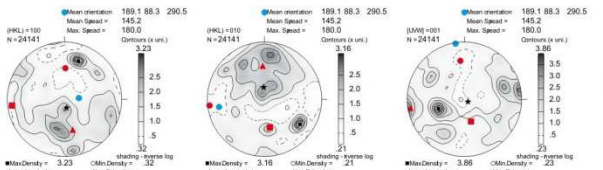

Cpx

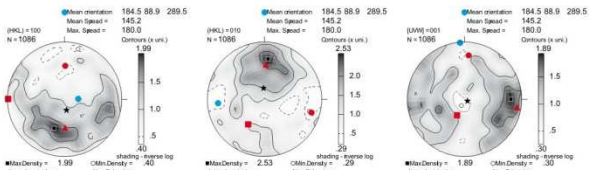

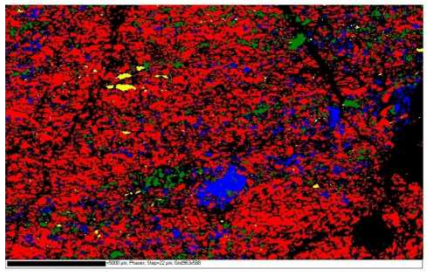

step=22µm

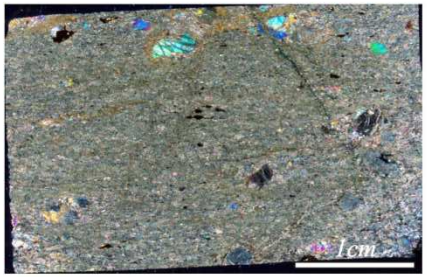

Geographic coordinates (1 point per grain)

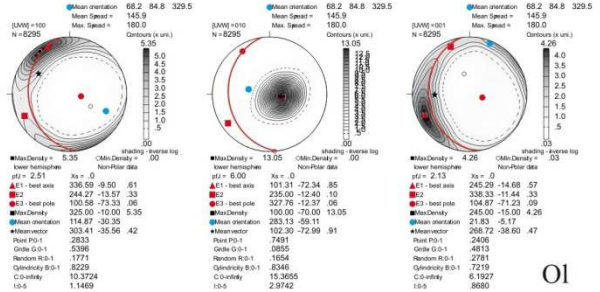

Ol

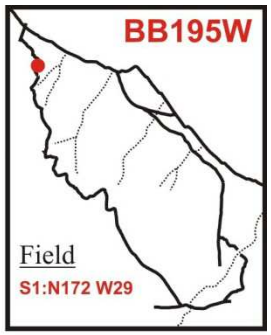

Sample coordinates (raw data)

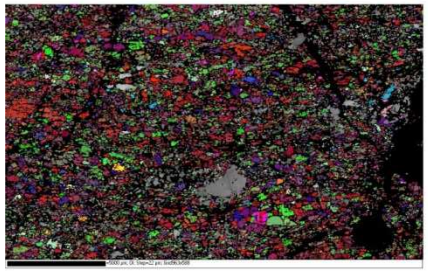

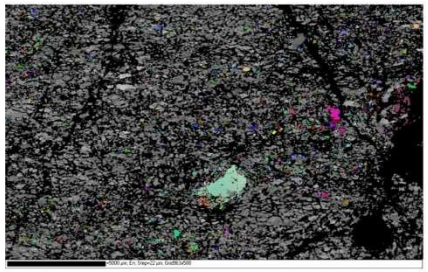

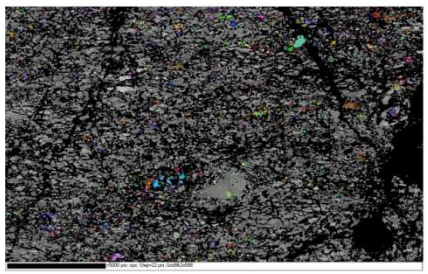

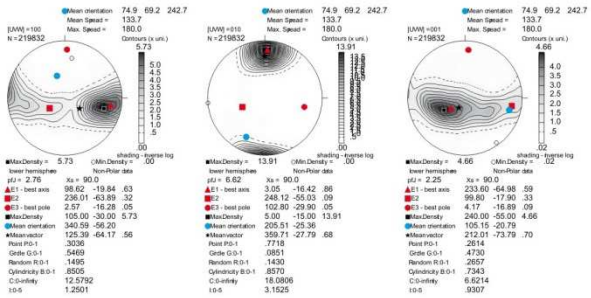

Ol

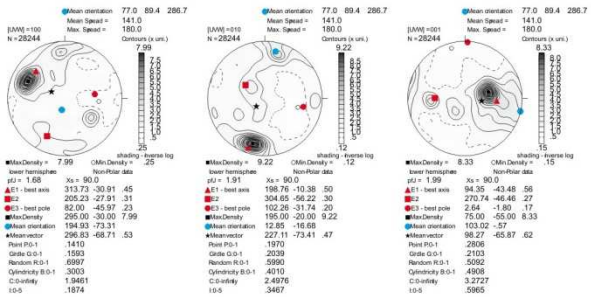

Opx

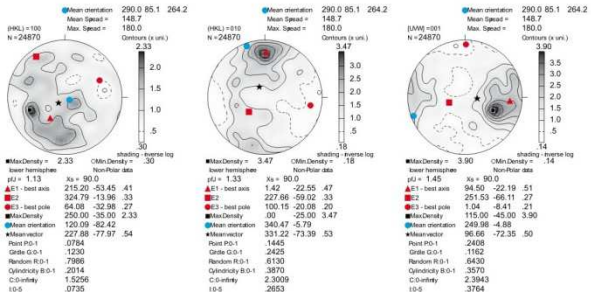

Cpx

Sample coordinates (1 point per grain)

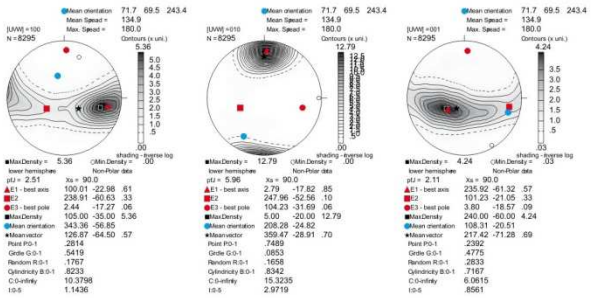

Ol

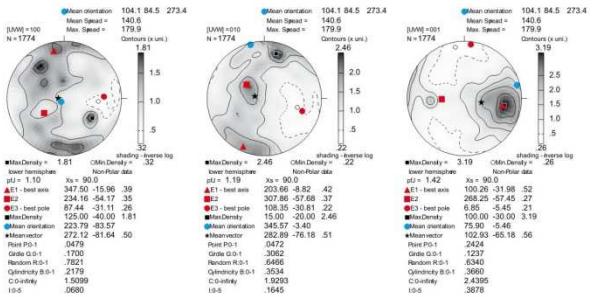

Opx

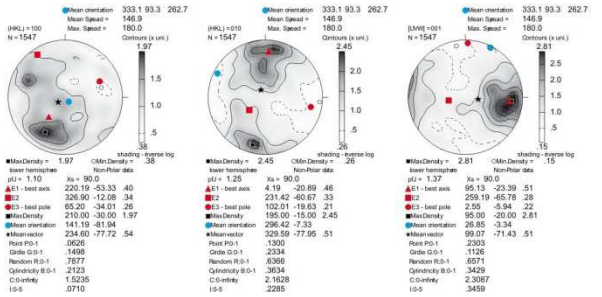

Cpx

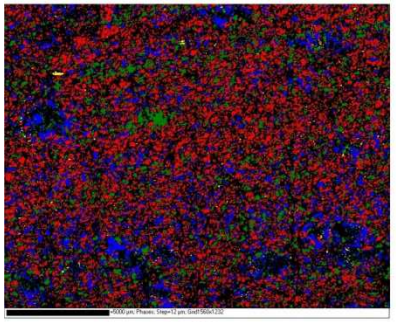

step=12µm

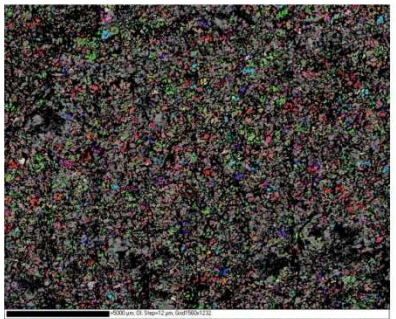

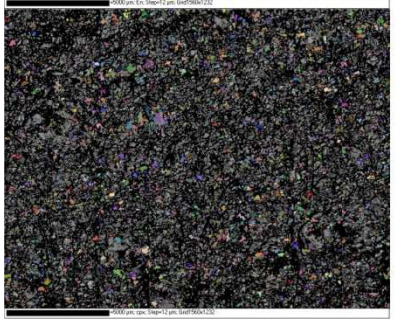

Geographic coordinates (1 point per grain)

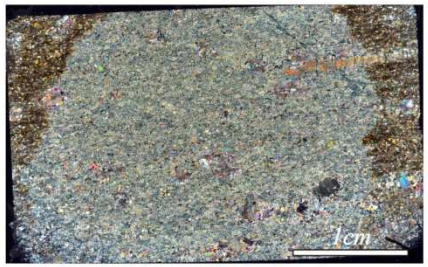

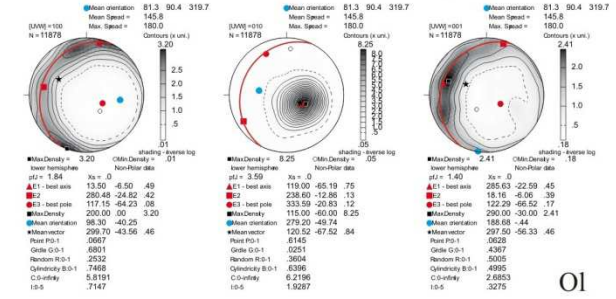

Ol

Sample coordinates (raw data)

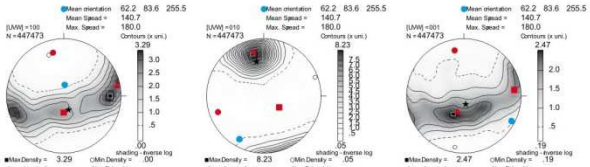

Ol

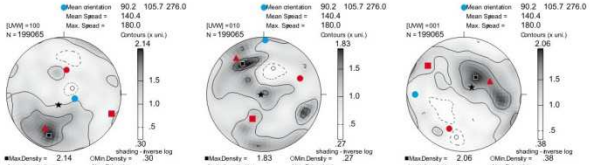

Opx

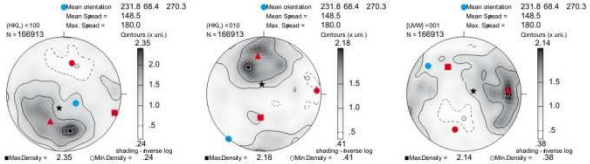

Cpx

Sample coordinates (1 point per grain)

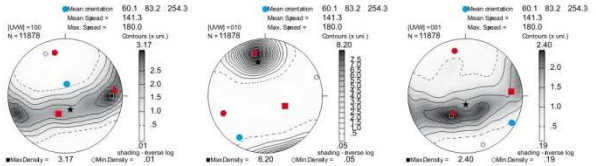

Ol

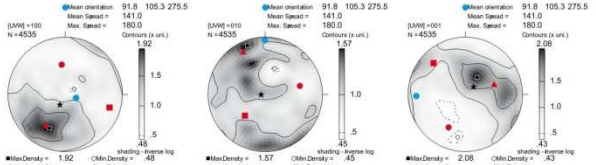

Opx

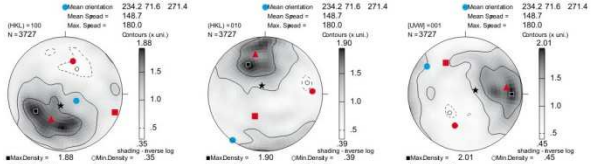

Cpx

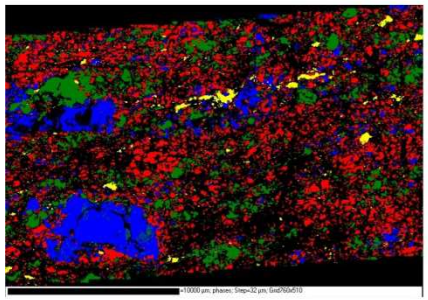

step=32µm

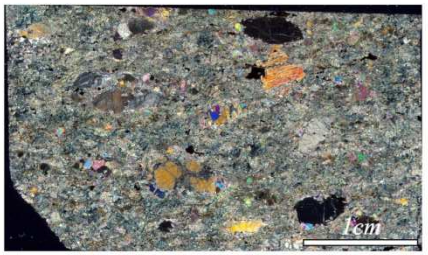

Geographic coordinates (1 point per grain)

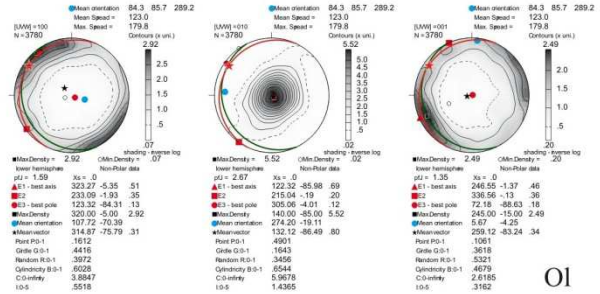

Ol

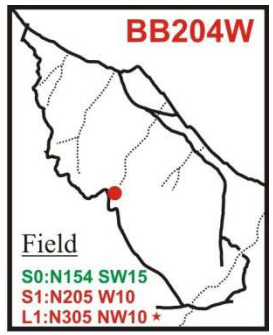

Sample coordinates (raw data)

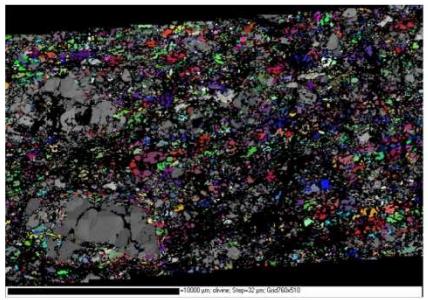

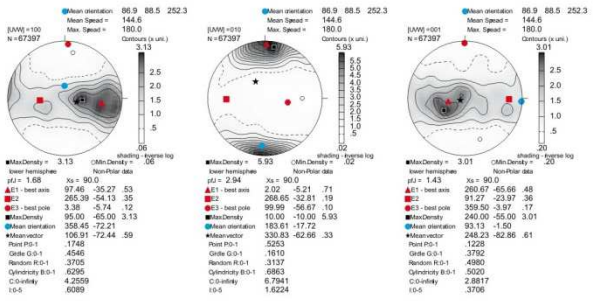

Ol

Sample coordinates (1 point per grain)

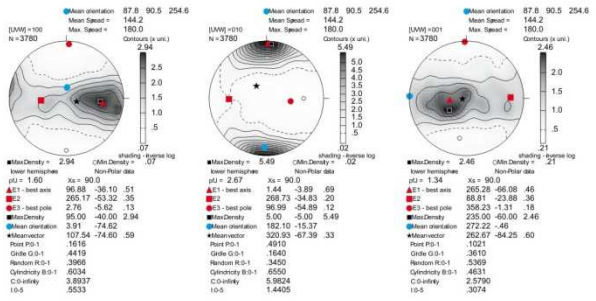

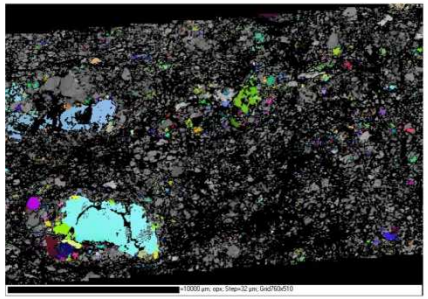

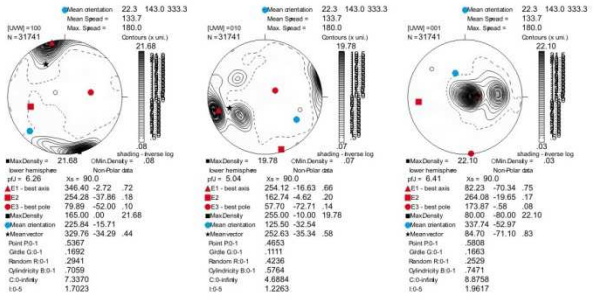

Opx

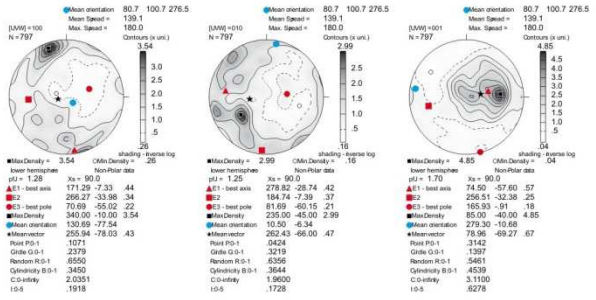

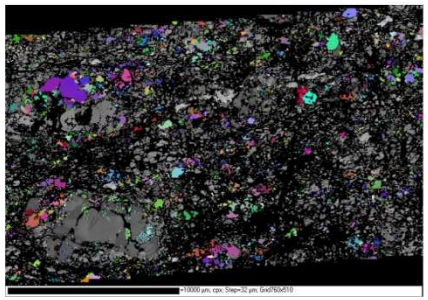

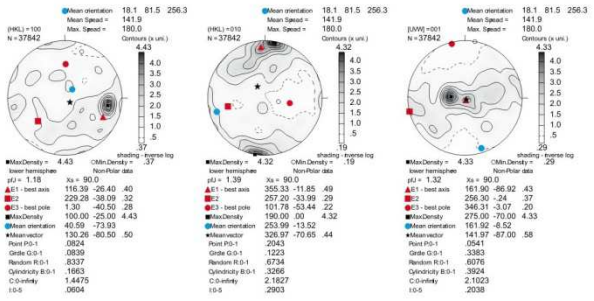

Cpx

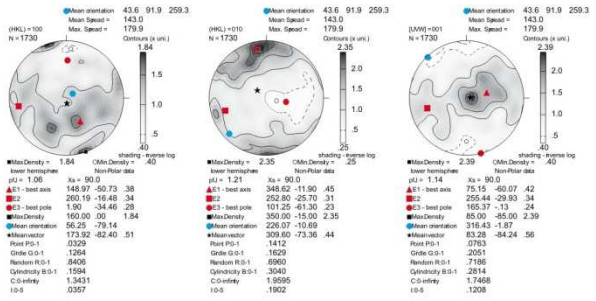

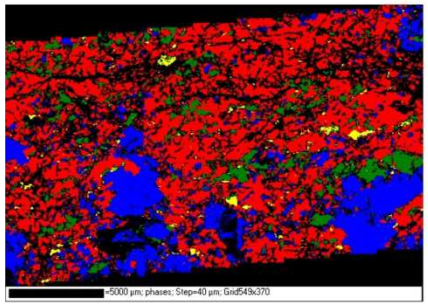

step=40µm

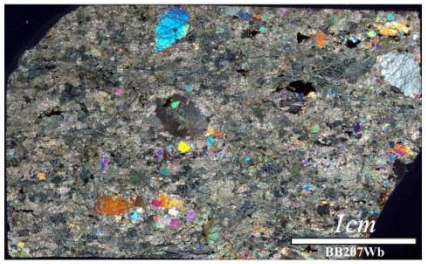

Geographic coordinates (1 point per grain)

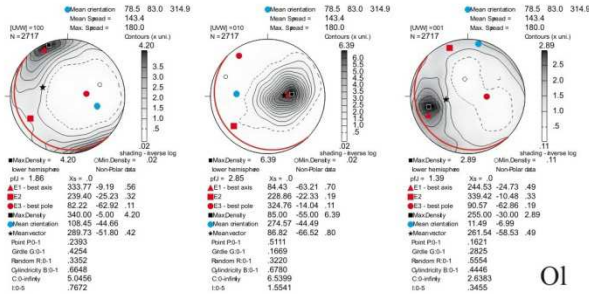

Ol

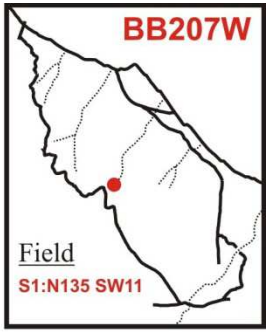

Sample coordinates (raw data)

Sample coordinates (1 point per grain)

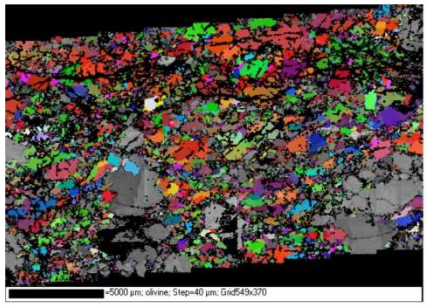

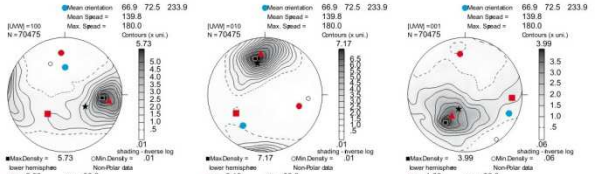

Ol

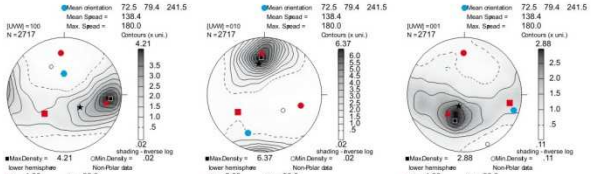

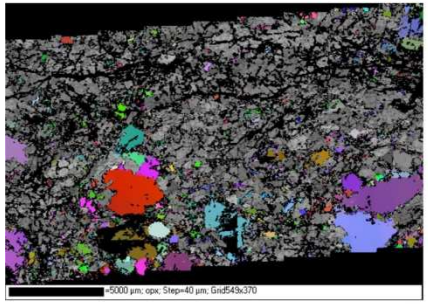

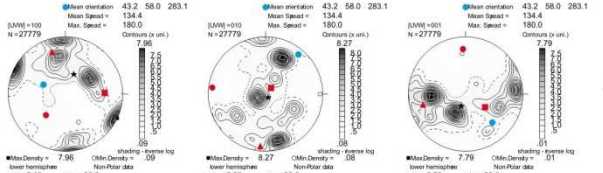

Opx

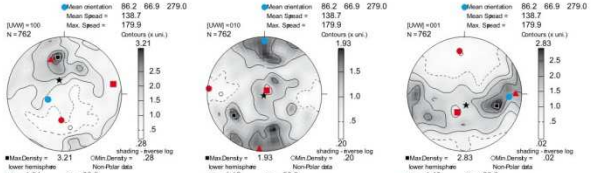

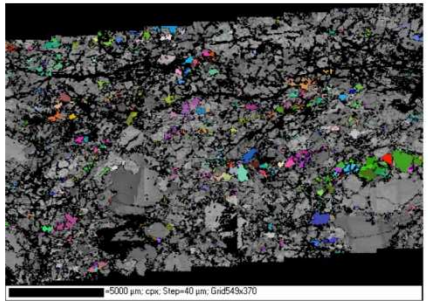

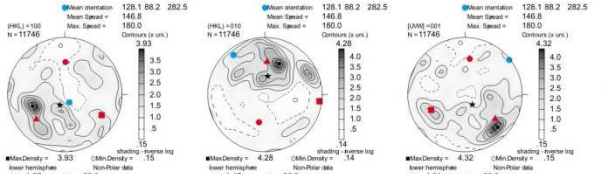

Cpx

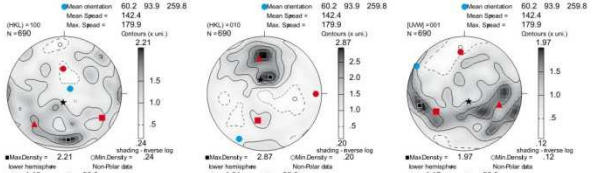

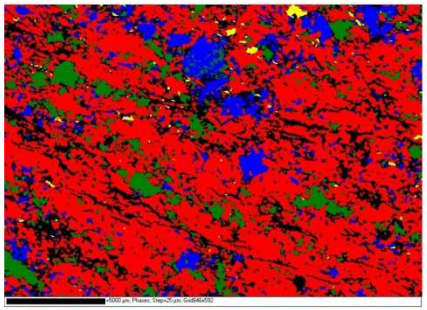

step=25µm

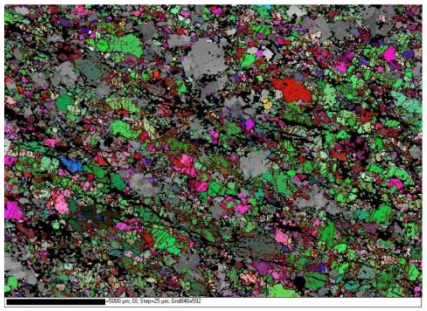

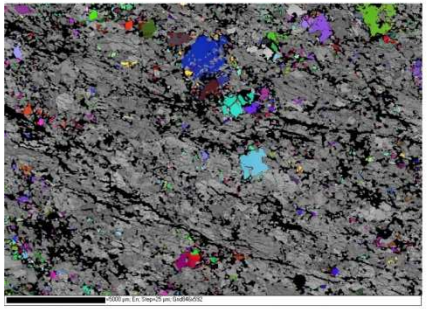

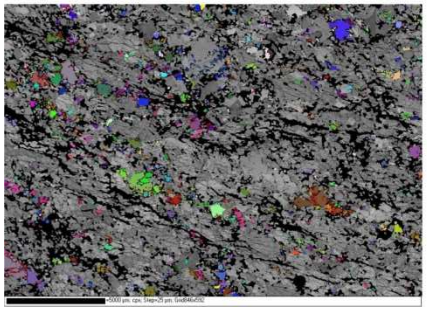

Geographic coordinates (1 point per grain)

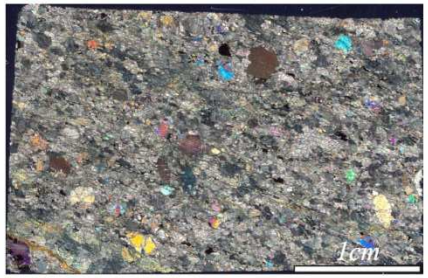

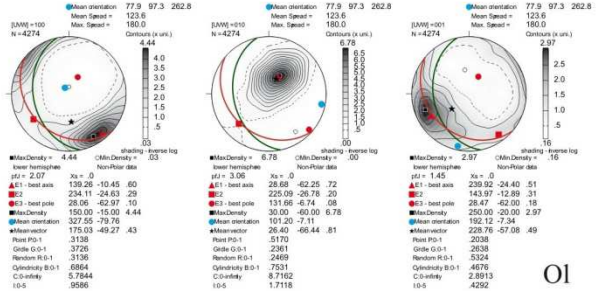

Ol

Sample coordinates (raw data)

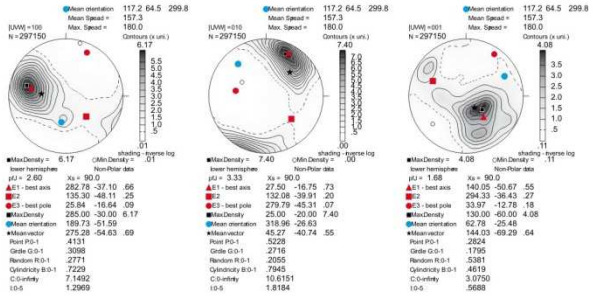

Ol

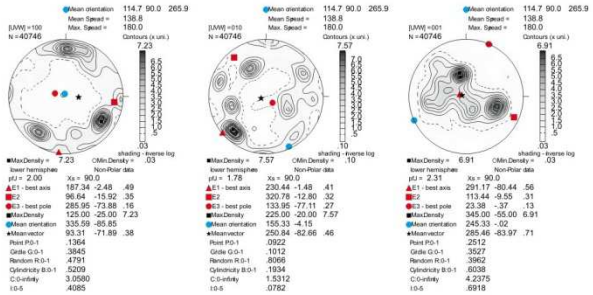

Opx

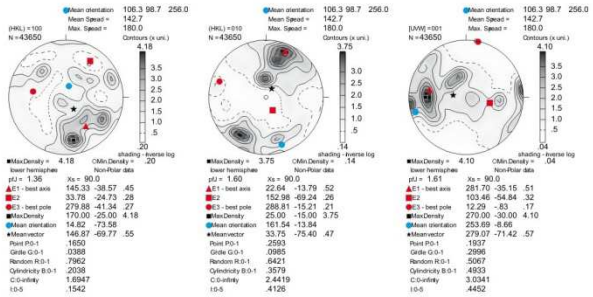

Cpx

Sample coordinates (1 point per grain)

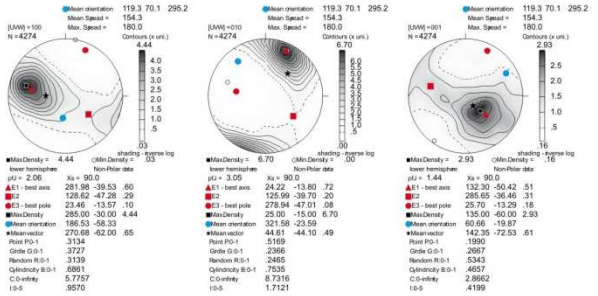

Ol

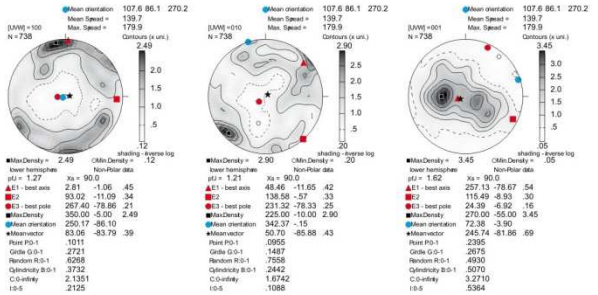

Opx

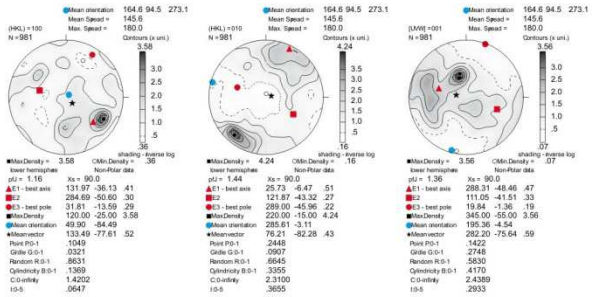

Cpx

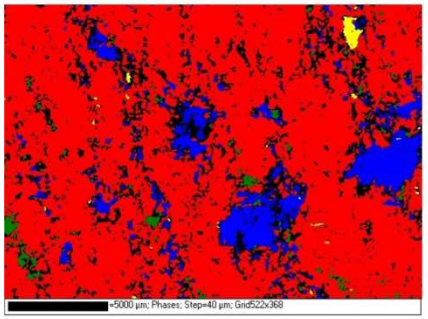

step=40µm

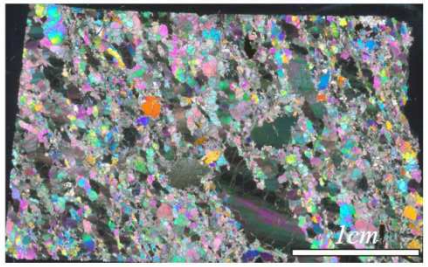

Geographic coordinates (1 point per grain)

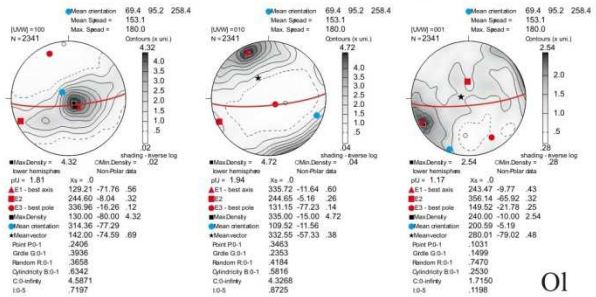

Ol

Sample coordinates (raw data)

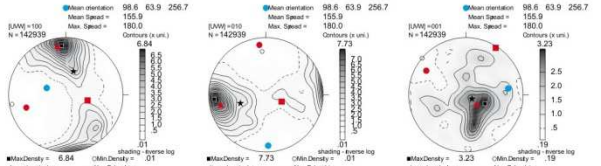

Ol

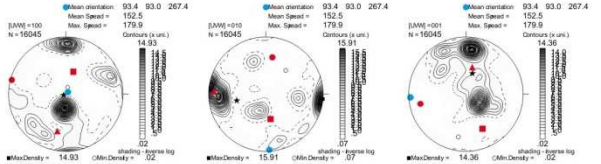

Opx

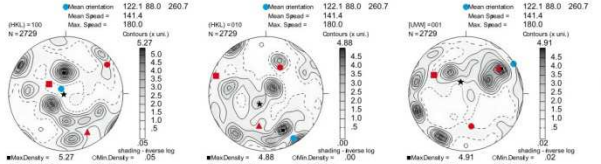

Cpx

Sample coordinates (1 point per grain)

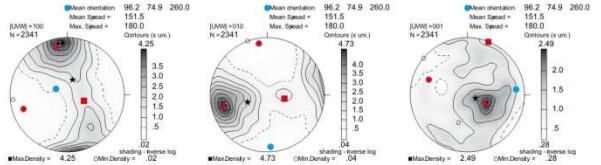

Ol

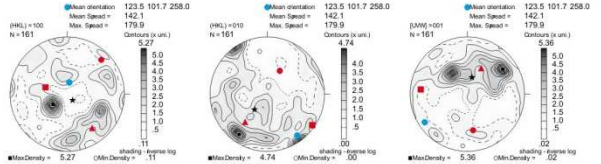

Opx

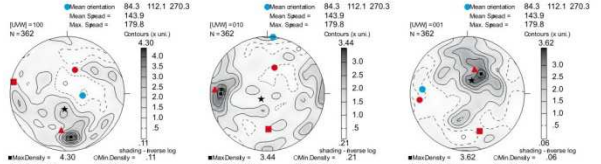

Cpx

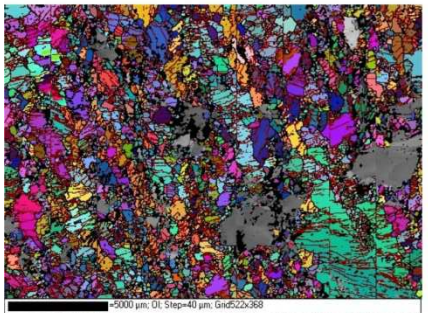

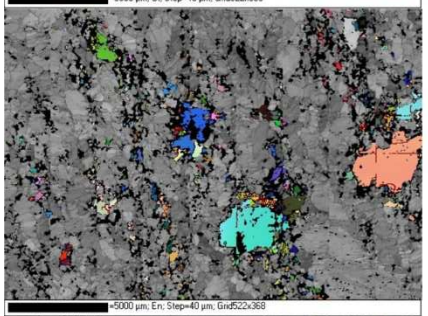

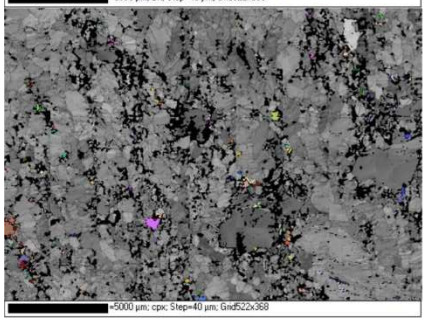

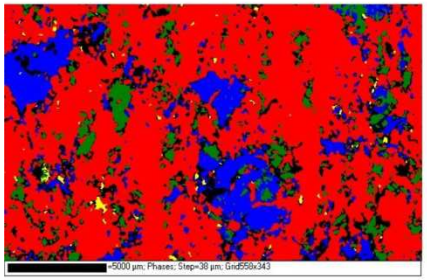

step=38µm

Geographic coordinates (1 point per grain)

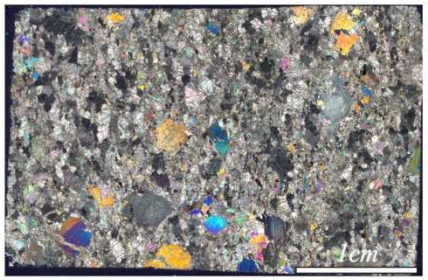

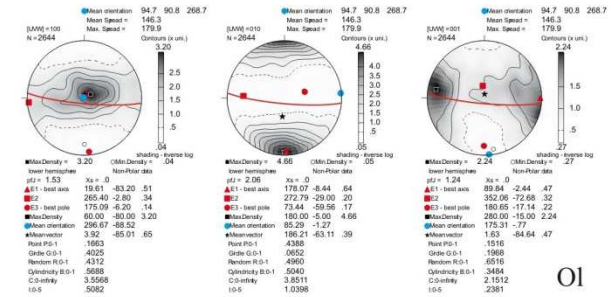

Ol

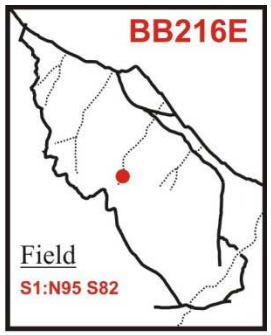

Sample coordinates (raw data)

Sample coordinates (1 point per grain)

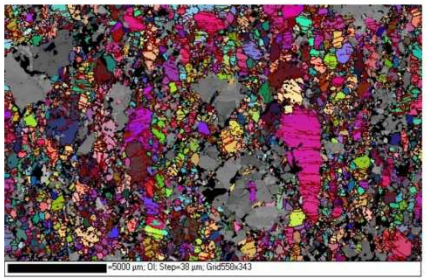

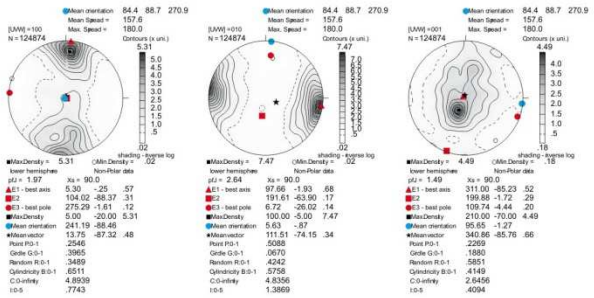

Ol

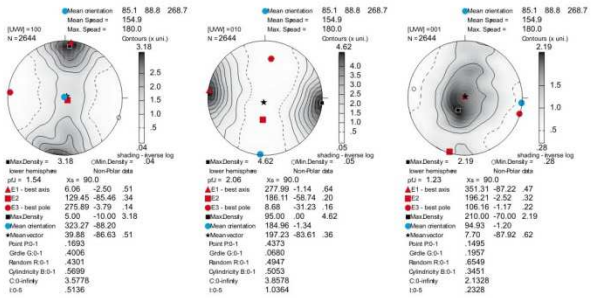

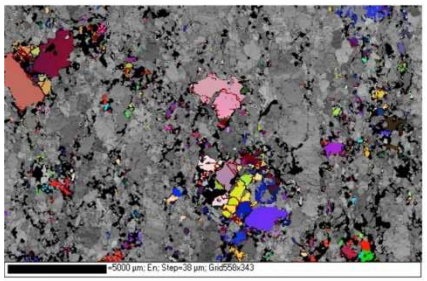

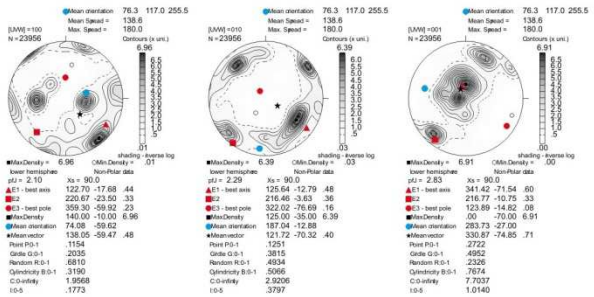

Opx

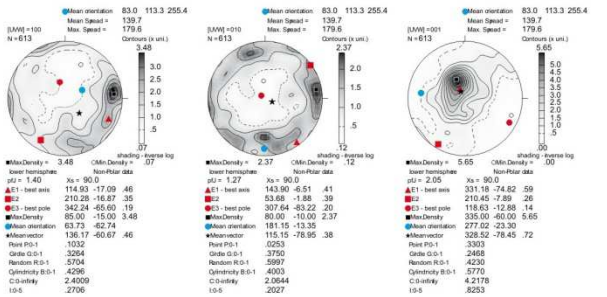

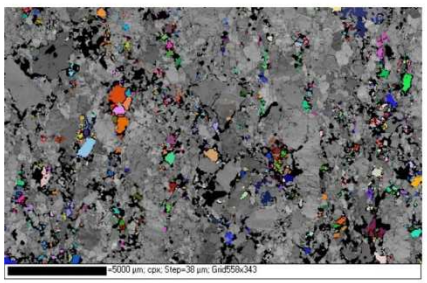

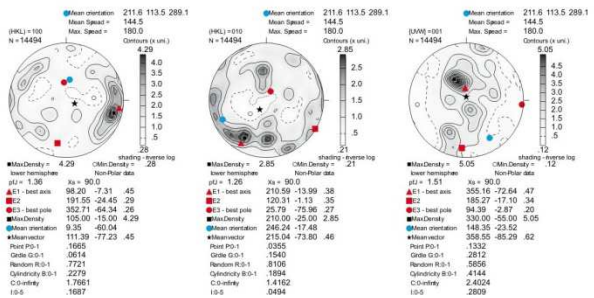

Cpx

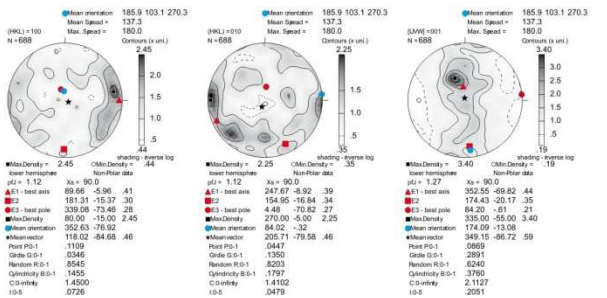

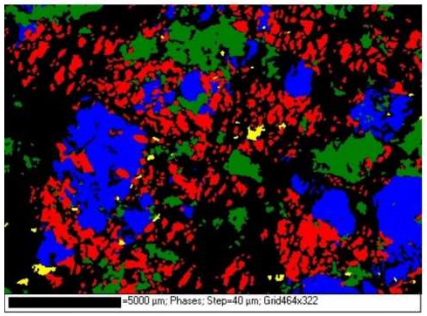

step=40µm

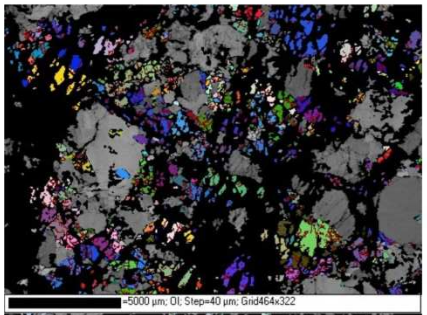

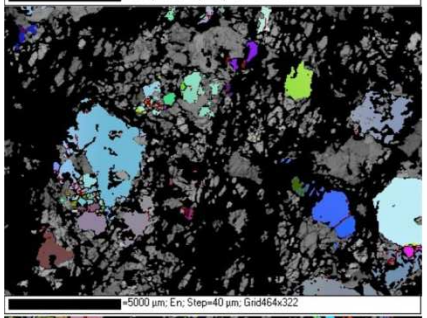

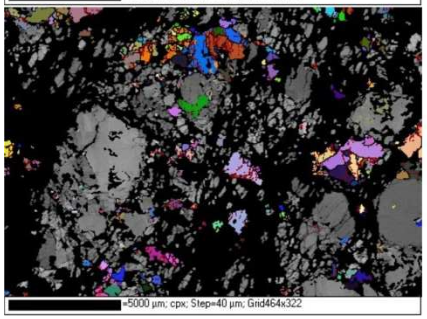

Geographic coordinates (1 point per grain)

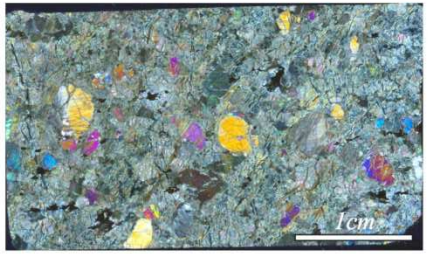

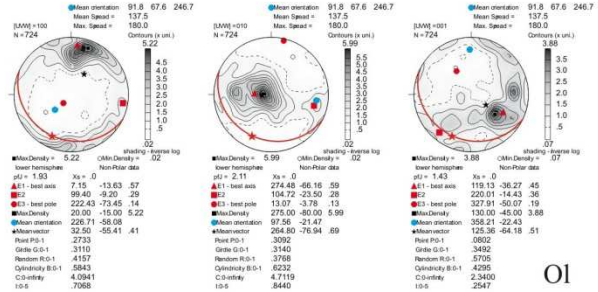

Ol

Sample coordinates (raw data)

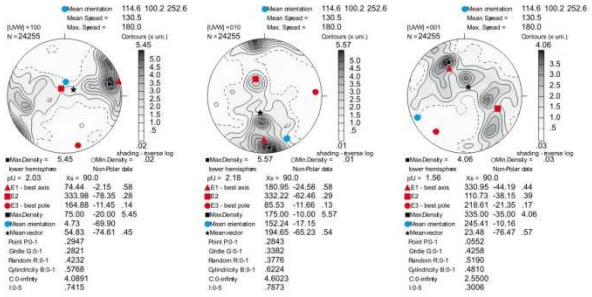

Ol

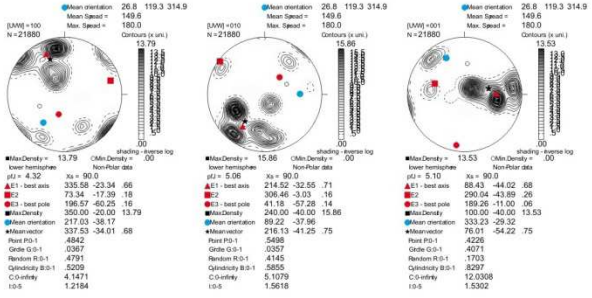

Opx

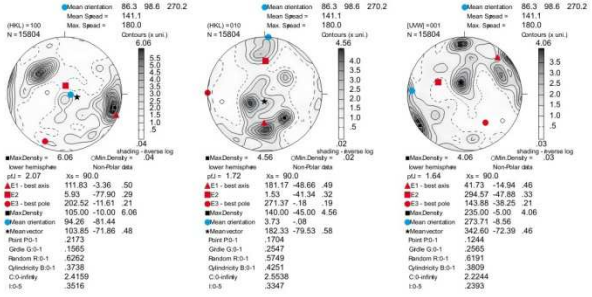

Cpx

Sample coordinates (1 point per grain)

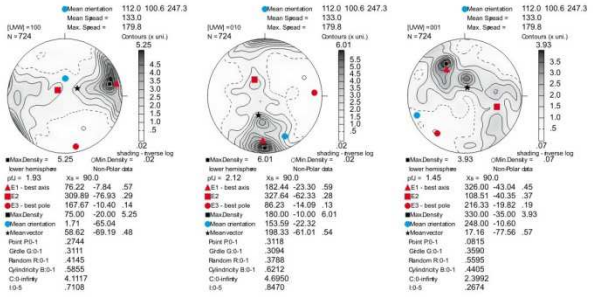

Ol

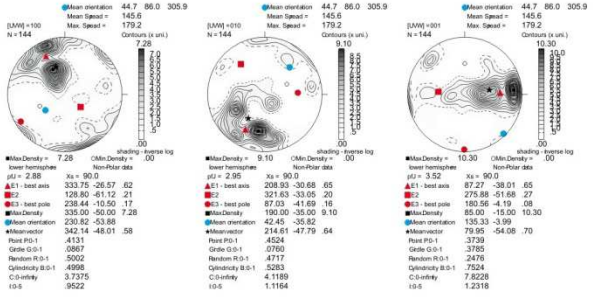

Opx

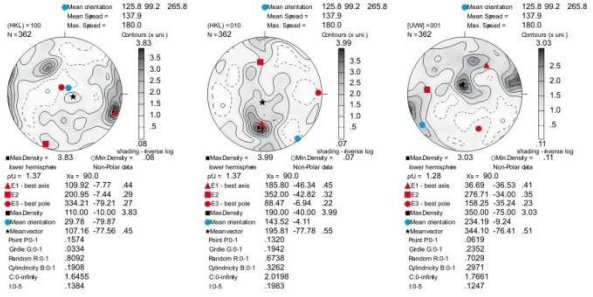

Cpx

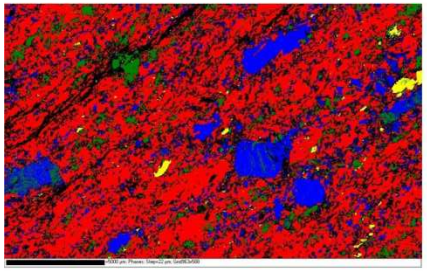

step=22µm

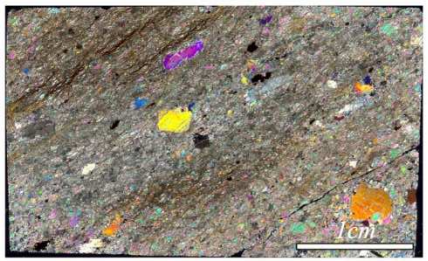

Geographic coordinates (1 point per grain)

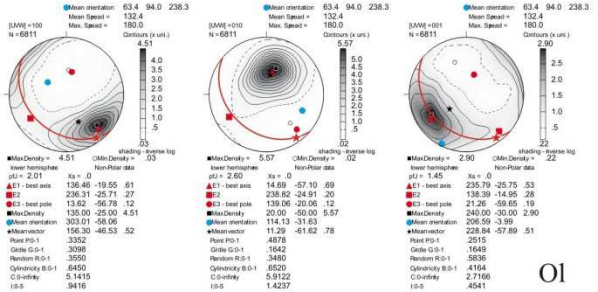

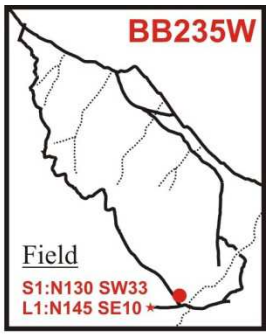

Ol

Sample coordinates (raw data)

Sample coordinates (1 point per grain)

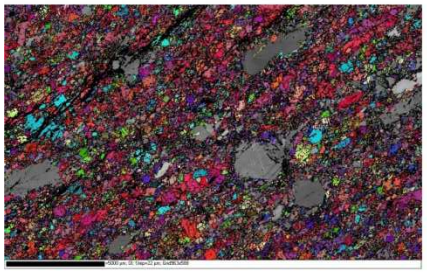

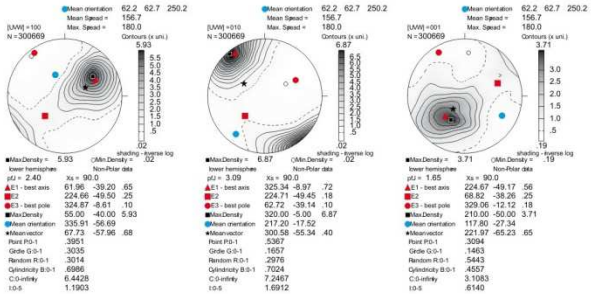

Ol

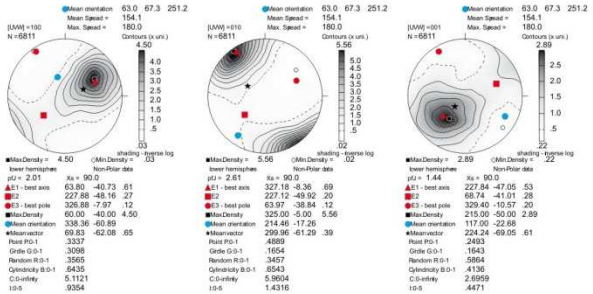

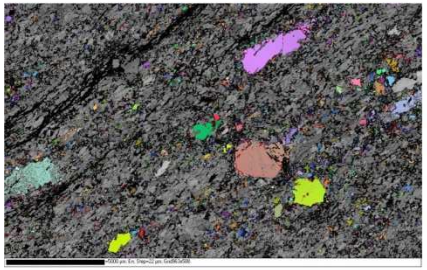

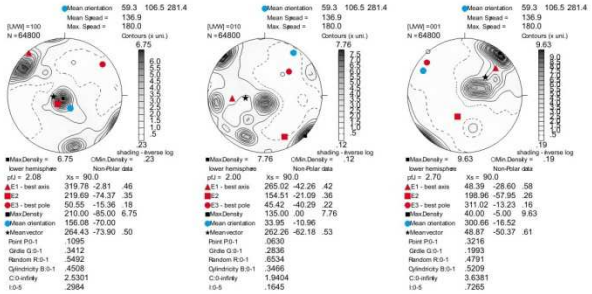

Opx

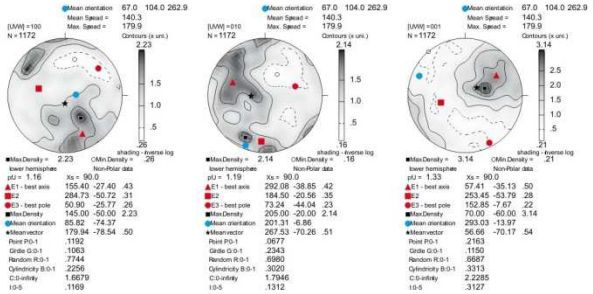

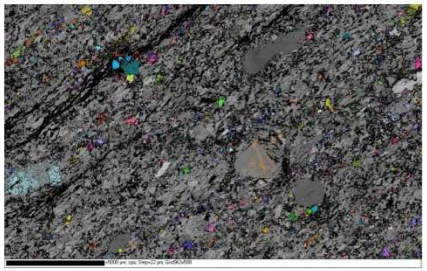

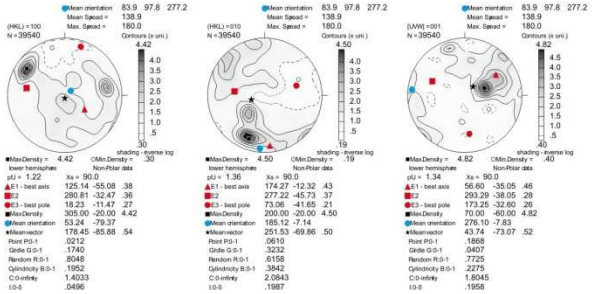

Cpx

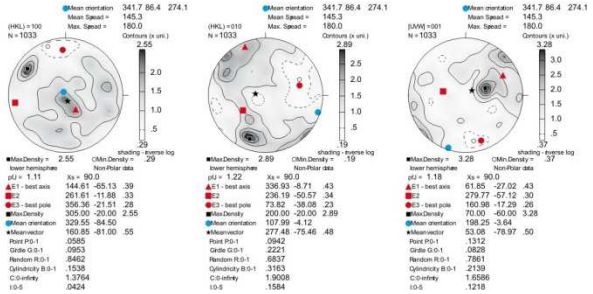

Geographic coordinates (1 point per grain)

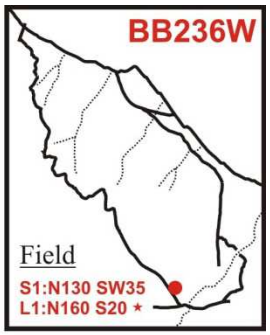

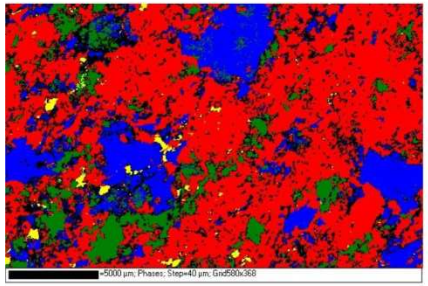

step=40µm

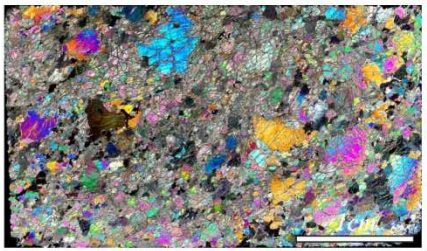

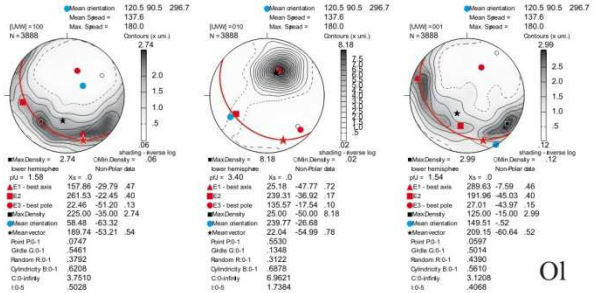

Ol

Sample coordinates (raw data)

Sample coordinates (1 point per grain)

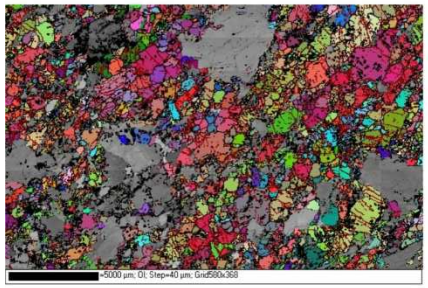

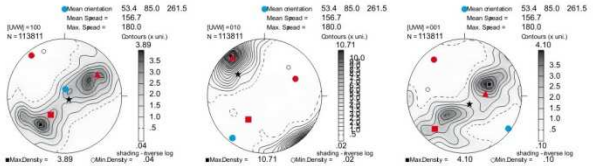

Ol

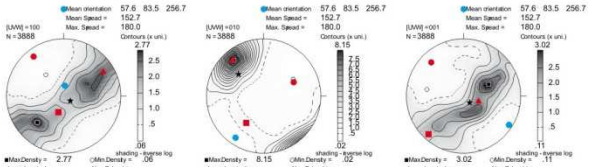

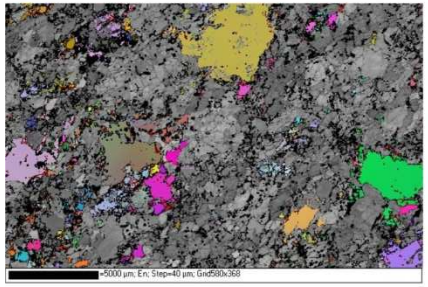

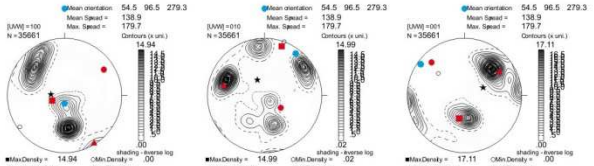

Opx

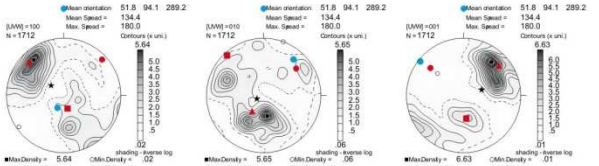

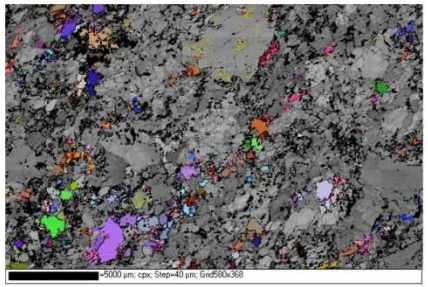

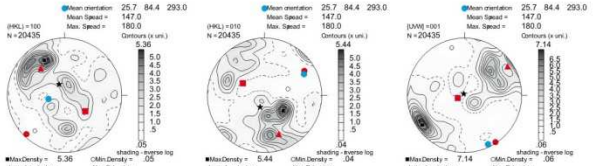

Cpx

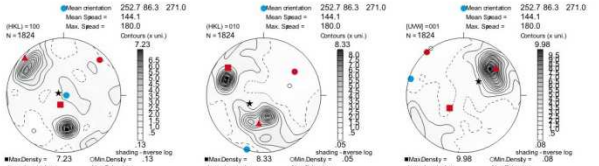

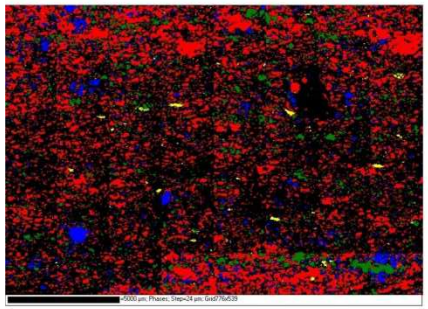

step=24µm

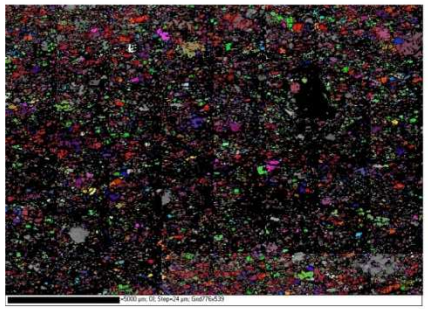

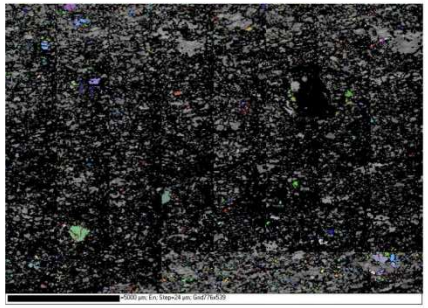

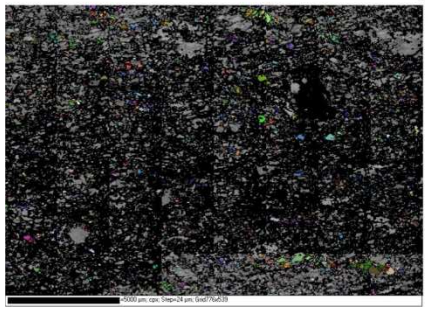

Geographic coordinates (1 point per grain)

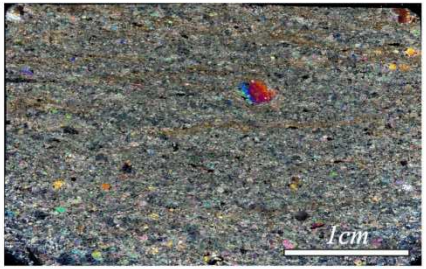

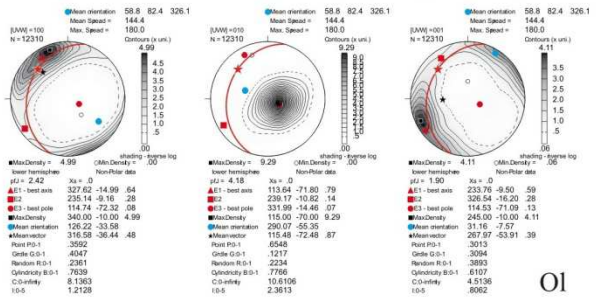

Ol

Sample coordinates (raw data)

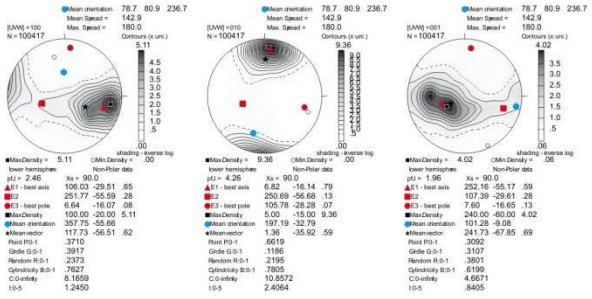

Ol

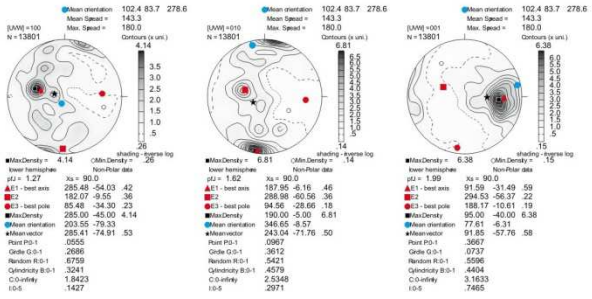

Opx

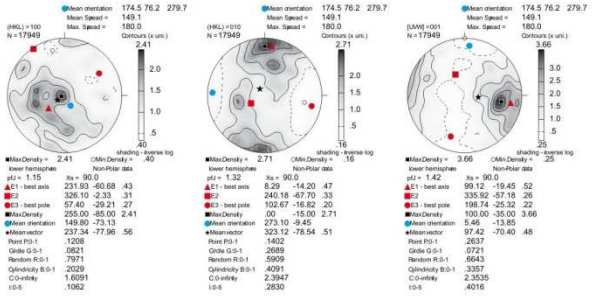

Cpx

Sample coordinates (1 point per grain)

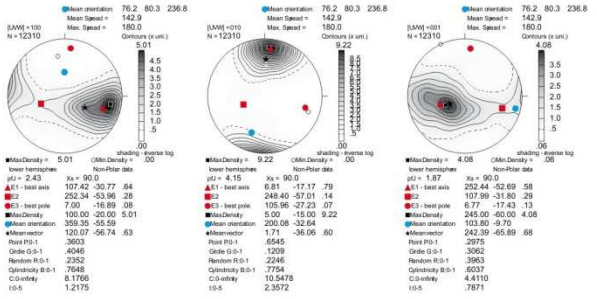

Ol

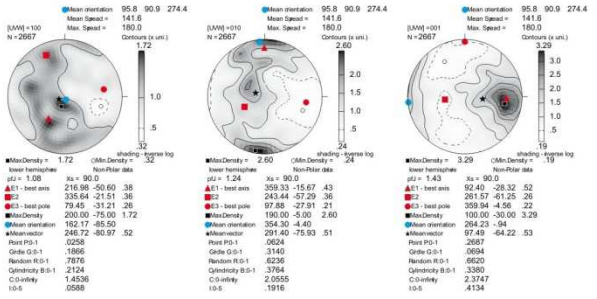

Opx

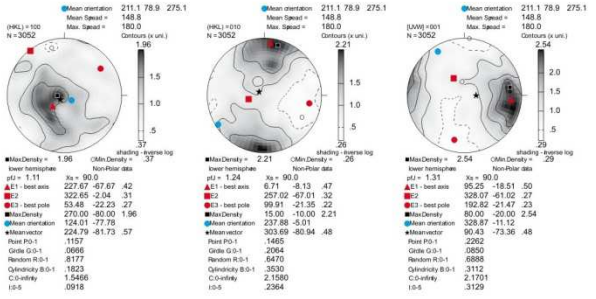

Cpx

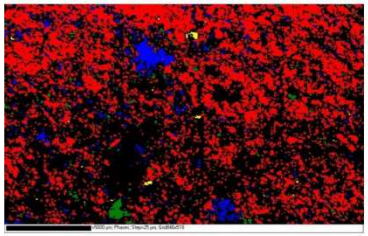

step=25µm

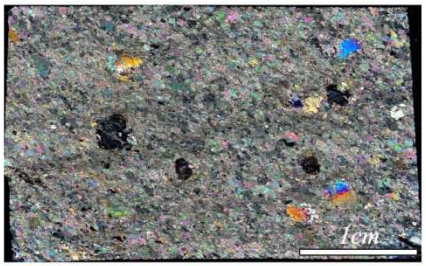

Geographic coordinates (1 point per grain)

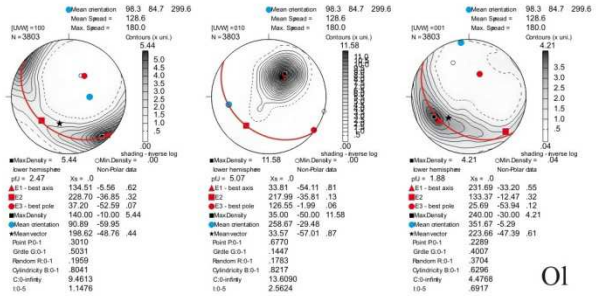

Ol

Sample coordinates (raw data)

Sample coordinates (1 point per grain)

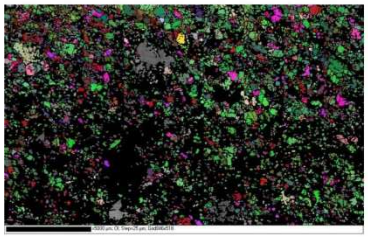

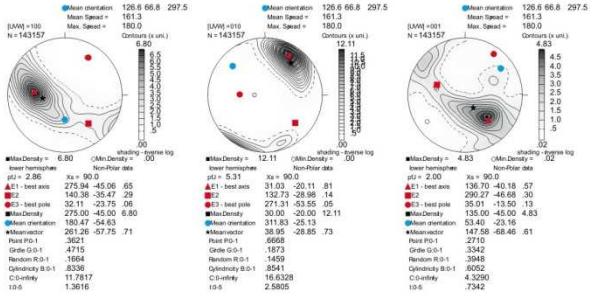

Ol

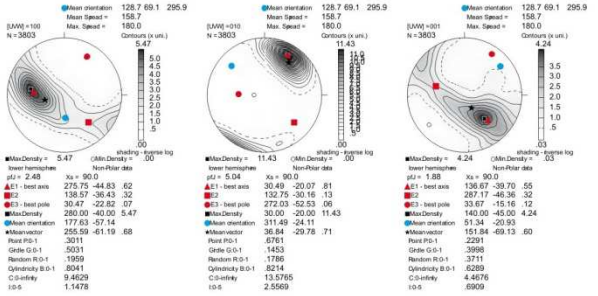

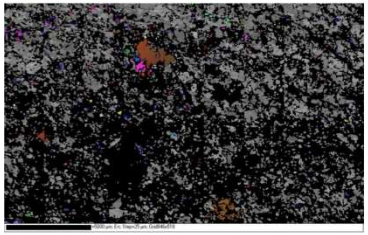

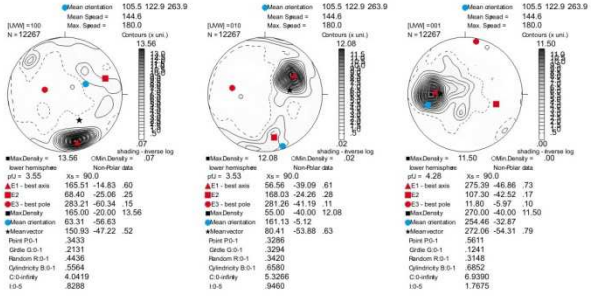

Opx

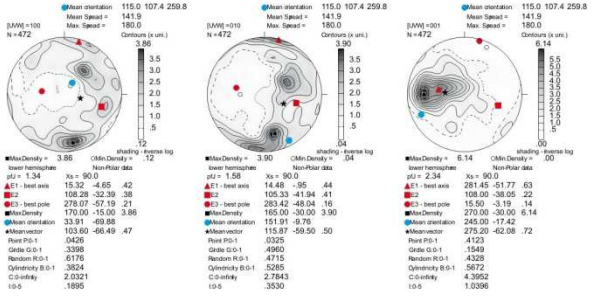

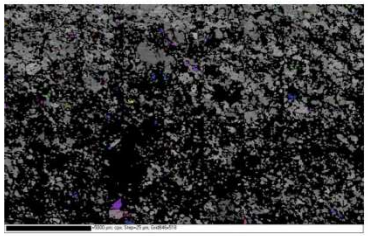

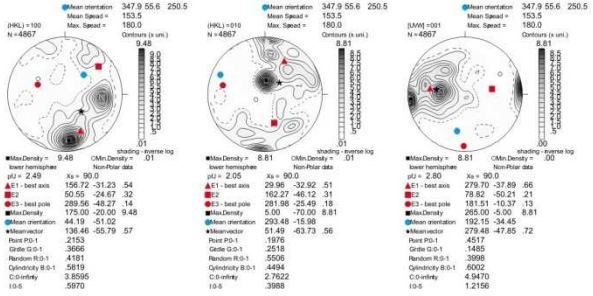

Cpx

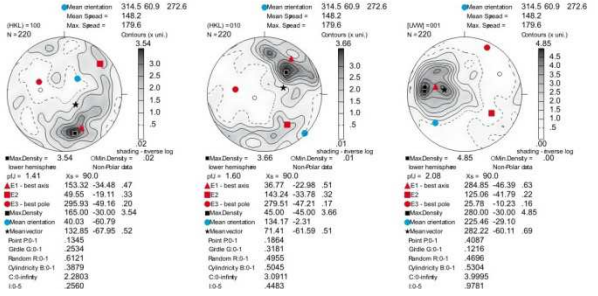

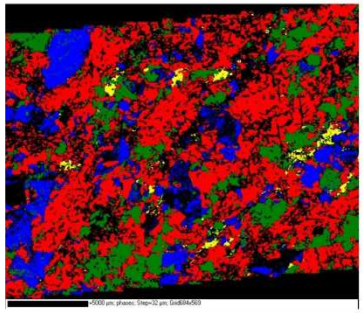

step=32µm

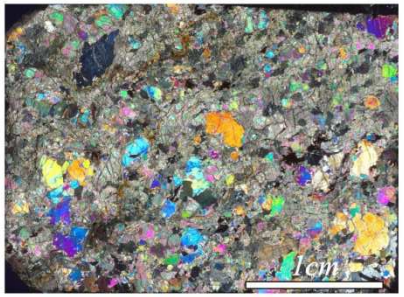

Geographic coordinates (1 point per grain)

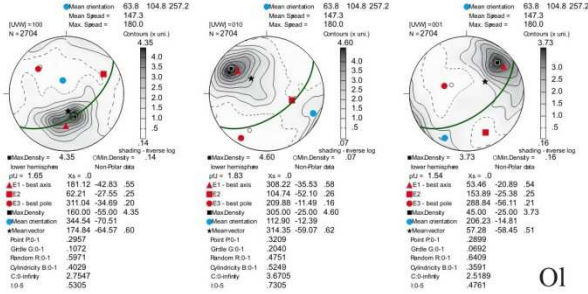

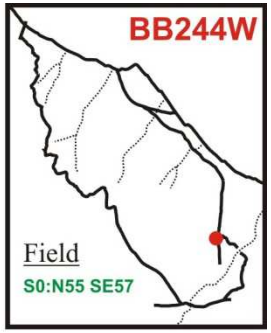

Ol

Sample coordinates (raw data)

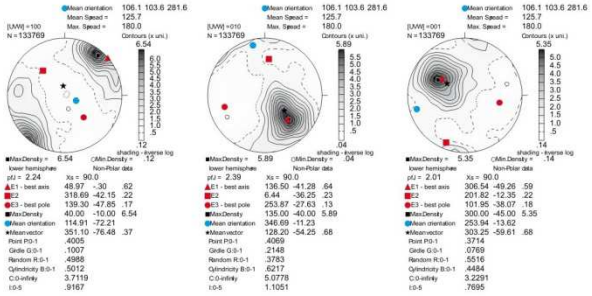

Ol

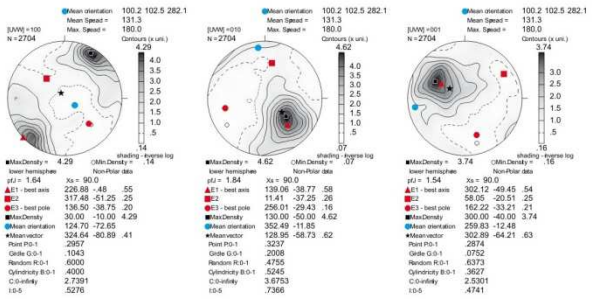

Sample coordinates (1 point per grain)

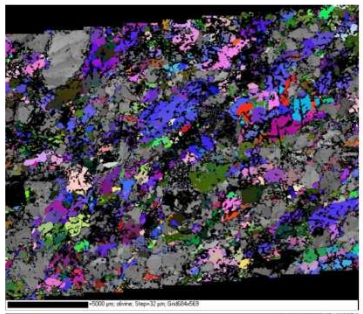

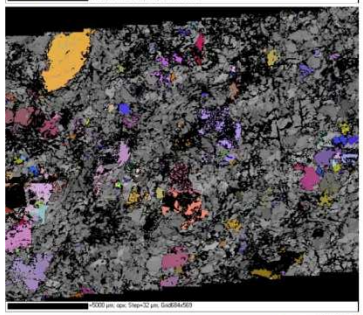

Opx

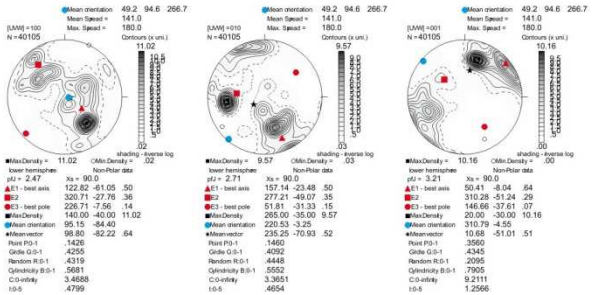

Opx

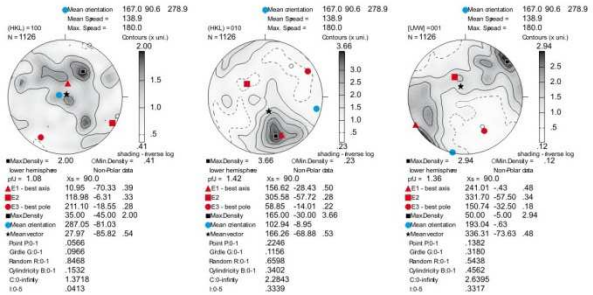

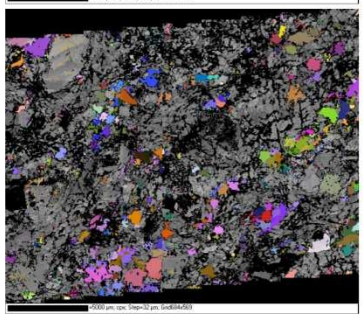

Cpx

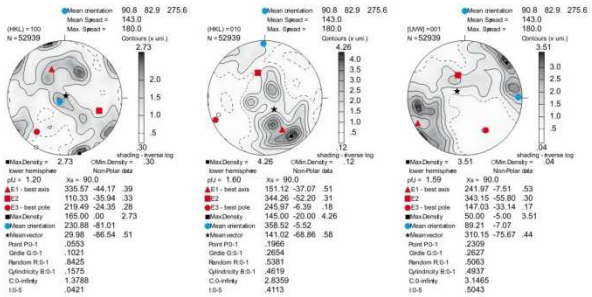

Cpx

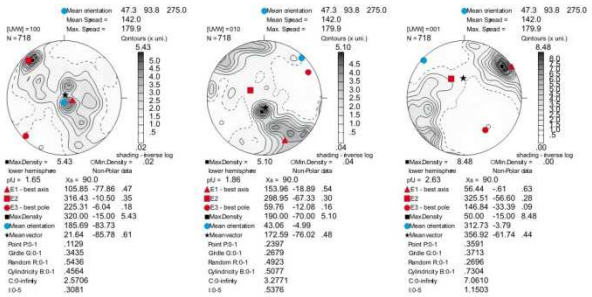

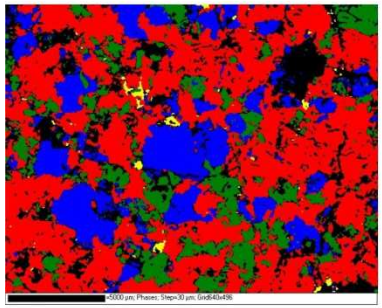

step=30μm

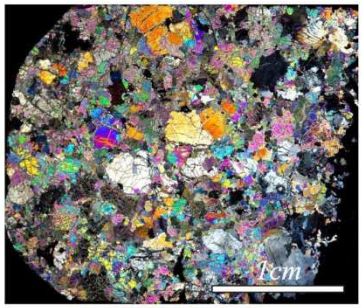

Geographic coordinates (1 point per grain)

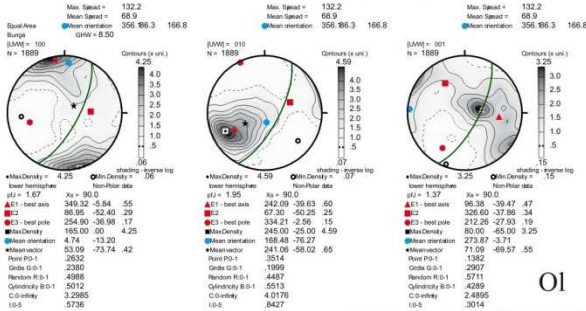

Ol

Sample coordinates (raw data)

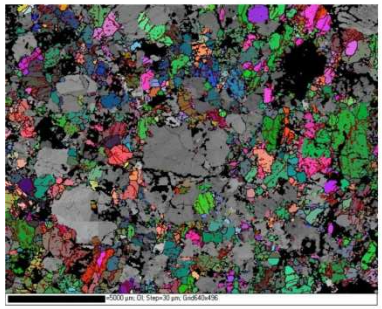

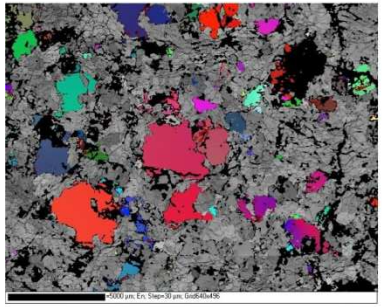

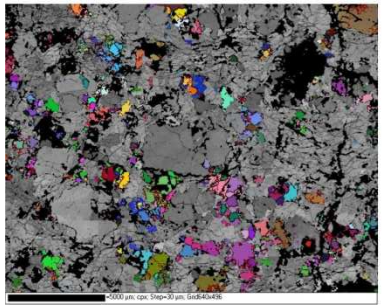

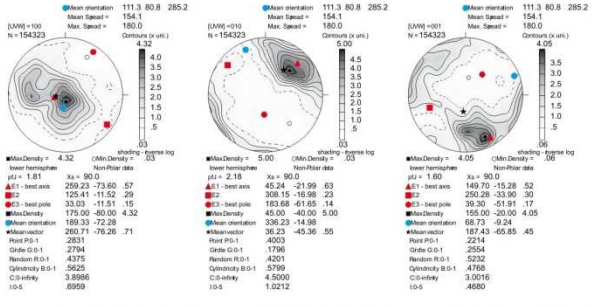

Ol

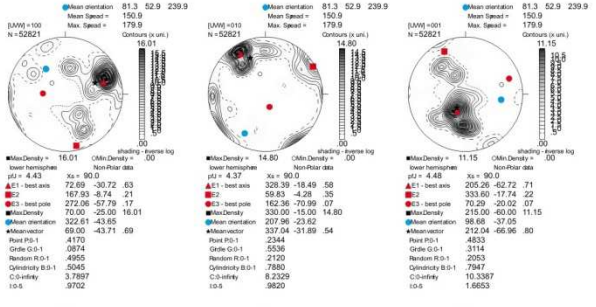

Opx

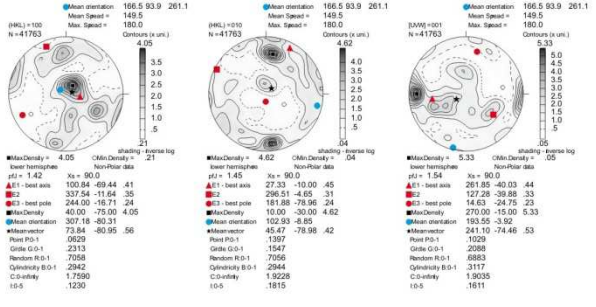

Cpx

Sample coordinates (1 point per grain)

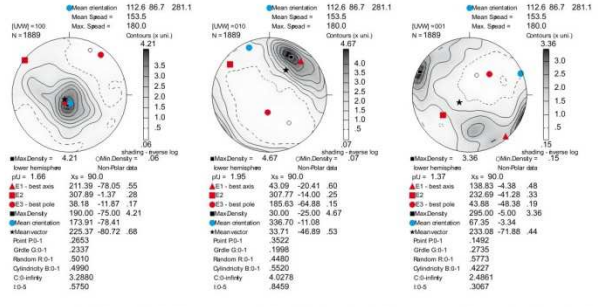

Ol

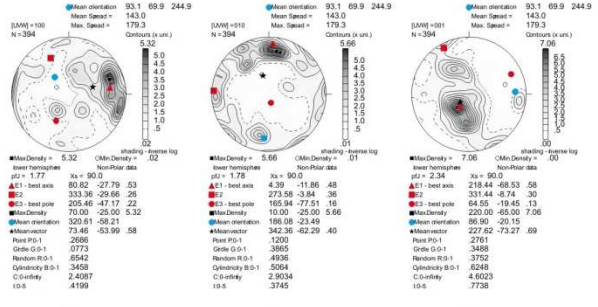

Opx

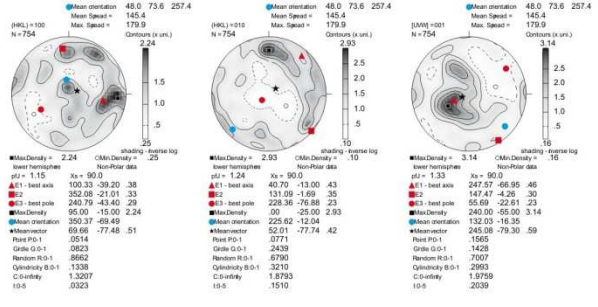

Cpx

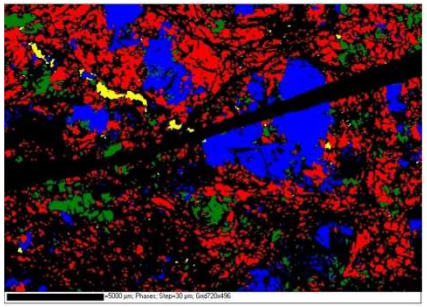

step=30μm

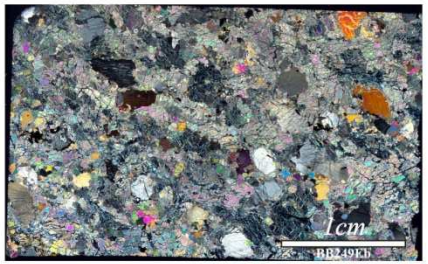

Geographic coordinates (1 point per grain)

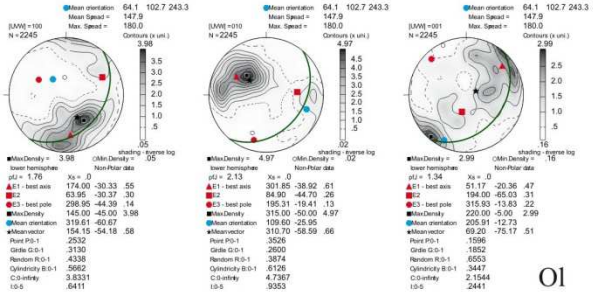

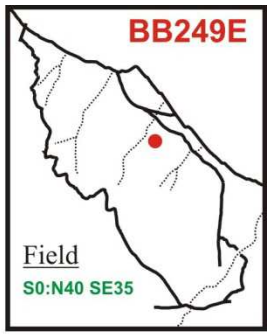

Ol

Sample coordinates (raw data)

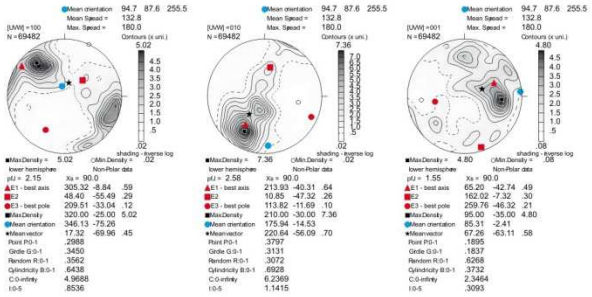

Ol

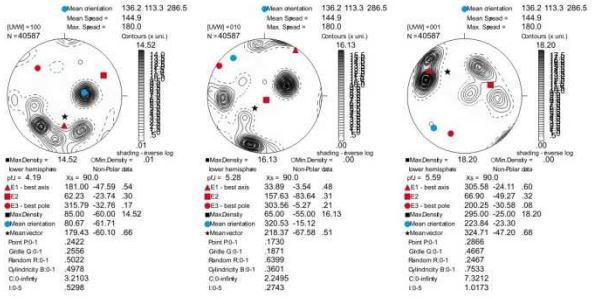

Opx

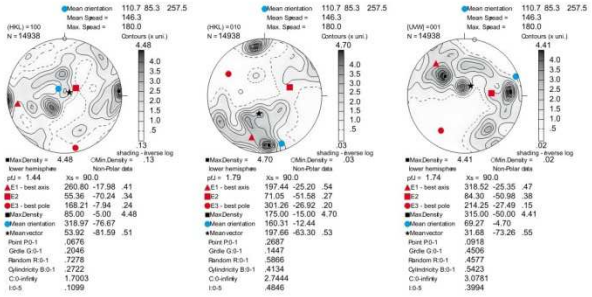

Cpx

Sample coordinates (1 point per grain)

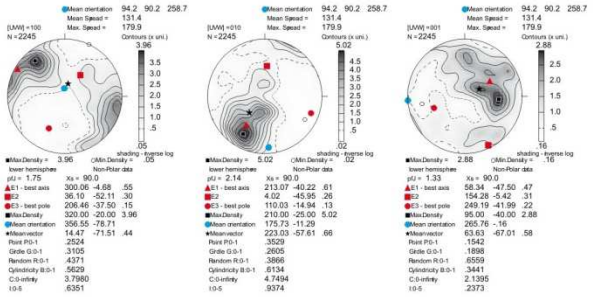

Ol

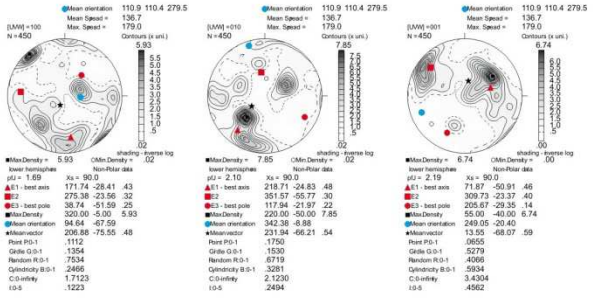

Opx

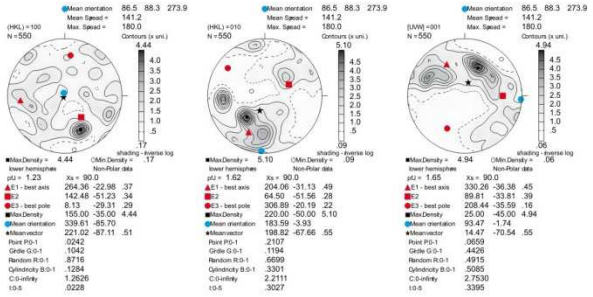

Cpx

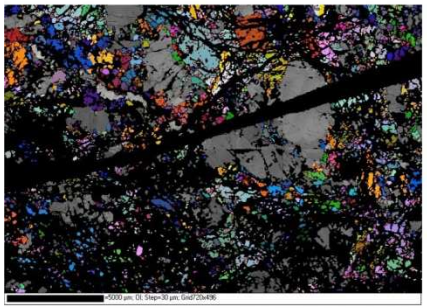

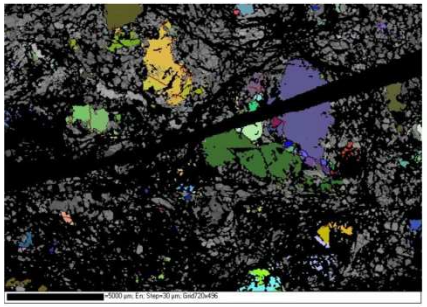

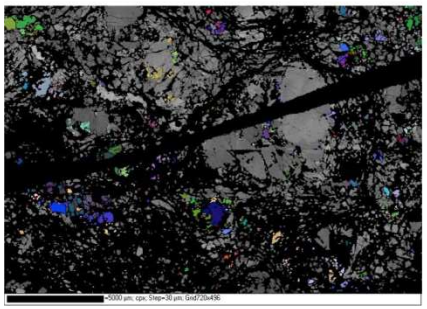

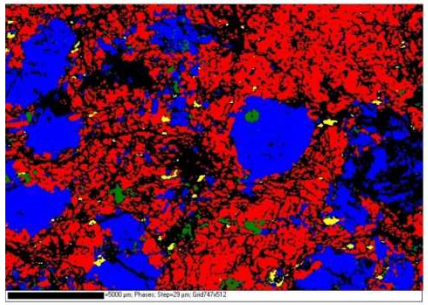

step=29µm

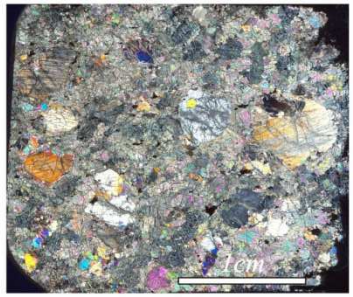

Geographic coordinates (1 point per grain)

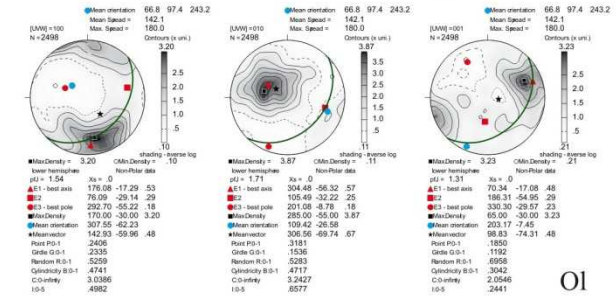

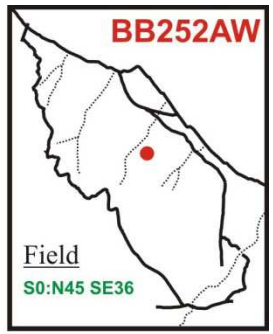

Ol

Sample coordinates (raw data)

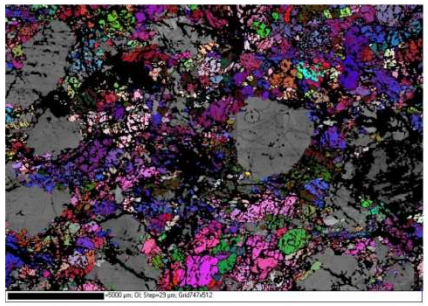

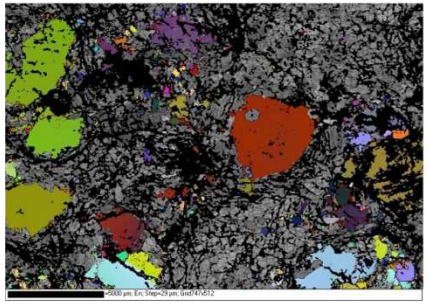

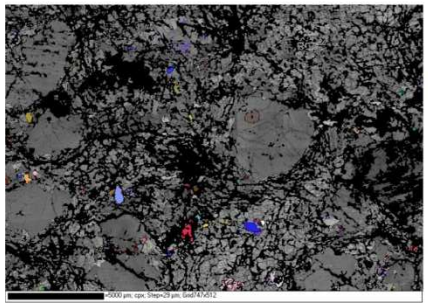

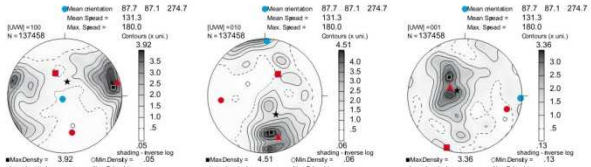

Ol

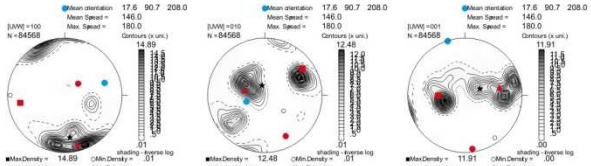

Opx

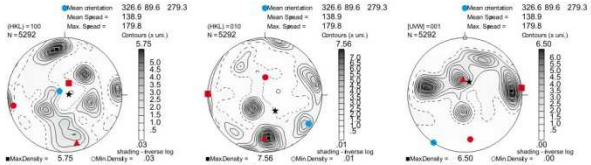

Cpx

Sample coordinates (1 point per grain)

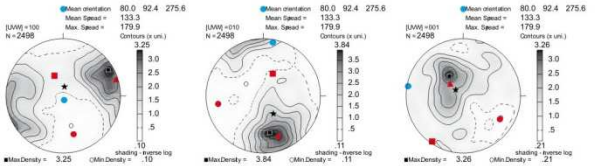

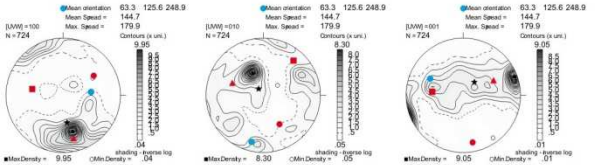

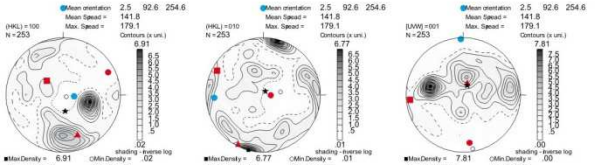

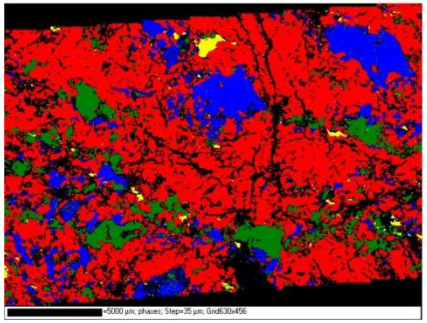

step=35µm

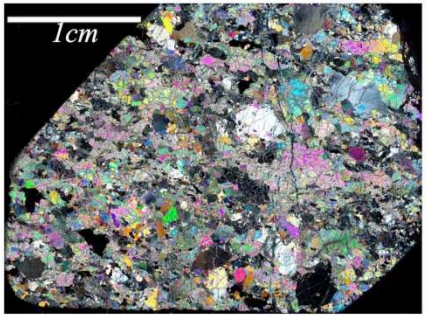

Geographic coordinates (1 point per grain)

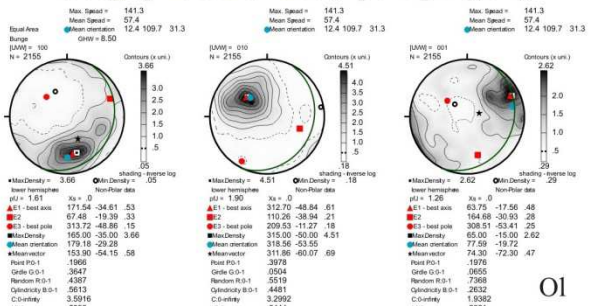

Ol

Sample coordinates (raw data)

Sample coordinates (1 point per grain)

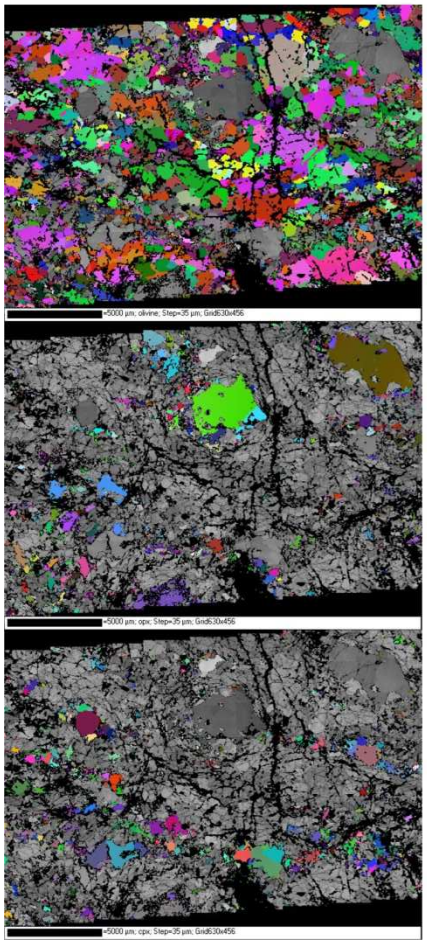

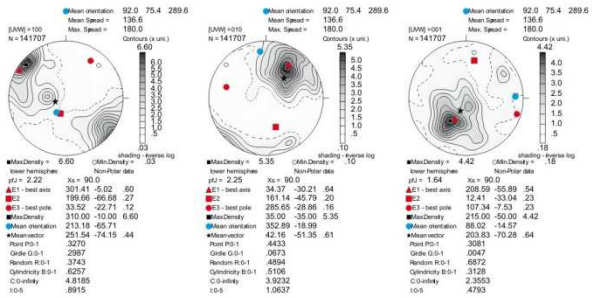

Ol

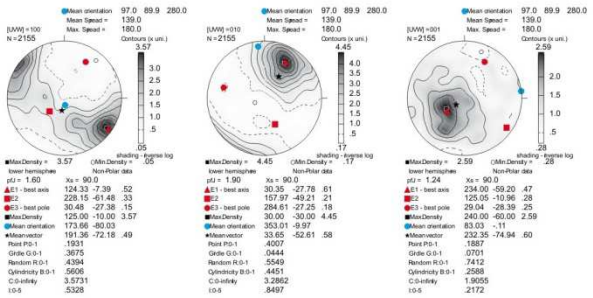

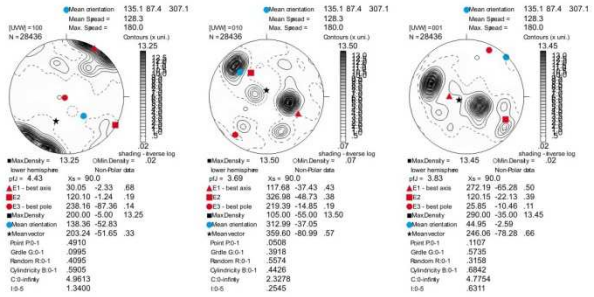

Opx

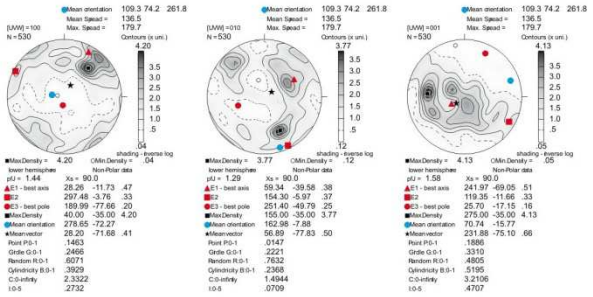

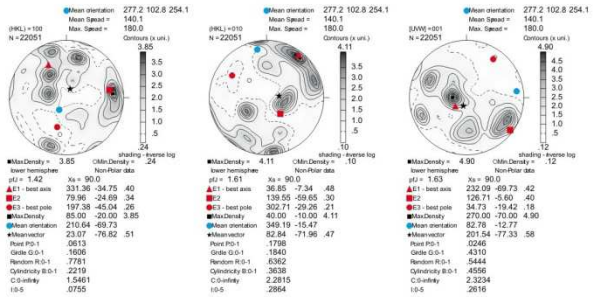

Cpx

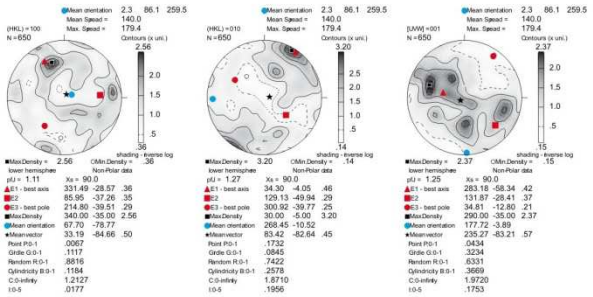

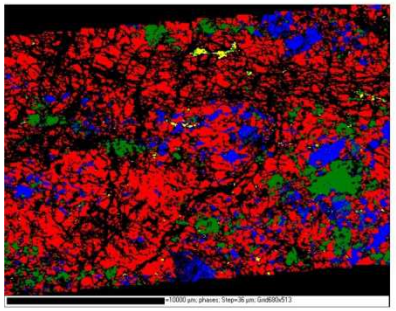

step=36µm

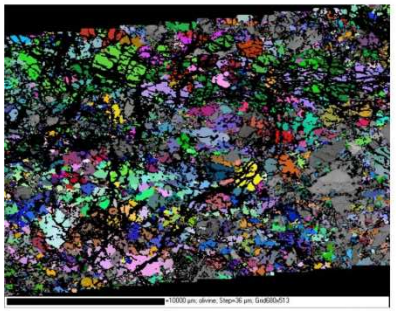

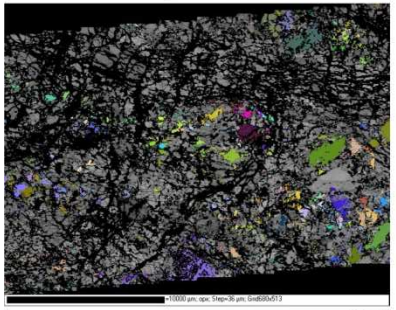

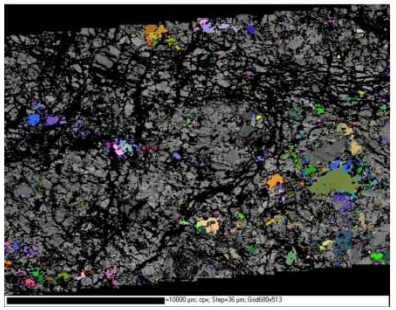

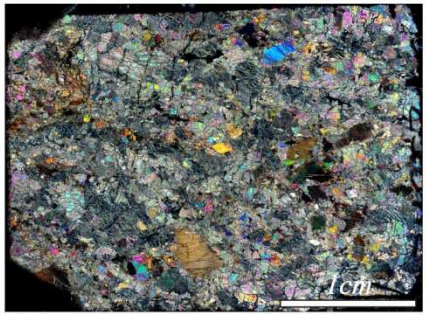

Geographic coordinates (1 point per grain)

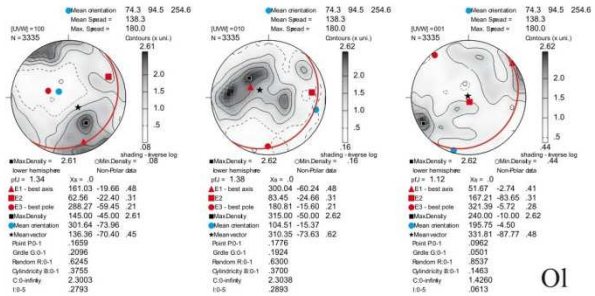

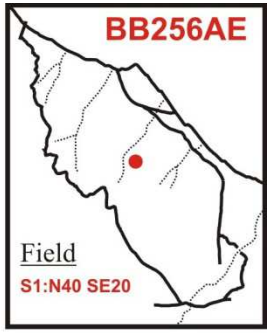

Ol

Sample coordinates (raw data)

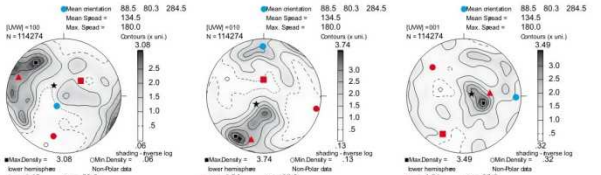

Ol

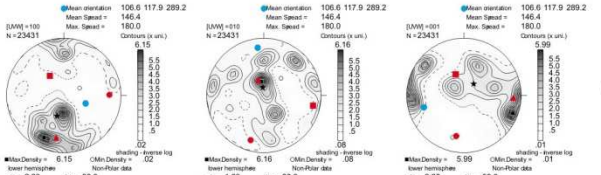

Opx

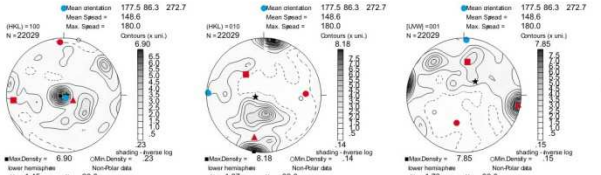

Cpx

Sample coordinates (1 point per grain)

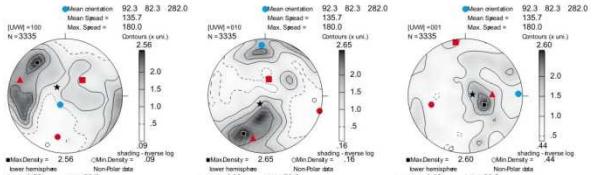

Ol

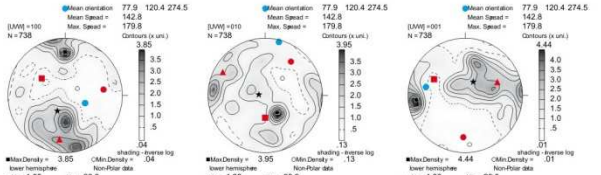

Opx

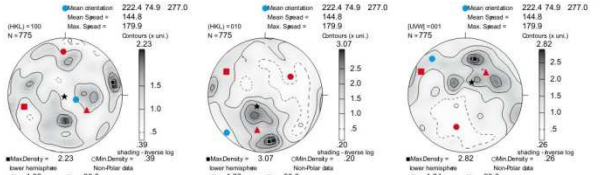

Cpx

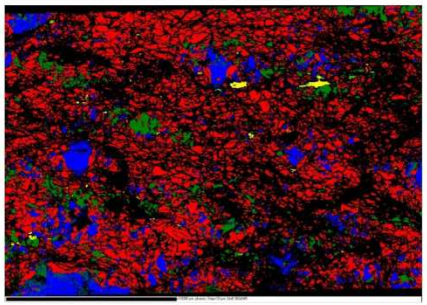

step=18µm

Geographic coordinates (1 point per grain)

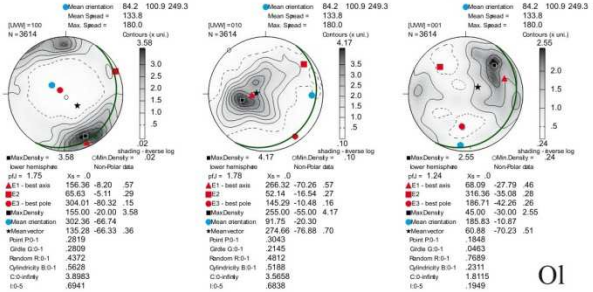

Ol

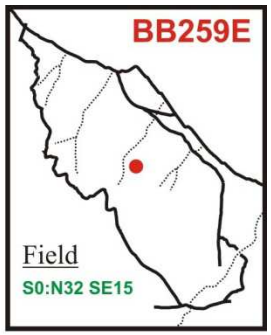

Sample coordinates (raw data)

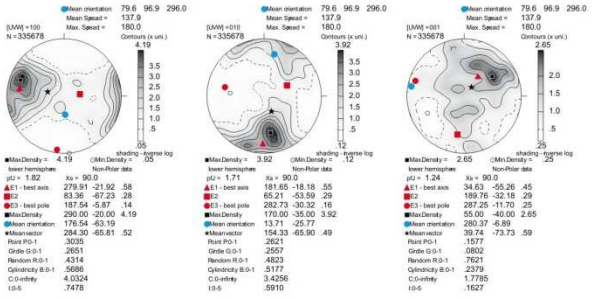

Ol

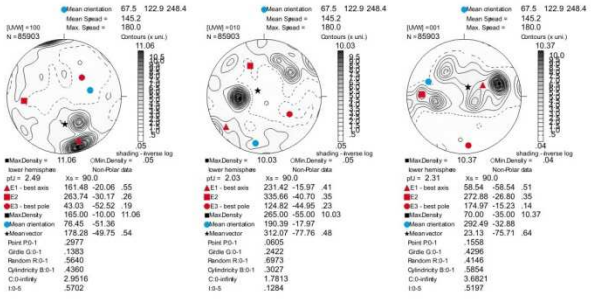

Opx

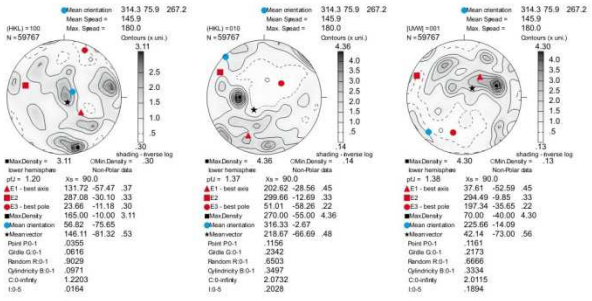

Cpx

Sample coordinates (1 point per grain)

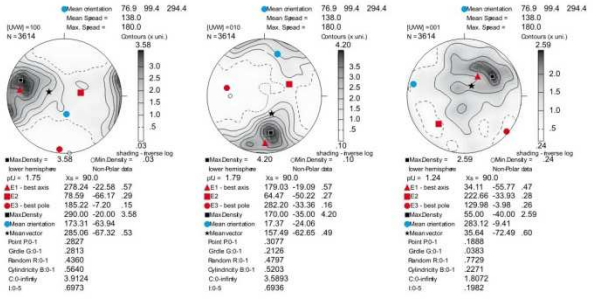

Ol

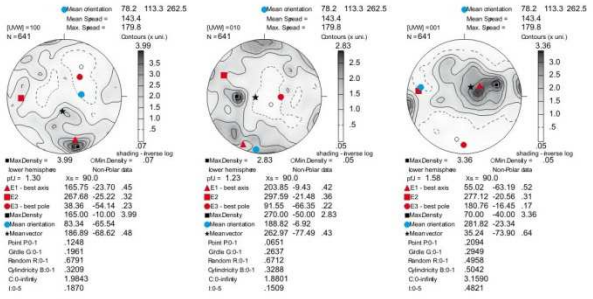

Opx

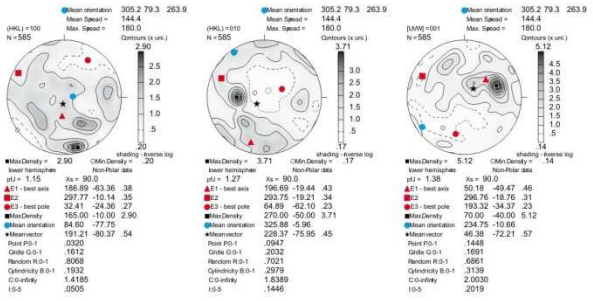

Cpx

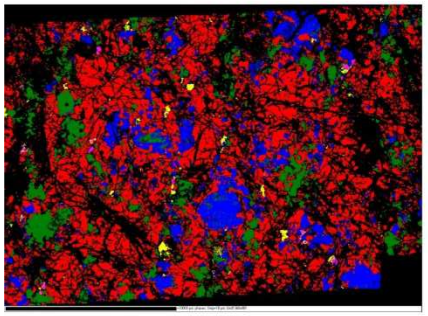

step=18µm

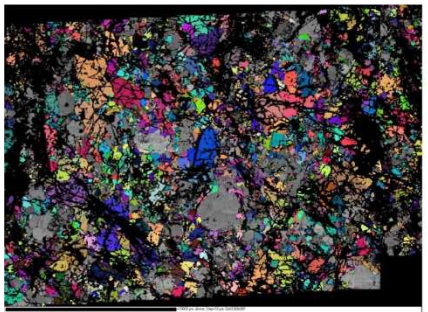

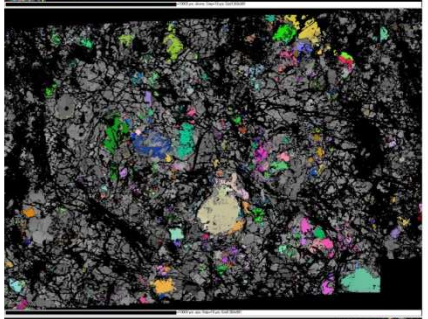

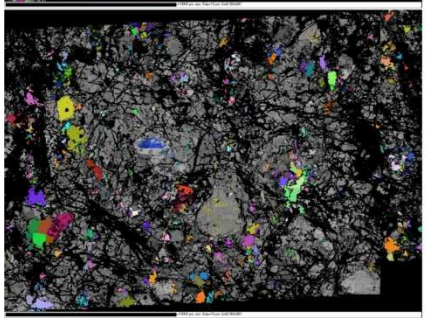

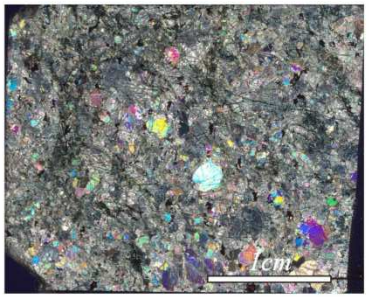

Geographic coordinates (1 point per grain)

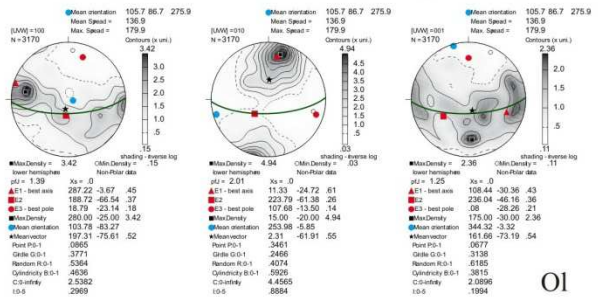

Ol

Sample coordinates (raw data)

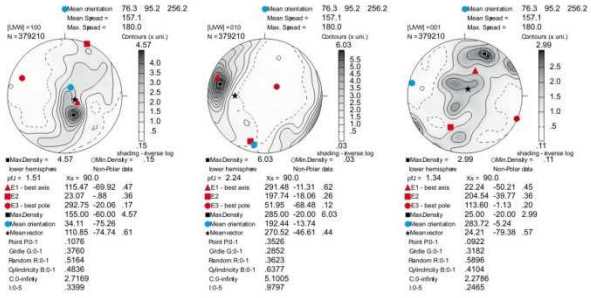

Ol

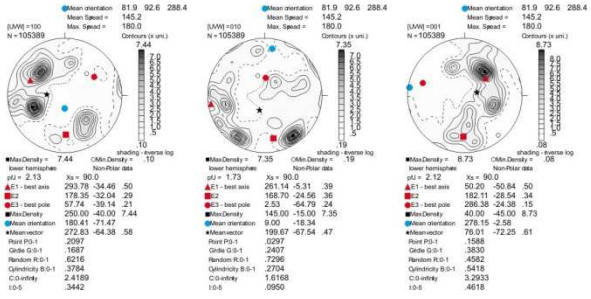

Opx

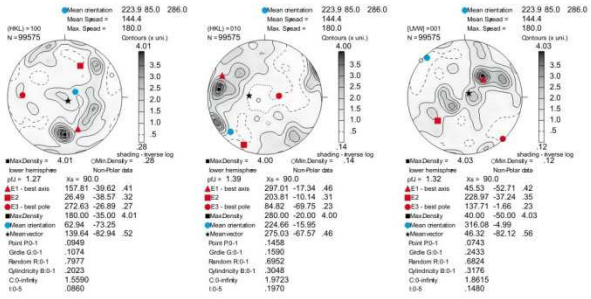

Cpx

Sample coordinates (1 point per grain)

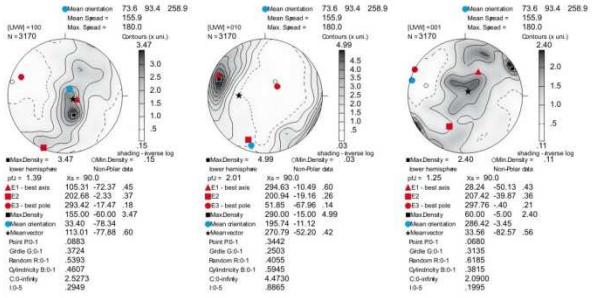

Ol

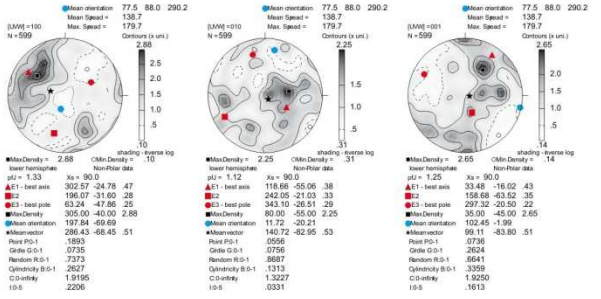

Opx

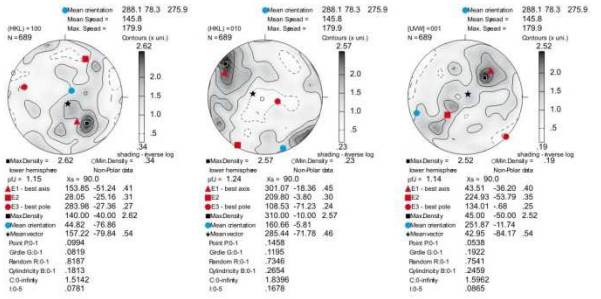

Cpx

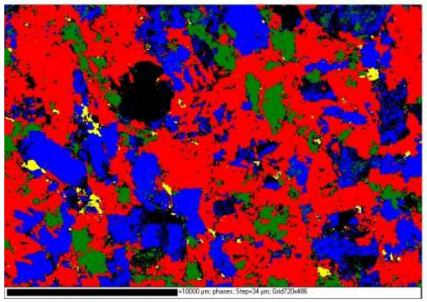

step=34µm

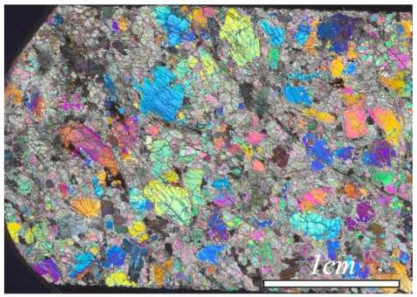

Geographic coordinates (1 point per grain)

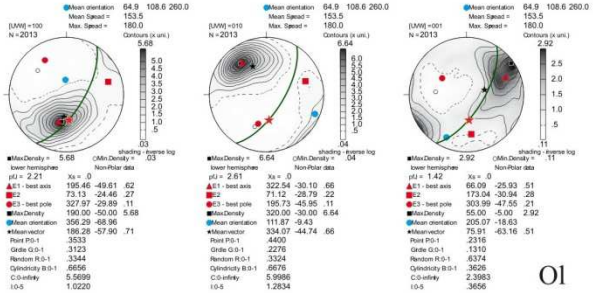

Ol

Sample coordinates (raw data)

Sample coordinates (1 point per grain)

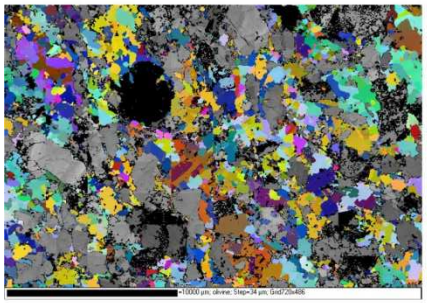

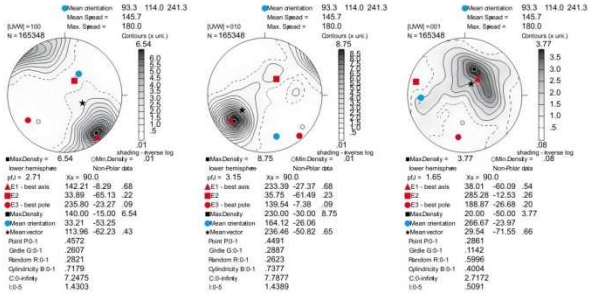

Ol

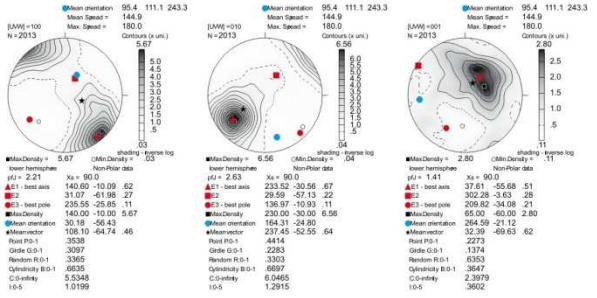

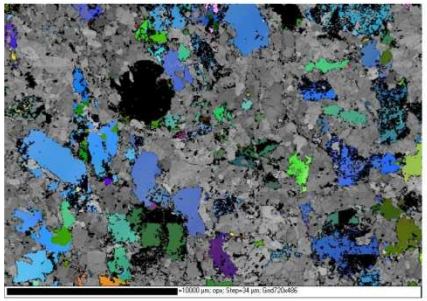

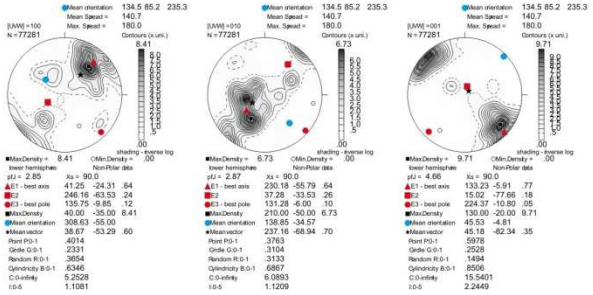

Opx

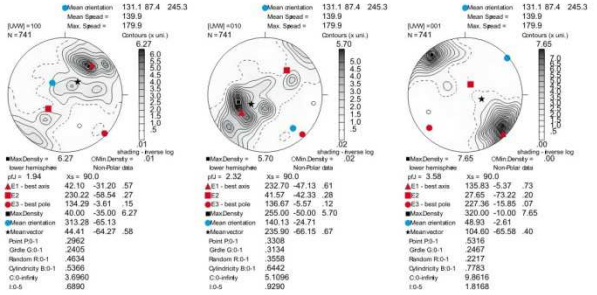

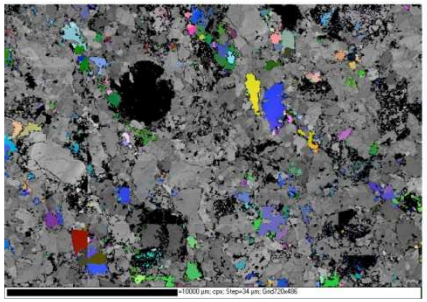

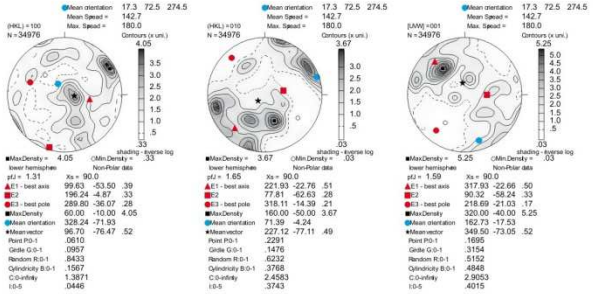

Cpx

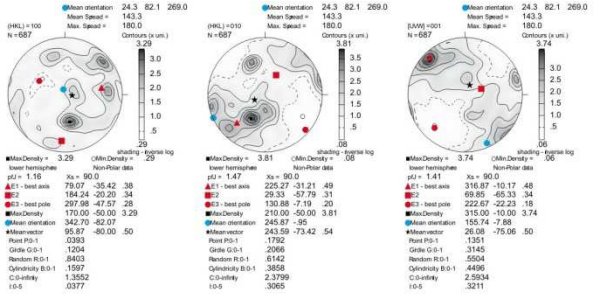

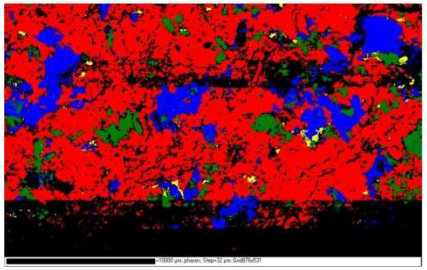

step=32µm

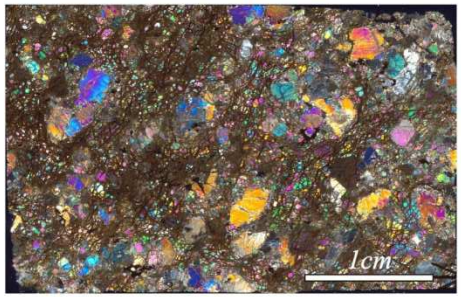

Geographic coordinates (1 point per grain)

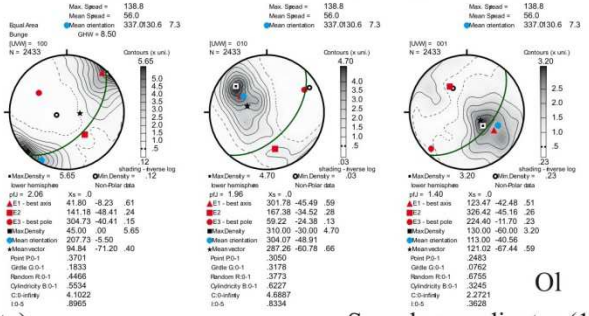

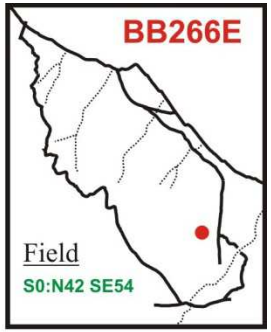

Ol

Sample coordinates (raw data)

Sample coordinates (1 point per grain)

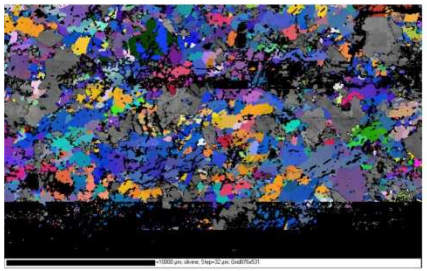

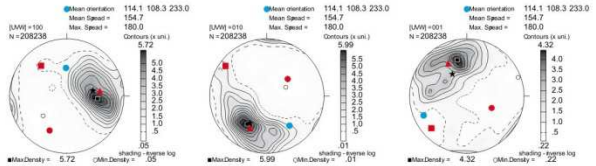

Ol

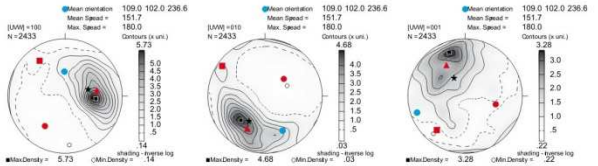

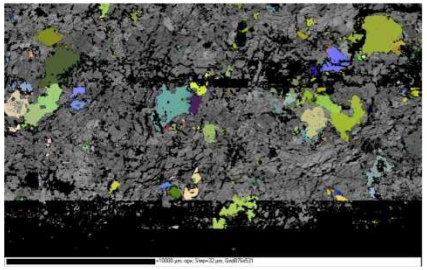

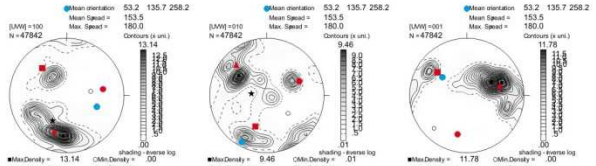

Opx

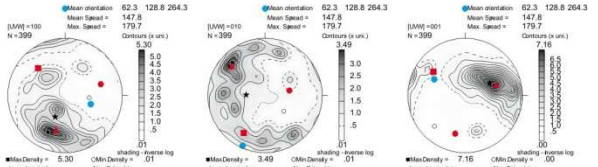

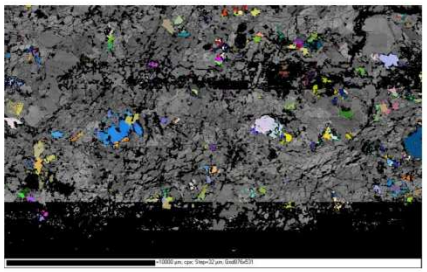

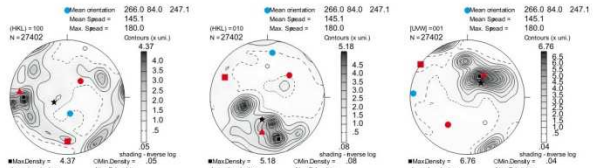

Cpx

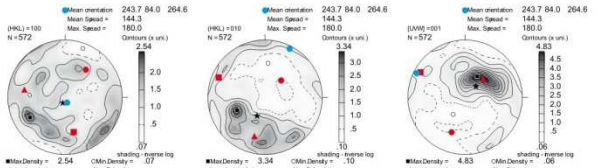

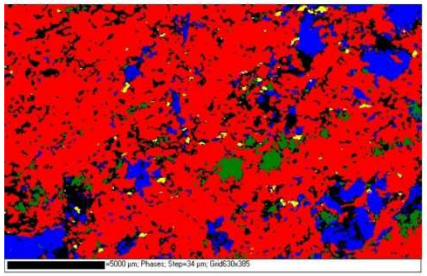

step=34µm

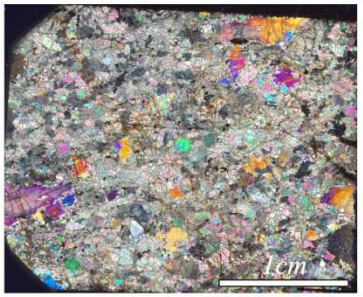

Geographic coordinates (1 point per grain)

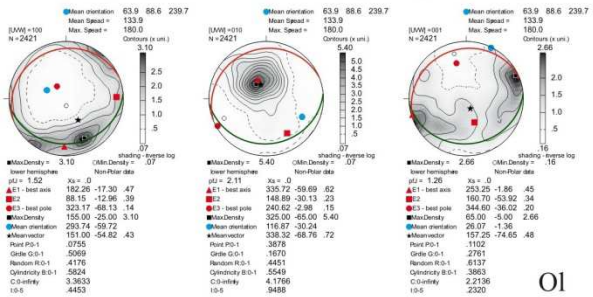

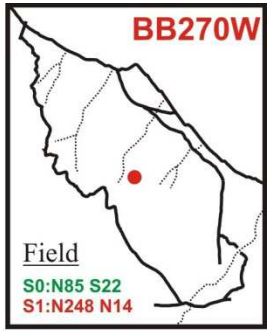

Ol

Sample coordinates (raw data)

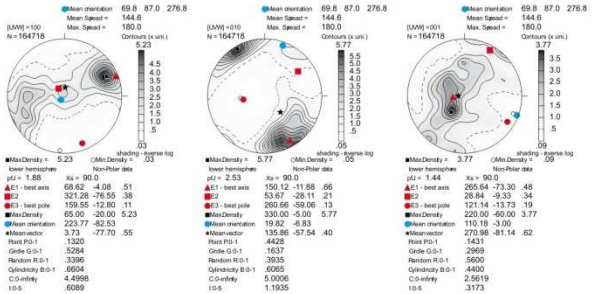

Sample coordinates (1 point per grain)

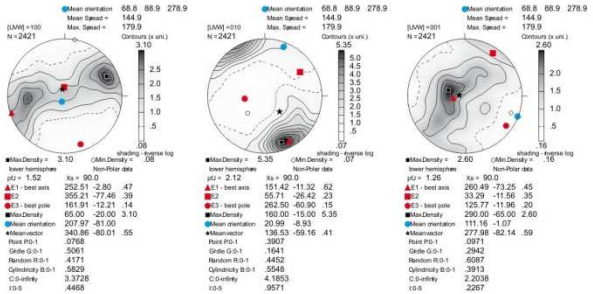

Ol

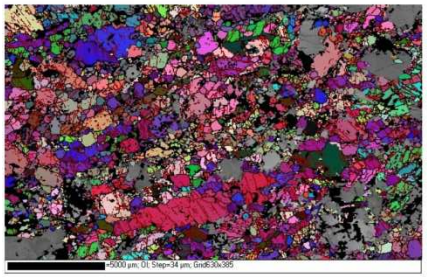

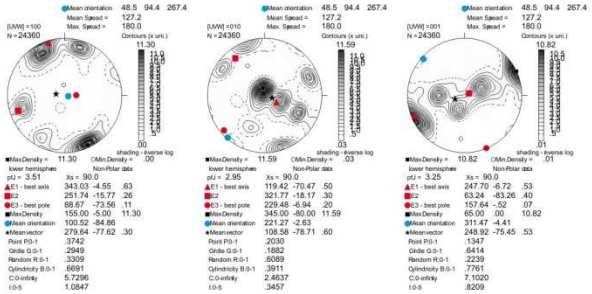

Opx

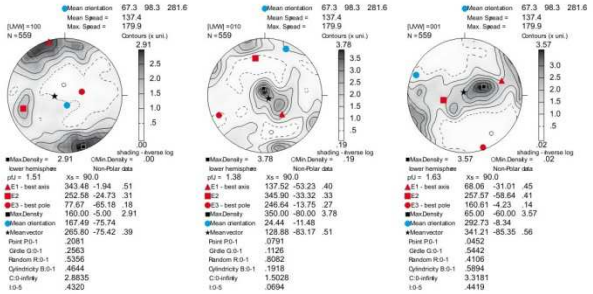

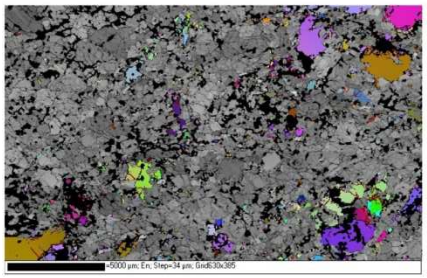

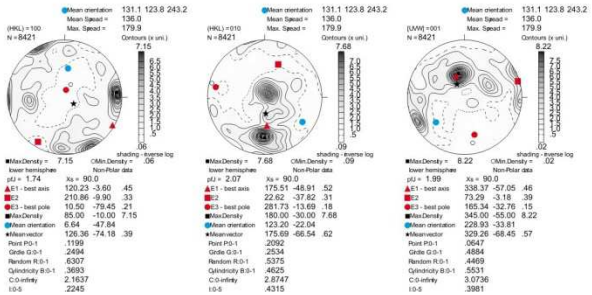

Cpx

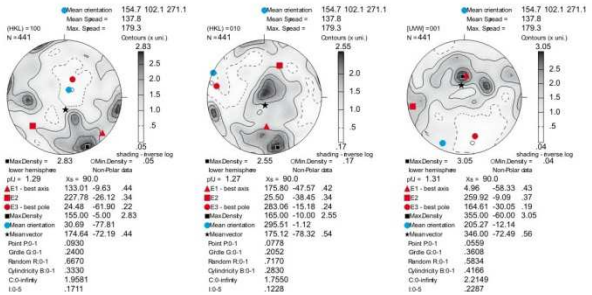

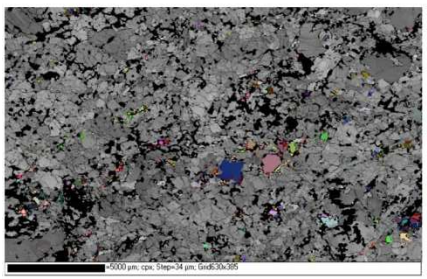

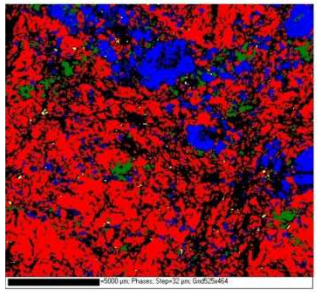

step=32μm

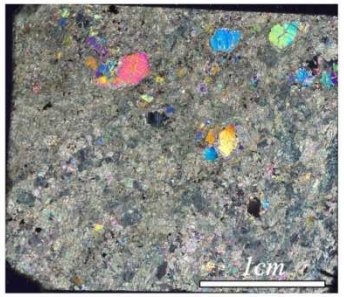

Geographic coordinates (1 point per grain)

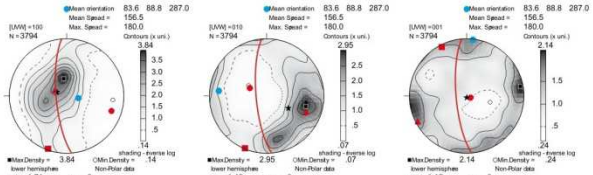

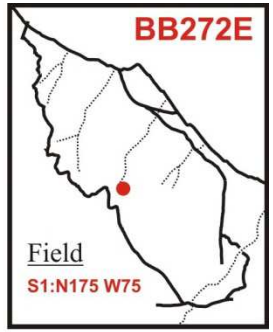

Ol

Sample coordinates (raw data)

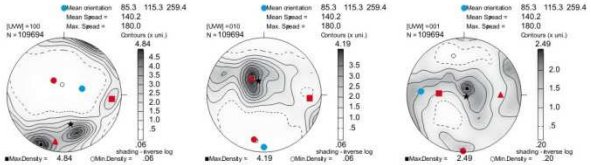

Sample coordinates (1 point per grain)

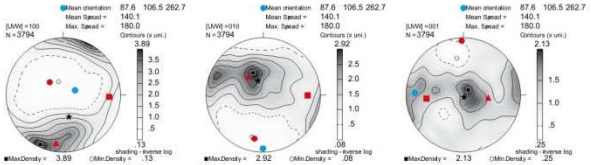

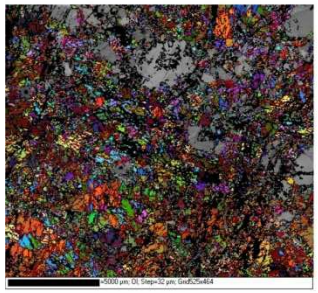

Ol

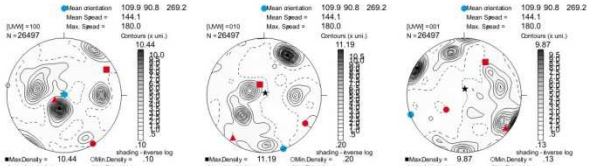

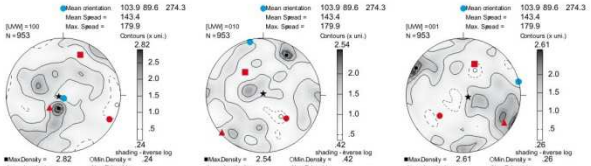

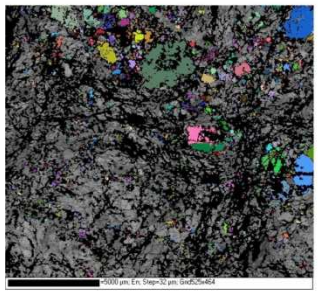

Opx

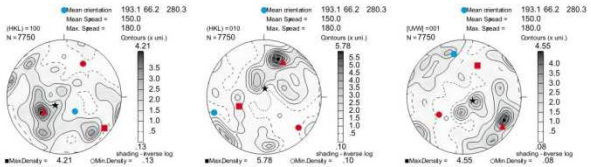

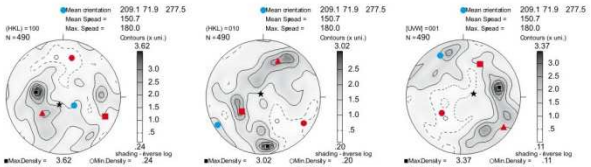

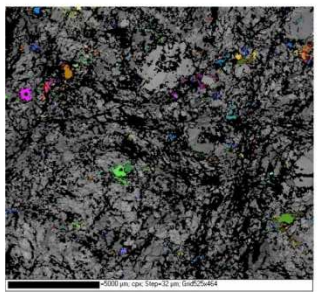

Cpx

The mantle deformation processes that control the thinning and break-up of continental lithosphere remain poorly understood. Our knowledge is restricted to either lithospheric scale thermo-mechanical models —that use experimentally derived flow laws—, geophysical imaging and/or rare xenoliths from active continental rifts, such as the East African Rift System. The originality of this work relies on the study of the two largest outcrops of diamond facies subcontinental lithospheric mantle in the world: the Beni Bousera and Ronda peridotite massifs in N Morocco and S Spain, respectively. The structures and petrologic and metamorphic zoning preserved in these massifs —implying a polybaric and polythermal evolution— provide a unique opportunity to investigate the thermo-mechanical evolution of thick subcontinental lithospheric mantle in extensional settings.

In this thesis we studied the deformation mechanisms in both peridotites and pyroxenites to constrain the modes of exhumation of subcontinental lithospheric mantle from garnet-, to spinel-, and finally, to plagioclase lherzolite facies conditions. We combined field mapping of tectono-metamorphic domains and structural mapping of ductile structures, microstructural analysis, crystal preferred orientations (CPO) measurements and conventional thermobarometric calculations and thermodynamic modeling (Perple_X) to unravel the pressure and temperature conditions of deformation. We showed that exhumation from garnet- to spinel lherzolite facies conditions was accommodated by fast shearing —in thermal disequilibrium— along a lithospheric scale transtensional shear zone. In this context, the petrological zoning and the large temperature gradient (ca. 100ºC/km) preserved in the Beni Bousera massif represent the mechanical juxtaposition of progressively deeper and hotter lithospheric levels at depths of ca. 60 km in the latest Oligocene (ca. 25 Ma). Final exhumation from spinel- to plagioclase facies lherzolite and emplacement into the crust is best recorded in the Ronda massif where it occurred by inversion and lithospheric scale folding of the highly attenuated continental lithosphere in a back-arc region, probably in relation with southward slab rollback and subsequent collision with the palaeo-Maghrebien passive margin in the early Miocene (21-23 Ma).

ugr Universidad de Granada
CSIC Consejo Superior de Investigaciones Científicas
UM2 Université Montpellier 2 Sciences et Techniques